*2017 IEEE International Conference on Telecommunications and Photonics (ICTP)*
*26-28 December, 2017, Dhaka, Bangladesh*



# Effect of Core Infiltration in the Birefringence of Photonic Crystal Fiber

Saleha Fatema†, Rubaya Absar†, Mohammad Istiaque Reja, and Aobaida Akhtar*

Department of Electrical and Electrical Engineering, Chittagong University of Engineering and Technology Chittagong-4349, Bangladesh

† Two first author made equal contribution

*lilyjobaida@cuet.ac.bd

***Abstract*—The effect of core infiltration in the birefringence of Photonic Crystal Fiber (PCF) is investigated. An elliptical soft glass rod infiltration is introduced in the core region of the fiber as it provides greater refractive index contrast between the core and the cladding. This modification also creates asymmetry in the core of the fiber which results in a resilient birefringence. Four structures (Hexagonal, Octagonal, Decagonal and Elliptical) are investigated and a comparative study is made to observe the change in birefringence due to the infiltration. It is observed that, by introducing this infiltration the birefringence is improved up to the order of $10^{-1}$. The birefringence is increased $4.82 \times 10^6$ times in the hexagonal PCF, $5.38 \times 10^5$ times in octagonal PCF, 546 times in decagonal PCF and about 8 times in the elliptical PCF at operating wavelength due to the core infiltration. The numerical investigation of the structure is conducted using full vector finite element method. The fabrication imperfection possibility is considered by analyzing $\pm 2\%$ tolerance in fiber dimension.**

***Index Terms*—Photonic crystal fiber; Core infiltration; Birefringence; Refractive index contrast; Full vector finite element method;**

## I. Introduction

Photonic Crystal Fiber, aims to address the challenge of higher channel capacity with increased data rate [1], has developed into being a well established area of research and commercialization. The main reason behind its growth is its ability to provide extra degrees of freedom in manipulating the optical properties of fiber such as high birefringence [2], ultra flattened dispersion [3], high nonlinearity [4], low confinement loss [5], endlessly single mode [6]. This is achieved by adjusting its structural parameters like pitch ($\Lambda$), air hole diameter (d) and shape, air filling ratio (d/$\Lambda$). This control over the optical properties of the fiber allows it to use in a wide range of application [7] instead of being limited to optical communication. One of the major fields of application is its uses as polarization maintaining fiber.

Polarization maintaining (PM) fibers play a very important role in high bit-rate optical transmission [8], fiber optic sensing [9], interferometry [10] and quantum key distribution systems [11]. It is also used in telecommunications for the connection between a source laser and a modulator [12]. Recently, PANDA (Polarization Maintaining and Absorption Reducing Fibers) [13], bow-tie [14] and elliptical jacket fibers [15] are used for polarization maintaining applications. These fibers operate by applying stress in the core region. Their modal birefringence is due to stress in the core region is up to $5 \times 10^{-4}$ [16]. These stresses impose unpredictable and uncontrolled birefringence on the fiber [17]. On the other hand, a controllable birefringence can be obtained by using polarization maintaining photonic crystal fibers [18].

To improve this highly growing technology, researchers are now introducing newer concepts in the design of photonic crystal fibers like creating various defects in the core or cladding , use of liquid or gaseous materials and materials with greater refractive index or lower refractive index than silica in the core or cladding respectively. In this article, we have modified the typical photonic crystal fibers with an elliptical soft glass rod in the core region. The material of this elliptical glad rod is selected as SF57 as it has greater refractive index than silica which provides a greater index contrast between the core and the cladding resulting in asymmetry in the core and cladding and thus the birefringence is increased significantly.

## II. Design and theory

An elliptical soft glass (SF57) rod is proposed in the core of four typical structures of PCF with circular air holes in the cladding. The cladding assembles multiple air hole rings. The background material is fused silica. For hexagonal structured PCF, the air hole diameters of $1^{st}$, $2^{nd}$, $3^{rd}$, $4^{th}$, $5^{th}$ rings are given as, $d_1$=$d_2$=$d_3$=$d_4$=$d_5$=0.5 $\mu m$ where, $d_1$, $d_2$, $d_3$, $d_4$, $d_5$ are the diameter of $1^{st}$, $2^{nd}$, $3^{rd}$, $4^{th}$, $5^{th}$ ring respectively. The pitch, $\Lambda$ of the structure is 1 $\mu$m and the air filling ratio, d/$\Lambda$ is 0.5. The major and minor axis of the elliptical glass rod is 0.8 $\mu$m and 0.2 $\mu$m respectively. For octagonal structured PCF, the air hole diameters of $1^{st}$, $2^{nd}$, $3^{rd}$, $4^{th}$, $5^{th}$ rings are given as, $d_1$=$d_2$=$d_3$=$d_4$=$d_5$=0.665 $\mu m$. The pitch, $\Lambda$ of the structure is 0.95 $\mu$m and the air filling ratio, d/$\Lambda$ is 0.7. The major and minor axis of the elliptical glass rod is 0.6 $\mu$m and 0.2 $\mu$m respectively. For decagonal structured PCF, the air hole diameters of $1^{st}$, $2^{nd}$, $3^{rd}$, $4^{th}$, $5^{th}$ rings are given as, $d_1$=$d_2$=$d_3$=$d_4$=$d_5$=0.5 $\mu m$. The pitch, $\Lambda$ of the structure is 1 $\mu$m and the air filling ratio, d/$\Lambda$ is 0.5. The major and minor axis of the elliptical glass rod is 0.9 $\mu$m and 0.2 $\mu$m respectively. For elliptical PCF, the air hole diameters of $1^{st}$, $2^{nd}$, $3^{rd}$, $4^{th}$, $5^{th}$, $6^{th}$ rings are given as, $d_1$=0.28 $\mu m$, $d_2$=0.30 $\mu m$, $d_3$=0.32 $\mu m$, $d_4$=0.34 $\mu m$, $d_6$=0.36 $\mu m$, $d_6$=0.4 $\mu m$. The major axis of the glass rod is 0.8 $\mu m$ and minor axis is 0.2 $\mu m$. In all four cases the central elliptical portion of the core is filled with SF57 glass rod. Since SF57 has higher refractive index than silica, this modification improvises the performance of the fiber by creating asymmetry which leads to an ultra high birefringence. It also enhances the overall field confinement. Fig. 1 represents the cross sectional view of the investigated structures.

The full vector finite element method with perfectly matched layer is used to solve Maxwell's equation. The refractive index

*978-1-5386-3374-8/17/$31.00 ©2017 IEEE*

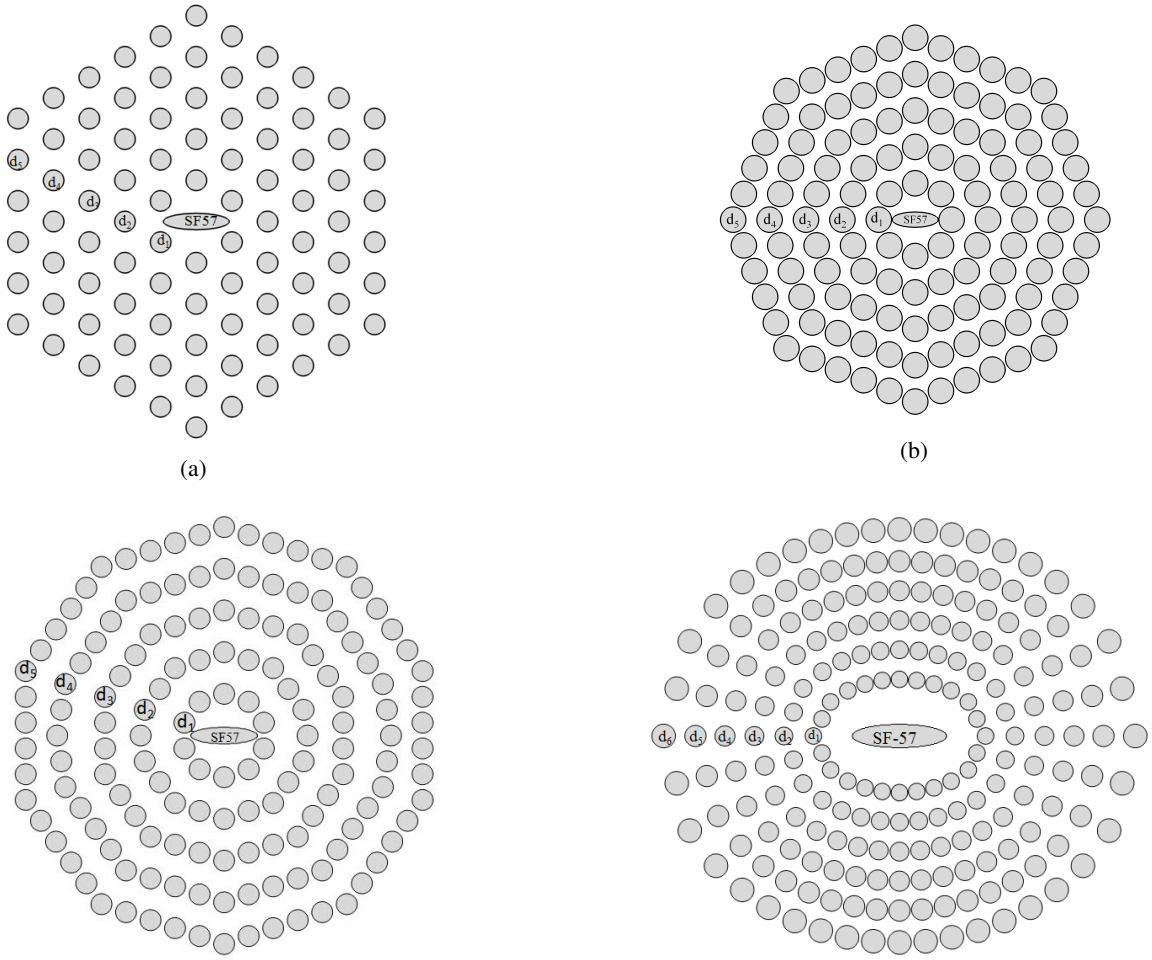


(a) (b) (c) (d)

Fig. 1: Cross sectional view of (a) hexagonal PCF (b) octagonal PCF, (c) decagonal PCF, (d) elliptical PCF with proposed infiltration where, $d_1$, $d_2$, $d_3$, $d_4$, $d_5$, $d_6$ are air hole diameters.

of the material is investigated over wavelength range from 1.3 $\mu m$ to 1.7 $\mu m$ covering E, S, C, L, U bands. The wavelength dependent refractive index of background material silica [19] and infiltration SF57 found by Sellmeier equation is included in simulation. The equation is given in (1)

$$n^2(\lambda) = 1 + \sum_i \frac{B_i \lambda^2}{(\lambda^2 - C_i)} \tag{1}$$

Here, n = refractive index; $\lambda$ = wavelength; $B_i$ (i=1,2,3) and $C_i$ (i=1,2,3) are Sellmeier coefficients for specific material. Solving the eigenvalue problem by simulation, effective refractive index $n_{eff}$ and effective area $A_{eff}$ are obtained. Birefringence is obtained from the difference between effective refractive index of both x and y mode using (2)

$$B = |n_{effx} - n_{effy}| \tag{2}$$

Here, $n_{effx}$ and $n_{effy}$ are the effective refractive index for x-mode and y-mode respectively.

The single modeness of the fiber is verified by using $V_{eff}$ parameter. The parameter is calculated by (3)

$$V_{eff} = \frac{(k \times \Lambda \times \sqrt{(A.F)})}{\lambda} \times \sqrt{(n_{eff}^2 - n_{air}^2)} \tag{3}$$

Where, K=$\frac{2\pi}{\lambda}$; $\lambda$=Wavelength; $\Lambda$=pitch; A.F=Air filling ratio; $n_{eff}$=Real part of effective refractive index; $n_{air}$= Refractive index of air.

It is known that, the fiber is considered as single mode if the value of $V_{eff}$ is lesser than 2.40 [20]. In this paper, the proposed four structures satisfy this condition so they are considered as single mode fiber. The calculated value of $V_{eff}$ over the wavelength 1.3 $\mu m$ to 1.7 $\mu m$ is plotted in the Fig. 2

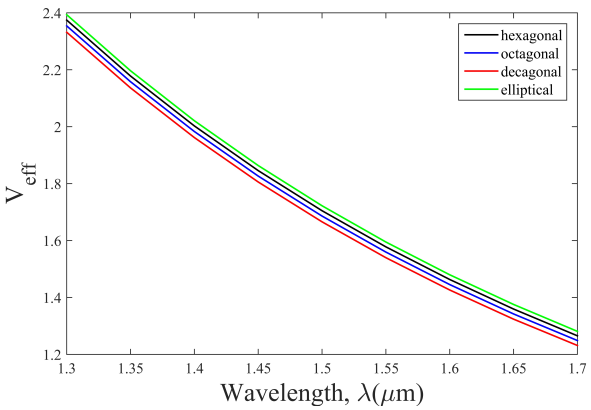


Fig. 2: V-parameter versus wavelength of the proposed structures with infiltration.

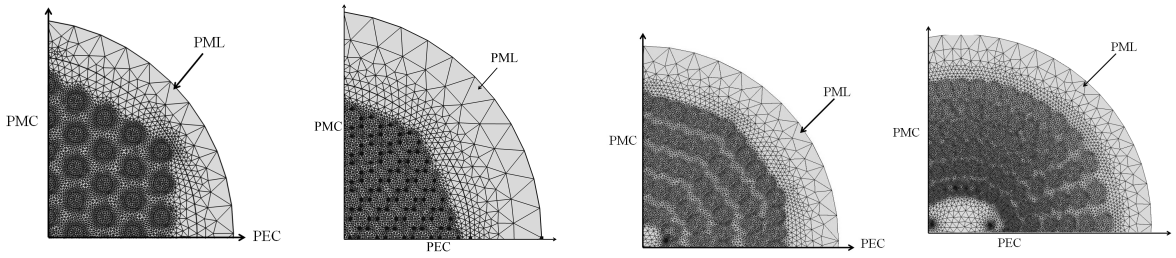


(a) (b) (c) (d)

Fig. 3: FEM mesh and boundary condition of (a) hexagonal infiltrated core PCF, (b) octagonal infiltrated core PCF, (c) decagonal infiltrated core PCF, (d) elliptical infiltrated core PCF.

## III. Results and Discussion

The simulation is performed using COMSOL Multiphysics. The fibers are divided into 53570 triangular elements with 401505 degree of freedom. Fig. 3 shows the corresponding mesh formation of the simulation.

Investigations were performed on some structures of PCF. Analysis shows that these structures exerts poor optical properties and are not suitable for any practical application. It is found that, if an elliptical soft glass rod of higher refractive index than silica is inserted in the core region of the fiber, due to increase of index contrast, light is propagated in a more confined way through the core. Besides it also introduces an asymmetry which leads to a higher birefringence. This enhances the polarization maintenance capability of the fiber so the fiber can be used in various polarization maintaining applications. The effect of this core infiltration on birefringence of different structures of photonic crystal fiber has been discussed here.

Electric and magnetic fields are distributed in the x-y plane and the wave propagates in the z direction. Electric field vector distribution of the two fundamental modes is transversely related. The difference of effective refractive index between two fundamental modes is defined as birefingence.

Fig. 4, Fig. 5, Fig. 6, Fig. 7 show the change of birefringence with wavelength of the investigated structures and the modified structures. It can be shown from the figures that birefringence increases gradually when the wavelength increases from 1.3 $\mu$m to 1.7 $\mu$m as the modal effective area increases with increasing wavelength. By investigating Fig. 4a, Fig. 5a, Fig. 6a, Fig. 7a it can be observed that the structures without the infiltration exert very low value of birefringence.

On the other hand, when infiltration is added, the value of birefringence is increased considerably since electric field distribution is dominated highly due to addition of the slot effect as shown in the Fig. 4b, Fig. 5b, Fig. 6b, Fig. 7b.

Birefringence of the hexagonal structured PCF with and without infiltration is shown in Fig. 4. At operating wavelength, 1.55 $\mu$m, birefringence of the structure without infiltration is found to be $5.517\times10^{-8}$ and that of with infiltration is $2.67 \times 10^{-1}$ which is about $4.82 \times 10^{-6}$ times greater than before. Birefringence of the octagonal structured PCF with and without infiltration is shown in Fig. 5. At operating wavelength, 1.55 $\mu$m, birefringence of the structure without infiltration is found to be $7.779 \times 10^{-8}$ and that of with infiltration is $4.0185 \times 10^{-2}$ which is about 537987 times greater than before. Birefringence of the decagonal structured PCF

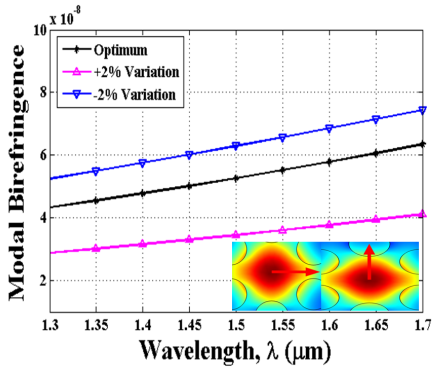


(a)

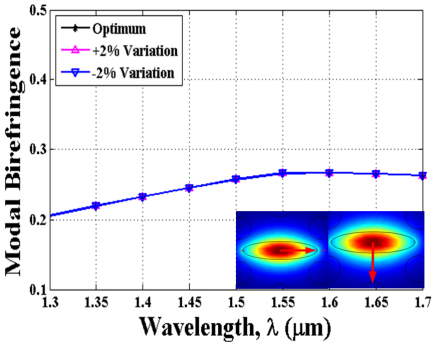


(b)

Fig. 4: Wavelength response of birefringence with $\pm2\%$ variation of hexagonal PCF (a) without infiltration, (b) with infiltration.

with and without infiltration is shown in Fig. 6. At operating wavelength birefringence of the fiber without infiltration is found to be $9.16\times10^{-5}$ and that of with infiltration is $5\times10^{-2}$ which is about 546 times greater than before. Birefringence of the elliptical PCF with and without infiltration is shown in Fig. 7. At operating wavelength the value of birefringence without infiltration is reported $6.828\times10^{-3}$ and that of with infiltration is $5.244 \times 10^{-2}$ which is about 8 times greater than before. It can be observed from these figures that the introduction of infiltration in the core region highly improve the birefringence. Since $\pm1\%$ variation may occur while fabrication [21], $\pm2\%$ tolerance has been taken under consideration for the fibers.

Table I summarizes the birefringence of the four investigated structures before and after adding the proposed modification. The comparison table clearly shows that the insertion of elliptical glass rod of the material SF-57 in the core region

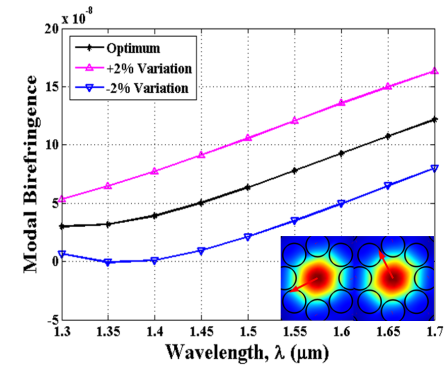


(a)

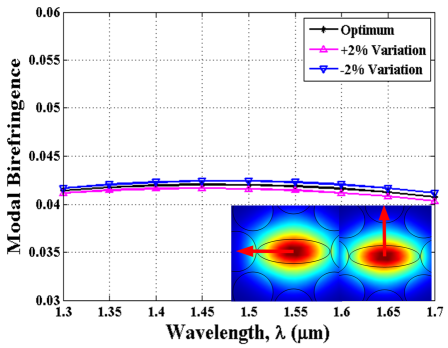


(b)

Fig. 5: Wavelength response of birefringence with $\pm 2\%$ variation of octagonal PCF (a) without infiltration, (b) with infiltration.

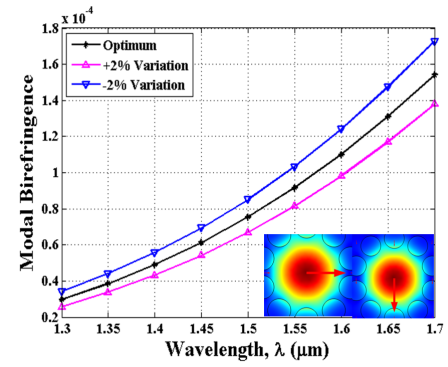


(a)

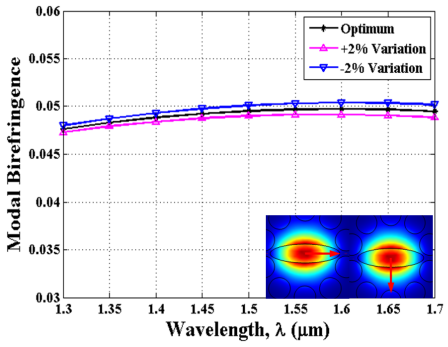


(b)

Fig. 6: Wavelength response of birefringence with $\pm 2\%$ variation of decagonal PCF (a) without infiltration, (b) with infiltration.

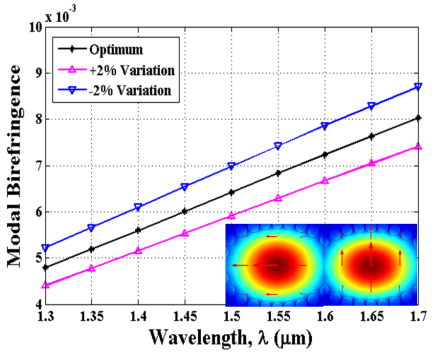


(a)

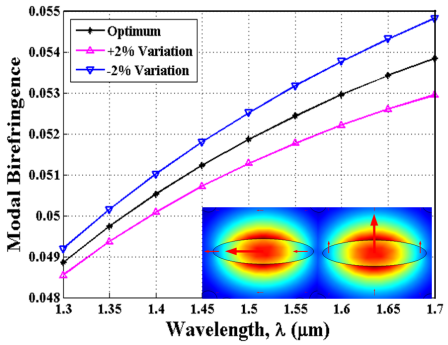


(b)

Fig. 7: Wavelength response of birefringence with $\pm 2\%$ variation of elliptical PCF (a) without infiltration, (b) with infiltration.

increases all the birefringence significantly.

Fabrication is a challenging issue when we are designing a PCF. PCF is fabricated using stack and draw process. Preform is made by stacking silica capillaries and a silica rod into a silica jacketing tube [22]. The preform is then drawn into fiber. Recently, significant development of the fabrication process permits fabrication of various complex structures [23] with reduced air hole diameter up to 110 nm [24]. Since smallest

TABLE I: Comparison of birefringence of different photonic crystal fiber without and with infiltration

| Structure | Birefringence | | |
|---|---|---|---|
| | Without Infiltration | With Infiltration | Increment factor |
| hexagonal | $5.517 \times 10^{-8}$ | $2.67 \times 10^{-1}$ | $4.82 \times 10^{6}$ |
| Octagonal | $7.779 \times 10^{-8}$ | $4.0185 \times 10^{-2}$ | $5.38 \times 10^{5}$ |
| Decagonal | $9.16 \times 10^{-5}$ | $5 \times 10^{-2}$ | 546 |
| Elliptical | $6.828 \times 10^{-3}$ | $5.244 \times 10^{-2}$ | 8 |

TABLE II: Comparison of birefringence of different reported photonic crystal fiber and that of proposed ones

| Structures | Characteristics | Birefringence | Comparison |
|---|---|---|---|
| Hexagonal | Reported [27] | $1.168 \times 10^{-2}$ | 23 times |
| | Proposed | $2.67 \times 10^{-1}$ | higher |
| Octagonal | Reported [28] | $2.04 \times 10^{-2}$ | 2 times |
| | Proposed | $4.0185 \times 10^{-2}$ | higher |
| Decagonal | Reported [29] | $1.02 \times 10^{-2}$ | 5 times |
| | Proposed | $5 \times 10^{-2}$ | higher |
| elliptical | Reported [30] | $10^{-2}$ | 5 times |
| | Proposed | $5.244 \times 10^{-2}$ | higher |

diameter used in the proposed design is 280 nm, this structure can be easily fabricated.

Here SF57 glass is used in the core. A number of works on the fabrication of a single mode SF57 glass fiber were reported in the early 2000 [25], [26]. So it is totally feasible to fabricate the proposed SF57 infiltrated fiber.

Adding this modification in the core not only improves the birefringence of the investigated fiber but also provides a higher value than any other reported structure. A comparative study has been made in Table II with the birefringence reported in very recent structures with that of proposed ones. The table helps to conclude that a multiple times higher birefringence can be ensured with this modification than the current reported configurations. Not only this, the configuration required to obtain such high value is comparatively much simpler than those of reported structures in [27], [28], [29], [30].

All the values in the table are considered at operating wavelength of 1550 nm.

## IV. Conclusion

The effect of elliptical glass rod in the core region of a photonic crystal fiber on birefringence has been demonstrated. Four basic structures have been investigated by adding this modification which increases the birefringence of the fiber considerably. This investigation led to the conclusion that the birefringence of any fiber can be improved for any polarization maintaining application. This insertion enhances the polarization property of the fiber by creating a greater difference between the two fundamental modes thus birefringence is increased notably. The birefringence can be improved upto the order of $10^{-1}$.

## References


[1] F. Poletti, N. Wheeler, M. Petrovich, N. Baddela, E. N. Fokoua, J. Hayes, et al., "Towards high-capacity fibre-optic communications at the speed of light in vacuum," Nature Photonics, vol. 7, pp. 279-284, 2013.

[2] D. Chen and L. Shen, "Ultrahigh birefringent photonic crystal fiber with ultralow confinement loss," IEEE Photonics Technology Letters, vol. 19, pp. 185-187, 2007.

[3] W. H. Reeves, J. Knight, P. S. J. Russell, and P. Roberts, "Demonstration of ultra-flattened dispersion in photonic crystal fibers," Optics express, vol. 10, pp. 609-613, 2002.

[4] T. Monro, K. Kiang, J. Lee, K. Frampton, Z. Yusoff, R. Moore, et al., "High nonlinearity extruded single-mode holey optical fibers," in Optical Fiber Communication Conference and Exhibit, 2002. OFC 2002, 2002, pp. FA1-FA1.

[5] K. Tajima, J. Zhou, K. Nakajima, and K. Sato, "Ultralow loss and long length photonic crystal fiber," Journal of Lightwave Technology, vol. 22, p. 7, 2004.

[6] M. D. Nielsen, N. A. Mortensen, J. R. Folkenberg, A. Petersson, and A. Bjarklev, "Improved all-silica endlessly single-mode photonic crystal fiber," in Optical Fiber Communication Conference, 2003, p. FI7.

[7] J. Broeng, D. Mogilevstev, S. E. Barkou, and A. Bjarklev, "Photonic crystal fibers: A new class of optical waveguides," Optical fiber technology, vol. 5, pp. 305-330, 1999.

[8] K. Suzuki, H. Kubota, S. Kawanishi, M. Tanaka, and M. Fujita, "High-speed bi-directional polarisation division multiplexed optical transmission in ultra low-loss (1.3 dB/km) polarisation-maintaining photonic crystal fibre," Electronics letters, vol. 37, pp. 1399-1401, 2001.

[9] S. Chung, J. Kim, B.-A. Yu, and B. Lee, "A fiber Bragg grating sensor demodulation technique using a polarization maintaining fiber loop mirror," IEEE Photonics Technology Letters, vol. 13, pp. 1343-1345, 2001.

[10] D.-H. Kim and J. U. Kang, "Sagnac loop interferometer based on polarization maintaining photonic crystal fiber with reduced temperature sensitivity," Optics Express, vol. 12, pp. 4490-4495, 2004.

[11] D. S. Bethune and W. P. Risk, "An autocompensating fiber-optic quantum cryptography system based on polarization splitting of light," IEEE Journal of Quantum Electronics, vol. 36, pp. 340-347, 2000.

[12] M. Nakazawa, E. Yoshida, and Y. Kimura, "Ultrastable harmonically and regeneratively modelocked polarisation-maintaining erbium fibre ring laser," Electronics Letters, vol. 30, pp. 1603-1605, 1994.

[13] Y. Sasaki, K. Okamoto, T. Hosaka, and N. Shibata, "Polarization-maintaining and absorption-reducing fibers," in Optical Fiber Communication Conference, 1982, p. ThCC6.

[14] M. Varnham, D. Payne, R. Birch, and E. Tarbox, "Single-polarisation operation of highly birefringent bow-tie optical fibres," Electronics letters, vol. 19, pp. 246-247, 1983.

[15] J. Simpson, R. Stolen, F. Sears, W. Pleibel, J. MacChesney, and R. Howard, "A single-polarization fiber," Journal of Lightwave Technology, vol. 1, pp. 370-374, 1983.

[16] K. Tajima and Y. Sasaki, "Transmission loss of a 125-mu m diameter PANDA fiber with circular stress-applying parts," Journal of Lightwave Technology, vol. 7, pp. 674-679, 1989.

[17] A. R. Chraplyvy, "Limitations on lightwave communications imposed by optical-fiber nonlinearities," Journal of Lightwave Technology, vol. 8, pp. 1548-1557, 1990.

[18] A. Ortigosa-Blanch, J. Knight, W. Wadsworth, J. Arriaga, B. Mangan, T. Birks, et al., "Highly birefringent photonic crystal fibers," Optics letters, vol. 25, pp. 1325-1327, 2000.

[19] K. Saitoh and M. Koshiba, "Single-polarization single-mode photonic crystal fibers," IEEE Photonics Technology Letters, vol. 15, pp. 1384-1386, 2003.

[20] C.-N. Liu, T.-H. Wang, T.-S. Rou, N.-K. Chen, S.-L. Huang, and W.-H. Cheng, "Higher Gain of Single-Mode Cr-Doped Fibers Employing Optimized Molten-Zone Growth," Journal of Lightwave Technology, 2017.

[21] M. Loncar, T. Doll, J. Vuckovic, and A. Scherer,"Design and fabrication of silicon photonic crystal optical waveguides," Journal of lightwave technology, vol. 18, pp. 1402-1411, 2000.

[22] H. Kubota, S. Kawanishi, S. Koyanagi, M. Tanaka, and S. Yamaguchi, "Absolutely single polarization photonic crystal fiber," IEEE Photonics Technology Letters, vol. 16, pp. 182-184, 2004.

[23] K. Suzuki, H. Kubota, S. Kawanishi, M. Tanaka, and M. Fujita, "Optical properties of a low-loss polarization-maintaining photonic crystal fiber," Optics Express, vol. 9, pp. 676-680, 2001.

[24] D. Tee, M. A. Bakar, N. Tamchek, and F. M. Adikan, "Photonic Crystal Fiber in Photonic Crystal Fiber for Residual Dispersion Compensation Over $\mathrm{E+S+C+L+U}$ Wavelength Bands," IEEE Photonics Journal, vol. 5, pp. 7200607-7200607, 2013.

[25] T. Monro, K. Kiang, J. Lee, K. Frampton, Z. Yusoff, R. Moore, et al., "High nonlinearity extruded single-mode holey optical fibers," in Optical Fiber Communication Conference and Exhibit, 2002. OFC 2002, 2002, pp. FA1-FA1.

[26] K. Kiang, K. Frampton, T. Monro, R. Moore, J. Tucknott, D. Hewak, et al., "Extruded singlemode non-silica glass holey optical fibres," Electronics Letters, vol. 38, pp. 546-547, 2002.

[27] M. Hasan, M. Anower, M. Rashid, and S. Ali, "A polarization maintaining hexagonal photonic crystal fiber for residual dispersion compensation," in Electrical Engineering and Information Communication Technology (ICEEICT), 2016 3rd International Conference on, 2016, pp. 1-6.

[28] M. M. Rashid, M. S. Anower, M. I. Hasan, and M. R. Hasan, "Highly birefringent octagonal shaped photonic crystal fiber with two zero dispersion wavelengths in Ti: Sapphire oscillator range," in Electrical Engineering and Information Communication Technology (ICEEICT), 2016 3rd International Conference on, 2016, pp. 1-6.

[29] M. De, R. K. Gangwar, and V. K. Singh, "Designing of highly birefringence, dispersion shifted decagonal photonic crystal fiber with low confinement loss," Photonics and Nanostructures-Fundamentals and Applications, vol. 26, pp. 15-23, 2017.

[30] A. K. Ghunawat, R. Chandra, and G. Singh, "Design of an ultra-flattened negative dispersion elliptical spiral photonic crystal fiber with high nonlinearity and high birefringence," in Computer, Communications and Electronics (Comptelix), 2017 International Conference on, 2017, pp. 623-627.

# Large Negative Flattened Dispersion over the S+C+L Bands Using Highly Birefringent Photonic Crystal Fiber

Md Borhan Mia,[1,*] Kanan Roy Chowdhury,[2] Animesh Bala Ani[1] and Mohammad Faisal[1]
[1]Bangladesh University of Engineering and Technology, Dhaka, Bangladesh
[2]Chittagong University of Engineering and Technology, Chittagong, Bangladesh
*mborhanm1110@gmail.com

*Abstract*—**Novel triangular lattice photonic crystal fiber (PCF) having vastly negative trodden chromatic dispersion over the S+C+L bands with a very high birefringence has been presented in this paper. To investigate different optical and electrical properties associated with the proposed fiber, finite element method (FEM) is deployed. The fiber presents a flattened negative dispersion of −698.5 ± 5 ps/(nm-km) over the wavelength of 1440 nm to 1600 nm. Besides, the proposed PCF displays a high birefringence of $1.886\times10^{-2}$ at 1550 nm wavelength. Furthermore, the nonlinearity, single modeness, effective area etc. of the proposed PCF are thoroughly discussed. The fiber would have important applications in broadband residual dispersion compensation as well as polarization maintaining applications**

***Index terms—Finite element method, chromatic dispersion, photonic crystal fiber, and birefringence.***

## I. Introduction

Recently high and ultra-high bit data are being transported by using dense wavelength division multiplexed (DWDM) and wavelength division multiplexed (WDM) systems [1]. In WDM system, bit rate of 40 Gb/s has been widely used [2]. Due to rapid grow of demand, 100 Gb/s [3] and 400 Gb/s [4] bit rate are employed to transport data for long haul communication. Standard single mode fibers (SMFs) are deployed in the transmission line which cause a huge stockpiled chromatic dispersion along the fiber optic line. Dispersion compensating fibers (DCFs) are used to recompense the accumulated dispersion of the SMFs. However, after compensation there exist some dispersion, known as residual dispersion due to slope mismatch arisen from the positive dispersion slope of SMFs. Therefore, residual dispersion compensating fibers (RDCFs) are indispensable to recompense the residual dispersion of the conventional DCFs. Besides, RDCFs exhibit very large negative and flattened dispersion, concurrently. There are many tunable properties of PCFs which are controllable and flexible. Therefore, PCFs have become very reasonable to design RDCFs.

Lately, PCFs with high negative flattened dispersion as well as large birefringence have been suggested by many authors. For instance, RDCF presented in [5] exhibits average negative dispersion of −457.4 ps/(nm-km) covering from 1360 nm to 1690 nm wavelength band. However, there is no information regarding birefringence and loss of the suggested PCF. In [6], Habib et al. proposed an octagonal shaped PCF. It shows a negative dispersion of −465.5 ps/(nm-km) and an out-and-out variation of 10.5 ps/(nm-km). Though, the design displays a high birefringence of $2.68\times10^{-2}$, the chromatic dispersion is small and the variation is high. Besides, the structure is hybrid which is difficult to fabricate. A PCF is suggested for residual dispersion purpose in [7] showing average negative dispersion of −138 ps/(nm-km) in the wavelength extending from 980 nm to 1580 nm with an out-and-out deviation of 12 ps/(nm-km). However, birefringence issue is ignored and flattened negative dispersion is very low. Ani et al. [8] proposed a RDCF exhibiting a flattened dispersion of −124 ps/(nm-km) covering the wavelength of 1350 to 1700 nm. Besides, fiber displays a dispersion deviation of ± 0.1252 ps/(nm-km). However, birefringence issue was disregarded. Li et al. [9] proposed a design, displaying a dispersion of −611.9 ps/(nm-km) in 1460 nm to 1625 nm wavelength bands. It also exhibits dispersion of −474 ps/(nm-km) over 1425 nm to 1675 nm wavelength. Hasan et al. [10] proposed photonic crystal fiber of spiral shape for broadband remaining dispersion reparation. The fiber shows flattened dispersion of −526.99 ps/(nm-km) over 1050 nm to 1700 nm with an absolute variation of ±3.7 ps/(nm-km) and birefringence of $2.26\times10^{-2}$. In [11], Hasan et al. proposed a photonic crystal fiber having high nonlinearity and high birefringent for dispersion purpose. Design fiber shows very high negative dispersion varying from −388.72 to −723.1 ps/(nm-km) in the wavelength array of 1460 to 1625 nm. However, transmission of data will be affected due to high nonlinearity of the suggested fiber.

In our article, we numerically investigated a triangular frame photonic crystal fiber for residual dispersion purpose. The fiber demonstrates a very high trodden dispersion of −698.5 ps/(nm-km) with a total variation of 5 ps/(nm-km) in S+C+L wavelength bands. To our knowledge, this is the utmost average negative dispersion than all recently printed articles. Moreover, the fiber exhibits a high birefringence of $1.885\times10^{-2}$ at the communication band, which will have important applications in sensor designs. Furthermore, the value of V-parameter recommends that fiber will operate only in fundamental mode.

## II. Fiber Design

The geometric view of the designed PCF is demonstrated in Fig. 1. The fiber comprises of 7 rings of circular air holes, divided into two regions, i.e., core and cladding. The cladding comprises of 5 air hole rings and core has two air hole rings without any doping to keep the design simple. The outer cladding has a pitch value of $\Lambda_2 = 0.671\mu m$ and at the core region, the pitch value is $\Lambda_1 = 0.667\mu m$. The diameter of the air hole, both in core and cladding profile is $d_1 = 0.58\mu m$. The air filling fractions at core and cladding are 0.87 and 0.864, respectively. Three air holes are removed from the center which

978-1-5386-3374-8/17/$31.00 ©2017 IEEE

breaks the symmetry in the core. Asymmetric core is the prerequisite to obtain high birefringence. In the design, we used silica ($SiO_2$) as background material which is accessible in fiber industry.

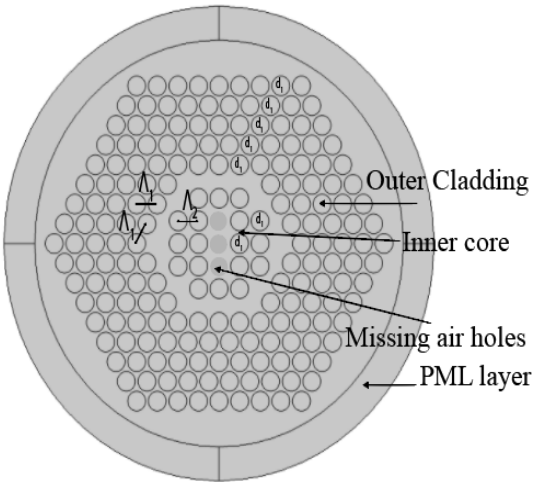


Fig. 1. Geometric view of the proposed PCF

## III. SIMULATION AND RESULT

Different belongings of the suggested fiber are tailored by using finite element method (FEM) and as a design simulator, COMSOL MULTIPHYSICS 5.0 is used. Perfectly matched layer (PML) is used to make simulation window compact and it produces no reflection. PML layer is placed nearby the outmost ring. Eigen value problems of Maxwell curl equation are solved to obtain the operative refractive index of the recommended fiber. Once $\eta_{eff}$ is obtained, other parameters; i.e., chromatic dispersion $D(\lambda)$, birefringence $B$, non-linear co-efficient $\gamma$, loss $L_c$, effective area $A_{eff}$ can be tailored from their respective equations [12]– [17]

$$D(\lambda) = -\frac{\lambda}{c}\frac{d^2\,\mathrm{Re}[\eta_{eff}]}{d\lambda^2} \quad (1)$$

$$B = \left|\eta_{eff}^{x} - \eta_{eff}^{y}\right| \quad (2)$$

$$A_{eff} = \frac{\left(\iint |E|^2\, dxdy\right)^2}{\iint |E|^4\, dxdy} \quad (3)$$

$$L_c = \frac{20\times 10^6}{\ln(10)} k_0 Im[\eta_{eff}] \quad (4)$$

$$V_{eff} = \frac{2\pi\Lambda}{\lambda}\sqrt{\eta_{eff}^2 - \eta_{FSM}^2} \quad (5)$$

Where, $Re\ [\eta_{eff}]$ and $Im\ [\eta_{eff}]$ are the real and imaginary fragment of the effective refractive index, respectively; $\eta_{eff}^{x}$ and $\eta_{eff}^{y}$ are the effective refractive indices alongside the x and y-polarization mode, respectively; c is the speed of light in void, $\lambda$ is the functional wavelength, $E$ is the electric field, $k_0 = \frac{2\pi}{\lambda}$ ,is the wave number in vacuum; $\eta_{eff}$ and $\eta_{FSM}$ are the refractive indices of the basic mode and basic space filling mode, respectively. The three termed Sellmeier principle is straightly included in simulation.

Fundamental mode profiles (x and y) of the suggested PCF is illustrated in Fig. 2 using parameters $d_1 = 0.58$ µm, $\Lambda_1 = 0.667$ µm and $\Lambda_2 = 0.671$ µm at wavelength of 1550 nm. Since higher refractive index is realized in core, optical fields are well restrained in core than cladding. From Fig. 2, it is enlightened that mode field spreads along the y-direction due to missing holes compared to x, which results in high birefringence.

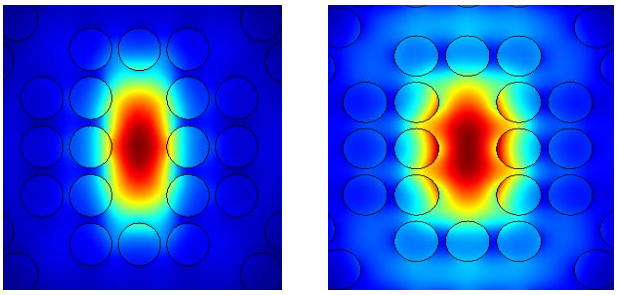

x-polarization y-polarization

Fig. 2. Basic mode profile of the suggested PCF for x and y-polarization mode at 1550 nm.

In Fig. 3 chromatic dispersion of presented PCF is demonstrated as a function of wavelength for both x and y-polarization mode. Since, in highly birefringent PCF two polarization modes (x and y) exhibit unlike dispersion characteristics, we limit our discussion only for y-polarization mode which displays a large negative flattened dispersion compared to x-polarization mode. Proposed PCF shows a large dispersion of −698.5 ± 5 ps/(nm-km) in the wavelength band of 1440 nm to 1600 nm. The dispersion of the suggested PCF at 1550 nm is -700 ps/(nm-km) which is clearly depicted in Fig. 3.

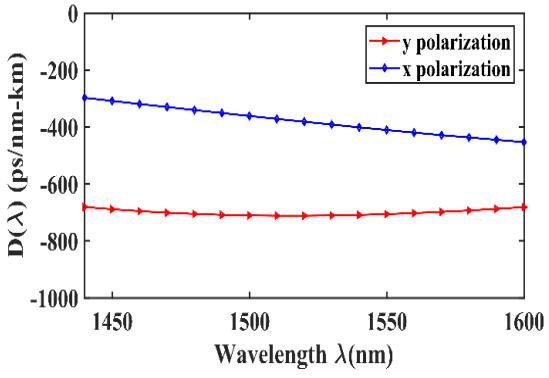


Fig. 3. Dispersion of proposed PCF as a function of wavelength alongside x and y polarization mode for the parameters $d_1 = 0.58$ µm, $\Lambda_1 = 0.667$ µm, $\Lambda_2 = 0.671$ µm.

To study, the effect of altering the diameter of the hole around the core region, we changed $d_1$ by taking the values of 0.57 µm, 0.58 µm and 0.59 µm and the corresponding chromatic

dispersion is illustrated in Fig. 4. It is seen form the Fig. 4, when $d_1$=0.58 µm, a large negative flattened dispersion is obtained.

The effect of altering pitch, both inner core and outer cladding is demonstrated in Fig. 5 and Fig. 6, respectively. It is clearly seen form Fig. 5 and Fig. 6 that when $\Lambda_1$ = 0.667 µm and $\Lambda_2$ = 0.671 µm, we have attained a very large negative flattened dispersion from the bands of wavelength, 1440 nm to 1600 nm. Therefore, the optimum parameters of the proposed design are $d_1$ = 0.58 µm, $\Lambda_1$ = 0.667 µm and $\Lambda_2$ = 0.671 µm.

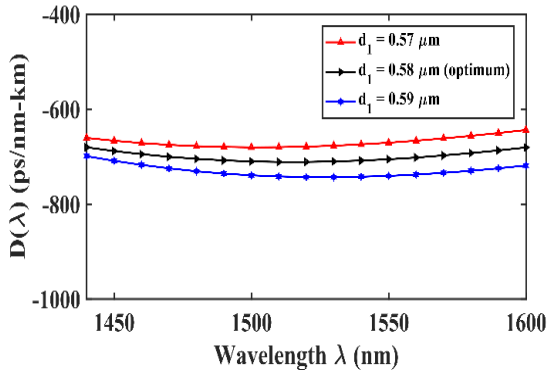


Fig. 4. Chromatic dispersion of the proposed PCF as function of wavelength altering $d_1$ keeping other parameters unaltered.

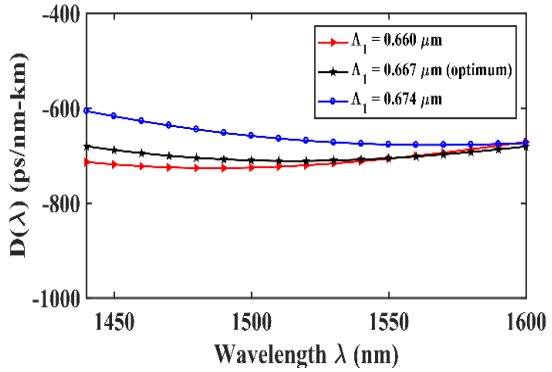


Fig. 5. Chromatic dispersion as a function of wavelength altering $\Lambda_1$, keeping other parameters unchanged.

The dispersion slope which is the variation of dispersion due to corresponding variation of wavelength, of the suggested PCF is demonstrated in Fig. 7 at optimum parameters. The dispersion slope is 0.35 ps/(nm$^2$-km) at communication band. Confinement loss of suggested PCF is also depicted in the same figure. In c band, confinement loss is $4\times10^{-5}$ dB/m, which is very low.

We carefully scrutinized birefringence, which is the variation between x and y-polarization mode, of the proposed fiber. To obtain birefringence, some air holes are intentionally removed from core to introduce asymmetry. Fig. 8 presents the birefringence of suggested PCF for finest factors $d_1$ = 0.58 µm, $\Lambda_1$ = 0.667 µm and $\Lambda_2$ = 0.671 µm. Form the Fig. 8, it is seen that, birefringence at 1550 nm wavelength is $1.885\times10^{-2}$, which is high enough compared to conventional polarization maintaining fibers.

The dependence of effective area on wavelength at finest parameters $d_1$, $\Lambda_1$ and $\Lambda_2$ is demonstrated in Fig. 9. The effective area of the suggested PCF is 4.2 µm$^2$ at 1550 nm wavelength and it decreases with the increment of the wavelength, due to guided mode of the fiber increases at longer wavelength. The nonlinear property of the proposed PCF is depicted in the same figure. The nonlinear co-efficient is 24.2 W$^{-1}$km$^{-1}$ at the exciting wavelength of 1550 nm. Since nonlinear co-efficient is low and it covers the wavelength of concern, the proposed fiber could be a proper choice for dispersion compensation.

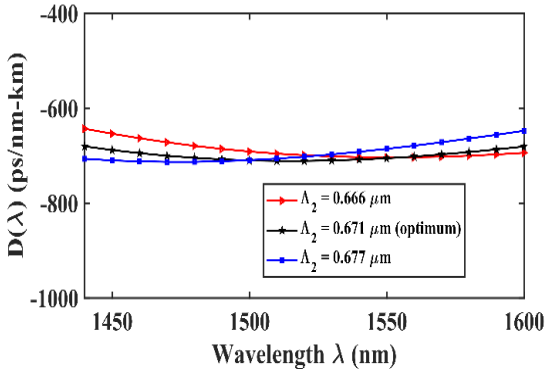


Fig. 6. Chromatic dispersion dependence on wavelength changing $\Lambda_2$, keeping other parameters constant.

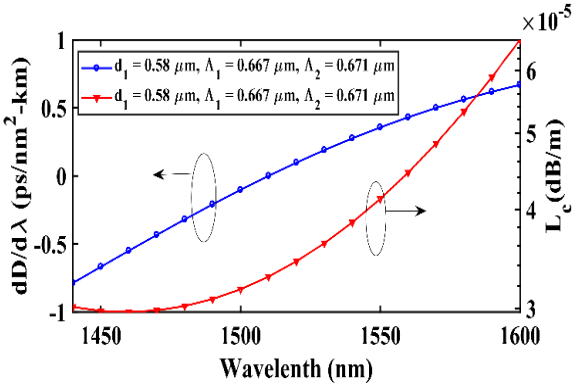


Fig. 7. Dispersion slope and loss as dependent on wavelength with parameters, $d_1$ = 0.58 µm, $\Lambda_1$ = 0.667 µm, $\Lambda_2$ = 0.671 µm.

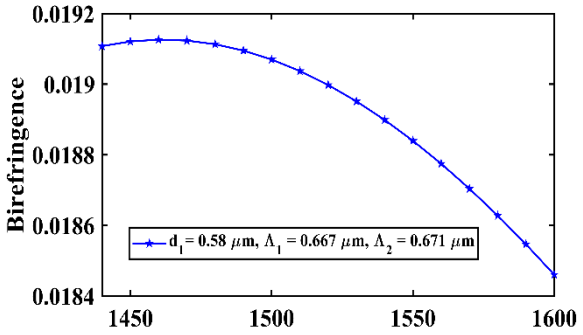


Fig. 8. Birefringence of the suggested fiber as a function of wavelength with parameters, $d_1$ = 0.58 µm, $\Lambda_1$ = 0.667 µm, $\Lambda_2$ = 0.671 µm.

The single modeness of the proposed PCF is carefully explored as discrepancy might happen because of different size of cores. The V- parameter assistances to verify whether the proposed fiber operates in single mode or not. The PCF will act as single mode fiber (SMF) if the V-parameter, $V_{eff} \leq \pi$. The V-parameter of the suggested PCF is showed in Fig. 10. From Fig. 10, it is realized that the V-parameter, $V_{eff} \leq \pi$ in wavelength band from 1440 nm to 1600 nm. Therefore, it guarantees that suggested PCF will operate in single mode only.

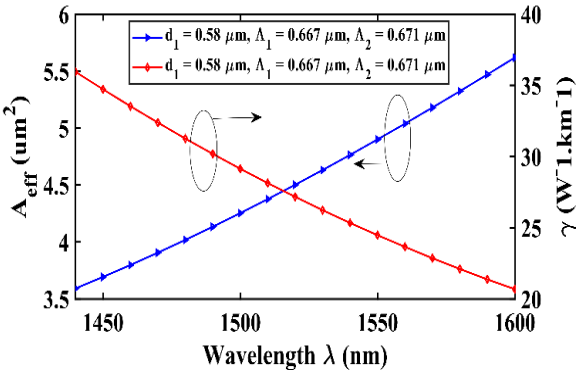


Fig. 9. Effective area and nonlinear co-efficient vs. wavelength with the finest parameters, $d_1$ = 0.58 μm, $\Lambda_1$ = 0.667 μm, $\Lambda_2$ = 0.671 μm.

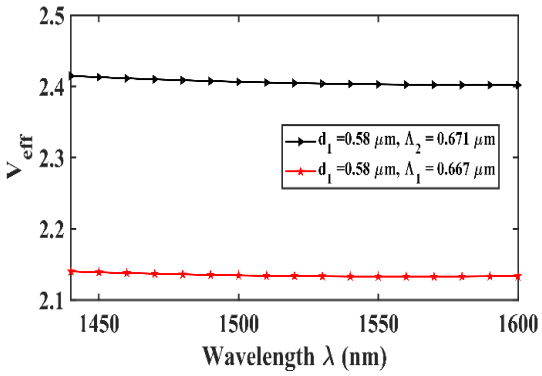


Fig. 10. V-parameter, $V_{eff}$ as a function of wavelength with optimum parameters, $d_1$ = 0.58 μm, $\Lambda_1$ = 0.667 μm, $\Lambda_2$ = 0.671 μm.

## IV. Conclusion

In this article, we demonstrated a novel PCF which shows a vast negative flattened dispersion over the wavelength S+C+L bands. The fiber exhibits large flattened dispersion of -698.5 ps/(nm-km) with a total variation of 5 ps/(nm-km). Therefore, fiber will be appropriate for dispersion compensation in optical transmission. Additionally, the proposed fiber exhibits large birefringence of $1.885\times10^{-2}$ at 1550 nm wavelength, which has probable applications in polarization maintenance. Furthermore, the nonlinear co-efficient is 24.2 $W^{-1}km^{-1}$ at the wavelength of 1550 nm confirming that transmission of data won't be much affected by the nonlinearity of the suggested PCF. To our awareness, the suggested PCF exhibits the largest negative dispersion of all formerly published articles.

## References


[1] M. L. Loeb and G. R. Stilwell, "High-speed data transmission on an optical fiber using a byte-wide WDM system," *J. Light. Technol.*, vol. 6, no. 8, pp. 1306–1311, 1988.

[2] K. Fukuchi *et al.*, "10.92-Tb/s (273/spl times/40-Gb/s) triple-band/ultra-dense WDM optical-repeatered transmission experiment," *Opt. Fiber Commun. Conf. Exhib. 2001. OFC 2001*, vol. 4, p. PD24-PD24, 2001.

[3] A. Sano *et al.*, "No-Guard-Interval Coherent Optical OFDM for 100-Gb/s Long-Haul WDM Transmission," *J. Light. Technol. Vol. 27, Issue 16, pp. 3705-3713*, vol. 27, no. 16, pp. 3705–3713, Aug. 2009.

[4] "High spectral efficiency 400 Gb/s transmission using PDM time-domain hybrid 32–64 QAM and training-assisted carrier recovery," *Technology*, 2013.

[5] D. Tee, M. Bakar, and N. Tamchek, "Photonic Crystal Fiber in Photonic Crystal Fiber for Residual Dispersion Compensation Over Wavelength Bands," *IEEE Photonics*, 2013.

[6] M. Samiul Habib, R. Ahmad, M. Selim Habib, and M. Imran Hasan, "Residual dispersion compensation over the S + C + L + U wavelength bands using highly birefringent octagonal photonic crystal fiber," *Appl. Opt.*, vol. 53, no. 14, p. 3057, May 2014.

[7] M. Samiul Habib, M. Selim Habib, M. I. Hasan, and S. M. A. Razzak, "A single mode ultra flat high negative residual dispersion compensating photonic crystal fiber," *Opt. Fiber Technol.*, vol. 20, no. 4, pp. 328–332, Aug. 2014.

[8] A. B. Ani and M. Faisal, "Ultra-flattened broadband dispersion compensating photonic crystal fiber with ultra-low confinement loss," in *2016 9th International Conference on Electrical and Computer Engineering (ICECE)*, 2016, pp. 243–246.

[9] X. Li, P. Liu, Z. Xu, and Z. Zhang, "Design of a pentagonal photonic crystal fiber with high birefringence and large flattened negative dispersion," *Appl. Opt.*, vol. 54, no. 24, p. 7350, Aug. 2015.

[10] M. I. Hasan, R. R. Mahmud, M. Morshed, and M. R. Hasan, "Ultra-flattened negative dispersion for residual dispersion compensation using soft glass equiangular spiral photonic crystal fiber," *J. Mod. Opt.*, vol. 63, no. 17, pp. 1681–1687, Sep. 2016.

[11] M. I. Hasan, M. Selim Habib, M. Samiul Habib, and S. M. Abdur Razzak, "Highly nonlinear and highly birefringent dispersion compensating photonic crystal fiber," *Opt. Fiber Technol.*, vol. 20, no. 1, pp. 32–38, Jan. 2014.

[12] A. Agrawal, N. Kejalakshmy, J. Chen, B. M. Rahman, and K. T. Grattan, "Golden spiral photonic crystal fiber: polarization and dispersion properties," *Opt. Lett.*, vol. 33, no. 22, p. 2716, Nov. 2008.

[13] K. Saitoh and M. Koshiba, "Leakage loss and group velocity dispersion in air-core photonic bandgap fibers," *Opt. Express*, vol. 11, no. 23, p. 3100, Nov. 2003.

[14] K. Suzuki, H. Kubota, S. Kawanishi, M. Tanaka, and M. Fujita, "Optical properties of a low-loss polarization-maintaining photonic crystal fiber.," *Opt. Express*, vol. 9, no. 13, pp. 676–680, Dec. 2001.

[15] A. Bala, K. R. Chowdhury, M. B. Mia, and M. Faisal, "Highly birefringent, highly negative dispersion compensating photonic crystal fiber," *Appl. Opt.*, vol. 56, no. 25, p. 7256, Sep. 2017.

[16] M. B. Mia, A. Bala, K. R. Chowdhury, and M. Faisal, "Highly Nonlinear and Low Confinement Loss Photonic Crystal Fiber Using GaP Slot Core," Oct. 2017.

[17] M. B. Mia, M. Faisal, S. I. Naz, A. Bala, and K. R. Chowdhury, "Heptagonal Photonic Crystal Fiber for Dispersion Compensation with a Very Low Confinement Loss," Sep. 2017.

# Highly Nonlinear and Low Confinement Loss Photonic Crystal Fiber Using GaP Slot Core

Md Borhan Mia,[1,*] Animesh Bala Ani,[1] Kanan Roy Chowdhury[2] and Mohammad Faisal[1]
[1]Bangladesh University of Engineering and Technology, Dhaka, Bangladesh
[2]Chittagong University of Engineering and Technology, Chittagong, Bangladesh
*mborhanm1110@gmail.com

*Abstract*—**This paper presents a triangular lattice photonic crystal fiber (PCF) with very high nonlinear coefficient. Finite element method is used to scrutinize different optical characteristics of proposed highly nonlinear PCF (HNL-PCF). The HNL-PCF exhibits a high nonlinearity up to $10\times10^4$ $W^{-1}km^{-1}$ over the wavelength band of 1500 nm to 1700 nm. Moreover, proposed fiber shows a very low confinement loss of $10^{-3}$ dB/km and chromatic dispersion of −9000 ps/(nm-km) at 1550 nm wavelength. Furthermore, dispersion slope, effective area are also analyzed thoroughly. The proposed fiber will be a suitable candidate for sensing applications, dispersion compensation, nonlinear signal processing and supercontinuum generation.**

***Index terms—Chromatic dispersion, Finite element method, nonlinear coefficient, photonic crystal fiber, and birefringence.***

## I. INTRODUCTION

Photonic crystal fibers or microstructure holey fibers exhibit diversified properties which furnish some new applications such as supercontinuum generation, fiber sensors and ability to uphold high polarization, broadband dispersion controlling etc. Nonlinearity is one of the indispensable belongings of photonic crystal fibers for many useful applications including optical switching, optical regeneration, supercontinuum generation, optical parameter magnification, and optical wavelength transformation [1], [2]. Compared to standard single mode fibers (SMFs), PCFs have many tunable properties, for example; air hole diameter, pitch, cladding, background material, doped core etc. These flexibilities provide better control over nonlinearity, dispersion slope, birefringence, splice loss and confinement loss etc. These are only possible in PCF which are unachievable in SMFs. PCFs are classified into two groups, index guiding and photonic band gap PCFs. In these two types of PCFs, high refractive index difference is upheld in the middle of core and cladding.

To attain high nonlinearity researchers have studied the behavior of PCFs by using nanostructure with large refractive index in the core section. Using pure silica core, nonlinear coefficient is only about 100 $W^{-1}km^{-1}$ due to very small nonlinear refractive index of silica, nominally $29.6\times10^{-21}$ $m^2/W$. Therefore, higher nonlinear refractive index materials are used in the core to improve nonlinearity. Recently, Liao et al. [3] suggested a PCF of high nonlinearity using nano scale slot core. The PCF exhibits a very high nonlinearity up to $3.5739\times10^4$ $W^{-1}km^{-1}$. However, confinement loss issue is ignored. Huang et al. proposed a slot coiled silicon PCF having a high nonlinear coefficient up to 1068 $W^{-1}m^{-1}$ [4]. Li and Zhao used nano wires of gold in core and attained boosted polarization reliant coupling and transmission [5]. Liao et al. [6] suggested a spiral PCF of high nonlinearity exhibiting nonlinear coefficient of 226 $W^{-1}m^{-1}$ at the communication band. Amin et al. [7] proposed a spiral high nonlinear photonic crystal fiber using GaP strips in the core. The fiber shows a high nonlinearity of $10^4$ $W^{-1}km^{-1}$. Nevertheless, fiber exhibits confinement loss of $10^3$ and $10^{-10}$ dB/km for x and y polarization modes, respectively at 1550 nm wavelength. To fabricate fibers having large nonlinearity with nanoscale slot core, recently article [8] is published.

In our article, a triangular lattice photonic crystal fiber is being suggested which shows a very high nonlinearity up to $8\times10^4$ $W^{-1}km^{-1}$ at wavelength of 1550 nm. It exhibits nonlinearity of $10\times10^4$ to $2\times10^4$ $W^{-1}km^{-1}$ in wavelength array of 1550 nm to 1770 nm. Additionally, it shows a very minute confinement loss of $10^{-3}$ dB/km at communication band. To our knowledge this is the best result compared to recently published articles. Moreover, HNL-PCF shows a very high dispersion up to −9000 ps/(nm-km) at 1550 nm wavelength. Therefore, suggested fiber can be useful supercontinuum generation, optical parameter amplification and broadband dispersion compensation.

## II. FIBER DESIGN

The geometric view of the proposed HNL-PCF with magnified sight of slot core is demonstrated in Fig. 1. The design is kept as simple as possible. The cladding region comprises of six air hole rings. The air hole diameter in cladding region, d = 0.58 µm with the pitch value of Λ = 0.75 µm. Air filling fraction in cladding is d/Λ = 0.77 which is fabrication feasible. Two alike rectangular strips of GaP are familiarized in core with a space of $L_s$ = 0.12 µm. The length and width of the strips are $d_x$ = 0.58 µm and $d_y$ = 0.096 µm, respectively. The amplified view of the core in Fig. 1(a) exhibits $d_x$, $d_y$ and $L_s$. The background material is silica ($SiO_2$) which is industrially accessible.

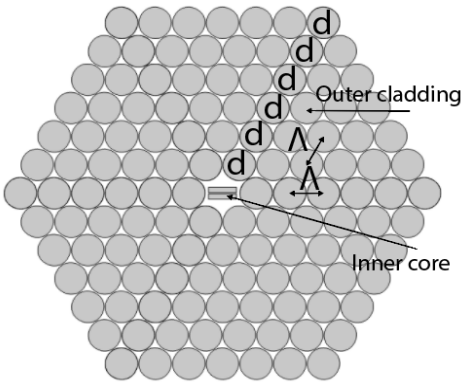


(a)

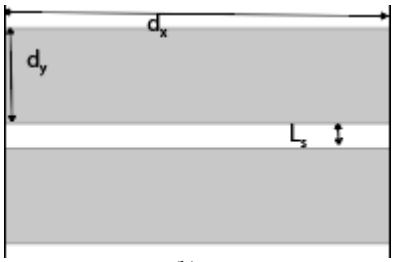


(b)

Fig. 1 (a) Geometric view of the suggested HNL- PCF (b) magnified view of core.

## III. Simulation and Result

Finite Element Method (FEM) is used to study different optical and electrical characteristics of the proposed design. COMSOL MULTIPHYSICS 5.0 is used to simulate the full design. Modal analysis has been studied by solving the Eigen value problems drawn from Maxwell's equations. A perfectly matched layer (PML) is placed at the outmost ring to avert reflection [9]. Since refractive indices depend on wavelength, Sellmeier's constants for silica ($SiO_2$) and GaP are directly employed in simulation to improve the accuracy. Once modal refractive index, $\eta_{eff}$ is obtained, other parameters like chromatic dispersion $D(\lambda)$, nonlinear coefficient $\gamma$, confinement loss $L_c$ and effective area $A_{eff}$ be able to be tailored from their equations [11]–[14].

$$\gamma = \frac{2\pi n_2}{\lambda A_{eff}} \tag{1}$$

$$A_{eff} = \frac{\left(\iint |E|^2 \, dxdy\right)^2}{\iint |E|^4 \, dxdy} \tag{2}$$

$$L_c = \frac{20\times 10^6}{\ln(10)} k_0 Im[\eta_{eff}] \tag{3}$$

$$D(\lambda) = -\frac{\lambda}{c}\frac{d^2 \,\mathrm{Re}[\eta_{eff}]}{d\lambda^2} \tag{4}$$

Where, $Re\,[\eta_{eff}]$ and $Im\,[\eta_{eff}]$ are the real and imaginary part of the effective refractive index, respectively; $c$ is the velocity of light in void, $\lambda$ is the operating wavelength, $E$ is the field vector, $k_0 = \frac{2\pi}{\lambda}$ ,is the wave number in vacuum; $n_2$ is the Kerr constant. For GaP, the $n_2 = 6.63 \times 10^{-18}$ $m^2W^{-1}$ [10]. Three termed Sellmeier formula for silica ($SiO_2$) and GaP are directly included in simulation.

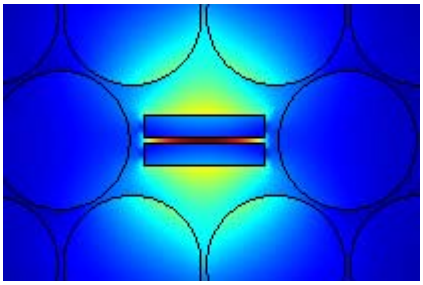

Fig. 2 Poynting vector profile of the proposed HNL-PCF.

Fundamental mode field distribution of the proposed fiber with parameters $\Lambda$ = 0.75 µm, d = 0.58 µm, $d_x$ = 0.5 µm, $d_y$ = 0.096 µm and $L_s$ = 0.12 µm is depicted in Fig. 2. It is seeming that fundamental mode field is well restrained in slot section of GaP meaning lesser effective mode be able to be achieved from the proposed fiber. Dependence of the effective mode on wavelength of the proposed fiber is explained in Fig. 3. From Fig 3, it is understood that effective area at 1550 nm wavelength is 0.3 $\mu m^2$, which is very small. This small area of the effective mode gives rise of huge nonlinearity.

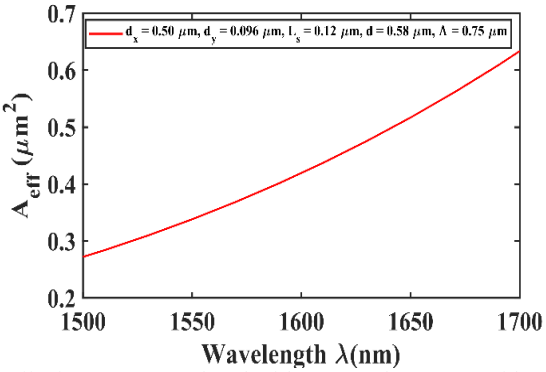


Fig. 3 Effective area vs. wavelength of the proposed HNL-PCF with parameters $\Lambda$ = 0.75 µm, d = 0.58 µm, $d_x$ = 0.5 µm, $d_y$ = 0.096 µm and $L_s$ = 0.12 µm.

Fig. 4 (a) shows the effects of variation in length of GaP strip on nonlinearity. It is apparent that increasing strip length $d_x$ results in decreasing nonlinearity from 1500 nm to 1700 nm. At 1500 nm, nonlinearity is up to 10 × $10^4$ $W^{-1}km^{-1}$ whereas it would be up to 4 × $10^4$ $W^{-1}km^{-1}$ at 1700 nm wavelength. Almost alike outcomes are deduced for increasing strip width $d_y$ in Fig. 4 (b). For lower strip width, HNL-PCF has higher nonlinearity. This is because, by decreasing the strip length or width improves the light confinement in HNL-PCF which reduces the effective area and enhances the nonlinear coefficient.

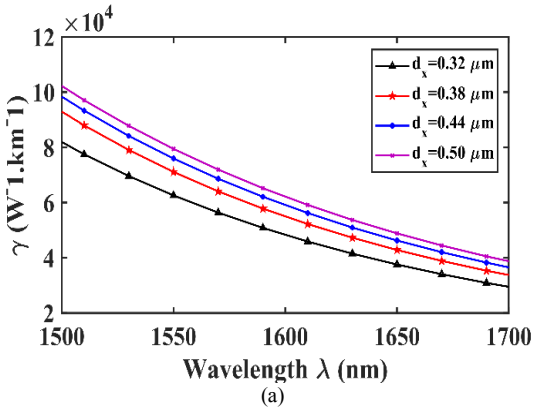


(a)

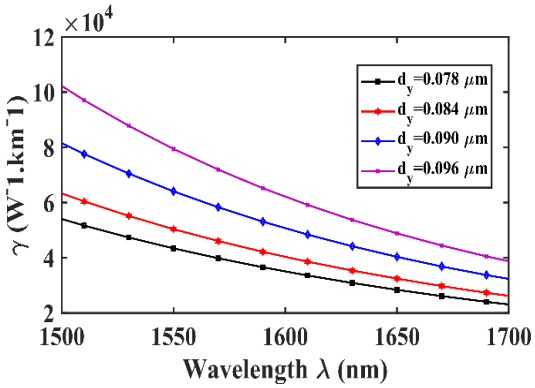


(b)

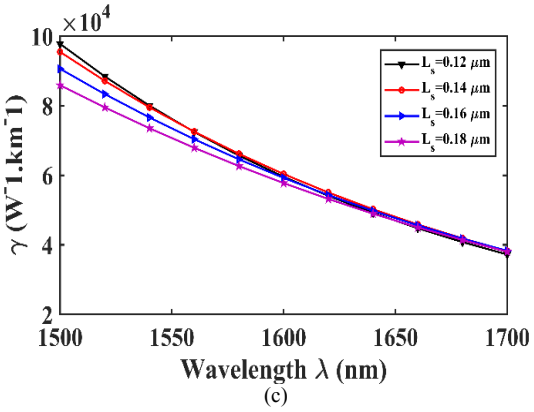


(c)

Fig. 4 Nonlinear coefficient vs. wavelength for variation of (a) strip length $d_x$, with $d_y$ = 0.096 µm, $L_s$ = 0.12 µm, Λ = 0.75 µm and d = 0.58 µm; (b) strip width $d_y$, with $d_x$ = 0.50 µm, $L_s$ = 0.12 µm, Λ = 0.75 µm and d = 0.58 µm and (c) slot width $L_s$, with $d_x$ = 0.50 µm, $d_y$ = 0.096 µm, $L_s$ = 0.12 µm, Λ = 0.75 µm and d = 0.58 µm.

Fig. 4 (c) exhibits the effects of changing slot width on nonlinearity. It is clear that, increasing $L_s$ reduces nonlinearity. At 1550 nm wavelength nonlinearity is 9.8 × $10^4$ $W^{-1}km^{-1}$ when $L_s$ = 0.12 µm. However when $L_s$ = 0.18, nonlinear coefficient reduces to 8.4 × $10^4$ $W^{-1}km^{-1}$. Since the slot width effective area increases, results in subsequent decrease in nonlinearity.

Chromatic dispersion of the suggested HNL-PCF is demonstrated in Fig 5(a), 5(b) and 5(c) by altering the parameters of $d_x$, $d_y$ and $L_s$, respectively. In Fig 5(a), chromatic dispersion decreases with the increment of strip length $d_x$. At the communication band dispersion reaches up to −9000 ps/(nm-km). In Fig 5(b), strip width $d_y$ is altered to see the effect of it. With the increment of strip width $d_y$, chromatic dispersion also increases and reaches up to −7500 ps/(nm-km) at 1550 nm wavelength. The effect of slot width $L_s$ is explored in Fig. 5(c). From Fig. 5(c), it is clear that with the maximum slot width, we obtain the less dispersion. When the slot width $L_s$ = 0.12 µm, we acquire maximum dispersion of −8000 ps/(nm-km) at communication band.

Confinement loss of the suggested HNL-PCF is depicted in Fig 6. In Fig 6(a), strip length of GaP is varied keeping other parameters constant. With the increment of strip length $d_x$, confinement loss decreases. Similar effect is shown for the increment of strip width $d_y$. In both, case confinement loss can be as low as $10^{-3}$ dB/km. However, slot width has opposite effect. With the slot width $L_s$, confinement loss increases.

In simulation, we varied the slot width $L_s$, strip length $d_x$ and strip width $d_y$ keeping other parameters unaltered; i.e., pitch Λ = 0.75 µm and air holes have diameter of d = 0.58 µm due to core length and width provided major effect on nonlinearity than cladding. Moreover, chromatic dispersion of the suggested HNL-PCF mainly depends on the $L_x$, $d_x$ and $d_y$ and these are justified by varying the core diameter which has less effect than strip width, length and slot width.

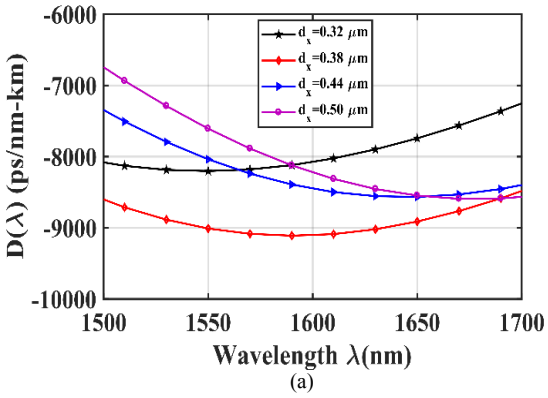


(a)

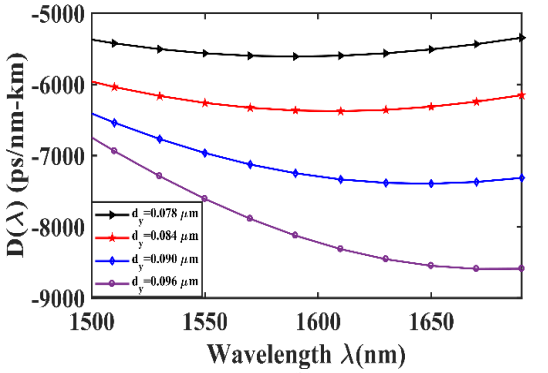


(b)

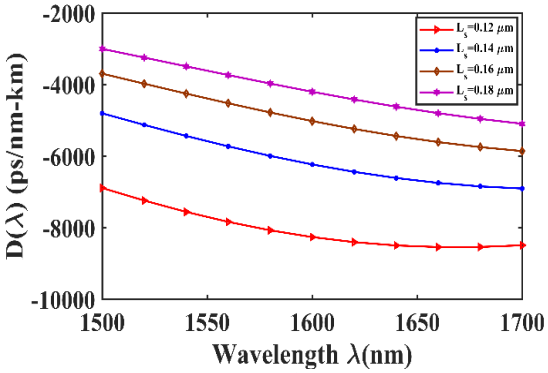


(c)

Fig. 5 Effects on chromatic dispersion depending on wavelength for variation of (a) strip span $d_x$, with $d_y$ = 0.096 µm, $L_s$ = 0.12 µm, Λ = 0.75 µm and d = 0.58 µm; (b) strip width $d_y$, with $d_x$ = 0.50 µm, $L_s$ = 0.12 µm, Λ = 0.75 µm and d = 0.58 µm and (c) slot width $L_s$, with $d_x$ = 0.50 µm, $d_y$ = 0.096 µm, $L_s$ = 0.12 µm, Λ = 0.75 µm and d = 0.58 µm.

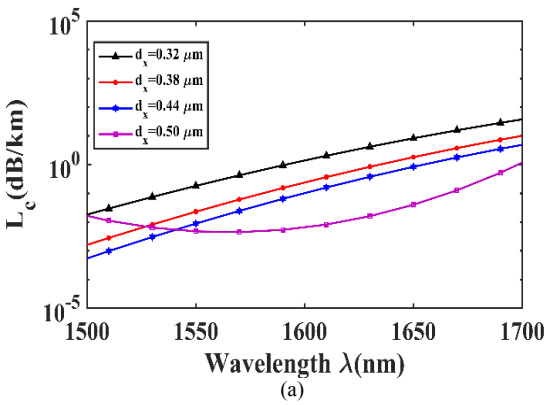


(a)

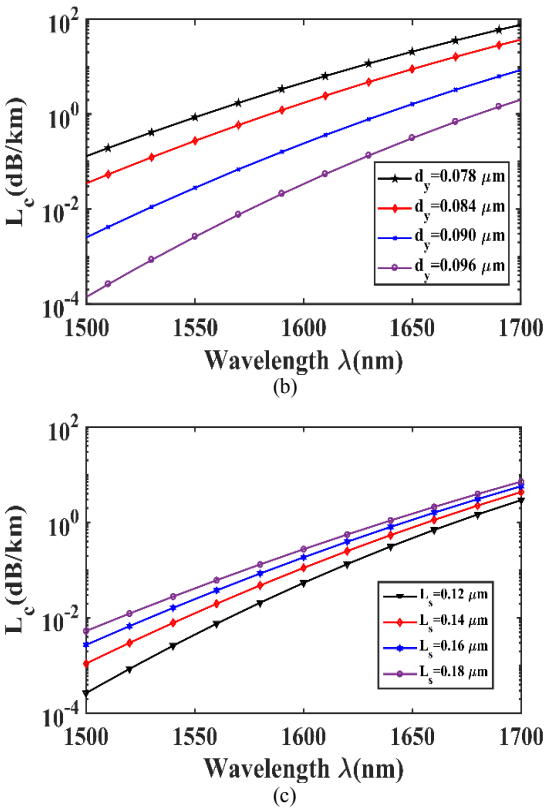


Fig. 6 Confinement loss vs. wavelength for variation of (a) strip span $d_x$, with $d_y$ = 0.096 μm, $L_s$ = 0.12 μm, Λ = 0.75 μm and d = 0.58 μm; (b) strip width $d_y$, with $d_x$ = 0.50 μm, $L_s$ = 0.12 μm, Λ = 0.75 μm and d = 0.58 μm and (c) slot width $L_s$, with $d_x$ = 0.50 μm, $d_y$ = 0.096 μm, $L_s$ = 0.12 μm, Λ = 0.75 μm and d = 0.58 μm.

## IV. Conclusion

In our paper, we numerically examined different optical properties of HNL-PCF using FEM and COMSOL MULTIPHYSICS as simulator. The proposed HNL-PCF shows a very high nonlinearity up to $10 \times 10^4$ $W^{-1}km^{-1}$ and a very low confinement loss of $10^{-3}$ dB/km at 1550 nm wavelength. The fiber can have potential application in supercontinuum generation, optical parameter amplification and broadband dispersion compensation. To our best knowledge, nonlinearity that HNL-PCF shows is the highest compared to recently published articles.

## References

[1] A. Wang *et al.*, "Visible Supercontinuum Generation With Sub-Nanosecond 532-nm Pulses in All-Solid Photonic Bandgap Fiber," *IEEE Photonics Technol. Lett.*, vol. 24, no. 2, pp. 143–145, Jan. 2012.

[2] Y. P. Yatsenko and A. D. Pryamikov, "Parametric frequency conversion in photonic crystal fibres with germanosilicate core," *J. Opt. A Pure Appl. Opt.*, vol. 9, no. 7, pp. 716–722, Jul. 2007.

[3] J. Liao and T. Huang, "Highly nonlinear photonic crystal fiber with ultrahigh birefringence using a nano-scale slot core," *Opt. Fiber Technol.*, vol. 22, pp. 107–112, Mar. 2015.

[4] T. Huang, J. Liao, S. Fu, M. Tang, P. Shum, and D. Liu, "Slot Spiral Silicon Photonic Crystal Fiber With Property of Both High Birefringence and High Nonlinearity," *IEEE Photonics J.*, vol. 6, no. 3, pp. 1–7, Jun. 2014.

[5] P. Li and J. Zhao, "Polarization-dependent coupling in gold-filled dual-core photonic crystal fibers," *Opt. Express*, vol. 21, no. 5, p. 5232, Mar. 2013.

[6] J. Liao, J. Sun, M. Du, and Y. Qin, "Highly Nonlinear Dispersion-Flattened Slotted Spiral Photonic Crystal Fibers," *IEEE Photonics Technol. Lett.*, vol. 26, no. 4, pp. 380–383, Feb. 2014.

[7] M. N. Amin and M. Faisal, "Highly nonlinear polarization-maintaining photonic crystal fiber with nanoscale GaP strips," *Appl. Opt.*, vol. 55, no. 35, p. 10030, Dec. 2016.

[8] J. Hou, D. Bird, A. George, S. Maier, B. Kuhlmey, and J. C. Knight, "Metallic mode confinement in microstructured fibres," *Opt. Express*, vol. 16, no. 9, p. 5983, Apr. 2008.

[9] S. Selleri, L. Vincetti, A. Cucinotta, and M. Zoboli, "Complex FEM modal solver of optical waveguides with PML boundary conditions," *Opt. Quantum Electron.*, vol. 33, no. 4/5, pp. 359–371, 2001.

[10] M. B. Mia, K. R. Chowdhury, A. Bala, and M. Faisal, "Large Negative Flattened Dispersion over the S+C+L Band Using Highly Birefringent Photonic Crystal Fiber," Oct. 2017.

[11] A. Bala, K. R. Chowdhury, M. B. Mia, and M. Faisal, "Highly birefringent, highly negative dispersion compensating photonic crystal fiber," *Appl. Opt.*, vol. 56, no. 25, p. 7256, Sep. 2017.

[12] A. B. Ani and M. Faisal, "Ultra-flattened broadband dispersion compensating photonic crystal fiber with ultra-low confinement loss," in *2016 9th International Conference on Electrical and Computer Engineering (ICECE)*, 2016, pp. 243–246.

[13] M. B. Mia, M. Faisal, S. I. Naz, A. Bala, and K. R. Chowdhury, "Heptagonal Photonic Crystal Fiber for Dispersion Compensation with a Very Low Confinement Loss," Sep. 2017.

[14] F. Liu *et al.*, "Three-photon absorption and Kerr nonlinearity in undoped bulk GaP excited by a femtosecond laser at 1040 nm," *J. Opt.*, vol. 12, no. 9, p. 95201, Sep. 2010.

# A 63fs Soliton Pulse Generation by Compression of Higher Order Soliton in Linear Dispersion Decreasing Fiber

Shah Md. Salimullah[#], Mohammad Faisal[*], Md. Saddam Hossain[#], Md. Monir Ahamed[#], Md. Shakhawath Hossain[#]
[#]Department of Electrical and Electronic Engineering, Bangladesh Army International University of Science and Technology (BAIUST), Comilla.
[*]Department of Electrical and Electronic Engineering, Bangladesh University of Engineering and Technology (BUET), Dhaka-1205.
[#]saikateee07@gmail.com,[*]mdfaisal@eee.buet.ac.bd

***Abstract*— A 2.05 m long linear dispersion decreasing fiber (LDDF) has been proposed for higher-order ultrashort soliton compression for nm-pm range soliton generation. We have obtained numerically ultrashort soliton of 63 fs after compression in LDDF. The spatial dimension has been found as 523.5 pm. Nonlinear Schrödinger equation (NLSE) has been solved using split-step Fourier (SSF) method for numerical analysis of ultrashort soliton propagation and compression. Such compressed pulse may have extensive applications in cancer cell treatment for creating smaller beam spot.**

***Keywords*— Liner dispersion decreasing fiber, split-step Fourier method, optical soliton**

## I. INTRODUCTION

Soliton pulse has become a subject of tremendous investigation. Ultrashort optical pulses with soliton nature possess vast applications in different fields like nonlinear optics, high speed communications [1], material science and processing (e.g., femtosecond laser ablation), attosecond physics etc. In recent years femtosecond pulse has become multifunctional surgery means for surgery by refraction [2], inner ear surgery [3], dental [4, 5], cardiovascular surgery [6] and so forth. At the same time, ultrashort soliton has become prominent in removal of tissue as well as cancer cell treatment [7, 8]. Side effects associated with radiation therapy [9] in treatment of cancer occur because of high doses of radiation (which has spatial dispersion in mm range) used to destroy cancer cells. As spatial dispersion of radiation is in mm range it affects healthy tissues and cells located near the treatment area. However, the ultrashort soliton maintains spatial dimension (nm or pm range [10]) lower than that of cancer cell, hence it may causes no side effect other than removing the specific affected tissue. To get this ultrashort pulse, compression is one of the techniques [11-16].

Although soliton of width 115 fs [17] and 100 fs [18] has been obtained using compression technique in DDF, however, the impact of the higher-order effects upon such pulse are not considered in those studies. At the same time most works use long length of DDF. In our study, higher-order effects like third-order dispersion (TOD), intrapulse Raman scattering (IRS) and self-steepening (SS) have been considered. The pulse width has been calculated as 63 fs after compression in our proposed LDDF with length of 2.05 m.

In this paper considering higher-order linear and nonlinear effects we have analyzed the soliton compression in LDDF according to nonlinear Schrödinger equation (NLSE). Sect. 2 describes basic physics of ultrashort soliton propagation. Compression of ultrashort fundamental soliton has been explored with the designed dispersion profile of LDDF in Sect. 3. Sect. 4 comprises LDDF based higher-order soliton compression up to 5th order.

## II. THEORETICAL ANALYSIS

Ultrashort (pulse width $\leqslant$1ps) optical pulse propagation through single-mode fiber can be given by the generalized NLSE considering higher-order effects as [19]

$$\frac{\partial E}{\partial z}+\frac{\alpha E}{2}+\frac{i\beta_2}{2}\frac{\partial^2 E}{\partial T^2}-\frac{\beta_3}{6}\frac{\partial^3 E}{\partial T^3}=i\gamma\left(E|E|^2+\frac{i}{\omega_0}\frac{\partial}{\partial T}E|E|^2-T_R E\frac{\partial|E|^2}{\partial T}\right) \quad (1)$$

where E stands for the complex envelop of the optical pulse, z describes the pulse propagation distance, T is for time, $\alpha$ gives the coefficient of fiber loss, $\beta_2$ and $\beta_3$ explains the second-order dispersion and TOD respectively. $T_R$ is the time related to Raman gain, the factor $1/\omega_0$ stands for the self-steepening effect and $\gamma$ is the nonlinearity. The normalized amplitude U can be given as

$$E(z,\tau)=P_0\left(\sqrt{\exp(-0.5\alpha z)}\right)U(z,\tau) \quad (2)$$

Where incident pulse peak power is given by $P_0$. In Eq. (2) fiber loss is denoted by the exponential factor. Hence the Eq. (1) takes the form

$$\frac{\partial U}{\partial z}+i\frac{\beta_2}{2L_D}\frac{\partial^2 U}{\partial\tau^2}-\frac{\beta_3}{6L'_D}\frac{\partial^3 U}{\partial\tau^3}=i\frac{e^{-\alpha Z}}{L_{NL}}\left(U|U|^2+is\frac{\partial}{\partial\tau}U|U|^2-\tau_R U\frac{\partial|U|^2}{\partial\tau}\right) \quad (3)$$

Where $L_D$ and $L'_D$ explains second-order and third-order dispersive length respectively and $L_{NL}$ explains nonlinear length defined as

978-1-5386-3374-8/17/$31.00 ©2017 IEEE

$$L_{NL}=\frac{1}{\gamma P_0}, L_D=\frac{T_0^{\,2}}{|\beta_2|}, L'_D=\frac{T_0^{\,3}}{|\beta_3|} \tag{4}$$

In Eq. (3) self-steepening effect and intrapulse Raman scattering are followed by the factor s and $\tau_R$ respectively, and are given by

$$\tau_R=\frac{T_R}{T_0}, s=\frac{\lambda}{2\pi c T_0} \tag{5}$$

Where $T_0$ defines the input pulse width. Although the two effects are quite negligible for picoseconds pulses but for ultrashort pulses (pulse width $T_0$<1 ps) should be considered. Considering normalized amplitude (U), distance (Z) and time ($\tau$) the Eq. (3) can be written as

$$\frac{\partial U}{\partial Z}+i\frac{1}{2}\frac{\partial^2 U}{\partial \tau^2}-i\frac{1}{6}\frac{\partial^3 U}{\partial \tau^3}=iN^2e^{-\alpha z}\left(U|U|^2+\frac{is}{\omega_0}\frac{\partial}{\partial \tau}U|U|^2-\tau_R U\frac{\partial |U|^2}{\partial \tau}\right) \tag{6}$$

Here $U=\frac{A}{\sqrt{P_0}}, \tau=\frac{T}{T_0}, Z=\frac{z}{L_D}$ (7)

For soliton pulse, $T_0$ is as follows

$$T_0=\frac{T_{FWHM}}{1.763} \tag{8}$$

Here N stands for the soliton order and is expressed as

$$N^2=\frac{L_D}{L_{NL}}=\frac{\gamma P_0 T_0^{\,2}}{|\beta_2|} \tag{9}$$

We have observed compression of ultrashort fundamental and higher-order soliton and explored our analysis solving Eq. (3) using SSF method. The time-bandwidth product for sech pulse is always 0.32. With temporal and spectral evolution of both fundamental and higher-order ultrashort soliton, the time-bandwidth product has also been checked.

## III. Fundamental Soliton Dynamics in LDDF

Soliton dynamics has been investigated for N = 1 using NLSE. Compression of fundamental soliton has been observed in LDDF. We have observed the temporal and spectral evolution of compressed soliton in an LDDF with following dispersion profile [20]:

$$\beta_{2n}=\beta_{2p}\left(1+\frac{z}{\beta L}-\frac{z}{L}\right) \tag{10}$$

Where $\beta_{2n}$, $\beta_{2p}$ are the changing group velocity dispersion (GVD) and starting GVD respectively. Here $\beta=\beta_{2p}/\beta_{2L}$, $\beta_{2L}$ = final GVD and L is the total fiber length. We have explored fundamental soliton compression in LDDF with parameters as full width half maximum (FWHM) pulse width, $T_{FWHM}$ = 2ps (initial pulse is chirp free), peak power, $P_0$ = 1.6W, $\beta_{2P}$ = –10 ps$^2$ /km, $\beta_{2L}$ = –1 ps$^2$/km, $\beta_3$ = 0.029 ps$^3$/km, $\gamma$ = 5, s = 0.29, and $\tau_R$ = 0.02. Although the GVD is decreasing along the length of DDF, TOD has been considered constant. The time-bandwidth product of the soliton pulse has been checked as 0.32 that means adiabatic compression has been happened during the propagation. Fig.1 (a) gives the temporal evolution whereas Fig.1 (b) shows the spectral evolution of ultrashort fundamental soliton compression in LDDF.

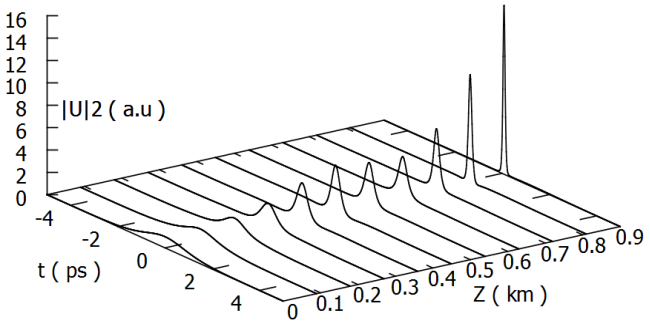


**(a)**

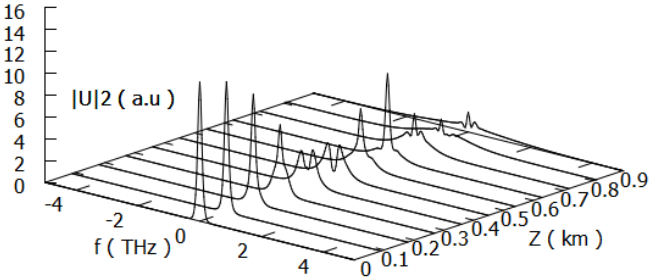


**(b)**

Fig. 1: Compression of fundamental soliton in LDDF, (a) Temporal Evolution and (b) Spectral Evolution.

Higher-order effects are not observed since pulse width is more than 1ps. The 2ps pulse has been compressed up to 200fs using LDDF with 0.9 km length. Fig. 2 shows pulse width (FWHM) vs. distance curve for fundamental soliton in LDDF. In LDDF, dispersion decreases with distance, so nonlinearity dominates gradually and consequently the pulse width decreases. With decrease of pulse width, the peak power increases, so we have to take care of that power to keep it below the capacity of fiber.

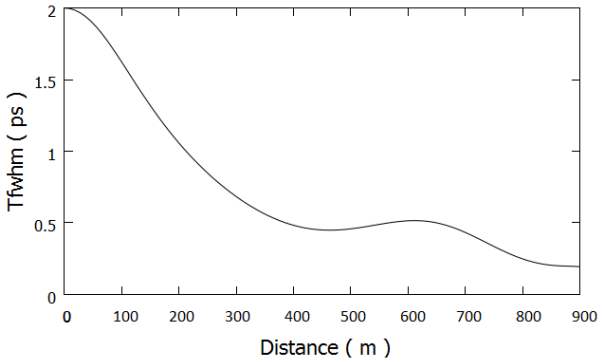


Fig. 2: Pulse width (FWHM) vs. distance curve for fundamental soliton in LDDF.

## IV. Higher Order Soliton Dynamics in LDDF

Here we will see the compression of higher-order soliton in LDDF. Using LDDF the compression of second order soliton has been shown in Fig. 3 (a) with parameters used as $T_{FWHM}$ = 500fs (initial pulse is chirp free), $P_0$ = 100W, $\beta_{2P}$ = –10 $ps^2$/km, $\beta_{2L}$ = –1 $ps^2$/km, $\beta_3$ = 0.029 $ps^3$/km, $\gamma$ = 5, s = 0.29, $\tau_R$ = 0.02, N = 2. What we have observed is that broadening of pulse is happened within first 10m of LDDF and then compression occurs in next 15m. The pulse width increases from 500fs to 800fs in first 10m and then decreases from 800fs to 340fs in next 15m through LDDF. This is because initially dispersive effect dominates and hence pulse broadening occurs (first 10m of LDDF in Fig. 3 (a)). With increase in fiber length dispersion decreases and nonlinear effect dominates here and we get pulse compression (next 15m of LDDF). The input and output pulse shape has been shown in Fig. 3 (b).

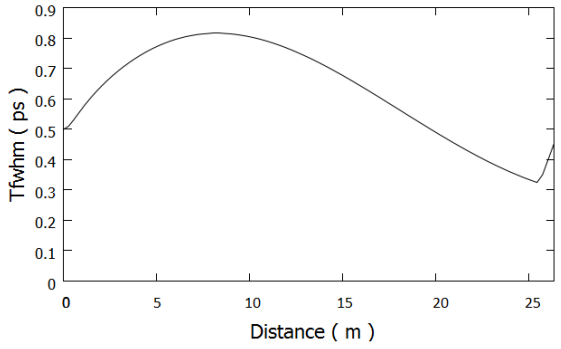


**(a)**

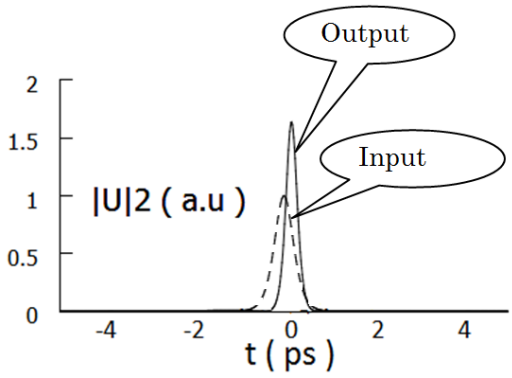


**(b)**

Fig. 3: (a) Pulse width (FWHM) vs. distance curve for second - order soliton in LDDF, (b) Input pulse and compressed output pulse after propagation of 25 m.

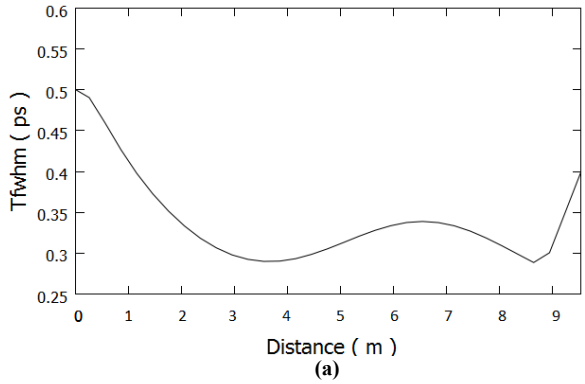


**(a)**

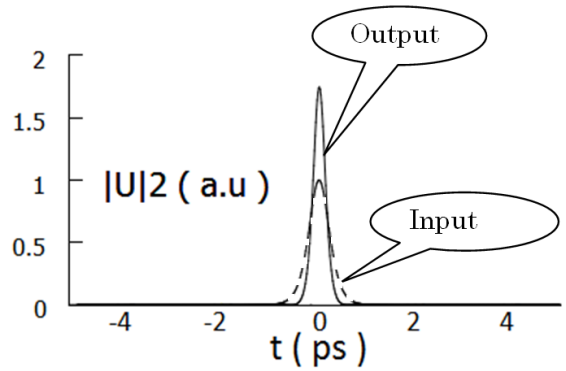


**(b)**

Fig. 4: (a) Pulse width (FWHM) vs. distance curve for third - order soliton in LDDF, (b) Input pulse and compressed output pulse after propagation of 8.5 m.

Fig. 4 shows the third-order soliton compression in LDDF. A smooth curve has been observed in LDDF that indicates compression of third-order soliton into 300fs from 500fs which is clear from Fig. 4 (a). The input/output pulse shape after compression has been shown in Fig. 4 (b).

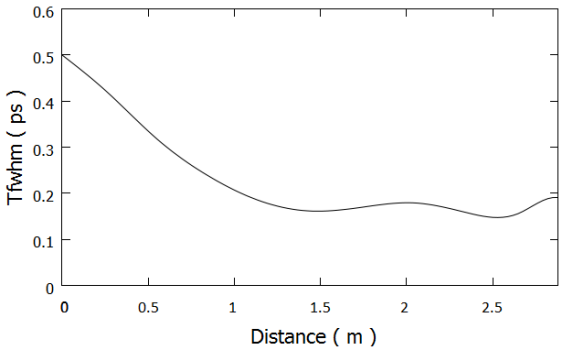


**(a)**

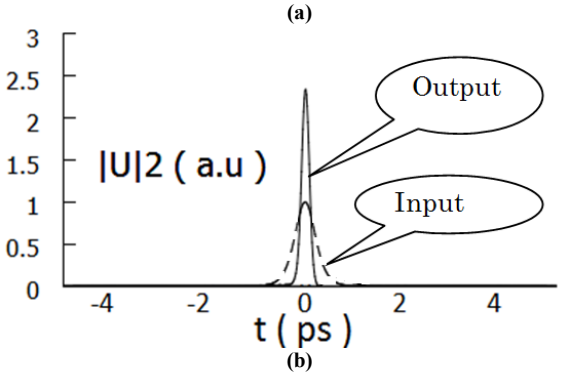


**(b)**

Fig. 5: (a) Pulse width (FWHM) vs. distance curve for fourth - order soliton in LDDF, (b) Input pulse and compressed output pulse after propagation of 2.5 m.

Let us see fourth-order sub-picosecond soliton compression shown in Fig. 5 for LDDF. We have found a very good compression of 500fs pulse into 150fs in LDDF briefed by Fig. 5 (a). Input pulse and output pulse after compression has been shown in Fig. 5 (b). For fifth-order soliton, the best compression has been found using LDDF where 500fs pulse is compressed to 63fs for 2.05m of fiber as shown in Fig. 6.

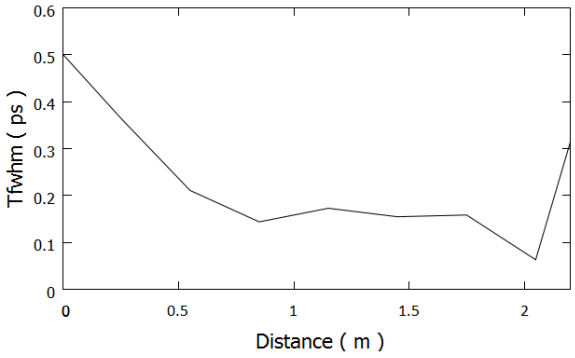


**(a)**

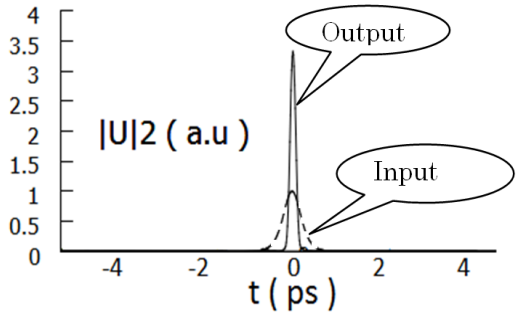


**(b)**

Fig. 6: (a) Pulse width (FWHM) vs. distance curve for fifth - order soliton in LDDF, (b) Input pulse and output pulse after compression through propagation of 2.05 m.

It is evident that with the more the soliton order increases, pulse width decreases at the end of LDDF. However, the peak power increases with increase of soliton order which could be so high and go beyond the tolerable limit of fiber. Even it may damage the fiber. Furthermore, higher-order dispersive and nonlinear effects will also be enhanced and pulse distortion may occur. The order of soliton and optimum length of LDDF for compression will be regulated by these factors.

## V. Result and Discussion

All the data for ultrashort soliton compression in LDDF are given in Table I.

TABLE I
PULSE WIDTH AFTER COMPRESSION AND SPATIAL SOLITON DIMENSION FOR 500FS INPUT PULSE

| Soliton order | Pulse width (post-compression) in LDDF | Spatial dimension of soliton in LDDF | Length of LDDF |
|---|---|---|---|
| 2nd | 340fs | 2.72nm | 25m |
| 3rd | 300fs | 2.408nm | 9m |
| 4th | 150fs | 1.2nm | 3m |
| 5th | 63fs | 523.5pm | 2.05m |

We can summarize the results for ultrashort fundamental and higher-order soliton compression in LDDF as follows. For 2ps input pulse, the compressed soliton FWHM has been found 200fs in LDDF. Second-order soliton compression has been explored with 500fs input pulse width. The compressed pulse width has been found about 340fs in LDDF. Again in fourth-order soliton compression, LDDF causes compression upto 150fs. Finally in fifth-order soliton compression, the best output has been observed in LDDF. The compressed pulse width is as low as 63fs. The spatial dimension has also been calculated which maintains nm range for second, third and fourth order soliton and the last one occupies 523.5pm.

From all of the above comparison and outcomes for ultrashort optical soliton compression for fundamental and higher-order soliton up to fifth order, we can say that LDDF has performed compression with excellence which has been shown in Table I.

## VI. Conclusions

Considering higher order dispersive effects i.e. TOD and higher order nonlinear effects i.e. SS and IRS, the compression of ultrashort optical soliton in LDDF has been investigated. LDDF of smaller length has been proposed for higher-order ultrashort soliton compression for formation of soliton in nm-pm range. Employing a small length of 2.05 m LDDF, we have obtained ultrashort soliton of 63 fs after compression. The spatial dimension has been found as 523.5pm.

## References

[1] S. M. Salimullah and M. Faisal, "Ultrashort soliton propagation in multi-clad optical fibers with per channel data rate of 1Tb/s," in *Telecommunications and Photonics (ICTP), 2015 IEEE International Conference on*, 2015, pp. 1-5.

[2] S. I. Mian and R. M. Shtein, "Femtosecond laser-assisted corneal surgery," *Current opinion in ophthalmology,* vol. 18, pp. 295-299, 2007.

[3] B. Schwab, D. Hagner, W. Müller, H. Lubatschowski, T. Lenarz, and R. Heermann, "Bone ablation using ultrashort laser pulses. A new technique for middle ear surgery," *Laryngo-rhino-otologie,* vol. 83, pp. 219-225, 2004.

[4] J. Serbin, T. Bauer, C. Fallnich, A. Kasenbacher, and W. Arnold, "Femtosecond lasers as novel tool in dental surgery," *applied surface science,* vol. 197, pp. 737-740, 2002.

[5] R. F. Lizarelli, M. Costa, E. Carvalho-Filho, F. Nunes, and V. S. Bagnato, "Selective ablation of dental enamel and dentin using femtosecond laser pulses," *Laser Physics Letters,* vol. 5, p. 63, 2007.

[6] H. Lubatschowski, A. Heisterkamp, F. Will, J. Serbin, T. Bauer, C. Fallnich, *et al.*, "Ultrafast laser pulses for medical applications," in *Proc. SPIE*, 2002, pp. 38-49.

[7] I. Amiri, A. Nikoukar, J. Ali, and P. Yupapin, "Ultra-short of pico and femtosecond soliton laser pulse using microring resonator for cancer cells treatment," *Quantum Matter,* vol. 1, pp. 159-165, 2012.

[8] M. Jalil, J. Phelawan, M. Aziz, T. Saktioto, C. Ong, and P. P. Yupapin, "Acne vulgarism treatment using ultra-short laser pulse generated by micro-and nano-ring resonator system," *Artificial cells, nanomedicine, and biotechnology,* vol. 41, pp. 92-97, 2013.

[9] D. P. Dearnaley, V. S. Khoo, A. R. Norman, L. Meyer, A. Nahum, D. Tait, *et al.*, "Comparison of radiation side-effects of conformal and conventional radiotherapy in prostate cancer: a randomised trial," *The Lancet,* vol. 353, pp. 267-272, 1999.

[10] S. M. Salimullah and M. Faisal, "Femtosecond Soliton Formation by Higher-Order Soliton Compression in Linear Dispersion Decreasing Fiber," in *Proceedings of 20th Microoptics Conference (MOC'15)*, Fukuoka, Japan., 2015, pp. paper no. H-11.

[11] T. Murphy, "10-GHz 1.3-ps pulse generation using chirped soliton compression in a Raman gain medium," *IEEE Photonics Technology Letters,* vol. 14, pp. 1424-1426, 2002.

[12] C.-C. Chang, A. Vengsarkar, D. Peckham, and A. Weiner, "Broadband fiber dispersion compensation for sub-100-fs pulses with a compression ratio of 300," *Optics letters,* vol. 21, pp. 1141-1143, 1996.

[13] Q. Li, P. Wai, K. Senthilnathan, and K. Nakkeeran, "Modeling self-similar optical pulse compression in nonlinear fiber Bragg grating using coupled-mode equations," *Journal of Lightwave Technology,* vol. 29, pp. 1293-1305, 2011.

[14] Q. Li, K. Senthilnathan, K. Nakkeeran, and P. Wai, "Nearly chirp-and pedestal-free pulse compression in nonlinear fiber Bragg gratings," *JOSA B,* vol. 26, pp. 432-443, 2009.

[15] S. M. Salimullah, "Analysis of higher-order soliton compression for formation of ultra-short pulses," 2015.

[16] J. H. Lee, T. Kogure, and D. J. Richardson, "Wavelength tunable 10-GHz 3-ps pulse source using a dispersion decreasing fiber-based nonlinear optical loop mirror," *IEEE Journal of selected topics in quantum electronics,* vol. 10, pp. 181-185, 2004.

[17] S. V. Chernikov, D. Richardson, D. Payne, and E. Dianov, "Soliton pulse compression in dispersion-decreasing fiber," *Optics letters,* vol. 18, pp. 476-478, 1993.

[18] P. Wai and W.-h. Cao, "Ultrashort soliton generation through higher-order soliton compression in a nonlinear optical loop mirror constructed from dispersion-decreasing fiber," *JOSA B,* vol. 20, pp. 1346-1355, 2003.

[19] G. Agrawal, *Applications of nonlinear fiber optics*: Academic press, 2001.

[20] D. Chao-Qing and C. Jun-Lang, "Ultrashort optical solitons in the dispersion-decreasing fibers," *Chinese Physics B,* vol. 21, p. 080507, 2012.

# Optimum Fiber Profile for Ultrashort Pulse Formation by Higher-Order Soliton Compression

Shah Md. Salimullah[#], Mohammad Faisal[*], Md. Saddam Hossain[#], Md. Monir Ahamed[#], Md. Shakhawath Hossain[#], Rakib Hossain[#]

[#]Department of Electrical and Electronic Engineering, Bangladesh Army International University of Science and Technology (BAIUST), Comilla.

[*]Department of Electrical and Electronic Engineering, Bangladesh University of Engineering and Technology (BUET), Dhaka-1205.

[#]saikateee07@gmail.com,mdfaisal@eee.buet.ac.bd

*Abstract*— **Linear dispersion decreasing fiber (LDDF) profiles has been found nearly optimum in regards to the pulse width (63fs) of the compressed pulse. Based on ultrashort soliton compression a comparative study has been carried out among dispersion compensating fiber (DCF), fiber Bragg grating (FBG) and LDDF. Considering higher order effects compression of higher-order solitons, produces high-quality compressed pulses in femtosecond regime. Nonlinear Schrödinger equation (NLSE) has been solved using split-step Fourier (SSF) method for numerical analysis of ultrashort soliton propagation and compression.**

***Keywords—Linear dispersion decreasing fiber, intrapulse Raman scattering, optical soliton***

## I. INTRODUCTION

For a few decades soliton pulse has become a subject of tremendous investigation as it offers the dynamic balance between self-phase modulation (SPM) and group-velocity dispersion (GVD). Extreme and single-cycle nonlinear optics, light-matter interactions, attosecond physics, higher-order harmonic generation, femtosecond laser ablation etc. are the extensive applications of ultrashort optical pulses with soliton nature. In recent years femtosecond pulse is tremendously used in applications like ultra-speed communications [1] refractive surgery [2], ear surgery [3] and cardiovascular surgery [4]. Again ultrashort soliton has become prominent in tissue removal for cancer cell treatment [5, 6]. To get this ultrashort pulse, compression is one of the techniques [7-10]. DCF based soliton compression was previously studied [11]. Compression using FBG was also observed [12, 13]. As a compressor DDF is of great interest [14, 15] also.

Although soliton of width 115fs [15] and 100fs [16] has been obtained using compression technique in DDF, however, the impact of the higher-order effects upon such pulse are not considered in those studies. At the same time most works use long length of DDF. In our study, higher-order effects like third-order dispersion (TOD) as higher-order dispersive effects and self-steepening (SS) and intrapulse Raman scattering (IRS) as higher-order nonlinear effects have been taken into consideration. The pulse width has been calculated as 63fs after compression in our proposed LDDF of 2.05m length. In this paper, comparative study among different fibers (DCF, LDDF and FBG) has been carried out for ultrashort optical soliton compression using fundamental and higher order soliton up to 5th order. Among these three fibers, DDF with linear decreasing dispersion profile has been proposed as the best soliton compressor whereas the compressed pulse width has been demonstrated about 63fs and spatially 523.5pm. For numerical analysis, Nonlinear Schrödinger equation (NLSE) has been solved using split-step Fourier (SSF) method.

In this paper considering higher-order linear and nonlinear effects we have analyzed NLSE governed by which ultrashort soliton propagates. Section 2 describes the basic physics of ultrashort soliton propagation. Section 3 comprises LDDF based higher-order soliton compression up to 5th order and a comparison based on soliton compression among LDDF, DCF and FBG.

## II. ULTRASHORT SOLITON DYNAMICS

Ultrashort optical pulse (pulse width ≤1ps) through a single-mode fiber can be described by the generalized NLSE considering higher-order nonlinear and dispersive effects as [17]

$$\frac{\partial E}{\partial z}+\alpha\frac{E}{2}+\beta_2\frac{i}{2}\frac{\partial^2 E}{\partial T^2}-\beta_3\frac{1}{6}\frac{\partial^3 E}{\partial T^3}=i\gamma\left(|E|^2E+i\frac{1}{\omega_0}\frac{\partial}{\partial T}|E|^2E-T_R E\frac{\partial|E|^2}{\partial T}\right). \quad (1)$$

Here $E$ is the complex envelop of the optical pulse, $z$ is propagated distance by the pulse and $T$ is the time, $\alpha$ stands for the fiber loss coefficient, $\beta_2$ and $\beta_3$ are the second-order and third-order dispersion respectively. $\gamma$ is the nonlinearity coefficient, $T_R$ stands as time related to the slope of the Raman gain [17], the term with the factor $1/\omega_0$ is related to the self-steepening effect [17]. Normalized amplitude $U$ of the pulse can be written as

$$E(z,\tau)=P_0\sqrt{\exp(-0.5\alpha z)}U(z,\tau). \quad (2)$$

Here $P_0$ denotes the peak power of the incident pulse. The exponential factor in (2) accounts for fiber loss. Hence the (1) takes the form

$$\frac{\partial U}{\partial z}+\frac{i\beta_2}{2L_D}\frac{\partial^2 U}{\partial \tau^2}-\frac{\beta_3}{6L'_D}\frac{\partial^3 U}{\partial \tau^3}=\frac{ie^{-\alpha Z}}{L_{NL}}\left(|U|^2U+is\frac{\partial}{\partial \tau}|U|^2U-\tau_R U\frac{\partial |U|^2}{\partial \tau}\right) \quad (3)$$

Where $L_D$, $L'_D$ and $L_{NL}$ are the second-order dispersive length, third-order dispersive length and nonlinear length respectively defined as

$$L'_D=\frac{T_0^3}{|\beta_3|}, L_{NL}=\frac{1}{\gamma P_0}, L_D=\frac{T_0^2}{|\beta_2|}. \quad (4)$$

The parameters $s$ and $\tau_R$ govern the effects of self-steepening and intrapulse Raman scattering respectively, and are given as

$$s=\frac{\lambda}{2\pi c T_0}, \tau_R=\frac{T_R}{T_0}. \quad (5)$$

Where $T_0$ is the input pulse width. Both of these effects must be considered for ultrashort pulses ($T_0$ <1 ps). In terms of normalized amplitude U with normalized distance Z and normalized time $\tau$ the (3) can be written as

$$\frac{\partial U}{\partial Z}+\frac{i}{2}\frac{\partial^2 U}{\partial \tau^2}-\frac{i}{6}\frac{\partial^3 U}{\partial \tau^3}=iN^2e^{-\alpha z}\left(|U|^2U+s\frac{i}{\omega_0}\frac{\partial}{\partial \tau}|U|^2U-\tau_R U\frac{\partial |U|^2}{\partial \tau}\right) \quad (6)$$

$$\text{Here } Z=\frac{z}{L_D}, U=\frac{A}{\sqrt{P_0}}, \tau=\frac{T}{T_0}. \quad (7)$$

For soliton pulse, $T_0$ is as follows

$$T_0=\frac{T_{FWHM}}{1.763}. \quad (8)$$

Parameter N is the soliton order that provides the measure of the strength of the nonlinear response compared to the fiber dispersion, and is defined as

$$N^2=\frac{L_D}{L_{NL}}=\frac{\gamma P_0 T_0^2}{|\beta_2|}. \quad (9)$$

We have observed compression of ultrashort fundamental and higher-order soliton and explored our analysis with return to zero hyperbolic secant pulse of 50% duty cycle. (3) has been solved using SSF method to simulate the compression characteristics of soliton.

## III. Higher-Order Soliton Dynamics in LDDF, DCF and FBG

Compression of higher-order soliton has been observed in LDDF, DCF and FBG. At first we have observed the temporal and spectral evolution of compressed soliton in an LDDF with following dispersion profile [18]:

$$\beta_{2n}=\frac{\beta_{2P}}{L\beta}(L\beta+z-z\beta) \quad (10)$$

Where $\beta_{2n}$, $\beta_{2p}$ are the changing group velocity dispersion (GVD) and starting GVD respectively. Here $\beta=\beta_{2p}/\beta_{2L}$, $\beta_{2L}$ = final GVD and L is the total fiber length. Using LDDF the compression of second order soliton has been shown in Fig. 1(a) with parameters used as $T_{FWHM}$=500fs, $P_0$=100W, $\beta_{2p}$ =−10 ps$^2$ /km, $\beta_{2L}$ =−1 ps$^2$/km, $\beta_3$ = 0.029 ps$^3$/km, $\gamma$ = 5, s = 0.29, and $\tau_R$ = 0.02, N=2. What we have observed is that expansion happened within first 10m of LDDF and then compression occurs in rest 15m. The pulse turns its shape from 500fs to 800fs for first 10m and 800fs to 340fs after compression and propagation within next 15m through LDDF. Fig. 1(b) shows second-order soliton pulse compression as well as reduction in FWHM of pulse width with respect to fiber length in DCF. The fiber shows compression and expansion alternatively. Finally a 500fs input pulse has been compressed up to 480fs by DCF of 2m length. Fig. 1(c) shows second order soliton compression using FBG with fiber parameters of TABLE I, where expansion has observed beyond 3ps and then compression happened up to 2.5ps.

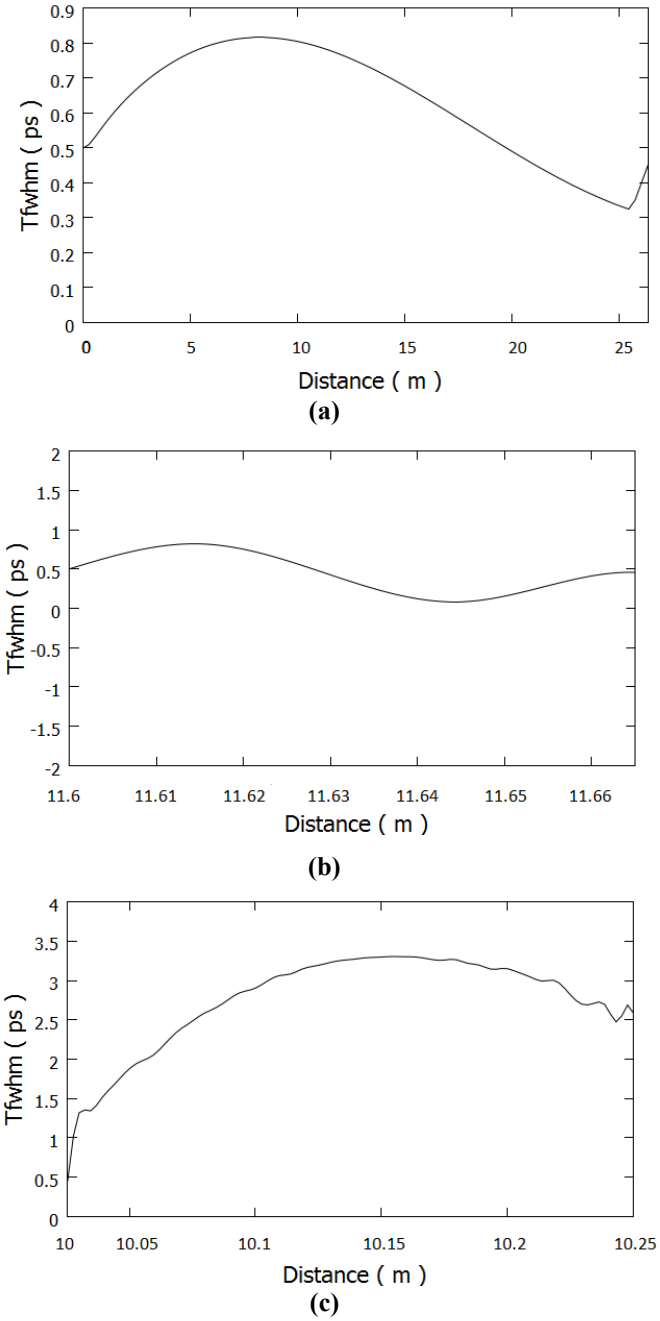


Fig. 1: Pulse width (FWHM) vs. distance curve for second - order soliton in (a) LDDF, (b) DCF and (c) FBG.

In comparison among LDDF, DCF and FBG for second order soliton compression, LDDF has performed best by compressing 500fs pulse into a 340fs pulse.

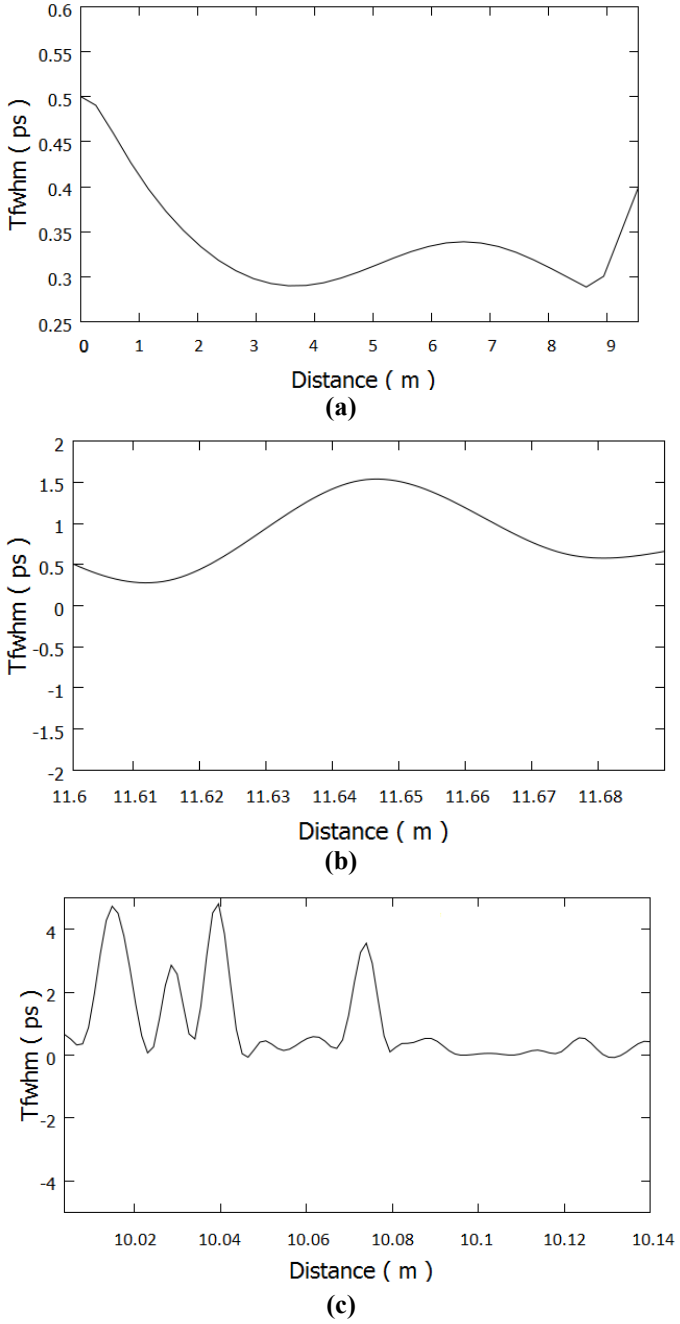


**Fig. 2**: Pulse width (FWHM) vs. distance curve for third - order soliton in (a) LDDF, (b) DCF and (c) FBG.

Fig. 2(a), 2(b) and 2(c) explore the third order soliton compression in LDDF, DCF and FBG respectively. A smooth curve has observed in LDDF that indicates compression of third order soliton into 300fs shown in Fig. 2(a). DCF based compression can be seen from Fig. 2(b) and an alternative compression and expansion has been observed. Finally a 350fs pulse has been obtained in DCF. FBG based compression has shown in Fig. 2(c). In comparison among LDDF, DCF and FBG for third order soliton compression, LDDF has performed best by compressing 500fs pulse into a 300fs pulse.

Let us divert our concentration for newer outcome with fourth order sub-picosecond soliton compression experienced in Fig. 3(a), (b) and (c). We have found a very good compression of 500fs pulse into 150fs in LDDF shown in Fig. 3(a). In DCF and FBG with same pulse and parameter we have got nothing but the figure as Fig. 3(b) and Fig. 3(c) respectively. Although the best result has been found above all of the analysis in Fig. 4(a), which shows the compression of ultrashort fifth order optical soliton in LDDF, but it was not so

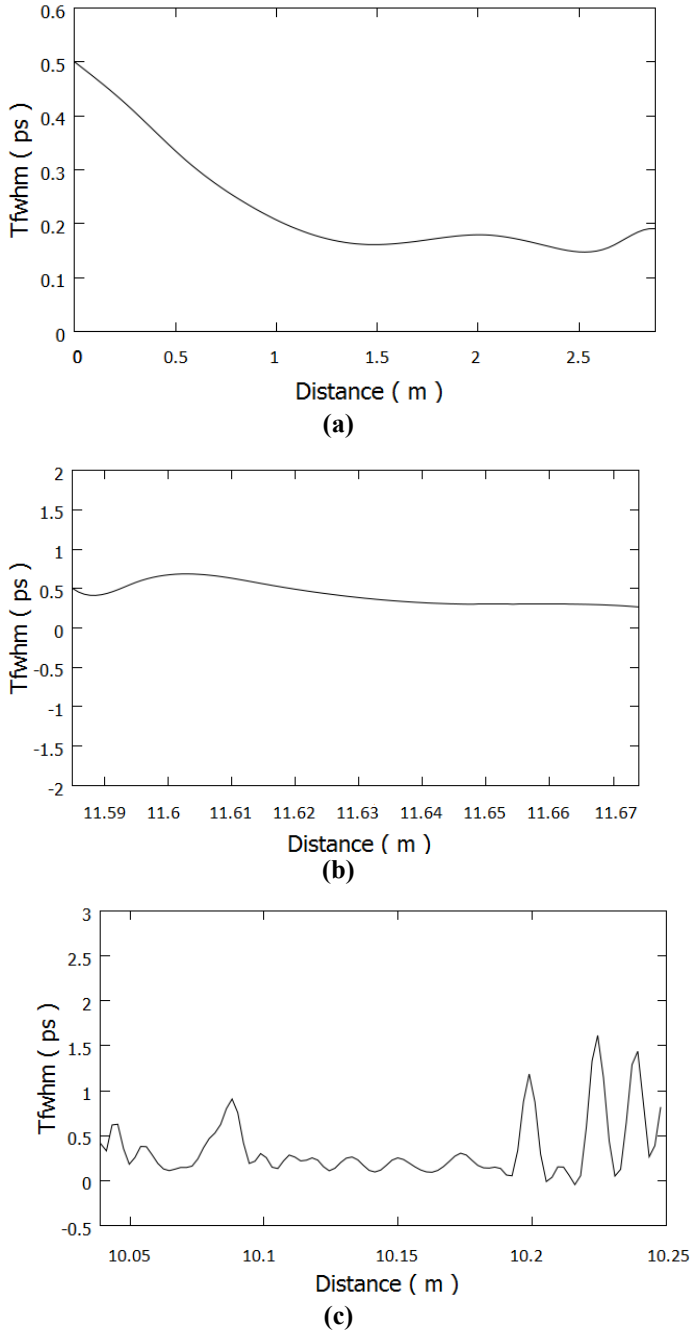


**Fig. 3**: Pulse width (FWHM) vs. distance curve for fourth - order soliton in (a) LDDF, (b) DCF and (c) FBG.

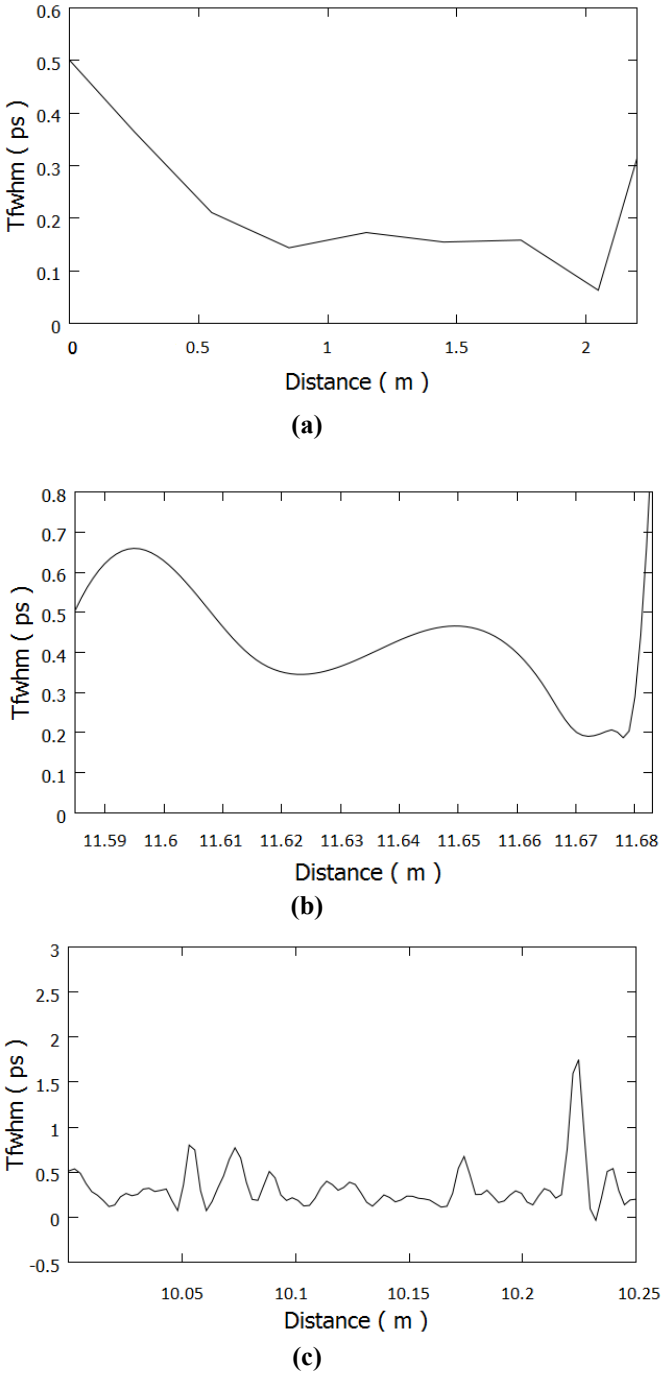


**Fig. 4**: Pulse width (FWHM) vs. distance curve for fifth - order soliton in (a) LDDF, (b) DCF and (c) FBG.

smooth. The result gives us a compression up to 63fs for fiber length of 2.05m. Beyond this fiber length pulse expansion happens which is clear from Fig. 4(a). This is because as the fiber length increases nonlinear effects dominate the linear effects. Fig. 4(b) and Fig. 4(c) show the result for compression of ultrashort fifth order optical soliton in DCF and FBG as well.

All the data for ultrashort soliton compression in DCF, FBG and LDDF are as follows:

TABLE I PULSE WIDTH AFTER COMPRESSION AND SPATIAL SOLITON DIMENSION FOR 500FS INPUT PULSE

| Soliton order | Pulse width (post-comp.) in DCF | Pulse width (post-comp.) in FBG | Pulse width (post-comp.) in LDDF | Spatial dimension of soliton in LDDF |
|---|---|---|---|---|
| 2nd | 480fs | Expansion (2.5ps) | 340fs | 2.72nm |
| 3rd | 350fs | 300fs | 300fs | 2.408nm |
| 4th | 250fs | 400fs | 150fs | 1.2nm |
| 5th | 200fs | 200fs | 63fs | 523.5pm |

From all of the above comparison and outcomes for ultrashort optical soliton compression of higher-order soliton up to fifth order we can say, it is obvious that DCF and FBG could not perform a good compression whereas LDDF has performed compression with excellence which has been clearly showed in TABLE I.

## IV. CONCLUSION

Considering higher order dispersive effects i.e. TOD and higher order nonlinear effects i.e. SS and IRS the compression of ultrashort optical soliton in DCF, LDDF and FBG has been investigated. Based on ultrashort soliton compression a comparative study has also been explored among dispersion compensating fiber (DCF), fiber Bragg grating (FBG) and LDDF. Finally LDDF of 2.05m length has been proposed for higher-order ultrashort soliton compression for formation of spatial soliton in nm-pm range. We have obtained numerically ultrashort soliton of 63fs after compression. The spatial dimension has been found as 523.5pm.

## REFERENCES

[1] S. M. Salimullah and M. Faisal, "Ultrashort soliton propagation in multi-clad optical fibers with per channel data rate of 1Tb/s," in *Telecommunications and Photonics (ICTP), 2015 IEEE International Conference on*, 2015, pp. 1-5.

[2] S. I. Mian and R. M. Shtein, "Femtosecond laser-assisted corneal surgery," *Current opinion in ophthalmology,* vol. 18, pp. 295-299, 2007.

[3] B. Schwab, D. Hagner, W. Müller, H. Lubatschowski, T. Lenarz, and R. Heermann, "Bone ablation using ultrashort laser pulses. A new technique for middle ear surgery," *Laryngo-rhino-otologie,* vol. 83, pp. 219-225, 2004.

[4] H. Lubatschowski, A. Heisterkamp, F. Will, J. Serbin, T. Bauer, C. Fallnich*, et al.*, "Ultrafast laser pulses for medical applications," in *Proc. SPIE*, 2002, pp. 38-49.

[5] I. Amiri, A. Nikoukar, J. Ali, and P. Yupapin, "Ultra-short of pico and femtosecond soliton laser pulse using microring resonator for cancer cells treatment," *Quantum Matter,* vol. 1, pp. 159-165, 2012.

[6] M. Jalil, J. Phelawan, M. Aziz, T. Saktioto, C. Ong, and P. P. Yupapin, "Acne vulgarism treatment using ultra-short laser pulse generated by micro-and nano-ring resonator system," *Artificial cells, nanomedicine, and biotechnology,* vol. 41, pp. 92-97, 2013.

[7] P. Reeves-Hall and J. Taylor, "Wavelength and duration tunable subpicosecond source using adiabatic Raman compression," in *Lasers and Electro-Optics, 2001. CLEO'01. Technical Digest. Summaries of papers presented at the Conference on*, 2001, pp. 228-229.

[8] T. Murphy, "10-GHz 1.3-ps pulse generation using chirped soliton compression in a Raman gain medium," *IEEE Photonics Technology Letters,* vol. 14, pp. 1424-1426, 2002.

[9] S. M. Salimullah and M. Faisal, "Femtosecond Soliton Formation by Higher-Order Soliton Compression in Linear Dispersion Decreasing Fiber," in *Proceedings of 20th Microoptics Conference (MOC'15)*, Fukuoka, Japan., 2015, pp. paper no. H-11.

[10] S. M. Salimullah, "Analysis of higher-order soliton compression for formation of ultra-short pulses," 2015.

[11] C.-C. Chang, A. Vengsarkar, D. Peckham, and A. Weiner, "Broadband fiber dispersion compensation for sub-100-fs pulses with a compression ratio of 300," *Optics letters,* vol. 21, pp. 1141-1143, 1996.

[12] Q. Li, P. Wai, K. Senthilnathan, and K. Nakkeeran, "Modeling self-similar optical pulse compression in nonlinear fiber Bragg grating using coupled-mode equations," *Journal of Lightwave Technology,* vol. 29, pp. 1293-1305, 2011.

[13] Q. Li, K. Senthilnathan, K. Nakkeeran, and P. Wai, "Nearly chirp-and pedestal-free pulse compression in nonlinear fiber Bragg gratings," *JOSA B,* vol. 26, pp. 432-443, 2009.

[14] J. H. Lee, T. Kogure, and D. J. Richardson, "Wavelength tunable 10-GHz 3-ps pulse source using a dispersion decreasing fiber-based nonlinear optical loop mirror," *IEEE Journal of selected topics in quantum electronics,* vol. 10, pp. 181-185, 2004.

[15] S. V. Chernikov, D. Richardson, D. Payne, and E. Dianov, "Soliton pulse compression in dispersion-decreasing fiber," *Optics letters,* vol. 18, pp. 476-478, 1993.

[16] P. Wai and W.-h. Cao, "Ultrashort soliton generation through higher-order soliton compression in a nonlinear optical loop mirror constructed from dispersion-decreasing fiber," *JOSA B,* vol. 20, pp. 1346-1355, 2003.

[17] G. Agrawal, *Applications of nonlinear fiber optics*: Academic press, 2001.

[18] D. Chao-Qing and C. Jun-Lang, "Ultrashort optical solitons in the dispersion-decreasing fibers," *Chinese Physics B,* vol. 21, p. 080507, 2012.

# Microstructure Fiber with Extremely High Nonlinearity for Supercontinuum Generation

Pranjol Sen Gupta*, Mohammad Faisal
Department of Electrical and Electronic Engineering, Bangladesh University of Engineering and Technology
Dhaka-1205, Bangladesh
*pranjolsengupta93@gmail.com

*Abstract*— **In this paper we present a modified hexagonal microstructure optical fiber (MOF) with circular air holes to achieve high nonlinearity as well as low confinement loss. To explore the chromatic dispersion, nonlinear properties and confinement loss, finite element method (FEM) has been used with an anisotropic, circular perfectly matched boundary layer. Throughout the arrangement of circular shaped holes with various diameters, the hexagonal PCF offers high nonlinearity up to 142 $W^{-1}km^{-1}$ at 1550 nm wavelength and chromatic dispersion of ~ 0±0.95 ps/(nm-km) in the range of 1250 to 1610 nm wavelength. This novel MOF with high nonlinearity and low dispersion is suitable for generating supercontinuum in telecommunication band (around 1300 nm and 1550 nm).**

***Index Terms***— **MOF, Nonlinearity, Supercontinuum, Dispersion, Finite Element Method**

## I. INTRODUCTION

A microstructure optical fiber (MOF) incorporates sub-wavelength air holes along the whole length of the waveguide. These MOFs featuring unprecedented properties [1]-[2] have been the subject of continuous research and development efforts for the past ten years and have fulfilled many of their promises that have further accelerated inventions in many sectors. In contrast with conventional fibers, MOF helps us to engineer various properties like birefringence [3], chromatic dispersion [4]-[5], nonlinearity [6]-[7] etc. MOFs support design parameters such as diameter of the air-hole, ring number, and spacing between air-hole to air-hole (the pitch) which enable us to tune those properties mentioned above. Ultra-short pulses are affected by a multitude of nonlinear effects as well as dispersion of fiber. The nonlinear effects can generate new frequencies in the outside region of input pulse spectrum. With sufficient intensity, a phenomenon like spectral broadening is occurred also known as supercontinuum (SC) generation [8] due to high nonlinearity of fiber. Property of the SC generation is particularly dependent upon the position of input pulse relative to the zero dispersion wavelength. SC generation has received great interest in applications like gas sensing, fluorescence lifetime imaging, frequency metrology and optical communication. Telecommunication window is the most preferable window in optical communication because of the minimal level of transmission loss in the fiber. Maintaining very high nonlinearity with tailoring the chromatic dispersion and restraining the losses to a minimum level are essential for SC generation. Index guiding photonic crystal fiber (PCF) offers unique dispersion and higher nonlinearity [8]-[13] that have been outlined up to date ranging from PCF with defects in core [8], PCF with a triangular lattice [9], with air holes uniformly optimized [10] and PCF having variation in air-hole diameters in cladding [12]. In [8], proposed hexagonal structure has a much lower nonlinearity of 25 $W^{-1}km^{-1}$ at 1300 nm wavelength and 20 $W^{-1}km^{-1}$ at 1550 nm wavelength whether our proposed structure has nonlinear coefficient of 220 $W^{-1}km^{-1}$ and 142 $W^{-1}km^{-1}$ at respective wavelength. In [9], the proposed structure has dispersion value of 2.0 ps/(nm-km) whereas we have achieved a much lower dispersion ~0.95 ps/(nm-km) in between 1250 to 1610 nm wavelength. PCFs in [10]-[11] have better dispersion attributes but they incorporate many rings to lessen the confinement losses. For instance, Reeves [11] have shown a dispersion lessened MOF with confinement loss of 0.57 dB/m using eleven rings whereas our proposed structure has a confinement loss of $10^{-8}$ dB/ km using only six rings of air-holes. As a result, the modified hexagonal MOF presented in this paper with low dispersion, very high nonlinearity and extremely low confinement loss will be a proper candidate for SC generation. Furthermore, we use silica as a background material without doping.

## II. DESIGN OF MOF AND GEOMETRICAL PARAMETERS

By carefully designing ring number, hole diameter and pitch, dispersion and confinement loss can be significantly altered in MOF. Moreover, existence of holes with various diameter in cladding also help to increase nonlinearity. The cross-sectional view of the hexagonal MOF with details is shown in Fig. 1 with core diameter 2a and pitch Λ. In our design, we have used four different sized hole diameters and six rings in the cladding. The diameter of the innermost ring is $d_1$, the second ring and third ring have a diameter of $d_2$ and $d_3$ respectively and the outermost three rings have a diameter of $d_4$. The spacing between adjacent air hole rings and distance between holes on the same ring has been kept fixed in whole analysis. Hence, the diameter of the core is 2Λ–d1. Use of air-hole of uniform diameters result in ultra-flattened dispersion but it will increase confinement loss. So many rings will be required to lessen the loss to a desired level. However, this will create complexities in fabrication with weak structure. In our case, the hexagonal structure with six air hole rings is adequate for obtaining a low dispersion and low confinement loss as well as higher nonlinearity. As PML is suitable for effective absorption boundary conditions [16], a circular PML has been

978-1-5386-3374-8/17/$31.00 ©2017 IEEE

incorporated to mask backscattering in the simulation domain. Sellmeier equation [17] has been employed for calculating accurate effective refractive index of fused silica.

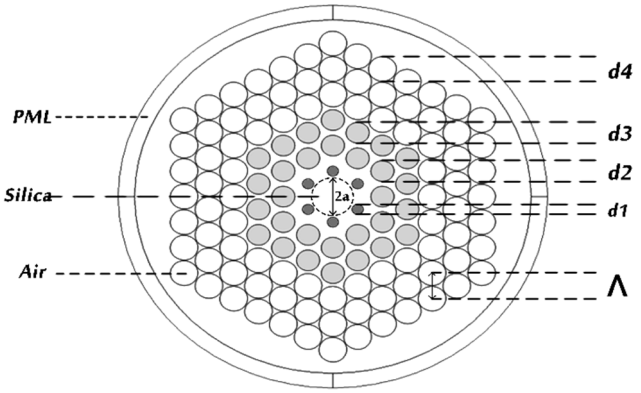


Fig. 1 Geometric Design and parameters of the proposed six ring PCF.

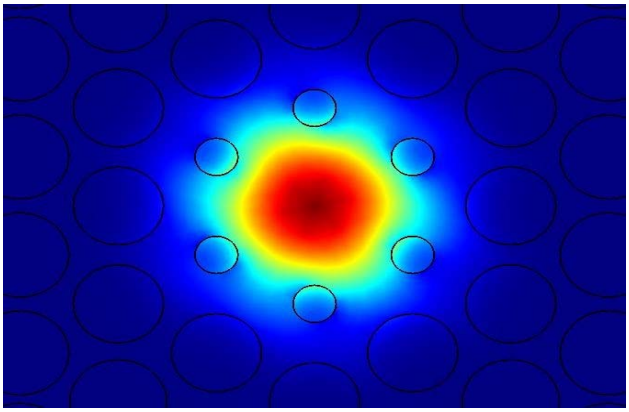

Fig. 2 Power flow distribution inside the proposed MOF at 1.55 µm.

## III. NUMERICAL SIMULATION RESULTS AND DISCUSSIONS

We have calculated effective modal index ($n_{eff}$) and the field distribution of the proposed fiber by using FEM with PML [16]. Power confinement of the proposed structure has been shown in Fig. 2 at 1550 nm wavelength, which clearly reveals the confinement of field in the core. We have used COMSOL multiphysics (v5.0) for numerical simulation. Once $n_{eff}$ is obtained by solving an eigen-value problem with Maxwell's equation by FEM method, the chromatic dispersion parameter ($D$), effective modal area ($A_{eff}$), nonlinearity ($\gamma$) and confinement loss ($L_c$) all are calculated by using the following equations [18].

$$D = -\frac{\lambda}{c}\frac{d^2 Re[n_{eff}]}{d\lambda^2} \quad (1)$$

$$A_{eff} = \frac{[\iint |E^2| dx\, dy]^2}{\iint |E|^4 dx\, dy} \quad (2)$$

$$\gamma = \frac{2\pi n_2}{\lambda A_{eff}} \quad (3)$$

$$L_c = 8.868 \times \mathrm{Im}[k_0\, n_{\mathrm{eff}}] \quad (4)$$

Here Re[$n_{eff}$] is the real part of $n_{eff}$, $c$ is the velocity of light and $\lambda$ is the wavelength. Im[$k_0$ $n_{eff}$] is termed as the imaginary part of $n_{eff}$. Nonlinear refractive index, $n_2 = 2.2\times 10^{-20}$ m$^2$/W [19] for silica and $E$ is the electric field inside the fiber derived from Maxwell's equations [18].

In Fig. 3, we have plotted the real part of effective refractive index against wavelength. The real part of refractive index decreases with wavelength. In Fig. 4, we can see the dispersion attributes of the fiber. During whole analysis Λ has been kept at 0.87 µm and the diameter of the innermost ring ($d_1$) is 0.33 µm and three outermost rings ($d_4$) is 0.84 µm. The second ring and third ring have a diameter of 0.693 µm and 0.747 µm, respectively. From Fig. 4 it is apparent that at 1300 nm and 1550 nm wavelength there are two zero dispersions and by optimizing the parameters $d_1$, $d_2$, $d_3$, $d_4$ and Λ, chromatic dispersion in the range of 0 ±0.95 ps/(nm-km) in between 1250 to 1610 nm wavelength has been achieved.

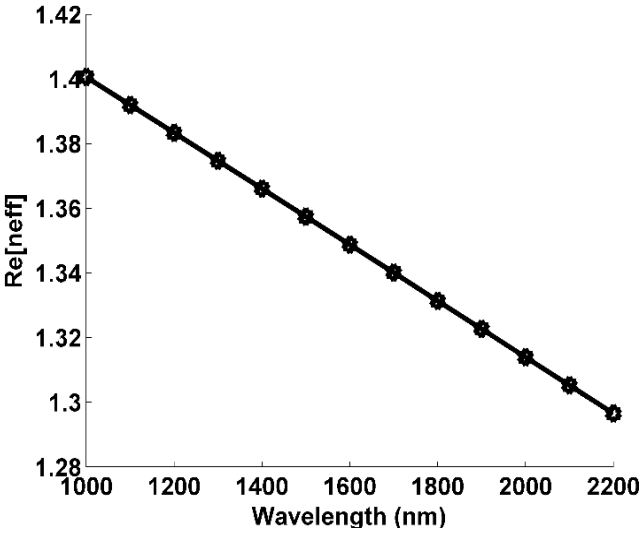


Fig. 3 Real component of effective refractive index.

Next, the design parameters, $d_2$ and $d_3$, have been varied and the effects are shown in Fig. 5 and Fig. 6. First, the diameter of 3rd ring is varied from 0.74 to 0.747 µm while the diameter of 2nd ring is remained unchanged. We can see that the dispersion curve has taken a downward shift. Then in Fig. 6 the diameter of 2nd ring is changed from 0.693 to 0.72 µm and the diameter of 3rd ring is kept at 0.747 µm which results in an upward movement of dispersion curve. It is important to note that other parameters such as pitch and air hole diameter for ring number 1,4,5,6 have been kept fixed. Only the diameters of the 2nd and 3nd ring have been tuned to shape the desired dispersion curve. Though dispersion is lower when diameter of third ring is decreased, consequently, it also reduces the overall wavelength band and shifts zero dispersion wavelength. That's why we have chosen 0.693 µm and 0.747 µm as an optimum diameter for 2nd and 3nd ring, respectively.

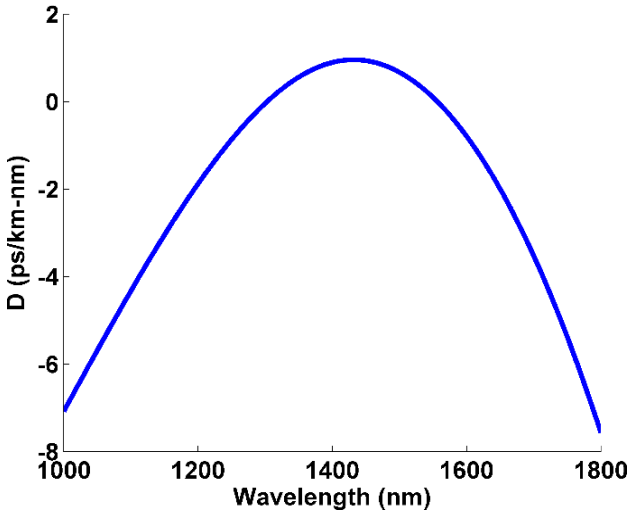


Fig. 4 Dispersion characteristic with optimum value for Λ=0.87 µm, d1=0.33µm, d2=0.693 µm, d3=0.747 µm, d4=0.84 µm.

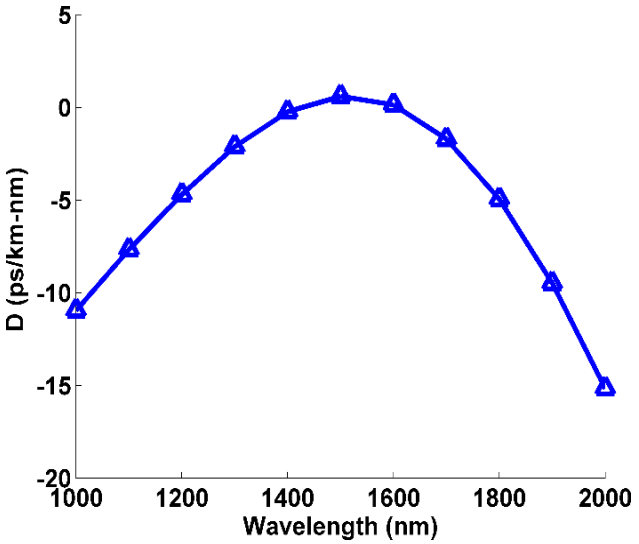


Fig. 5 Dispersion characteristic with optimum value for Λ=0.87 µm, d1=0.33 µm, d2=0.693 µm, d3=0.74 µm, d4=0.84 µm.

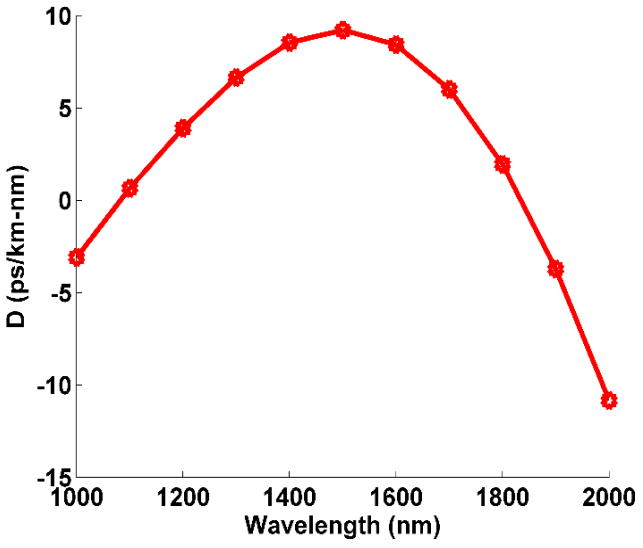


Fig. 6 Dispersion characteristic with optimum value for Λ=0.87 µm, d1=0.33 µm, d2=0.72 µm, d3=0.747 µm, d4=0.84 µm.

From Eq. (3) it is evident that nonlinearity of a fiber is inversely proportional to effective area of the fiber. Fig. 7 illustrates the variation of effective area with respect to wavelength for different pitch variation. At 1550 nm wave length, effective mode area is 2.85 $\mu m^2$ when pitch is 0.87 µm. If the pitch is increased to 0.90 µm, effective area also increases from 2.85 $\mu m^2$ to 3.1 $\mu m^2$ and effective area is 2.37 $\mu m^2$ when pitch is 0.80 µm, at the same wavelength. In Fig. 8, we have plotted nonlinear co-efficient γ with respect to wavelength for different pitch variation. Because of inverse relation between effective area and nonlinearity, nonlinear coefficient is about 170 $W^{-1}km^{-1}$ when pitch is 0.80 µm at 1550 nm wavelength. However, with a 0.80 µm pitch the overall dispersion is much higher which is not suitable for SC generation. On the other hand, with a pitch of 0.90 µm nonlinear coefficient is 132 $W^{-1}km^{-1}$ which is lower and not accepted. Finally, the pitch of 0.87 µm has been considered as the optimum value that offers nonlinear coefficient of 142 $W^{-1}km^{-1}$ at 1550 nm wavelength since here dispersion is zero. We also achieved nonlinearity of 220 $W^{-1}km^{-1}$ at 1300 nm wavelength where dispersion is also zero.

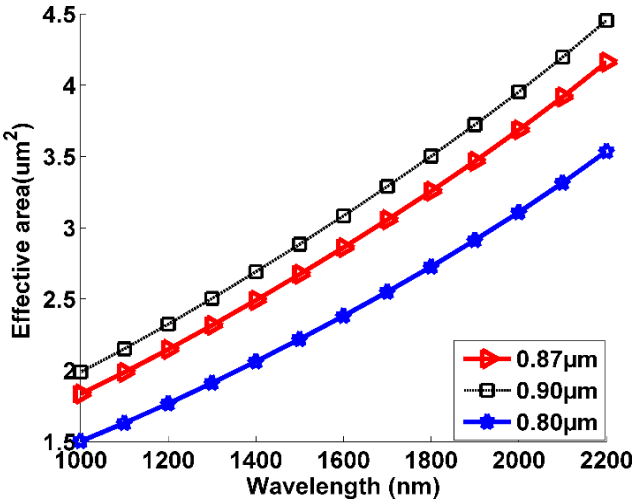


Fig. 7 Effect of pitch variation on effective area with optimum value for d1=0.33 µm, d2=0.693 µm, d3=0.747 µm, d4=0.84 µm.

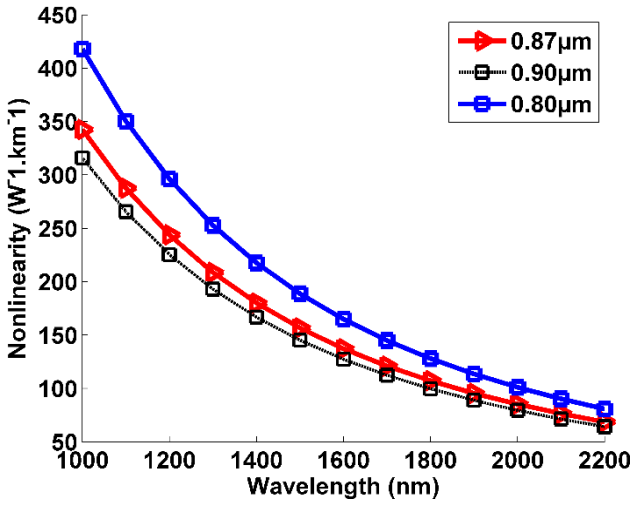


Fig. 8 Effect of pitch variation on nonlinear coefficient with optimum value for d1=0.33 µm, d2=0.693 µm, d3=0.747 µm, d4=0.84 µm.

In Fig. 9, we have shown the effect of ring number on

confinement loss while all the other parameters are kept at their optimum values. With six rings in the cladding, loss in the fiber is nearly $10^{-8}$ dB/km at 1550 nm operating wavelength, which is extremely low. It is also evident that loss increases as ring number in the cladding is decreased. With six rings, loss is at minimum level and an increase in number of rings do not affect the overall confinement loss significantly. From Fig. 9 it is evident that with seven rings in the cladding confinement loss does not vary much. The diameter of the outer ring has been kept larger in order to avoid leakage loss and poor mode confinement. Only the diameter of first three rings has been altered significantly to get the desired dispersion curve. Now we would like to talk about the possible fabrication of the proposed MOF. Since we are using all circular air holes and hexagonal lattice, we can predict that such simple design could be fabricated using current versatile technology like stack and draw.

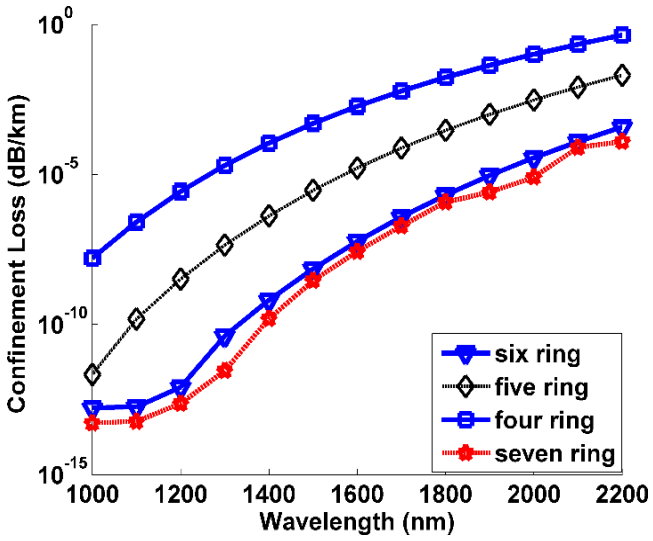


Fig. 9 Effect of ring number on confinement loss with optimum value for Λ=0.87 µm, d1=0.33 µm, d2=0.693 µm, d3=0.747 µm, d4=0.84 µm.

## IV. Conclusions

We have presented a hexagonal MOF with only six rings in cladding and achieved very low dispersion approximately 0±0.95 ps/(nm-km) in between 1250 and 1610 nm wavelength. We have also achieved two zero dispersion at 1300 and 1550 nm wavelength which is important in the application of supercontinuum generation. We have also shown a lower confinement loss of about $10^{-8}$ dB/km and very high nonlinearity about 142 $W^{-1}km^{-1}$ at 1550 nm wavelength and 220 $W^{-1}km^{-1}$ at 1300 nm wavelength. So this proposed design can be a potential candidate for supercontinuum generation.

## References

[1] J.K. Ranka, R.S. Windeler, A.J. Stentz, "Optical properties of high delta air-silica microstructure optical fibers," *Opt. Lett.*, vol. 25, no. 1, pp. 796-798, 2000.

[2] P. St.J. Russell, "Photonic crystal fibers," *Journal of Lightwave Technol.*, vol. 24, no. 12, pp. 4729-4749, 2006.

[3] J. Ju, W. Jin, and M. S. Demokan, "Properties of a highly birefringent photonic crystal fiber," *IEEE Photon. Technol. Lett.*, vol. 15, no. 10, pp.1375–1377, Oct. 2003.

[4] K. Saitoh and M. Koshiba, "Chromatic dispersion control in photonic Crystal fibers: Application to ultra-flattened dispersion," *Opt. Exp.*, vol. 11, no. 8, pp. 843–852, Apr. 2003.

[5] F. Ge´rome, J. L. Auguste, and J. M. Blondy, " Design of dispersion-Compensating fibers based on a dual-concentric core photonic crystal Fiber," *Opt. Lett.,* vol. 29, no. 23, pp. 2725–2727, Dec. 2004.

[6] J.C. Knight, T. A. Birk, P. J. St. Russell, and J. P. Sandro, "Properties of photonic crystal fiber and the effective index model," *J. Opt. Soc. Am. A*, vol. 15, no. 3, pp. 748–752, Mar. 1998.

[7] T. Matsui, J. Zhou, K. Nakajima, and I. Sankawa, "Dispersion-flattened photonic crystal fiber with large effective area and low confinement loss," *J. Lightwave Technol.,* vol. 23, no. 12, pp. 4178–4183, Dec. 2005.

[8] F. Begum, Y. Namihira, T. Kinjo, S. Kaijage, "Supercontinuum generation in square photonic crystal fiber with nearly zero ultra-flattened chromatic dispersion and fabrication tolerance analysis," *Opt. Comm.*, vol. 284, no. 4, pp. 965-970, 2011.

[9] A. Ferrando, E. Silvestre, P. Andres, J. Miret, and M. Andres, "Designing the properties of dispersion-flattened photonic crystal fibers," *Opt. Express*, vol. 9, pp. 687–697, 2001.

[10] A. Ferrando, E. Silvestre, P. Andres, J. J. Miret, and M. Andres, "Nearly zero ultraflattened dispersion in photonic crystal fibers," *Opt. Lett.*, vol. 25, pp. 790–792, 2000.

[11] W. H. Reeves, J. C. Knight, and P. St. J. Russell, "Demonstration of ultraflattened dispersion in photonic crystal fibers," *Opt. Express*, vol. 10, pp. 609-613, 2002.

[12] K. Saitoh, M. Koshiba, T. Hasegawa, and E. Sasaoka, "Chromatic dispersion control in photonic crystal fibers: application to ultraflattened dispersion," *Opt. Express*, vol. 11, pp. 843-852, 2003.

[13] K. Saitoh, N. J. Florous, and M. Koshiba, "Ultraflattened chromatic dispersion controllability using a defected core photonic crystal fiber with low confinement losses," *Opt. Express*, vol. 13, pp. 8365-8371, 2005.

[14] G. Renversez, B. Kuhlmey, and R. McPhedran, "Dispersion management with microstructured optical fibers: ultraflattened chromatic dispersion with low losses," *Opt. Lett.*, vol. 28, pp. 989-991, 2003.

[15] H. Ademgil and S. Haxha, "Highly birefringent photonic crystal fiber with ultra low chromatic dispersion and low confinement losses," *J. Lightwave Technol.*, vol. 26, no. 4, pp. 441–448, Feb. 2008.

[16] S. Guo, F. Wu, S. Albin, H. Tai, R.S. Rogowski, "Loss and dispersion analysis of microstructured fibers by finite difference method," *Optics Express*, vol. 12, pp. 3341-3352, 2004.

[17] I.H. Malitson, "Interspecimen comparison of the refractive index of fused silica," *J. Opt. Soc. Am.*, vol. 55, no. 10, pp. 1205-1209, 1965.

[18] K. Kaneshima, Y. Namihira, N. Zou, H. Higa, and Y. Nagata, "A unique approach in ultraflattened dispersion photonic crystal fibers containing elliptical air holes," *Opt. Rev.*, vol. 15, pp. 91-96, 2006.

[19] K. S. Kim, R.H. Stolen, W. A. Reed, and K. W. Quoi, "Measurement of the nonlinear index of the silica core and dispersion shifted fibers," *Opt. Lett.*, vol.19, no. 4, pp. 257-259, 1994.

# Smart Health Care System for Underdeveloped Countries

*Md. Sultanul Arefin, Tania Haider Surovi, Nazmun Nahar Snigdha, Md. Firoz Mridha, Md. Akhtaruzzaman Adnan

Computer Science and Engineering, University of Asia Pacific
74/A, Green Road, Farmgate, Dhaka - 1215, Bangladesh
*mhmdarefin@gmail.com

***Abstract*—Nowadays state of the art health care systems are either based on hospital or household environs and its scope is confined to urban areas of a country. Yet traditional healthcare systems are facing challenges such as lack of ubiquity, use of backdated techniques, inadequacies in tracking, observing and reporting status of patients and diseases as well as unaffordability. However, modern updates in IoT, cloud computing, mobile and web development and computer vision technology are offering us a wider scope in providing an effective health care system to everyone. The assistance includes automation in systematic monitoring of patients, transmission of medical data at real-time, saving those data in cloud servers, manipulate data for future use, presenting real time scenario to stake holders and many more. Here we suggest a wireless network infrastructure that will provide useful health and medical services to children and adults as well as assist in distributing vaccines, tablets and personnel to monitor endemic diseases. We have two components in our system, first one is the clinic booth accompanied by health workers. This system assists health workers in their work and acquire personalized data and sends them to an online server for future use. Second is the administration and presentation of the ground data to stake holders. In our preliminary network evaluation of the IoT powered clinic booth design we found average response time of 1.5 seconds with uptime of 98.16%.**

***Keywords*— Cloud computing, internet of things, tiny and affordable computers , health care system, sensors, mobile and web development.**

## I. INTRODUCTION

Internet is everywhere, thanks to wide spread use of computers, cheap price of devices, heavy demand, new invention, optimization, miniaturization etc. Devices today became so small that a few years ago television sets dominated the living room. Now we can watch television in a handheld device and do much more than just watching soap operas or games. With these new devices and the internet connectivity comes the idea of Internet of Things (IoT). IoT is a novel idea in internet which targets to connect anything with anyone, at any given time, utilizing proper connection and services [1].

The IoT conglomerate is strengthened by connecting it to cloud servers. Application of IoT technologies have bright future in health care systems and it is already being used in different settings. Health related information of patients is very important and requires protection from manipulation and theft. It also requires efficient and secure distribution of devices and servers (application and database servers) to render good service to the end user.

Bulk of the IoT related work focuses mainly on devising a network of wireless human body sensors encompassing a hospital or home environment. These approaches don't cover the full spectrum of patients and their problems. For instance, what if a patient/child doesn't want to move or may have problems in moving from home to hospital. Thus in order to cover the full spectrum of patients; we need to employ both traditional and mobile systems which will be portable.

Apart from premature birth the leading causes of death of children under 5 are Pneumonia, Diarrhea, Malaria and Malnutrition. The consequences of malnutrition and illness in childhood are visible in subsequent periods of human growth. One of the key indexes of child health and wellbeing is child mortality rate, which continues to be an issue for majority of under developed countries. One of the 8 Millennium Development Goals (MDGs) was to reduce child mortality by two-thirds by 2015 [2].

Many developing countries are showing good results in preventing child mortality. For instance, in Bangladesh from 1990 to 2011, under age 5 mortality decreased from 151 to 53 per 1000 childbirths. Mortality wanes are connected to social awareness, preventive measurements, improvements in socioeconomic conditions, initiate programs to enlarge coverage area for vaccines, treatment of diarrhea, implementation of IMCI, etc. [3]. Most vaccines are given to children aged between 0 to 10.

However in many countries modern equipment's are confined to provincial health centers and is often very far away [4]. Health workers in developing countries setup clinics in rural areas use backdated techniques to determine and handle problems. Workers typically investigate fever by putting their hand on a child's brow. They measure heart rate using stop watch. height and weight were measured and feedback were given based on the weight chart e.g. normal, over weighted, underweighted or obese [5]. To provide improved health care services, updated and refined actions are required. As of 2015, UN's sustainable development goal number 3 is, to ensure "Good health and well-being" of the people [6].

Portable diagnostic tools and electronic health care services can play an important role in achieving this goal if utilized in an exact and timely manner. If clinical data is provided at actual time, it will be very effective in treating patients and allocate resource. Which can also detect outbreaks of diseases as well

978-1-5386-3374-8/17/$31.00 ©2017 IEEE

as find cases of drug-resistance. Thus we emphasize that further achievements in reducing child mortality can be realized if health workers are equipped with a detection system that is compact, portable and cheap.

These portable devices will also be useful in countries that are suffering from wars and catastrophic events like tsunami, earthquake, etc. In 2017 we often hear that in Yemen people are affected by Cholera, by consuming contaminated water. Children in Syria are suffering from malnutrition. Thus challenges in different parts of the world may vary. We can tailor our system for a particular area which will help prevent region specific challenges. We can take data from children at real time and store it to cloud-based storage facility for future processing.

In our work, we propose a bundled and generic system where sensors and devices are connected to one tiny and affordable computer either by cable or wireless technology. The proposed system contains a unit that can be transported through land, river, lakes and seas. We call it clinic booth. These booths are connected to 3rd party data server. We administer this data and present these data to stakeholders by creating mobile and web applications as shown in figure 1.


*Fig. 1 Division wise demographic report on the number of people who are affected by Malaria in a selected period in Bangladesh.*

## II. OBJECTIVES

The role of modern technology is yet to be exploited fully in advancing health management in most parts of the world. Management of data relating to medical treatments and tests as well as execution of e-health continues to be a headache since paper-based systems are still used today, especially in hard-to reach rural areas. For instance, there had been some undertakings in countries like India, Malawi, Bangladesh to use SMS as a reporting tool for child health care monitoring. Maintaining processes like these are hard, requires double entry and are prone to human mistakes. Furthermore, the data is impersonal [5]. However, a system that is capable of automatically interpreting and transmitting personalized measurement data to cloud based servers at runtime would deal with these troubles.

We emphasize that our system be incorporated with other arms of a government. In most of the countries people have identification cards like National ID cards to identify themselves. Because our system is portable, we can move it across every corner of a country. Which will help us in relating children with their parents. We can take pictures of children, collect their ages and also store the number of vaccines they have taken over a period. We can also ensure whether a child is taking the same medicine twice. One problem arises in Bangladesh is often children die from taking medicines that have expired their service date. What occurs is the government buys more medicine than they actually need and tablets that were not distributed in one year were put in stock so that it can be used in the next year. Thus many children die when they consume those expired tablets. Health workers have an extended reach in every corner of a country. They know how much tablets or vaccines are required in a particular area. Thus policy makers can make decision about how much medicine they need to buy or import each season or year. Thus we can prevent child death and wastage of money. Our aim here is to monitor the growth, check crucial parameters, updating child vaccination chart, taking images, taking child and parent identification data, uploading data to the main server, present data to stake holders and give options for administrative tasks. Assessing body temperature and respiration rate is performed with sensor as it provides critical information about the child's well-being and guide the medical personnel about what to do next. Each child has a vaccination chart which maintains vaccination and dose report in the cloud server. Weight and height measurement is also performed to detect malnutrition.

Ambitions of our work are as follows:

1. Door to door delivery of simplified health services, enhancing accuracy and providing elegant quality of diagnostics through automatic review, record maintenance and spotting cases of malnutrition, fever, endemics, etc.
2. Improving existing health care systems by creating wireless network infrastructure and software as well as establishing storage structure in order to maintain personalized and customized clinical data to secure cloud-based storage systems.
3. Adjust child health care system with existing governmental systems of a country. like National ID Card number, child birth certificate number, social security number. Thus we can relate a child with their parents using their SSN or NID number. We can store locational information relating to pregnant women, suggest medication. Preserve information about vaccines and dosages, a child may have taken as well as prevent redundant usage of same medicine and vaccine. We can also store the level of medication and information relating to medicine brands.
4. Distribute and monitor the medicine flow to different areas in the country. Policy makers can see the medicine and vaccination distribution area at a particular moment. For instance, they can view demographic report of a particular country about how much area is vaccinated with polio vaccine. They can also view which of the areas are prone to which diseases and move assets like medicine and personnel to that area. In figure 1, we have shown a scenario about the number of people who were affected by Malaria disease with in the month of January in Bangladesh.

## III. METHODOLOGY

For our health care system, these accompanying elements are suggested: portable clinic booth, Raspberry Pi, cloud platform, sensors, mobile application server, web server, image processing software and mobile and web based health monitoring software. Each clinic booth has internet access through wireless technologies, e.g. WiMAX, 3G or 4G.

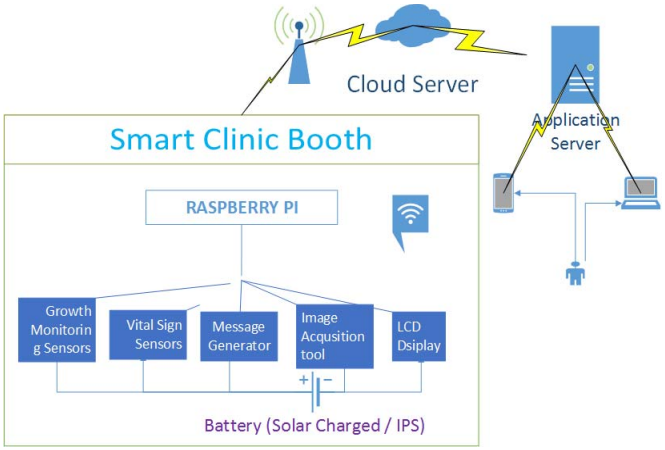


*Fig. 2 Configuration of different components used in the proposed health care system.*

A configuration of the suggested system is shown in figure 2. We use IPS and solar panels to power the electronic materials accompanied with the health workers.

### A. Architecture of the Clinic Booth


*Fig. 3 Portable Smart clinic booth with accompanying components.*

A construct of the booth is picturized in figure 3. It comprises of a collapsible, small, handy booth that is transportable through car, motorcycle, canoes or by hand. The length, breadth and height of the booth is 70 by 70 by 130 cm respectively, as this device will only be used for babies. Inner height of the booth is 120cm allowing us to measure babies aged from 0-7 in standing position. The parts that comprises our clinic booth are: Raspberry Pi, camera, mobile phone and laptops to use the software, temperature sensor, weight-height measurement device, display device, audible message generator. some sensors and devices are handled by Raspberry Pi which has its own Wi-Fi ports and software. Child growth is audited through a scaling device that can measure weight, water percentage, muscle mass and bone mass. Measurement of sleeping child is also possible with health worker's assistance. We avoided using traditional technologies instead we used sensors to measure individuals pulse rate, respiration rate and temperature. Measurements are displayed on the software and health workers can overwrite the data if need. Findings from the derived data can be narrated to guardians or users.

## IV. TECHNICAL DETAILS

Several ideas and elements were consolidated for effective service delivery of our system such as skilled design, technology alternatives, stability, scalability, security, integration, accessibility, pricing of elements, response time, accuracy, evaluation result, communication bandwidth, etc. Here, we describe about the underlying technology for clinic booth; Software associated with its operation, connectivity of the booth to the cloud platform, administration of data and servers and presentation of data to stakeholders.

### A. Underlying hardware and software modules

There have been encouraging developments in every sectors of ICT. From our strength point of view, we have preferred to use mini-computer instead of microcontrollers which ensure us fast prototyping, greater software control, reliability on the hardware, good community support, scalability and many more. Our system is constructed using Raspberry Pi, a tiny and affordable computer, with a processor speed of 700Mhz to 1200 MHz, RAM size of 512 MB or 1 GB with built in USB, Ethernet, Wireless and Bluetooth capabilities depending on the model. The price of this device varies from $5 -$35 depending on the model [7].

We have used "Windows 10 IoT Core" operating system for our Raspberry Pi devices. It is an operating system that is built for IoT. It is not the same operating system that we use in our desktop computers. Windows 10 IoT Core is the environment that will allow us to deploy our applications to Raspberry Pi. We used a compatible SD card in order to setup the "Windows 10 IoT Core Dashboard". Resources like documentation, Software, compatibility issues, source codes and IEDs related to Windows 10 IoT Core are available online [8].

Computer vision is a field that aims to gain remarkable understanding from videos or images. We used image recognition software in order to match images of our patients. A number of open source software(OSS) in computer vision are available online for example [9], GitHub [ https://github.com/ageitgey/face_recognition], etc. These open source software aims to motivate people and collaborate with other scientists.

### B. Data storage, manipulation and security

The application is developed using Firebase which offers a complete backend solution. It has supports for authentication [10] (supports OAuth 2.0) [11] , analytics, remote configuration, cloud messaging, crash reporting, REST API, NoSQL and many more. NoSQL database is more applicable compared to relational database in regards to real-time web application development and is known for its simplicity of design and control. Applications store data as JSON objects and interact with the database using a JavaScript API. Developers can add Firebase to their Android or iOS project very easily. Thus providing us future scaling and optimization option. The data store is designed to scale with application demand, so there

is no need to add additional servers, partition data or perform other database administration tasks that were required to preserve database back end.

The RESTful API includes query operations but not SQL operations. The query API is tailored to work with channels of data. There are also query operators with SQL-equivalents, such as orderByKey, orderByValue and orderByPriority. For instance, limit, limitToLast and limitToFirst query operations can restrict the number of JSON documents returned by the query [12].

Firebase will validate domain ownership, provision of SSL certificate and deploy it across the Firebase content delivery network. Once users or in the case of IoT, when the devices are authenticated, security rules control the operations they can execute and the data they can access.

At last we will access Firebase data through REST API. There are not many C# REST libraries to access Firebase. We use NuGet package manager to install the desired library(FirebaseDatabase.net). We give the opportunity to our admin of this system to view demographic reports, bar charts, create and send emails to stakeholders, view stock, ship medicine, tablets and personnel depending on the situation.

## V. DEVELOPMENTS

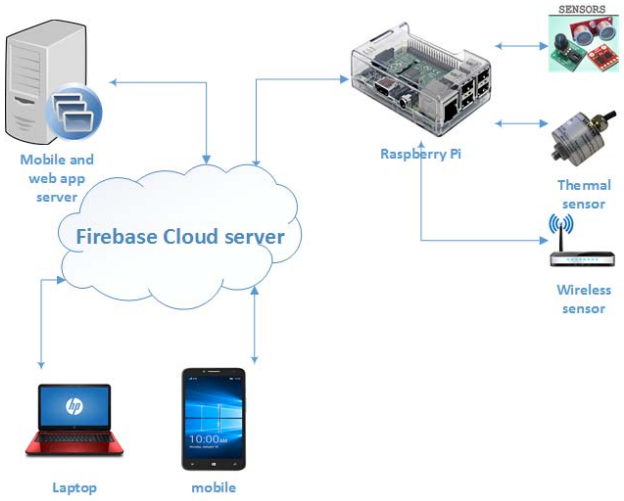


Fig. 4 Development phase (communication between hardware and software).

Our primary task was to establish connection between the cloud infrastructure and the booth. Then we focused on controlling the devices and sensors from Raspberry Pi. Take automated readings and save them to cloud servers. Give input and view output on application window and finally administer and present data as well as provide administrative options to stakeholders. In our work we have check our system in terms of responsiveness, dependability, accessibility and security.

As illustrated in figure 4, our device is built with Raspberry Pi that communicates with sensors. Controlling the devices and sensors from Windows 10 IoT operating system is done through dedicated USB, Wi-Fi ports and pins. There is admin for each booth who have a unique user name and password. Apart from helping the patient admin of the booth can also input and update data in the storage system. Personalized data of a patient are saved to the cloud storage at run time. Health workers communicate with the storage system and the Raspberry Pi device through our dedicated android and web apps. They can perform create, edit, update and delete operations on the cloud data. Log information about access to the storage are saved to the system automatically. Our Web app was created with Asp.net MVC technology. Stake holders having unique username and password can view demographic report, bar report (shown in figure 5), current distribution of personnel, stock and endemics in a particular area as well as create and send emails from this site. We have stored detailed patient data in our system in order to build trust in our system. Furthermore, we designed our system in such a way so that any human error would come to light very easily.

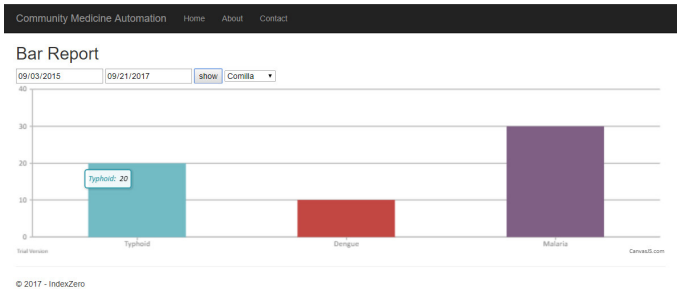


Fig. 5 Disease and district wise endemics bar report based on some selected date ranges in 2017.

## VI. RESULTS

### A. Performance

We measure performance in terms of latency. Latency is the time from when a user sends an instruction from the mobile or web application to the time when a response is received by the application. Latency is measured by deducting the transmitted message (TX) date-time stamp from the Received message (RX) date-time stamp. We measured time in terms of milliseconds by using different analytical tools.

### B. System Availability

Availability is the quality of being at hand when needed is a proof of a systems reliability. For our system, system availability is measured in terms of the reachability of the main component of clinic booth (Raspberry Pi) and its corresponding data store on Firebase from our software platforms. During the period 13th to 18th June 2017, the clinic booth was connected to its data store, representing a total duration of 432000s. The activity was monitored from the Google analytics, our mobile and web app servers as well as using 3rd party analytical tools. Our hardware and software components performance were extremely satisfactory.

## VII. MERITS

Our campaign mainly focused on targeting 3 kind of people: citizens with less privileged health access, health workers and policy makers. We expect our system will ensure better service delivery to people in rural areas of underdeveloped countries. It can even more effectively provide services in disaster hit areas and can be accompanied by field workers working for NGOs or health workers of a state. With this system the tasks of health workers will be automated by our system; all collected and log data are automatically stored at our cloud servers; data can be processed/updated for any future use and presented to policy makers at any given time. This benefits ensures that our system will supported by policymakers as well as other stakeholders. Furthermore, it will give an exact scenario about current distribution of health agents, vaccinators, vaccines and

medicines to a certain region. If medicine shortage or disease outbreak is reported in an area, this system will assist people in the government to take decisions in order to remedy the situation. Moreover, avoiding the use of paper-based systems would help us to protect the environment, reduce human errors and hardships as well as protect us from corruption. This system also awards us market spaces in cloud platform, data mining, data analysis, sensor technology, mini-computer and IC production technology.

## VIII. Conclusions

In the aforementioned work, we propose a health care system consisting of IoT, cloud computing, Raspberry Pi, sensors, software, web and mobile app servers. All test experiment results involving sensors and measurement devices, transmission of readings to Firebase backend server and presentation of data to stakeholders were remarkable.

We recorded an average delay of 1.5 seconds in our experiment of sending a command from the application software and receiving a response in the same application window. System availability of 98.16% was recorded. Thus, the network operation of our system reasserts the suitability of the IoT system in underdeveloped rural areas.

Although many tasks performed here are automatic but health workers can intervene when taking images or inputting NID/ SSN/ birth certificate numbers to the system. We have plans to develop a more sophisticated image recognition tools and integrate the system with our existing system. We have also plans to develop a customized mini-computer like Raspberry Pi, to minimize the production cost. There are not many REST API libraries available in dot net for accessing Firebase. Developing a web server with Python or Ruby seemed to be more preferable.

## References


[1] S. M. R. Islam, D. Kwak, H. Kabir, M. Hossain, and K.-S. Kwak, "The Internet of Things for Health Care : A Comprehensive Survey," *Access, IEEE*, vol. 3, pp. 678–708, 2015.

[2] Statistics Division of United Nations, "The Millennium Development Goals Report 2015," UN Statistics Division, New York, 2015.

[3] B. Ministry of Health and Family Welfare, *Success factors for women's and children's health: Bangladesh I.World Health Organization.* Geneva, 2015.

[4] O. Vermesan and Peter Friess, *Internet of Things: Converging Technologies for Smart Environments and Integrated Ecosystems*. 2013.

[5] T. Nyasulu, "Smart under-five health care system," in *2016 IST-Africa Conference, IST-Africa 2016*, 2016.

[6] U. N. UN Web Services Section, Department of Public Information, "Sustainable Development Goals launch in 2016." [Online]. Available: http://www.un.org/sustainabledevelopment/blog/2015/12/sustainable-development-goals-kick-off-with-start-of-new-year/. [Accessed: 17-Aug-2017].

[7] R. P. FOUNDATION and U. R. C. 1129409, "Raspberry Pi FAQs - Frequently Asked Questions." [Online]. Available: https://www.raspberrypi.org/help/faqs/. [Accessed: 10-Aug-2017].

[8] Microsoft, "Windows 10 IoT Core Official Website | Developer Resource | Windows IoT." [Online]. Available: https://developer.microsoft.com/en-us/windows/iot. [Accessed: 17-Aug-2017].

[9] U. of S. CVSSP Webpages, "University of Surrey - Centre for Vision, Speech and Signal Processing - Home." [Online]. Available: https://www.surrey.ac.uk/centre-vision-speech-signal-processing. [Accessed: 17-Aug-2017].

[10] L. A. R. R. Copyright © 2006-2017 How-To Geek, "What Is OAuth? How Those Facebook, Twitter, and Google Sign-in Buttons Work." [Online]. Available: https://www.howtogeek.com/53275/exchanging-data-safely-with-oauth/. [Accessed: 17-Aug-2017].

[11] D. Hardt, "The OAuth 2.0 Authorization Framework [RFC 6749]," *RFC 6749*, pp. 1–76, 2012.

[12] S. M. Sohan, C. Anslow, and F. Maurer, "SpyREST in action: An automated RESTful API documentation tool," in *Proceedings - 2015 30th IEEE/ACM International Conference on Automated Software Engineering, ASE 2015*, 2016, pp. 813–818.

# Iris Recognition using Machine Learning from Smartphone Captured Images in Visible Light

Md. Fahim Faysal Khan,[1*] Ahnaf Akif,[1] and M. A. Haque[1]

[1]Department of Electrical and Electronic Engineering
Bangladesh University of Engineering and Technology
Dhaka -1205, Bangladesh
[*]fahim.faysal11@gmail.com

*Abstract*—**This work shows the applicability and feasibility of different machine learning techniques on iris recognition from smartphone captured eye images. First, the iris is localized using the popular Daugman's method and the eyelids are suppressed with canny edge detection technique. Then normalization of the extracted iris region is performed in a novel way by setting an adaptive threshold. Next, the normalized image is decomposed using Haar wavelets to obtain the feature vectors. Histogram equalization is performed for better classification accuracy. After that, different classifiers are trained using the extracted feature vectors which yield about 99.7% accuracy for training and 97% accuracy for testing. Finally, the results are compared with other previously applied methods on the same dataset and it is found that the proposed method outperforms most of them.**

***Index Terms***—**Iris recognition, machine learning, visible spectrum, eyelash removal, smartphone**

## I. Introduction

Human iris is well known for its uniqueness, stability and non-evasiveness [1]. Hence iris recognition is a very popular problem for the researchers in the field of bioinformatics, cryptography, computational intelligence etc. Many successful approaches have been taken so far. This approaches can be classified into two categories based whether they used machine learning or not. A significant thing to notice that the datasets which are used in these approaches are iris images captured by NIR (Near Infrared) camera as they offer very good visibility of iris texture, even for heavily pigmented regions [2]. As a result, the extracted iris region provides more accurate information implying better chances for recognition. However, the setup complexity with the above mentioned camera is difficult especially when the issue of portability and simplicity arises. On the other hand, smartphones with cameras are within everyone's reach now a days. The only problem with these cameras is that they capture images in visible light spectrum resulting in less detailed iris images compared to the NIR cameras. So the usual question arises "Are they good enough for iris recognition?"

A good number of studies [2,8] replied positively towards the question. The one thing to notice here that almost all the above mentioned approaches paid a little or no effort to state the feasibility or usability of machine learning techniques in case of the smartphone captured iris database. This is important because machine learning techniques have provided very good results in case of NIR camera captured datasets [3]. As iris images in visible light are likely to offer relatively less details, the question of applicability of ML techniques in this case still remain unanswered. However, one studyRaja *et. al*[4] used Sparse Reconstruction Classifier with K-means clustering which gave a very low EER percentage (Equal Error Rate).It is in other words a very good indication but it does not compare or give any further info on the feasibility of other machine learning techniques.

In our work, we investigate further on the use of machine learning techniques on iris recognition using smartphone captured iris images in visible light spectrum. In order to do so we develop a complete segmentation and feature extraction technique and try to use same set of extracted features to train different classifier. Finally, we compare the classification accuracy of the trained classifiers and decide whether the machine learning techniques are feasible in case of smartphone captured database.

## II. Related Works

Several works have been done with the publicly available datasets UBIRISv1 [5], UBIRISv2 [6], MICHE [7] etc. containing iris images in visible light spectrum. The challenges of iris recognition associated with unconstrained iris images in visible light were discussed by Proenca *et al* [8]. Noisy iris images and independent segmentation and noise recognition procedures are most likely the sources of errors. Santos *et al.* [9] explored best illumination configurations for visible light iris images.

Raja *et al.* [10] used deep sparse filtering with visible spectrum iris dataset VSSIRIS, BIPLab and obtained a very promising result (EER less than 2%).

Another interesting study from Trokielewicz *et al.* [2] where a completely new dataset was created by themselves, showed that iris images captured with a mobile phone offer sufficient visibility of iris texture details for all level of pigmentation. And they also justified that this images are readily usable with already available iris recognition solutions such as VeriEye [11], MIRLIN [12], OSIRIS [13], IriCore [14] etc. All of these algorithms offered more than 95% accuracy for the dataset.

Machine learning techniques have also been proved to be very successful in iris recognition. A study from De Marsico*et al.* [3] compared different machine learning techniques in iris recognition. In these studies, they used mostly CASIA-Iris [15] dataset which is created from images taken with NIR camera. Among different approaches, Rai and Yadav [16] were able to obtain 99% accuracy with a combination of Support Vector Machines and Hamming distance.

## III. Dataset

In our study, the dataset created by Trokielewicz [2] and their group was used. Total 70 people participated and the photos were taken by iPhone 5s (8 megapixels and *f/2.2*). The final dataset comprises about 3192 images acquired in 2 sessions. We used these images for iris recognition. And to the best of our knowledge, no one used machine learning techniques on this dataset before.

978-1-5386-3374-8/17/$31.00 ©2017 IEEE

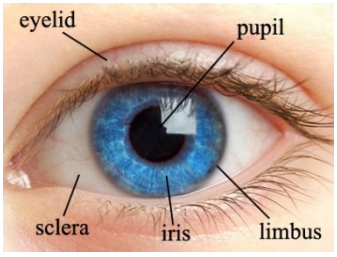


Fig. 1 The typical components in an eye image [20].

## IV. METHODOLOGY

### A. Image Pre-processing

The images provided in the dataset were in RGB format. We had to convert it into a single channel to proceed. While converting, red channel was used as wavelengths corresponding to red light (closest to near infrared) are the longest in our visible spectra, the best iris pattern should be visible this way [2].

### B. Iris Localization

For extracting the iris region first, the classic Daugman's Integro-differential operator is used. The Integro-differential operator [17] is defined as

$$max_{(r,x_o,y_0)} \left| G_\sigma(r) * \frac{d}{dx} \oint_{x_o,y_0} \frac{I(x,y)}{2\pi r} ds \right| \quad (1)$$

Where $I(x,y)$is the eye image, r is the radius of the search, $G_\sigma(r)$is Gaussian smoothing function and s is the contour of the circle given by $(r, x_o, y_0)$ i.e. circle of radius r whose centre is at $(x_o, y_0)$. The operator searches for the circular path where there is maximum change in intensity occurs by varying the radius and centre x and y position of the circular contour. First, the iris boundary is localized as the maximum gradient is usually there. Then a fine search detects the pupillary boundary. We used variance ( $\sigma = 0.5$ ) for the Gaussian smoothing function. For faster run the image was scaled down to find $(r, x_o, y_0)$. These values were then rescaled to get the co-ordinates and radius in the original image. Under normal circumstances, this operator successfully localized the iris region. However, if there is any reflection, it might fail locally. So for fine search instead of brute force, we adaptively ran the search for a selected set of points inside the iris region with pupil radius varying from 10% to 90% than that of the iris. By this way, we were able to localize the iris region of all eye images in our database successfully.

Red Channel Localized Iris

Fig. 2 Iris localization

### C. Eyelid Suppression

The visible portion of the iris part is not exactly circular. It is partly covered by the eyelids which needs to be suppressed. To do so, we followed an approach inspired from Masek [18]. The total search region was divided into two parts, upper eyelid and lower eyelid. The width of the search region is exclusively the difference between the iris and the pupil radius. First the edges were detected using canny edge detection followed by the gamma adjustment and hysteresis thresholding. Finally, the edge-image was radon transformed to get the eyelid line both for upper and lower sections.

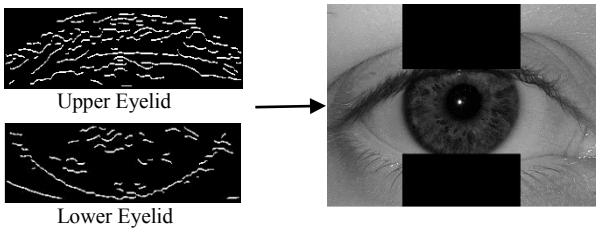


Fig. 3 Eyelid Suppression

### D. Normalization

So far we have successfully segmented the iris part and suppressed eyelids. Now we have to transform it into fixed dimensions for further processing. To do that, we used the very popular homogenous rubber sheet model introduced by Daugman [17]. In the homogenous rubber sheet model, each point within the iris region is remapped to a pair of polar coordinates $(r, \theta)$ where r is on the interval [0, 1] and $\theta$ is angle in the range $[0, 2\pi]$.

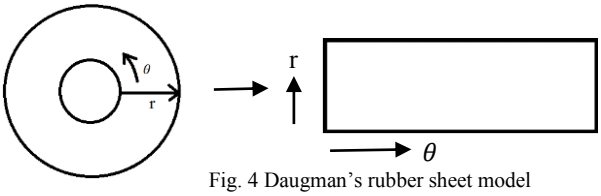


Fig. 4 Daugman's rubber sheet model

The remapping can be modelled as

$$I(x(r,\theta), y(r,\theta)) \rightarrow I(r,\theta) \quad (2)$$

With,

$$x(r,\theta) = (1-r)x_p(\theta) + rx_i(\theta) \quad (3)$$

$$y(r,\theta) = (1-r)y_p(\theta) + ry_i(\theta) \quad (4)$$

Where $I(x,y)$ is the iris region, $(x,y)$ are the original Cartesian coordinates, $(r,\theta)$ are the corresponding normalized polar coordinates, $(x_p,y_p)$ and $(x_i,y_i)$ are the centre coordinates of pupil and iris boundary along the $\theta$ direction.

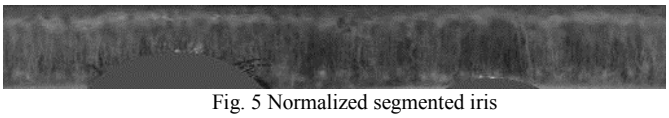

Fig. 5 Normalized segmented iris

### E. Eyelash Removal

Even though eyelash removal is a part of noise cancellation, it was done after the normalization in our work. Developing a method to do so was a tough job as the eyelashes differ largely from image to image. The most obvious option was applying a threshold. But if a hard threshold value is applied, there is no guarantee that it will work for every image. In some images the iris region was darker than the others. So we had to develop an adaptive algorithm to set the threshold value in each image separately. We did it by analysing the histogram of the normalized iris image. As the eyelashes are usually the darkest parts of the image, histogram inspection led us to find the pixel values of those. These pixel values were used as thresholds to detect the occluded regions. The detected pixels were set to "0" at first and then were restored from the non-occluded regions in the neighbourhood of those pixels.

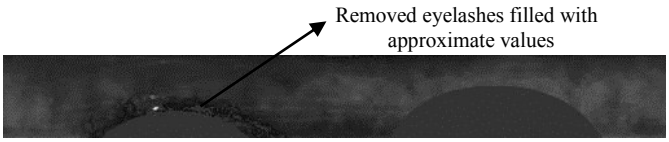


Fig. 6 Eyelash removal

### F. Histogram Equalization

Once the iris region is segmented, normalized and noise has been removed, the relevant texture and intensity information needs to be extracted to train a classifier. But before doing that a histogram equalization was performed on the normalized images. This is because the histogram analysis of the normalized image revealed that the image intensities were congested in a very small region making it harder for the classifier to differentiate. In our study we found that the histogram equalization improved the recognition and training accuracy over 2%.

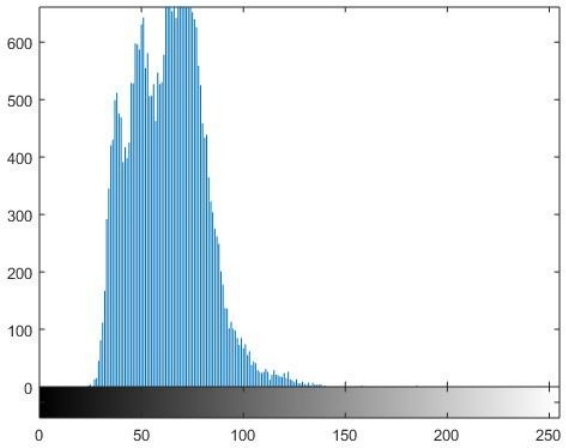


Fig. 7 Before histogram equalization

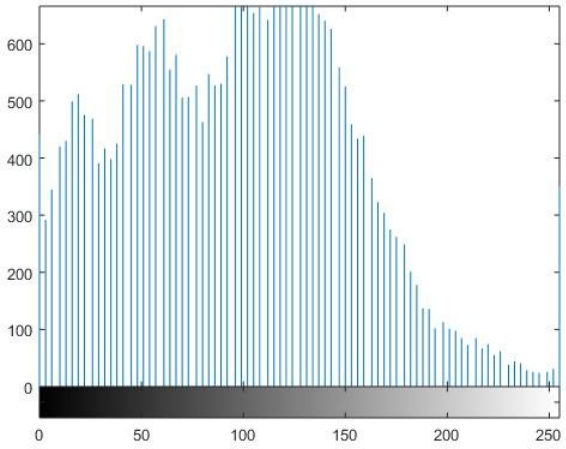


Fig. 8 After histogram equalization

### G. Feature Extraction

A typical iris consists of lots of complex patterns such as *arching ligaments, furrows, ridges, crypts, rings, corona, freckles* and a *zigzag collarette*. These complex patterns are very much complicated to extract. That is why we chose to train with the image itself. So far we have a normalized image of size 64 x 512 pixels. If we want to train the classifier with this amount of data, it will be too heavy and training will take a very long period of time. So we need to scale it. But scaling may result in loss of important information.

The solution to this problem lies in wavelet decomposition as the wavelets have localized frequency data i.e. features having same resolution can be matched up. As we know of now that if a 2-d wavelet transformation is applied on an image, it decomposes it into 4 segments: LL, LH, HL and HH. The LL is called the approximation of the image. LH is the horizontal detail, HL is the vertical detail and HH represents the diagonal detail of the image. The most energy and information is contained within the LL coefficients. So these are our desired values. Figure 9 shows the wavelet decomposed iris image after two stages. Finally, we were able to make the image ready for training after successive 3 stages of wavelet decomposition. The LL3 coefficients were taken which contained 8 x 64 = 512 features. For decomposition, Haar wavelets were used.

The extracted feature vector was 2D with dimension 8 x 64. Before Training the classifier, it was converted to a 1D vector of length 512 by placing the rows side by side (Fig- 10).

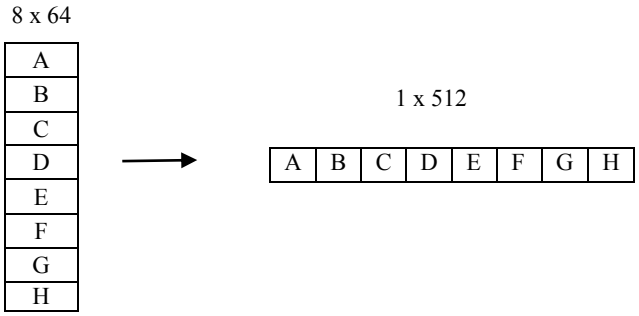


Fig. 10 1-d feature vector of size 512

### H. Training Classifier

In the given database, we had eye images of 70 people. For training the model we took 5 images for each person and rest of the images were kept aside for testing the classifier. For training we used 5-fold cross validation method so that each image in the training set can be tested once against the others. We tried several classifier and among them support vector machines, k-nearest neighbour, linear discriminants etc. showed great promise. The results are summarized in the next section.


Fig. 9 Wavelet decomposition after 2 stages

### I. Results

For training and testing several classifiers were used. Starting from decision trees, discriminant analysis, support vector machines, RUSBoosted trees, K-nearest-neighbours, Subspace KNN etc. The following table summarizes the best performed classifier accuracy:

TABLE I
CLASSIFIER ACCURACY

| Classifier | Train Accuracy (%) | Test Accuracy (%) |
|---|---|---|
| SVM (Linear Kernel) | 99.1 | 96.46 |
| SVM (Quadratic) | **99.7** | **97** |
| KNN | 99.4 | 95.1 |
| LDA | 99.4 | 94.28 |

It is evident from the above data that Support Vector Machines give the best results. K-nearest-neighbours also performs very well. Though its accuracy is slightly lower than that of SVMs, it takes much less time to train and test. Similar is the case for Linear Discriminant Classifier (LDA). The ROC (Receiver Operating Characteristics) curve matrix attained during training for the best model i.e. SVM with quadratic kernel is given below:

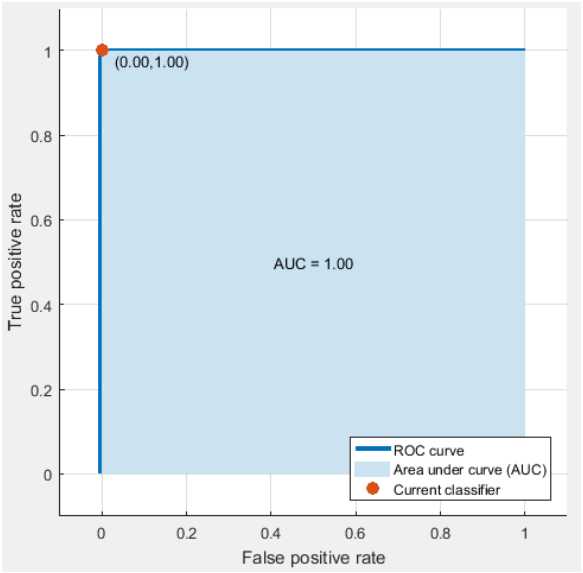


Fig. 11 ROC curve for SVM model

It is evident from the result that our very first doubt about the feasibility and applicability of machine learning techniques on iris recognition from smartphone captured visible light images is well answered through this work.

Now if we compare our approach and its results with the other approaches that is already applied on the same dataset, we see that our approach indeed shows a great promise.

TABLE II
DIFFERENT APPROACHES' RESULT ON SAME DATASET

| Classifier | Accuracy (%) |
|---|---|
| VeriEye[11] | 94.57[2] |
| MIRLIN[12] | 95.63[2] |
| OSIRIS[13] | 95.25[2] |
| IriCore[14] | **99.67**[2] |
| **Proposed Method** | **97** |

### J. Sources of Errors

The Major Source of errors in our findings is failure in segmentation of eye images. Despite our efforts, there were

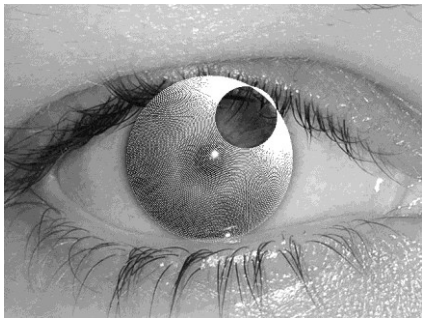

Fig. 12 Failure in correct segmentation

one or two such images whose segmentation could not be done properly. And these are the images who were falsely labelled. Another source of errors are eye images with extremely dark pigments. As a result, it becomes very difficult to extract distinct information from them. Some other noise sources might be blurred images or images with excessive eyelid/eyelash occlusion.

## V. CONCLUSION

In this paper a machine learning based approach on iris recognition from smartphone captured images is proposed. With the results above, this paper successfully showed that in case of smartphone captured visible spectrum iris images, the machine learning techniques are equally as good as the other ones, in some cases even better. Still accuracy can be further improved. And in our findings, accuracy largely depends on accurate segmentation. So some robust approaches may be taken to improve the segmentation result. In our approach we tried to stick to some basic segmentation approaches. This was done keeping in mind their easy implementation. As smartphones of todays' are equipped with very good camera, the whole recognition system shows great promise to be implemented on these smartphones for recognition, security and identification purpose. Already Samsung® [19] has developed a built in iris scanner which works for the user who is using it. Our next task would be to develop a cloud based server where iris data can be easily sent through the smartphone. The classifier will run on the server and the sent data would be matched and verified. Thus by just using the smartphones, it will be possible to develop a full security system.

## ACKNOWLEDGEMENT

This work was performed in the laboratories of the Dept. of EEE of BUET. The authors would like to thank the concerned authorities of BUET for providing the facilities and help in getting the datasets.

## REFERENCE

[1] J. Daugman, "How iris recognition works.," in *IEEE Transactions on circuits and systems for video technology*, 2004.

[2] M. Trokielewicz, "Iris Recognition with a Database of Iris Recognition with a Database of Iris Images Obtained in Visible Light Using Smartphone Camera," in *The IEEE International Conference on Identity, Security and Behavior Analysis (ISBA 2016)*, Sendai, Japan, 2016/02.

[3] M. D. Marsico, A. Petrosino and S. Ricciardi, "Iris recognition through machine learning techniques: A survey," *Pattern Recognition Letters,* vol. 82, pp. 106-115, 2016.

[4] K. B. Raja, R. Raghavendra and C. Busch, "features, Smartphone based robust iris recognition in visible spectrum using clustered k-means," in *Biometric Measurements and Systems for Security and Medical Applications (BIOMS) Proceedings, 2014 IEEE Workshop on*, IEEE, 2014, pp. 15-21.

[5] H. Proença and L. A. Alexandre, "{UBIRIS}: A noisy iris image database," in *13th International Conference on Image Analysis and Processing - ICIAP 2005*, Cagliari, Italy, Springer, 2005, pp. 970-977.

[6] H. Proenca, S. Filipe, R. Santos, J. Oliveira and L. A. Alexandre, "The {UBIRIS.v2}: A Database of Visible Wavelength Images Captured On-The-Move and At-A-Distance," *IEEE Trans. PAMI,* vol. 32, pp. 1529-1535, 2010.

[7] M. D. Marsico, M. Nappi, D. Riccio and H. Wechslerd, "Mobile Iris Challenge Evaluation (MICHE)-I, biometric iris dataset and protocols," *Pattern Recognition Letters,* vol. 57, pp. 17-23, 2015.

[8] H. Proenca and L. A. Alexandre, "The NICE. I: noisy iris challenge evaluation-part I," in *Biometrics: Theory, Applications, and Systems*, IEEE, 2007, pp. 1-4.

[9] G. Santos, M. V. Bernardo, H. Proenca and P. T. Fiadeiro, "Iris Recognition: Preliminary Assessment about the Discriminating Capacity of Visible Wavelength Data," in *2010 IEEE International Symposium on Multimedia*, IEEE, 2010, pp. 324-329.

[10] K. B. Raja, R. Raghavendra, V. K. Vemuria and C. Busch, "Smartphone based visible iris recognition using deep sparse filtering," *Pattern Recognition Letters,* no. 57, pp. 33-42, 2015.

[11] Neurotechnology, "VeriEye SDK, version 4.3".

[12] Smart Sensors Ltd., "MIRLIN SDK, version 2.23," 2013.

[13] G. Sutra, B. Dorizzi, S. Garcia-Salicetti and N. Othman, "A biometric reference system for iris. OSIRIS," 2014.

[14] IriTech Inc., "IriCore Software Developers Manual," 2013.

[15] http://www.sinobiometrics.com, "Casia Iris Image Database".

[16] H. Rai and A. Yadav, "Iris recognition using combined support vector machine and Hamming distance approach," *Expert systems with applications,* vol. 41, pp. 588-593, 2014.

[17] J. Daugman, "High confidence visual recognition of persons by a test of statistical independence," 1993.

[18] L. Masek and P. Kovesi, "MATLAB Source Code for a Biometric Identification System Based on Iris Patterns," in *The School of Computer Science and Software Engineering, The University of Western Australia*, 2003.

[19] "http://www.samsung.com/global/galaxy/galaxy-s8/security/".

[20] "Courtesy: https://www.pinterest.com/".

# Numerical Modeling and Simulation of Quantum Key Distribution Systems under Non-Ideal Conditions

Sadman Shafi,[1,*] Md. Serajum Monir,[1] and Md. Saifur Rahman[1]

[1] Department of Electrical and Electronic Engineering, Bangladesh University of Engineering and Technology
Dhaka-1000, Bangladesh

[*]sadmanshafi10@gmail.com

***Abstract*—Quantum key distribution is a very promising technology that can complement the classical cryptographic protocols. However, since the exploitation of the laws of quantum mechanics for any useful purpose is limited by the non-idealities of modern-day devices, researches are required on how these imperfections can be overcome. In this paper, we propose a QKD system and talk about implementation tradeoffs in real world design. We also propose a method for simulating this QKD system including its non-ideal factors. The results obtained by the simulation of the model try to justify a QKD system implementation instead of classical cryptography. The results also show that a real QKD system can be accurately simulated in a classical computer before it is physically set up.**

***Index terms*—Quantum cryptography, quantum key distribution, simulation, modeling, BB84, quantum communication, quantum information**

## I. Introduction

Quantum mechanics, although highly counter-intuitive in nature, has proven to be the most successful theory to explain and give predictions about the nature. Its wildest of predictions has had many useful applications in modern civilization. One of the most recent of these is Quantum Key Distribution (QKD). In theory, this works just fine, but the non-idealities that occur in practical implementation severely limit its performances. In this paper we tried to model the non-idealities that arise from different devices and the environment and study how the performance of a QKD system varies with these non-idealities.

There are several approaches to Quantum Key Distribution depending on what type of property is exploited. They can be divided in two categories: prepare and measure protocols, and entanglement based protocols. In 1983, Stephen Wiesner presented the idea how information can be stored or transmitted by encoding in two "conjugate observables" [1], for example, linear and circular polarization states of light. Based on his idea Charles H. Bennett and Gilles Brassard proposed a secure cryptographic protocol which is known as BB84 [2]. Several other protocols have been suggested later, such as B92 [3], E91 [4], MSZ96 [5], SARG04 [6], KMB09 [7] etc. Numerous modifications of these protocols have been developed throughout the course of time, including a particularly significant one named the decoy state protocol [8]. Various experiments have been carried out in many parts of the world to implement QKD systems, and there are several companies that commercially manufacture QKD systems. However, the speed of communication in realized QKD systems has been a limitation. Therefore, efforts are being made to increase the speed so that it can replace classical systems around the world.

Several QKD protocols can be shown to be unconditionally secure in principle. This security is what makes QKD systems a significant and attractive alternative to classical cryptographic systems. However, practical QKD systems suffer from various non-ideal factors which create security vulnerabilities in the systems. Hence much research is being conducted in studying the effects of these non-idealities on QKD systems, and developing possible countermeasures. A utility for simulating QKD systems incorporating these non-ideal conditions can greatly help in these studies, and developing such a simulation utility is our objective.

The remainder of the paper is organized as follows: In section II we talk about the basic principle of the QKD protocol BB84. In section III we give an illustration of the results and error rates that can be theoretically obtained under ideal conditions. In section IV we propose the QKD system based on the BB84 protocol that can be implemented in practice. We also discuss about various devices and components in the QKD system and the sources of non-idealities. We provide mathematical modeling for these non-idealities, and in section V, we define some system parameters necessary for characterization of the system performance. Based on the mathematical models we show the simulation results in section VI. Finally, in section VII we give conclusions and provide future research efforts.

## II. Basic Principle

The BB84 protocol requires two parties- Alice, the sender, and Bob, the receiver. Alice prepares two random bit-streams – the message bit-stream $a$ and the basis bit-stream $b$. She prepares qubits in two bases according to $a$ and $b$. We assume that she prepares the qubits by "encoding" single photons with four polarization states – horizontal $|H\rangle$, vertical $|V\rangle$, diagonal $|+\rangle$ and antidiagonal $|-\rangle$. She then sends the prepared qubits to Bob through a quantum channel.

TABLE I. Polarization States and Bases

| Polarization State | Basis | Dirac Notation Representation | Encoded Bit |
|---|---|---|---|
| **Horizontal** | Rectilinear | $\|0\rangle = 1 \cdot \|H\rangle + 0 \cdot \|V\rangle$ | 0 |
| **Vertical** | Rectilinear | $\|1\rangle = 0 \cdot \|H\rangle + 1 \cdot \|V\rangle$ | 1 |
| **Diagonal** | Diagonal | $\|+\rangle = \frac{1}{\sqrt{2}} \cdot \|H\rangle + \frac{1}{\sqrt{2}} \cdot \|V\rangle$ | 0 |
| **Anti-diagonal** | Diagonal | $\|-\rangle = \frac{1}{\sqrt{2}} \cdot \|H\rangle - \frac{1}{\sqrt{2}} \cdot \|V\rangle$ | 1 |

Bob prepares a random basis bit-stream $b'$ and measures the states of the qubits according to $b'$. Using the outcome of the measurements, he obtains a raw message bit-stream $a'$. If the

978-1-5386-3374-8/17/$31.00 ©2017 IEEE

bit-streams are long, about 75% of the bits of $a$ and $a'$ will match, and about 50% of the bits of $b$ and $b'$ will match. Alice and Bob then publicly compare $b$ and $b'$ and discard those bits of $a$ and $a'$ corresponding to the bits of $b$ and $b'$ that do not match. This process is called "sifting", and the message bit-streams thus obtained after sifting are the "sifted keys" $a_{\text{sift}}$ and $a'_{\text{sift}}$. Ideally, without any noise and any eavesdropper, $a_{\text{sift}} = a'_{\text{sift}}$. Thus, there will be no error in the sifted keys formed.

Now suppose an eavesdropper, Eve, is present, who tries to intercept the qubits sent by Alice. Eve measures the states of the intercepted qubits. However, this destroys the states of those qubits, and by the "no-cloning theorem" [9], she will not be able to reproduce those states. She then prepares qubits according to the outcomes of her measurements, and sends them to Bob to avoid suspicion. This hacking strategy is called intercept-and-resend attack. If this attack is made, then the error in Bob's $a'$ will be more than 25%, and thus Bob will be able to detect the presence of Eve.

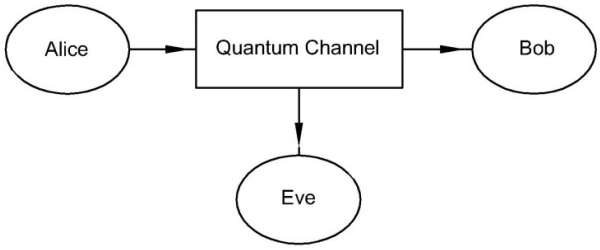


Fig. 1. Schematic diagram of a generic quantum key distribution system

It can be shown that the BB84 protocol is theoretically unconditionally secure under ideal conditions [10].

## III. Simulation under Ideal Conditions

We have carried out a simulation of the BB84 protocol under ideal conditions. The simulation was done using MATLAB. We have included the presence of Eve who performs an intercept-and-resend attack in the system. The eavesdropping rate of Eve (the ratio of the number of qubits intercepted by Eve to the total number of qubits transmitted by Alice) is varied and its effects are observed on the error rate and the message match rate of Bob's received message with the transmitted message of Alice before and after sifting. The results are shown in Fig 2.

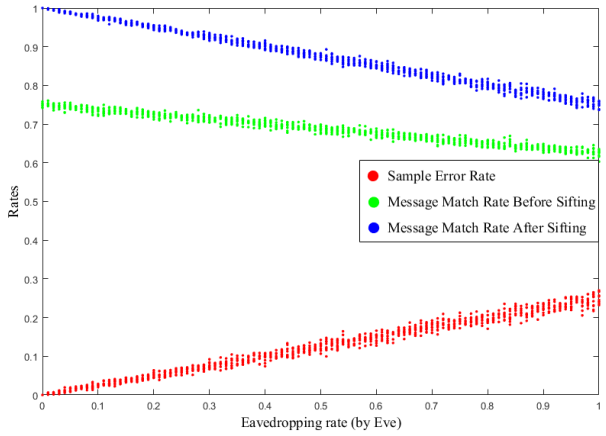


Fig. 2. Sample error rate, message match rates before and after sifting vs. eavesdropping rate by Eve

The results match with those predicted theoretically. The sample error rate (error rate in a sample of bits chosen randomly from the sifted key by Alice and Bob) increases with the increase in eavesdropping rate, because increased eavesdropping causes increased disturbance in the states of the qubits, and thus results in an increased error rate. This also causes the message match rates before and after sifting to decrease.

## IV. Implementation of the Proposed Quantum Key Distribution System and Non-Ideality Simulation

The QKD system consists of three parts - Alice's module (transmitter), quantum channel and Bob's module (receiver).

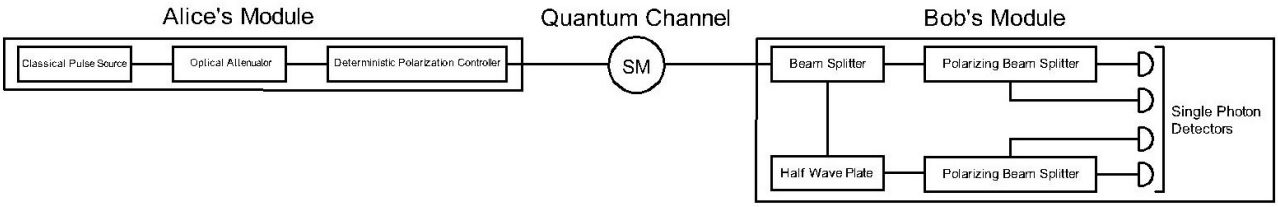


Fig. 3. Schematic diagram of the modelled quantum key distribution system employing the BB84 protocol

### A. Alice's Module

Alice's module consists of a classical pulse source, an optical attenuator and a deterministic polarization controller. The classical pulse source produces strong optical pulses of light plane polarized in a particular direction at a certain rate. The optical attenuator strongly attenuates these pulses to "weak coherent pulses" having a very low mean photon number (less than 1). The weak coherent pulses act as "single photons". The deterministic polarization controller sets the polarization states of these pulses according to Alice's message and basis bits.

*1) Classical Pulse Source:* The classical pulse source consists of a laser diode and a polarizer. The laser diode produces unpolarized light pulses of wavelength 1550 nm. Each pulse has millions or billions of photons and behaves as a "classical" pulse. The polarizer plane-polarizes these pulses at a certain orientation angle.

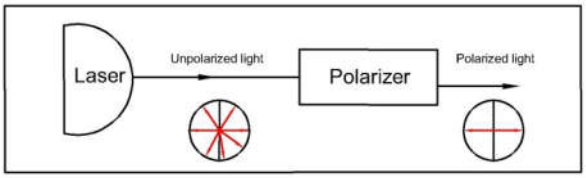


Fig. 4. Schematic diagram of the classical pulse source

Commercially available optical fibers and most other optical devices used in optical fiber communication have been optimized for the wavelength 1550 nm, and so this wavelength has been chosen [11].

*2) Optical Attenuator:* The optical attenuator block consists of a fixed optical attenuator (FOA) and an electronic variable optical attenuator (EVOA).

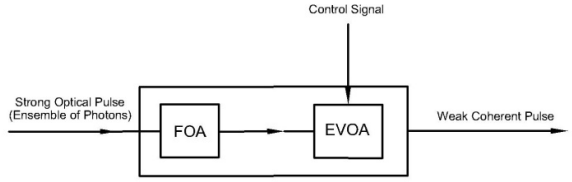


Fig. 5. Schematic diagram of the optical attenuator

The photon numbers in the weak coherent pulses produced obey Poisson statistics [11], [12]. If the mean photon number of the weak coherent pulses is $\mu$, then the probability that a weak coherent pulse will contain $n$ photons is given by

$$P(n) = \frac{\mu^n e^{-\mu}}{n!} \tag{1}$$

If a pulse contains more than 1 photon, it can cause security vulnerabilities. They can be mitigated by several ways, such as the use of decoy states [8].

*3) Deterministic Polarization Controller:*

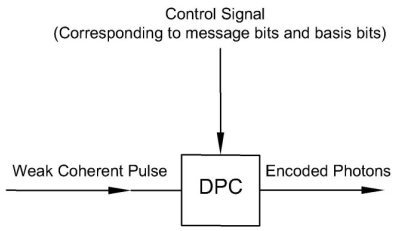


Fig. 6. Schematic diagram of the deterministic polarization controller

The deterministic polarization controller (DPC) can change the polarization state of light passing through it in a known and controlled manner. It is used to "encode" photons by setting their polarization states according to the bit streams $a$ and $b$ of Alice.

## B. Quantum Channel

The photons emitted from the source travel through a "quantum channel". A single mode optical fiber can be used as this "quantum channel". We have used photons of wavelength 1550nm since at this value the attenuation through the fiber is very low, about $0.2dB/km$. A real optical fiber can introduce several non-idealities, such as polarization change, depolarization, polarization mode dispersion etc. We have included the polarization change of photons transmitted through the channel in the simulation.

## C. Bob's Module

Bob's module consists of a beam splitter, a half wave plate, two polarizing beam splitters and four single photon detectors.

*1) Beam splitter:* The beam splitter (BS) splits light incident on it into two parts by transmitting a certain portion of the light and reflecting the remaining light in another direction. In this work, we have used a 50:50 beam splitter that transmits half of the incident light and reflects the other half.

Real beam splitters exhibit some non-ideal properties such as attenuation, ghosting, polarization dependent losses etc. Consider a BS with a split ratio $r = T:R$. Let the amplitudes of the incident light, the transmitted light and the reflected light be $E_0 E_T$ and $E_R$ and their intensities be $I_0 I_T$ and $I_R$ respectively. Suppose, their polarization orientation angles are $\theta_0 \theta_T$ and $\theta_R$, the horizontal components of their amplitudes are $E_{0x} E_{Tx} E_{Rx}$ and their vertical components are $E_{0y} E_{Ty} E_{Ry}$ respectively. Let the attenuation of the beam splitter be $\alpha$ (in decibels) and the polarization dependent losses for horizontal and vertical polarization states be $PDL_x$ and $PDL_y$ (in decibels) respectively. Then

$$\alpha + PDL_x = 10\log_{10}\left(\frac{E_{Tx}^2}{E_0^2\cos^2\theta_0}\times\frac{T+R}{T}\right) = 10\log_{10}\left(\frac{E_{Rx}^2}{E_0^2\cos^2\theta_0}\times\frac{T+R}{R}\right) \tag{2}$$

$$\alpha + PDL_y = 10\log_{10}\left(\frac{E_{Ty}^2}{E_0^2\sin^2\theta_0}\times\frac{T+R}{T}\right) = 10\log_{10}\left(\frac{E_{Ry}^2}{E_0^2\sin^2\theta_0}\times\frac{T+R}{R}\right) \tag{3}$$

$$I_T \propto E_T^2 = E_{Tx}^2 + E_{Ty}^2 \tag{4}$$

$$I_R \propto E_R^2 = E_{Rx}^2 + E_{Ry}^2 \tag{5}$$

For a single photon incident on a BS, whether it will be transmitted or reflected is a purely random event - a feature of quantum mechanics. For a real BS, if we incorporate attenuation and polarization dependent losses, then the probability that an incident photon will be transmitted is

$$P(T) = \frac{I_T}{I_0} = \frac{E_T^2}{E_0^2} = \frac{T}{T+R}\cdot 10^{\frac{\alpha}{10}}\left(10^{\frac{PDL_x}{10}}\cos^2\theta_0 + 10^{\frac{PDL_y}{10}}\sin^2\theta_0\right) \tag{6}$$

And the probability that it will be reflected is

$$P(R) = \frac{I_R}{I_0} = \frac{E_R^2}{E_0^2} = \frac{R}{T+R}\cdot 10^{\frac{\alpha}{10}}\left(10^{\frac{PDL_x}{10}}\cos^2\theta_0 + 10^{\frac{PDL_y}{10}}\sin^2\theta_0\right) \tag{7}$$

Thus, a photon passing through a real BS has a finite probability of being "destroyed" (e.g. scattered or absorbed), and that probability is

$$P(\text{destroy}) = 1 - P(T) - P(R) \tag{8}$$

The beam splitter performs a "passive basis selection" for Bob by randomly transmitting or reflecting an incident photon. A transmitted photon will be measured in the horizontal-vertical basis, whereas a reflected photon will be measured in the diagonal-antidiagonal basis.

*2) Half wave plate:* The half wave plate rotates the plane of polarization of a plane polarized incident beam of light by a specified amount. In our work, the half wave plate is aligned so that it rotates the plane of polarization of the incident light by 45° clockwise.

*3) Polarizing Beam Splitter:* The polarizing beam splitter (PBS) splits the incident beam of light into two beams of light with different polarization states. Real polarizing beam splitters display several non-idealities, such as attenuation,

polarization dependent losses etc. Using the quantities mentioned in case of the normal beam splitter, we have

$$\alpha + PD\,L_x = 10\log_{10}\left(\frac{E_{Tx}^2}{E_0^2\cos^2\theta_0}\right) \quad (9)$$

$$\alpha + PD\,L_y = 10\log_{10}\left(\frac{E_{Ry}^2}{E_0^2\sin^2\theta_0}\right) \quad (10)$$

$$r_e\ (dB) = 10\log_{10}\left(\frac{E_{Tx}^2}{E_{Ty}^2}\right) = 10\log_{10}\left(\frac{E_{Ry}^2}{E_{Rx}^2}\right) \quad (11)$$

Here, $r_e$ is the extinction ratio of the PBS. Equations (4), (5) also apply here.

Similar to a normal BS, if a single photon is incident on a PBS, whether it will be transmitted or reflected is a random event. The probability that an incident photon will be transmitted is

$$P(T) = \frac{I_T}{I_0} = 10^{-\frac{\alpha + PD\,L_x}{10}}\left(1 + 10^{-\frac{r_e}{10}}\right)\cos^2\theta_0 \quad (12)$$

And the probability that it will be reflected is

$$P(R) = \frac{I_R}{I_0} = 10^{-\frac{\alpha + PD\,L_y}{10}}\left(1 + 10^{-\frac{r_e}{10}}\right)\sin^2\theta_0 \quad (13)$$

The probability that an incident photon will be annihilated is thus similar to (12).

*4) Single photon detector:* The single photon detector (SPD) can detect and count single photons and weak coherent pulses incident on it. One of the most feasible single photon detectors suitable for quantum communication using photons at the telecommunication wavelength 1550 nm is the InGaAs avalanche photodiode, which has been modeled in our work. Real single photon detectors have several limitations, including dark counts, time jitter, afterpulsing, limited quantum efficiency, lack of ability of photon number resolution etc.

The two PBS's, the half-wave plate and the 4 SPDs "measure" the received photons. In Fig. 3, the upper PBS and the two associated SPDs measure the photons transmitted by the BS in the rectilinear basis. The half-wave plate, the lower PBS and the two associated SPDs measure the photons reflected by the BS in the diagonal basis. The detections in the SPDs determine the outcomes of the measurements.

## V. System Parameters and Performance Measures

Three system parameters – the mean photon number (MPN) of the weak coherent pulses, the optical fiber length and the dark count probability of the avalanche photodiodes – are varied in the simulation to observe their effects on the system performance. Several quantities can be used to characterize the system performance, such as the quantum bit error rate (QBER) of the sifted key, the signal gain, the sifted key generation rate etc.

QBER of the sifted key

$$= \frac{\text{Number of correct bits in the sifted key}}{\text{Total number of bits in the sifted key}} \quad (14)$$

Signal gain

$$= \frac{\text{No. of Bob's sifted signal detections}}{\text{No. of Alice's classical signal pulses sent}} \quad (15)$$

The sifted key generation rate is the number of bits in the sifted key generated per unit time. For example, if the sifted key generation rate is 100 kbps, then $100 \times 10^3$ bits is obtained in the sifted key in 1 second.

## VI. Simulation Results

The entire experimental setup was simulated several times with a certain number of optical pulses generated (e.g. $10^6$) in each run. The simulation was performed with MATLAB. The mean photon number, the optical fiber length and the dark count probability of the avalanche photodiodes were varied separately, and their effects on the signal gain, quantum bit error rate (QBER) and the sifted key generation rate were observed. The results are shown in figures 7-12.

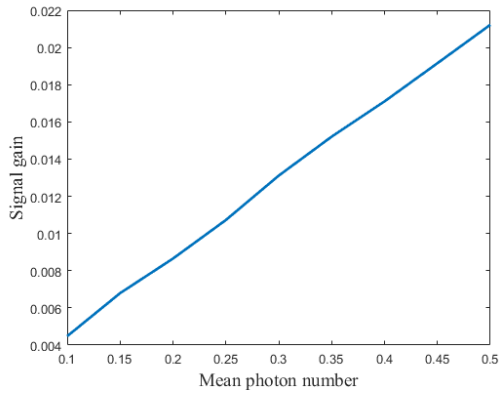


Fig. 7. Signal gain vs. mean photon number

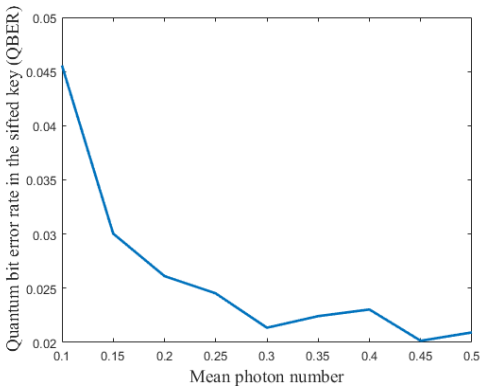


Fig. 8. Quantum bit error rate of the sifted key vs. mean photon number

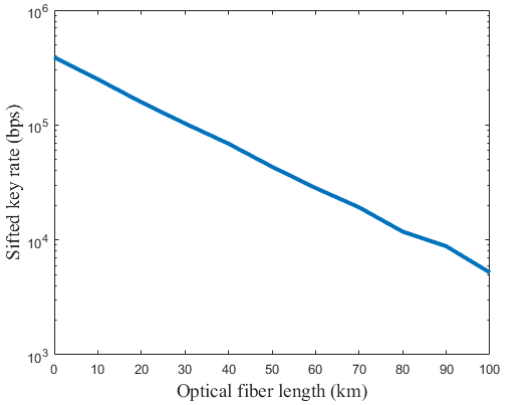


Fig. 9. Sifted key generation rate vs. optical fiber length

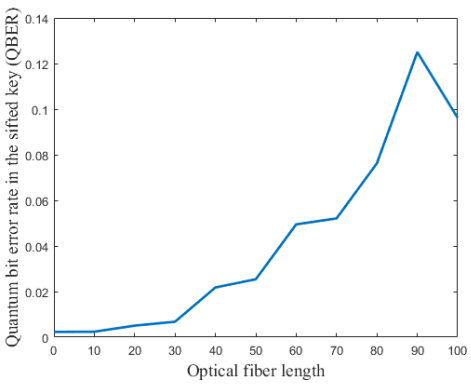


Fig. 10. Quantum bit error rate of the sifted key vs. optical fiber length

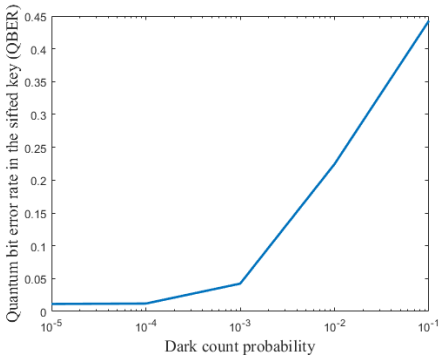


Fig. 11. Quantum bit error rate of the sifted key vs. dark count probability

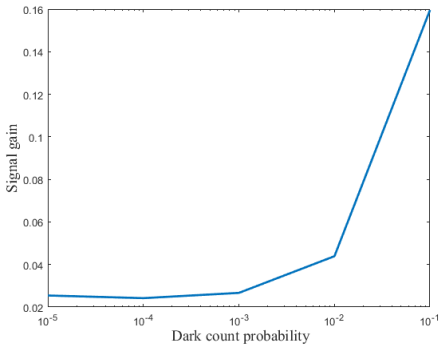


Fig. 12. Signal gain vs. dark count probability

From figures 7 and 8, it is seen that the signal gain increases with the mean photon number, and the QBER decreases, which is expected. Increasing the mean photon number increases the number of non-empty weak coherent pulses and thus the number of pulses received by Bob and so the number of sifted signal detections increases. This increases the signal gain.

Figure 9 shows that the sifted key rate decreases with the increase in optical fiber length. A longer optical fiber results in greater attenuation of the transmitted pulses, and the number of pulses detected by Bob decreases. This causes a reduction in the sifted key rate. Increasing the optical fiber length also increases the change of the polarization states of the photons, which leads to more errors, and thus increases the QBER, as shown in figure 10.

Figure 11 and 12 depict that the QBER and the signal gain increase with the increase in dark count probability. If the dark count probability of the avalanche photodiodes increases, the number of erroneous dark count detections at Bob's module increases, which in turn decreases the message match rate between Alice and Bob before sifting and increases the QBER of the sifted message. Since increased dark count detections increase the number of sifted message bits, so the signal gain also increases with the increase in dark count probability, albeit with more errors in the sifted message. The highest acceptable dark count probability for this experimental setup is about $10^{-3}$, above which the QBER increases to unacceptable levels (the maximum theoretical upper limit of QBER for secure key generation is about 11% when privacy amplification and one-way error correction are applied and about 20% when privacy amplification and two-way error correction are used [13], [14], [10]).

## VII. Conclusion

The simulation results show the effects of some non-ideal conditions on the performance of a real QKD system, and these effects are realistic and expected. The non-ideal behavior of the system as found in the simulation closely resemble the real-life behavior of the system. Thus, the simulator can reliably simulate a real QKD system and can be used to estimate the performance of the system. The simulator can also be modified to simulate other QKD systems with different QKD protocols. Further research can be done to include more non-ideal factors of the devices used in different QKD systems to make the simulation more accurate.

## References


[1] S. Wiesner, "Conjugate Coding," *ACM SIGACT News - A special issue on cryptography,* vol. 15, no. 1, pp. 78-88, 1983.

[2] C. H. Bennett and G. Brassard, "Quantum cryptography: Public key distribution and coin tossing," in *Proc. IEEE Int. Conf. Comput., Syst. Signal Process.*, 1984.

[3] C. H. Bennett, "Quantum cryptography using any two nonorthogonal states," *Phys. Rev. Lett.,* vol. 68, no. 21, pp. 3121-3124, 1992.

[4] C. H. Bennett, G. Brassard and A. Ekert, "Quantum cryptography," *Scientific Am.,* no. (int. ed.), pp. 26-33, 1992.

[5] Y. Mu, J. Seberry and Y. Zheng, "Shared cryptographic bits via quantized quadrature phase amplitudes of light," *Optics Communications,* vol. 123, no. 1-3, pp. 344-352, 1996.

[6] C. Branciard, N. Gisin, B. Kraus and V. Scarani, "Security of two quantum cryptography protocols using the same four qubit states," *Phys. Rev. A,* vol. 72, no. 3, p. 032301, 2005.

[7] M. M. Khan, M. Murphy and A. Beige, "High error-rate quantum key distribution for long-distance communication," *New Journal of Physics,* vol. 11, no. 6, p. 063043, 2009.

[8] H. -K. Lo, X. Ma and K. Chen, "Decoy state quantum key distribution," *Phys. Rev. Lett.,* vol. 94, no. 3, p. 230504, 2005.

[9] W. Wootters and W. Zurek, "A Single Quantum Cannot be Cloned," *Nature,* no. 299, pp. 802-803, 1982.

[10] P. Shor and J. Preskill, "Simple Proof of Security of the BB84 Quantum Key Distribution Protocol," *Phys. Rev. Lett.,* vol. 85, no. 2, pp. 441-444, 2000.

[11] N. Gisin, G. Ribordy, W. Tittel and H. Zbinden, "Quantum cryptography," *Rev. Modern Phys.,* vol. 74, no. 1, p. 12, 2002.

[12] R. H. Hadfield, "Single-photon detectors for optical quantum information applications," *Nature Photon.,* vol. 3, p. 698, 2009.

[13] K. Tamaki, M. Koashi and N. Imoto, "Unconditionally Secure Key Distribution Based on Two Nonorthogonal States," *Phys. Rev. Lett.,* vol. 90, no. 16, p. 167904, 2003.

[14] D. Gottesman, H.-K. Lo, N. Lütkenhaus and J. Preskill, "Security of Quantum Key Distribution with Imperfect Devices," *Quantum Inf. Comp.,* vol. 4, no. 5, pp. 325-360, 2004.

[15] T. F. d. Silva, G. B. Xavier and J. P. v. d. Weid, "Real-Time Characterization of Gated-Mode Single-Photon Detectors," *IEEE Journal of Quantum Electronics,* vol. 47, no. 9, pp. 1251 - 1256, 2011.

# Evaluation of Butterworth Coupling Arrangement and Line Trap Circuit for PLC Integrated Power System

Hasan Mahamudul[1,*], Cagil Ozansoy[2], and Ershadul Haque[3]
[1,2] College of Engineering and Science, Victoria University
Melbourne, Australia
[3]Z. H. Sikder University of Science & Technology
Modhupur, Kartikpur, Bangladesh
[*] md.hasan5@live.vu.edu.au

*Abstract*- **Coupling Circuits (CCs) and Line Traps (LTs) are the two most important elements of PLC-integrated power system networks. CCs are used for selectively injecting PLC signals into the network, whereas the LT is used to restrict the PLC signal from entering into areas of the network where such signals may damage equipment. In this paper, a Butterworth filter based CC and a T-type LT circuit have been modelled, simulated and evaluated. The objective was to design power systems complaint coupling and line trap circuits to operate within the CENELEC frequency band. The key finding is that sufficient performance can be achieved in terms of the insertion loss profile of the CC and LT when such circuits are designed using commercially available off-the-shelf components. For the designed CC, the insertion loss was measured as -3 dB in the 55 kHz to 100 kHz range. For the LT circuit, the insertion loss was measured as more than -53 dB. This ensures low attenuation of the PLC signal by the CC, and high attenuation by the LT.**

***Index Terms*—Powerline communication, Coupling, Line-trap, CENELEC, Evaluation, Commercial.**

## I. INTRODUCTION

Application of Powerline Carrier (PLC) systems in power system networks can be used in numerous smart grid applications such as controlling home appliances, monitoring of distributed generators, data communications, and fault detection in power system networks [1]. A complete PLC integrated power system network will be associated with lots of peripherals including CCs, LT units, line tuner, and impedance matching units. Amongst the above listed peripherals, the CCs and LTs are the most important elements in the design and operation of an efficient PLC integrated power system network. These two elements are often said to form the heart of a PLC system.

Most research in this area is focusing on the application of PLC systems, rather than how PLC transmitters can be efficiently coupled to networks with minimal signal losses. For example, works in [2, 3] have outlined the suitability of PLC techniques in smart metering applications. Milidius et al. [4-6] has worked on the implementation of a three-phase power line fault detection system using the PLC technique. There are also works, which investigated the possibility of establishing a data connection over the Single Wire Earth Return (SWER) network using the PLC technique [7-12]. Beyond this, few researchers have also worked on modelling and evaluation of LTs and coupling circuits [13-17]. However, there is not much research reported in the literature, which has focused on the evaluation of the coupling arrangement and LT unit on the same network and in the same frequency range. Existing works [13, 17] focus on individual analysis of these two vital components, rather than a holistic analysis including both. This paper aims to address this knowledge gap by considering both in the same network.

The CENELEC band of frequencies (9 kHz to 150 kHz) has been allocated for the use of power utilities. In a PLC-integrated power system, the CC and LT serves opposite purposes. CC is expected to permit the transmission of signals into the network in a given frequency range. The LT, on the other hand, must block signals in this same frequency range to prevent signals from entering into and interfering with the parts of the network such as substations and generation units.

The highlight in this paper is a wide-band study where the CC and the LT unit have both been analyzed for the same frequency band and in the same network. Others [10, 11] have individually analyzed these components, which is a weakness and knowledge gap as these must work together in harmony in real networks. Considering the aforesaid issues, in this paper, a Butterworth bandpass filter based CC and a wideband LT circuit have been modelled and evaluated.

The key objective, in this paper, is to discuss the modeling of Butterworth CCs and LT units and evaluate these in terms of insertion losses within the 45 kHz to 130 kHz frequency band. In terms of insertion loss, it was found that the Butterworth CC produces very low insertion loss (around -3 dB) in the designated frequency band, but the LT unit produces very high insertion loss (more than -53 dB) in the same band.

978-1-5386-3374-8/17/$31.00 ©2017 IEEE

The key feature of this work that separates it from other published work [18, 19] is the fact that commercially available capacitors have been used in modelling the designed CC and LT rather than building models based on non-commercially available values obtained from theoretical calculations. The significance of this work lies in the fact that the designed CC and LT will be appropriate for use within real power networks because they produce desirable results within the designated frequency band. The designated frequency band (55 kHz to 100 kHz) forms a portion of the CENELEC frequency band.

The organization of the paper is as follows: Section 2 summarizes the basic concept of the work with a schematic arrangement and Section 3 presents the modelling and simulation of the Butterworth filter. The modelling and evaluation of the LT circuit has been presented in Section 4, followed by discussion of results in Section 5 and conclusions in Section 6.

## II. BASIC CONCEPT OF THE WORK

A schematic arrangement of the PLC-integrated power system network is shown in Fig. 1, which includes the PLC transmitters and receivers, coupling circuits, line traps, and the electrical network. The PLC modem can generate signals in the 1-500 kHz frequency range. The desired Butterworth CC is expected to attenuate all signals outside the 45 kHz to 130 kHz range, and only allow PLC signals within the designated frequency band to be transmitted onto the electrical network. The function of the LT, connected to either end of the network, is to block signals in the same frequency range from penetrating into substations.

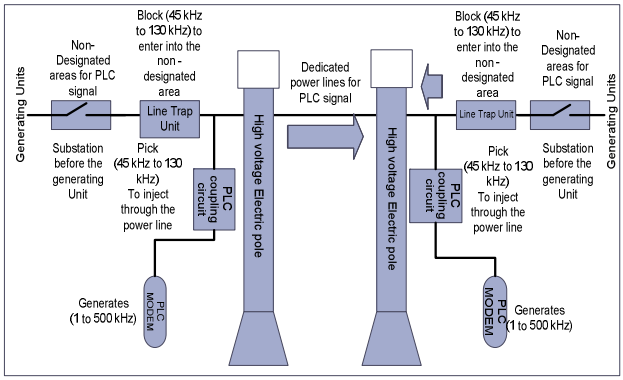


Fig.1 A PLC-integrated power system

## III. MODELLING OF THE BUTTERWORTH COUPLING CIRCUIT

This section presents the modelling of the Butterworth filter type CC. The function of CC is to block the 50/60 Hz power frequency from entering into the PLC modem, but allow the high frequency PLC signals into the power line. Different types of filter circuits may serve this purpose such as the high-pass filters, the notch filter, and the band-pass filter.

As part of this research, the Butterworth type band-pass filter has been selected and modelled. There are two types of Butterworth filters, known as the π-type and T-type circuit arrangements. The Butterworth filter consists of different combination of LC pairs. Fig. 2 shows the π-type circuit arrangement and Fig. 3 shows the T-type circuit arrangement.

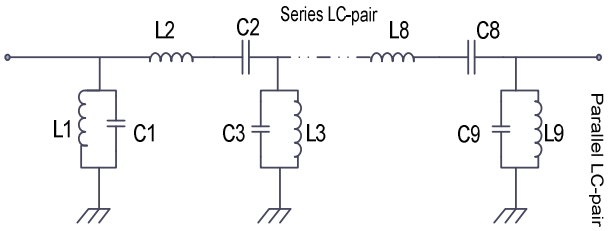


Fig.2 π-type Butterworth coupling circuit

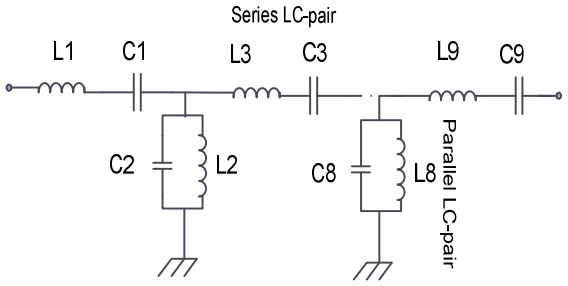


Fig 3 T-type Butterworth filter

The order of a filter, given by the number of cascaded pairs, has to be selected according to design requirements and the application area. The higher is the order of a filter, the sharper the slope of the filter would be. This is useful in applications such as military radio communication where a strict frequency band may be required.

To demonstrate the frequency response of a Butterworth filter, it is important to first calculate the value of the LC-pairs. The standard equations [18] that are used for calculating the filter LC-parameters are given in Eq. (1) to Eq. (4). Eq. (1) and Eq. (2) are used for calculating the inductance of the shunt and series connected inductors of the $i^{th}$ order respectively. Eq. (3) and Eq. (4) give the capacitances of the series and shunt connected capacitors of the $i^{th}$ order respectively.

$$L_{shunt} = \frac{g_i Z_0}{(2\pi)^2 BW \ f_c} \quad (1)$$

$$L_{series} = \frac{BW * f_c Z_0}{g_i (2\pi f_c)^2} \quad (2)$$

$$C_{series} = \frac{g_i}{(2\pi) BW \ Z_o} \quad (3)$$

$$C_{shunt} = \frac{BW}{(2\pi (f_c)^2 g_i Z_o} \quad (4)$$

where, n is the number of LC pairs,
i designate the order of the filter,
$f_c$ gives the cut-off frequency,
BW is the pass band,
$Z_o$ is the transmitting side impedance
$g_i$ is the immittance of the circuit

A 3rd order Butterworth band pass filter, shown in Fig. 4, has been designed and simulated first limiting the number of LC pairs to two. The objective is to identify the performance that can be achieved when such theoretically calculated ideal values are used. The theoretical values, shown in Table 1, were calculated using using Eqs. (1) to (4) and adapted in the circuit configuration below.

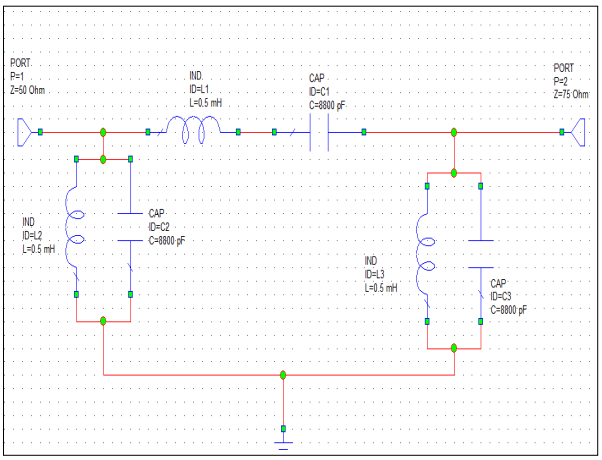


Fig. 4. 3rd order Butterworth band pass filter

For analyzing the frequency response of the Butterworth circuit, the cut-off frequency was chosen as 100 kHz because it allows the Butterworth filter passband cover the CENELEC band of frequencies. The strength of PLC signal will be highest around 100 kHz and the insertion loss is expected to be lowest at the cut-off frequency. Two different LC pair combinations were used to evaluate this circuit. The first one is a standard power line to modem (with a 50 Ω/75 Ω impedance ratio) with the theoretical LC component values given in Table 1. The second one is a similar circuit, where the same impedance ratio has been used with practically available LC off-the-shelf component values.

TABLE 1. LIST OF THE THEORETICAL VALUE OF THE COMPONENTS FOR STANDARD 50 Ω/75 Ω IMPEDANCE COMBINATIONS

| Parameters | Values |
|---|---|
| $L_{series}$ | 0.5 mH |
| $L_{shunt}$ | 0.5 mH |
| $C_{series}$ | 8800 pF |
| $C_{shunt}$ | 8800 pF |

Fig. 5 shows the insertion loss graph for the first circuit with theoretical values. The insertion loss graph shows that if theoretically calculated values are used, the circuit would give an almost perfect response. For example, in this particular case, the insertion loss is under -3 dB band in the 55 kHz to 160 kHz range. This implies that by setting circuit components to the theoretically obtained values, a very good CC may be obtained, with minimum attenuation of the PLC signals.

But, the required capacitance and inductance values are not practical and not commercially available.

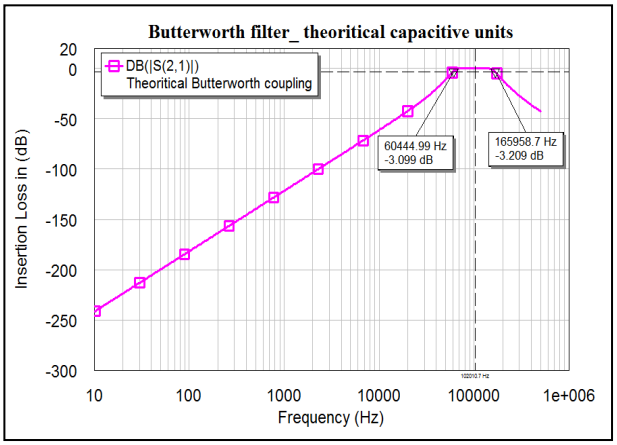


Fig. 5 Insertion Loss graph for (50/75) Ω theoretical Butter worth coupling circuit

Many researchers [18, 20] in the literature assume such theoretically calculated practical values in their designs. This work aims to target this shortcoming by demonstrating how good responses could still be obtained by using commercially available off-the-shelf components. Therefore, in the second part of the simulation, the theoretically obtained component values were changed to practically available values, ratings of which are given in Table 2. As shown in Table 2, capacitance has been chosen as 8800 pF, which is a very common value capacitor that is commercially manufactured by ABB electronics. Similarly, the value of the inductance has been chosen as 0.5 mH, which is also commercially available.

TABLE 2. LIST OF THE PRACTICALLY AVAILABLE COMPONENTS FOR STANDARD 50 Ω/75 Ω IMPEDANCE COMBINATIONS

| Parameters | Values |
|---|---|
| $L_{series}$ | 159154.943 nH |
| $L_{shunt}$ | 79577.472 nH |
| $C_{series}$ | 15915.494 pF |
| $C_{shunt}$ | 31830.989 pF |

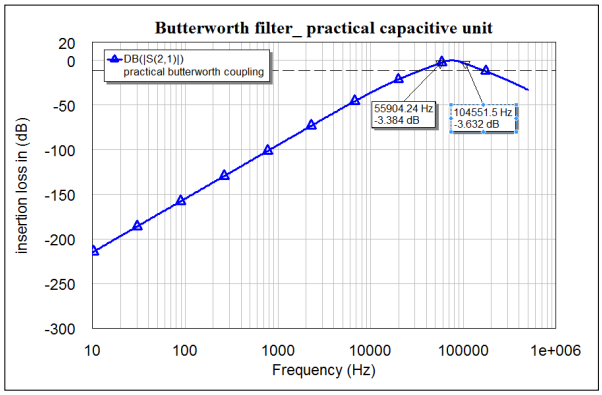


Fig. 6 Insertion Loss graph for (50/75) Ω practical Butter worth coupling circuit

The insertion loss graph of the modified circuit is shown in Fig. 6. As shown, for the lower part of the CENELEC band,

this circuit produces a very high insertion loss more than -53 dB, but from 55 kHz to 100 kHz, the insertion loss is very low (less than -3 dB) which is very promising for use in real-time PLC applications over power networks. Even though the designed circuit will not be adequate in the 9 kHz to 55 kHz range, its insertion loss performance will be quite ample in the 55 kHz to 100 kHz range. This result validates the feasibility of using the practical Butterworth filter as a coupling arrangement for real world PLC applications.

## IV. Modelling of Wide Band Line Trap Circuit

Different types of LT circuits such as band-stop, the notch filter, wide-band LC resonant and the T-type filter circuits can be used as the LT circuit. However, amongst them, the T-type LT circuit is the most widely used according to the literature. Most LT circuits have been designed and modelled to isolate signals over 1 MHz in high frequency data communications applications. In the previous section, a Butterworth filter based CC was designed to operate with minimum attenuation in the 55 kHz to 100 kHz frequency band. In this section, the objective is on designing a LT circuit that would block frequencies in this range. Fig. 7 and Fig. 8 show the circuit diagrams of the single stage and double stage T-type LT circuits, appropriate for power system networks.

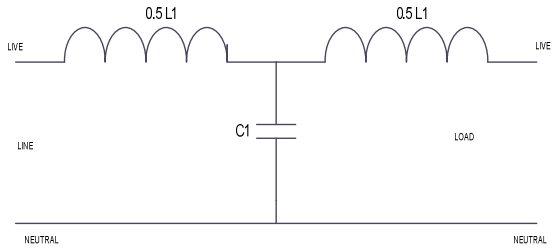


Fig. 7 Single stage T-type line trap circuit

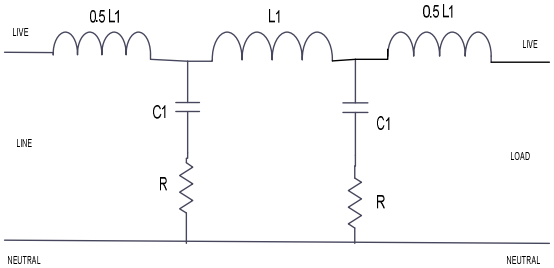


Fig. 8 Double stage line trap circuit

Eqs. (5) to (6) are the fundamental equations [20] that can be used to calculate any ratio such as the S-parameters, gain and etc. associated with LT circuits.

$$\begin{bmatrix} V_{in} \\ I_{in} \end{bmatrix} = \begin{bmatrix} 1 & \frac{jk\,R_d}{2} \\ 0 & 1 \end{bmatrix} \begin{bmatrix} 1 & 0 \\ \frac{jk}{R_d} & 1 \end{bmatrix} \begin{bmatrix} 1 & \frac{jk\,R_d}{2} \\ 0 & 1 \end{bmatrix} \begin{bmatrix} V_{out} \\ I_{out} \end{bmatrix} \qquad (5)$$

$$\Rightarrow \begin{bmatrix} V_{in} \\ I_{in} \end{bmatrix} = \begin{bmatrix} \frac{2-k^2}{2} & \frac{jk\,R_d}{4}(4-k^2) \\ \frac{jk}{R_d} & \frac{2-k^2}{2} \end{bmatrix} \begin{bmatrix} V_{out} \\ I_{out} \end{bmatrix} \qquad (6)$$

Where, J is an imaginary term,

$R_d$ is the filter design impedance,

$K$ is the normalized frequency defined by the trouble frequency F and cut off frequency $F_C$ as in Eq. (7)

$$k = \frac{F_C}{F} \qquad (7)$$

Using the Eqs. (5) to (6), frequency co-relation between any types of LT circuits can be modelled. For this work, a double-stage T-type LT circuit has been modelled and evaluated with the same practical LC components that were used in building the CC stages. These include the 8800 pF capacitance and the 50 mH inductance.

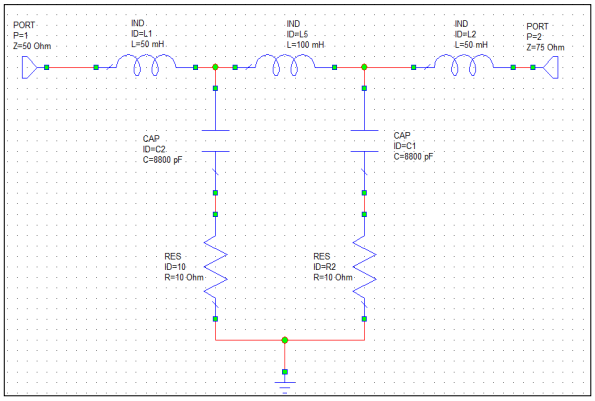


Fig. 9 Double stage T- type line trap circuit in Microwave window view

Fig. 9 shows the Microwave Office design view of the LT circuit that has been modeled using commercially available capacitive and inductive components. The insertion loss of the designed circuit is shown in Fig. 10.

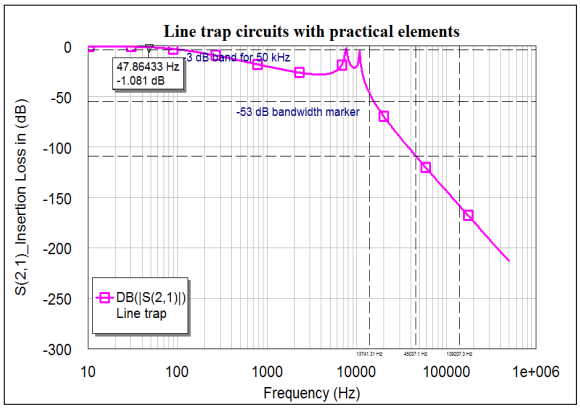


Fig. 10 Insertion loss graphs of the line trap circuit

The results demonstrate that the circuit permits the power signal (50 Hz) with a low attenuation (< -3 dB) and for the CENELEC band of frequencies, the circuit produces high

insertion losses. Specifically, for frequencies above 55 kHz, this circuit provides a large attenuation more than -53 dB. This design would therefore ensure that the LT will block PLC signals in the 55 kHz to 100 kHz range from penetrating into areas of the network where generating units may be present.

## V. DISCUSSION

A comparative discussion of the LT vs. CC is presented in this Section. Fig. 11 plotted to show the comparative insertion loss curves for both circuits. The pink curve is for the Butterworth CC circuit, where the peak of the insertion curve lies on the 55 kHz to 100 kHz range, and the insertion loss in this range is less than -3 dB. The blue curve is for the LT circuit, which exhibits very high insertion loss (larger than -53 dB) in the same band. The results achieved confirm that these two circuits can be used in power system PLC applications where the frequency of the PLC signal must be chosen between 55 kHz to 100 kHz.

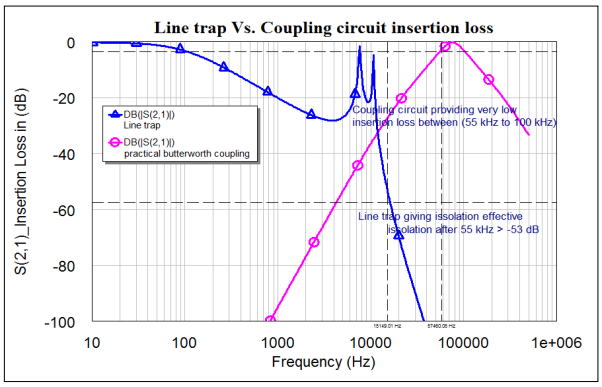


Fig. 11 Insertion loss graphs for the LT vs. practical Butterworth CC

## VI. CONCLUSION

In this paper, a Butterworth type CC and a T-type LT circuit have been modelled, simulated and evaluated for use in power system applications where the PLC signal frequency is to be selected within the CENELEC frequency band. The circuits were designed using commercially available off-the-shelf components. The insertion loss of the CC was measured as -3 dB in the 55 kHz to 100 kHz range, and the insertion loss of the LT was measured as more than -53 dB. Therefore, sufficient performance was achieved in terms of insertion loss profile of the circuits. This shows that if the PLC signal transmission frequency can be chosen within the 55 kHz to 100 kHz portion of the CENELEC frequency range, then the designed circuits can be perfectly used in real-time applications.

## VII. REFERENCES


[1] C. Sridhathan and F. Samsuri, "Application of power line communication in healthcare for ECG and EEG monitoring," in Proc. Of Int. Conf. on Advances in Power Electronics and Instrumentation Engeneering, 2013: Citeseer.

[2] M. Yigit, V. C. Gungor, G. Tuna, M. Rangoussi, and E. Fadel, "Power line communication technologies for smart grid applications: a review of advances and challenges," Computer Networks, vol. 70, pp. 366-383, 2014.

[3] A. B. Batiller, E. F. I. Bugayong, A. A. Caisip, N. P. Coligado, C. A. C. Padilla, and M. A. A. Pedrasa, "Prepaid metering system for isolated microgrids," in Innovative Smart Grid Technologies-Asia (ISGT-Asia), 2016 IEEE, 2016, pp. 529-534: IEEE.

[4] A. N. Milioudis, G. T. Andreou, and D. P. Labridis, "Detection and location of high impedance faults in multiconductor overhead distribution lines using power line communication devices," IEEE Transactions on Smart Grid, vol. 6, no. 2, pp. 894-902, 2015.

[5] A. N. Milioudis, G. T. Andreou, and D. P. Labridis, "Enhanced protection scheme for smart grids using power line communications techniques—Part II: Location of high impedance fault position," IEEE Transactions on Smart Grid, vol. 3, no. 4, pp. 1631-1640, 2012.

[6] A. Milioudis, G. Andreou, and D. Labridis, "High impedance fault evaluation using narrowband power line communication techniques," in PowerTech, 2011 IEEE Trondheim, 2011, pp. 1-6: IEEE.

[7] C. J. Kikkert and S. Zhu, "Measurement of powerlines and devices using an inductive shunt on-line impedance analyzer," in Power Line Communications and its Applications (ISPLC), 2015 International Symposium on, 2015, pp. 41-46: IEEE.

[8] S. Zhu, C. J. Kikkert, and N. Ertugrul, "Software for control and calibration of an inductive shunt on-line impedance analyzer," in Power Line Communications and its Applications (ISPLC), 2015 International Symposium on, 2015, pp. 53-58: IEEE.

[9] C. J. Kikkert, "A PLC frequency model of 3 phase power distribution transformers," in Smart Grid Communications (SmartGridComm), 2012 IEEE Third International Conference on, 2012, pp. 205-210: IEEE.

[10] C. J. Kikkert, "MV to LV transformer PLC bypass coupling networks for a low cost smart grid rollout," in Innovative Smart Grid Technologies Asia (ISGT), 2011 IEEE PES, 2011, pp. 1-6: IEEE.

[11] C. J. Kikkert, "Effect of couplers and line branches on PLC communication channel response," in Smart Grid Communications (SmartGridComm), 2011 IEEE International Conference on, 2011, pp. 309-314: IEEE.

[12] C. J. Kikkert, "Modelling power transformers at power line carrier frequencies," 2010.

[13] M. Rastogi, D. Mitra, and A. Bhattacharya, "A Novel Implementation of Bidirectional Coupling Circuit for Broadband, High-Voltage, Power-Line Communications," in Communications, 2005 Asia-Pacific Conference on, 2005, pp. 38-42: IEEE.

[14] P. L. So and Y. Ma, "Development of a test bed for power line communications," IEEE Transactions on Consumer Electronics, vol. 50, no. 4, pp. 1174-1182, 2004.

[15] P. A. J. van Rensburg, M. P. Sibanda, and H. C. Ferreira, "Integrated Impedance-Matching Coupler for Smart Building and Other Power-Line Communications Applications," IEEE Transactions on Power Delivery, vol. 30, no. 2, pp. 949-956, 2015.

[16] P. A. J. van Rensburg and H. C. Ferreira, "Design and evaluation of a dual impedance-adapting power-line communications coupler," IEEE Transactions on power Delivery, vol. 25, no. 2, pp. 667-673, 2010.

[17] P. A. J. van Rensburg and H. C. Ferreira, "Coupler winding ratio selection for effective narrowband power-line communications," IEEE Transactions on power Delivery, vol. 23, no. 1, pp. 140-149, 2008.

[18] S. Wei, W. Gao, L. Zhang, and Z. Cao, "High frequency and broadband coupling characteristics of filter circuit based on low voltage power lines," Procedia Engineering, vol. 15, pp. 1978-1982, 2011.

[19] I. H. Cavdar and E. Karadeniz, "Measurements of impedance and attenuation at CENELEC bands for power line communications systems," Sensors, vol. 8, no. 12, pp. 8027-8036, 2008.

[20] P. J. Van Rensburg and H. C. Ferreira, "Coupling circuitry: Understanding the functions of different components," in Proc. 7th Int. Symp. Power-Line Comm, 2003, pp. 204-209

# Identification and Volume Estimation of Dental Caries using CT Image

Sabbir Ahmed[1, *], Khaled Mohammed Saifuddin[1], Abu Shakil Ahmed[2], A. B. M. Aowlad Hossain[1], and Md. Taslim Iqbal[3]

[1]Electronics and Communication Engineering, Khulna University of Engineering & Technology
Khulna-9203, Bangladesh

[2]Electrical and Electronic Engineering, Khulna University of Engineering & Technology
Khulna-9203, Bangladesh

[3]City Dental College
Dhaka-1219, Bangladesh

[*]sabbir.ahmed.delu@gmail.com

**Abstract— Early detection of dental caries is vital as it causes several fatal diseases like cancer if it spreads into the root of the teeth. Therefore, early detection, tracking, and testing the depth of carious lesion may be lifesaving. In this paper, a carious detection method has been presented, and the volume of caries has been investigated. We have applied K-means clustering and threshold method for segmentation and utilized Computed Tomography (CT) images in order to construct the three-dimensional view of the carious lesion which is an integral part of the diagnosis of dental cavity. Result shows that the average Peak Signal-to-Noise Ratio (PSNR) has been obtained 19.98 and 20 by applying K-means clustering and threshold method respectively along with satisfactory visual interpretation of the three-dimensional structure of dental carries. This contribution can be applied for several other medical detection purposes with a slight adjustment.**

***Index Terms*—Dental caries, K-means clustering method, Threshold method, 3D construction.**

## I. INTRODUCTION

Dental caries is alternatively known as tooth decay or dental cavities. Bacterial infections and deposition of acid on the enamel surface erode the hard tissues on the upper layer of teeth. This disease is so severe that even if in the developed countries over 60 to 90 percent children fall victim to dental caries due to bacterial infection where access to healthcare is comparatively easier [5]. If carious lesion spreads into the root of the teeth, it can cause cancer and several other fatal diseases. Therefore, it is better to detect dental caries as well as the depth of its spreading as early as possible. Different methods are used for detection of dental caries such as Electronics Caries Monitor (ECM), Fiber Optic Transillumination (FOTI), Digital Fiber-Optic Transillumination (DIFOTI), and Quantitative Light-induced Fluorescence (QLF) most of which are based on subjective interpolation of visual examination and tactile sensation [2-4] [7-8]. However, most of these methods have their limitations, for example, the sensitivity of FOTI and DIFOTI based methods are very low. Dentists often get confused to the results these methods produce, and they have to perceive the result with their expertise which puts patients at risk. As per ECM method, a single tooth has to be extracted in order to apply this method for the detection of dental caries which is not feasible. Moreover, the infrastructure of ECM and QLF is very expensive and hence, the cost of treatment rises [4]. QLF offers better performance than FOTI and DIFOTI as it has a high level of specificity although the sensitivity is low for this method as well. Radiography is also one of the most widely used methods to diagnose the proximal and interproximal carries though patients are exposed to radiation which is harmful to their health [6]. The Diagnodent method offers higher value for both sensitivity and specificity. Therefore, this method yields more accurate result than any of these methods. At present, computerized tomography is a well-known method for anatomic imaging of oral cavity instead of conventional imaging procedures prior to different treatments those involves surgery. Dental CT image plays a vital role in the detection of the carious lesion as we can extract various parameters from the image including the area and the depth.

In this research work, we have applied two different segmentation algorithms to determine the carious lesion affected area of an adult head part from its CT image with a view to extracting necessary information. Moreover, we have reconstructed the three-dimensional view and pixel-wise estimation of caries lesion to analyze its formation and evaluate the depth. Affected area is the region of interest (ROI) that situates inside the border of the CT image which has been identified by observing change in several properties like similarity criterion and discontinuity. The segmentation of CT images has been conducted as per the intensity of ROI.

This paper has been organized in four sections. In Section II, we have elaborated the methodology with a particular focus on the working principle of the segmentation algorithms. In section III, we have explained the simulation procedure step by step, presented the graphical results, evaluated the outcomes of the simulation works, and clarified the contribution of this paper. Section IV contains the summary of the study.

## II. METHODOLOGY

The primary concentration of this research work is to investigate for a more efficient technique to detect dental caries from the CT images. In order to meet this objective, segmentation is the most critical part. Two algorithms we have applied for segmentation are K-means clustering and threshold method. Clustering is a classification technique that indicates the similarity among different regions to search the distinct groups in the feature space. It arranges data in several

978-1-5386-3374-8/17/$31.00 ©2017 IEEE

partitions which can be represented in n-dimensional features space. K-means clustering is a widely used method for segmentation because of its simplicity and high convergence rate, and it operates based on iteration technique [11]. This algorithm can split new classes into several regions as per similarity of the objects [9]. In fact, this algorithm compares between the index of similarity and dissimilarity for pairs of data components and divides the image into different channels. The threshold method compares every pixel in an image with a threshold value T and replaces it with a white pixel if the original pixel intensity is less than or equal to the threshold value. The threshold method has several variations such as global threshold, mean threshold, and Otsu threshold. In this paper, we have applied mean threshold method. The threshold method uses the average grey level contained within the different groups to calculate the threshold value, unlike the Otsu which is based on the discrimination criteria defined by between-class variance. In comparison with Otsu, mean threshold method offers better segmentation, and it is easier to implement [1]. An overview of the mean threshold method has been presented in Fig. 1.

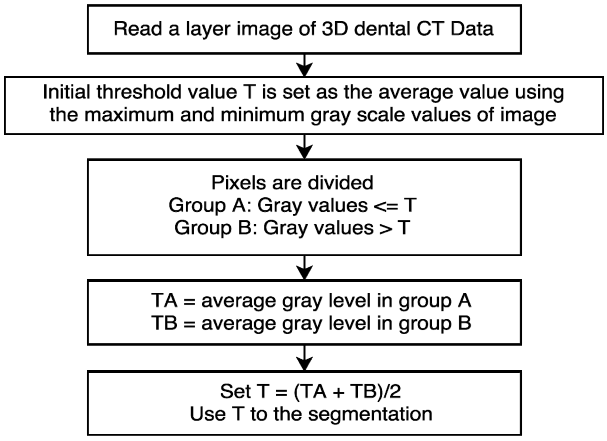


Fig. 1 Flow chart of the mean threshold method.

The feature extraction procedure separates the unnecessary portions of the image while the feature selection decreases the number of features to make classification easier. The feature extraction is the most complex procedure among the mentioned ones since the effectiveness of the classification depends upon it [10]. The workflow of the K-means clustering and the threshold method have been shown step by step graphically in Fig. 2 and Fig. 3. Moreover, we have reconstructed the three-dimensional orientation of the two-dimensional CT images constructed after feature extraction.

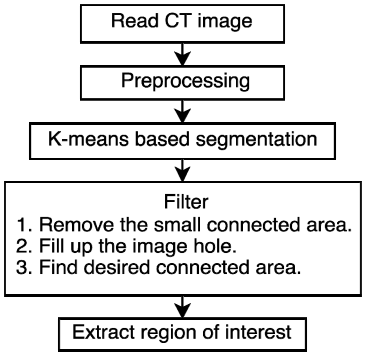


Fig. 2 Segmentation and feature extraction from CT image (2D slice) of an adult head part using K-means clustering method.

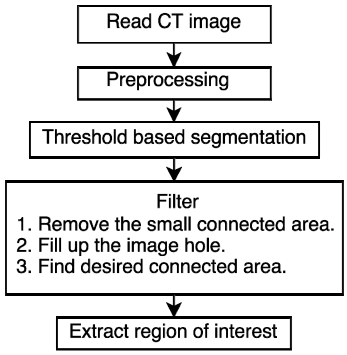


Fig. 3 Segmentation and feature extraction from CT image (2D slice) of an adult head part using threshold method.

## III. Result and Discussion

### A. Pre-processing

Several pre-processing tasks are required to perform prior to begin the segmentation procedure. The DICOM dental CT images have been collected from OsiriX library [12]. The two-dimensional medical CT images of dimension of 512*512 are then converted and consequent simulations are performed in MATLAB. The redundant and unwanted portion of the images has been removed in the following step. In this regard, we have cut out the redundant part of the images and put zero in the vacant places.

*1) Cutting the Redundant Part*: We have cropped only the region of interest from an image and discarded the rest of it as we cannot extract any necessary information from those areas. After cropping, the CT image with of dimension 512*512 has been reduced to a 234*234 matrix that forms an image shown in Fig. 4.

Fig. 4 Input image after removal of the redundant part.

*2) Putting Zero for Vacant Space*: We have placed a series of zeros in the vacant spaces after removal of the redundant parts as illustrated in Fig. 5.

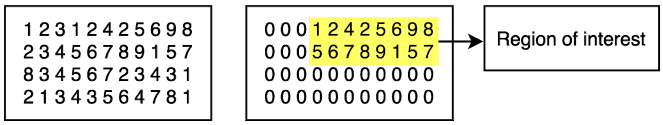


Fig. 5 Unwanted pixel elimination.

Since the image becomes less complex after elimination of the unwanted pixels as portrayed in Fig. 6, the detection process of dental caries operates faster which makes the system more efficient.

Cutting the redundant parts and putting zero for the vacant spaces both are essential for pre-processing before segmentation and they have to be performed sequentially. If we remove the unwanted regions without putting zero values, the three-dimensional representation of CT images will lose their connectivity. Therefore, we have filled the vacant

regions with zeros instead of permanently removing them. Moreover, the number of necessary pixels, the operation time, and the segmentation complexity have also been reduced by this way.

Fig. 6 CT image after putting zero to the redundant pixel.

*B. Segmentation*

We have applied two different algorithms for segmentation and determined the optimum one by evaluating their performances. Moreover, the working procedures of the algorithms have been illustrated step by step in this section.

*1) K-means Clustering Method*

We have selected spatial coordinates and L*a*b components of a pixel as the set of distinguishing features and created a five-dimensional feature vector. The K-means clustering method has been applied afterward in order to generate K clusters and hence the image is subdivided into K disjoint subsets. The segmentation algorithm assigns its pixel to its nearest centroid so that the Euclidean distance between them can be minimised into the five-dimensional features space. This algorithm completes the segmentation as intended for an arbitrary value of K. The number of segmentation varies proportionally with the value of k as the intensity level rises with the increase in K. The partition of a CT image into three channels by this algorithm has been shown in Fig. 7.

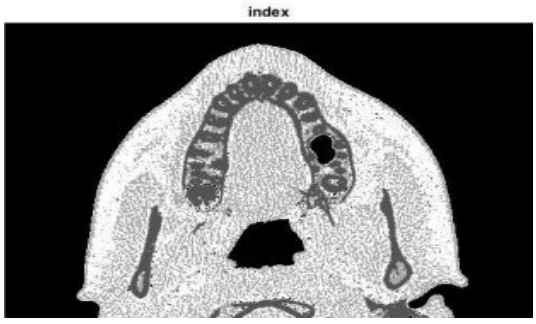


Fig. 7 CT image after segmentation using K-means clustering method.

The application of K-means clustering method has yielded each image with three different indexes, i.e., index 1, index 2, index 3 as shown in Fig. 8.

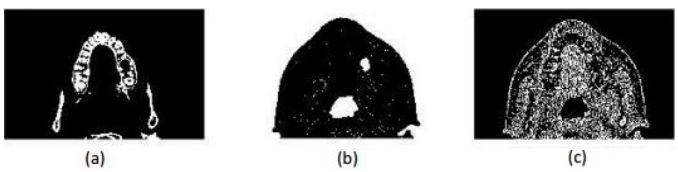


Fig. 8 Images of different index. (a) index=1 (b) index=2 (c) index=3.

Out of these three regions, one contains the region of interest. Feature extraction process can be initiated by choosing the right index, and a two-dimensional image can be formed using the extracted parametric values.

*2) Threshold Method*

We have used histogram shape based method in order to separate the carious lesion from other dental parts where the ISODATA is responsible for computing the global image threshold applying an iterative technique. As per the threshold method, a threshold value T has been set at first, and its value has been determined from the ISODATA. We have converted the image into binary format applying the IM2BW technique. The histogram has been segmented into several parts by comparing with the threshold value. Moreover, the sample mean of the grey value associated with both the foreground and the background pixels has been calculated. The grey value has been set 0 if it is beyond the preset threshold value and 1 otherwise. The threshold value has been updated after conducting these steps, and the process has been continued until the further change in threshold value. By this way, the CT images have been segmented. Fig. 9 represents the scenario of dental CT image after pre-processing and segmentation using threshold method.

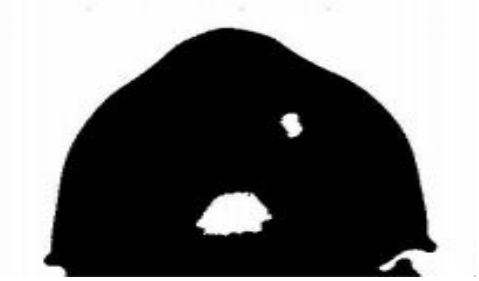

Fig. 9 Dental CT Image after segmentation using threshold method.

*C. Extraction*

We have extracted the region of interest from the segments of CT images by applying feature extraction method with a view to conducting further analysis. The chosen parameters are the pixel intensity of each pixel and the number of connected pixels which are selected for the quantitative reflection of similarity and discontinuity.

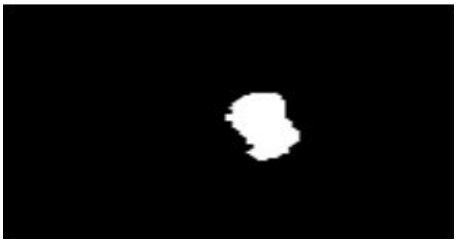

Fig. 10 The extracted region of interest for K-means clustering method.

A separate matrix has been formed containing the parametric values, and an image has been generated that incorporates all the connected components. In this manner, the region of interest has been extracted as a two-dimensional image that facilitates further analysis on the area, depth, and several other properties. Fig. 10 and Fig. 11 shows the extracted region of interest for K-means clustering method and threshold method respectively. Here, a sharp segmented region has been obtained for threshold method.

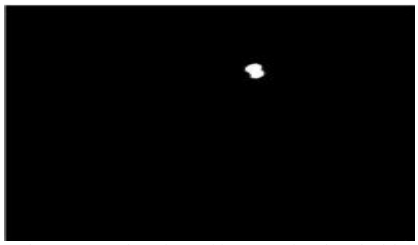

Fig. 11 The extracted region of interest for threshold method.

### D. 3D Construction of Cavity

After conducting pre-processing, segmentation, and extraction process, we have constructed a three-dimensional image of the dental cavity. The dimension consists of X, Y, and Z-axis where the two-dimensional images generated by extraction process have been placed along the XY plane, and the Z-axis maintains the serial number of images. The serial number or image sequence as per the three-dimensional matrix is vital to retain the connectivity among the images. We have used a 3D viewer software to observe the three-dimensional images of the dental cavity presented in Fig. 12.

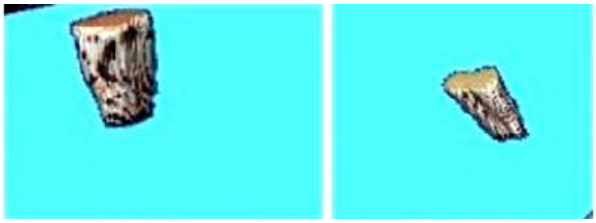

Fig. 12 Three-dimensional orientation of dental cavity.

We have evaluated the performance of the detection method illustrated earlier and clarified the contribution of this study. While conducting the simulation, we have measured the value of several parameters in order to track the progress of the dental cavity along with its detection. We have measured the PSNR = $10\log_{10}$(peak value/MSE) of the segmented images for both the K-means clustering and the threshold method corresponding to the original CT images. The recorded PSNR values of the segmented images have been presented in TABLE I. It can be observed that the two segmentation methods negligibly differ from each other regarding the PSNR value. Therefore, it is evident that the same PSNR has been maintained throughout the simulation. However, the threshold method is more convenient for segmentation as a sharper segmented region has been obtained for this method in comparison with the K-means clustering.

TABLE I PSNR OF THE SEGMENTED IMAGES

| Main Image | PSNR (K-means clustering) | PSNR (Threshold method) |
|---|---|---|
| IM-0001-0050.dcm | 20.01 | 20.04 |
| IM-0001-0051.dcm | 20.05 | 20.07 |
| IM-0001-0052.dcm | 19.92 | 19.92 |
| IM-0001-0053.dcm | 20.01 | 20.00 |
| IM-0001-0054.dcm | 19.91 | 19.91 |
| IM-0001-0055.dcm | 20.02 | 20.06 |

We have measured the number of pixels in each segment of the images during the simulation process as the number of affected pixels can be determined by comparing with the number of pixels of the original CT image. By this way, we have identified the areas affected by dental caries. Moreover, using the pixel information we have determined the volume of the carious lesion. TABLE II represents the number of actual pixels in each segmented volume.

TABLE II NUMBER OF ESTEMATED PIXEL IN EACH SEGMENTED IMAGE

| Main image | No. of estimated pixel in segmented volume (K-means clustering) | No. of estimated pixel in segmented volume (Threshold algorithm) |
|---|---|---|
| IM-0001-0050.dcm | 140339 | 150167 |
| IM-0001-0050.dcm | 116847 | 120764 |
| IM-0001-0050.dcm | 101862 | 102582 |
| IM-0001-0050.dcm | 79163 | 790821 |
| IM-0001-0050.dcm | 58852 | 58359 |
| IM-0001-0050.dcm | 33426 | 38669 |

## IV. CONCLUSION

The key concentration of this paper is to identify dental caries as well as examining the depth of the carious lesion. In this regard, we have prepared the medical CT images for simulation through some pre-processing works. The segmentation of the images has been performed using K-means clustering method and threshold method separately in order to compare the performances of these two algorithms. The necessary features have been extracted from the segmented images to form a two-dimensional matrix at first and later a three-dimensional matrix in order to construct a three-dimensional orientation of the dental cavity. During conducting the simulation, we have recorded the values of PSNR and calculated the number of effective pixels with a view to detecting dental caries and estimating its volume. The effectiveness of this study has been justified by both graphical and numerical measures.

## REFERENCE


[1] Z. Hu, P. Wu, J. Gui, Y. Chen and H. Zheng, "Teeth segmentation using dental CT data", 2014 7th International Conference on Biomedical Engineering and Informatics, 2014.

[2] S. Tikhe, A. Naik, S. Bhide, T. Saravanan and K. Kaliyamurthie, "Algorithm to identify enamel caries and interproximal caries using dental digital radiographs", 2016 IEEE 6th International Conference on Advanced Computing (IACC), 2016.

[3] R. Agarwal, A. Agrawal, H. Singh and S. Tyagi, "A review paper on diagnosis of approximal and occlusal dental caries using digital processing of medical images", 2016 International Conference on Emerging Trends in Electrical Electronics & Sustainable Energy Systems (ICETEESES), 2016.

[4] L. Karlsson, "Caries detection methods based on changes in optical properties between healthy and carious tissue", International journal of dentistry, 2010.

[5] P. E. Petersen, D. Bourgeois, H. Ogawa, S. Estupinan-Day, and C. Ndiaye, "The global burden of oral diseases and risks to oral health," Bulletin of the World Health Organization, vol. 83, pp. 661–669, 2005.

[6] S. Datta and N. Chaki, "Detection of dental caries lesion at early stage based on image analysis technique", 2015 IEEE International Conference on Computer Graphics, Vision and Information Security (CGVIS), 2015.

[7] I. Pretty, "Caries detection and diagnosis: Novel technologies", Journal of Dentistry, vol. 34, no. 10, pp. 727-739, 2006.

[8] A. Lussi, S. Imwinkelried, N. Pitts, C. Longbottom and E. Reich, "Performance and reproducibility of a laser fluorescence system for detection of occlusal caries in vitro", Caries Research, vol. 33, no. 4, pp. 261-266, 1999.

[9] A. S. M. Burney, H. Tariq, "K-means cluster analysis for image segmentation", International Journal of Computer Applications, vol. 96, no. 4, pp. 1-8, June 2014.

[10] A. K. Jain, R. Bolle, S. Pankanti, "Biometrics: personal identification in networked society", MA, Norwell:Kluwer, 1999.

[11] P. Sharma, J. Suji, "A review on image segmentation with its clustering techniques", Int. J. Signal Process. Image Process. Pattern Recogn. 9(5), 209–218, 2016.

[12] "OsiriX | The world famous medical imaging viewer", Osirix-viewer.com, 2017. [Online]. Available: http://www.osirix-viewer.com. [Accessed: 10- Oct- 2017].

# A Proposed Framework for Biometric Electronic Voting System

Md. Mahboob Karim[1], Nabila Shahnaz Khan[2], Ashratuz Zavin[3], Shusmoy Kundu[4], Asibul Islam, Brazab Nayak
Department of Computer Science and Engineering, Military Institute of Science and Technology, Dhaka-1216, Bangladesh
[1]mahboob4146@yahoo.com, {[2]nabilakhan1024, [3]ashzavin, [4]kshusmoy14}@gmail.com

***Abstract*— In this modern age of digitization, Bangladesh Election Commission (EC) still uses manual system during election for vote casting. Recently, it is considering to introduce Electronic Voting Machine (EVM) in parliamentary elections though EVM is not entirely automated and has many limitations. In this work, we have designed an automated biometric voting system with a convenient user interface and integrated database system containing all voters' information. Casted votes will be counted automatically at the end of the voting process and result will be generated centrally with less time. Therefore, the proposed system will improve the voting management of Bangladesh by ceasing fraudulent activities, corruptions, ensuring security, transparency, fairness, accuracy and keeping backup trails of voting process.**

***Index Terms*—Automated result calculation, Biometric authentication, Central integrated database, Electronic Voting Machine (EVM).**

## I. Introduction

Bangladesh is a democratic country where election of the government is a part and parcel of this democracy. Being a citizen of Bangladesh voting is the fundamental right. It expresses the choice of the people and that is why voting process needs to be fair, transparent and legal. Under many circumstances the voting system has become a debatable issue. At current time manual voting process using ballot papers is followed in the electoral system of Bangladesh. In the manual ballot system, people need to cast their votes on the paper provided by the Election Commission, no bio-metric identification of the voter is required. As a result transparency of the voting process is always in question [1]. Also the votes are preserved and counted manually which is a long time consuming process.

Bangladesh EC is looking forward to make the voting process digitized for which they are considering about using EVM [2]. At Chittagong and Narayanganj city corporation election EVM was used in the voting process [3]. It has mainly two units: Control Unit and Ballot Unit. The Control Unit is the main unit which stores all data and controls the functioning of EVM. In the EVM, people need to cast vote by pressing a button against the candidate in the Ballot Unit. EVM then automatically update the number of votes against the candidate in the Control Unit which is supervised by a presiding officer [4]. But the problem is that the system is vulnerable to corruption and security issues. No integrated database and biometric authentication are integrated to this method, hence EVM is considered to be unsuitable for general election [5].

Both the ballot paper voting system and EVM system failed to achieve proper security and authenticity as false vote casting is very easy in these systems by threatening people. Sometimes by creating terror, antisocial intruders force genuine voters to cast illegal votes. Considering these problems and to overcome the consequences, we have proposed an automated biometric voting model keeping in mind the electoral rules and regulations of this country. Biometrics are distinct and measurable characteristics of human beings used to identify each individual separately [6]. At present different biometric identification methods like fingerprint identification, hand geometry, palm vein authentication, retina scan, iris scan, digital signature, voice analysis etc are commonly in use [7]. For our model we have used the most commonly used and verified fingerprint identification biometric method.

In this paper, we have focused on designing an biometric electronic voting machine (BEVM) along with fingerprint authentication and centralized database. Based on total number of voters, several BEVM will be installed in each polling station for different elections in Bangladesh which will help to deploy the fingerprint matching task accurately within less time. Furthermore, the system is applicable to use anywhere in the world with some adjustment according to their election process.

We organize the rest of the paper as follows. Background study of related work is discussed in Section II. In Section III, we present the system model and architecture. System implementation steps are stated in Section IV. Section V states the result analysis while Section VI focuses on the limitations and future plans. Finally Section VII concludes the paper.

## II. Related Works

Recently biometric EVM has gained the attention of many researchers. In this section, the related works on electronic voting system with biometric authentication are discussed briefly.

In a study [8], a model of electronic voting machine was discussed where user verification was done using Near Field Communication (NFC) ID card and biometric technologies. In this process, multiple vote casting was restricted by marking this NFC card after the user had casted his vote once. Use of different biometric identification in e-voting and their security aspects were analyzed in another study conducted by Hof [9].

978-1-5386-3374-8/17/$31.00 ©2017 IEEE

He discussed some of the weaknesses of biometric systems such as spoofing, false accept and reject rate etc and therefore, suggested to implement biometric in e-voting with precautions. In a study [10], an abstract model of voting system with fingerprint authentication and details matching process in fingerprint minutiae were introduced.

A study conducted by Sarkar et al. [4] provided a brief overview on existing e-voting systems and their framework and protocols. They discussed the recent developments of EVM in context of Bangladesh and suggested some strategies to improve the security, accuracy of the existing design. In another study, Sarker et al. [11] proposed a conceptual design of electronic voting machine with fingerprint authentication that helped to eradicate defrauding of the manual voting systems and prior versions of electronic voting. They used four layer network system with three application server and a client to send data from client to database.

In [12], Chakraborty et al. introduced a biometric voting system (BVS) with fingerprint recognition in context of India. In their designed model, voter's information was stored in Adhar card- government ID card database and the data was accessed from this card during voting process. Adhar card contains biometric information such as fingerprint and iris of every citizens of India. Some other studies [13]–[15] also introduced Adhar card such as in study [13], [15], a conceptual design to link up the biometric data of Adhar card with e-voting machine was proposed. Stephen et al. [14] designed an IOT based e-voting system with Adhar card database model.

A study conducted by Khasawneh et al. [16] proposed an idea of multifaceted online e-voting system with combined biometric authentication like fingerprint, facial recognition, iris scanning etc. In this model, electronic ballot paper with multiple scope was introduced and computer simulations were run to test the robustness and accuracy.

Reddy mentioned several existing problems in EVM of India in this case study [17] and those problems are- unauthorized vote casting, rigging, netwrork threats and poor software support. He proposed to use biometric authentication with this EVM. Yinyeh [18] provided an overview of electronic voting system in Ghana using biometric authentication which was implemented at each polling station over a LAN (local area network).

In another study [19], the authors proposed a voting system where voter could give vote in two ways - online and offline. In online voting system, voters could give vote through internet with only a password verification, therefore hackers may apply brute-force attack and get succeed. In offline method, voters could give vote by using a voting matching appearing in the booth where iris recognition technology and finger print sensor were used. A study conducted by Baig [20] discussed an e-voting system where user can give vote using smart phone application with QR code verification and this application uses the user information stored in Adhar card.

In sum, each of the research work introduces different ways for the authentication of electronic voting system. Though some studies show the implementation of BEVM, each of them has pros and cons in their own use of context. Such as NFC or Adhar card needs to use in some proposed system which introduces the issues of losing or stealing IDs. Some of the designed model did not ensure convenient user interface and integrated database, biometric authentication etc like EVM that was tested in some countries- Bangladesh, India [21]. Therefore, our contribution in this paper is to introduce a conceptual design and development of BEVM which is unique, secured and convenient to solve the raised problems.

## III. Our Proposed System

### A. Proposed System Model

The proposed system is a biometric e-voting system which has two main sections- 1) voter registration & 2) voting control and result calculation. Each user needs to register first as a voter through the system with biometric (fingerprint) verification. The information of the voter will be saved in a central database. Then during the election, digital ballot paper will be used instead of paper ballot paper and it will contain the list of candidates and their respective logos. A registered voter can cast only one vote by verifying his finger print. The registration and voting process of the proposed system is explained below:

*1) Registration Process:* As shown in Figure 1, at the beginning of the registration process system will store detailed information of voters along with their NID numbers. Then the fingerprints of the voters will be collected under complete supervision of the registration officers using their NID numbers. If the fingerprints are valid, the system will generate templates for respective fingerprints which will be stored in the database alongside the voters' other information. To check the authentication of a voter during registration process following cases will be considered:

(I) Case A: If the NID number provided by the user isn't valid then the system will show '*Invalid ID*' and terminate the process. If fingerprint has already been taken for that NID number then system will show '*Voter already registered*'. At the same time the buzzer will beep and an SMS will be send to the authority in charge to notify them about false registration attempt.

(II) Case B: If the given NID number is valid but match is found for the given fingerprint then system will display a message that '*Fingerprint Already Exists*' and generate the ID number with which the fingerprint match was found. Then after beeping buzzer and sending SMS to the authority in charge the process will terminate.

(III) Case C: If no match is found then system will save the template for that specific NID in the database and will display a message saying '*Registration Complete*'.

*2) Voting Process:* As shown in Figure 2, the system will ask for the voter's fingerprint until properly scanned. Then it will try to find a match with templates existing in the database. During voting process following cases will be considered:

(I) Case A: If the match is not found then system will display a message saying '*Voter Not Registered*' and send SMS to the control.

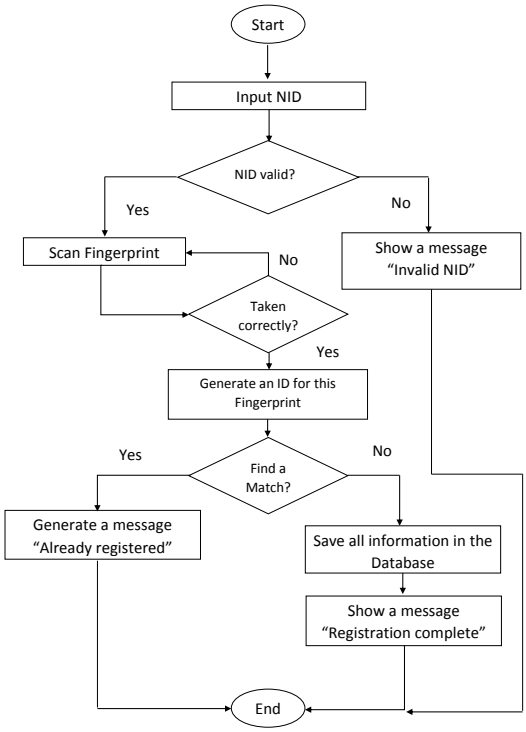


Fig. 1: The Work Flow Diagram of Registration Process

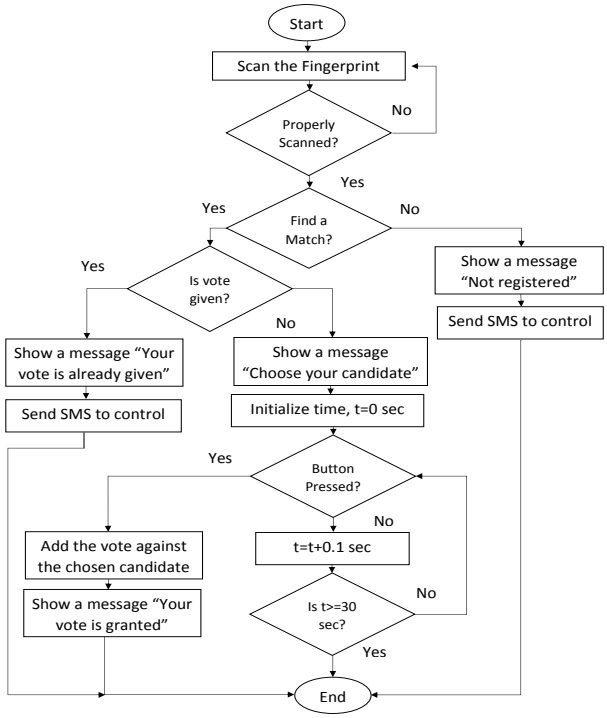


Fig. 2: The Work Flow Diagram of Voting Process

(II) Case B: If the match is found then system will check if vote has been already given or not against that fingerprint.

a) If vote is already given against that fingerprint then system will display a message '*Your vote is already given*' and notify authority with SMS.

b) If vote is not given against that fingerprint then system will ask to vote displaying a message '*Choose your candidate*'. The voter will be able to see the candidate list on the display. Then the system will initialize time with 0 second and will wait for a certain time for the the voter to give his vote.

c) If the button is pressed then system will add the vote against the candidate, display a message that '*Vote is granted*' and an SMS will be sent to the voter to avoid any kind of miscommunication.

d) If the button is not pressed then system will wait for 30 second for the button to be pressed. If time exceeds 30 second, the process will terminate.

The voting process will be held in each polling station by comparing a fingerprint with the voters of that specific station for faster operation. At the end of the election, the result of each polling station will be calculated automatically and will be integrated to the central database for overall result.

### *B. System Architecture*

The overall conceptual architecture of the system has been highlighted in Figure 3. A fingerprint sensor will be used for the biometric identification process of the proposed system. LCD display will be used to show candidate list, their logos and which button to press to vote for a specific candidate. There will be another small LCD display to show the users various instructions like which button to press for selecting which option during the registration and voting process. A keypad will be used which will take user input for various

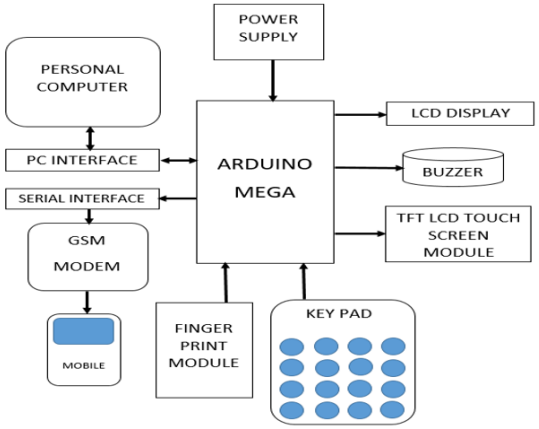


Fig. 3: Conceptual Architecture of the System

options. A GSM Modem will be used to send SMS to the central authority for any kind of complication during the voting process and also to the voters after they have successfully cast votes. Buzzers will be used to generate different types of alert sounds at different situations.

## IV. System Implementation

Different hardware which have been interfaced together for implementing a prototype of the system as shown in Figure 4 are given bellow:

1) Arduino Mega R3 2560
2) Finger Print Module FPM 10A
3) GSM modem
4) 16x2 LCD Display
5) Ethernet Shield
6) TFT LCD Touch Screen Module
7) 4*4 flexible keypad
8) Adapter 12v 2amp
9) Buzzer
10) Jumper wire
11) TP link Router

Fig. 4: Implemented System Prototype

According to the system architecture, a model of the system is developed by integrating Arduino Mega with 16x2 LCD, 4x4 keypad, finger print module, Ethernet Shield, TFT LCD Touch Screen, GSM, Buzzer etc. A database is designed on MYSQL server which is used to store the fingeprint templates generated through the fingerprint module, voter's detailed information, list of candidates for specific election and other necessary information. A wired connection using ethernet shield and router is established for the database connection with Arduino. A user interface is designed using HTML, CSS, PHP, JavaScript and JQuery to access the data stored in the database and also to provide an integrated platform to the election controllers for the central control. The implemented features are:

### A. Procedural Instructions and Option Selection

During the whole process, the LCD display shows the user all kind of necessary instructions and displays different kinds of messages to make the system easier to understand and use. For different types of operations like giving user id, voting for a candidate, the user has to press different buttons in the keypad.

### B. Registration

Only users, whose information are already stored in database, are eligible for the registration process. For checking process user has to input his id at first. If eligible, user will be asked for the same fingerprint twice for better accuracy. If the same fingerprint already exists in the system, the system will notify about that and user won't be registered. Otherwise the user will be registered successfully.

### C. Voting

In the voting process, the user will have to give his fingerprint first. If the fingerprint exists in the database and the id holding that fingerprint has not voted yet, then the user will be granted the permission to vote any candidate.

### D. Candidate List

The candidate list along with their serial number for the voting process is displayed on the TFT monitor which tells the user which button to press to vote for a specific candidate.

### E. Generating SMS and Buzzer Alarm

When a voter has voted successfully, the system will generate a message to the voter's number to notify him. For any kind of disturbance sms will be sent to authority. In case of any kind of false attempt like - trying to register with invalid id or same id, trying to register twice with same fingerprint, non-voter trying to vote or voter trying to vote twice, the system will generate an alarm using the buzzer.

### F. Voter Profile

Voter's all information can be viewed by the control officer from the central website. So, during the registration process registration officer can easily see voter's detailed information and his picture to verify if he is actually the person he is claiming to be and only then take his fingerprint for registration.

### G. Stored Voting Information

During the voting process the exact date and time of giving vote along with the name of candidate who has been voted will be stored in the database. But for security purpose, the name of the candidate will be stored in an encrypted format.

## V. Result and Discussion

The implemented prototype of the system was tested for various constraints and loopholes but the result was quite satisfying. There is no way a user can register or vote falsely. All information regarding the voting process (voter, voting date, time) is stored in the database but the user name is encrypted using algorithm. Message from GSM and data from server are sent in an encrypted form using SHA-1 algorithm which is then decrypted in the receiver end to protect data from eavesdropping, spoofing or any kind of network breach.

In order to test accuracy of the system fingerprints of around 65 people were collected. Later on, while conducting voting process, among 70 people (5 not registered) fingerprints of 63 people were recognized correctly by the system. So, the value of True Positive (TP) and False Negative (FN) was calculated to be 63 and 2 respectively with a sensitivity of 97%. The system was found to be quite user friendly and easy-to-understand so that general people (both literate and illiterate) can easily get used to it.

## VI. Limitation and Future Implementation

Few limitations of the prototype are given below which we plan to work on in future to make the system foolproof to a great extent.

### A. Huge Volume of Fingerprints

The matching of fingerprints may take some more time than expectation when the matching has to be done with a huge volume of fingerprints existing in the database.

### B. Better Interface

At present the voters have to press buttons in the keypad to vote for specific candidate which might be difficult for people with less educational knowledge. We plan to solve this problem by using different fingerprint sensors for each candidate, the voter will only need to put his finger in the fingerprint sensor appointed for the specific candidate he is willing to vote for.

### C. Multi-biometric System

Result of fingerprint matching may not always be correct so depending only on fingerprints will increase the risk of error. Again, people with no hands won't be able to cast votes following this procedure. So in future we plan to extend our biometric identification system to a multi-biometric system by integrating facial recognition, retinal scan and iris scan system to our model.

## VII. Conclusion

Being a democratic country, Bangladesh needs a fair and transparent election. Use of a biometric EVM is one of the most secured ways of coducting a fair election. Using biometric identification process, no one will be able to cast someone elses vote or vote multiple times. BEVM helps to overcome the drawbacks of the current EVM system recollecting the voting information (audit trails) which will provide evidence of the EVM's integrity and accuracy. Therefore we can say that implementation of BEVM can provide transparent, fair, secure and accurate election process which is the main desire of every democratic country like Bangladesh and thus hold democracy upright in our country.

## References


[1] B. B. Sarma, *Election and democracy in Bangladesh: A case for introducing proportional voting system*, 2012 [Accessed October 08, 2017]. [Online]. Available: http://print.thefinancialexpress-bd.com/old/more.php?news_id=131158&date=2012-05-30.

[2] D. Tribune, *EC publishes roadmap, says use of EVMs still possible*, July 16, 2017 [Accessed October 06, 2017]. [Online]. Available: http://www.dhakatribune.com/bangladesh/politics/2017/07/16/ec-lays-path-11th-national-elections/.

[3] J. U. Md. Meftaul Islam, Dept. of International Relations, *EVM and Digital Bangladesh*, 2011 (accessed Sep 22, 2017). [Online]. Available: http://www.thedailystar.net/news-detail-215643

[4] M. M. Sarker and M. N. Islam, "Management of sustainable, credible and integrated electronic voting (e-voting) system for bangladesh," *Management of Sustainable Development*, vol. 5, no. 1, pp. 15–21, 2013.

[5] T. Kohno, A. Stubblefield, A. D. Rubin, and D. S. Wallach, "Analysis of an electronic voting system," in *Security and Privacy, 2004. Proceedings. 2004 IEEE Symposium on*. IEEE, 2004, pp. 27–40.

[6] J. Wayman, A. Jain, D. Maltoni, and D. Maio, "An introduction to biometric authentication systems," *Biometric Systems*, pp. 1–20, 2005.

[7] Technovelgycom, *Biometric identification systems*, [Accessed October 02, 2017]. [Online]. Available: http://www.technovelgy.com/ct/Technology-Article.asp?ArtNum=12

[8] S. M. Hasan, A. M. Anis, H. Rahman, J. S. Alam, S. I. Nabil, and M. K. Rhaman, "Development of electronic voting machine with the inclusion of near field communication id cards and biometric fingerprint identifier," in *Computer and Information Technology (ICCIT), 2014 17th International Conference on*. IEEE, 2014, pp. 383–387.

[9] S. Hof, "E-voting and biometric systems?" *Electronic Voting in Europe Technology, Law, Politics and Society*, 2004.

[10] D. A. Kumar and T. U. S. Begum, "A novel design of electronic voting system using fingerprint," *International Journal of Innovative Technology & Creative Engineering*, vol. 1, no. 1, pp. 12–19, 2011.

[11] T. M. N. U. A. M. S. U. M. Mesbahuddin Sarker, Md. Ariful Islam Shah, "An approach of automated electronic voting management system for bangladesh using biometric fingerprint," *International Journal of Advanced Engineering Research and Science*, vol. 3, 2016.

[12] S. Chakraborty, S. Mukherjee, B. Sadhukhan, and K. T. Yasmin, "Biometric voting system using aadhar card in india," *International journal of Innovative research in Computer and Communication Engineering*, vol. 4, no. 4, 2016.

[13] N. S. Tilwani, N. Majumdar, and P. Bhargava, "Fair election system in india using uid data and biometric technology," *International Journal of Scientific Engineering Research*, vol. 4, 2013.

[14] M. S. G. M. Stephen, "Aadhar based electronic voting system using biometric authentication and iot," *International Journal of Recent Trends in Engineering Research (IJRTER)*, 2017.

[15] R. M. Prasad, P. Bojja, and M. Nakirekanti, "Aadhar based electronic voting machine using arduino," *International Journal of Computer Applications (0975–8887) Volume*.

[16] M. Khasawneh, M. Malkawi, O. Al-Jarrah, L. Barakat, T. S. Hayajneh, and M. S. Ebaid, "A biometric-secure e-voting system for election processes," in *Mechatronics and Its Applications, 2008. ISMA 2008. 5th International Symposium on*. IEEE, 2008, pp. 1–8.

[17] A. Reddy, "A case study on indian evms using biometrics." *International Journal of Engineering Science & Advanced Technology*, vol. 1, no. 1, pp. 40–42, 2011.

[18] M. Yinyeh and K. Gbolagade, "Overview of biometric electronic voting system in ghana," *International Journal of Advanced Research in Computer Science and Software Engineering*, vol. 3, no. 7, 2013.

[19] R. Alaguvel, G. Gnanavel, and K. Jagadhambal, "Biometrics using electronic voting system with embedded security," *International Journal of Advanced Research in Computer Engineering & Technology*, vol. 2, no. 3, pp. 1065–1072, 2013.

[20] Baig, Hidayat, Taslim, B. Jeba, Rajesh, A. Prof., J., and Prof., "Secured e voting via smart phone app," *International Journal on Future Revolution in Computer Science Communication Engineering (IJFRSCE)*, vol. 2, pp. 20–23, 2016.

[21] *Elections in India*, November 06, 2017 [Accessed November 16, 2017]. [Online]. Available: https://en.m.wikipedia.org/wiki/Elections_in_India

# Module-Based Edukit for Teaching and Learning 8051 Microcontroller Programming

Liakot Ali,[1] Lutfor Rahman,[2] and Shahin Akhter [3]

[1, 2, 3]Institute of Information and Communication Technology, Bangladesh University of Engineering and Technology Dhaka-1000, Bangladesh

[1]liakot@iict.buet.ac.bd

*Abstract*- **A microcontroller unit (MCU) is the critical part of an embedded system. The knowledge of MCU is essential for every field of science and technology which in turn directs that a strong curriculum based on MCUs at various levels of education is necessary for universities, colleges, and schools. For learning Atmel MCU programming, various trainer board models are available in the local market. But these currently available trainer board components are assembled on a large single printed circuit board (PCB) which is expensive, consumes high power and inconvenient for portable applications. Moreover, it is not possible to integrate new components in these trainer boards. This paper presents a module-based Edukit to overcome those problems. Miniaturization is the main contribution of Edukit. an ice-cream size box contains the whole Edukit which proves that the Edukit is simple, portable, low cost, consuming less power. Moreover, the Edukit is module based which in turn makes it a low-cost and suitable educational tool for any disciplines of science and engineering.**

***Index Terms***—**Educational Kit, Microcontroller, Embedded System, Printed Circuit Board, 8051.**

## I. Introduction

Low power portable embedded system is a demand in this era of information and communication technology. A microcontroller is one of the powerful but low-cost devices to realize an embedded system. At present, a microcontroller unit (MCU) is being widely used in almost all areas of science and engineering disciplines. It is imposed by the Accreditation Board for Engineering and Technology (ABET) that engineering students must demonstrate a knowledge of data acquisition, processing and control in which use of computers, MCUs are essential [1]. Considering the high demand for MCU knowledge, curriculum containing MCUs at various levels of education are being introduced in different universities, colleges and schools [2], [3]. This requires suitable simulation tools and Educational kits (Edukit) for teaching and learning MCU programming as well as for real-time application development [4], [5]. In the market there are many types of MCUs such as Motorola, Intel, Microchip, Zilog, Atmel etc. and their educational MCU boards are available for this purpose. Among all the MCUs, 8051 family has many unique features such as inexpensive, low power consumption, and good cross-platform support. Usually, educational boards are manufactured for general purpose and so components are assembled on a big size single printed circuit board (PCB). Due to the crowdedness of components and big size of the board, this may appear inconvenient and cumbersome for MCU beginners [6].

Hence, the scope of our current study in this paper is to develop 8051 MCU based educational boards having the following features:

- It will simple and portable,
- It will affordable for everybody,
- It will suitable for any disciplines of science and engineering.

## II. Prior Work

There have been remarkable efforts in literature for developing multi-module 8051 MCU experimental board for teaching MCU courses in different disciplines of science and engineering [7]. This experimental board is multi-module based where the 8051 MCU is on the main module and other modules are related to interfacing application such as the 16X2 LCD display, 7-segment display, dc motor speed control, DAC, etc. Texas A&M University-Corpus Christi recently established a Digital Systems Laboratory (DSL) that provides interdisciplinary educational and research capabilities in several sciences and engineering areas [8]. A research in [9] describes teaching aid – platform for courses of embedded systems programming. This platform consists of an MCU unit (evaluation kit), an industrial computer (panel PC), several models of real-world processes and I/O modules and other supporting circuitry for connecting the computer systems to the models. A project-based MCU system laboratory has been designed and developed using BK300 development board with PIC16F887 chip [10]. A modular-approach of multi-microcontroller based educational training system with IDE has been designed for MCU training system that is based on 8-bit MCU Intel® MCS51 and Motorola®MC68HC11 [11]. Considering the importance of MCU in the academic curriculum of BUET, a concept of module-based Educational kit for Edukit programming was proposed in [12].

## III. Conceptual Design Of Edukit

Our current study considered MCU of 8051 architecture due to its low cost, simplicity, availability and many other attractive features [13].

Fig. 1 shows a conceptual design of the Edukit where 1(a) and 1(b) indicates a sample of motherboard and daughterboard respectively. The motherboard was equipped with an AT89S51 processor, power supply and usually used common components such as resistors, capacitors, switches, and connectors. The oval icon in Fig. 1(b) is used to indicate the

978-1-5386-3374-8/17/$31.00 ©2017 IEEE

typical components in the motherboard. There were male connectors around the periphery of the motherboard. The daughterboard was equipped with components for developing specific applications as indicated by the oval icon. The male connector resided in the periphery. It is to be mentioned that the motherboard and the daughterboard can be easily connected through the connector wires. MCU port pins were not kept fixed for any components to ease the adoption of a new daughterboard with the motherboard.

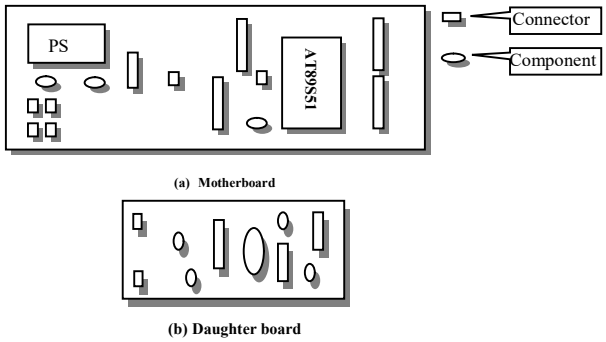


Fig. 1 Conceptual motherboard and daughter board of the proposed Edukit.

## IV. IMPLEMENTATION

The Orcad software was used for preparing the schematic design and layout of motherboard and daughter board of Edukit and the simulation was carried out in the Proteus software. Finally, the prototype of the Edukit from Orcad was implemented in Printed Circuit Board (PCB). Fig. 2 shows the motherboard of the Edukit.

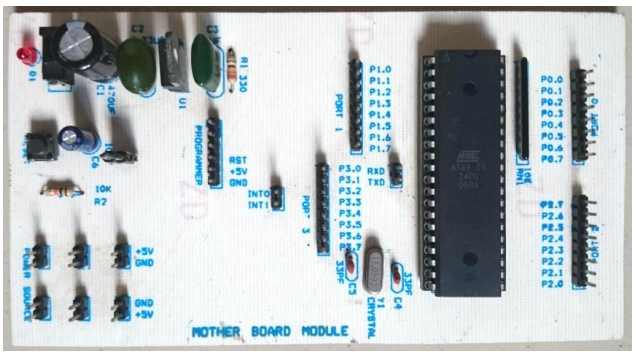


Fig. 2 Mother Board Module.

It is to be observed in Fig. 2 that there is a port connector, programmer connector, power connector, and reset button on the motherboard. Port connectors are used to establish a connection between motherboard and daughter board module for various application purpose. The program connector in the MCU is to connect with MCU programmer and the power connector is to supply power to the daughter board module. A reset button is kept for restarting the MCU program.

Other components such as the LED module, 7 segment modules, 8×8 dot matrix module, 16×2 LCD module, ADC module, a serial communication module, a motor driver module, keypad, and RTC respectively are shown in Fig. 3 to Fig. 11.

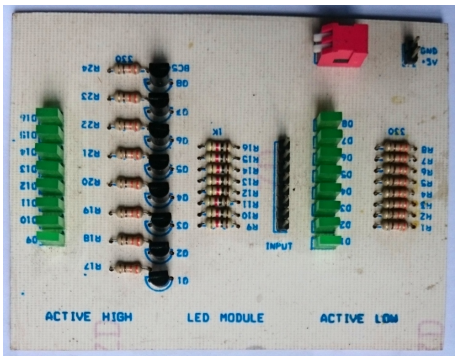


Fig. 3 LED Module.

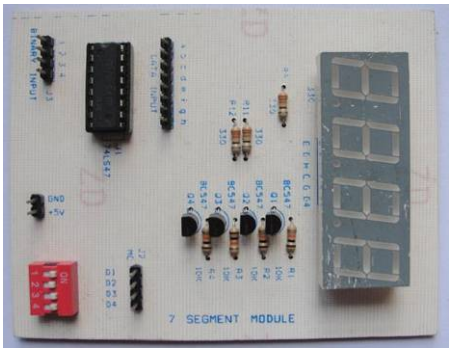


Fig. 4 7 Segment Module.

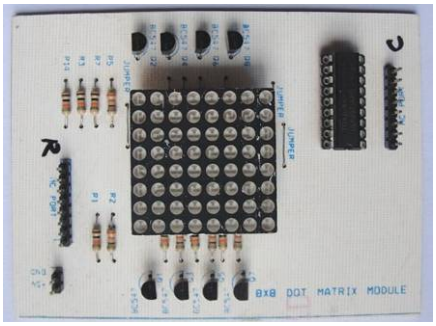


Fig. 5 8×8 Dot Matrix Module.

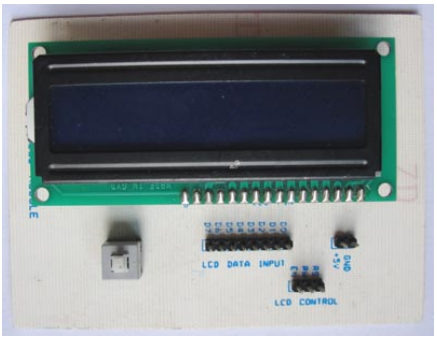


Fig. 6 16×2 LCD Module.

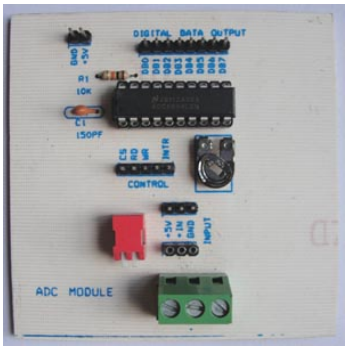


Fig. 7 ADC Module.

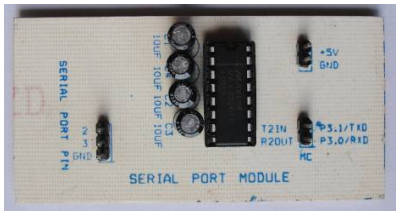


Fig. 8 Serial Port Module.

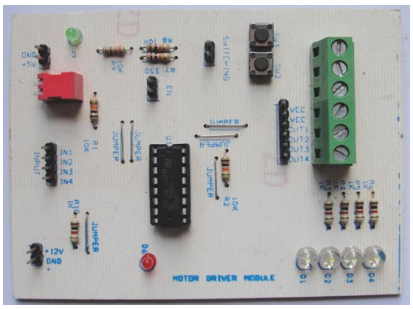


Fig. 9 Motor Driver Module.

Fig. 10 Keypad


Fig. 11 RTC module.

In LED module in Fig. 3 has one input connector, one power connector, one two-digit switch, resistors, transistors and two row LEDs. The basic component of the 7-segment module was a four-digit common anode 7-segment display. The module has digit selection connector, digit selection switch, data input connector, a binary input connector, power connector, 74LS47 and other peripheral components.

In 8×8 dot matrix module in Fig. 5, there were two 8 pin connectors to connect with the motherboard, power connector, ULN2803A IC, resistors, transistors. The ULN2803A contained a high-voltage, high-current Darlington transistor array. The 16 pins female connector LCD module in Fig. 6 contained a 3-pin connector for LCD control, power connector, an sw1 switch for LCD back light and VR1 variable resistor for adjusting display contrast in the LCD module.

In the ADC module of Fig. 7, there were input connectors for analog input voltage, control connector for controlling ADC operation, digital data output connector for digital signal output and power connector. The serial communication module in Fig. 8 consists of an MC connector, power connector, and serial port pin to connect with RS232 DB9 pin. The motor module in Fig. 9 was developed to operate DC motor and stepper motor. Here, L293D acted as a motor driver and D1-D4 LED were for displaying the correspondent output value status in the motor module.

The RTC module in Fig. 11 was developed to provide the time (hour, minute, second) and the date (year, month, day) continuously, regardless of whether the power is on or off. DS1307 was used as RTC in this module.

The whole kit including the motherboard, daughterboard, cables, adapter, and programmer can be packed in an ice cream box as shown in Fig. 12.

Fig. 12 Edukit in an Ice-cream Box.

## V. Test Results

The Keil µVision compiler and Hex code were used to compile the necessary codes and burned inside the MCU. Finally, the daughter board was tested for different applications.

### *A. LED module*

Fig. 13 displays the microcontroller port status through LED. Here, MCU P0 port of motherboard was connected to the input connector of LED module through connector wire.

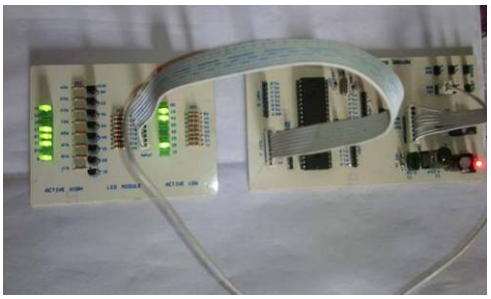

Fig. 13 LED Module Testing Result Output.

### *B. 7 segment module*

A sample numeric value in the 7-segment display is shown in Fig. 14 by connecting the MCU port P2 of motherboard to the input port of 7-segment module.


Fig. 14 7 Segment Module Testing Result Output.

### C. Dot matrix module

Fig. 15 shows the symbol 'A' in the Dot Matrix module by connecting the P1 and P3 ports of the motherboard MCU to the input port of Dot Matrix module.

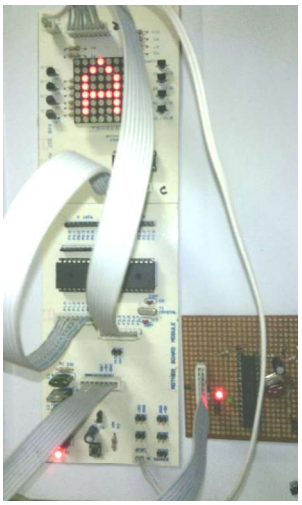

Fig. 15 Dot Matrix Display Module Testing Result Output.

### D. LCD module and Keypad

The keypad port was connected to the P0 port and the LCD data input port was connected to the P2 port of the motherboard. Fig. 16 displays the keypad assigned values to the LCD module.

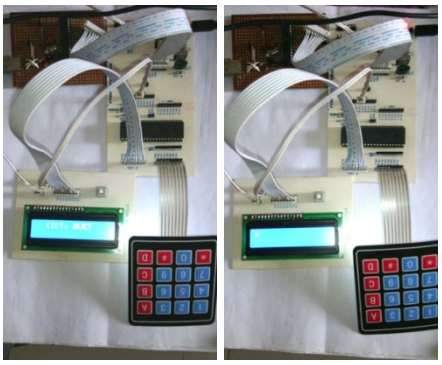

Fig. 16 Keypad Interfacing Testing Result Output.

### E. LCD module and ADC module

The ADC module for digital data output was connected to the P1 port and the LCD data input port was connected to the P2 port of the motherboard. We provided analog voltage to the +VIN of the ADC module. Fig. 17 displays a sample decimal value on the LCD display.

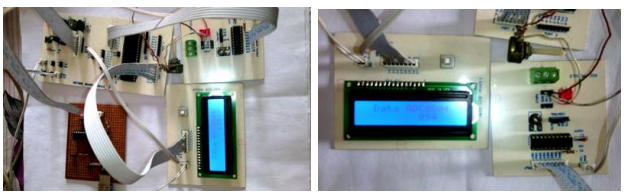

Fig. 17 ADC Module Testing Result Output.

### F. Serial communication module

The MC connector in serial port module was connected to the P3.1 and P3.0 of the motherboard. Fig. 18(a) shows the connection within the PC, motherboard and serial communication module, while Fig. 18(b) displays a sample output in the hyper terminal.

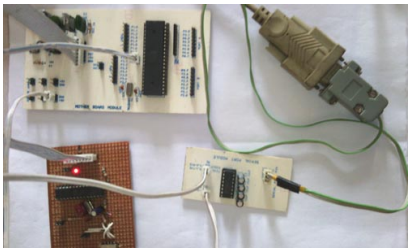

(a)

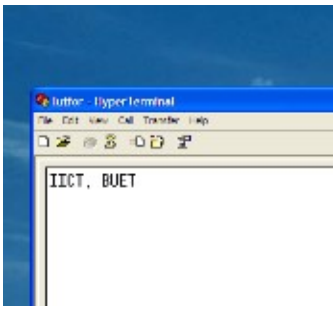


(b)

Fig. 18 Serial Port Module Testing Result Output.

### G. Motor driver module for DC motor

P2.0 and P2.1 pins of the motherboard were connected to the input terminal of motor driver terminal and P1.7 pin of the motherboard was connected to the switching terminal of motor driver terminal. Different LED status is shown in Fig. 19 indicates that a change in the direction of motor rotations (i.e., clockwise in Fig. 19(a) and anti-clockwise in Fig. 19(b)).

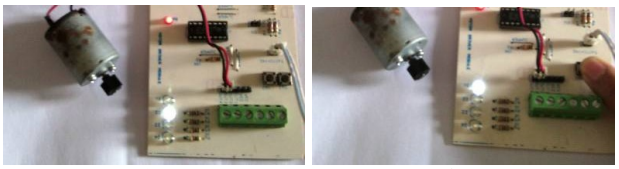

(a) (b)

Fig. 19 Motor driver module testing result output using DC motor.

### H. Motor driver module for stepper motor

P1 port of motherboard was to the input terminal of motor driver terminal and stepper motor was connected to the output terminal of motor driver module. The 4-step sequence of the stepper motor rotation is displayed in Fig. 20 through LED status.

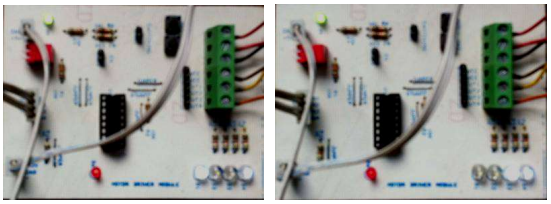

Fig. 20 Motor Driver Module Testing using Stepper motor.

### I. LCD module and RTC module

RTC SCL and SDA pin were connected to P1.0 and P1.1 pins of the motherboard, respectively. LCD data input port was connected to the P2 port of the motherboard. LCD RS and EN pin was connected to the P3.5 and P3.4 pins of the motherboard, respectively. The following figure in Fig. 21 shows time and date in the LCD display.

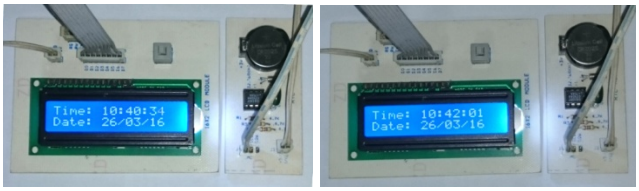


Fig. 21 RTC module testing result.

A list of available features in the traditional Edukit and module-based Edukit is presented below in Table 1. It is evident from Table 1 that the module-based Edukit is simple, inexpensive and suitable for further integration of external modules.

TABLE I
COMPARISON BETWEEN THE TRADITIONAL AND MODULE-BASED EDUKIT

| **Traditional Edukit** | **Module-Based Edukit** |
|---|---|
| Expensive. | Low cost. |
| Single size big PCB. | Not in a single size big PCB. |
| Use is complex. | Use is simple. |
| Not possible to adopt new component. | It is easy to adopt new daughter board. |
| MCU port pin is fixed for specific application. | MCU port pin is free for any application. |
| Program must be written according to the Edukit layout. | It is easy to connect between motherboard and daughter board according to program code. |

## VI. CONCLUSIONS

Based on the comparative performances listed in Table 1, it is expected that the developed Edukit will be complementary for the new MCU curriculum and will satisfy the needs of the students and instructors in the most effective way. This will module based Edukit could be a cost-effective and portable solution for delivering the MCU curriculum. Considering its modular architecture, the daughter board of the Edukit can be of use for various fields of science and technology as well.

## ACKNOWLEDGMENT

The authors are grateful to IICT, BUET for allowing us to conduct research using its Advanced Embedded System Laboratory and all kinds of facilities here.

## REFERENCES

[1] Engineering Accreditation Commission, Accreditation Board of Engineering and Technology, Inc., Criteria for Accrediting Programs in Engineering in the United States, pp. 11-12, 1996- 1997.
[2] Anon., http://www.abet.org/. Accessed on October 2005.
[3] E. Montanez, "Micro-controller in Education: Embedded control-Everywhere and Everyday", in *Proc. of American Society for Engineering Education Annual Conference & Exposition*, USA, 2005.
[4] T. K. Hamariata and R.W. McClendon, "A New Approach for Teaching and Learning Micro-controller Courses", *Int. Journal of Engineering Education,* vol. 13, pp. 269-274, 1997.
[5] Anon., http://www.futurlec.com/. Accessed on October 2005.
[6] Sickle, "Programming Micro-controller in C", Hightext, 1994.
[7] Kumbhar D. S., Bhujbal, R. V., "Development and use of multi-module 8051 micro-controller board for teaching and learning micro-controller programming", in *Proc. of National Conference on Emerging Trends in Electronics & Computer Science*, 2010.
[8] R. Bachnak, "Teaching microcontrollers with hands-on hardware experiments", *Journal of Computing Sciences in Colleges*, vol. 20, pp. 207-213, Apr. 2005.
[9] Dolinay J., Dostálek P., Vašek V., Vrba P., "Teaching platform for lessons of embedded systems programming", in *Proc. 13th WSEAS International Conference on Automatic Control, Modelling & Simulation*, Lanzarote, Canary Islands, 2011, pp.158-161.
[10] L. A. Ajao, O. M. Olaniyi, J. G. Kolo, A. O. Ajao, "Project-based microcontroller system laboratory using BK300 development board with PIC16F887 chip", *International Journal of Embedded systems and Applications (IJESA)*, vol. 5, pp. 15-18, Sept. 2015.
[11] R. S. K. Selvakumar, K. H. Ghazali, N. M. K. Nik Yusoff, "Designing a modular-approach of multi-microcontroller based educational training system with IDE", *National Conference on Postgraduate Research,* Malaysia, 2009.
[12] M. L. Ali, S. M. L. Kabir, M. J. B. Alam, and M. A. Kashem, "Module-based Edukit for Teaching and Learning Micro-Controller Programming", in *Proc. of Methods, Materials and Tools for Programming Education*, Finland, pp. 67-70, 2006.
[13] AT89S51 Datasheet from Atmel Corporation, www.atmel.com

# Minimization of Fading Effect through Novel Method of Beamforming for NGN Wireless Systems

A. K. M. Baki
Department of Electrical and Electronic Engineering
Ahsanullah University of Science and Technology (AUST)
141-142 Love Road, Tejgaon I/A, Dhaka-1208, Bangladesh
Dr.AKM.Baki@ieee.org

*Abstract*—**This paper describes a novel multipath fading effect minimization technique through a novel method of Beamforming algorithm. RMS Delay Spread (RDS) of a channel is highly dependent on beamwidth of deployed antenna systems. Deep fade, which is a bottle neck for high speed wireless networks, causes larger RDS and higher bit error rate (BER). A frequency flat fading channel can trasmit data with smaller RDS and higher bit rate. RDS is reduced if the beamwidth of deployed antenna system becomes narrower. Binomial array and Dolph-Chebyshev array are popular methods of array antenna beamforing, though each of these methods has its own technical limitations. The method of Beamforming described in the paper is technically better which uses a novel concept of Fractional-Powered Binomial coefficients. The method performs better than Binomial and Dolph-Chebyshev array. Superiority of the described method is validated through simulations of realistic antennas and technical analysis of RDS.**

***Index Terms***— **Antenna radiation patterns; Bit error rate; Channel models; Fading; Next generation networking; Rayleigh channels; Rician channels; Radio propagation;**

## I. INTRODUCTION

Some of the bottlenecks for next generation networking (NGN) wireless systems (e.g. 5G) are increased number of devices with increased energy consumption, increasingly crowded environment with high rise buildings, requirement of very high speed data channels, shortage of spectrum, and mobility issues. Some goals of 5G systems are:

a. 100 Mbps throughputs;
b. Extremely low latency (1 msec or less), ten times lower than 4G;
c. Data rate at least ten times higher than that of 4G;
d. Use of higher frequencies (30 GHz and above);
e. Wider channel bandwidth (1 to 2 GHz, or even wider).

In a wireless communication system with multipath fading channels, different versions of transmitted signal at the receiver spread in time. This phenomenon is called delay spread. Delay spread can be characterised by Power Delay Profile (PDP) of a channel. PDP is the measure of time distribution of the received signal power when an impulse signal is transmitted through a channel. A time dispersive channel can be characterized by RMS Delay Spread (RDS). RDS is a measure of how the multipath power in a channel is spread over the delay. RDS depends on several factors such as propagation channel, shadowing, types of antennas, polarization, and array signal processing techniques. Channel modelling is required for different purposes of wireless communication systems [1]. Performance evaluation of Long Term Evaluation (LTE) network is done in [2]. Performance evaluation of LTE Rayleigh fading and pedestrian channels are reported in [3]. Another important parameter that describes the channel characteristics is the Rician K-factor. K is the ratio of power through the line of sight (LOS) component to those of other scattered components [4]-[5]. Channels can be classified as Rician or Rayleigh fading channels based on RDS and K-factors [6]-[8]. Rician K depends on several channel factors and beamwidth of antenna system [4]-[5]. Generally higher K-factors and lower RDS represent frequency-flat Rician channels. On the other hand lower K-factors and higher RDS represent frequency selective Rayleigh fading channels. Frequency flat channel is better in terms of higher bandwidth and lower bit error rate (BER).

A channel can be considered as Rician channel if the Rician- K $\geq 0$ dB [9]. Antennas with narrower beamwidth result in higher K-factor [9]. RDS of a channel is also highly dependent on beamwidth of antenna radiation pattern. RDS can be minimized by using high gain antennas [10] with narrower beamwidth. High gain antenna for LTE and 5G system is discussed in [11]. Rician-K of a wireless channel can be expressed [4], [5], [12] as:

$$K \cong F_s F_h F_B K_0 d^{\gamma} \quad (1)$$

where,
$F_s$ is the seasonal factor;
$F_h$ is height factor (meter);
$F_B$ is the beamwidth factor which can be expressed as [4]-[5]:

$$F_B = \left(\frac{B}{17}\right)^{-0.62} \quad (2)$$

B is the beamwidth in degrees;
d is distance in kilometres;
$K_0, \gamma$ are constants.
The values of $K_0$ and $\gamma$ are reported as 10 dB and -0.5 dB in [5].

Equation (2) states that Rician-K depends on beamwidth of antenna system. Antennas with lower beamwidth give rise to higher K-factors. Bit rate decreases and inter-symbol-interferences (ISI) increases with increased RDS and decreased K-factors. Fig. 1 shows a plot of $F_B$ vs. beamwidth for different values of beamwidth. It can be inferred from (1), (2) and Fig. 1 that a channel with lower K-factor can be transformed into a channel with higher K-factor by using antennas with reduced beamwidth.

In an antenna system, weightings of antenna elements are adjusted to achieve maximum transmission/ reception in a desired direction by rejecting interfering signals in other directions. In order to ensure a robust and power efficient wireless communication system, propagating signal from antenna should have narrower beamwidth and negligible side lobe levels (SLL). Beamwidth-SLL trade-off can be optimized [13] through optimization of antenna excitation coefficients. There exists different types of power distributions of array antennas. Some of the non-uniform amplitude distributions of array antenna, those can produce lower SLL (at the cost of

978-1-5386-3374-8/17/$31.00 ©2017 IEEE

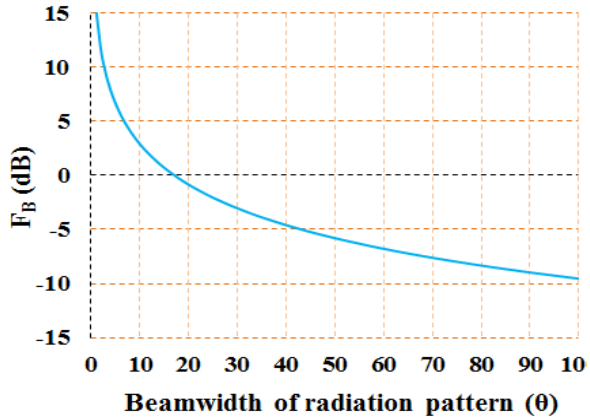


Fig. 1. Beamwidth factor vs. beamwidth of antenna radiation pattern.

wider beamwidth), are Binomial distribution [14]-[15], Dolph-Chebyshev distribution [14], and Gaussian distribution [16]-[17]. Array antenna with Binomial excitation coefficients does not produce any SLL with element spacing $0.5\lambda$ or less [14]-[15]. Coefficients of an N-element Binomial array can be calculated as [14]-[15]:

$$1, N-1, \frac{(N-1)(N-2)}{2!}, \ldots\ldots\ldots\ldots \quad (3)$$

This paper describes a minimization technique of multi-path fading effects through a novel concept of Fractional-Powered Binomial Array (FPBA) [15]. The novel FPBA is better than popular Dolph-Chebyshev or Binomial array from the perspective of beamwidth-SLL trade off [15]. The paper is organized in the following way. Section II compares the radiation parameters of Binomial array, Dolph-Chebyshev array and FPBA considering different number of isotropic antenna elements and different set of excitation coefficients. Section III analyses the radiation parameters of FPBA with realistic antennas (e.g. microstrip patches). Section IV describes the effect of frequency flat and frequency selective fading channels on RDS. Finally, section V concludes the paper.

## II. Analysis of Excitation Coefficients and Radiation Patterns For Different Array Distribution

In this section a comparative analysis of radiation patterns for Binomial array, Dolph-Chebyshev array and the proposed FPBA [15] is made by using different set of excitation coefficients and number of antenna elements. Effect of different main beam steering angle on radiation patterns is also investigated. Binomial and Dolph-Chebyshev array antennas have some limitations. Beamwidth of Binomial array is the widest. Widest main beam will result in maximum power loss in some wireless applications. Magnitudes-variation of Binomial array is also too wide which can lead to an impractical implementation of power amplifier at the output stage of transmitter. Too wide variation of amplifier output causes non-linearity of the system. Though element spacing of $\leq 0.5\lambda$ increases mutual coupling effects, Binomial array does not produce any SLL when element spacing of $\leq 0.5\lambda$ is used [14]. Another problem with Binomial array is the increase of SLL when element spacing becomes higher than $0.5\ \lambda$. Mutual coupling effects can be minimized with element spacing of $\geqslant 0.6\lambda$ and will be discussed further in section III.

Beamwidth of Binomial array can be reduced further by using excitation coefficients according to FPBA [15]. Instead of using Binomial coefficients of (3), following FPBA excitations coefficients can be used [15]:

$$1^{\beta}, (N-1)^{\beta}, \left[\frac{(N-1)(N-2)}{2!}\right]^{\beta}, \quad (4)$$

$\beta$ in (4) is a variable within the range $0 < \beta < 1$.

Coefficients of (4) can reduce beamwidth and 'wide-variation of excitation coefficients of convention Binomial array'. FPBA becomes Binomial array when $\beta$ is set to 1. Following sub-sections describe radiation patterns of FPBA, Binomial array, and Dolph-Chebyshev array for different cases of number of antenna elements, main beam steering angle, and different sets of excitation coefficients. Isotropic element spacing for all cases was chosen as $0.6\lambda$ (for 60 GHz system).

### *A. Excitation Coefficients and Radiation Patterns for 25-elements Array (MSLL=20 dB)*

Fig. 2 shows the relative excitation coefficients (dB) for Binomial array, 20 dB Dolph-Chebyshev array, and FPBA ($\beta = 0.07$). The number of elements for each of these three distributions was 25. Fig. 2 shows that reverse tapering occurs in case of Dolph-Chebyshev array which may lead to technical difficulties. Fig. 3 shows the radiation patterns for the respective distributions.

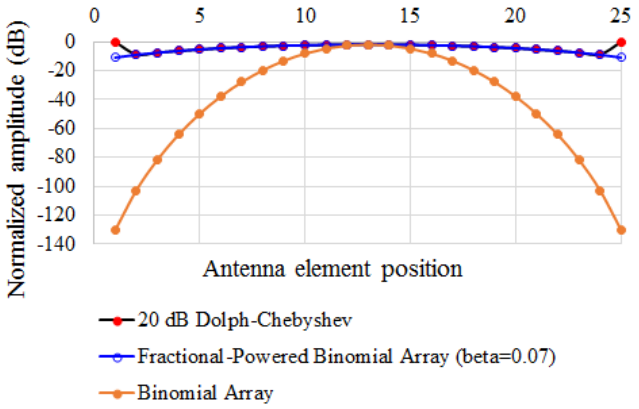


Fig. 2. Excitation coefficients of 25 antenna elements for 20 dB Dolph-Chebyshev, Binomial, and Fractional-powered-Binomial array ($\boldsymbol{\beta = 0.07}$).

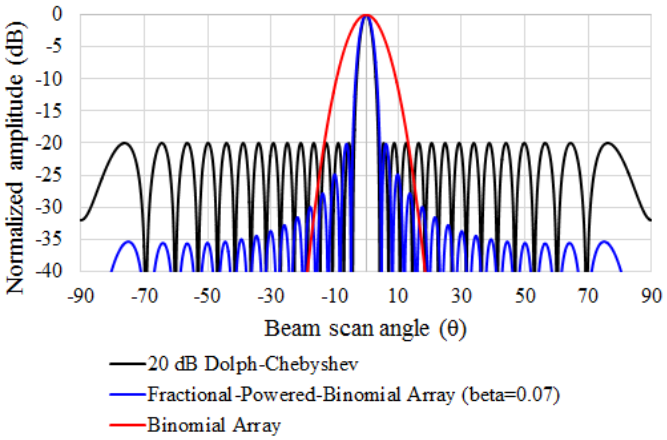


Fig. 3. Radiation patterns of 20 dB Dolph-Chebyshev array, Binomial array and FPBA at $\mathbf{0}^{\circ}$ beam steering angle (respective excitation coefficients are shown in Fig.2.)

Fig. 3 shows that the main beamwidth is the highest in case of Binomial array. First Null Beamwidth (FNBW) are same in case of Dolph-Chebyshev array and FPBA ($\beta = 0.07$). Maximum SLL (MSLL) are also same in case of Dolph-

Chebyshev array and FPBA (-20 dB in this case). Though other SLLs of FPBA are lower than those of Dolph-Chebyshev array. Fig. 4 shows the radiation patterns for the respective distributions and at 30° beam steering angle. FPBA also shows the best performance along this 30°direction.

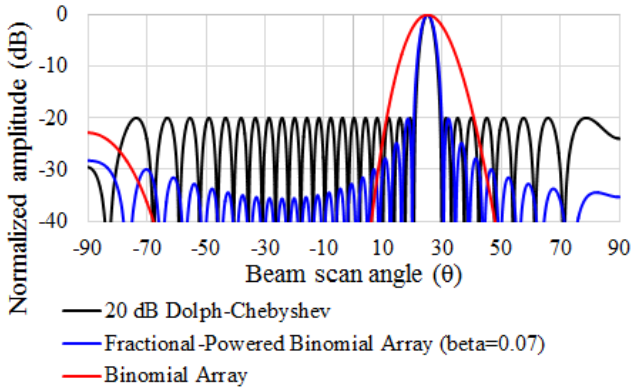


Fig. 4. Radiation patterns of 20 dB Dolph-Chebyshev array, Binomial array and FPBA($\boldsymbol{\beta = 0.07}$) at $\mathbf{30}^{\circ}$ beam steering angle (respective excitation coefficients are shown in Fig.2.)

### *B. Excitation Coefficients and Radiation Patterns for 45-elements Array (MSLL =40 dB)*

Fig. 5 shows the excitation coefficients for 45-element Dolph-Chebyshev array (40 dB), and 45-element FPBA ($\beta = 0.11$). Fig. 6 shows the corresponding radiation patterns. In this case, main beam direction was at $35^{\circ}$ from array broad side. Fig. 5 and Fig. 6 show that FPBA is also technically better than Dolph-Chebyshev array for higher number of antenna elements with lower MSLL. It was shown in [15] that GL appears with 8-element FPBA/Dolph-Chebyshev array when main beam angle is greater than $25^{\circ}$. Therefore number of antenna elements is a deciding factor for larger beam steering angle without any GL.

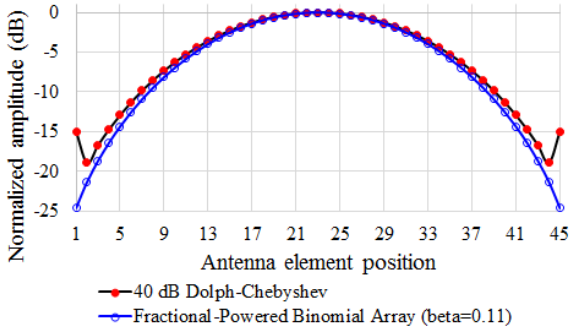


Fig. 5. Excitation coefficients of 45 antenna elements for 40 dB Dolph-Chebyshev array and FPBA ($\boldsymbol{\beta = 0.11}$). Respective radiation patterns are shown in Fig. 5.

From the above analysis of radiation patterns it is evident that FPBA is better than Dolph-Chebyshev array when SLL and excitation coefficients are compared. FPBA does not produce any reverse tapering. It is technically difficult to implement reverse tapering. Though Binomial array does not produce any SLL in some cases, the main beamwidth is the widest in this case. Directivities of FPBA are also higher than those of Dolph-Chebyshev arrays. The reason of these higher directivities are the lower SLL of FPBA. Higher directivities imply higher received power and lower RDS. Table I summarizes the radiation parameters for Dolph-Chebyshev array and FPBA.

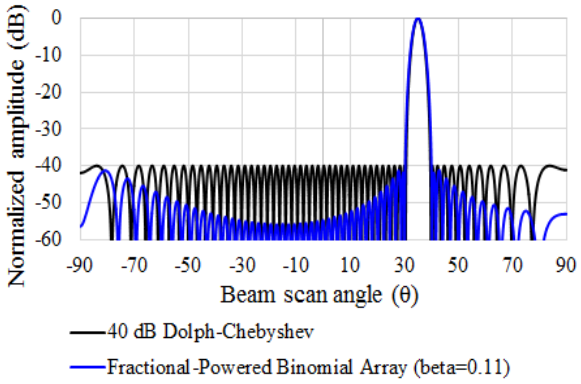


Fig. 6. Radiation patterns of 40 dB Dolph-Chebyshev array and FPBA ($\boldsymbol{\beta = 0.11}$) at $\mathbf{35}^{\circ}$ beam steering angle (respective excitation coefficients are shown in Fig.5.)

## III. Radiation Patterns of FPBA With Realistic Patch Antenna Elements

Radiation patterns of isotropic antennas [15] and those of realistic antennas are not the same due to some technical reasons. In this section analysis of radiation patterns of FPBA is done considering realistic antenna elements. Both rectangular and circular Microstrip patch elements were considered for the analysis of the radiation patterns, directivities, and the mutual coupling effects. Different inter-element spacing within the range 0.25 cm~0.37 cm ($0.5\lambda$~$0.74\lambda$) was considered for 60 GHz arrays. Antenna elements were placed along the X-axis (Fig. 7) in PCAAD simulation software. Effects of both X-axis polarization and Y-axis polarization were investigated. Fig. 8 shows the directivity versus 'inter-element spacing' graphs of rectangular and circular patch arrays. Total number of antenna elements was 8 in each case. It is noteworthy to mention here that in [15] only the isotropics cases of 8-element FPBA were investigated.

It is well known that the directivity decreases with the increased mutual coupling effect. On the other hand, directivity increases with increased inter-element spacing. Graphs of Fig. 8 also verify that the directivity increases with increased inter-element spacing of realistic antennas. Fig. 9 shows the radiation patterns of 8-element array (β=0.68) with different polarization. Some of the parameters of patch elements and radiation patterns are summarized in Table II. It is noteworthy to mention here that the Half-Power Beamwidth (HPBW) and MSLL for the FPBA (β=0.68; element spacing $0.6\lambda$) were respectively $16^{\circ}$ and – 50 dB when isotropic elements were considered (not shown in the figure). Simulation results show that circular patch array (both X and Y polarizations) is better than rectangular patch array in terms of directivity, HPBW and SLL. Results of Table II also suggest that the mutual coupling effect is less in case of circular patches. Radiation parameters of Table II verify that the FPBA is better than Binomial or Dolph-Chebyshev array even when practical antenna shapes are considered.

## IV. RMS Delay Spread vs. Fading Channels

Results of sections II-III show that FPBA is better than Binomial or Dolp-Chebyshev array, particularly in terms of directivity, SLL, and beamwidth. It was discussed in previous

TABLE I
COMPARISON OF RADIATION PARAMETERS FOR DOLPH-CHEBYSHEV AND FRACTIONAL-POWERED BINOMIAL ARRAYS (ISOTROPIC CASE)

| Types of excitation | Number of elements | Element spacing | Directivity (dB) | FNBW (deg.) | MSLL (dB) |
|---|---|---|---|---|---|
| Dolph-Chebyshev array | 25 | 0.6 $\lambda$ | 14.16 | 8.8 | -20 |
| | 45 | 0.6 $\lambda$ | 16.60 | 8 | -40 |
| FPBA | 25 | 0.6 $\lambda$ | **15.10** | 8.8 | -20 |
| | 45 | 0.6 $\lambda$ | **17.11** | 8 | -40 |

TABLE II
COMPARISON OF DIFFERENT RADIATION PARAMETERS OF FRACTIONAL-POWERED BINOMIAL ARRAY (FPBA) WITH RECTANGULAR AND CIRCULAR PATCH ELEMENTS (TOTAL ELEMENTS = 8).

| Patch Type | Dimensions | Element spacing (cm) | Polarization | Directivity (dB) | HPBW (deg.) | MSLL (dB) |
|---|---|---|---|---|---|---|
| Rectangular | 0.2×0.2 cm$^2$ | 0.31 | X | 15.1 | 15.43 | -48 |
| | | 0.31 | Y | 15.1 | 15.44 | -48.3 |
| Circular | Radius = 0.2 cm | 0.31 | X | **16.2** | **14.82** | **-53** |
| | | 0.31 | Y | **16.7** | **15.23** | **-50.7** |

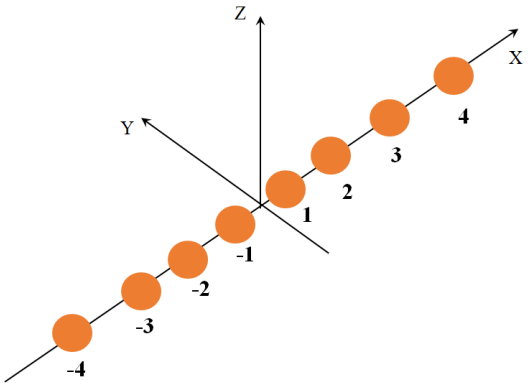


Fig. 7. Element position (x) of array antenna.

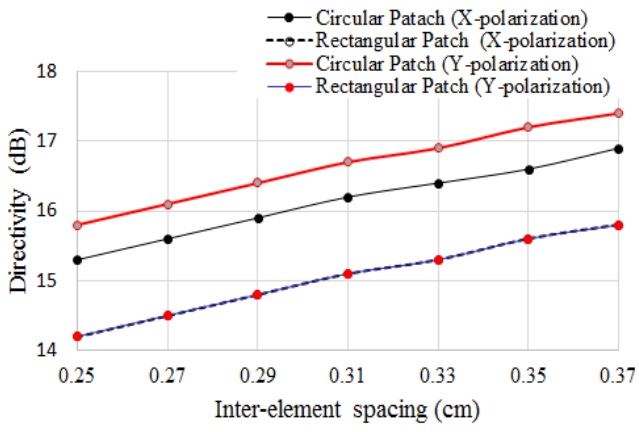


Fig. 8. Directivities of FPBA ($\beta = 0.68$) with rectangular and circular patch elements and for different polarization.

sections that narrorwer beamwidth of antenna radiation pattern gives rise to lower RDS (higer Rician-K) in a multipath fading channels [12]. The effect of fading on RDS will be investigated in this section. RDS of a channel can be defined as [12], [18]:

$$RMS\ delay\ spread\ (RDS),\ \sigma_\tau = \sqrt{\overline{\tau^2} - (\bar{\tau})^2} \qquad (5)$$

where $\bar{\tau} = mean\ ecess\ delay\ = \frac{\sum_k^N a_k^2 \tau_k}{\sum_k^N a_k^2} = \frac{\sum_k^N P(\tau_k)\tau_k}{\sum_k^N P(\tau_k)}$ (6)

and $\overline{\tau^2} = \frac{\sum_k^N a_k^2 \tau_k^2}{\sum_k^N a_k^2} = \frac{\sum_k^N P(\tau_k)\tau_k^2}{\sum_k^N P(\tau_k)}$ (7)

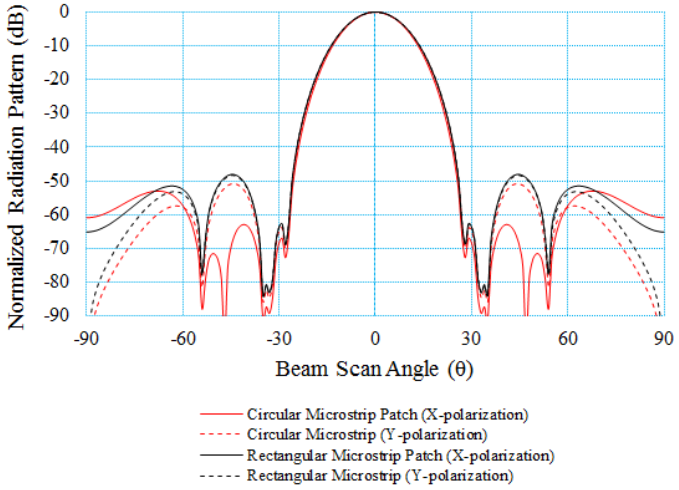


Fig. 9. Radiation patterns (E-θ plane) of FPBA ( $\beta = 0.68$ ) with different polarizations and patch shapes (element spacing 0. 31 cm).

In (6),(7), and (8):
N: Total multipath components;
$P(\tau_k)$: power of the k-th multipath component;
$\tau_k$: time of arrival of the k-th multipath component;

Delays are measured relative to the first detectable signal arriving at the receiver at $\tau_0 = 0$. Equations (6)-(8) do not rely on absolute power level of $P(\tau)$, but only on the relative amplitudes of multipath components with in $P(\tau)$. Delay spread is highly dependent on beamwidth of antenna radiation pattern [12]. About 6 ns RDS is found in a residential environment, though it can be reduced to 1 ns by using high gain antennas [10], [12].

The nature (Rayleigh or Rician) of a fading channel can be predicted from RDS and K-factor of the respective channel [9], [12]. Higher RDS with lower K-factor suggests that the channel is a Rayleigh channel; on the other hand lower RDS with higher K-factor suggests that the channel is a Rician channel [9], [12]. IEEE 802.11b Task Group has adopted an indoor channel model that follows an exponential power delay profile [12]. Fig.

10 and Fig. 11 show the simulation results of average channel power distributions and frequency response of an IEEE 802.11 channel model for two different values of RDS [12]. Maximum amplitude-variation in Fig. 11 is 25.38 dB (RDS= 42ns). Fig. 11 suggests that a channel can be considered as frequency-flat Rician channel when then RDS of the channel becomes 12.5 ns. On the other hand a channel can be considered as frequency-selective Rayleigh fading channel with RDS of 42 ns. These results agree well with those of [9]. Larger RDS corresponds to deep fade and vice versa. Deep fade of a channel can be minimized by implementing antenna system with narrower beamwidth (e.g. FPBA). It is noteworthy to mention here that FPBA can be implemented in any frequency range.

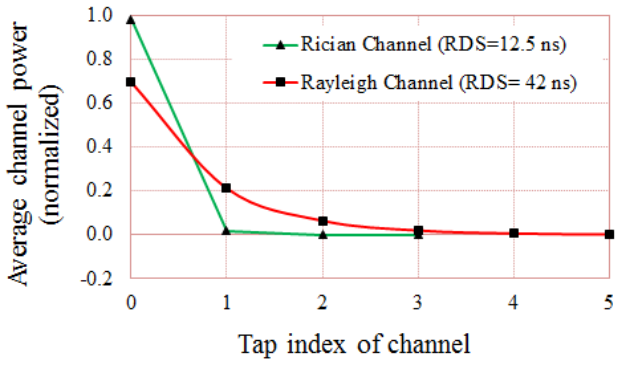


Fig. 10. Channel powers of IEEE 802.11 indoor channel model for two different values of RMS Delay Spread (RDS).

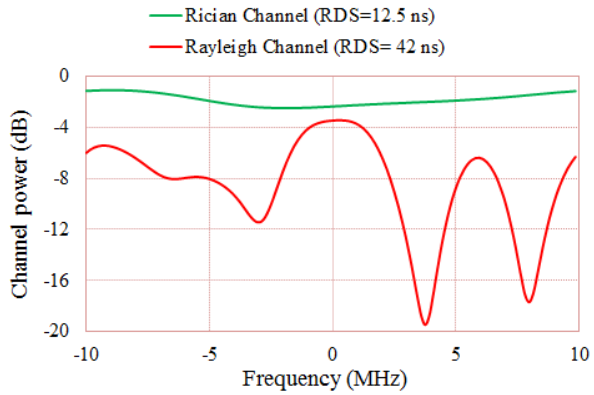


Fig. 11. Frequency spectra of IEEE 802.11 indoor channel model for two different values of RMS Delay Spread (RDS).

## V. Conclusions

Next generation State of the Art (SOA) wireless networks will require very high speed wireless communication channels with lower bit error rate (BER), lower RMS delay spread (RDS), and higher values of Rician-K factors. Lower RDS and higher K-factors of a wireless channel can be achieved if an antenna system with narrower beamwidth can be implemented. This paper compares the radiation patterns of array antenna considering Binomial Array, Dolph-Chebyshev Array, and novel Fractional Powered Binomial Array (FPBA) [15]. It is seen that FPBA outperforms Binomial Array and Dolph-Chebyshev array from the technical perspectives. FPBA can achieve better radiation pattern with lower side lobe level (SLL) and narrower beamwidth. Narrower beamwidth and lower SLL of FPBA can enhance received power and reduce RDS of a wireless channel. Since RDS is a function of beamwidth. Narrower beamwidth of FPBA is also helpful in mitigating deep fade of a multipath channel. Large number of antenna elements at higher frequencies (e.g. within mm-range) can be deployed with novel FPBA Beamforming for next generation wireless system.

## References


[1] Stefania Sesia *et.al*, 'LTE, The UMTS Long Term Evaluation: From Theory to Practice', *2nd Edition, John Wiley & Sons, Ltd., Publication*, UK, 2011.

[2] Zeeshan Hameed Mir and Fethi Filali, 'LTE and IEEE 802.11p for vehicular networking: a performance evaluation', *EURASIP Journal on Wireless Communications and Networking*, vol. 89, pp.1-15, 2014.

[3] Edward Kasem, Roman Marsalek, 'The Performance of LTE Advanced Uplink in Flat Rayleigh and Pedestrian Channels' *Electro revue*, vol. 4. No. 3. pp. 45-50, Dec. 2013.

[4] 'Channel Model for Fixed Wireless Applications: IEEE 802.16 Broadband Wireless Access Working Group' (http: ieee802.org.16).

[5] Larry J. Greenstein *et. al*, 'Ricean *K*-Factors in Narrow-Band Fixed Wireless Channels: Theory, Experiments, and Statistical Models', *IEEE Trans. Vehicular Tech.* (Digital Object Identifier, 2009 10.1109/TVT.2009.2018549).

[6] Janssen, G. J. M., P.A. Stigter, and R. Prasad, 'Wideband Indoor Channel Measurements and BER Analysis of Frequency Selective Multipath Channel at 2.4, 4.75 and 11.5 GHz', *IEEE Trans. on Communications*, vol. 44. No. 10, pp. 1272-1288, Oct. 1996.

[7] Bohdanowicz, A., G. J. M. Janssen, and S. Pietrzyk, 'Wideband Indoor and Outdoor Multipath Channel Measurements at 17 GHz', Proc. VTC'99- Fall (IEEE Vehicular Technology Conference), Amsterdam, 1999, pp. 1998-2003.

[8] Davies, R., *et. al*, 'Wireless Propagation Measurements in Indoor Multipath Environments at 1.7 GHz and 60 GHz for Small Cell Systems', Proc. 41st IEEE Veh. Techn. Conf., St. Louis, MS, 1991, pp. 589-593.

[9] R. Prasad, 'OFDM for Wireless Communications Systems' Artech House Inc. London, 2004.

[10] Peter F. M. Smulders, "Statistical Characterization of 60-GHz Indoor Radio Channels," *IEEE Trans. Antennas Propagat.*, vol. 59, pp. 2820–2829, Oct. 2009.

[11] T. Thomas, G. Charishma, K. Veeraswamy, 'MIMO Antenna System with High Gain and Low SAR for UE of 5G Operating at MM Wave: Design', 10th International Conference on Information, Communications and Signal Processing (ICICS), Singapore, 2015.

[12] A. K. M. Baki *et al.* 'Investigation of Rayleigh and Rician Fading Channels for State of the Art (SOA) LTE-OFDM Communication System', Proceedings of the 2017 4th International Conference on Advances in Electrical Engineering (ICAEE), 28-30 September, Dhaka, Bangladesh

[13] Stutzman, Warren L. and Thiele, Gary A. (1997), "Antenna Theory and Design", 2nd edition, John Wiley & Sons, Inc.

[14] Constantine A. Balanis, **"**Antenna Theory, Analysis and Design**"**, John Wiley & Sons, NY, 1997.

[15] A. K. M. Baki, 'Beamwidth Reduction of Binomial Array for 5G Communications', presented at the 5th IEEE Region 10 (Asia Pacific) Humanitarian Technology Conference (R10HTC), Dhaka, 2017.

[16] Goubau, G. and Schwering, F. (1961), "On the guided propagation of electromagnetic wave beams", *IRE Trans. AP* (pp. 248-256), AP-9.

[17] Brown, W. C. and Eugene, Eves E., "Beamed Microwave Power Transmission and its Application to Space", *IEEE Trans. Microwave Theory and Techniques*, vol. 40, no. 6. pp. 1239-1250, June 1992.

[18] T. S. Rapport, 'Wireless Communications: Principles and Practice' *2nd edition, Prentice Hall Communications and Emerging Technologies Series*, 2002.

# Effect of Radiation Patterns on WLAN Delay Spreads for 60 GHz Living Room Environments

A. K. M. Baki[1], Shaela Sharmin[2]
Dept. of Electrical and Electronic Engineering, Ahsanullah University of Science and Technology (AUST)
141 & 142 Love Road, Tejgaon I/A, Dhaka, Bangladesh
[1]Dr.AKM.Baki@ieee.org, [2]shaela.ritu@gmail.com

*Abstract*— **The Parameters, those can affect an indoor Wireless Local Area Network (WLAN) at 60 GHz, are multi-path reflections, polarization-effects, shadowing, interior of the room, main beam lobe, and side lobe level (SLL) of radiation patterns. RMS Delay Spread (RDS) of a channel can be reduced if SLL of antenna radiation pattern can be minimized. RDS is a measure of channel delay and fading characteristics. Minimum RDS can reduce channel deep-fade and multipath effects. This paper investigates the effect of different level of SLL on RDS characteristics considering two different living room environments. One of the approaches is IEEE 802.11ad living room channel model, and the other is Full-3D ray tracing simulation model of a residential apartment. The investigations show that reduced SLL of radiation pattern can effectively reduce the RDS.**

***Index Terms— antenna radiation patterns, channel models, multipath channels, millimeter wave propagation, line of sight propagation.***

## I. INTRODUCTION

Due to an increasingly higher rate of demand for high-speed wireless networks, the utilization of millimeter-wave frequency bands has been receiving more attention. Specially, 57–64 GHz frequency regions have been used for short-distance and indoor communications. 60 GHz wireless system is one promising candidate for short range communication systems [1], [2]. In a wireless communication system with multipath fading channels, arrival of different versions of transmitted signal at the receiver spreads in time. This phenomenon is called delay spread. Propagation at 60 GHz is quasi-optical in nature and most of the transmitted power is propagated between the transmitter and the receiver through LOS, 1st order and 2nd order reflections [3], [4].

Statistical channel model should be used to describe the properties of a channel when detailed knowledge of propagation channel is not available [3]. Some of the Parameters of statistical channel model are Power Delay Profile (PDP), RMS Delay Spread (RDS), and Rician-K factor. RDS is highly dependent on beamwidth [5], [6] and SLL of the antenna radiation pattern. Channel delay at 60 GHz also depends on multipath reflections [7], [8]. Reduced RDS is the indication of a faster communication channel. Deep fade of frequency selective fading channel as well as Inter Symbol Interference (ISI) can be minimized if delay spread is minimized. Some of the factors those affect the RDS of an indoor propagation channel are shown in Fig. 1.

Clustering approach is followed for channel modeling at 60 GHz. A cluster can be defined as a group of multi-path [9] or LOS components having similar delays and directions of departure/arrival. Angular characteristics of clusters are closely related to the geometry of the room and environment that makes it infeasible to model the delay and angular domains independently [9]. In a 60 GHz indoor channel environment it is insufficient to consider only walls, glass wind, floor and Tables. Finer structures such as ceiling lamps, chairs and bookshelves are also needed to be considered [9]. Diffraction at 60 GHz is an insignificant propagation due to sharp shadow zones [9], [10]. 3rd order reflections, diffused reflections, and diffraction can be neglected in case of a 60 GHz outdoor radio propagation channel [11].

Accurate modeling of intra-cluster distributions is very important for the performance evaluation of 60 GHz WLAN channels since the characteristic of beamformed-channel directly depends on the intra-cluster Parameters [8]. Intra-cluster ray identification in angular domain requires very high angular resolution that can be achieved by using highly directional beamforming antennas with very high gain. In case if the LOS path is absent the signal can be steered towards the best reflected path (or cluster). It is possible to reduce the channel delays by using highly directional antennas with minimum side lobe level (SLL). Highly directional antennas with narrower beamwidth (20° ~ 30°) at both Tx/Rx sites are suggested for 60 GHz WLAN systems to compensate the high propagation loss in this band [10].

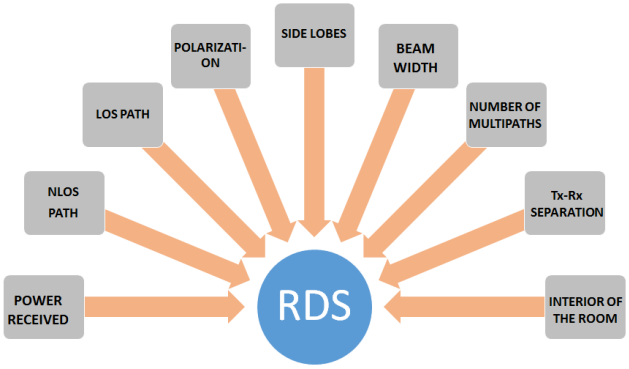


**Fig. 1**. Some of the factors those affect the RMS Delay Spread (RDS) of an indoor wireless propagation channel.

978-1-5386-3374-8/17/$31.00 ©2017 IEEE

Three different types of antenna models, which can be applied to the generated space-time channel realizations, are proposed in the channel model described in [12]. The antenna types are isotropic antenna, basic steerable directional antenna and phased array antennas. Antenna with constant side lobe levels [13], [14] is reported in [12] for the channel modeling. Average side lobe level (AvSLL) was calculated through averaging the side lobe power over the angle out of the main lobe [14]. The considered AvSLL for the IEEE 802.11ad indoor channel model was -11.54 dB [12]. It is possible to reduce this value of AvSLL further through an appropriate choice of array antenna system. It is mentioned in the previous paragraph that reduced SLL minimizes channel RDS. Radiation from antenna system should have negligible SLL and narrower main beam for a robust, power efficient, and faster wireless communication system. SLL and main beam of radiation pattern are functions of excitation coefficients of antenna elements. Width of the main lobe and SLL can be optimized by choosing appropriate excitation coefficients of antenna elements [15]. Non-uniform excitation coefficients of antenna elements can produce lower SLL. Dolph-Chebyshev power distribution [16], and Gaussian power distribution [17], [18] are two popular non-uniform power distribution systems of array antenna. Though Dolph-Chebyshev array has some limitations which will be discussed in subsequent sections.

This paper describes the effect of SLL on RDS in different indoor scenarios such as LOS/NLOS paths, Tx-Rx distances, and different half-power beam width (HPBW). The paper is organized in the following way. Section II describes IEEE 802.11ad channel model. Section III describes the effect of SLL on RDS for an IEEE 802.11ad living room model. Section III also describes that lower AvSLL can reduce the RDS. Section IV describes the effectiveness of reduced SLL for a living room propagation model at 60 GHz by using Wireless Insite Full-3D simulation software. Section V compares and discusses the results of section III and IV. Finally, section VI concludes the paper.

## II. IEEE 802.11ad WLAN CHANNEL MODEL

The IEEE 802.11ad standard describes the channel models for Wireless Local Area Networks (WLANs) which is based on the results of experimental and statistical data at 60 GHz [12]. The model generates a channel realization considering space, time, amplitude, phase, and polarization characteristics of all rays [12]. Spatial characteristics of the rays consider both azimuth and elevation angles for both Tx-Rx sides. The model evaluated three basic propagation model scenarios: conference room, cubicle and living room. Detailed of the modelling techniques can be found in [12]. The following sub-section describes the IEEE 802.11ad channel model for a living room scenario.

### *A. Channel Model in Living Room Environment*

The IEEE 802.11ad living room model considers the floor plan [19] scenario according to [20]. Fig. 2 shows the simplified model of the living room used in realizing the channel model [12], [20]. Following are some dimensions and furniture of the living room [19]:

i. Dimensions of the home living room: 7 m x 7 m x 3 m (L x W x H),
ii. A Table in the room,
iii. Two sofas,
iv. An armchair placed around the Table, and
v. One outer wall has two windows and a cabinet is placed between them.

All furniture dimensions are chosen according to [19]. In the simulation scenario the communication can be established between a set top box (STB) transmitting uncompressed video, and a TV receiving the transmitted video. The TV is placed in the middle of one of the walls. The position of the STB in the horizontal plane can be different. A '6m x 7m' rectangular sector of possible STB positions in the horizontal plane is also introduced in the model. The size of the sector is chosen considering all the sitting places around the Table [12]. The average distance between the STB and the TV is approximately 4m~6m for the simulation considered in this paper.

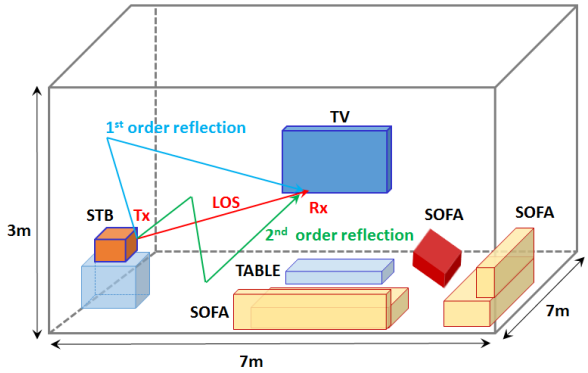


**Fig. 2.** 3D simplified model of the living room for IEEE 802.11ad channel model [adopted from ref. 12].

### *B. Intra-Cluster Parameters in Living Room Environment*

IEEE 802.11ad channel model [10], [12] generates impulse response of the channel that supports both with/without polarization characteristics. The model also considers beamforming performance. The impulse response of the model with polarization characteristics can be expressed as [10], [12]:

$$h\left(t,\varphi_{tx},\theta_{tx},\varphi_{rx},\theta_{rx}\right)= \sum_i \mathbf{H}^{(i)} C^{(i)}\left(t-T^{(i)},\varphi_{tx}-\Phi_{tx}^{(i)},\theta_{tx}-\Theta_{tx}^{(i)},\varphi_{rx}-\Phi_{rx}^{(i)},\theta_{rx}-\Theta_{rx}^{(i)}\right) \quad (1)$$

where,

$h$ : channel impulse response.

$t$, $\varphi_{tx}$, $\theta_{tx}$, $\varphi_{rx}$, $\theta_{rx}$ : time, azimuth and elevation angles respectively at the transmitter and receiver.

$\mathbf{H}^{(i)}$ : 2x2 cluster polarization matrices [Gain of the channel impulse response is merged in to $\mathbf{H}^{(i)}$]. Detailed discussions on $\mathbf{H}^{(i)}$ is outside of the scope of the paper.

$C^{(i)}$ : channel impulse response for $i^{\text{th}}$ cluster which can be expressed as [10], [12]:

$$C^{(i)}\left(t,\varphi_{tx},\theta_{tx},\varphi_{rx},\theta_{rx}\right)= \sum_k \alpha^{(i,k)}\delta\left(t-\tau^{(i,k)}\right)\delta\left(\varphi_{tx}-\varphi_{tx}^{(i,k)}\right)\delta\left(\theta_{tx}-\theta_{tx}^{(i,k)}\right)\delta\left(\varphi_{rx}-\varphi_{rx}^{(i,k)}\right)\delta\left(\theta_{rx}-\theta_{rx}^{(i,k)}\right) \quad (2)$$

$\delta(\,)$: Dirac delta function.

$T^{(i)}$, $\Phi_{tx}^{(i)}$, $\Theta_{tx}^{(i)}$, $\Phi_{rx}^{(i)}$, $\Theta_{rx}^{(i)}$ : time-angular coordinates of $i^{\text{th}}$ cluster.

$\alpha^{(i,k)}$ :amplitude of the $k^{th}$ ray of $i^{th}$ cluster.
$\tau^{(i,k)}$, $\varphi_{tx}^{(i,k)}$, $\theta_{tx}^{(i,k)}$, $\varphi_{rx}^{(i,k)}$, $\theta_{rx}^{(i,k)}$ : relative time-angular coordinates of the $k^{th}$ ray of $i^{th}$ cluster.

Fig. 3 shows the time-domain characteristic of the cluster [12]. The cluster consists of a central ray $\alpha^{(i,0)}$ with fixed amplitude and pre-cursor $\alpha^{(i,-N_f)} \ldots \alpha^{(i,-1)}$ and post-cursor rays $\alpha^{(i,1)} \ldots \alpha^{(i,N_b)}$. Table I summarizes the Parameters for the living room model [12]. The same Parameters were used in this paper for the investigation of SLL effect on RDS. Similar characteristic of cluster for a conference room channel model is described in [10].

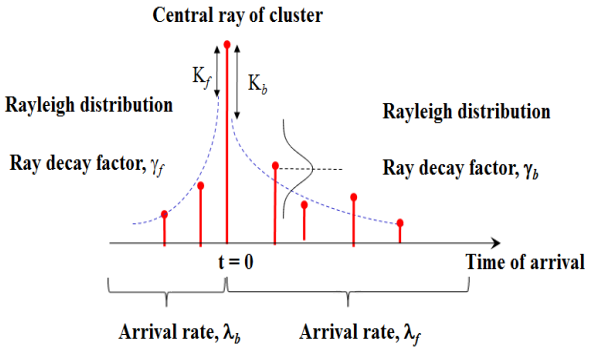


**Fig. 3.** Time domain characteristic of the cluster.

TABLE I INTRA CLUSTER TIME DOMAIN PARAMETERS FOR THE LIVING ROOM CHANNEL MODEL [12]

| Parameter | Notation | Value |
|---|---|---|
| *K*-factor for pre-cursor rays | $K_f$ | 11.5 dB |
| Power decay time for pre-cursor rays | $\gamma_f$ | 1.25 ns |
| Arrival rate of pre-cursor rays | $\lambda_f$ | 0.28 $ns^{-1}$ |
| Amplitude distribution of pre-cursor rays | | Rayleigh |
| Number of pre-cursor rays | $N_f$ | 6 |
| *K*-factor for post-cursor rays | $K_b$ | 10.9 dB |
| Power decay time for post-cursor rays | $\gamma_b$ | 8.7 ns |
| Arrival rate of post-cursor rays | $\lambda_b$ | 1.0 $ns^{-1}$ |
| Amplitude distribution of post-cursor rays | | Rayleigh |
| Number of post-cursor rays | $N_b$ | 8 |

## III. EFFECT OF SLL ON RDS FOR IEEE 802.11ad LIVING ROOM CHANNEL MODEL

It was mentioned in section I that reduced RDS, which is highly dependent on beamwidth and SLL of antenna radiation pattern, is the indication of a faster communication channel. The effect of beam width on RDS can be found in some literatures [8], [10]. But the effect of AvSLL on RDS is hardly found in the literatures. In this section the effect of AvSLL on RDS is investigated for the described living room channel model. Probability of arrival (used in the simulations) of different type of ray at the receiver is shown in Table II. The same probability was used for different AvSLL within the range of -51.54 dB ~ -11.54 dB. Though the probability is variable in real scenario and in most cases these probabilities may decrease with the decrement of AvSLL. The reason of considering the AvSLL within the range of -51.54 dB ~ -11.54 dB is discussed briefly hereafter.

A novel and technically better method of array-elements' excitation by using novel concept of Fractional-Powered Binomial coefficients is proposed by the first author in [21]-[22]. The new method is named as Fractional Powered Binomial Array (FPBA) [21]-[22]. FPBA shows better performance than Binomial or Dolph-Chebyshev array from the perspective of beamwidth-SLL trade off [21]-[22]. Fig. 4 shows the radiation pattern of 25-element FPBA along with that of 20 dB Dolph-Chebyshev array. Fig. 4 also shows the main lobes and AvSLL for the respective array distributions. Element spacing was chosen as $0.6\lambda$ for both the distributions. Fig. 4 shows that AvSLL of FPBA is 20 dB lower than that of 20 dB Dolph-Chebyshev array. Estimation process of AvSLL is described in [14]. Detailed discussions of FPBA is outside the scope of this paper.

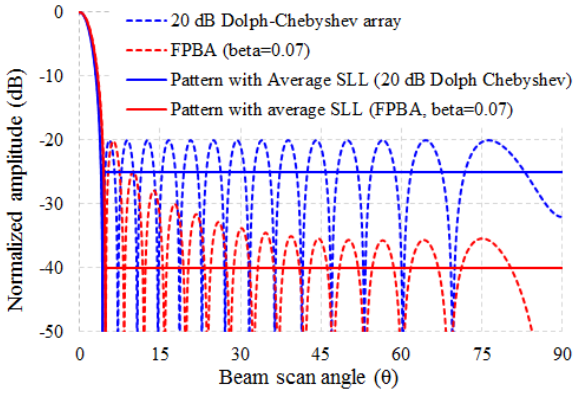


**Fig. 4.** Radiation patterns of 20 dB Dolph-Chebyshev array and FPBA (β=0.07) showing Average SLL (AvSLL) of radiation patterns for the respective array distributions.

Fig. 5 shows RDS vs. AvSLL graphs for different LOS/NLOS scenario, HPBW, and Tx-Rx separation. Fig. 5 shows that RDS decreases with the decrease in AvSLL. Variation of RDS due to variation of HPBW is less. In some cases reduced-HPBW should reduce the RDS, though there might be exception. Since change of SLL and HPBW also influences some other factors such as multipath effects, polarization effects, and ray paths. Polarization mismatches reduce the received power and increases the RDS. Left Hand Circular Polarization (LHCP) was used for Tx/Rx antennas of all the scenarios of Fig. 5. In the simulation it was found that LHCP-LHCP combination generates the lowest RDS.

TABLE II PROBABILITY OF ARRIVAL OF DIFFERENT TYPE OF RAY FOR THE LIVING ROOM SIMULATION MODEL

| Type of Ray | Probability of Arrival at the Receiver |
|---|---|
| 1st order reflections from ceiling | 0.3 |
| 1st order reflections from floor | 0.3 |
| 1st order reflections from walls | 0.5 |
| 2nd order reflections from two walls | 0.2 |
| 2nd order reflections from ceiling and floor | 0.2 |
| 2nd order reflections from wall-ceiling and ceiling-wall | 0.2 |
| 2nd order reflections from wall-floor and floor-wall | 0.2 |

Results of Fig. 5 show that the decrease in RDS is about 4.5 pico-second per dB decrement of AvSLL. Therefore even a one dB change in SLL influences the channel characteristics.

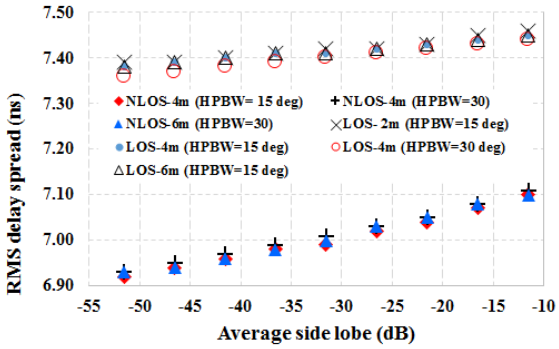


**Fig. 5.** RMS Delay Spread (RDS) for different values of average side lobe level (AvSLL) and for the NLOS/LOS scenarios.

Fig. 5 shows that the values of RDS are higher in LOS scenarios than those of NLOS scenarios. Average RDS for NLOS scenarios was about 7 ns and that for LOS scenarios was about 7.4 ns. Main reason of this higher RDS is the dissimilar Tx/Rx antenna heights in LOS cases. In LOS scenario Tx-antenna height was 1.5 meter and Rx-antenna height was 1.0 meter. In NLOS scenario Tx/Rx antenna height was 1.0 meter. It is noteworthy to mention here that the values of RDS in LOS and NLOS scenarios are not precisely comparable, mainly due to difference in multipath effects and overall received power. Variation of RDS, shown in Fig. 5, due to variation of Tx-Rx separation is also insignificant in the considered living room. These results agree well with the results of [8].

## IV. Full-3D Simulation Model For a Residential Environment Using Wireless Insite

Ray tracing propagation model in a residential indoor apartment (shown in Fig. 6) was also investigated by using Wireless InSite software that supports Full-3D simulations.

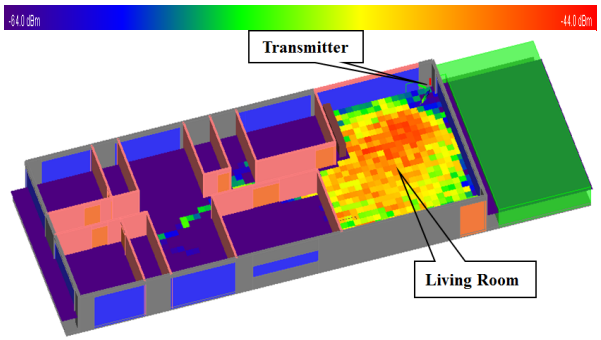


**Fig.6.** Indoor residential environment with one transmitting antenna array (8 nos. of circular patch elements) and 32×13 receivers-grid. The figure also shows the received power on an XY receivers-grid of the indoor residential apartment.

In this case, size of the apartment was 33m ×13m ×3m (L x W x H) and size of the living room was 10m ×13m ×3m (L x W x H). Full-3D simulation model of Wireless Insite has some attractive features. The software considers all antenna types, all antenna heights, all environments, building of any shapes, frequency upto 100 GHz, geometric ray of diffraction (GFD), ray tracing method, reflection, transmission, and diffraction of electric fields. Total number of receivers for the whole apartment was (32×13). In this paper only the propagation model of living room is discussed. Total number of receivers in the living room was (9×13). At the transmitting side 8-element circular patch array with LHCP was considered. Other antenna Parameters used in the simulations are shown in Table III. In this section two different amplitude-distributions of transmitting antenna elements were considered. One type of distribution is the mentioned FPBA and the other type is Uniform Array (UA). Each receiving antenna was a single element isotropic antenna. Isotropic receiver was considered only for the investigation purpose of total received power from all directions. Table IV summarizes different statistical Parameters of RDS found in the living room simulations. Average RDS for UA was 10.40 ns and that for FPBA was 9.87 ns. Standard deviation of RDS for UA was 9.15 ns and that for FPBA was 8.51 ns. Parameters of Table IV show that FPBA is better than UA from the perspective of RDS. SLL of 8-element FPBA was much lower than that of UA (not shown in the paper). Performance of FPBA over Dolph-Chebyshev array has been discussed in section III. Fig. 7 shows the excess delay of a receiver location in the living room. Tx-Rx distance was 15 m in this case. Fig. 7 shows that the excess delay follows the exponential decay curve. Arrival times of some clusters (LOS-NLOS) are also shown in the figure. In the figure the LOS ray is considered as Cluster-1.

**Table III** Different Parameters of Tx/Rx antennas used in the indoor living room channel model for Full-3D simulations of Wireless Insite.

| **Parameters of antenna systems** | |
|---|---|
| ***Parameters of transmitting antenna array*** | |
| Types of amplitude distribution | FPBA |
| Number of elements | 8 |
| Dielectric constant | 3.9 |
| Radius of circular patch | 0.0025 m |
| Height | 0.001 m |
| Inter-element spacing | 0.0035 m |
| Polarization | LHCP |
| Input power | 20 dBm |
| Tx antenna height | 1.5 m |
| HPBW | 14.5 degree |
| Maximum SLL | -54 dB (normalized) |
| ***Parameters of receiving antenna*** | |
| Rx antenna height | 1 m |
| Rx antenna type | Single element (isotropic) |
| Total number of receivers | 9 ×13 |

**Table IV** Summary of RMS delay spreads within the living room for the new FPBA and UA.

| **Delay Spread** | **UA (nS)** | **FPBA (nS)** |
|---|---|---|
| Maximum RDS | 44.70 | 41.73 |
| Average RDS | 10.40 | 9.87 |
| Standard Deviation of RDS | 9.15 | 8.51 |

## V. Comparison of RDS of Section III and Section IV

In section III RDS Parameters were calculated considering different average SLL. On the other hand in section IV realistic side lobe levels (SLL) of radiation patterns were considered. Properties of building materials (conductivities, permittivities and thicknesses of brick, concrete, glass, wood etc.) were also considered in section IV. Average RDS found in section III was about 7 ns~ 7.4 ns. On the other hand in section IV, the lowest average RDS was 9.87 ns. The difference in RDS of the two sections was mainly due to the difference in room dimensions and multipath environments. In section IV, beam forming was considered only at the transmitter side. In case of simulations described in section IV, RDS can be reduced further through

beam forming at the receiver sites. It was reported in [3] that the measured RDS at 60 GHz indoor rooms falls within the range of 10.89 ns ~ 41.01 ns. RDS values at 60 GHz within the range of 15 ns~45 ns for small rooms and within the range of 30 ns ~70 ns for large indoor environment was reported in [11]. About 6 ns RDS was found in a residential environment [8]. It was also reported in [8] that the value of RDS can be reduced to 1 ns by using high gain antennas. RDS values found in sections III and IV agree well with the results found in [3], [8], and [11]. Results of section III and IV also confirm that lower SLL can minimize RDS.

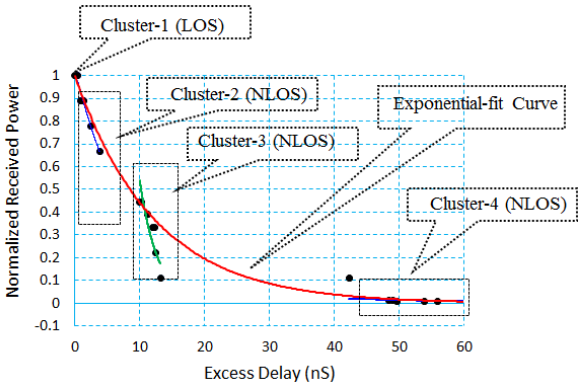


**Fig. 7.** Power Delay Profile (PDP) of a receiver in the living room of Fig.10. Tx-Rx distance was 15 meter for this scenario.

## VI. CONCLUSIONS

This paper presents the delay characteristics of a 60 GHz wireless indoor channel model. Lower RMS Delay Spread (RDS) of a multipath channel increases the bit rate and decreases the bit error rate (BER). RDS depends on many factors, one of them is the side lobe level (SLL) of radiation pattern. It was found that RDS of a multipath channel can be reduced if SLL or average SLL (AvSLL) of antenna radiation pattern can be reduced. The effects of reduced SLL on RDS were investigated through the simulations of IEEE 802.11ad channel model and the Wireless Insite Full-3D ray tracing simulation software. Simulation results discussed in this paper confirmed that lower level of AvSLL can reduce the RDS of a 60 GHz wireless indoor fading channel.

**Acknowledgments**

The authors acknowledge the support of REMCON Inc. for providing Wireless InSite software and the valuable comments from the anonymous reviewers those helped in improving the paper.

## REFERENCES

[1] P. F. M. Smulders, "60 GHz radio: prospects and future directions," *in Proceedings of the IEEE Symposium Benelux Chapter on Communications and Vehicular Technology*, pp. 1–8, Eindhoven, The Netherlands, 2003.

[2] M. Nedil *et al.* "Design of new mm-Wave Antenna fed by CPW Inductively Coupling fo mining communication," *IEEE Antenna and Propagation Society*, pp. 1–4, 2009.

[3] H. Xu, V. Kukshya, and T. S. Rappaport, 'Spatial and Temporal Characteristics of 60-GHz Indoor Channels', *IEEE Trans. Selected Areas Comm.* vol. 20, pp. 620–630, April 2002.

[4] A. Maltsev *et al.* 'Impact of Polarization Characteristics on 60-GHz Indoor Radio Communication Systems', *IEEE Antennas Wireless Propag. Lett.,* vol. 9, pp. 413-416, 2010.

[5] 'Channel Model for Fixed Wireless Applications: IEEE 802.16 Broadband Wireless Access Working Group' (http: ieee802.org.16).

[6] Larry J. Greenstein *et. al*, 'Ricean *K*-Factors in Narrow-Band Fixed Wireless Channels: Theory, Experiments, and Statistical Models', *IEEE Trans. Vehicular Tech.* (Digital Object Identifier, 2009 10.1109/TVT.2009.2018549).

[7] F. Yıldırım, Ali S. Sadri, and H. Liu, 'Polarization Effects for Indoor Wireless Communications at 60 GHz', *IEEE Commun. Lett.*, vol. 12, pp. 660–662, Sept. 2008.

[8] Peter F. M. Smulders, "Statistical Characterization of 60-GHz Indoor Radio Channels," *IEEE Trans. Antennas Propagat.*, vol. 59, pp. 2820–2829, Oct. 2009.

[9] Gustafson C. *et al.* "On mm-Wave Multi-path Clustering and Channel Modeling," *IEEE Trans. Antennas Propagat.*, vol. 62, pp. 1445–1455, Jan. 2014.

[10] A. Maltsev *et al.* 'Statistical Channel Model for 60 GHz WLAN Systems in Conference Room Environment', *Radio Engineering,* vol. 20, pp. 409-422, June 2011.

[11] Smulders, P. F. M., & Correia, L. M.,' Characterisation of propagation in 60 GHz radio channels', *Electronics and Communication Engineering Journal*, 9(2), pp. 73-80, April 1997.

[12] MALTSEV, A., *et al*. Channel models for 60 GHz WLAN systems. *IEEE Document* 802.11-09/0334r8, May 2010.

[13] Spatial channel model text description, SCM text v.7.0, Spatial channel model AHG (combined ad-hoc from 3GPP&3GPPs), Aug. 19, 2003.

[14] IEEE doc. 802.15-06/474r0, Reference antenna model with side lobe for TG3c evaluation, I. Toyoda *et al*, Nov. 2006.

[15] Stutzman, Warren L. and Thiele, Gary A. (1997), "Antenna Theory and Design", 2nd edition, John Wiley & Sons, Inc.

[16] Constantine A. Balanis, **"**Antenna Theory, Analysis and Design**"**, John Wiley & Sons, NY, 1997.

[17] Goubau, G. and Schwering, F. (1961), "On the guided propagation of electromagnetic wave beams", *IRE Trans. AP*, pp. 248-256, AP-9.

[18] Brown, W. C. and Eugene, Eves E., "Beamed Microwave Power Transmission and its Application to Space", *IEEE Trans. Microwave Theory and Techniques*, vol. 40, no. 6. pp. 1239-1250, June 1992.

[19] IEEE doc. 802.11-09/0499r1. Simulation scenario floor plans, E. Perahia, R. Maslennikov, May 9, 2009.

[20] IEEE doc. 802.11-10/0296r14. TGad evaluation methodology, E. Perahia, Jan. 20, 2010.

[21] A. K. M. Baki, 'Beamwidth Reduction of Binomial Array for 5G Communications', presented at the 5th IEEE Region 10 (Asia Pacific) Humanitarian Technology Conference (R10HTC), Dhaka, 2017.

[22] A. K. M. Baki, 'Minimization of Fading Effect through Novel Method of Beamforming for NGN Wireless Systems', Proceedings of The 2nd IEEE International Conference on Telecommunications and Photonics (ICTP) 2017, Dhaka, 2017.

2017 IEEE International Conference on Telecommunications and Photonics (ICTP)
26-28 December, 2017, Dhaka, Bangladesh


# A Novel Technique for Underwater Object Detection Using 3D EM Sensor Network

Sarah Tanzina[1], Sultan Hassan Mahmud[2] and Md. Farhad Hossain[3]
Department of Electrical and Electronic Engineering
Bangladesh University of Engineering and Technology (BUET), Dhaka-1205, Bangladesh
[1]sarah30h@gmail.com, [2]satej.sultan@gmail.com, [3]mfarhadhossain@eee.buet.ac.bd

***Abstract*—Localization of objects in underwater environment using electromagnetic (EM) wave based underwater wireless sensor networks (UWSNs) provides the opportunity of faster object detection in comparison with acoustic wave based networks. For this purpose, we propose a novel technique using the law of reflection and spheres with different radii in three dimensional (3D) space. The overall system comprises of a source (transmitter), sensors in a sensor field, cluster heads and an onshore base station (BS). The system is divided in various zones with each zone having a number of spheres. If the object is in the propagation path of the transmitted EM wave, signal gets reflected and is received by one or multiple sensors. Information of location of these sensors is subsequently transferred to the onshore BS which then calculates the location of the object using the proposed algorithm. To assess the performance of the proposed system in a seawater environment, substantial simulations are carried out.**

***Index Terms*—localization; underwater environment; EM wave communication; UWSN.**

## I. Introduction

Underwater sensor networks (UWSNs), utilized in underwater wireless communications is a widely used practical strategy for coastal surveillance, environmental research, oceanography and control of autonomous underwater vehicle (AUV), submarine and surface vessel [1]. In most cases UWSNs use acoustic as transmission medium due to relatively longer transmission capability compared with EM wave. However, slow propagation speed, very slow data rate, severe attenuation at the water-air boundary etc have raised serious concerns over the feasibility of underwater acoustic networks [2], [3]. In case of EM wave, though it suffers from having shorter transmission range due to severe attenuation, underwater EM wave communications provide some advantages, like higher bandwidth, faster data rates, lower propagation delays and robustness to channel [1]. Also, in case of optical wave, although higher data rates are achievable from optical wave transmission, it requires clear water with line-of-sight (LOS) propagation [3]. The overall advantages facilitate the use of EM wave over acoustic medium and optical wave in the underwater surroundings. Underwater object detection is really significant as it helps to detect enemy war submarines and if such one is detected, necessary measures can be taken by the concerned authority.

For detection of objects in underwater, most of the works that have been accomplished, are done in two dimensional (2D) space. In [4], the writers proposed a propagation model and evaluated it by maximum likelihood (ML) estimation and Cramer-Rao bound (CRB) method. Furthermore, the writers in [5] introduced 2D distributed particle filter based object locating and tracking strategies using clustered USWNs. But works related to this topic in 3D are being carried out recently. In [6], a 3D underwater acoustic sensor network (UW-ASN) is implemented which works in two phases, namely passive listening and active listening. The arrival time of the echo coming from an object is utilized to measure the distance from object to sensor. Trilateration is then used to determine the location of the object. Most prominently, in [7], [8], 3D cluster based cubic sensor architectures are proposed and implemented. When an intruder comes in the presence of the sensor network, the sensors in the cube sense the arrival of the intruder and the locations of these sensors are transmitted to the CH in the cube. Then this data from the CH is transferred to the upper cube's CH and subsequently to an onshore BS. The BS then calculates the location of the intruder. In [9], underwater target tracking technique is explored in EM-acoustic combination.

In this paper, the purpose is to explore a different technique to detect an underwater object in 3D space using EM wave with the help of law of reflection and drawing spheres. The model comprises of a signal source or a transmitter, a 3D sensor field, CHs and a BS. If there is an object on the transmission signal line, the signal from the source gets reflected from the surface of the object and received by the sensors which in turn transfer the location of the sensors to the BS. From the data collected in the BS, the location of the surface point is calculated. We have proposed an algorithm that eliminates the sensors according to the power they receive. If the sensor power is less than a certain threshold, the particular sensor is excluded from the next step of calculation. The number of effective sensors is dependent on the number of the spheres. Meticulous simulations are done to evaluate the overall system performance by varying different parameters of the setup.

The rest of the paper is organized as follows: general outline of the system model in Section II with object detection technique in section III. Simulation results are discussed and analyzed in section IV followed by the summary of findings in section V.

978-1-5386-3374-8/17/$31.00 ©2017 IEEE

## II. System Model

### A. Proposed Architecture

This section of the paper discusses the overall network model of the system and how the components of the network are distributed. The system comprises of a source that transmits an EM wave by varying the angle of incidence on the surface of the underwater object. If the signal is incident on the surface, then the signal gets reflected from a particular point of the surface of the object. Our objective is to determine this surface point. For this, a 3D sensor field is proposed throughout the whole region of observation with each small block of SNs having it's own CH for data transmission. The SNs are distributed in equal distance in a cubic pattern. When a SN receives the reflected signal, the power received at the sensor ($P_s$) is calculated and if the power is greater than a certain threshold ($P_{th}$), then the SN is assumed to be fully active. The SNs whose received power is less than the threshold, are excluded from the next steps. The active SNs transfer the data to CH and from then the data is transferred to BS and the overall location estimation calculation is done there. Fig. 1 shows the basic view of the network model of the system.

In the figure, there are only a few small blocks of the cubic sensor field is shown for understanding. In practical situation, the sensor field will be distributed throughout the whole region. The sensor field and source are assumed to be framed in a corrosion free steel cage, which is firmly tied with the ground level. This system works by following the law of reflection, i.e, angle of incidence, $\theta_i$ = angle of reflection, $\theta_r$. The distance from source to object and sensor is assumed to be in short range due to EM communication. The overall detection technique is discussed in the section III in details.

### B. Link Model

Propagation path loss $P_L$ (dB) of EM wave in underwater environment can be given by [10]

$$P_L = L_{\alpha,\epsilon} \qquad (1)$$

where $L_{\alpha,\epsilon}$ is the attenuation loss in water due to water conductivity and complex permeability in dB. The path loss is

$$20 \times 2\pi \times (log_{10}e) \times \sqrt{(\sigma \times f \times 10^{-7})} \qquad (2)$$

which is in dB/m, $f$ is the transmission frequency in Hz and $\sigma$ is the conductivity of the water in S/m.

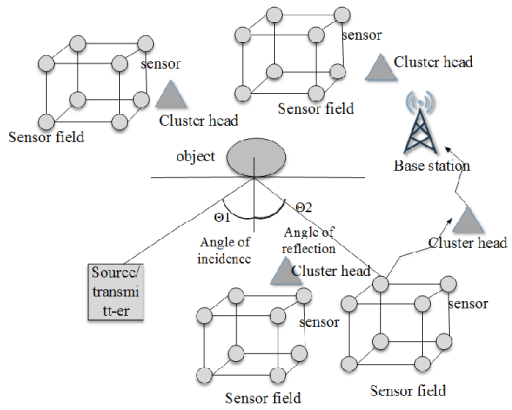


Fig. 1. A 2D overview of the network model.

### C. Performance Metric

For evaluating the performance of the proposed detection technique which will be discussed in section III, performance metrics are defined below, which is used to calculate the error in location estimation in perspective of distance.

If *(x,y,z)* is the true position of the source, then the absolute distance *r* between the true source location and approximated target location is assumed as a measure of error and *r* is given by

$$r = \sqrt{(x_{est} - x)^2 + (y_{est} - y)^2 + (z_{est} - z)^2} \qquad (3)$$

where $(x_{est}, y_{est}, z_{est})$ is the estimated target point on the object. Then, the absolute percentage of error is denoted as $e_p$ and determined by

$$e_p = |\frac{r_{est} - r_{act}}{r_{act}}| \times 100\% \qquad (4)$$

where $r_{act}$ is the actual distance from the source to the point on the surface of the object and $r_{est}$ is the estimated distance from the source to the object point.

## III. Proposed Object Detection Technique

The detection scheme proposed here involves drawing spheres with different radii around the approximated location of the object. The radius of each sphere is determined from the minimum threshold power $P_{th}$ required for a sensor to be in active mode and the distance of the propagating wave.

### A. Selection of Range for Object Detection

At first, an EM signal is transmitted from the source in a particular angle in reference with *x* axis of the *xy* plane. We assume a directional antenna with low beamwidth. As the highest power will be transmitted through the center of the main lobe, a line is assumed in this direction through the center. This transmission signal line is represented by AB as shown in Fig. 2.

Next, the highest possible distance point C is selected as the initial estimated position of the object on the AB line on the basis of the furthest CH whose coverage area intersects with the AB line. This point is selected such that the reflected wave traveling back is detected by one SN at or above threshold power. If the point is estimated very far, then the signal will not propagate back to be detected by any SN. The distance from A to C is the range for the object detection technique.

### B. Zones and Points

The range for object detection is then divided into *n* number of zones. *k* equidistant points are then selected for each zone, where the first point is the rightmost point of the corresponding zone as shown in Fig. 3. Therefore, *P = nk* is the total number of points.

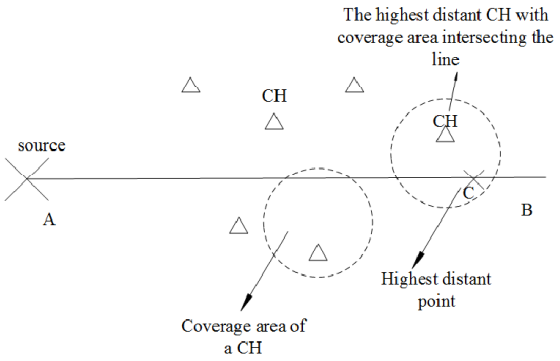


Fig. 2. A 2D view of transmission signal line and the highest possible range on it.

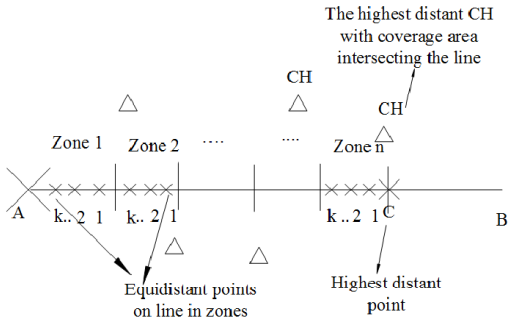


Fig. 3. Range of detection is divided in various zones.

### C. Spheres

Next, spheres are drawn for each zone for detection purpose. The rightmost point of each zone is selected as the first point for drawing spheres. To determine the radius of a sphere for a zone, the power received from the source at this point is calculated via path loss model. If there were an object at this point on the way of transmitted signal, the signal would have got reflected and a far positioned SN would have received the signal at power equal to threshold power. The distance from the rightmost point and this SN is calculated. A sphere is then drawn by taking this distance as it's radius and the rightmost point as it's center. The spheres along the transmission signal line (one sphere for each zone) are shown in Fig. 4.

Each zone can have a single sphere or multiple spheres depending on how many points per zone are being used in calculation. For drawing the next sphere, next point in the same zone closer to the source on line AB is selected.

### D. Algorithm

The source transmits the signal in a particular direction. If there is no reflected signal, the algorithm decides that the object does not lie on the signal line. Then the source will change the direction of signal transmission. If some part of an object lies on the propagation line AB, the signal gets

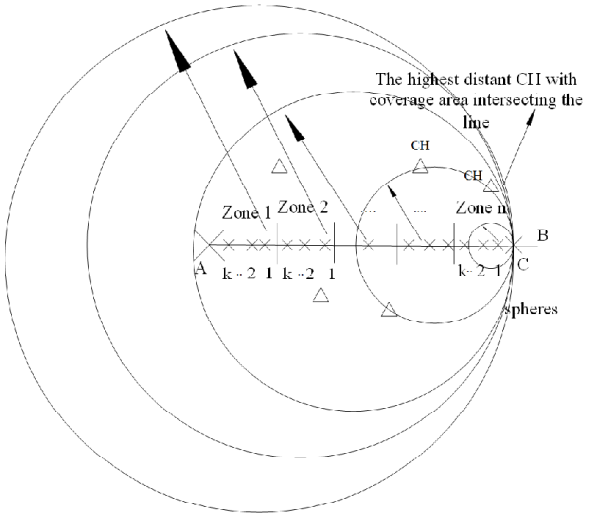


Fig. 4. Spheres along the line of transmission signal, one sphere for each zone.

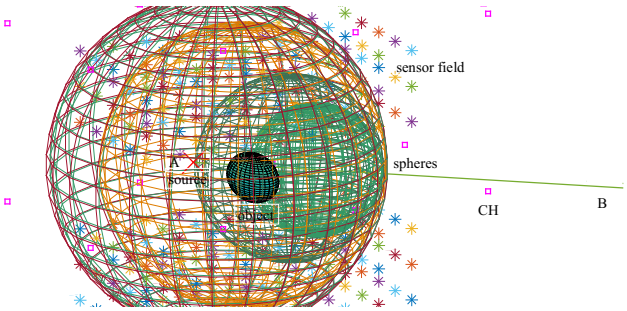


Fig. 5. Spheres along the signal propagation line.

reflected and the necessary information is transferred to the BS. Then the algorithm determines the range, divides the range into zones and points and draws spheres as discussed in section III.A-C. For demonstration, diagram for four zones and a sphere per zone is shown in Fig. 5.

The SNs inside these spheres which receive the reflected signal at threshold power or more, are differentiated from the other SNs by encircling them as shown in Fig. 6.

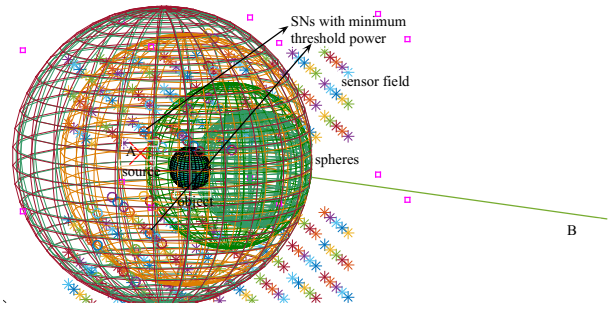


Fig. 6. Sensors with minimum threshold power are distinguished from other SNs.

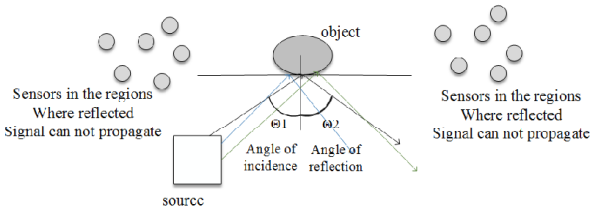


Fig. 7. Regions where reflected signal can not propagate.

According to law of reflection, reflected signal can not propagate in some regions as shown in Fig. 7. The SNs in these regions are excluded from the encircled ones for the next step.

A line CD is fitted through these remaining encircled SNs. If this line intersects the transmission signal line, then the intersection point is the desired surface point of the underwater object as shown in Fig. 8.

If CD line does not intersect the AB line, then the combination of SNs with at least minimum power or more are changed in a way that this line intersects AB. For example, if this line is far right from AB, then some SNs from the encircled ones are excluded from upper right side and lower right side of CD and new SNs are included to it's upper left side and lower left side for a new line fitting. In Fig. 9, a 2D representation of the reflected wave CD shifting through SN exclusion and inclusion is shown. A 2D view is shown instead of 3D view due to the convenience of presenting the system before and after SN inclusion and exclusion. When this line CD intersects with the transmitted signal line AB, the algorithm stops shifting the SNs and decides the intersection point as the object location.

## IV. Result and Analysis

### A. Simulation Setup

Substantial MATLAB based simulations are carried out for evaluating the performance of the proposed object detection technique. The results presented here are found by averaging the result for more than 1000 individual and independent locations of the object. SN-SN distance in a small cubic sensor block is assumed as 5 m and the dimension of the network coverage region is $60 \times 60 \times 100$ m$^3$. Usually for fresh water,

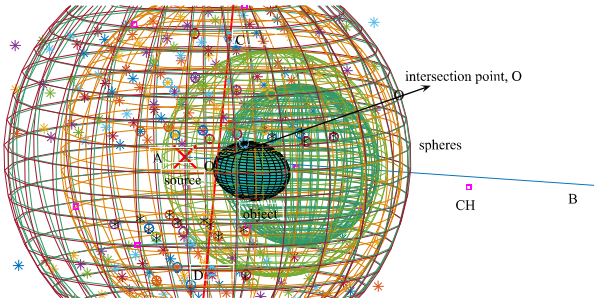


Fig. 8. Intersection point of incident signal and reflected signal.

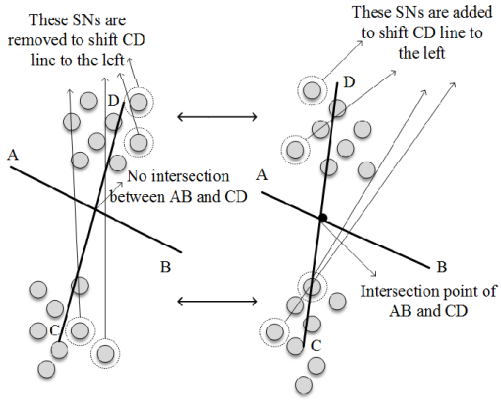


Fig. 9. Shifting of the reflected signal to intersect the transmission signal.

the value of $\sigma$ is 0.01 S/m. But as we have considered saline water, $\sigma$ = 4 S/m is taken [11]. Frequency, transmission power and detection threshold power values are taken as $f$ = 5 kHz, $P_{tX}$ = 3 W, $P_{th}$ = -70 dBm respectively.

### B. Result Analysis

When CDF of error is plotted for 1000 different positions of the object, it is observed how the CDF for each zone differs with one another. For demonstration, CDF of error for $n$ = 2, 3 and 4 with $k$ = 2 is shown in Fig. 10. For $n$ = 2, $e_p$ starts from 0.36, whereas for $n$ = 3 and 4, $e_p$ starts from 0.86 and 1.31 respectively. This plot shows that for $n$ = 2, CDF curve is the least steep and for $n$ = 4, CDF curve is the steepest. This implies that for $n$ = 4, the variance in error is the smallest and a small variance indicates that the errors tend to be very close to the mean, and to each other. This is in line with the proposed method as with the increase in number of zones, SNs with minimum $P_{th}$ for line fitting increase and the errors get close to one another for different positions of the object.

Fig. 11 illustrates the impact of number of spheres per zone on $e_p$. In this figure, $e_p$ between actual distance and estimated distance from source to object is plotted against number of spheres per zone. This graph shows that in case of two zones ($n$ = 2), when number of spheres per zone is

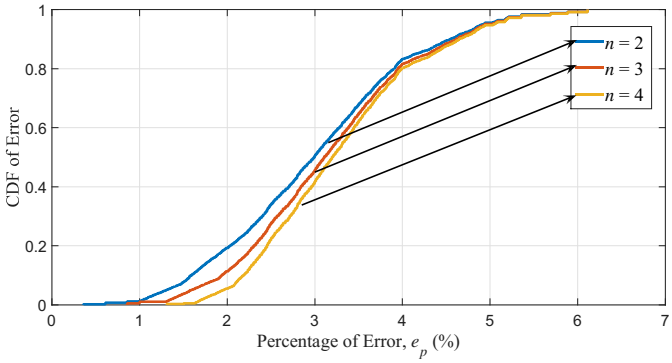


Fig. 10. CDF of percentage of error for different zones for two spheres.

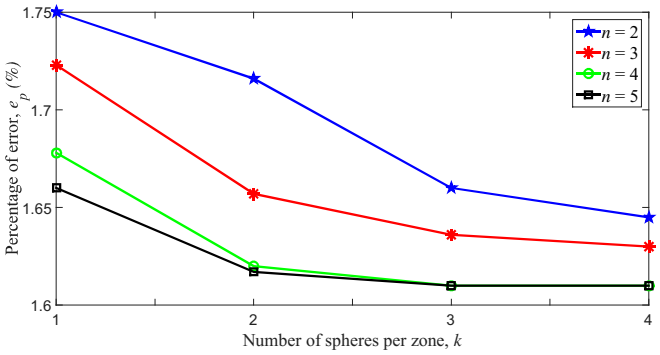


Fig. 11. Error curve for spheres per zone.

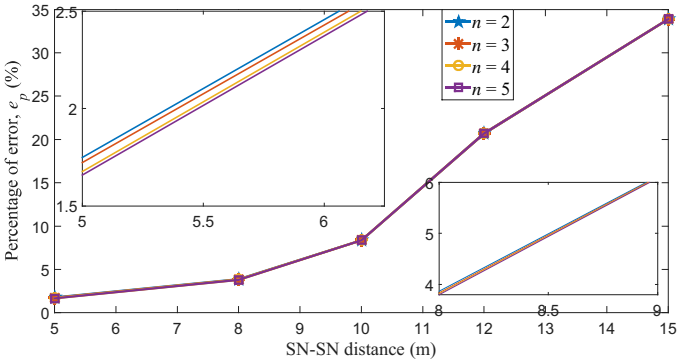


Fig. 12. Impact of SN-SN distance on percentage of error.

equal to 1, $e_p$ starts from 1.75. As the number of spheres per zone increases, $e_p$ decreases. This happens because with the increase in number of spheres per zone, the number of SNs that receive the reflected signal at $P_{th}$ or more also increases. Consequently, as the number of SNs with minimum threshold power increases, the line fitting becomes more accurate. Therefore, the determination of intersection point of AB and CD becomes a more accurate estimation of the object location. As a result, $e_p$ decreases. It is also observed that as $n$ increases, $e_p$ values for all the zone combinations decrease. This also reflects the notion that with the increase of zones, number of SNs with minimum threshold power increases. As a result, starting $e_p$ values decrease. For $n$ = 3, 4 and 5, the similar decreasing pattern of $e_p$ with the increment in the number of spheres per zone is observed. This plot also reflects that $e_p$ becomes constant with the increase of number of zones and spheres after a certain value.

Finally, Fig. 12 demonstrates the impact of SN-SN distance on the $e_p$ for $n$ = 2, 3, 4 and 5 with $k$ = 1. For $n$ = 2, $e_p$ starts from 1.75 as can be seen from the top left inset. We can observe that with the increase in SN-SN distance, $e_p$ increases as the number of SNs decreases. As a result, there are less SNs for line fitting and determination of the intersection point of the transmitted signal and fitted line becomes more erroneous. For $n$ = 3, 4 and 5, $e_p$ starts from 1.72, 1.68 and 1.66 respectively, which implies that with the increment in number of zones, object location algorithm has higher accuracy. Furthermore, the similar increasing pattern of $e_p$ with the increment in SN-SN distance is observed.

## V. Conclusion

In this paper, a novel technique for object detection, specifically a point on the surface of the object in underwater environment is proposed using EM wave. The proposed method involves determining a range for object detection, then dividing the range into a number of zones and points and finally drawing spheres with the points as the centers of the spheres. This method is assessed through percentage of error estimation between actual and estimated distances from source to object. The number of spheres and zones have substantial impact on the result. It is observed that the greater the number of spheres and zones, the less the error is in object detection i.e., the more is the accuracy of the method.

Shadow fading is not included in the process as then the shape of the spheres would become irregular and great difficulty would arise in detection. Future works will include the impact of shadow fading and object velocity on the overall system performance. We will also evaluate the detection delay performance and compare it with the acoustic counterpart.

## References


[1] X. Che, I. Wells, G. Dickers, P. Kear, and X. Gong, "Re-Evaluation of RF Electromagnetic Communication in Underwater Sensor Networks," *IEEE Communications Magazine,* vol. 48, no. 12, pp 143-151, Dec 2010.

[2] J. Partana, J. Kurosea, and B. N. Levinea, "A Survey of Practical Issues in Underwater Networks," *ACM Mobile Computing and Communications Review,* vol. 11, no. 4, pp. 2333, Oct 2007.

[3] B. F. Bush, V. K. Tripp, and K. Naishadham, "Practical Modeling of Radio Wave Propagation in Shallow Seawater," *IEEE Antennas and Propagation Society International Symposium,* pp. 1-2, Jul 2012.

[4] S. Zhou, and P. Willett, "Submarine Location Estimation Via a Network of Detection-Only Sensors," *IEEE Transactions on Signal Processing* vol. 55, no. 6, pp. 3104-3115, 2007.

[5] Y. Huang, W. Liang, H. B. Yu, and Y. Xiao, "Target Tracking Based on a Distributed Particle Filter in Underwater Sensor Networks," *Wireless Communications and Mobile Computing,* vol. 8, no. 8, pp. 1023-1033, Oct 2008.

[6] G. Isbitiren, and O. B. Akan, "Three-Dimensional Underwater Target Tracking With Acoustic Sensor Networks," *IEEE Transactions on Vehicular Technology,* vol. 60, no. 8, pp. 3897-3907, 2011.

[7] M. F. Hossain, M. B. Wali, K.S. Munasinghe, and A. Jamalipour, "Three Dimensional (3D) Underwater Sensor Network Architectures for Intruder Localization Using EM Wave," *IEEE Wireless Communications and Networking Conference (WCNC),* pp. 1-6, Apr 2016.

[8] K. Munasinghe, M. Aseeri, S. Almorqi, M. F. Hossain, M. B. Wali and A. Jamalipour, "EM-Based High Speed Wireless Sensor Networks for Underwater Surveillance and Target Tracking," *Journal of Sensors,* vol. 2017, Article ID 6731204, pp. 1-14, Feb 2017.

[9] E. Dalberg, A. Lauberts, R.K. Lennartsson, M.J. Levonen, and L. Persson, "Underwater Target Tracking by Means of Acoustic and Electromagnetic Data Fusion," *IEEE $9^{th}$ International Conference on Information Fusion (ICIF),* pp. 1-7, Jul 2006.

[10] S. Jiang, and S. Georgakopoulos, "Electromagnetic Wave Propagation into Fresh Water," *Journal of Electromagnetic Analysis and Applications,* vol. 3, no. 7, pp. 261-266, Jul 2011.

[11] A. I. Al-Shamma'a, A. Shaw, and S. Saman, "Propagation of Electromagnetic Waves at MHz Frequencies Through Seawater," *IEEE Transactions on Antennas and Propagation,* vol. 52, no. 11, pp. 2843-2849, Nov 2004.

# Designing and Performance Evaluation of GSM/GPS Based Helicopter Tracking Device

Md Imdadul Hoque,[1,*] Abdullah Al Amin,[1] Md Jumshadur Rahaman,[1] and Mohammad Hossam-E-Haider[1]

[1]Electrical Electronic & Communication Engineering Department
Military Institute of Science and Technology, Dhaka, Bangladesh
[*]imdad_7138@yahoo.com

*Abstract*— **Low flying aircrafts are always tough to track due to the radar horizon limitation. But an aircraft is always to be tracked for the safety purpose. However, there are means to augment the radar detection like aircraft to ground data link or satellite phone.The combination of Global Positioning System (GPS) and Global System for Mobile Communications (GSM) can also perform the job satisfactorily. This work proposes the design for GPS/GSM based helicopter tracking device and evaluates the performance. In this work, two GSM networks were utilized to track low flying aircrafts in different routes. The device design is proposed basing on the experimental results of tracking. Possible future modifications of the device are also suggested to achieve more accurate and precise results in future experiments.**

***Index Terms*—GPS, GSM, Helicopter, SMS, Tracker.**

## I. INTRODUCTION

In aircraft detection systems, the radar horizon is the distance at which radar beam rises much above the earth's surface to make the low-level detection impossible[1]. The presence of clutter zone also restricts the radar beam. Clutter zone can be defined as the zone where radar energy is in the lowest altitude of the troposphere. These make the tracking of low flying aircrafts troublesome in some cases. But for security purpose, the positioning information of these aircrafts is very important[2]. Though Radio Detection and Ranging (RADAR) is an excellent tool for tracking, still the radar shadow and clutter zone needs to be covered up with any alternative communication mean.

Helicopters are low flying aircrafts. Most helicopters do not have pressurized cabins. So they normally fly in low altitude, generally around 1000 feet. If a helicopter is flying at an altitude of 1000 feet, Radar can detect it up to maximum 75 km of distance. This happens due to the earth's curvature[3]. Thus, obtaining the real-time position information of the helicopter is troublesome which increases flight safety hazards.

Presence of the radar shadow and clutter zone allows the helicopters to take Nap-of-the-Earth (NOE). NOE is the very low altitude flying, usually by the military aircrafts to avoid the radar detection. However, it may be useful for aircrafts to avoid the enemy radar detection. But it is of obvious importance to remain in constant communication with own detection system. Secondary Surveillance Radar (SSR) is a means for covering the communication missing zone. But this is not also free of limitation with height. GPS is a trusted and widely accepted tool for obtaining position information[4]. Combination of GSM and GPS communication system may satisfactorily cover up the zone that is blank for a radar and augment the communication throughout.

GSM is the most common and widely used communication technology which is readily available at most of the parts around the globe[5]. It allows to send General packet radio service (GPRS) at a cheap rate. This provision can be utilized to transmit the positioning data which can be obtained by GPS. GSM primarily works on line of sight (LOS) principle and designed for surface communication. However, the lower altitudes can be covered by the GSM. This can successfully cover the radar shadow and augment other means of communication. In Spain, A study by Juan showed that, signal transmitted by GSM upwards are traceable by GSM devices up to the height of approximately 3000 meters[6]. Thus, it was confirmed that GSM works at low altitude and can be used for communicating with helicopters.

It is easier for GSM network to cover the whole area of Bangladesh as it is the most densely populated country of the world. At present four separate GSM networks are operating in this country. All the networks have widespread network coverage; though may not be the whole country for all. The strengths of these networks are also not similar. Again, the network strength differs from place to place. Even the strongest network at one place may show poor network strength in some other place.

Bangladesh is a land of geo-diversity. Though mostly plain, Bangladesh has a widespread hilly region as well. Obviously, the hilly region causes the radar shadows and radar clutters in some of the areas. Thus, those areas remain untraceable by the radar coverage. But GSM can successfully cover the undulating lands as well.

## II. RELATED TECHNOLOGIES

Different technological terms are described here which will help to explain the working procedure of this project.

### *A. GPS Technology*

The Global Positioning System (GPS) is a network of about 30 satellites. Those keep on orbiting the Earth at an altitude of 20,000 km. The purpose of the development of GPS was military navigation and implemented by the United States (US) government. At present, GPS devices are so available that almost every single person is in the possession

978-1-5386-3374-8/17/$31.00 ©2017 IEEE

of GPS devices, be it a mobile phone or handheld GPS unit. These devices can receive the radio signals which are broadcasted by the satellites.

These 30 satellites are so positioned that, any point of the planet is covered by at least four GPS satellites at any time. Those satellites individually transmit the data informing the positional data. Once any GPS receiver has information on the distance from at least three satellites, it can pinpoint the location. This process is known as trilateration. For a moving object, the time-based position, altitude, speed and direction can be extracted from the GPS satellite data.

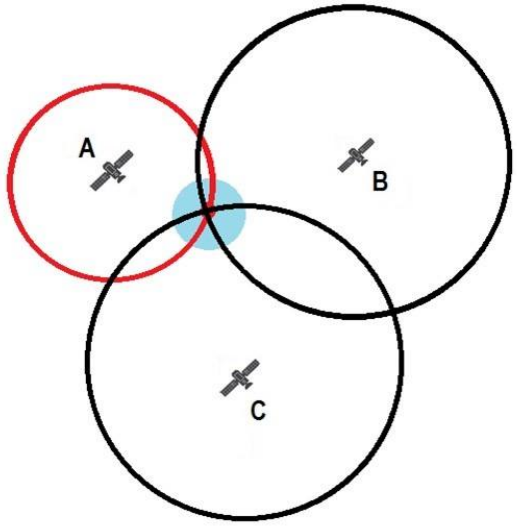


Fig. 1 GPS trilateration technique.

## B. GSM Technology

In the year of 1970 at Bell Laboratories, the idea of GSM was developed. It is the most widely used mobile communication system around the globe. GSM can operate at 850MHz, 900MHz, 1800MHz and 1900MHz frequency bands.GSM system was developed using time division multiple access (TDMA) technique as a digital system for the purpose of the communication. Data rates from 64kbps to 120Mbps can be carried by the GSM technology. A typical GSM architecture is shown in Fig. 2.

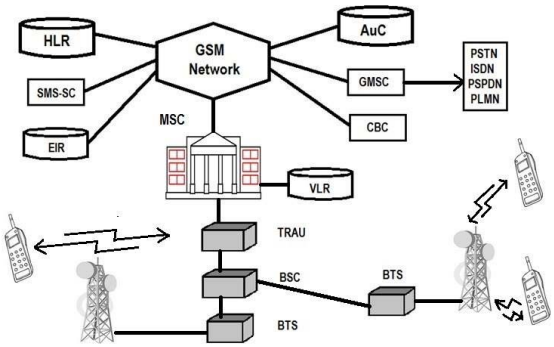


Fig. 2 GSM architecture.

## C. RADAR Horizon

The radar horizon is the distance at which radar beam rises much above the earth's surface to make the low-level detection impossible. The presence of clutter zone also restricts the radar beam. Clutter zone can be defined as the zone where radar energy is in the lowest altitude of the troposphere.

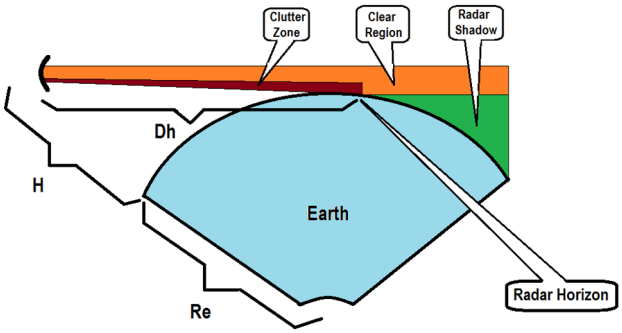


Fig. 3 RADAR horizon.

## D. Nap-of-the-Earth

NOE is the provision of very low altitude flying to avoid being detected by enemy, particularly at a high-threat environment. During NOE flight, the aircrafts follow geographical features to keep themselves in radar shadow and thereby avoiding being detected. Fig. 4 shows a low flying aircraft (helicopter) following NOE route.

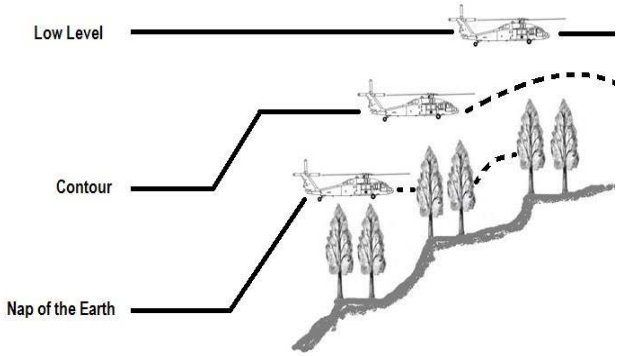


Fig. 4 NOE.

## E. Google Maps

'Google Maps' is a service of technology giant Google. It is basically a web mapping service. It is very much useful to plot the positional data on a google map for the understanding at user end. Just plotting the position on google maps offers much better assimilation than merely mentioning the data as a list. A flight route of an aircraft plotted on google maps is shown here at Fig. 5.

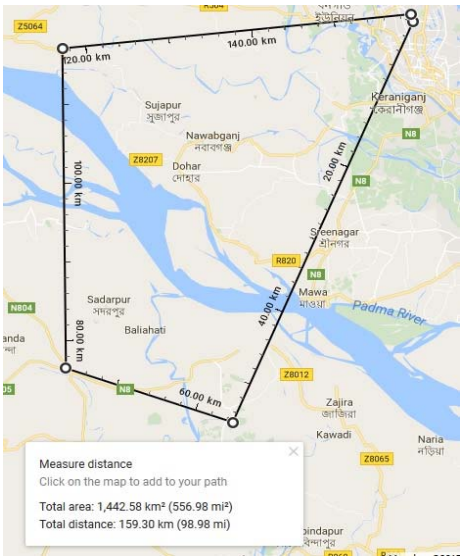


Fig. 5 Google maps.

## III. METHODOLOGY

Two devices were designed for evaluating the performance of helicopter path profile tracking, based on GSM network. The devices were developed using commercially available hardware comprising GPS receiver, GSM modem, microcontroller unit (MCU), micro Secure Digital (SD) card and power source. The main aim of this work is to develop an affordable and reliable tracking system for helicopter.

### *A. Architechture of Modules*

To analyse the performance a device was developed and put into real-time experiment. The architecture of module-1 is shown in Fig.6. Here an algorithm was developed for transmission of data based on better network signal. The MCU determines the signal quality among the GSM networks and transmit data through the better one. The result obtained through the first module was not satisfactory. There after the module was redesigned using two MCU and two GSM modules keeping one GPS module. The block diagram is shown in Fig .7.

### *B. Atmel Xmega Microcontroller*

The Atmel Xmega Microcontroller(AXM) is used with the GPS/GPRS/GSM Module for data management from the GPS and transmission of processed data to the remote server. This microcontroller having 100 pins among those 78 are digital Input/Output (IO) pins. The AXM has 128KB program memory. It can be connected to computer through USB cable. The boot loader occupies only 0.5 KB. It contains 8 KB of SRAM and 4 KB of EEPROM.

### *C. U-Blox 6 GPS Module*

The NEO-6 GPS is a stand-alone GPS receiver featuring high performance u-blox 6 positioning engine. The 50-channel u-blox 6 positioning engine claims a Time-To-First-Fix (TTFF) of under 1 second. The devoted acquisition engine, with 2 million correlators, is capable of massive parallel time/frequency space hunts, allowing it to find satellites instantaneously. Compact design and technology overpowers jamming sources and mitigates multipath effects, giving NEO-6 GPS receivers brilliant navigation performance even in the most hostile environments.

### *D. SIM800 GSM Module*

Simcom SIM800 is a quad-band GSM module is designed as a data communication equipment. It supports quad-band 850/900/1800/1900 Mhz. It can transmit voice, data and SMS with low power consumption. It provides a full modem serial port which is used for data transmission and sending command. The modem is controlled via AT commands. It operates within 3.4 volts to 4.4volts and -40°C to 85°C. The module was configured in GPRS mode for sending data to the remote server.

### *E. Operating Principle of Module-1*

The module-1 was designed with one GPS module, two GSM module and one MCU. The GPS receives positional data from satellite and MCU extract the required data. Then MCU compares the signal strengths among two mobile operators and transmit to the server using best available network. After receiving data on the server side, data validation is conducted and stored in database. A web based application named (ONNESHA) has been developed on the server which projects the real-time location and related information of the device like speed, altitude, direction and time on digital map. The block diagram of module-1 is shown in Fig.6. Total five real-time performance tests were conducted by the module-1.

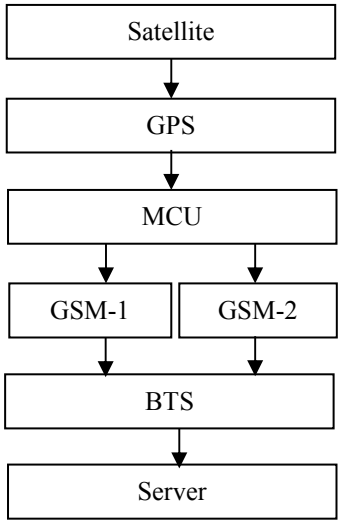


Fig.6 Block diagram of module-1.

### *F. Operating Principle of Module-2*

The operating principle is almost same like module-1 except algorithm and number of MCU. The operating block diagram is shown in Fig.7. The main difference between module-2 from module-1 is the use of two MCU. Each MCU extracts data from the same GPS module but transmit data to the server following separate GSM network individually. The algorithm is also different from module-1. A provision of SD card was kept but intentionally it was disabled to analyze the unsuccessful transmission without storing to memory device. So far two tests were conducted

through Bell-212 helicopter and in future, more tests will be conducted in different routes covering more area.

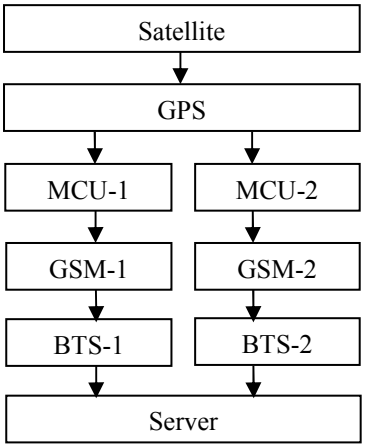


Fig. 7 Block diagram of module-2.

## IV. Experimental Results

### A. Result from Device-1

The helicopter flew at 200kph and maintained average height of 1000 feet. Total flight time was about 3 hour 30 minutes. After analysing the data received from the device it was found that, only 20-25% data could be sent. The test was conducted using two mobile networks but every time with different network combination. One of the test results is plotted in Fig. 8.

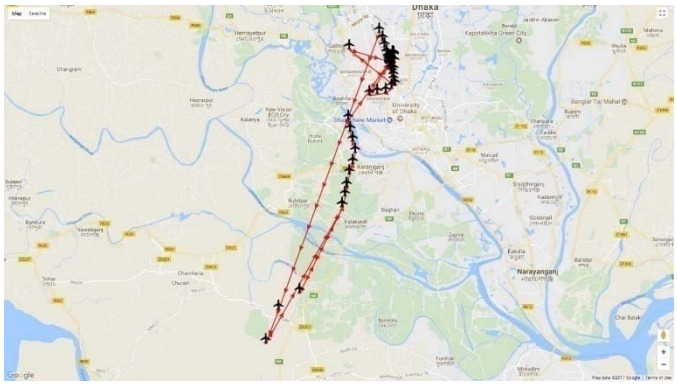

Fig. 8 Helicopter routes tracked by device-1.

### B. Result from Device-2

The helicopter flew twice at a speed of 200kph maintaining average height of 1000 feet. Total flight time was 2hr 25min covering distance of 160km per flight. This device could track approximately 92% of total path profile. The algorithm was programmed to send data after each 15 seconds. The maximum height travelled by the helicopter was 1250 feet from where the device could successfully transmit data except few places. The transmitted data was much better than the previous one. The transmitted data vs received data chart is shown in the Fig. 9and the tracked route is plotted on map shown in Fig. 10.

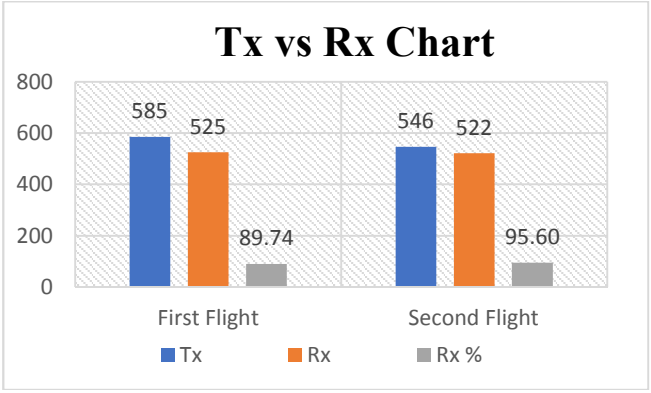


Fig. 9 Transmitted vs received data.

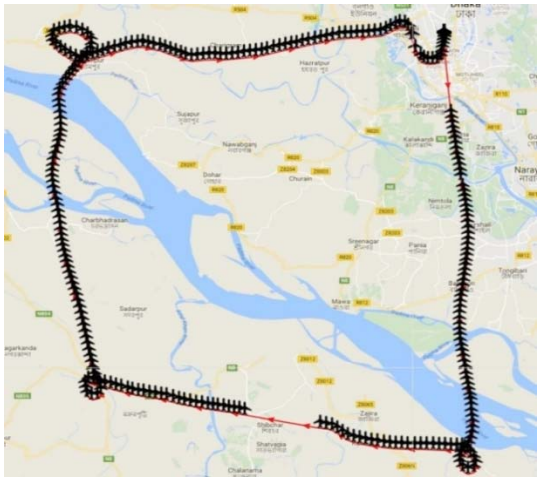

Fig. 10 Helicopter route, tracked by device-2.

## V. Conclusions

After conducting number of experiment through module-1 it was observed that, the device was unable to transmit data despite availability of GSM network. While the MCU compares the strengths and tries to connect a BTS, the helicopter leaves behind the BTS due to its high speed. Since the signal strength is weak and changes vary rapidly, therefore single MCU can not operate two GSM modules effectively. Due to the high speed and low signal quality, the MCU fails to conduct handoff/re-registration of GSM module effectively. On the other side, module-2 with two MCU gave much better result compared to module-1. Each MCU of module-2 operates single GSM module separately. Transmission of 100% data instantly is not possible because of non-availability of network in some particular places. GSM network is not available across wide river and the places where habitation is absent. To get the complete flight path unsuccessful data need to be stored in SD card and transmitted to the server once the device reaches within the range of GSM network. In our future experiment, we will store unsent data in SD card and transmit as soon as the helicopter comes within the GSM network. The block diagram of data transmission and storing is shown in Fig.11. In this experiment two GSM networks were used. Use of even more GSM networks will help to achieve much better tracking result because a particular area not covered by one GSM network may be covered by another GSM network.

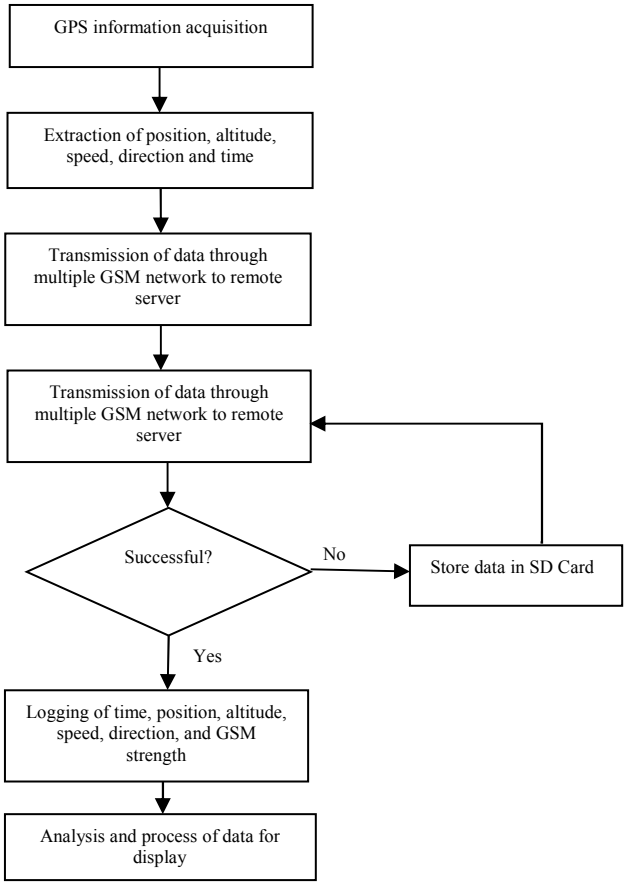


Fig.11 Block diagram of data transmission and storage procedure.

## REFERENCES

[1] K.-W. Gurgel, H.-H. Essen, and S. Kingsley, "High-frequency radars: physical limitations and recent developments," Coastal Engineering, vol. 37, pp. 201-218, 1999.

[2] D. McCallie, J. Butts, and R. Mills, "Security analysis of the ADS-B implementation in the next generation air transportation system," International Journal of Critical Infrastructure Protection, vol. 4, pp. 78-87, 2011.

[3] D. L. Knepp, "Radar measurement of ionospheric scintillation in the polar region," inGeneral Assembly and Scientific Symposium, 2011 XXXth URSI, 2011, pp. 1-4.

[4] M. S. Amin, M. A. S. Bhuiyan, M. B. I. Reaz, and S. S. Nasir, "GPS and Map Matching Based Vehicle Accident Detection System," in 2013 IEEE Student Conference on Research and Development (SCOReD), Putrajaya, Malaysia, 2013, pp. 1-4.

[5] M. S. Amin, M. B. I. Reaz, and S. S. Nasir, "Integrated Vehicle Accident Detection and Location System," TELKOMNIKA Telecommunication, Computing, Electronics and Control,vol. 12, pp. 73-78, 2014.

[6] J. A. Romo, G. Aranguren, J. Bilbao, I. Odriozola, J. Gómez, and L. Serrano, "GSM/GPRS signal strength measurements in aircraft flights under 3,000 meters of altitude," WSEAS Transactions on Signal Processing, vol. 5, pp. 219-228, 2009.

# Clustering Approach Delay Sensitive Application in Wireless Sensor Network (WSN)

Md. Saiful Islam Rubel*, Nahi Kandil, Nadir Hakem, Md. Jahirul Islam Zuyal
Laboratoire de recherche Télébec en communications souterraines (LRTCS)
Université du Québec en Abitibi-Témiscamingue (UQAT)
675, 1ère avenue, Val d'Or, QC, J9P 1Y3, QC, Canada.
*md.saifulislam.rubel@uqat.ca, Nahi.Kandil@uqat.ca, nadir.hakem@uqat.ca, jewel205@ymail.com

***Abstract*—Energy efficiency is considered as the key issue in the design of WSN. Saving energy often introduces additional network delay, which is not desirable especially in case of sensitive-delay application. For such application, the system should be time responsive. Most of the recent scenarios have not introduced any management of delay-sensitive data applications to their works in order to achieve energy efficiency. However, managing the delay sensitive data along with regular data is not often good for energy efficiency. Clustering is one technique that used very effectively to achieve scaling up and power saving in WSNs. However, it does not take care of application delay constraints. In this work, we consider only two kinds of sensors, one is used for sensitive-delay application and the other one is used for best effort or regular application. The proposed clustering scheme manages both sensitive and best effort sensors and meets both delay and energy constraints.**

***Keywords*—Energy efficiency, delay, delay-sensitive data, clustering.**

## I. Introduction

Wireless Sensor Networks (WSNs) have recently come into prominence because they hold the potential to revolutionize many segments of our economy and life. Environmental monitoring and conservation, manufacturing and business asset management, automation in transportation industries and healthcare industries are the different application of wireless sensor application.

WSNs are composed of a large number of sensor nodes and sink which is also a node used for collecting data from all the nodes. And these nodes are densely deployed either inside a physical phenomenon or very close to it. It has become an effective paradigm to gather information on a large-scale area through the collaboration of sensors. As the advances in micro-sensor and wireless communication technologies, WSNs are capable of monitoring many sensitive-delay applications, such as detections of forest fires, toxic gases, etc. These kinds of application [3] should transmit data to the monitoring station or sink as quickly as possible comparing to best-effort or regular application.

All existing WSNs are designed to achieve high energy saving and take little account of application delay constraints. The reported work in [6], [7] and [11] give much information about the need of a real-time WSN, but there is no clarification on how to achieve this purpose. Recently some researchers have given importance to use mobile element [2] or sink moving strategy [1] to collect data from sensors in order to make the WSN system both real-time and energy efficient. But this approach is impracticable for such physical environment like underground mines and not cost effective. And there is also no indication about the sensitive-delay application at all. To resolve the WSN scaling effect, sensors often need to organize themselves into clusters. Clustering allows hierarchical structures [5] to be built on the nodes and enables more efficient use of scares resources, such as frequency spectrum, bandwidth and power.

In this work, we propose a new clustering scheme able to give more transmitting time to sensitive-delay sensors against the regular one. In other words, we introduce a Quality of Service (QoS) mechanism that gives more priority to sensitive-delay sensors by managing different duty cycle for both types of data used in our proposal.

The next section of this paper presents the statement. In section III, related work is outlined. The proposed approach's description and performance analysis are given in two following sections. Finally, section VI presents our conclusions.

## II. Problem Definition

As previously mentioned, our main goal is to manage a wireless sensor network where sensors belong to two different kinds. The first one has non-delay constraint on data transmission wherein the second one, sensors support a critical or constraint time application. This assumption affects the lifespan of sensors and the network.

To define the problem, let us consider the RSD as network parameter that gives the ratio between the number of sensitive-delay sensors and the number of sensors in WSN. The issue is how to give more transmission time to sensitive-delay sensors against regular sensors. Which means, how to attribute more priority to sensitive-delay sensors. It is obvious that, if we

978-1-5386-3374-8/17/$31.00 ©2017 IEEE

give more transmission time to sensitive-delay sensors then it will quickly consume the battery energy of sensitive-delay sensors comparing to regular sensors. Furthermore, we know that sensor networks consist of limited battery-powered nodes. So, when a sensitive-delay sensor dies after spending all its energy, the purpose of applications that rely on this sensor will be affected.

## III. Related Work

In recent years, many studies focus on solving the problem of energy issue in WSNs. However, in most of the cases, it is not concerned about the sensitive-delay application and managing it with regular nodes. Sink moving strategy for making the system durable and energy efficient by using LEACH proposed in [1]. Where sink itself visits all the nodes and collect data from them. A hybrid approach called Node density based clustering and mobile collection (NDCMC) proposed in [2], where a number of Cluster Heads (CHs) gather information from cluster members and then an ME (Mobile Element) visits these CHs to collect data. In [3], the authors proposed a sensitive-delay application (toxic gas monitoring system) in real time. However, it is the regular nodes, who sense this sensitive-delay data. In [4], authors propose two new distance-based clustering routing protocols, which called DB LEACH and DBEA-LEACH. The first approach (distance-based) selects a CH node by considering the distance between the candidate nodes to the base station and the second approach considers both distance and residual energy to select a CH. Energy and delay efficient hierarchical clustering scheme called BHC (Bruijn Hierarchical Clustering) for WSNs has been proposed in [5], which shows the end-to-end delay for data transmission. But, there is no indication of sensitive-delay application. In [6], the authors describe an investigation of the trade-off between two objectives in WSN design: minimizing energy consumption and minimizing end-to-end delay by using DCEM (Distributed Clustering) scheme. A new localized quality of service (QoS) routing protocol for wireless sensor networks (WSN) is proposed in [7]. Here the proposed protocol targets WSN's applications having different types of data traffic. A clustering approach for the homogeneous network is proposed in [8], which select CH based on distance from the sink. In [9], the authors have proposed a cross-layered real-time data broadcast on the K-coverage configuration for sensitive-delay applications, called RTBK, which propagates emergent messages within time constraints. In [10], the authors have defined non-uniform QoS for WSN to extend the network lifetime. Paper [11] presents a QoS aware Energy Efficient Routing (QEER) protocol for Clustered Wireless Sensor Network. Here to address energy efficiency (hotspot problem) and high end-to-end delay problem, a combination of the mobile and static sink is used for data gathering.

## IV. Proposed Approach

In our proposal we have assumed that the sensors are deployed in fixed (not moving) position that is when they are first randomly distributed, they will remain in the same place throughout the lifetime of network. Each sensor node has a unique ID and knows its current position and its remaining energy and also each sensor node has enough power (Threshold value) to communicate directly with the sink. There is no different energy for sensitive-delay and regular sensors. All nodes have the same initial energy because we want to maintain the homogeneous network. In addition, their batteries are not rechargeable. Sensor nodes die at the end of their battery. Network is assumed to be connected.

### *A. Management of Critical and Regular data*

In this approach, we define SDC as a ratio between the number of duty cycle required by sensitive-delay sensors and the number of cycles allocated for regular sensors during a time period. Which means sensitive-delay sensors will have 1/SDC duty cycles more than the regular ones.

So, if a regular sensor sense any sensitive-delay data then it will be forwarded to Cluster Head (CH) as a sensitive-delay data using the same duty cycle, which was dedicated for the sensitive-delay sensors. The duty cycle can also be increased or decreased in our approach. If the duty cycle of sensitive-delay sensors increase then it will consume more energy and the sensitive-delay sensor will die soon. To resolve this problem we can consider sensitive-delay sensors not to be a Cluster Head (CH). This will save more energy to keep the sensitive-delay sensors alive as long as possible.

### *B. CH Selection Algorithm*

Since we are using clustering approach, it will draw additional network delay. To solve this problem, we have to improve CH selection algorithm to obtain a reasonable end-to-end delay. In this approach, we will select CH based on minimum distance from sink and based on residual energy available in sensors.

*1) CH Selection Based on Minimum Distance:* This algorithm will select that node as CH, which is nearest to the sink. The energy cost ($E_T$) of a network is given by:

$$E_T = E_{RX} + E_{TX} + E_S + E_I \qquad (1)$$

Where $E_{RX}$ indicates the receiving energy, $E_{TX}$ is the transmission energy, $E_I$ is energy cost during idle state and $E_S$ is the energy cost during sensing mode. Generally, the three energy costs except the transmission cost are constant. The transmission energy mainly depends on the distance. To minimize the transmission energy, we have taken this criterion into consideration.

For the CH selection, based on minimum distance from the sink, we have defined an equation, which is as follows:

$$P_i = 1 - \frac{d_i^2}{\sum_{j=1}^{j=n} d_j^2} \quad (2)$$

Where n is the total number of nodes, $d_i$ is the distance from sensor i to sink, $d_j$ is the distance from each other node j to the sink. The ratio of this two values will give $P_i$, which is a uniform value between 0 and 1. The sensor i will be selected as CH if the probability of $S_i \leq P_i$. Where $S_i$ is the random probability between 0 and 1. Here, randomness and probability are introduced. If we select those nodes as CH, which have the minimum distance from the sink, then those nodes will die soon because of selecting them as CH repeatedly. That is why we have introduced new variable $S_i$ for selecting randomly those nodes as CH nodes, which are the nearest to sink on the basis of probability.

*2) CH Selection Based on Residual Energy:* In this algorithm, the CH will be selected on the basis of maximum remaining energy. Similarly, for this algorithm, we have defined an equation, which is as follows:

$$P_i = \frac{E_i}{\sum_{j=1}^{j=n} E_j} \quad (3)$$

Where $E_i$ is the residual energy of sensor i, $E_j$ is the residual energy of each other node j and $P_i$ indicates the ratio of this two values which gives a uniform value between 0 and 1. Similarly, the sensor i will be selected as CH if the probability of $S_i \leq P_i$. Where $S_i$ is the random probability between 0 and 1. That means CH will be selected randomly which has the maximum residual energy after each round on the basis of probability.

*3) Hybrid CH Selection:* In this algorithm, the CH will be selected on the basis of both above mentioned criteria. That means, based on maximum remaining energy and minimum distance from the sink. The basic equation of Hybrid CH selection is as follows:

$$P_i = (\alpha) \times \left(1 - \frac{d_i^2}{\sum_{j=1}^{j=n} d_j^2}\right) + (1 - \alpha) \times \left(\frac{E_i}{\sum_{j=1}^{j=n} E_j}\right) \quad (4)$$

Where α is the factor of both energy and distance. Suppose, if we take α=0.5, that means we consider 50% of distance and 50% of residual energy to select CH. Similarly, we can take only distance or only residual energy into consideration, if we take α=1 and α=0 respectively. We can evaluate the performance of Hybrid CH selection algorithm by taking the value of α between 0 and 1.

The diagram below shows the CH formation of Hybrid approach. Where we have taken α=0.2. That means we have given priority to residual energy compared to the distance to select CH of the network. In our proposal, we have taken a sensor threshold value and CH threshold value. That means a sensor and a CH should have a minimum level of energy to transmit the data to sink. Otherwise, it will not transmit the data. In diagram below, Pi indicates the equation (4) and CS indicates the sensitive-delay sensors. The logic CS>0 indicates, if there is any sensitive-delay sensor then it will not be selected as CH to save energy.

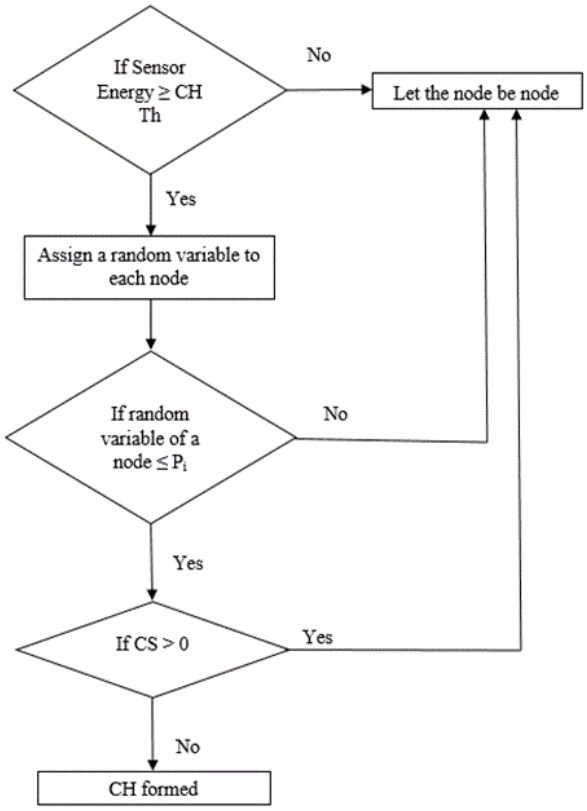


Fig. 1. Hybrid CH selection approach chart

### C. DBEA-LEACH

We will compare our approach with DBEA-LEACH [4] to observe our proposal's performance. But, to do so, we have to make some adaptation to keep the same input as our proposal. Generally, LEACH does not have specific sensitive-delay or regular sensors. It uses the same sensors to sense both sensitive-delay and regular data. But, we will take the same ratio of sensitive-delay sensors to sense sensitive-delay data. However, we will keep the duty cycle same for the regular and sensitive-delay cycle to see our proposal's performance.

In DBEA-LEACH, the CH is selected on the basis of distance and energy to achieve energy efficiency. Here a node is more likely to be selected as a cluster head if the distance of it from the BS is nearly equal to the average distance of the network sensor nodes to the BS and that node which has a high residual energy.

## V. Performance Evaluation

In this section, we will evaluate the performance of our proposed approach and compare it with DBEA-LEACH. We have used MATLAB to simulate our approach. Table 1 summarizes the main parameters that we have assumed for simulation of our approach.

TABLE I. PARAMETERS CONSIDERED

| Parameters | Value |
|---|---|
| Network size | 100*100 |
| Number of nodes | 100 |
| Ratio of sensitive-delay sensors (%) | 10 |
| Sink location | 1m*1m |
| Initial energy of sensors | 0.2J |
| Quality of Service factor | 0.1 |
| Transmission/ Receiving energy | 50 nJ |
| Alpha (α) | 0.2 |
| Data aggregation energy | 5 nJ |
| Maximum round | 12000 |
| Transmission speed | 10 Kbits |
| Packet size regular | 400 bytes |
| Packet size sensitive-delay | 80 bytes |
| Duty cycle ratio | 1:10 |

All the parameters are the same in case of DBEA-LEACH except the duty cycle ratio and the Alpha (α) factor. As Alpha (α) is used to select CH on the basis of residual energy and minimum distance from sink. In DBEA-LEACH, we will not take any duty cycle ratio to see the transmission delay and lifespan effect of sensitive-delay sensors. Now we will observe two main metrics: the transmission delay and the number of sensors, which have not exhausted their batteries.

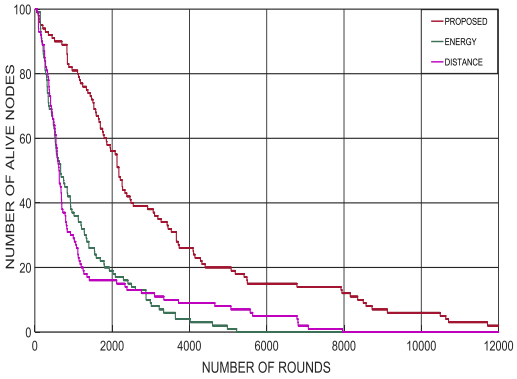


Fig. 2. Comparision of lifespan

From figure 2, we observe that the hybrid or proposed one has the best energy efficiency than the other two. The distance method has the worst energy efficiency. Because the nodes which are nearest to the sink will be used as CH most often and will exhaust their energy fast. If CHs are selected which are far from sink then they will consume more energy to transmit through the long distance over network. Hence we have taken α=0.2 in equation (4). That means we have given 20% priority on distance and 80% priority on residual energy to achieve the best energy efficiency.

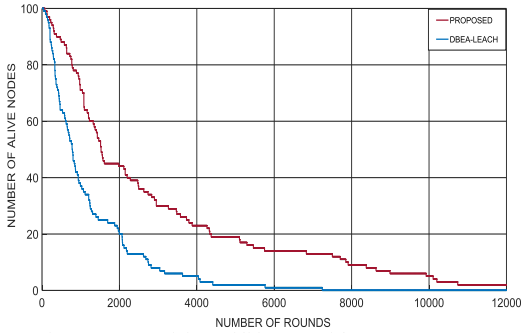


Fig. 3. Comparision of lifespan with DBEA-LEACH

As shown in Fig. 3, the proposed protocol has a more improved network lifetime than the DBEA-LEACH protocol. This enhancement is due to the optimal clustering and hybrid mechanism. The proposed approach is much more stable. But in DBEA LEACH there is a sharp breakdown before 2000 rounds. All the sensor nodes in case of DBEA LEACH die before 8000 rounds whereas few sensors are still alive till 12000 rounds in our proposed approach. This improvement in network lifetime is due to the efficient energy conservation approach employed by the hybrid protocol and the threshold value of the sensors.

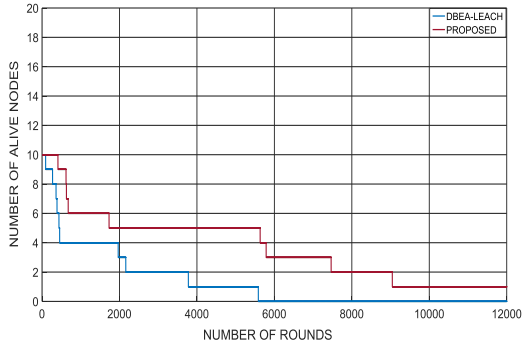


Fig. 4. Lifespan of delay-sensitive sensors

Fig. 4 presents the lifespan of sensitive-delay sensors in both cases. As we take 10% ratio of sensitive-delay sensors in both cases, there are only 10 sensitive-delay sensors. All the sensitive-delay sensors are dead before 6000 rounds in DBEA-LEACH approach. But in our approach, a sensitive-delay sensor exists at more than 12000 rounds. Because in our approach, we have set the criteria that sensitive-delay sensors will not be selected as CH node. This gives more lifespan to sensitive-delay sensors. Therefore, our approach is very much applicable for sensitive-delay applications.

The time taken for packets going from sensors to sink is defined as the end-to-end delay. Here, we have taken the mean of delay because in one cycle there are many packets go from sensor to sink. To make it clear in the figure, we have taken the mean of all delay.

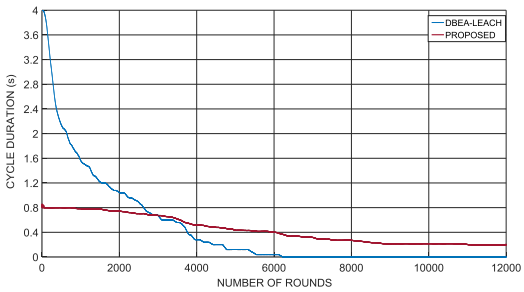


Fig. 5. End-to-End delay of regular sensors

From figure 5, we can see that the average delay time of our approach is much better than the DBEA-LEACH till 3000 rounds (approximately). But the proposed approach shows consistently low average delay over the network. In DBEA-LEACH, initialy there is high delay encountered which is not good at all especially in case of delay-sensitive applications. As the lifespan of DBEA-LEACH ends around 6000 rounds, so there is no packet delivered to sink after 6000 rounds and hence, there is no delay time considered after 6000 rounds for the DBEA-LEACH approach.

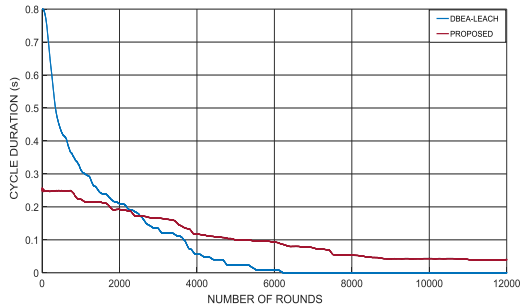


Fig. 6. End-to-End delay of delay-sensitive sensors

Finally, from figure 6, we can see the end-to-end delay of sensitive-delay sensors of both approaches. This result is very important in case of sensitive-delay applications. As we are giving more duty cycle to sensitive-delay data in our approach it will take less time for packets going from sensitive-delay sensors to sink. Here we can see it clearly that our approach takes less time to transmit the data to sink. Which is most important in case of sensitive-delay applications.

## VI. Conclusion

In this work, our main goal was to manage the sensitive-delay sensors along with regular ones. We can also manage the sensors of different priorities by using our approach. We have proposed a clustering approach that gives more transmission priority to sensitive-delay sensors compare to regular sensors. We have also introduced hybrid CH selection approach taking consideration of energy efficiency. Moreover, by comparing with DBEA-LEACH, which is used to achieve energy efficiency, our proposed scheme shows more energy efficiency and give a better delay transmission for non-regular sensors. There is some problem may arise like offloading problem. In future, we will work on this kind of problem.

## References

[1] Makhl ouf Aliouat, Zibouda Aliouat, “Improved Wireless Sensor Networks Durability through Efficient Sink Motion Strategy,” in IEEE Conference on Wireless Sensors (ICWiSE), 2014, pp. 61-66.

[2] Ruonan Zhang, Jianping Pan, Di Xie, “NDCMC: A Hybrid Data Collection Approach for Large-Scale WSNs Using Mobile Element and Hierarchical Clustering,” in IEEE internet of things journal, 2016, vol. 3, no. 4, pp. 533-543.

[3] K. A. Unnikrishna Menon, Deepa Maria, Hemalatha Thirugnanam,“Energy Efficient Clustering Protocol for Early Warning System for Miner's Safety in Coal Mines,” in IEEE 21st Annual Wireless and Optical Communications Conference(WOCC), 2012, pp. 99-104.

[4] Tri Gia Nguyen, Chakchai So-In, Nhu Gia Nguyen, “Two Energy-Efficient Cluster Head Selection Techniques Based on Distance for Wireless Sensor,” in 2014 International Computer Science and Engineering Conference (ICSEC), pp. 33-38.

[5] Networks Trong Thua Huynh, Anh-Vu Dinh-Duc, Cong Hung Tran, “Energy Efficient Delay-aware Routing in Multi-tier Architecture for Wireless Sensor Networks,” in International Conference on Advanced Technologies for Communications (ATC), 2013, pp. 603-608.

[6] Trong-Thua Huynh, Anh-Vu Dinh-Duc, Cong-Hung Tran, “Delay-Constrained Energy-Efficient Cluster-based Multi-Hop Routing in Wireless Sensor Networks,” in Journal of Communications and Networks, 2016, vol. 18, no. 4, pp. 580-588.

[7] Djamel Djenouri, Ilangko Balasingham, “Traffic-Differentiation-Based Modular QoS Localized Routing for Wireless Sensor Networks,” in IEEE Transactions on Mobile Computing, 2011, vol. 10, no. 6, pp. 797-809.

[8] S. Taruna, Sheena Kohli, N.Purohit, “Distance Based Energy Efficient Selection of Nodes to Cluster Head in Homogeneous Wireless Sensor Networks,” in International Journal of Wireless & Mobile Networks (IJWMN) 2012, vol. 4, no. 4, pp. 243

[9] I-Shyan Hwang, Meng-Chun Wueng, Ling-Fei Sung, “Real-time data broadcast in K-covered wireless sensor networks,” in IEEE 13th Asia-Pacific Network Operations and Management Symposium, 2011, pp. 1-5.

[10] Anna Egorova-Forster, Amy L. Murphy, “Exploring Non Uniform Quality of Service for Extending WSN Lifetime,” in Proceedings of the Fifth Annual IEEE International Conference on Pervasive Computing and Communications Workshops (PerComW), pp. 285-289.

[11] Babar Nazir, Halabi Hasbullah, “QoS aware Energy Efficient Routing Protocol for Wireless Sensor Network,” in IEEE Conference on Open System (ICOS) , 2011, pp. 375-380.

# Reduction of Packet Delay in a WLAN with Multi-round Contention Based CSMA MAC Protocol

Manobendu Sarker[1] and Md. Forkan Uddin[2,*]
[1]Department of Electrical and Electronic Engineering
University of Asia Pacific, Dhaka-1215, Bangladesh
[2]Department of Electrical and Electronic Engineering
Bangladesh University of Engineering and Technology, Dhaka-1205, Bangladesh
*mforkanuddin@eee.buet.ac.bd

***Abstract*—The conventional single-round contention based carrier sense multiple access (CSMA) medium access control (MAC) protocols are not able to effectively utilize the opportunities of advanced physical layer techniques of multi-packet receptions in wireless local area networks (WLANs). Researchers proposed various multi-round contention based CSMA MAC protocols to increase throughput in WLANs by taking the full benefits from those advanced physical layer techniques. However, delays of the packets of a WLAN becomes high under non-saturated traffic due to the waiting time by the access point (AP) for contending multiple packets from multiple users when multi-round contention based MAC protocol is used. In this paper, a multi-round contention based CSMA MAC protocol is considered in a WLAN with successive interference cancellation (SIC) technique. An algorithm is proposed for dynamically adapting the waiting time for multi-round contentions to improve the delay performance in a WLAN under a multi-round contention based MAC protocol and SIC. The simulator of multi-round contention based CSMA protocol is modified including the proposed algorithm. Delay and throughput performances of WLANs are evaluated under non-saturated traffic via simulation with and without the proposed algorithm. The simulation results show that the proposed algorithm is very effective in reducing the packet delay in WLANs with multi-round contention based MAC protocol without degradation of throughput performance.**

***Index Terms*—Wireless local area network, carrier sense multiple access, successive interference cancellation, multi-round contention, throughput, delay.**

## I. Introduction

With the massive expansion of utilizing wireless devices in this modern era, wireless local area networks (WLANs) attain vast popularity to deploy in many countries for accommodating the wireless traffic demands efficiently. Currently, the physical and data link layers of WLANs are based on IEEE 802.11 standard and its data link layer uses carrier sense multiple access with collision avoidance (CSMA/CA) medium access control (MAC) protocol [1]. This MAC protocol uses a carrier sensing mechanism to avoid collision and provide single round contention of the users through a contention resolution algorithm. Due to the single round contention, the number of users accessing the medium at a time varies hence the number of successful transmissions depends on the employment of physical layer technique at the access point (AP).

There are many advanced physical layer techniques available for significantly increasing throughput in WLANs. Multi-user multiple-input multiple-output (MU-MIMO) and successive interference cancellation (SIC) are the two important techniques among them. MU-MIMO [2] is an advanced antenna technology, vastly used in wireless communication which enables multiple simultaneous transmissions between transmitter and receiver utilizing their multiple antennas. Besides, SIC [3] is an effective approach which allows a receiver to decode multiple signals based on their signal to interference plus noise ratio (SINR) in an iterative manner.

The traditional single-round contention based CSMA/CA MAC protocol cannot exploit the full advantage of the physical layer techniques [4], [5] since most of the cases the number of users getting access to the channel at a time becomes less than the number of packets that can be received by the AP simultaneously. As a result, researchers have been proposed different multi-round contention based CSMA protocols. The proposals in [6]-[8] are based on two round contention and they manifest good performance improvement in throughput. In [9], the authors propose a SIC-aware multi-round contention based CSMA MAC protocol under the *physical interference model* [10] and demonstrate that the proposed protocol can improve throughput significantly by exploiting SIC. The authors in [4] propose a joint uplink-downlink MAC protocol called Uni-MUMAC where data transmitted users are selected by multi-round contentions. In [11], the authors present a joint uplink-downlink MU-MIMO based MAC protocol utilizing multi-round contentions in uplink while considering *physical interference model* with attenuation, fading and shadowing.

In the multi-round contention based MAC protocols, the AP has to wait some time for extracting the requests from desired number of users which is called waiting time. This leads to increase of packet delay in the system. Thus, multi-round contention based MAC protocols suffer from higher packet delay [9], [11]. Both the throughput and delay are very important performance metrics for any network. Unfortunately, the existing multi-round contention based MAC protocols only focus on throughput improvement but they do not consider the reduction of packet delay. This research motivates to reduce the packet delay in a WLAN with multi-round contention based MAC protocol.

In this paper, we consider the multi-round contention based MAC protocol proposed in [9] considering SIC. Only uplink transmission is examined for a single channel and single rate WLAN. The transmit power of all the users are assumed to be equal. The AP of the WLAN employs SIC technique. We consider the *physical interference model* along with some

978-1-5386-3374-8/17/$31.00 ©2017 IEEE

wireless channel characteristics like path loss, Rayleigh fading and log-normal shadowing. Our contributions in this paper are as follows.

- The delay and throughput performances of the multi-round contention based MAC protocol in [9] are analyzed via simulation.
- An adaptive algorithm is proposed to reduce packet delay of the proposed multi-round contention based MAC protocol by dynamically adapting the waiting time of the AP.
- The simulator in [9] is modified to include the adaptive algorithm.
- The delay and throughput performances of the multi-round contention based MAC protocol under the proposed adaptive algorithm are evaluated via simulation. The effectiveness of the proposed algorithm is demonstrated.

The remainder of this paper is organized as follows. The system model is described in Section II. Section III describes the proposed algorithm to reduce packet delay. The results are presented and analyzed in Section IV. This paper is, finally, concluded in Section V.

## II. System Model

### A. Network Architecture

The network architecture of the WLAN system is assumed as in [9] where one access point (AP) is surrounded with $N$ users. Each of the nodes has a single antenna which can radiate omni-directionally with a fixed power. The positions of the users are distributed randomly within a circle of unity radius. The distance between a user and the AP is taken to be a random variable $r$ and its probability density function (PDF) is defined as

$$f_r(x) = 2x, 0 \leq x \leq 1. \tag{1}$$

We consider a half-duplex system, i.e., the nodes in the WLAN system cannot transmit or receive simultaneously. The AP has a receiver which employs SIC to extract maximum $M$ packets.

### B. Wireless Propagation Model

In any practical wireless channel, the transmitted power from a user is affected by attenuation, fading and shadowing. By taking these phenomena into account, the received power by the AP from a user at a distance $r$ is considered as [9],

$$P_r = A^2 e^{\alpha} \left(\frac{r}{r_0}\right)^{-\eta} P_t \tag{2}$$

where, $P_t$ is the transmit power of the user, $\left(\frac{r}{r_0}\right)^{-\eta}$ is considered as the attenuation at distance $r$ with far field cross-over distance $r_o$ and path loss exponent $\eta$, $A$ is a random variable with Rayleigh distribution of unit power and $e^{\alpha}$ is the signal variation for shadowing with Gaussian distributed random variable $\alpha$ with zero mean and variance $\sigma^2$. Each random variable $\alpha$ and $A$ is considered to be independent and identically distributed for one user to another and from one data packet transmission to next data packet transmission. Furthermore, we consider

$$f_\alpha(\alpha') = (e^{\frac{-\alpha'^2}{2\sigma^2}})/\sqrt{2\pi}\sigma \tag{3}$$

and

$$f_A(y) = 2ye^{-y^2} \tag{4}$$

as the PDFs of $\alpha$ and $A$, respectively.

### C. Multi-round Contention Based CSMA MAC Protocol

In [9], the authors propose a multi-round contention based uplink MAC protocol where they assume the time is divided into mini-slots and all users transmit DATA packets with same size. According to the MAC protocol, an idle user having a DATA packet senses the medium in each mini-slot to send request. If the user finds the medium as busy then it tries again to access the medium in the next mini-slot. Besides, if the medium is found free, the user sends a request to send (RTS) packet with a transmission probability $p$. More than one user can send RTS packet simultaneously but the transmission of one user can be successful which depends on the interference model based on SIC technique. After receiving a RTS packet, the AP sends an acceptance notification (AN) packet to the RTS transmitted user after a short inter-frame space time (SIFS). If any user sends RTS packet but does not get AN packet, the user tries again to access the channel to transmit RTS packet. If a user receives an AN packet, the user waits for a clear to send (CTS) or not CTS (NCTS) packet from the AP. However, the AP waits for a certain time to receive $M$ successful RTS packets. It is called the waiting time. From the $M$ users, the AP determines the maximum number of users such that data transmission of all of those users are successful using SIC. The AP sends CTS packet to those users and NCTS packet to the others. If the AP does not receive $M$ RTS packets within this time duration, the AP transmits CTS/NCTS packet to the user(s) from which it receives RTS packet(s) during this time. The users who receive CTS packet, transmit their DATA packets to the AP. On the other hand, if a user receives NCTS packet, it does not transmit DATA packet to the AP and goes to the idle mode and tries later to send RTS packet. The DATA packets transmitted by the users are extracted by the AP by employing SIC technique. Then the AP sends a common acknowledgement (ACK) packet to the users from which it extracted DATA packets successfully. After receiving ACK packet, the users tries again to access the channel to send their RTS packets. The transmission of AN, CTS/NCTS and ACK packets are considered always successful.

### D. Interference Model for RTS Packet Reception

The received power by the AP from any user may vary due to attenuation, fading and shadowing. According to the *physical interference model*, the transmission of a user having the strongest SINR among all the transmitting users can be successful if the SINR is greater than a certain threshold. We assume that all the users use the same modulation and coding scheme comprising data rate $R$ and the SINR threshold for successful decoding of a packet at that rate is $\beta$. If $y$ be the set of simultaneous RTS packet transmitted users at a time, the condition for successful RTS transmission of any user $i$ is given as

$$SINR_i = \frac{P_r^i}{\sum_{z \in y \setminus i} P_r^z + N_o} > \beta \tag{5}$$

where, $P_r^z$ is the power received by the AP from a user $z$ and $N_o$ is the background noise power.

### E. Interference Model for Data Packet Reception with SIC

Let $v$, $|v| \leq M$ be the set of users from which the AP receives RTS packets. The AP chooses a set of users $s$ from the user-set $v$ such that all the DATA packets transmitted by

the users in $s$ are successful. Moreover, the AP always tries to maximize the number of users in set $s$. Let the users in $s$ are arranged based on descending received power levels by the AP and $s = \{1, 2, .., |s|\}$. According to SIC, the condition for successful DATA packet extraction by the AP is given as

$$\frac{P_r^1}{\sum_{z\in s\setminus 1} P_r^z + N_o} > \beta, \frac{P_r^2}{\sum_{z\in s\setminus\{1,2\}} P_r^z + N_o} > \beta, ..... \\ ....., \frac{P_r^{|s|}}{N_o} > \beta. \quad (6)$$

## III. Algorithm for Adapting the Waiting Time

In any multi-round contention based MAC protocol, packet delay is high because the AP has to wait a fixed duration of time to extract the desired number of RTS packets. Sometimes, there may be some cases when the AP waits unnecessarily till the expiration of the waiting time although transmission of RTS packets from the desire number of users does not occur. This happens mainly at non-saturated traffic condition. As a result, packet delay in the WLAN system increases. Thus, it is necessary to adapt the waiting time dynamically considering the traffic condition in the network. In the following, the proposed algorithm of adapting waiting time to reduce the delay in WLAN with multi-round contention based MAC protocol is described.

According to the MAC protocol, AP collects requests from a number of users during the waiting time and receives a number of data packet(s) simultaneously using SIC. We assume that AP can calculate the delay of each of the simultaneously received data packets. It is possible since the generation time of a packet is stamped in each data packet during its generation and hence, the AP can easily calculate the delays of the packets. After receiving a number of data packets at a time, the AP calculates the maximum delay of those packets which is referred as the new maximum delay $\tau_{max}^{new}$. This new maximum delay is then compared with the old maximum delay $\tau_{max}^{old}$, i.e., the maximum delay of the simultaneously received data packets in the previous iteration. Initially, $\tau_{max}^{old}$ is set to an initial value $T_0$. If $\tau_{max}^{new} < \tau_{max}^{old}$, the waiting time, i.e., the new waiting time $T_{wait}^{new}$ is set to $(T_{wait}^{old} + \Delta)$, where $T_{wait}^{old}$ is existing waiting time and $\Delta$ is small amount of time. Initially, the value of $T_{wait}^{old}$ is set to a fixed minimum waiting time, $T_{wait}^{min}$. On the other hand, if $\tau_{max}^{new} \geq \tau_{max}^{old}$, the new waiting time $T_{wait}^{new}$ is set to $(T_{wait}^{old} - \Delta)$ when $(T_{wait}^{old} - \Delta) > T_{wait}^{min}$. However, $T_{wait}^{new}$ is set to $T_{wait}^{old}$ if $(T_{wait}^{old} - \Delta) \leq T_{wait}^{min}$. In this manner, the AP adapts the waiting time dynamically whenever it receives data packets for reducing packet delay in WLAN. The proposed adaptive algorithm is illustrated by the flowchart in Fig. 1.

## IV. Results

The custom simulator written in MATLAB [9] is modified according to the proposed algorithm of adaptive waiting time. Then delay and throughput performances of the multi-round contention based MAC protocol with and without the adaptive algorithm are evaluated via simulation. Moreover, the average packet delay and throughput of the WLAN under the conventional single-round CSMA MAC protocol with SIC are also determined via simulation.

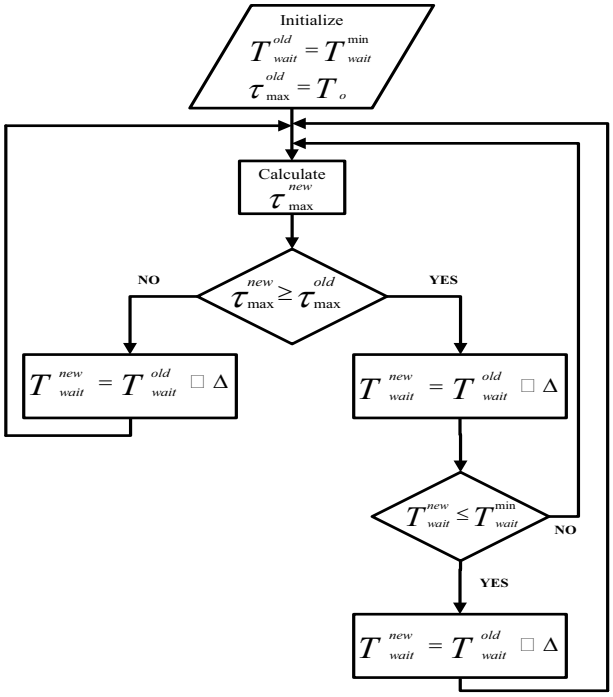


Fig. 1: Algorithm for dynamically adapting the waiting time.

### A. Networks and Parameters

A WLAN system is considered with 20 users and one AP. We consider data rate 5.5 Mbps with SINR threshold $\beta$ = 9.4 dB. The transmit power $P_t$ of the users are taken to be 12 watts. The far field cross-over distance $r_o$ is considered to be 0.01 m. Considering the indoor WLAN environment, the path loss exponent $\eta$ is chosen to 4. The value of $\sigma$ is taken to be 6 dB. We consider the duration of a mini-slot, $\phi = 20\ \mu s$. The values of different types of packet in mini-slots are considered as: $L_{RTS} = 7$, $L_{AN} = L_{ACK} = 6$, $L_{CTS} = 2M + 4$, and $L_d = 500$, where $L_{RTS}$, $L_{AN}$, $L_{CTS}$, $L_{ACK}$ and $L_d$ are the transmission times of RTS, AN, CTS, ACK and DATA packets, respectively. Moreover, the duration of a SIFS time is taken to be one mini-slot. We only consider $M = 4$ in our simulation.

### B. Modification of the Simulator

Two major modifications are done on the simulator used in [9]: (i) generation of non-saturated traffic and (ii) implementation of the algorithm for adaptive waiting time. For a given traffic arrival rate of the users, packet arrivals of the users are generated by using the Poisson process. The generation time of each packet is recorded such that the AP can determine the delay of a received packet. A user tries to access the channel if packet(s) is available in its queue. We assume infinite buffer at the users. In simulator, the process of RTS packet transmission to ACK packet reception remains unchanged. However, waiting time to send the CTS/NCTS packet by the AP is dynamically changed based on the algorithm whenever the AP receives data packets.

### C. Determination of Total Throughput and Packet Delay

We consider 100 instances of 20 user WLAN by randomly generating the positions of the users and each instance is run for 100 s. The total throughput of the users is determined

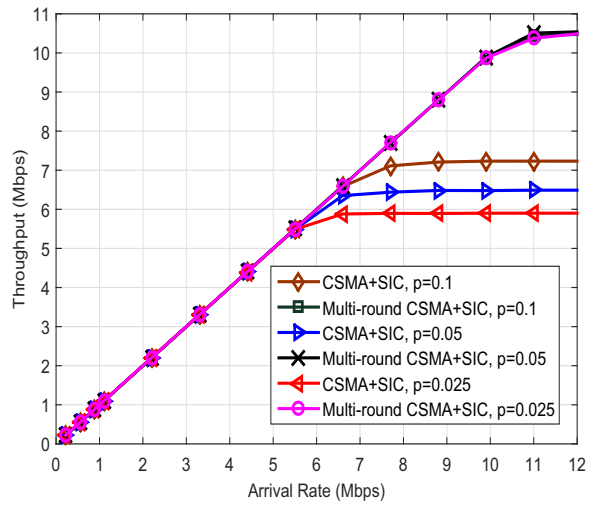


Fig. 2: Comparison of the total throughputs under the single-round and the multi-round contention based MAC protocols with SIC.

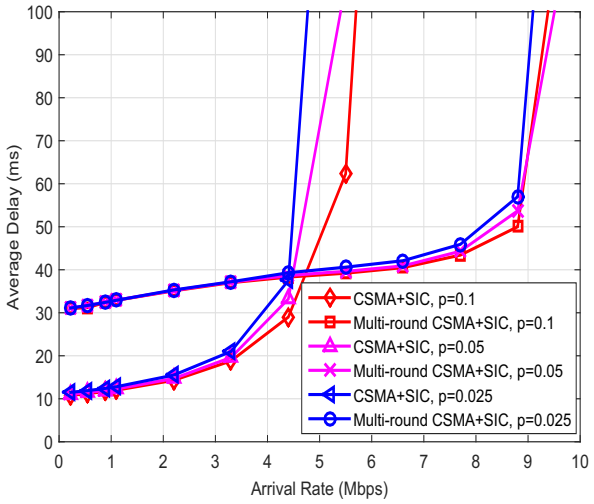


Fig. 3: Comparison of the average packet delays under the single-round and the multi-round contention based MAC protocols with SIC.

from the total received packets by the AP at the end of the simulation of all the instances. To determine the average packet delay, delay of each received packet is recorded by the AP. At the end of simulation of all the instances, the average delay of the packets is calculated.

### *D. Performance Analysis of the Multi-round and the Single-round Contention Based MAC Protocols*

To investigate the performance of multi-round contention based CSMA MAC protocol, the total throughput and the average packet delay are determined via simulation. The fixed waiting time is taken to be 500 mini-slots. The total throughput of the users for different transmission probabilities of the users by varying the traffic arrival rate is shown in Fig. 2. At lower traffic arrival rate, i.e., non-saturation condition, throughput and arrival rate are the same since all the generated packets can be transfer to the AP. However, the network becomes saturated with increasing the traffic rate and hence, the throughput becomes constant even the traffic rate is increased. It is clear that the maximum achievable throughput of the multi-round contention based MAC protocol is significantly higher than that of the single-round contention based MAC protocol. It can be observed that the maximum achievable throughput of the single-round contention based CSMA MAC protocol increases with the increase of transmission probability. It is due to the fact that the number of RTS packet transmitted users increases during the waiting time with increasing the transmission probability hence the opportunities for employing SIC are also increased. However, the throughput of the multi contention based CSMA MAC protocol does not change with changing the transmission probability. We attribute this to the fact that in multi-round contention based MAC protocol, the AP collects $M$ requests during the waiting time for any transmission probability of the users.

The average packet delay for different transmission probabilities of the users by varying the traffic arrival rates is presented in Fig. 3. The results show that for the both MAC protocols, the average delay increases with increasing the traffic arrival rate and it sharply increases when the traffic leads to saturation. At a low traffic rate, the average delay of the single-round contention based MAC protocol is lower than that of the multi-round contention based MAC protocol. Although the average delay of the multi-round contention based MAC protocol at lower traffic rate is only around 30-40 ms but this kind of delay may affect some critical services with low latency requirement.

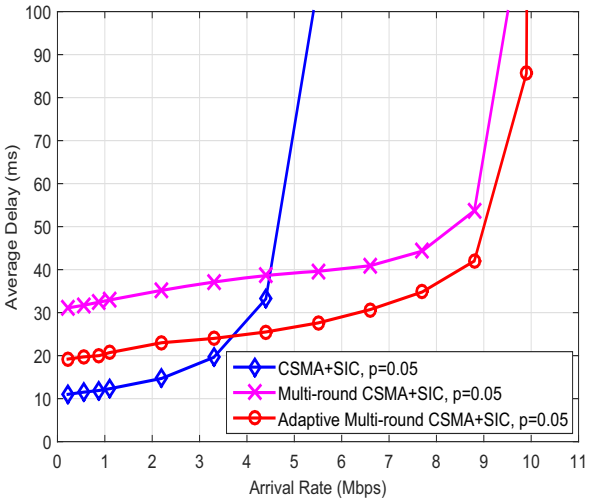


Fig. 4: Comparison of the average packet delays under the single-round, multi-round and the adaptive multi-round contention based MAC protocols with SIC.

### *E. Performance Analysis of the Proposed Algorithm*

The 100 instances of 20-user WLAN system is simulated under the multi-round contention based MAC protocol with the proposed algorithm of adaptive waiting time. The total throughput and the average packet delay are determined at the end of the simulation of all the instances. In simulation, we consider $T_{wait}^{min} = 100$ mini-slots, $T_0 = 50$ ms and $\Delta = 20$ mini-slots. The transmission probability of the users is taken to be 0.05.

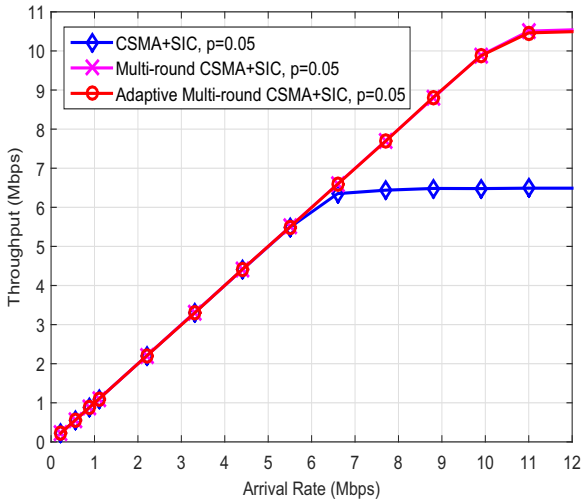


Fig. 5: Comparison of the total throughputs under the single-round, multi-round and the adaptive multi-round contention based MAC protocols with SIC.

Comparison of the average delays under the different MAC protocols is depicted in Fig. 4. The results show that the proposed algorithm reduces the average delay of the packets. To investigate whether the total throughput of the system reduces for implementing the proposed algorithm, the total throughput of the users is shown in Fig. 5. It is clear that the proposed algorithm reduces the average packet delay without affecting the throughput performance.

## V. Conclusion

We have studied the delay and throughput performances in WLANs with multi-round contention based SIC-aware CSMA MAC protocol. It is found that the multi-round contention based SIC-ware MAC protocol provides significantly higher throughput than the traditional single-round contention based MAC protocol. However, the multi-round contention based MAC protocol causes higher packet delay due to the fixed waiting time at the AP for choosing the desired number of users. To reduce the delay of the multi-round contention based MAC protocol, we have proposed a simple algorithm to dynamically adapt the waiting time at the AP based on the traffic condition in the network. We have demonstrated via simulation that by using the proposed algorithm the average packet delay can be reduced in WLANs with multi-round contention based MAC protocol without hampering the throughput performance.

The proposed algorithm in this paper is iterative and it may not provide the optimal results. Further research is necessary to obtain the minimum delay in WLANs with multi-round contention based MAC protocol. Development of an analytical model of delay as function of traffic rate of the users may be the possible drive for future research to adapt the waiting time of the multi-round contention based CSMA MAC protocol.

## References

[1] IEEE Std. 802.11, "Wireless LAN medium access control (MAC) and physical layer (PHY) specification," *IEEE*, New York, USA, Nov. 1997.

[2] D. Gesbert, M. Kountouris, R. W. Heath Jr., C. b. Chae and T. Salzer, "Shifting the MIMO paradigm," *IEEE Signal Processing Magazine*, vol. 24, no. 5, pp. 36-46, Sept. 2007.

[3] S. Verdu, *Multiuser Detection*. Cambridge, U.K.: Cambridge Univ. Press, 1998.

[4] R. Liao, B. Bellalta, T. C. Minh, J. Barceló and M. Oliver, "Uni-MUMAC: A unified down/up-link MU-MIMO MAC protocol for IEEE 802.11ac WLANs," *Wireless Netw.*, vol. 21, no. 5, pp. 1457-1472, Jul. 2015.

[5] M. F. Uddin, "Throughput analysis of a CSMA based WLAN with successive interference cancellation under Rayleigh fading and shadowing," *Wireless Netw.*, vol. 22, no. 4, pp. 1285-1298, May 2016.

[6] P. X. Zheng, Y. J. Zhang and S. C. Liew, "Multipacket reception in wireless local area networks," in Proc. *ICC*, vol. 8, pp. 3670-3675, 2006.

[7] S. Barghi, H. Jafarkhani and H. Youse'zadeh,"MIMO-assisted MPR-aware MAC design for asynchronous WLANs," *IEEE/ACM Trans. on Netw.*, vol. 19, no. 6, pp. 16521665, 2011.

[8] S. Zhou and Z. Niu, "Distributed medium access control with SDMA support for WLANs," *IEICE Transactions*, vol. 93-B, no. 4, pp. 961-970, 2010.

[9] M. F. Uddin and S. Mahmud, "Carrier sensing based medium access control protocol for WLANs exploiting successive interference cancellation," *IEEE Trans. on Wireless Commun.*, vol. 16, no. 6, pp. 4120-4135, June 2017.

[10] A. Iyer, C. Rosenberg and A. Karnik, "What is the right model for wireless channel interference?" *IEEE/ACM Trans. on Netw.*, vol. 8, no. 5, May 2009.

[11] M. Sarker and M. F. Uddin, "Saturation throughput analysis of a carrier sensing based MU-MIMO MAC protocol in a WLAN under fading and shadowing," *Wireless Netw. (Early access),* Nov. 2017.

# Design and Fabrication of a Fiber-Optic Deep-Etched Silicon Fabry-Perot Temperature Sensor

Sanaz Zarei,[1,*] Shamsoddin Mohajerzadeh,[1] and Mahmoud Shahabadi[2]

[1] Thin Film Laboratory, School of Electrical and Computer Engineering, College of Engineering, University of Tehran, Tehran, Iran

[2] Photonics Research Laboratory, School of Electrical and Computer Engineering, College of Engineering, University of Tehran, Tehran, Iran

[*] szarei@ut.ac.ir

*Abstract*— **Design and fabrication of a silicon-based fiber-optic temperature sensor is reported. It is based on a planar Fabry-Perot resonator fabricated on a silicon substrate using highly anisotropic deep reactive ion etching process. Due to the large thermo-optic coefficient and thermal expansion coefficient of silicon, we have typically achieved a sensitivity of 0.5mV/°C in our measurements. The paper also includes a summary of our computational method to analyze the propagation of an optical Gaussian beam throughout the Fabry-Perot cavity fabricated in the silicon substrate.**

***Index Terms***— **Anisotropic deep reactive ion etching, Silicon sensor, Fabry-Perot sensor, Integrated Optics, Optical fiber sensors, Temperature sensors.**

## I. Introduction

In recent years, there have been numerous demands for monitoring temperature in a variety of industrial scenarios in oil/gas exploration, environmental engineering, and high-voltage power systems, to name a few. Fiber-optic temperature sensors are useful in most of the above-mentioned applications due to their compact size, immunity to electromagnetic interference, multiplexing capability, etc. In particular, the thermo-optic effect, which is defined as refractive index variation due to temperature, has been exploited in optical temperature sensors with wide range of measurable temperature and without any self-heating effect.

Crystalline silicon is desirable for high-resolution and high-speed temperature sensing, as it is highly transparent over infrared wavelengths and shows a large thermo-optic coefficient which yields a higher temperature sensitivity. Silicon-based temperature sensors also ensure short response time because of the large thermal diffusivity of silicon. Moreover, silicon-based sensors have inherent low processing cost and can be integrated with conventional electronic integrated circuits through fully matured fabrication technologies.

Diverse silicon photonic structures have been demonstrated for implementation of temperature sensors. These include ring resonator structures fabricated in a silicon substrate [1-6], silicon photonic-crystal fiber tip sensors [7-11], an array of silicon Fabry-Perot interferometers working on the principle of optical phase shift [12], silicon Fabry-Perot sensors fabricated by sputtering an approximately one-micron thick silicon layer on the tip of an optical fiber [13-15]. A silicon pillar on the tip of a single-mode fiber on the basis of Fabry-Perot interferometry [16].

In this paper, we propose an optical temperature sensor based on the thermo-optic effect of silicon. It consists of a vertical Fabry-Perot resonator fabricated on a silicon substrate. The in-plane design of our sensor, in which the Fabry-Perot resonator is realized by vertically etched walls, facilitates fiber alignment. Moreover, this sensor can readily be integrated inside electronic devices to enable direct measurement of the device temperature, which is usually required in high-precision measurements and calibration. The proposed silicon Fabry-Perot resonator is fabricated by deep reactive-ion etching of silicon in a capacitively coupled plasma etcher, which was challenging due to the large depth of the cavity. The fabricated sensor is characterized by direct monitoring of optical power at a fixed wavelength. To design this sensor, a numerical analysis is developed based on the transfer-matrix formulation to estimate propagation path of Gaussian beams within a silicon Fabry-Perot resonator. Here, we begin with introducing our numerical analysis.

## II. Operation Principle

### A. Optical Analysis

The proposed structure consists of a Fabry-Perot resonator with two deep-etched silicon bars located at the end of a fiber U-groove. Figure 1 shows a schematic of the resonator assembly. A Gaussian beam emerging from the input fiber end facet at $z = 0$ irradiates the air-silicon interface at $z = d$. To simplify the analysis, we assume two-dimensional beam propagation. An analogous analysis to the one presented here was pursued in [17] for propagation of optical beams through one-dimensional photonic band-gap structures.

The silicon resonator is characterized by $l$ (resonator length) and $n$ (resonator refractive index). The following equations are used in our analysis to predict the experimental results. The two-dimensional Gaussian beam at the output interface of the fiber is as follows:

$$E(x) = e^{\frac{x^2}{\sigma^2}} = \frac{1}{2\pi}\int_{-\infty}^{\infty} \widetilde{E}(k_x)\, e^{-jk_x x} dk_x \quad at\ z = 0 \tag{1}$$

The plane-wave expansion equivalent to this optical beam can be obtained using the Fourier transform:

$$\widetilde{E}(k_x) = \int_{-\infty}^{\infty} E(x)\, e^{jk_x x} dx = \sqrt{\pi}\sigma\, e^{-\frac{1}{4}k_x{}^2\sigma^2} \tag{2}$$

where $\sigma$ determines the Gaussian beam width.

978-1-5386-3374-8/17/$31.00 ©2017 IEEE

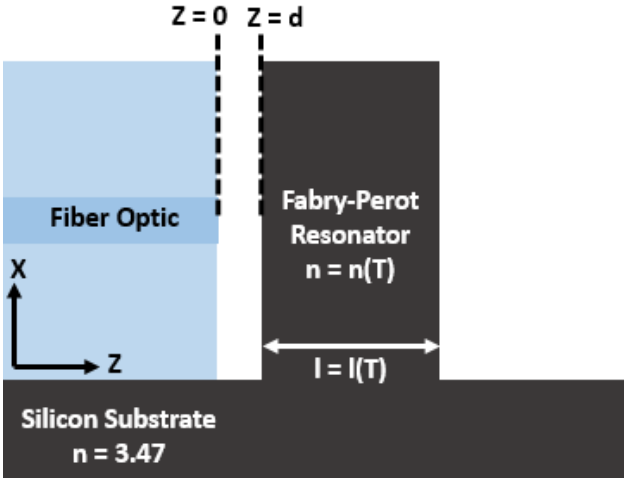


Fig. 1 Schematic of the proposed silicon-based sensor.

Hence, the incident Gaussian beam $E^i$ at the input plane of the Fabry-Perot resonator at $z = d$ is described by:

$$E^i = \frac{1}{2\pi}\int_{-\infty}^{\infty} \tilde{E}(k_x)\, e^{-jk_x x} e^{-jk_z d}\, dk_x \quad at\ z = d \tag{3}$$

where $k_z = \sqrt{k_0^2 - k_x^2}$ . To calculate the electric field of the reflected beam, the transfer matrix formulation is used in which propagation through the resonator is described by a 2×2 chain matrix:

$$M = \begin{bmatrix} a_{11} & a_{12} \\ a_{21} & a_{22} \end{bmatrix} = \begin{bmatrix} \cos(\delta) & j\eta_T \sin(\delta) \\ j\eta_T^{-1} \sin(\delta) & \cos(\delta) \end{bmatrix} \tag{4}$$

where the phase $\delta$ is:

$$\delta = k_0\, n\, l \cos\theta \tag{5}$$

and the characteristic impedance is:

$$\eta_T = \begin{cases} \eta \cos\theta & for\ TE_Z\ polarization \\ \eta / \cos\theta & for\ TM_Z\ polarization \end{cases} \tag{6}$$

in which $\eta = \sqrt{\mu_o / n^2 \varepsilon_o}$ . In the above equations, $k_0 = \frac{2\pi}{\lambda}$ denotes the free-space wavenumber and $\theta$ is the angle of incidence within the resonator, which is calculated for a given $k_x$ using Snell's law, i.e., $n \sin\theta = k_x / k_o$ . Thus, the wave reflected from the Fabry-Perot resonator $E^r$ is obtained as

$$E^r = \frac{1}{2\pi}\int_{-\infty}^{\infty} \tilde{E}(k_x)\Gamma_{in}(k_x)\, e^{-jk_x x} e^{-j2k_z d}\, dk_x \quad at\ z = 0 \tag{7}$$

where $\Gamma_{in}(k_x)$ is the electric field reflection coefficient. Finally, the overlap integral

$$\eta(\lambda) = \frac{\left|\left\langle E^r, E_{fiber}\right\rangle\right|^2}{\left\langle E^r, E^r\right\rangle\left\langle E_{fiber}, E_{fiber}\right\rangle} \tag{8}$$

is calculated to determine that portion of the reflected beam which is coupled into the fundamental mode of the single-mode fiber. Obviously, $\left\langle E^r, E_{fiber}\right\rangle$ depicts the inner product of the reflected wave by the mode field of the fiber.

The spectrum of the reflected wave is obtained from the reflected and incident fields and the overlap integral as:

$$I(\lambda) = \eta(\lambda)\frac{\left\langle E^r, E^r\right\rangle}{\left\langle E^i, E^i\right\rangle} \tag{9}$$

The outcome of this calculation depends on the phase factor $\delta$ which is related to the length $l$ of the Fabry-Perot resonator, the wavelength $\lambda$ of the radiation, the wavenumber $k_x$, and the refractive index of silicon $n$ . Figure 2 depicts the reflected wave intensity as a function of wavelength for cavity length of 100um. The reflected wave is calculated for three different temperature values, due to temperature dependence of the refractive index of silicon. The Gaussian beam width is assumed to be 9um as is for commercially available single-mode fibers.

Due to operation wavelength of 1.55um for available laser diodes, the main concern is whether this wavelength is the proper one for sensor operation. As is inferred from fig. 2, at the wavelength of 1.55um, the reflection intensity is maximum at zero temperature and reaches its minimum at 20℃.

Therefore, in the temperature range of 0 to 20℃, the sensor has maximum reflection variations at the wavelength of 1.55um. Thus, this wavelength is a suitable choice for input light in terms of dynamic range and sensitivity through the device temperature range.

### *B. Temperature Analysis*

Any temperature variation alters silicon refractive index due to the thermo-optic effect. It also alters the cavity length due to thermal expansion effect.

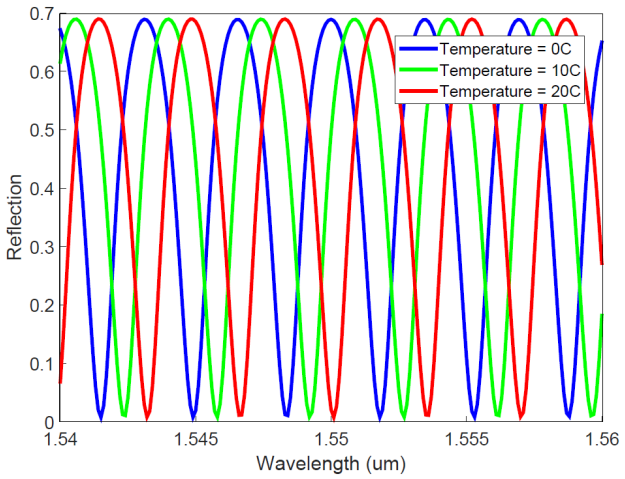


Fig. 2 Reflected wave intensity as a function of wavelength for cavity length of 100um for three different temperature values.

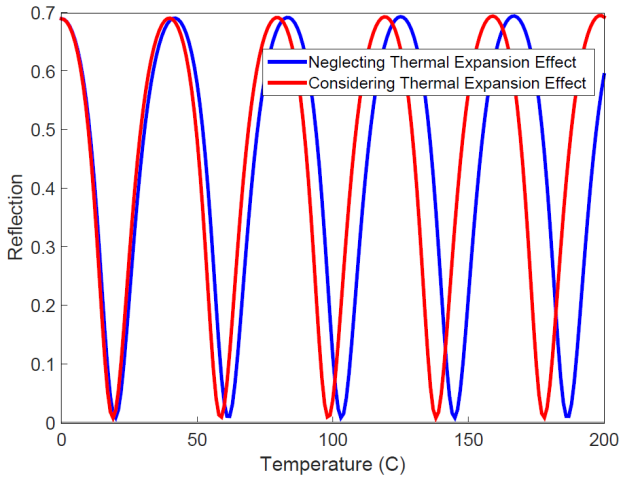


Fig. 3 Reflected wave intensity as a function of temperature for cavity length of 100um. The red curves indicate the simulation results for the case of considering thermal expansion effect and the blue curves indicate the case of neglecting thermal expansion effect.

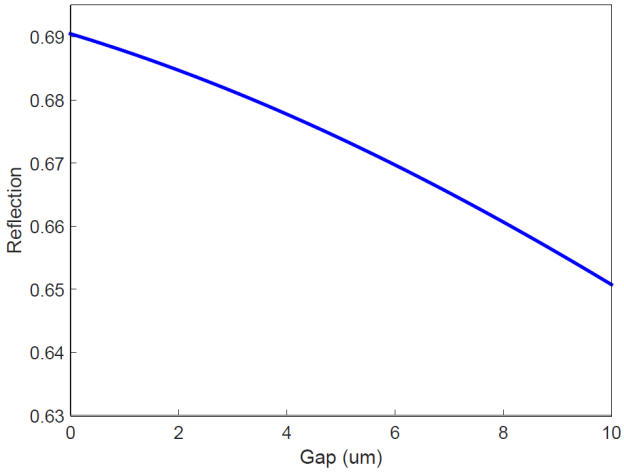


Fig. 4 Reflected wave intensity as a function of the existing gap between cleaved fiber tip and the Fabry-Perot resonator input facet for cavity length of 100um for a temperature of zero degree centigrade.

They finally lead to a variation of the reflected light which is being measured as the sensor output. Differentiating $\delta$ with respect to $T$ leads to the temperature sensitivity of the cavity [12]:

$$\frac{d\delta}{dT} = \frac{2\pi}{\lambda} nl\cos\theta\left(\frac{1}{n}\frac{dn}{dT} + \frac{1}{l}\frac{dl}{dT}\right) \tag{10}$$

Here, the first term on the right hand side consists of $\frac{dn}{dT}$, which is the thermo-optic coefficient of silicon, and the second term is the thermal expansion of silicon. For single-crystal silicon, $\frac{\partial l}{l\partial T} = 2.6\times10^{-6}\,K^{-1}$ and $\frac{\partial n}{\partial T} = 1.86\times10^{-4}\,K^{-1}$. Variation in $\delta$ due to thermal expansion coefficient of silicon is a factor of 100 smaller than that of the thermo-optic effect of silicon. However, it can't be neglected for large cavity lengths. Figure 3 shows the computed reflected wave intensity as a function of temperature for cavity length of 100um. This figure includes two cases, the one considering thermal expansion effect and the one neglecting thermal expansion.

### C. *Effect of Air Gap on Temperature Response*

In all the above figures, it is assumed that $d = 0$, which means that the fiber end facet is in contact with the input interface of the Fabry-Perot resonator. However, in real case, an air gap always exists between the two interfaces due to an unwanted curvature in the input facet of the cavity during vertical etching of silicon. We have estimated the impact of this gap on the response of our sensor. This is shown in Fig. 4.

As can be seen in this diagram, when the air gap is increased, the reflection amplitude decreases. The maximum reflected wave is obtained as the fiber is in direct contact with the cavity. However, the performance of the sensor is not too much affected by the existence of the gap.

## III. EXPERIMENTS

### A. *Device Fabrication*

In this research, the fabrication process is mainly based on deep reactive ion etching of silicon. For the sake of highly-vertical walls as well as smooth vertical surfaces and to preserve time and cost, we presented a novel semi-sequential method which is based on a two separate sub-cycles of etching and passivation in which the etching step utilizes $SF_6$ gas and passivation step employs $H_2$, $O_2$ and $SF_6$ gases.

The etching is achieved in a reactive ion etching (RIE) machine operating at 13.56 MHz with an effective area of 20×15cm2 (Fig. 5). The operation of all parts of this unit is controlled by computers. The gas flow is controlled by means of mass flow meters. A combination of roots and rotary mechanical pumps control pressure in our process. A typical pressure of 200-800mTorr is used in this process. Here, P-type (100) silicon wafers are used. After cleaning the silicon substrates using a RCA No.1 solution, they are blow dried and a 80-nm chromium layer is deposited as a masking film using an electron-beam evaporation system. After patterning the masking layer using standard photolithography, the sample is ready for loading into etching reactor. To avoid serious variations in the etch rate, the silicon samples have to be placed in the central rectangle.

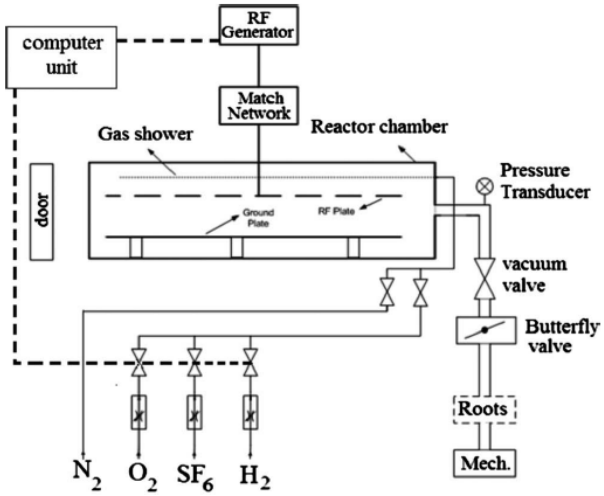


Fig. 5 Schematic of the reactive ion etching machine.

The etching process which is employed in this work is very similar to the one presented in [18-19] where a sequential etching/passivation procedure is utilized. In the passivation sub-cycle, a mixture of $SF_6$, $H_2$ and $O_2$ gases are fed into the chamber. Oxygen radicals oxidize the side surfaces of the sample, whereas hydrogen ion bombardment removes the bottom oxide and results in an improvement of etching directionality. To initiate the etching sub-cycle, $SF_6$ gas which contains fluorine radicals flows into the chamber. These radicals which react with exposed silicon can cause isotropic etching of silicon.

However, opposed to the method presented in [18-19], there is no purging steps between the sub-cycles to evacuate the chamber and ensure proper switching between gases. So a little trace of reactant gases from the previous sub-cycle remains in the chamber and assist to the process in the current step. Especially, in etching sub-cycle, a little trace of $O_2$ and $H_2$ gases helps to minor passivation of the sidewalls. This helps to achieve more verticality and smoothness of sidewalls as well as fast etching progress with high etch-rate.

By adjusting plasma parameters of both sub-cycles, such as plasma power, flow of gases, chamber pressure and duration of etching and passivation step, verticality and smoothness of sidewalls can be enhanced. The obtained optimum parameters are shown in table 1.

TABLE I
PLASMA PARAMETERS IN OUR SEMI-SEQUENTIAL PROCESS

| | $SF_6$ (sccm) | $O_2$ (sccm) | $H_2$ (sccm) | Power (W) | Time (s) |
|---|---|---|---|---|---|
| Etching | 0 | 140 | 0 | 140-190 | 10 |
| Passivation | 230 | 13 | 620 | 270 | 6 |

Figure 6 shows the obtained structure with the etch depth of 85um. This process has a moderate etch rate of 0.53um/min caused by longer etching duration and shorter passivation period, which makes this method more cost-effective comparing with the one presented in [18-19]. Due to longer etching duration with respect to passivation, we set the passivation power to the maximum obtainable power of the RIE machine in order to strengthen passivation while keeping it short.

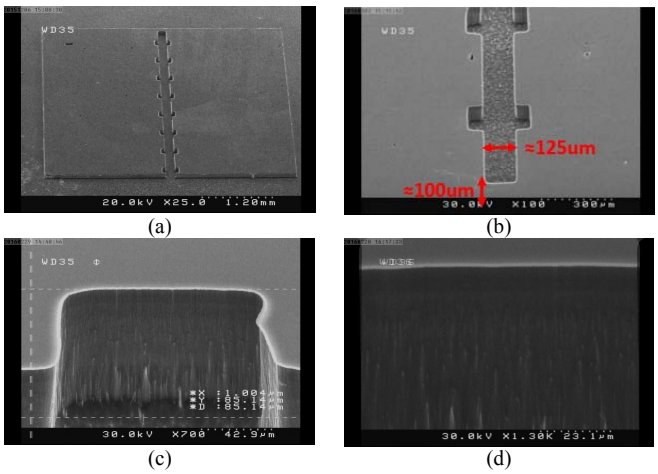


(a) (b) (c) (d)

Fig. 6 SEM images of the fabricated sensor. (a) and (b) show the top-view of the sensor. It consists of a U-groove for mounting the fiber and some side teeth to fix the fiber with high-temperature glue. (c) and (d) show the close-up view of the sidewalls. The sidewalls are sharp and vertical with low roughness.

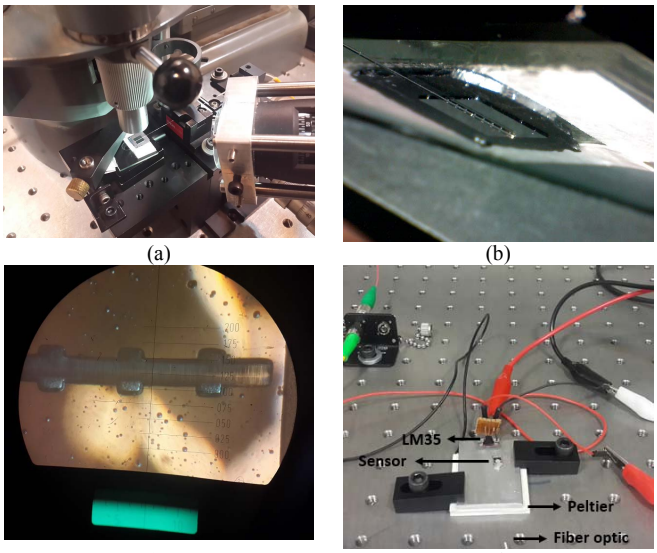


(a) (b) (c) (d)

Fig. 7 (a) The alignment setup for the sensor along with a single-mode fiber. (b) and (c) The microscope photograph of the fiber mounted into the U-groove. (d) The measurement setup.

## B. *Setup Description*

Our measurement setup consists of the fiber sensor connected to a 3dB coupler. The sensor chip is glued onto a peltier heat pump together with a calibrated LM35 thermocouple which allows independent monitoring of temperature.

The sensor is tested at the fiber-optic wavelength of 1.55um using a pigtailed single-mode fiber. The alignment and measurement setup are shown in Fig. 7. Mounting the input fiber into the U-groove is a rather critical step.

The radiation was launched into the cavity via a 3 dB dual directional coupler, while the intensity of the wave reflected from the input facet was collected by the same coupler and delivered to an InGaAs photodiode which was connected to an oscilloscope to monitor the variations of the reflected signal (Fig. 8) without any required expensive spectral monitoring.

## C. *Measurement*

Our measurements include only a small verification of our theoretical analysis. More complete measurements are now underway. The measured reflected wave intensity for a 100um-long cavity is reported in Fig. 9. As shown in this figure, the reflection intensity is changing periodically with increasing temperature as predicted by our simulations (See Fig. 3). Note that due to unwanted under-etching of the cavity walls, the actual length of the fabricated cavity is shorter than the designed value. Also an air gap exists between the fiber and the cavity facet. These phenomena result in a small discrepancy between the measurements and simulations.

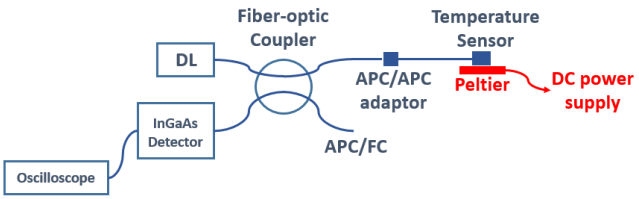


Fig. 8 Optical setup for amplitude reflection measurement: diode laser source DL, InGaAs photodiode detector, along with other components are seen in this figure.

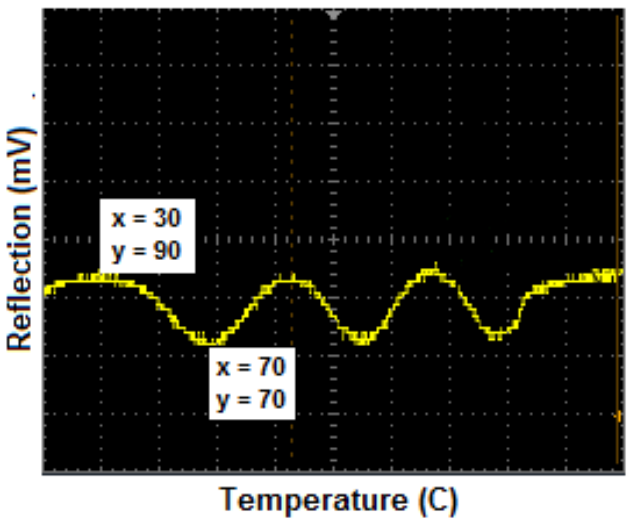


Fig. 9 Reflected wave amplitude as a function of temperature.

As can be deduced from figure, the temperature range of this sensor is between 30℃ to 70℃, which is approximately the linear region between a maximum and a minimum of reflection. Also it is seen that with a temperature change of 40℃ across the temperature range of 30℃ to 70℃, the reflected intensity varies by 20mV. This results in temperature sensitivity of 0.5mV/℃ in this temperature range.

## IV. Conclusion

We have designed, analyzed, and fabricated a temperature sensor composed of a vertical silicon Fabry-Perot resonator operating based on the thermo-optic effect in silicon. The resonator walls have been fabricated by deep reactive ion etching of silicon which facilitates compatibility with other optoelectronic devices. The lowest measured temperature sensitivity of the sensor is 0.5mV/℃, which is obtained at the telecommunication wavelength of 1.55μm. We also presented the design procedure for the sensor using a transfer-matrix formulation for Gaussian beams.

## Acknowledgment

The authors would like to thank Mr. Hamidreza Neshasteh and Mr. Amideddin Mataji-Kojouri from the Photonics Research Lab., School of ECE, University of Tehran, for their invaluable help in these measurements.

## References

[1] G. Kim, H. Lee, C. Park, S. Lee, B. Lim, H. Bae and W. Lee, "Silicon photonic temperature sensor employing a ring resonator manufactured using a standard CMOS process", *Opt. Express*, vol. 18, no. 21, pp. 22215-21, Oct. 2010.

[2] H. Xu, M. Hafezi, J. Fan, J. Taylor, G. Strouse and Z. Ahmed, "Ultra-sensitive chip-based photonic temperature sensor using ring resonator structures", *Opt. Express*, vol. 22, no. 3, pp. 3098-3104, Feb. 2014.

[3] H. Lee, G. Kim, W. Kim, S. Lee and W. Lee, "Tunable-Resonator-Based Temperature Sensor Interrogated through Optical Power Detection", *Appl. Phys. Express*, vol. 4, no. 10, p. 102201, Oct. 2011.

[4] H. Kim and M. Yu, "Cascaded ring resonator-based temperature sensor with simultaneously enhanced sensitivity and range", *Opt. Express,* vol. 24, no. 9, pp. 9501-10, May 2016.

[5] C. Qiu, T. Hu, P. Yu, A. Shen, F. Wang, X. Q. Jiang, and J. Y. Yang, "A temperature sensor based on silicon eye-like microring with sharp asymmetric fano resonance," *IEEE 9th International Conference on Group IV Photonics (GFP),* Aug. 2012.

[6] N. Klimov, M. Berger and Z. Ahmed, "Towards Reproducible Ring Resonator Based Temperature Sensors," *Sensors & Transducers J.*, vol. 191, no. 8, pp. 63-66, Aug. 2015.

[7] I. Jung, B. Park, J. Provine, R. Howe and O. Solgaard, "Highly Sensitive Monolithic Silicon Photonic Crystal Fiber Tip Sensor for Simultaneous Measurement of Refractive Index and Temperature", *J. Lightwave Technol.,* vol. 29, no. 9, pp. 1367-74, March 2011.

[8] B. Park, I. W. Jung, J. Provine, A. Gellineau, J. Landry, R. Howe and O. Solgaard, "Double-Layer Silicon Photonic Crystal Fiber-Tip Temperature Sensors", *IEEE Photon. Technol. Lett.*, vol. 26, no. 9, pp. 900-903, March 2014.

[9] B. Park, J. Provine, I. Jung, R. Howe and O. Solgaard, "Photonic Crystal Fiber Tip Sensor for High-Temperature Measurement", *IEEE Sensors J.*, vol.11, no. 11, pp. 2643-48, May 2011.

[10] I. Jung, B. Park, J. Provine, R. T. Howe and O. Solgaard, "Photonic Crystal Fiber Tip Sensor for Precision Temperature Sensing," *IEEE LEOS Annual Meeting Conference*, Oct. 2009.

[11] B. Park, I. Jung, J. Provine, R. T. Howe and O. Solgaard, "Monolithic Silicon Photonic Crystal Fiber Tip Sensor for Refractive Index and Temperature Sensing," *IEEE Conference on Lasers and Electro-Optics and Quantum Electronics and Laser Science*, May 2010.

[12] G. Cocorullo, F. Della Corte, M. Iodice, I. Rendina and P. Sarro, "A temperature all-silicon micro-sensor based on the thermo-optic effect", *IEEE Trans. on Electron Devices*, vol. 44, no. 5, pp. 766-774, May 1997.

[13] G. Beheim, J. Sotomayor, M. Tuma, "Laser-annealed thin-film fiber-optic temperature sensor," *Proc. SPIE*, vol. 2045, pp. 217-221, Aug. 1993.

[14] L. Schultheis, H. Amstutz, and M. Kaufmann, "Fiber-optic temperature sensing with ultrathin silicon etalons", *Opt. Lett.*, vol. 13, no. 9, pp. 782-784, Sept. 1988.

[15] J. W. Berthold, S. E. Reed, and R. G. Sarkis, "Reflective fiber optic temperature sensor using silicon thin film", *Opt. Eng.*, vol. 30, no. 5, pp. 524-528, May 1991.

[16] G. Liu, M. Han, and W. Hou, "High-resolution and fast-response fiber-optic temperature sensor using silicon Fabry-Perot cavity", *Opt. Express*, vol. 23, no. 6, pp. 7237-47, March 2015.

[17] A. Lipson and E. M. Yeatman, "A 1-D photonic band gap tunable optical filter in (110) silicon", *J. Microelectromech. Syst.*, vol. 16, no. 3, pp. 521-527, June 2007.

[18] S. Azimi, M. Mehran, A. Amini, A. Vali, S. Mohajerzadeh and M. Fathipour, "Formation of three-dimensional and nanowall structures on silicon using a hydrogen-assisted high aspect ratio etching", *J. Vac. Sci. Technol. B,* vol. 28, no. 6, pp. 1125-31, Oct. 2010.

[19] A. Sammak, S. Azimi, N. Izadi, B. Hosseinieh and S. Mohajerzadeh, "Deep Vertical Etching of Silicon Wafers Using a Hydrogenation-Assisted Reactive Ion Etching", *Journal of Microelectromech. Syst.*, vol. 16, no. 4, pp. 912-918, Aug. 2007.

*2017 IEEE International Conference on Telecommunications and Photonics (ICTP)*
*26-28 December, 2017, Dhaka, Bangladesh*


# Analytical Model for Coupling Whisperring Gallery Mode Spherical Microresonator for Sensing Application

Shovasis Kumar Biswas*, Abdullah al Noman, Md. Rubayet Islam, S. M. Rakibul Islam,
Md. Tawhid Islam Opu, Feroz Ahmed
Department of Electrical and Electronic Engineering
Independent University, Bangladesh
*shuvoapece@gmail.com

***Abstract*—An analytical expression for the coupling of whispering gallery mode is derived by adding the coupling and intrinsic loss terms. We found smaller negative frequency shift for higher order mode when nonlinear coefficient is smaller consistent with the reported experimental observations. The resonant frequency of a weak probe mode can be shifted by a strong pump mode due to XPM and the frequency shift of the probe is proportional to the pump energy. We found large negative frequency shift when pump and probe power are perfectly matched. This result opens up a range of new applications in nonlinear sensing and quantum optics.**

**Keywords - Coupled-mode theory, microcavity, microsphere, resonator.**

## I. Introduction

Whispering gallery modes (WGM) microcavity have played an ubiquitous role due to their high quality factor Q and small effective mode volume $V_{eff}$. They are suitable for different applications and scientific research which includes quantum electrodynamics (QED) [1], microlasers [2]–[5], Raman lasers [6]–[9], sensing [10]–[12], parametric oscillation [13], frequency comb [14], [15] and so forth. In huge numbers of these applications, light should be coupled into the micro sphere without any changing of high quality factor, Q. There are a number of methods to couple light into the micro sphere. Among all of the methods, the most widely used are the tapered fiber [16], prism coupler [17], and polished half-block coupler. Tapered fibre are widely used for device applications. The main goal of this paper is to derive an analytical formula for coupling Whispering gallery mode by taking into account the intrinsic loss and coupling loss terms.

We developed an analytical model to explain the impact of Kerr nonlinearity on silica microsphere and we found large negative frequency shift for resonant modes which is proportional to the mode energy [18], [19]. Recently, We investigated nonlinear interaction between two WGMs due to cross phase modulation (XPM) and stimulated Raman scattering (SRS) and we found negative frequency shift for resonant mode which depends on both the energy of resonant mode and the energy of the other mode. Taking into account the delayed Raman response, we also developed analytical expressions for transferring energy between Stokes and pump wave considering SPM and XPM effects.

In this paper, we present a new extension of the impact of Kerr effect to study the multimode coupling of Whisperring gallery mode due to cross-phase modulation (XPM). We develop an analytical expression for the coupling of whispering gallery mode is by adding the coupling and intrinsic loss terms. We found large negative frequency shift depending on pump power and probe power. Our result show that frequency shift is large when both pump power and probe power are perfectly matched. However, to the best of our knowledge, coupling of Whispering gallery mode has not been analytically modelled previously to explain cross-phase modulation effect by taking tensor in spherical co-ordinates.

## II. Mathematical description of coupling to whispering gallery mode microcavity resonators

In a Whispering gallery mode microcavity, optical energy transfer in between cavity resonator and wave guide can be explained with a simple model which is shown in Fig.1. The resonant frequency is the most important coupling parameter. Another two important coupling parameters are internal lifetime, $\tau_p^{-1}$ and external lifetime $\tau_{ex}^{-1}$. Internal lifetime is the cavity decay rate due to cavity internal loss and external time is the decay rate due to coupling resonator to the waveguide.

According to the H. Haus, coupling of Whispering gallery modes can be explained by the following equation [21]–[23]

$$\frac{dq}{dt} = -\frac{1}{2}\left(\frac{1}{\tau_0} + \frac{1}{\tau_{ex}}\right)q + i\kappa_0 s \tag{1}$$

where q signifies the slowly varying amplitude in the cavity resonator and s denotes the input wave. The coupling into the waveguide is denoted by $\tau_{ex}$ (external lifetime). The coupling coefficient $\kappa_0$ is related to the $\tau_{ex}$ which denotes the coupling in to the waveguide and is given by

$$\kappa_0 = \sqrt{\frac{1}{\tau_{ex}}} \tag{2}$$

*978-1-5386-3374-8/17/$31.00 ©2017 IEEE*

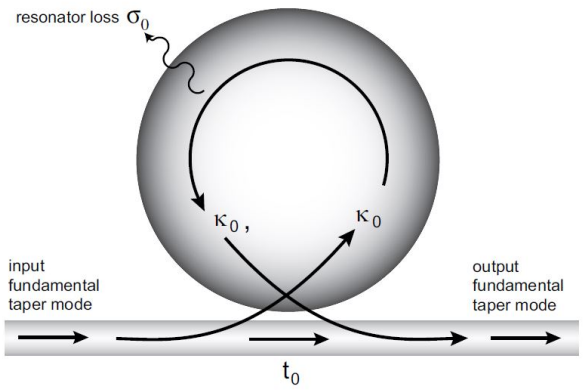


Fig. 1. Schematic of a waveguide coupled resonator.

Depending on the relation between $\tau_0$ and $\tau_{ex}$, the transmission through the waveguide can be described by the following equation

$$T = \Big(\frac{\tau_{ex} - \tau_0}{\tau_{ex} + \tau_0}\Big)^2 = \Big(\frac{1-K}{1+K}\Big)^2 \tag{3}$$

where $K$ is the dimensionless coupling parameter which is defined as the ratio of coupling between resonator and waveguide to intrinsic resonator loss. Depending on $K$, the transmission profile can be characterized by the three coupling regime.

Under coupling ($K = 1$): Under coupling means the waveguide coupling is weak and the rate of cavity decay $\tau_0^{-1}$ exceeds the cavity coupling rate $\tau_{ex}^{-1}(\tau_0^{-1} > \tau_{ex}^{-1})$. This regime is called undercoupled due to the fact that in this regime cavity loss is always greater than the coupling loss.

Over coupling ($K > 1$): Over coupling refers to the regime where output coupling dominates the loss. In this case cavity coupling loss larger than the cavity internal loss.

Critical coupling ($K = 1$): At critical coupling, both input coupling and cavity internal loss are equal i.e. ($K = 1$). As there is no waveguide transmission at critical coupling, so complete power is coupled into the microcavity.

## III. Single Mode Coupling of WGMs resonators

We developed an analytical model to describe the Kerr effect on a spherical microcavity by treating loss as perturbations [18].

$$i\Big(\frac{\partial q}{\partial t} + \frac{q}{2\tau_p}\Big) = \gamma|q|^2 q, \tag{4}$$

where $\tau_p$, denote the photon lifetime with the resonant frequency $\omega$.

If the resonator is coupled to an external waveguide or to the outside space, one can easily proceed and add coupling and intrinsic loss terms in Eqs. (4). Now, considering the input wave $s$ and coupling coefficients $\kappa_0$, we find

$$i\Big(\frac{\partial q}{\partial t} + \frac{q}{2\tau_p}\Big) = \gamma|q|^2 q + i\kappa_0 s, \tag{5}$$

For solving Eqs. (5), let

$$q(t) = B(t)e^{i\theta(t)}, \tag{6}$$

where $B(t)$ denote the amplitude and $\theta(t)$ denote the pahse. Now, solving Eq. (6) and Eq. (5), we find

$$\frac{dq}{dt} = \big(\frac{dB}{dt} + i\frac{d\theta}{dt}B\big)e^{i\theta}. \tag{7}$$

From Eq. (5), we have

$$i\frac{dB}{dt} - \frac{d\theta}{dt}B + i\frac{B}{2\tau_p} = \gamma B^2 B + i\kappa_0 s. \tag{8}$$

Separating real and imaginary parts of Eq. (8), we obtain

$$\frac{dB}{dt} + \frac{B}{2\tau_p} = \kappa_0 s, \tag{9}$$

$$\frac{d\theta}{dt} = -\gamma B^2(t). \tag{10}$$

Integrating Eqs. (9) and (10), we obtain

$$B(t) = 2\kappa_0 s\tau_p(1 - e^{-t/2\tau_p}), \tag{11}$$

$$\theta(t) = -\gamma\Big[4\kappa_0^2 s^2\tau_p^2\big\{t + \big(1 - e^{-t/\tau_p}\big)\tau_p - \big(1 - e^{-t/2\tau_p}\big)4\tau_p\big\}\Big], \tag{12}$$

Frequency shift in a microsphere can be written as

$$f(t) = -\frac{\gamma}{2\pi}\Big[4\kappa_0^2 s^2\tau_p^2\big(1 + e^{-t/\tau_p} - 2e^{-t/2\tau_p}\big)\Big]. \tag{13}$$

## IV. multi mode Coupling of WGMs resonators

We have derived an analytical model for describing the impact of self phase modulation and cross phase modulation in a Whispering gallery mode microcavity by considering tensor nature of $\chi^3$ in spherical co-ordinates [19], [20].

$$i\Big(\frac{dq_1}{dt} + \frac{q_1}{2\tau_{p1}}\Big) = \Big[\gamma_{11}|q_1|^2 + \gamma_{12}|q_2|^2\Big]q_1, \tag{14}$$

$$i\Big(\frac{dq_2}{dt} + \frac{q_2}{2\tau_{p2}}\Big) = \Big[\gamma_{21}|q_1|^2 + \gamma_{22}|q_2|^2\Big]q_2, \tag{15}$$

where $\tau_{pj}$, $(j = 1, 2)$ denote the photon lifetime with the resonant frequency $\omega_j$, given by

$$\tau_{pj} = \frac{\int \vec{f}^{(j)}(\vec{r}).\vec{f}^{(j)^*}(\vec{r})dv}{\omega_j \int \big[n_i^2(r)\vec{f}^{(j)}(\vec{r}).\vec{f}^{(j)^*}(\vec{r})\big]dv/n^2(r)}, \tag{16}$$

If the resonator is coupled to an external waveguide or to the outside space, one can easily proceed and add coupling and intrinsic loss terms in Eqs. (4) and (5)

$$i\Big(\frac{dq_1}{\partial t} + \frac{q_1}{2\tau_1}\Big) = \Big[\gamma_{11}|q_1|^2 + \gamma_{12}|q_2|^2\Big]q_1 + i\kappa_1 s_1, \tag{17}$$

$$i\Big(\frac{dq_2}{\partial t} + \frac{q_2}{2\tau_2}\Big) = \Big[\gamma_{21}|q_1|^2 + \gamma_{22}|q_2|^2\Big]q_2 + i\kappa_2 s_2, \tag{18}$$

where

$$\frac{1}{\tau_j} = \frac{1}{\tau_{pj}} + \frac{1}{\tau_{ex,j}}, \qquad j = 1, 2, \tag{19}$$

Here $q_j(j = 1, 2)$ signifies the slowly varying amplitude and $s_j(j = 1, 2)$ denotes the input wave. $\tau$ denote the whole life time of incident photons in the WGM microcavity, which is summation of intrinsic lifetime, $\tau_{pj}(j = 1, 2)$ and external lifetime (coupling into the waveguide), $\tau_{ex,j}(j = 1, 2)$. The coupling coefficient $\kappa_j(j = 1, 2)$ is related to $\tau_{ex,j}(j = 1, 2)$, which is given by

$$\kappa_j = \sqrt{\frac{1}{\tau_{ex,j}}}, \qquad j = 1, 2. \tag{20}$$

For large amount of coupling we consider critical coupling ($\tau_{pj} = \tau_{ex,j}$). At critical coupling, complete power is coupled into the microcavity. To solve Eqs. (7) and (8), let

$$q_j = B_j(t)e^{i\theta_j(t)}, \qquad j = 1, 2, \tag{21}$$

where $B_j(t)$ indicate amplitude and $\theta_j(t)$ indicate phase, respectively. Subtituting Eq. (21) in Eqs. (14) and (15), we find

$$\frac{dq_j}{dt} = \Big(\frac{dB_j}{dt} + i\frac{d\theta_j}{dt}B_j\Big)e^{i\theta_j}. \tag{22}$$

From Eqs. (7) and (8), we have

$$i\frac{dB_1}{dt} - \frac{d\theta_1}{dt}B_1 + i\frac{B_1}{2\tau_1} = \big(\gamma_{11}B_1^2 + \gamma_{12}B_2^2\big)B_1 + i\kappa_1 s_1, \tag{23}$$

$$i\frac{dB_2}{dt} - \frac{d\theta_2}{dt}B_2 + i\frac{B_2}{2\tau_2} = \big(\gamma_{21}B_2^2 + \gamma_{22}B_1^2\big)B_2 + i\kappa_2 s_2. \tag{24}$$

Separating real and imaginary parts of Eqs. (13) and (14), we obtain

$$\frac{dB_j}{dt} + \frac{B_j}{2\tau_j} = \kappa_j s_j, \qquad j = 1, 2, \tag{25}$$

$$\frac{d\theta_j}{dt} = -[\gamma_{jj}B_j^2 + \gamma_{jk}B_k^2], \qquad j = 1, 2, \quad k = 3 - j. \tag{26}$$

Integrating Eqs. (15) and (16), we obtain

$$B_j(t) = 2\kappa_j s_j \tau_j (1 - e^{-t/2\tau_j}), \qquad j = 1, 2, \tag{27}$$

$$\theta_j(t) = \theta_{j,SPM}(t) + \theta_{j,XPM}(t), \tag{28}$$

$$\theta_{j,SPM}(t) = -\gamma_{jj}\Big[4\kappa_j^2 s_j^2 \tau_j^2\big\{t + \big(1 - e^{-t/\tau_j}\big)\tau_j - \big(1 - e^{-t/2\tau_j}\big)4\tau_j\big\}\Big], \tag{29}$$

$$\theta_{j,XPM}(t) = -\gamma_{jk}\Big[4\kappa_k^2 s_k^2 \tau_k^2\big\{t + \big(1 - e^{-t/\tau_k}\big)\tau_k - \big(1 - e^{-t/2\tau_k}\big)4\tau_k\big\}\Big], \quad j = 1, 2, \quad k = 3 - j. \tag{30}$$

Instantaneous frequency shift can be written as

$$f_j(t) = f_{j,SPM}(t) + f_{j,XPM}(t) \tag{31}$$

Where, $f_{j,SPM}$ is frequency shift due to self phase modulation and written as

$$f_{j,SPM}(t) = -\frac{\gamma_{jj}}{2\pi}\Big[4\kappa_j^2 s_j^2 \tau_j^2\big(1 + e^{-t/\tau_j} - 2e^{-t/2\tau_j}\big)\Big], \tag{32}$$

and $f_{j,XPM}$ is frequency shift due to cross phase modulation and written as

$$f_{j,XPM}(t) = -\frac{\gamma_{jk}}{2\pi}\Big[4\kappa_k^2 s_k^2 \tau_k^2\big(1 + e^{-t/\tau_k} - 2e^{-t/2\tau_k}\big)\Big], \quad j = 1, 2, \quad k = 3 - j. \tag{33}$$

## V. Results and Discussion

Figs. (2) shows the phase $\theta(t)$ and corresponding instantaneous frequency shift $\Delta f(t)$ calculated using Eq. (12) and Eq. (13) respectively for different injected powers. As can be seen in the Fig. (2), the frequency shift increases with time due to the presence of input power. It can also be seen that negative frequency shift is increasing with time from higher order mode to lower order mode because lower order mode coupled more power as compared with higher order mode. More importantly mode order is inversely related to nonlinear coefficient. So, smaller mode order provides larger nonlinear coefficients and hence we found larger negative frequency shift.

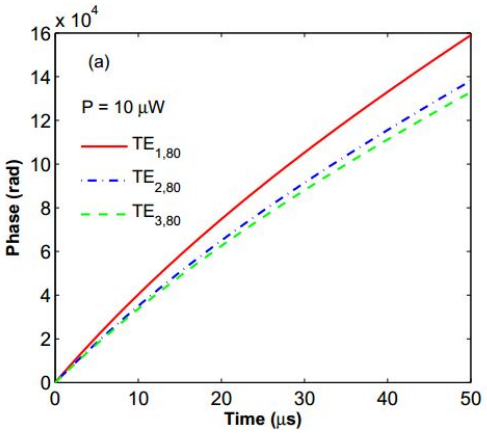


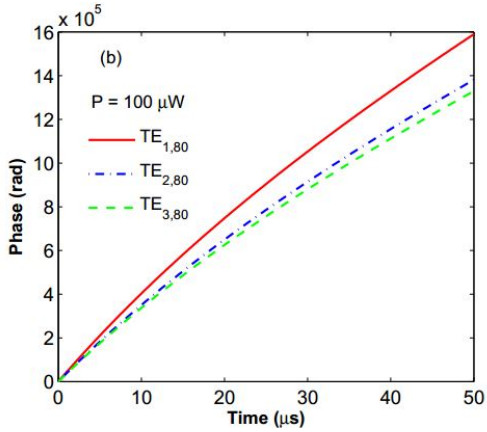

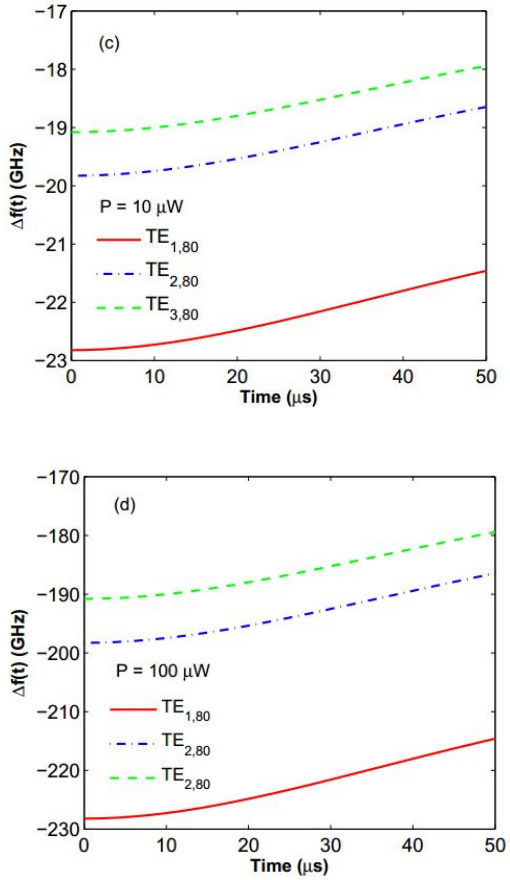


Fig. 2. Observation of phase change and frequency shift as a function of time for different injected powers in the microsphere with a radius of $15\mu m$.

Fig. 3 shows the phase $\theta_1(t)$ and corresponding frequency shift $f_1(t)$ calculated using Eq. (28) and Eq. (31), respectively for different injected powers $p_j$. Comparing Figs. 3(c) and (d), we find that, the XPM induced frequency shift is much smaller in Fig. 3(d) due to the lower power coupled to mode 2. Comparing Figs. (1) in Ref [19] and 3, we note that the frequency shift in Fig. (1) in Ref [19] becomes zero after a time scale comparable to the life time whereas in Fig. 3 the frequency shift increases monotonically with time and then saturates. This difference is due to the fact that in Fig. (1), optical impulses at t = 0 excite the modes whereas in Fig. 3, the cw beams couple powers to the modes.

These results can be used to analyze the experimental work related to frequency comb, third harmonic generation and parametric oscillation. WGMs have been used for sensing applications in which the object placed in the microcavity alters the refractive index profile of the microcavity which leads to the frequency shift of the WGMs. In addition, the object changes the nonlinear polarization properties of the microcavity and it could lead to additional frequency shifts due to SPM and XPM as discussed in this paper and hence, the analysis developed in this paper could be used for nonlinear sensing applications.

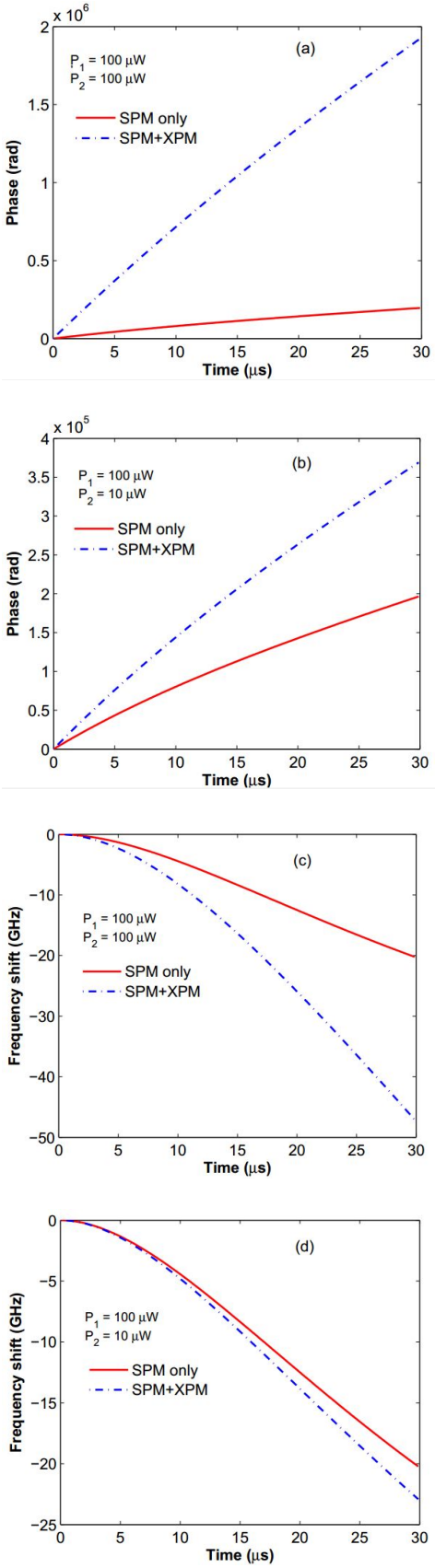


Fig. 3. The phase change and frequency shift as a function of time for different injected powers in the microsphere with a radius of $15\mu m$.

## VI. Conclusion

In this paper, coupling equations for WGMs microsphere are derived by adding coupling and intrinsic loss terms. We showed that the difference between SPM induced frequency shift and SPM+XPM induced frequency shift is $26.88GHz$ when both pump and probe power are perfectly matched. These results can be used for sensing applications in which the object placed in the microcavity alters the refractive index profile of the microcavity which leads to the frequency shift of the WGMs.

## References


[1] D. K. Armani, T. J. Kippenberg, S. M. Spillane & K. J. Vahala, "Ultra-high-Q toroid microcavity on a chip, Nature, 421(6926), 925 (2003).

[2] F. Treussart, V. S. Ilchenko, J. F. Roch, P. Domokos, J. Hare, V. Lefevre, & S. Haroche, "Whispering gallery mode microlaser at liquid helium temperature, Journal of luminescence, 76, 670-673 (1998).

[3] K. An, J. J. Childs, R. R. Dasari, & M. S. Feld, "Microlaser: A laser with one atom in an optical resonator, Physical review letters, 73(25), 3375 (1994).

[4] L. He, S. K. Ozdemir and L. Yang, "Whispering gallery microcavity lasers," Laser and Photonics Reviews **7**, 60-82 (2013).

[5] L. He, S. K. Ozdemir, J. Zhu, W. Kim and L. Yang, "Detecting single viruses and nanoparticles using whispering gallery microlasers," Nature Nanotechnology **6**, 428-432 (2011).

[6] S. M. Spillane, T. J. Kippenberg and K. J. Vahala, "Ultralow-threshold Raman laser using a spherical dielectric microcavity," Nature **415**, 621-623 (2002).

[7] T. J. Kippenberg, S. M. Spillane, D. K. Armani and K. J. Vahala, "Ultralow-threshold microcavity Raman laser on a microelectronic chip," Optics Letters **29**, 1224-1226 (2004).

[8] S. K. zdemir, J. Zhu, X. Yang, B. Peng, H. Yilmaz, & L. Yang, "Highly sensitive detection of nanoparticles with a self-referenced and self-heterodyned whispering-gallery Raman microlaser Proceedings of the National Academy of Sciences, 111(37), E3836-E3844 (2004).

[9] T. Carmon, T. J. Kippenberg, L. Yang, H. Rokhsari, S. Spillane, & K. J. Vahala, "Feedback control of ultra-high-Q microcavities: application to micro-Raman lasers and micro-parametric oscillators," Optics Express, 13(9), 3558-3566 (2005).

[10] L. Maleki & V. Ilchenko, "U.S. Patent No. 6,490,039" Washington, DC: U.S. Patent and Trademark Office (2002).

[11] M. R. Foreman, J. D. Swaim & F. Vollmer, "Whispering gallery mode sensors. Advances in optics and photonics," 7(2), 168-240 (2015).

[12] E. Krioukov, D. J. W. Klunder, A. Driessen, J. Greve & C. Otto, "Sensor based on an integrated optical microcavity. Optics letters, 27(7), 512-514 (2002)

[13] A. A. Savchenkov, A. B. Matsko, D. Strekalov, M. Mohageg, V. S. Ilchenko & L. Maleki, "Low Threshold Optical Oscillations in a Whispering Gallery Mode C a F 2 Resonator," Physical review letters, 93(24), 243905 (2004)

[14] T.J. Kippenberg, R. Holzwarth and S. A. Diddams,"Microresonator-based optical frequency combs," Science **332**, 555-559 (2011).

[15] T. J. Kippenberg, R. Holzwarth & S. A. Diddams, "Microresonator-based optical frequency combs," Science, 332(6029), 555-559 (2011).

[16] J. C. Knight, G. Cheung, F. Jacques, and T. A. Birks, Phase-matched excitation of whispering-gallery-mode resonances by a fiber taper, Opt. Lett., vol. 22, pp. 11291131, 1997.

[17] L. Collot, V. Lefevre-Seguin, M. Brune, J. M. Raimond, and S. Haroche, Very high-Q whispering-gallery mode resonances observed on fused silica microspheres, Europhys. Lett., vol. 23, pp. 327334, 1993.

[18] S. K. Biswas and S. Kumar, "Impact of Kerr nonlinearity on the whispering gallery modes of a microsphere," Optics Express **23**, 26738-26753 (2015).

[19] S. K. Biswas, "Impact of Kerr and Raman Nonlinear Effects on the Whispering Gallery Modes of a Spherical Microcavity," M.A.Sc. thesis (McMaster University, 2016).

[20] S. Kumar, & S. K. Biswas "Impact of Kerr nonlinearity and stimulated Raman scattering on the whispering gallery modes of an optical microsphere. JOSA B, 33(8), 1677-1687(2016).

[21] H. A. Haus, Waves and Fields in Optoelectronics (Prentice-Hall series in solid state physical electronics, 1984).

[22] M. L. Gorodetsky and V. S. Ilchenko, "Optical microsphere resonators: optimal coupling to high-Q whispering-gallery modes," JOSA B, 16(1), 147-154 (1999).

[23] M. L. Gorodetsky, A. D. Pryamikov and V. S. Ilchenko, "Rayleigh scattering in high-Q microspheres," JOSA B, 17(6), 1051-1057 (2000).

# SPR Biosensor Based on Microstructured Fiber with Lens Shaped Air Holes

Ahasan Ullah, M. M. Sajjad Hossain, and M. Shah Alam†

Department of Electrical and Electronic Engineering
Bangladesh University of Engineering and Technology (BUET)
Dhaka-1205, Bangladesh
†Corresponding author ( shalam@eee.buet.ac.bd)

***Abstract* — In this work, we propose a microstructured optical fiber with lens shaped air holes as a surface plasmon resonance biosensor. The fiber material is fused silica and in the central core region there is a small air hole which is surrounded by four biconvex lens shaped air holes acting as the cladding. The lens shaped holes helped bring design flexibility to tune sensor performance by enhancing plasmon excitation. The gold layer is placed outside the cladding to expedite real time in situ sensing. We have analyzed the sensor performance by using finite element method. Results have shown a maximum wavelength sensitivity of 5000 nm/RIU, maximum amplitude sensitivity of 500 RIU$^{-1}$ and a resolution of $2\times10^{-5}$ RIU.**

**Keywords—*Microstructured optical fiber, biosensor, surface plasmon resonance, high sensitivity, finite element method.***

## I. Introduction

The use of surface plasmon resonance (SPR) in sensing applications has proliferated in the last few decades due to its higher sensitivity, reliable label free sensing procedure and versatility. Under proper conditions, a surface wave of conduction electrons known as surface plasmon wave (SPW) can be generated at the interface of a dielectric and a conductor excited by a p-polarized light, whose propagation constant depends on the dielectric functions of the constituent materials of the interface.

The first idea of an SPR sensor was proposed by Kretschmann in 1968, where direct deposition of a thin metal layer on the base of a prism coupler was demonstrated [1]. The potential of SPR at metal interfaces [2] for monitoring processes and characterization of thin films was recognized in the late seventies. Nylander and Liedberg [3] demonstrated the use of SPR for gas detection and biosensing in 1983. Since then scientific communities' attention towards SPR sensing has been growing continuously. After the birth of PCF in 1995, PCF based sensors attracted the attention of researchers. T. Monro et al. explored the possibility of sensing by microstructured optical fibers [4]. Their design criteria showed the possibility for achieving significant overlap between the light guided in the fiber and the air holes and hence for producing efficient evanescent field devices. They have also shown the dispersive properties combined with the high mode confinement that make the ultra-broadband single mode sources and new source wavelengths a possibility.

In 2004, a novel PCF biosensor based on a PCF Bragg grating was proposed [5] which detects the presence of selected single-stranded DNA molecules, hybridized to a biofilm in the air holes of the PCF, by measuring their interaction with the fiber modes. The idea of SPR biosensors based on PCF are recent. Many researchers are proposing novel PCF sensor designs based on SPR. The metal-dielectric combination and the structure are diverse in these researches. PCF sensors based on graphene silver deposited core [13], copper with graphene [6] were proposed, different structural design to achieve the phase matching condition are also found in literature [7-9,12,14]. N. Luan et al. [10] proposed a D-shaped microstructured fiber to solve analyte filling and metal deposition problem. Recently a PCF based SPR probe was reported with a sensitivity of 6000 nm/RIU for low RI detection [11].

In this work, we have proposed a microstructured fiber with lens shaped air holes to facilitate mode coupling and obtain sensing characteristics. The structure provides a greater flexibility in terms of control parameter. Besides the central air hole, the radii of curvature of the lens shaped air holes have a strong influence on phase matching and excitation. By tuning this parameter, one can change the operating wavelength range. Thus, the proposed sensor can be operated with high sensitivity by selecting the operating wavelength range conveniently. By changing the lens size the coupling between core and plasmon mode can be controlled easily. The proposed structure can be operated with lower confinement loss, which will be a potential advantage in remote sensing applications. The proposed sensor can be fabricated by sputter deposition technology and stack and draw method [8].

## II. Structure and Theoretical Modeling

The proposed structure is a novel one, where four identical biconvex lens shaped air holes surround a small central air hole. The central hole serves the purpose of lowering the core mode effective index and thus helps phase matching with the plasmonic mode. The lens shaped holes are defined by their radii of curvatures (rand $r_1$) and the distance between the

978-1-5386-3374-8/17/$31.00 ©2017 IEEE

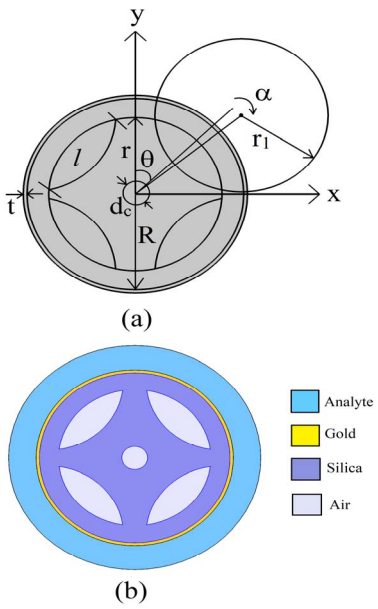


Fig. 1. (a) Cross sectional geometric specification (b) Cross section of proposed structure.

intersecting points ($l$). By tuning these parameters, we can control the resonance wavelength, modal confinement loss and sensitivity of the sensor. Thus, the structure gives higher flexibility and control in terms of sensor performance and operation.

The outer circle of the air holes is concentric with the central hole and have a radius of curvature r. The centers of the inner circles are symmetrically placed on a circle concentric to the central air hole (θ=45°). The birefringence is added by rotating the centers towards the x-axis by 1° (α= 1°). Fig. 1 shows the geometric model of the structure, where the central hole diameter is $d_c$ and the gold layer thickness is t. The substrate material of the MOF is silica, which is most widely used and readily available. The core is formed of silica with the small central air hole. The material property of silica is described by the Sellmeier equation [12]

$$n(\lambda) = \sqrt{1 + \frac{B_1\lambda^2}{\lambda^2 - C_1} + \frac{B_2\lambda^2}{\lambda^2 - C_2} + \frac{B_3\lambda^2}{\lambda^2 - C_3}} \qquad (1)$$

Here, n and λ are the refractive index of silica and the operating wavelength in μm, respectively. The Sellmeier coefficients are $B_1$= 0.696163, $B_2$= 0.4079426, $B_3$= 0.8974794, $C_1$= $4.67914826\times10^{-3}$ μm², $C_2$=$1.35120631\times10^{-2}$ μm² and $C_3$ = 97.9340025 μm².

Here the plasmonic material is gold. It is preferred over silver due to its chemical stability. The gold layer is added at the outer surface of the cladding which makes the metal deposition easier. The characteristics of gold are modeled by the equation [8],

$$\varepsilon_{Au}(\omega) = \varepsilon_\infty - \frac{\omega_D^2}{\omega^2 + j\gamma_D\omega} - \frac{\Delta\varepsilon.\Omega_L^2}{(\omega^2 - \Omega_L^2) + j\Gamma_L\omega} \qquad (2)$$

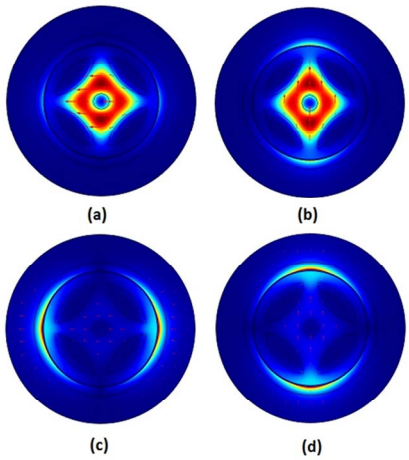


Fig. 2. Electric field distribution of core guided mode, (a) and (b) for X- and Y-polarization, respectively, (c) and (d) for SPP mode X- and Y- polarization, respectively.

Here, $\varepsilon_{Au}$ represents the permittivity of gold, $\varepsilon_\infty$ is the high frequency permittivity having a value of 5.9673, ω is the angular frequency, $\gamma_D$ and $\omega_D$ are the damping and plasma frequencies, respectively, where $\gamma_D/2\pi$ = 15.92 THz and $\omega_D/2\pi$ = 2113.60 THz.Δε = 1.09 is the weighting factor while, $\Gamma_L/2\pi$ = 104.86 THz and $\Omega_L/2\pi$ = 650.07 THz. The numerical calculations of the proposed MOF sensor were carried out using the structural parameters: R=2 μm, r = 1.6μm, $r_1/r$ = 1, $d_c/r$ = 0.27, $l/r$ = 1.2 and t=40nm.

## III. Results and Analysis

The MOF structure shown in figure has two tunable parameters, the inner radius ($r_1$) and the length ($l$), by which one can achieve resonance or phase matching at wavelengths in visible and near-infrared band. The effects of changing these two parameters on sensor performance will be discussed herein details, but a qualitative description is possible observing the structure. The effect of increasing the inner radius keeping the length constant is an increase in effective index of the core mode. Because an increase in $r_1$ decreases the curvature and results in an effective increase in core region. Thus, it is expected to have lower confinement loss for a higher inner radius. Similarly, the effect of increasing the length of the hole keeping other parameters unchanged is a decrease in the coupling between plasmonic mode and core mode, as the core mode field gets narrower space to leak into the gold layer to excite plasmonic mode. We have used water as analyte ($n_a$=1.33) and $r_1$= r while $l$=1.2r. In this work, y-polarized fundamental and the corresponding SPP mode were preferred over the x-polarized mode due to their higher modal loss. The dissimilarity between these two polarizations is because of added birefringence in the structure which creates a possibility of multianalyte sensing.

Fig. 3 shows the variation of effective refractive indices of both y-polarized core mode and plasmonic mode respectively along with the confinement loss of the fundamental core mode with respect to wavelength. It is found that for an analyte with index of 1.33 (water), the resonant wavelength where the

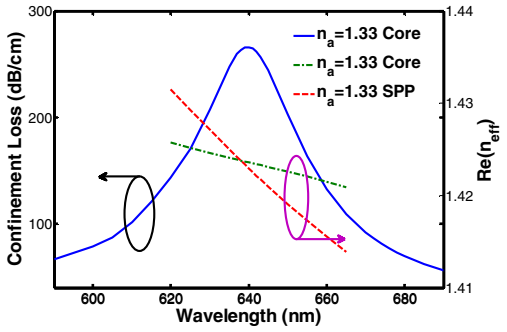


Fig. 3. Dispersion relation of core mode (green) and SPP mode (red) and confinement loss of core mode (blue).

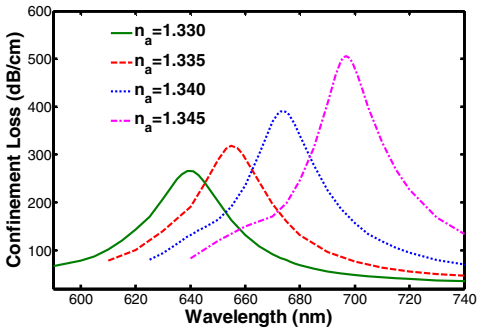


Fig. 4. Confinement loss and shift of resonance peak with respect to analyte refractive index.

confinement loss is maximum matches with the intersection point of the real part of the effective RI ($n_{eff}$) of the two modes. This wavelength is found to be 640 nm in this case. The confinement loss is dependent on the imaginary part of the effective RI, and is given by [13]

$$\alpha = \frac{40\pi.\mathrm{Im}(n_{eff})}{\lambda.\ln(10)} = 8.686 \times k_0 \times \mathrm{Im}(n_{eff})\mathrm{dB(cm)}^{-1} \quad (3)$$

where $k_0 = 2\pi/\lambda$ represents the free space wave number and $\lambda$ is the free space wavelength expressed in μm. At the resonant wavelength, power transferred from core mode to the SPP mode is maximum, and therefore we can see a loss peak at that wavelength. This wavelength is extremely sensitive to the refractive index of the analyte surrounding the gold region. A change in the analyte will shift the resonant wavelength, and thus sensing is possible by interrogating the resonant wavelength.

Next, we examine the sensing performance by varying the analyte refractive index. Fig. 4 shows the loss versus wavelength for different analytes with refractive indices from 1.33 to 1.345 at 0.005 steps. It is found that the resonant wavelength shifted to the right as the analyte refractive index increases. Also, the amplitude of the loss peak has visibly increased. Thus, there can be two detection techniques, namely wavelength-interrogation method and amplitude-interrogation method. Wavelength-interrogation method uses the shift in resonant wavelength to detect the analyte, while amplitude-interrogation method makes use of the difference in modal loss for detection. Sensor performance according to

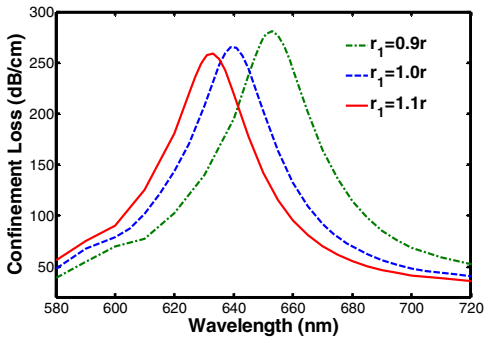


Fig. 5. Confinement loss and shift of resonance peak with respect to radius $r_1$ for $n_a$=1.33.

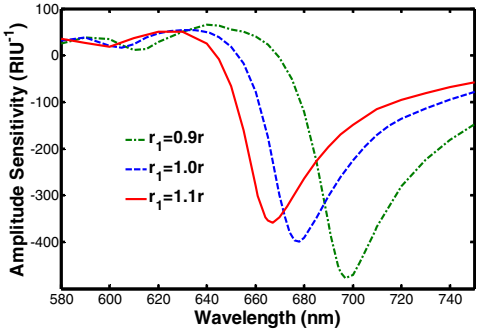


Fig. 6. Amplitude sensitivity with respect to radius $r_1$ for $n_a$=1.33.

wavelength interrogation technique is given by wavelength sensitivity, defined as, shift of resonant wavelength per unit change in analyte index, i.e.,

$$S_\lambda = \frac{\Delta\lambda_{peak}}{\Delta n_a}\mathrm{nm/RIU} \quad (4)$$

Here, $\Delta\lambda_{peak}$ is the resonant peak wavelength shift and $\Delta n_a$ is the change is analyte refractive index corresponding to that shift. The proposed sensor has a maximum wavelength sensitivity of 5000 nm/RIU. Another important measure of sensor performance is the resolution. The resolution of a sensor is defined as the minimum change of analyte refractive index detectable by the sensor, and is given by,

$$R = \frac{\Delta\lambda_{min}\times\Delta n_a}{\Delta\lambda_{peak}} = \frac{\Delta\lambda_{min}}{S_\lambda} \quad (5)$$

where $\Delta\lambda_{min}$ is the minimum spectral shift detectable by the sensor. Assuming $\Delta\lambda_{min}$ = 0.1 nm, the proposed sensor has a resolution of $2\times10^{-5}$ RIU, and signifies that the sensor can detect very tiny change in the index of the analyte.

Now we investigate the effects of changing $r_1$ and *l* on the sensor performance. Fig 5 shows the confinement loss for different values of $r_1$. It can be seen that higher values of $r_1$ shifts resonance wavelength to the left, along with a decrease in the confinement loss peak. For example, for $r_1$ = 0.9r, the resonant peak modal loss is 230 dB/cm. The amplitude sensitivity of the sensor versus wavelength for different values of $r_1$ are shown in Fig. 6. Amplitude sensitivity is calculated using the equation [13],

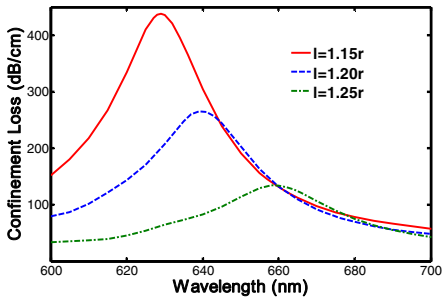


Fig. 7. Confinement loss and shift of resonance peak with respect to length *l* for $n_a = 1.33$.

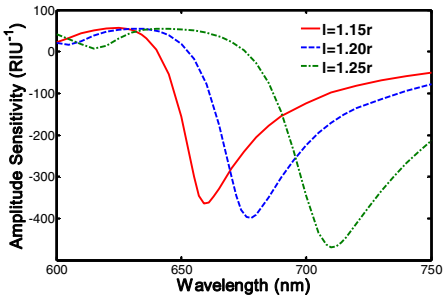


Fig. 8. Amplitude sensitivity with respect to length *l* for $n_a = 1.33$.

$$S_A = -\frac{1}{\alpha(\lambda,n_a)}\frac{\partial\alpha(\lambda,n_a)}{\partial n_a}\text{RIU}^{-1}. \qquad (6)$$

Here, the overall propagation loss at wavelength λ at a specific analyte refractive index $n_a$ is given by $\alpha(\lambda, n_a)$. It can be inferred from the figure that maximum amplitude sensitivity increases with the decrease of $r_1$. This can be explained observing the loss of Fig. 5. The modal loss increases and shift towards higher wavelength with the decrease of $r_1$, hence the difference $\Delta\alpha\ (\lambda,n_a)$ also increases and shift towards higher wavelengths and thus maximum sensitivity is achieved at higher wavelengths for lower $r_1$. The maximum sensitivity for $r_1$=0.9r is 500 $\text{RIU}^{-1}$. Assuming an accurate sensing of minimum 1% change in the transmitted intensity, this corresponds to a resolution of $2\times10^{-5}$ RIU.

Fig.7 shows the modal loss versus wavelength for different lengths of the holes, keeping $r_1$=r. The curves in this figures show that increasing the length of the holes spreads out the loss and shift it towards higher wavelengths. This spreading out of the loss over the wavelength is predictable as increased hole length resists leaking of field towards gold layer. Despite a clear dip in intensity, an increase in amplitude sensitivity is observed for increasing *l* in Fig. 8. This is because the effect of increasing *l* is to shift the resonant point to higher wavelength. As sensitivity increases with operating wavelength [10], hence the observed increase in sensitivity is due to this right shift of resonant wavelength. The amplitude sensitivity versus wavelength curves for three different values of *l* are shown in Fig. 8, which shows that increasing the length also increases the maximum amplitude sensitivity. For *l*=1.25r, the highest amplitude sensitivity is 500 $\text{RIU}^{-1}$. For an accurate measurement of 1% change in the transmitted intensity, the corresponding resolution will be $2\times10^{-5}$ RIU.

# IV. Conclusion

The sensor we have proposed is novel in its structural design and performance. Four biconvex lens shaped air holes around the core gives us the design flexibility to enhance its sensitivity and resolution, even better than the results reported here. The FEM was used here with finer triangular meshes over the cross section. Analysis shows a maximum sensitivity of 5000 nm/RIU for wavelength-interrogation method corresponding to a resolution of $2\times10^{-5}$ RIU and 500 $\text{RIU}^{-1}$ for amplitude-sensitivity method with similar resolution. By tuning the operating wavelength range, this proposed structure can be operated with very high sensitivity for a small particular range of analyte index.

## *References*


[1] E. Kretschmann and H. Raether, "Notizen: Radiative Decay of Non Radiative Surface Plasmons Excited by Light", *Zeitschrift für Naturforschung A*, vol. 23, no. 12, 1968.

[2] I. Pockrand, J. D. Swalen, J. G. Gordon, and M. R. Philpott, "Surface plasmon spectroscopy of organic monolayer assemblies," *Surface Science*, vol. 74, no. 1, pp. 237–244, May 1978.

[3] B. Liedberg, C. Nylander, and I. Lunström, "Surface plasmon resonance for gas detection and biosensing," *Sensors and Actuators*, vol. 4, pp. 299–304, Jan. 1983.

[4] T. Monro, W. Belardi, K. Furusawa, J. Baggett, N. Broderick and D. Richardson, "Sensing with microstructured optical fibres", *Measurement Science and Technology*, vol. 12, no. 7, pp. 854-858, 2001

[5] N. Burani and J. Lægsgaard, "Perturbative modeling of Bragg-grating-based biosensors in photonic-crystal fibers", *Journal of the Optical Society of America B*, vol. 22, no. 11, p. 2487, 2005.

[6] A. Rifat, G. Mahdiraji, R. Ahmed, D. Chow, Y. Sua, Y. Shee and F. Mahamd Adikan, "Copper-Graphene-Based Photonic Crystal Fiber Plasmonic Biosensor", *IEEE Photonics Journal*, vol. 8, no. 1, pp. 1-8, 2016.

[7] A. A. Rifat, G. A. Mahdiraji, Y. G. Shee, M. J. Shawon, and F. R. M. Adikan, "A novel Photonic crystal fiber Biosensor using surface Plasmon resonance," *Procedia Engineering*, vol. 140, pp. 1–7, 2016.

[8] A. Rifat, G. Mahdiraji, Y. Sua, Y. Shee, R. Ahmed, D. Chow and F. Adikan, "Surface Plasmon Resonance Photonic Crystal Fiber Biosensor: A Practical Sensing Approach", *IEEE Photonics Technology Letters*, vol. 27, no. 15, pp. 1628-1631, 2015.

[9] R. Otupiri, E. Akowuah, S. Haxha, H. Ademgil, F. Abdel Malek and A. Aggoun, "A Novel Birefrigent Photonic Crystal Fiber Surface Plasmon Resonance Biosensor", *IEEE Photonics Journal*, vol. 6, no. 4, pp. 1-11, 2014.

[10] N. Luan, R. Wang, W. Lv and J. Yao, "Surface plasmon resonance sensor based on D-shaped microstructured optical fiber with hollow core", *Optics Express*, vol. 23, no. 7, p. 8576, 2015.

[11] C. Liu, L. Yang, Q. Liu, F. Wang, Z. Sun, T. Sun, H. Mu and P. Chu, "Analysis of a Surface Plasmon Resonance Probe Based on Photonic Crystal Fibers for Low Refractive Index Detection", *Plasmonics*, 2017.

[12] E. Akowuah, T. Gorman, H. Ademgil, S. Haxha, G. Robinson and J. Oliver, "Numerical Analysis of a Photonic Crystal Fiber for Biosensing Applications", *IEEE Journal of Quantum Electronics*, vol. 48, no. 11, pp. 1403-1410, 2012.

[13] A. Rifat, G. Mahdiraji, D. Chow, Y. Shee, R. Ahmed and F. Adikan, "Photonic Crystal Fiber-Based Surface Plasmon Resonance Sensor with Selective Analyte Channels and Graphene-Silver Deposited Core", *Sensors*, vol. 15, no. 5, pp. 11499-11510, 2015.

[14] Y. Lu, C. Hao, B. Wu, X. Huang, W. Wen, X. Fu and J. Yao, "Grapefruit Fiber Filled with Silver Nanowires Surface Plasmon Resonance Sensor in Aqueous Environments", *Sensors*, vol. 12, no. 12, pp. 12016-12025, 2012.

# Laser-ablated Clad Grating Sensors for Reinforcement Corrosion Measurement in Wet Conditions

Md. Rajibul Islam,[1,*] Abdul Kawsar Tushar,[1] and Kok-Sing Lim[2]
[1]Department of Computer Science and Engineering, University of Asia Pacific, Dhaka - 1215, Bangladesh
[2]Photonics Research Centre, University of Malaya, 50603 Kuala Lumpur, Malaysia
{[*]md.rajibul.islam, tushar.kawsar}@gmail.com, kslim@um.edu.my

***Abstract*—Laser-ablated Clad Grating is applied for the first time to monitor corrosion of reinforced concrete structure in wet conditions. In this study, the galvanostatic method is executed to speed up the entire process of corrosion in a controlled environment. Red-shifts in the cladding resonant wavelengths are observed in the course of the corrosion process and the wavelength shifts of these resonances are used to monitor corrosion.**

***Keywords*—Fiber optic sensor, impressed current technique, steel rebar corrosion measurement, laser-ablated clad grating.**

## I. Introduction

One of the crucial factors undermining small as well as large engineering and movable transport structures is corrosion. The risk of damage from corrosion is proportional to how old the structure is, increasing as the structure ages and service life is expired. Corrosion has the dual disadvantage of lowering stiffness leading to loss of structural integrity, and introducing undesirable stresses due to expansive corrosion products that can result in cracking of concrete [1]. In order to ensure prevention of structural damage and mitigate financial and collateral risk, detecting corrosion as early as possible poses great importance. An associated exhaustive monitoring system will go a long way in estimating the remaining service life of a structure.

A number of techniques, including non-optic as well as optic based methods has been proposed to monitor corrosion in structures in wet conditions. With long-term monitoring and detection of corrosion initiation in mind, a wireless passive sensor based on 91-mm long PCB has been proposed in [2]. This system poses strenuous requirements on both time and labor and therefore not always helpful for detection of multiple points. Electrochemical impedance was used to quantify the corrosion level of corroding metal, which can then be judged against the scale of by-corrosion processes that occur naturally, including electrochemical noise [3]. Yet, only uniform corrosion process can be measured in this method. On the other hand, a range of fiber-optical methods has been employed for the same purpose, including long-period gratings (LPGs) [4] and fiber Bragg gratings (FBGs) [5]. The sensitivity of FBGs are often increased by removing the cladding, which significantly weakens the mechanical strength of fiber, which renders it inappropriate to be used in hostile environment. Moreover, although LPGs show significant sensitivity to surrounding refractive index (SRI) caused by the light coupling between the forward propagation clad mode, and core mode [6], they are also highly sensitive to strain and temperature. This can lead to undesirable effects as an SRI sensor.

In this paper, a laser-ablated clad grating (LaCG) sensor is used for the measurement of corrosion in steel structures surrounded by wet environment. Smaller diameter of fiber ($80\mu$) is chosen for LaCG fabrication because of its higher sensitivity to RI variations. The asymmetric photo-induced index modulation in the cladding of LaCG triggers the couplings between core and cladding modes that contributes to generate cladding resonances. These cladding resonances are too sensitive to SRI which drives the main motivation for selecting such sensor to measure corrosion. The rest of this paper is organized as follows. Section II discusses the experimental setting. Section III elaborates on the obtained results and their implications. Finally, Section IV concludes the paper.

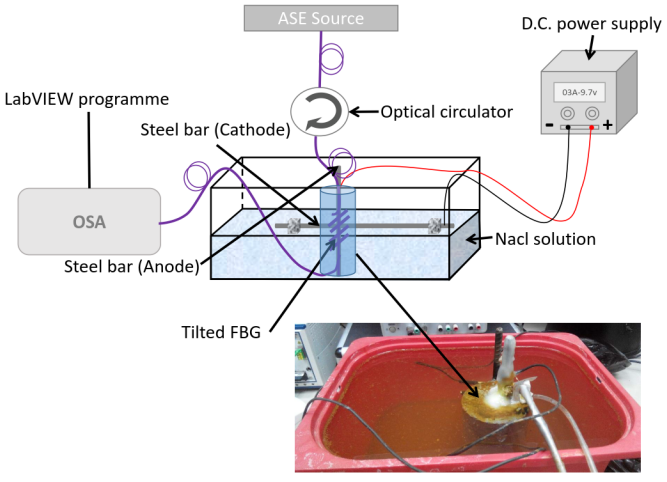


Fig. 1. Schematic of the LaCG sensor to the rebar and galvanostatic method setup for corrosion measurement test.

978-1-5386-3374-8/17/$31.00 ©2017 IEEE

## II. Optical Sensor Setup and Stimulated Corrosion Process

In this section, the stimulated corrosion process of the steel rebar used in the experiments is described, after which the entire setup of the experiment is explained. The galvanostatic method, otherwise known as the impressed current technique, is a common technique which is employed to expedite corrosion process in longevity experiments for steel reinforcement, in order to simulate the real life scenario over a much shorter period [7]. A steady and uninterrupted flow of current is required to the steel rebar that is implanted in concrete in order to produce corrosion. MEGURO MP 303-3 was utilized as the source of portable dc power to supply this current. The quantity of induced corrosion in this process is mathematically determined from the percentage of real mass loss, which in turn is theoretically calculated by Faradays law that is rooted on the applied current and time or gravimetric experiment on the eroded rebars. If the actual quantity of steel loss is known, then the density of current of a corresponding erosion procedure could also be calculated from it [8].

Together with the dc power source, an electrolyte and a counter electrode was utilized to conduct the galvanostatic method to induce corrosion in reinforcement steel. Both cathode and anode are steel rebars in this experiment. The anode and cathode were attached with the positive and negative terminals of the power source, respectively. NaCl solution was used to get the rebars immersed. By nature, the electrolyte (NaCl solution) would act as a medium for the current to be passed from the cathode to the anode [9], [10]. By this process, several corrosion products would start emerging into the electrolyte, including Iron hydroxide ($Fe(OH)_2$), iron trihydroxide ($Fe(OH)_3$), and goethite ($\alpha - FeOOH$) as major items [11]. Fig. 1 shows the experimental setup.

The LaCG is engraved in the photosensitive single-mode optical fiber via a hydrogenation process by using highly focused UV laser pulse energy from an ArF excimer laser. As a result, a periodic ablation is composed on the surface of the fiber and the optical damage is expanded from the surface of the fiber cladding towards the fiber core. The diameter of cladding is 80 $\mu$ and salinity measurement is performed to calibrate the

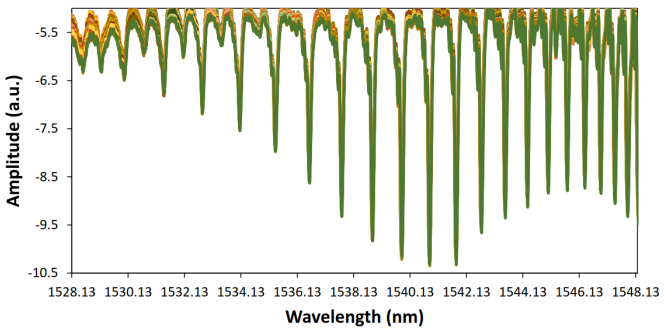


Fig. 2. Chosen spectra of transmission for analysis of fluctuation of responses from low-order to high-order modes.

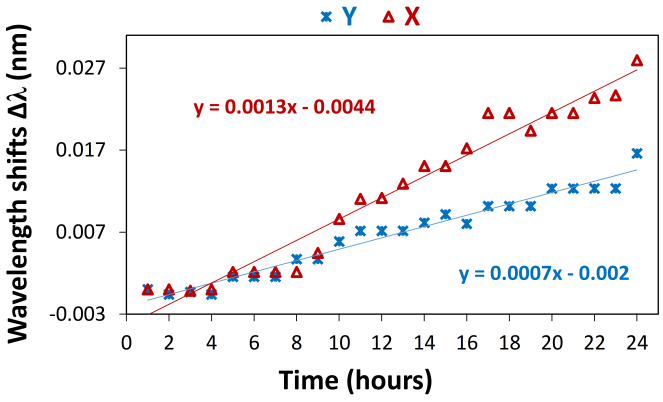


Fig. 3. Measured dynamic response of high-order and low-order cladding mode of the LaCG corrosion sensor.

LaCG [12]. The cladding is made up of fused silica glass layer devoid of any photosensitive material [13] and therefore, in general, grating cannot be inscribed on it. In order to make this task possible, the fiber needs to be hydrogenated up to a specific mark, at which level the photosensitivity of the fiber increases by around 40 times. However, the photosensitivity to be achieved for this process must be at a precise level while inscribing LaCGs with high-intensity ultraviolet (UV) laser [12]. A laptop using a LabVIEW program was utilized to monitor the transmission spectra with a frequency of 1 hour during the expedited corrosion process.

## III. Result Analysis

During the expedited corrosion process by galvanostatic method, the mass of the cathode rebar was decreased from 260 to 184.9 g which is equal to loss of 28.9% mass after 24 h of experiment time. $1528.13 - 1547.6\ nm$ is considered in order to observe the cladding resonances in the spectrum, as shown in Fig. 2 [14]. The reason for selecting this particular wavelength region is that this region contains lower levels of noise, and noise could be removed to another extent with the help of a moving average filter. We consider higher and lower-order modes based on this considered spectra for corrosion sensing. This figure depicts the superimposed transmission spectra of the LaCG during the erosion procedure. A point to note here is that low-order and high-order modes of cladding have different wavelength shifts. The high-order cladding modes, when excited, are especially sensitive to the outer surroundings, since these resonances demonstrate considerably more wavelength shifts compared to resonances of low-order cladding, as shown in Fig. 3 [14]. Low-order and high-order cladding resonances demonstrate wavelength shifts of 0.7 and 1.3 $pmh^{-1}$, respectively. The variations of wavelength shifts from high-order to low-order cladding resonances are taken into consideration for the calculation of magnitude of the level of corrosion.

Persistent temperature was ensured in the experiment environment, which was controlled for corrosion measurement experiment. In our experimental procedure, Bragg wavelength

did not demonstrate any shift during the whole expedited corrosion procedure. By taking the unresponsiveness of Bragg wavelength to RI changes into consideration, it can be said that variation of strain and temperature to the LaCG was absent throughout the procedure. However, practical effects of strain and temperature cannot be evaded, and therefore comes the necessity to use a supplementary FBG, which could be included in the sensing system to differentiate strain and temperature from the calculation of RI variations of LaCG.

## IV. Conclusion

In this research, the LaCG has been employed in order for in-position observation of the corrosion in steel rebars submerged in solution of NaCl. To expedite the procedure of corrosion, galvanostatic method is utilized. Throughout the corrosion procedure, it is noticed that the higher order cladding resonances revealed comparatively higher responsiveness to the fluctuations of corrosion in comparison with the lower order cladding resonance existing close to the Bragg wavelength. For the wavelength range of $1528.13 - 1547.6\ nm$ in the spectrum of transmission, the lowest sensitivity of $0.7\ pmh^{-1}$ and the highest sensitivity of $1.3\ pmh^{-1}$ have been acquired for high-order as well as low-order cladding modes, respectively.

## References


[1] C. Fang, K. Lundgren, L. Chen, and C. Zhu, "Corrosion influence on bond in reinforced concrete," *Cement and concrete research*, vol. 34, no. 11, pp. 2159–2167, 2004.

[2] K. Perveen, G. E. Bridges, S. Bhadra, and D. J. Thomson, "Corrosion potential sensor for remote monitoring of civil structure based on printed circuit board sensor," *IEEE transactions on instrumentation and measurement*, vol. 63, no. 10, pp. 2422–2431, 2014.

[3] J. M. Smulko, K. Darowicki, and A. Zielinski, "On electrochemical noise analysis for monitoring of uniform corrosion rate," *IEEE transactions on instrumentation and measurement*, vol. 56, no. 5, pp. 2018–2023, 2007.

[4] K. Cooper, J. Elster, M. Jones, and R. Kelly, "Optical fiber-based corrosion sensor systems for health monitoring of aging aircraft," in *AUTOTESTCON Proceedings, 2001. IEEE Systems Readiness Technology Conference*. IEEE, 2001, pp. 847–856.

[5] J. A. Greene, M. E. Jones, T. A. Tran, K. A. Murphy, P. M. Schindler, V. Bhatia, R. G. May, D. Sherrer, and R. O. Claus, "Grating-based optical fiber-based corrosion sensors," *Smart Sensing Processing and Instrumentation*, vol. 2718, pp. 170–174, 1996.

[6] V. Bhatia, D. K. Campbell, T. D'Alberto, G. A. Ten Eyck, D. Sherr, K. A. Murphy, and R. O. Claus, "Standard optical fiber long-period gratings with reduced temperature sensitivity for strain and refractive-index sensing," in *Optical Fiber Communication. OFC 97., Conference on*. IEEE, 1997, pp. 346–347.

[7] S. Caré and A. Raharinaivo, "Influence of impressed current on the initiation of damage in reinforced mortar due to corrosion of embedded steel," *Cement and concrete research*, vol. 37, no. 12, pp. 1598–1612, 2007.

[8] O. Almubaied, H. K. Chai, M. R. Islam, K.-S. Lim, and C. G. Tan, "Monitoring corrosion process of reinforced concrete structure using fbg strain sensor," *IEEE Transactions on Instrumentation and Measurement*, 2017.

[9] T. A. El Maaddawy and K. A. Soudki, "Effectiveness of impressed current technique to simulate corrosion of steel reinforcement in concrete," *Journal of materials in civil engineering*, vol. 15, no. 1, pp. 41–47, 2003.

[10] S. Ahmad, "Techniques for inducing accelerated corrosion of steel in concrete," *Arabian Journal for Science and Engineering*, vol. 34, no. 2, p. 95, 2009.

[11] P. Refait, J.-B. Memet, C. Bon, R. Sabot, and J.-M. Génin, "Formation of the fe (ii)–fe (iii) hydroxysulphate green rust during marine corrosion of steel," *Corrosion Science*, vol. 45, no. 4, pp. 833–845, 2003.

[12] M. R. Islam, D. S. Gunawardena, Y.-S. Lee, K.-S. Lim, H. Z. Yang, and H. Ahmad, "Fabrication and characterization of laser-ablated cladding resonances of two different-diameter photosensitive optical fibers," *Sensors and Actuators A: Physical*, vol. 243, pp. 111–116, 2016.

[13] L. Dong, W. Loh, J. Caplen, J. Minelly, K. Hsu, and L. Reekie, "Efficient single-frequency fiber lasers with novel photosensitive er/yb optical fibers," *Optics letters*, vol. 22, no. 10, pp. 694–696, 1997.

[14] M. R. Islam, M. Bagherifaez, M. M. Ali, H. K. Chai, K.-S. Lim, and H. Ahmad, "Tilted fiber bragg grating sensors for reinforcement corrosion measurement in marine concrete structure," *IEEE Transactions on Instrumentation and Measurement*, vol. 64, no. 12, pp. 3510–3516, 2015.

# A 2.4 GHz Gain-boosted CMOS Amplifier Using Multibias Points for Improved Linearization

Abu Md. Raihan*, Md. Ekramul Hoque, and Apratim Roy
Department of Electrical and Electronic Engineering,
Bangladesh University of Engineering and Technology, Dhaka, Bangladesh
*raihan150.buet@gmail.com

***Abstract*—A highly linear two stage CMOS amplifier using 130 nm technology is presented. A linearization technique is employed using multibias points through a combination of bulk bias control and floating bulk devices to achieve significant improvement of intercept points. Forward gain boosting is ensured by utilizing a cascode topology followed by a common source stage while maintaining a low ceiling for noise in the S band. Including a bias controlled feedback path between the stages further improves the architecture's expected gain compression. The final design reports 27.6 dB simulated power gain with third order input intercept of 9.92 dBm and noise figure of 1.22 dB at the center frequency. Input and output impedances have been matched with the help of passive appendages to ensure -24 dB input return loss and -27.5 dB output return loss, respectively. Optimized radio frequency parameters are achieved along with a linearity upgrade which is better than reported CMOS amplifiers.**

***Index Terms*—Multistage Amplifier, Bulk Bias, Floating Bulk, Bias-controlled Feedback.**

## I. Introduction

With the development of radio frequency (RF) technologies, the linearity requirement of submicron CMOS Amplifiers has become increasingly stringent to overcome the limiting effect of robust interferers in the band of interest [1]. This issue assumes particular significance in determining the overall linearization of an RF receiver as its performance depends largely on the figures of the front-end low-noise amplifier (LNA). Additionally, as a part of the linearization process, trade-offs between other RF parameters like port reflection and signal amplification may become necessary for the amplifier. Therefore, while optimizing a linearity setting parameter like the input referred third order intercept point (IIP3), it is important to ensure that the outcome does not infringe on the design targets of power and gain overhead set beforehand [2].

In an RF system with multiple cascaded blocks, the system IIP3 is typically dominated by the later stages as they encounter larger signal amplitudes resulting from processing by the preceding blocks while the noise figure (NF) of the architecture is dominated by the noise performance of the input stage [3] [4]. But in the crowded wireless environment offered by modern communication standards, the LNA at the start of the receiver should also be able to sufficiently suppress the out-of-band interferers as well. Without this capability, the following block (e.g., mixer) encounters unreasonably strong interferers which demands a higher performance from it (in terms of linearity) possibly compromising its other specifications like conversion gain. Thus, an amplifier that is able to achieve high levels of linearity and consequently high IIP3 is desired. But the key function of an LNA is to achieve gain without adding significant noise to the received signal. Therefore, any circuitry that is used in the CMOS amplifier for the betterment of linearity should not achieve that at the expense of elevated noise. In this regard, various techniques have been used by front-end amplifiers to achieve high linearity such as derivative superposition [5], body biasing [6], post distortion [7], current reused topology [8], fixed biasing, floating body stages [9] and modified derivative superposition [10]. But an enhancement in linearization often comes at a cost of a decrease in gain performance and adversely affecting other RF parameters.

In order to overcome this limitation, a linearization method is proposed which exploits a combination of bulk bias controlled and floating bulk devices to achieve reduction in gain compression and low noise figure at the same time. The design based on multibias points for its active devices is realized through a cascode amplifier followed by a common source gain boosting stage. The multistage configuration allows the attainment of high gain performance whereas a feedback network between the stages maintains linearity for the structure and provides stability by ensuring the absence of oscillations. Matching circuit is appended to both port terminals to achieve optimized scattering parameters and reduce the noise ceiling. Additionlly, negative bulk voltages are provided to the feedback transistor while the bulk of the second stage driver is kept floating to reduce the intermodulation product and consequently improve linearity. This work particularly focuses on the 2.4 GHz range in the S band, which makes it compatible with modules used in wireless applications like Wi-Fi, bluetooth, cordless phone, car alarm, emergency response information portal (ERIP) and ZigBee, an IEEE 802.15.4-based specification. Apart from the targeted applications, the topology offers the feature of reconfigurable operating point where it is possible to vary its center frequency range by changing a component reactive element. The paper is arranged in the following sections: in section II, the proposed configuration is explained in terms of enhancement in linearity. In section III, the simulated results along with contributions of the presented techniques are explained and designs parameters are compared with recently proposed configurations. Finally, the findings are summarized in section IV.

## II. Proposed Architecture for Improved Linearization

Among various CMOS amplifier topologies, the cascode structure offers relatively high gain while maintaining an acceptable degree of linearity. In this work, the linearity performance of the cascode topology was bolstered by introducing bias controlled feedback between the driving block and a linear output common source stage. The multistage architecture is

978-1-5386-3374-8/17/$31.00 ©2017 IEEE

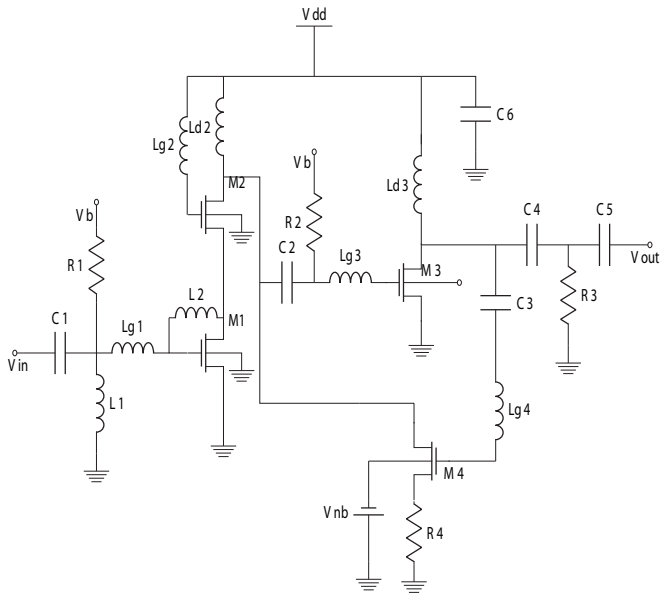


Fig. 1. Schematic diagram of the linearized multistage amplifier.

supported by bulk bias control [6] and floating body [9] techniques. A careful application of these methods is able to provide good linearity and low noise figure despite maintaining a high enough gain. The resultant circuit is formed by the adjoining of two blocks followed by the formation of a feedback path from the second stage output to its input provided by the driving block. The feedback transistor includes a degenerative resistance along with negative biasing to its bulk to control the current flow in feedback path. Negative feedback provided by this branch possibly reduces the voltage gain to some extent but compensates by improving the gain sensitivity and bandwidth. The driving stage transistors have bulk connected to ground whereas the second stage CS transistor has a floating bulk connection for providing higher linearity by mitigating the effect of third order intermodulation product.

### A. Linearized Multistage Amplifier

In the proposed design, as presented in Fig. 1, M1 and M2 comprise the first stage cascode driver. Acting as a standalone stage, this driver is able to provide reasonable noise performance for a given power, but it suffers from significant gain compression due to second order non-linearity effects. Resistive input matching is avoided in the input stage as it contributes additional noise to the amplifier. Additionally, a drain to gate feedback inductor is used in the architecture for regulating noise figure and reflectance. To boost the gain further, a following common source stage in the form of $M_3$ is adopted. To complete the cascading, a capacitor $C_2$ and an inductor $L_{g3}$ are used in between the stages to maintain flat gain accomplished by series resonance in the midband [10].

For a two stage cascaded system, each stage contributes individually to the overall system noise performance and linearity. If the noise figure of the component stages are given, the overall figure can be calculated from the following equation [4]:

$$NF - 1 = NF_1 - 1 + \frac{NF_2 - 1}{G_1} \tag{1}$$

where $G_1$ denotes first stage gain and $NF_i$ denotes the standalone noise figure of the *i*th stage. Similarly, the overall IIP3 of a multistage structure can be calculated as [3]

$$\frac{1}{IIP3} \approx \frac{1}{IIP3_1} + \frac{G_1}{IIP3_2} \tag{2}$$

where $IIP3_i$ denotes the input referred third order intercept point of the *i*th stage. The formulations suggest that first stage dominates the system noise whereas the second stage has a stronger influence in determining system IIP3. For this reason, the second stage is targeted in this architecture for accomodating the multibias point linearization technique. Additionally, $M_3$ is biased as a floating bulk transistor as it offers better linearity performance than a conventional grounded CS device by reducing third order intermodulation product with increasing power.

### B. Feedback Branch and Output Matching

Gain and linearity performance can be improved for an amplifier using transconductance feedback techniques and proper biasing in the second stage [11]. In the presented design, the bulk of the feedback device $M_4$ is biased with a small negative voltage to control the closed loop transconductance and hence regulate linearity parameters. It manipulates the threshold voltage of the active element which minimizes the third order intermodulation product as a part of the linearization process. For output matching, a capacitive-resistive network has been used which improves both linearity and high frequency output matching as it balances the impedance seen by the load section with the output impedance of the core amplifier.

## III. Simulated Results

The presented multistage linearized amplifier is simulated with an RF simulator using 130 nm CMOS technology. Essential scattering, reflectance, noise and linearity parameters are obtained which helps to quantify the gain-noise performance and linearization of the architecture. The effect of multibias points on linearity improvement is shown by deriving input referred intercept points with and without the linearizing scheme. In addition to specifications in the targeted frequency, gain and noise performance at reconfigured operating points are also simulated and the obtained parameters are compared with some recently proposed configurations.

### A. RF Parameters

The presented amplifier's performance is demonstrated in Fig. 2-6 with the presentation of voltage gain, power gain (S21), input return loss (S11), output return loss (S22), insertion loss (S12), noise figure and input intercept point (IIP3). The peak voltage gain of the two stage amplifier is 28.1 dB at 2.41 GHz as shown Fig. 2. Maximum forward gain (S21) is 27.6 dB at the center point of 2.4 GHz with a 3 dB bandwidth spanning from 2.23 GHz to 2.53 GHz. Reverse isolation (S12) is always better than -35.2 dB and is presented in Fig. 4. Input and output matching parameters (S11 and S22) are -24 dB and -27.5 dB, respectively, in the demonstration of Fig. 5. Noise figure and minimum noise figure are plotted in Fig. 3 where NF is 1.22 dB at the center frequency and remains below 1.26 dB over the entire bandwidth. Simulation results also reveal that input referred third order intercept point (IIP3) of the optimized amplifier is 9.92 dBm. Along with IIP3, the output intercept point (OIP3) is also presented in Fig. 6.

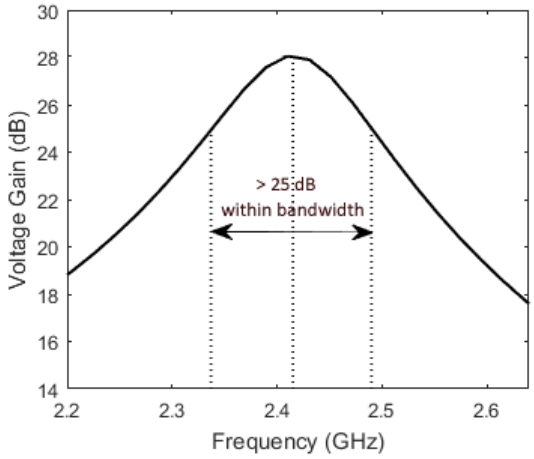


Fig. 2. Voltage gain of the multistage amplifier.

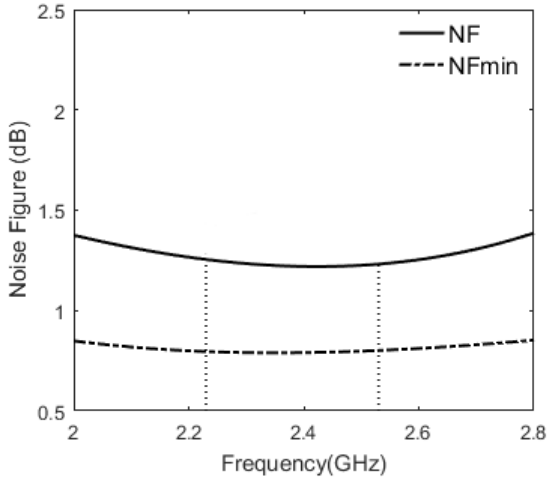


Fig. 3. Noise parameters of the amplifier.

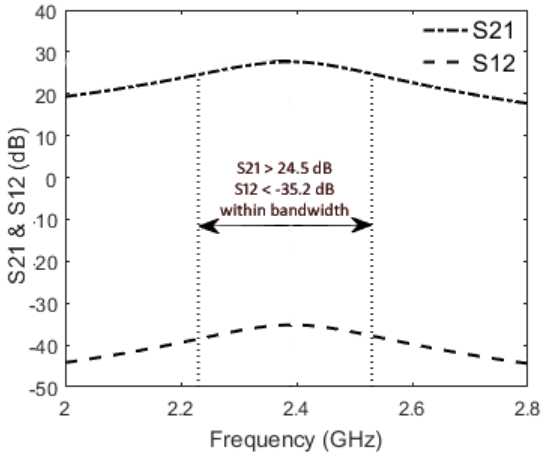


Fig. 4. Forward gain and reverse isolation parameters.

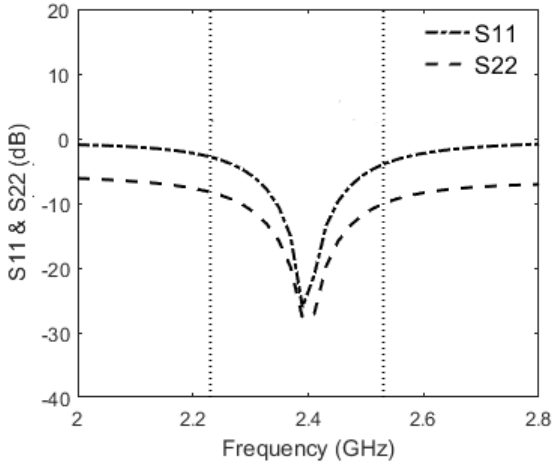


Fig. 5. Return loss parameters.

### *B. Effect of Multibias Points on Linearity*

As mentioned earlier, the input stage dominates the architechtures's noise performance and the system IIP3 is typically set by later stages, so the focus for IIP3 improvement is on the output stage to minimize the impact on noise factor. The multibias technique refers to the application of multiple bias conditions to the active elements to optimize linearity. In this design, the common source stage transistor has a floating bulk condition and the feedback transistor uses a small negative voltage in its bulk. This biasing combination is able to improve the system IIP3 by more than 10 dBm from the linearity obtained with the use of grounded bulk transistors. The result shows that, with grounded transistors, IIP3 has a value of -0.14 dBm which improves to 9.92 dBm with the help of the multibias point technique, as shown in Fig. 7. This method is advantageous as the improvement in linearity is achieved without any significant loss of gain or increase in noise parameters.

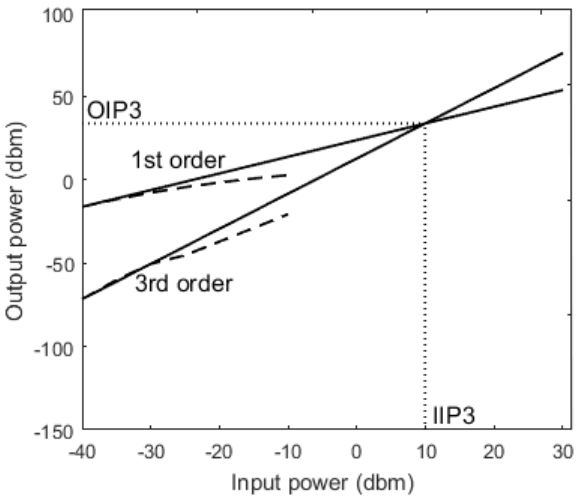


Fig. 6. Port referred third order intercept points (IIP3 and OIP3).

### *C. Reconfigurable Operating Point*

The range of peak operating frequency for the amplifier can be configured by controlling the reactance provided by the first stage load inductor. Therefore, the CMOS amplifier is able to achieve a tunable operating range from 1.6 GHz to 3.6 GHz, where the gain remains relatively unchanged. In this domain, the peak voltage gain varies between 25 dB to 29 dB and increase in peak noise figure remains reasonable (1.22 dB to 1.78 dB), as shown in Fig. 8. Simulation of scattering parameters at different peak operating frequencies show stable

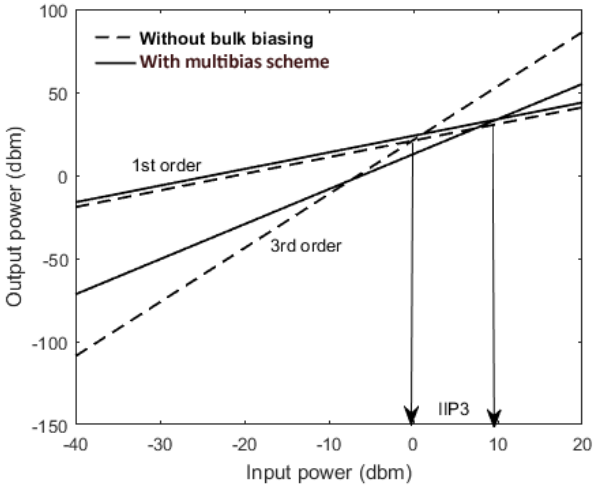


Fig. 7. Effect of multibias points on linearization.

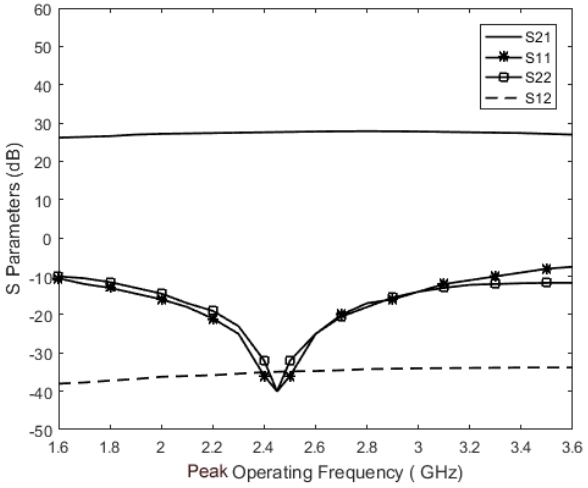


Fig. 9. Range of scattering parameters achieved with tuned operating frequencies.

S21 and S12 but an increase in input and output return losses as the operating point shifts away from 2.4 GHz. Peak S11 ranges from -8 dB to -40 dB and S22 ranges from -10 dB to -40 dB which is shown in Fig. 9.

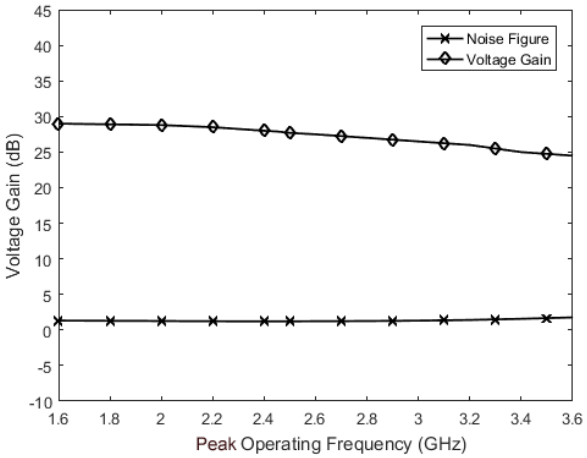


Fig. 8. Peak voltage gain and noise performance at different peak operating frequencies.

TABLE I
COMPARATIVE PERFORMANCE OF AMPLIFIERS.

| Ref. | This work | [12] | [13] | [14] | [15] | [16] |
|---|---|---|---|---|---|---|
| Tech. ($\mu$m) | .13 | .18 | .18 | .13 | .13 | .18 |
| Freq. (GHz) | 2.4 | 2.5 | 2.45 | 2.4 | 2.4 | 5 |
| S11 (dB) | -24 | -26.4 | -15 | -14 | -21.5 | -8 |
| S22 (dB) | -27.5 | -20 | - | -15 | - | -12 |
| S21 (dB) | 27.5 | 20.1 | 12 | 20.8 | 18.2 | 15 |
| S12. (dB) | -35.2 | -47.15 | - | - | - | - |
| NF. (dB) | 1.22 | 1.44 | 1.597 | 1.39 | 4.54 | 3.2 |
| IIP3 (dBm) | 9.92 | 8.9 | 12 | -15 | -2 | -15.9 |
| FOM | 15.45 | - | - | 4.75 | - | 0.067 |

### *D. Comparison of Results*

The results of the linearized CMOS amplifier is compared with the simulation data of other reported low noise amplifiers in Table I ([12-16]). From the table, it is apparent that the presented amplifier exhibits excellent simulated performance in terms of power gain, insertion loss, noise figure, output return loss, and input intercept point. Only current reused architecture [12] and post distortion architecture [13] show linearity parameters comparable to this work, but the feat comes at the cost of reduced gain and noise performance. Considering the parameters presented in Table I, the demonstrated CMOS amplifier can be useful in simultaneously achieving gain-boosted and highly linear performance. To evaluate the performance of different low noise amplifiers, the following figure of merit (FOM) formula is used.

$$FOM = \frac{gain(abs).IIP3(mW)}{(NF-1)(abs).power(mW)} \quad (3)$$

## IV. CONCLUSIONS

This work presents a highly linear, gain-boosted, low NF CMOS amplifier in 130 nm technology for wireless applications. The architecture exhibits excellent linearity performance with the help of a multibias scheme resulting in a positive IIP3 of 9.92 dBm. This is achieved after an increment in linearization of 10.06 dB which is rarely reported among linearity enhancement techniques. Linearity compensation is further improved by bulk bias settled interstage feedback which is supported by passive networks for impedance matching. Besides, noise figure of 1.22 dB and power gain of 27.5 dB are achieved which makes it a good candidate for low voltage and low power applications.

## REFERENCES

[1] B. Razavi, *Design of Analog CMOS Integrated Circuits*, 1st ed. New York, NY, USA: McGraw-Hill, Inc., 2001.

[2] M. Sanduleanu and E. van Tuijl, *Power Trade-offs and Low-Power in Analog CMOS ICs*. Springer US, 2006.

[3] T. H. Lee, "The design of cmos radio-frequency integrated circuits, 2nd edition," *Communications Engineer*, vol. 2, no. 4, pp. 47–47, Aug 2004.

[4] H. T. Friis, "Noise figures of radio receivers," *Proceedings of the IRE*, vol. 32, no. 7, pp. 419–422, 1944.

[5] W. Gao, Z. Chen, Z. Liu, W. Cui, and X. Gui, "A highly linear low noise amplifier with wide range derivative superposition method," *IEEE Microwave and Wireless Components Letters*, vol. 25, no. 12, pp. 817–819, Dec 2015.

[6] A. Mabrouki, T. Taris, Y. Deval, and J. B. Begueret, "Cmos low-noise amplifier linearization through body biasing," in *2009 IEEE International Symposium on Radio-Frequency Integration Technology (RFIT)*, Jan 2009, pp. 150–153.

[7] B. Guo and X. Li, "A 1.6 to 9.7 ghz cmos lna linearized by post distortion technique," *IEEE Microwave and Wireless Components Letters*, vol. 23, no. 11, pp. 608–610, Nov 2013.

[8] C. M. Chou and K. W. Cheng, "A sub-2 db noise-figure 2.4 ghz lna employing complementary current reuse and transformer coupling," in *2016 IEEE International Symposium on Radio-Frequency Integration Technology (RFIT)*, Aug 2016, pp. 1–3.

[9] A. Madan, M. J. McPartlin, C. Masse, W. Vaillancourt, and J. D. Cressler, "A 5 ghz 0.95 db nf highly linear cascode floating-body lna in 180 nm soi cmos technology," *IEEE Microwave and Wireless Components Letters*, vol. 22, no. 4, pp. 200–202, April 2012.

[10] A. Galal, R. Pokharel, H. Kanaya, and K. Yoshida, "High linearity technique for ultra-wideband low noise amplifier in 0.18μm cmos technology," *AEU - International Journal of Electronics and Communications*, vol. 66, no. 1, pp. 12 – 17, 2012.

[11] M. T. Lai and H. W. Tsao, "Ultra-low-power cascaded cmos lna with positive feedback and bias optimization," *IEEE Transactions on Microwave Theory and Techniques*, vol. 61, no. 5, pp. 1934–1945, May 2013.

[12] R. Dai, Y. Zheng, J. He, W. Kong, and S. Zou, "A 2.5-ghz 8.9-dbm iip3 current-reused lna in 0.18 um cmos technology," in *2014 IEEE International Symposium on Radio-Frequency Integration Technology*, Aug 2014, pp. 1–3.

[13] I. Umoh, T. Al-Attar, and T. Ogunfunmi, "A 0.18 um cmos narrow-band lna linearization using digital base-band post-distortion," in *2010 Conference Record of the Forty Fourth Asilomar Conference on Signals, Systems and Computers*, Nov 2010, pp. 998–1001.

[14] A. Taibi, A. Slimane, S. A. Tedjini, M. T. Belaroussi, D. Maafri, and M. Trabelsi, "A 0.9 v low power reconfigurable cmos folded cascode lna for multi-standard wireless applications," in *2014 9th International Design and Test Symposium (IDT)*, Dec 2014, pp. 185–188.

[15] C. h. Chang and M. Onabajo, "Linearization of subthreshold low-noise amplifiers," in *2013 IEEE International Symposium on Circuits and Systems (ISCAS2013)*, May 2013, pp. 377–380.

[16] E. Kargaran, Y. Mafinejad, K. Mafinezhad, and H. Nabovati, "A new gm-boosting current reuse cmos folded cascode lna," *IEICE Electronics Express*, vol. 10, no. 24, pp. 20 130 264–20 130 264, 2013.

# A Novel Zeonex based photonic sensor for alcohol detection in beverages

Md. Saiful Islam[1,*], Jakeya Sultana[1,2], Alex Dinovitser[1], Kawsar Ahmed[3],Mohammad Rakibul Islam[2], Mohammad Faisal[4], Brian W.-H. Ng[1], and Derek Abbott,[1]

[1]School of Electrical & Electronic Engineering, The University of Adelaide, Adelaide, 5005, Australia
[2] Electrical & Electronic Engineering, Islamic University of Technology, Gazipur, 1704, Bangladesh
[3] Information & Communication Technology, Mawlana Bhashani Science & Technology University, Tangail,1902, Bangladesh
[4] Electrical & Electronic Engineering, Bangladesh University of Engineering & Technology, Dhaka, 1000, Bangladesh
*mdsaiful.islam@adelaide.edu.au

***Abstract*—A novel Zeonex based photonic crystal fiber (PCF) is proposed in terahertz frequency band for alcohol detection in beverages. Characterizing the fiber using Finite Element Method (FEM), simulation results shows an extremely high relative sensitivity of $88.6\%$ with very low effective material (EML) loss of $0.0222$ cm$^{-1}$ and negligible confinement loss of $3.63 \times 10^{-11}$ cm$^{-1}$ at an operating frequency of $1.9$ THz. Another important advantage of the proposed fiber is that it shows nearly flat characteristics of relative sensitivity and EML in a broad frequency of $1$–$4$ THz. The design of the sensor is extremely simple in that it facilitates the fabrication possibilities. The proposed PCF based sensor can be used for the alcohol detection in beverages as well as low loss transmission of terahertz waves in a bandwidth of $3$ THz.**

***Index Terms*—Alcohol sensor, terahertz, PCF, EML, dispersion.**

## I. Introduction

In the last few years, porous core PCF have demostrated enormous potential in the field of optical fiber communications, nonlinear optical devices, fiber lasers, highly sensitive sensors [1], [2], [3], [4], [5], [6] as well as low loss transmission of terahertz waves [7], [8], [9]. The main reason for this interests is that, the fiber characteristics including relative sensitivity, EML, confinement loss, dispersion, effective area can be modified easily just by tuning the position and size of air holes used to design the PCF. In a PCF, the key design parameters including pitch size, air hole radius, size of core diameter, and operating frequency can be adjusted freely based on the requirements of terahertz applications [10]. In a porous core PCF, the absorption loss of the used material is reduced compared to a solid core fiber, as much of the energy is guided through air [8]. Moreover, using a number of microstructured air holes inside the core increases the probability of transmitting signal through air. In addition, instead of using air inside the air holes different analytes like gas/liquid can be used. This provides enhanced light-matter interaction with great potential for sensing applications.

For the detection of alcoholic beverages it is important to detect ethanol (ethyl-alcohol) as it is the primary active ingredient [11]. There are a number of PCF have been proposed [12], [13], [14] for sensing application in the optical wavelength (100 nm to 1 mm). In 2006, Cordeiro *et al.* [1] proposed a PCF using different analytes in the core air holes. After, theoretical and experimental study of their proposed PCF based sensor they obtained a low relative sensitivity with high absorption loss. Monro *et al.* [5] for the first time shows that porous structure both in core and cladding can be used for evanescent PCF sensing. To improve the sensitivity, Ademgil *et al.* in 2014 proposed an octagonal PCF with only 21% relative sensitivity [13]. In the following year, for liquid analyte sensing application a highly birefringent PCF was proposed by the same research group proposed [14]. But, again they failed to improve the sensitivity of their proposed fiber. Later, a number of research works [15], [16], [17], [18], [19] were carried out to increase the relative sensitivity and reduce the confinement loss. But in most of the cases researchers failed to achieve both at the same time. Recently, Paul *et. al* [20] proposed a folded cladded PCF and obtained a relative sensitivity of $65.18\%$ and confinement loss of $2.07 \times 10^{-5}$ dBm$^{-1}$.

Therefore, from the proposed [12], [13], [14], [15], [16], [17], [18], [19], [20] PCF it is found that the designed sensor only operates in the optical wavelength and used silica as the material. Also, their applications are limited to low frequency region.

In order to bring diversity in application it is necessary to design sensor to operate at high frequencies. In the electromagnetic frequency spectrum, terahertz waves (0.1-10 THz) have immense potential to the researchers due to its enormous demand in the field of sensing, communication, time domain spectroscopy, pharmaceutical drug testing and in biomedical engineering [21], [22], [23], [24], [25], [26]. Though optical wavelength is technologically well developed for sensing applications, there are few areas where terahertz sensing is better. Firstly, in terahertz sensing it is possible to achieve few times sharper spatial resolution and better spectroscopy of the concealed material that needs to be detected. This is because terahertz waves have few times

978-1-5386-3374-8/17/$31.00 ©2017 IEEE

lesser wavelength than optical wavelength. Moreover, in terahertz sensing, it is possible to detect skin cancer [27], [28] because it can go through few millimeter of human body. In addition, due to non-ionizing effect it is safer to human body than $x$-ray radiation [29], [30], [31], [32]. Moreover, terahertz signal can go through non-mettalic and non-polar mediums so it can easily detect any harmful materials contained within those mediums. Again many hazardous chemicals have transmission spectra in the terahertz band so a terahertz sensor can detect those concealed chemicals easily.

In this manuscript, we propose a novel Zeonex based terahertz sensor for alcoholic beverage detection. The proposed terahertz sensor contains a simplified kagome structure with circular shaped air holes inside the core. In addition to high relative sensitivity, the terahertz sensor shows extremely low EML and negligible confinement loss over a broad operating frequency range. Another advantage of the proposed sensor is its extraordinary simplicity in design that can be fabricable easily using the existing fabrication techniques.

## II. PHYSICAL CHARACTERIZATION OF THE PROPOSED TERAHERTZ SENSOR

The physical architecture of the proposed Zeonex based terahertz sensor is shown in Fig. 1. The full-vector FEM based software COMSOL v $4.3b$ is used to compute different characteristics of the PCF. In the cladding region, simplified kagome lattice with few simple struts are used while the core consists of hexagonal structure with only circular shaped air holes. The compact geometry of core is responsible for high relative sensitivity as well as EML. Moreover, the simplified kagome lattice and core air hole diameter is responsible for negligible confinement loss. We selected extremely finer mesh in COMSOL during simulation and found an average element quality of $0.93$ that indicates the computational error using COMSOL is less than $1\%$.

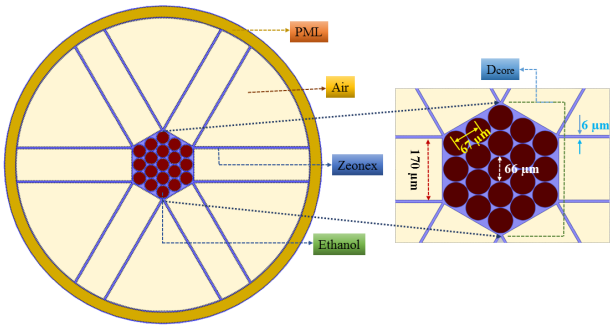


Fig. 1. Cross section of the proposed terahertz PCF based sensor.

In the cladding, the parallel struts are $170$ $\mu$m apart where the strut width is $6$ $\mu$m. The core diameter ($D_{core}$) and diameter of each air holes in the core were kept fixed at $350$ $\mu$m and $66$ $\mu$m respectively. The pitch distance between the air holes in the core region was kept fixed at $67$ $\mu$m. Attention were also given so that the air holes do not overlap with each other. The distances between the air holes were taken as such it does not affect the fabrication process. A $4$ $\mu$m distance was kept from the beginning of the cladding region from the core. A perfectly matched layer boundary condition has been used at the outer part of the cladding, which is about $10\%$ of the fiber radius.

There are a number of polymer materials that can be used as the base material to design a PCF based sensor. These include Teflon, polymethylmethacrylate (PMMA), high density polyethylene (HDPE), Silica, Topas and Zeonex. We use Cyclo-olefin Polymer (COP) commercially named as Zeonex as the bulk material of our proposed PCF because Zeonex have a lower material absorption loss of $0.2$ cm$^{-1}$ in terahertz frequency range, a constant index of refraction of $n_{mat}$= $1.53$, negligible material dispersion and other optical properties that are suitable for terahertz sensing [33].

## III. SIMULATION AND RESULTS

The intensity of light interaction with the given analyte inside the core air hole at $1.9$ THz is shown in Fig. 2. It is observed that mode fields are well confined to the porous core region, which is essential for efficient terahertz signal propagation.

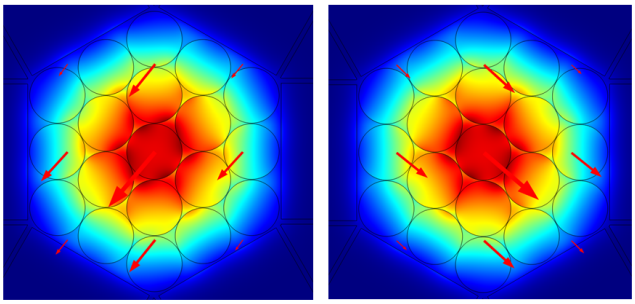

(a) (b)

Fig. 2. Intensity of light interaction with ethanol at 1.9 THz frequency with fixed ($D_{core}$) and core air hole radius (a) $x$-polarization,(b) $y$-polarization

It is also observed from Fig. 2 that, the core structure is a purely symmetrical and the light interaction with ethanol is almost same for both the polarization mode. For the $x$-pol the obtained effective refractive index is $1.358$ and as the structure is symmetrical so the effective refractive index for the $y$-pol is found to be the same at $1.358$. From the effective refractive index of $x$ and $y$ pol it can be said that the fiber operates in one mode. So when a light pulse is emerged at the centre of the core only the fundamental modes will be excited and the fiber will operate in the single mode region [33].

The relative sensitivity of a PCF sensor can be measured from the intensity of light interaction with the matter to be sensed. The amount of light interaction with matter is measured through the absorption coefficient at a particular frequency. According to the Beer-Lambert law, amount of light attenuation with the intensity of absorbance of the evanescent field can be calculated by [18],

$$I(f) = I_0(f)exp[-r\alpha_m l_c] \quad (1)$$

Where, $I(f)$ and $I_0(f)$ are the intensities of light at the input and output of PCF, $r$ is the relative sensitivity, $\alpha_m$ indicates the absorption coefficient, $l_c$ is the channel length and $f$ is the operating frequency.

The absorbance of the material to be detected can be calculated by [18],

$$A = log(\frac{I}{I_0}) = -r\alpha_m l_c \tag{2}$$

The relative sensitivity of a PCF based sensor can be calculated by [14],

$$R = \frac{n_{\rm r}}{n_{\rm eff}} \times e \tag{3}$$

where, $R$ denotes the relative sensitivity, $n_{\rm r}$ represents the refractive index of the analyte needs to be detected which is $1.354$ in case of ethanol, $n_{\rm eff}$ denotes the effective refractive index of the guided mode and $e$ is the amount of light interaction with the analyte which can be calculated by [14],

$$e = \frac{\int_{\rm sample} R_e(E_x H_y - E_y H_x)\ dxdy}{\int_{\rm total} R_e(E_x H_y - E_y H_x)\ dxdy} \times 100 \tag{4}$$

here, $E_x$, $E_y$ and $H_x$, $H_y$ are the electric field and magnetic field component of the guided mode respectively.

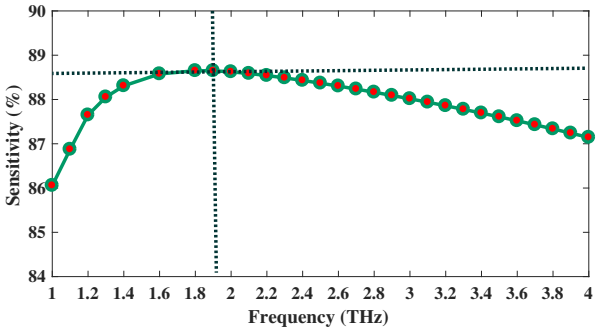


Fig. 3. Relative sensitivity of ethanol with respect to frequency at fixed core diameter and core air hole radius

At a fixed core diameter and core air hole radius the relative sensitivity as a function of frequency is shown in $Fig.$ 3. It is observed from the figure that sensitivity is increases up to 1.9 THz and then start to decrease with further frequency increase. This technical explanation is that at 1.9 THz the interaction of light and matter reaches a maximum. Further increase of frequency tends to reduce the light interaction with matter, as more of the light penetrates the cladding, leading to a decreased sensitivity. We set 1.9 THz, $66\mu$m core air hole diameter and $350\mu$m core diameter as optimum because at 1.9 THz the obtained sensitivity is highest, also the core air hole diameter is chosen as optimum in such a consideration so that $66\mu$m$\pm 2\%$ variation in diameter is suitable for fabrication, and there may be $66\mu$m$\pm 2\%$ variation from optimum parameters. So at optimum design parameters the obtained sensitivity is $88.6\%$. To our knowledge, this is the highest sensitivity obtained in any form of PCF sensing for ethanol detection.

In the terahertz frequency bands, most of the polymer materials are very leaky, so it is a major challenge to design a low loss terahertz waveguide. The so-called effective material loss can be calculated by [35],

$$\alpha_{\rm eff} = \sqrt{\frac{\epsilon_0}{\mu_0}} \left( \frac{\int_{\rm mat} n_{\rm mat} |E|^2 \alpha_{\rm mat} dA}{|\int_{\rm all} S_{\rm z} dA|} \right) \tag{5}$$

where, $\epsilon_0$ and $\mu_0$ designates the relative permittivity and permeability in free space respectively, $\alpha_{\rm mat}$ is called the bulk material loss of Zeonex, $n_{\rm mat}$ indicates the refractive index of Zeonex and $S_{\rm z}$ implies the $z$-component of Poynting vector $S_{\rm z} = \frac{1}{2}(\mathbf{E} \times \mathbf{H}^*)z.$, here, $\mathbf{E}$ is the electric field component and $\mathbf{H}^*$ is the magnetic field component.

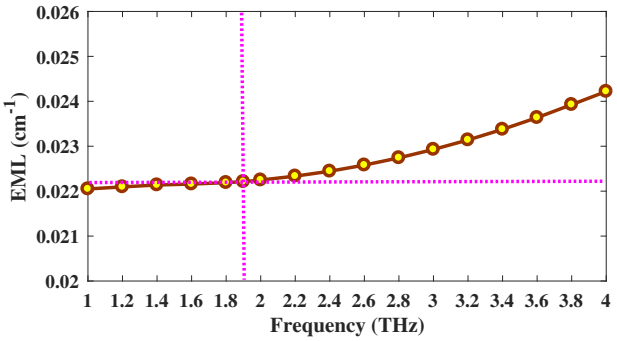


Fig. 4. EML vs frequency at fixed core diameter and core air hole radius

Fig. 4 shows the nature of EML variation with frequency at optimum design parameters. It is observed that, the EML is not constant over the frequency but increases with frequency [35]. This is true because according to the empirical formula [35]: $\alpha(\nu) = \nu^2 + 0.63\nu - 0.13$ [dB/cm], it is experimentally found that, the bulk material absorption loss depends on frequency. This matter is carefully handled when calculating the frequency response of EML. It is seen that, the obtained EML is almost flat throughout the whole numerical simulation. The EML variation is $0.023 \pm 0.01$ cm$^{-1}$ within the frequency range of 1 THz to 4 THz. At 1.9 THz the obtained EML is $0.0222$ cm$^{-1}$ which is extremely low in terahertz frequency range.

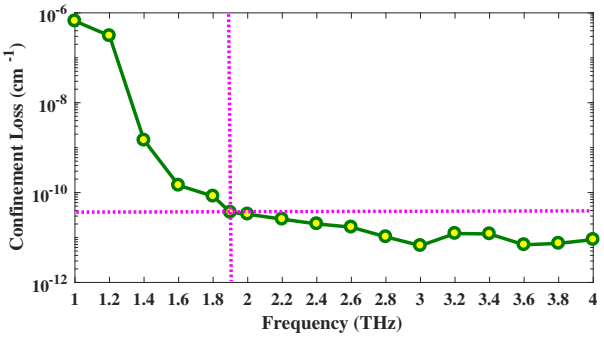


Fig. 5. Confinement loss with respect to frequency at optimal design parameters

Confinement loss is also an important guiding property that can limit the length of terahertz transmission system. Confinement loss depends on the core air hole radius and the number of air hole rings used in the cladding. It can be calculated by [9],

$$L_{\rm c} = \left(\frac{4\pi f}{c}\right) {\rm Im}(n_{\rm eff}), {\rm cm}^{-1} \tag{6}$$

where, ${\rm Im}(n_{\rm eff})$ reflects the imaginary part of effective refractive index and $c$ is called the velocity of light in free space.

TABLE I
COMPARISON OF THE PROPOSED PC-PCF SENSOR WITH PRIOR PCF SENSORS FOR ETHANOL DETECTION

| Ref. | Operating Region | Relative Sensitivity(%) | $\alpha_{\text{eff}}$ ($\text{cm}^{-1}$) | $L_{\text{c}}$ ($\text{cm}^{-1}$) | Background Material |
|---|---|---|---|---|---|
| [13] | $1.0\mu$m | 21.1 | - | $1.319 \times 10^{-4}$ | Silica |
| [14] | $1.5\mu$m | 23.75 | - | $5.5 \times 10^{-5}$ | Silica |
| [15] | $1.33\mu$m | 49.17 | - | $6.3 \times 10^{-11}$ | Silica |
| [16] | $1.3\mu$m | 53.35 | - | $3.7 \times 10^{-11}$ | Silica |
| [37] | $1.33\mu$m | 67.66 | - | $7.5 \times 10^{-12}$ | Silica |
| This manuscript | 1.9 THz | 88.6 | 0.0222 | $3.63 \times 10^{-11}$ | Zeonex |

Fig. 5 shows the characteristics of confinement loss with the variation of frequency. It can be seen that, confinement loss is scaled down with frequency increase because as the frequency increases more light start to constrict strongly in the porous core region. At optimal design parameters, the obtained confinement loss is in the order of $3.63 \times 10^{-11}$ $\text{cm}^{-1}$ which is better than previously reported [12], [13], [14], [15], [16], [17], [18], [19], [20].

It is also necessary to explore the fabrication possibilities of the proposed PCF. There are a number of ways to fabricate porous core PCF. The most frequently used methods are capillary stacking, drilling, stack and draw, extrusion and sol-gel etc. The hexagonal structured circular shaped air holes can easily be fabricated using capillary stacking [8] or sol-gel [36] technique. Moreover, we proposed a simplified kagome cladding structure instead of complex kagome structure. The complex Kagome structure has already been fabricated using the existing fabrication technology [37], [38], [39], [40]. Moreover, the extrusion technique [37], [38] and 3D printing [39], [40] technique paves the way of fabricating complex structures in both core and cladding region. So, it can be said that, the proposed PCF based sensor is feasible to fabricate using the existing fabrication techniques.

Table 1 indicates that this sensor has the higher relative sensitivity compared to other proposed PCFs, as well as low EML and negligible confinement loss.

## IV. CONCLUSIONS

We have presented a Zeonex based PCF sensor for Alcoholic beverage detection in the terahertz range. After theoretical modelling and numerical simulation using COMSOL we obtain a high relative sensitivity of $88.6\%$ and negligible confinement loss of $3.63 \times 10^{-11}$ $\text{cm}^{-1}$ at $1.9$ THz. Moreover, a flat sensitivity of $87.3 \pm 1.3\%$ and flat EML with a variation of $0.023 \pm 0.01$ $\text{cm}^{-1}$ is obtained within a broad frequency range of $1$ THz to $4$ THz. The obtained high relative sensitivity is suitable for detecting alcohols in beverages as well as skin cancer in human body. Moreover, the obtained ultra-low loss properties potentially have a significant application in longer distance transmission of terahertz waves. Again, simplicity in design and the realistic size makes the proposed PCF feasible in terms of fabrication. So, considering all the aforementioned properties, we can conclude that, if the proposed fiber can be utilized properly with state of the art technology then it will open a new window for sensing application as well as longer distance transmission of terahertz waves.

## REFERENCES


[1] C. M. B. Cordeiro, M. A. R. Franco, G. Chesini, E. C. S. Barretto, R. Lwin, C. H. B. Cruz, and M. C. J. Large "Microstructured-core optical fibre for evanescent sensing applications," *Opt. Express*, vol. 14, no. 26, pp. 13056–13066, 2006.

[2] T. Kiwa, J. Kondo, S. Oka, I. Kawayama, H. Yamada, M. Tonouchi, and K. Tsukada, "Chemical sensing plate with a laser-terahertz monitoring system," *Appl. Opt.*, vol. 47, no. 18, pp. 3324–3327, 2008.

[3] Y. L. Hoo, W. Jin, H. L. Ho, D. N. Wang, R. S. Windeler, "Evanescent-wave gas sensing using microstructure fiber" *Optical Eng*, vol. 41, no. 1, pp. 8–9, 2002.

[4] Y. Yu, X. Li, X. Hong, Y. Deng, K. Song, Y. Geng, H. Wei, W. Tong, "Some features of the photonic crystal fiber temperature sensor with liquid ethanol filling," *Opt. Express*, vol. 18, no. 15, pp. 15383–15388, 2010.

[5] T. M. Monro, W. Belardi, K. Furusawa, J. C. Baggett, N. G. R. Broderick and D. J. Richardson, "Sensing with microstructured optical fibres," *Measurement Science and Technology.*, vol. 12, no. 7, 854, 2001.

[6] A. M. R. Pinto and M. Lopez-Amo, "Photonic crystal fibers for sensing applications, " *Journal of Sensors*, vol. 2012, 598178, 2012.

[7] J. Sultana, Md. S. Islam, J. Atai, M. R. Islam and D. Abbott "Near-zero dispersion flattened, low-loss porous-core waveguide design for terahertz signal transmission," *Opt. Eng.*, vol. 56, no. 7, 076114, 2017.

[8] M. S. Islam, S. Rana, M. R. Islam, M. Faisal, H. Rahman, and J. Sultana, "Porous core photonic crystal fiber for ultra-low material loss in THz regime," *IET Communications*, vol. 10, no. 16, pp. 2179–2183, 2016.

[9] Md. S. Islam, J. Sultana, J. Atai, M. R. Islam and D. Abbott,"Design and characterization of a low-loss, dispersion-flattened photonic crystal fiber for terahertz wave propagation," *Optik - International Journal for Light and Electron Optics.*, vol. 145, pp. 398–406, 2017.

[10] S. Rana, Md. S. Islam, M. M. Faisal, K. C. Roy, R. Islam, and ,S. F. Kaijage "Extremely low-loss, dispersion flattened porous-core photonic crystal fiber for terahertz regime," *Optical Engineering.*, 55, 076117, 2016.

[11] Chemical Ingredients in Alcohol. Accessed on 9th October' 2017 [Online]. Available: https://en.wikipedia.org/wiki/Alcohol.

[12] K. Lee, S. A. Asher, "Photonic crystal chemical sensors: pH and ionic strength," *J. Am. Chem. Soc.*, vol. 122, no. 39, pp. 9534–9537, 2000.

[13] H. Ademgil "Highly sensitive octagonal photonic crystal fiber based sensor" *Optik - International Journal for Light and Electron Optics.*, vol. 125, no. 20, pp. 6274–6278, 2014.

[14] H. Ademgil, and S. Haxha "Highly PCF based sensor with high sensitivity, high birefringence and low confinement losses for liquid analyte sensing applications," *Sensors*, vol. 15, no. 12, pp. 31833–31842, 2015.

[15] S. Asaduzzaman, K. Ahmed. T. Bhuyan and T. Farah "Hybrid photonic crystal fiber in chemical sensing," *SpringerPlus*, vol. 15, no. 1, 748, 2016.

[16] Md. F. H. Arif, Md. J. H. Biddut, "A new structure of photonic crystal fiber with high sensitivity, high nonlinearity, high birefringence and low confinement loss for liquid analyte sensing applications, " *Sensing and Bio-Sensing Research,*, vol. 12, pp. 8–14, 2017.

[17] B. K. Paul, Md. S. Islam, K. Ahmed, S. Asaduzzaman, "Alcohol sensing over O+E+S+C+L+U transmission band based on porous cored octagonal photonic crystal fiber," *Photonic Sensors*, vol. 7, no. 2, pp. 123–130, 2017.

[18] Md. F. H. Arif, K. Ahmed, S. Asaduzzaman, Md. A. K. Azad, "Design and optimization of photonic crystal fiber for liquid sensing applications," *Photonic Sensors*, vol. 6, no. 3, pp. 279–288, 2016.

[19] S. Asaduzzaman, and K. Ahmed. "Microarray-core based circular photonic crystal fiber for high chemical sensing capacity with low confinement loss," *Optica Applicata*, vol. 47, no. 1, pp. 41–49, 2017.

[20] B. K. Paul, K. Ahmed, S. Asaduzzaman, Md. S. Islam, "Folded cladding porous shaped photonic crystal fiber with high sensitivity in optical sensing applications: design and analysis," *Sensing and Bio-Sensing Research,*, vol. 12, pp. 36–42, 2017.

[21] M. I. Hasan, S. M. Abdur Razzak, G. K. M. Hasanuzzaman, and Md. S. Habib, "Ultra-low material loss and dispersion flattened fiber for THz transmission," *IEEE Photonics Technol. Lett.*, vol. 26, no. 23, pp. 2372–2375, 2014.

[22] M. Walther, B. M. Fischer, A. Ortner, A. Bitzer, A. Thoman, and H. Helm, "Chemical sensing and imaging with pulsed terahertz radiation," *Analytical and Bioanalytical Chemistry*, vol. 397, no. 3, pp. 1009–1017, 2010.

[23] B. M. Fischer, H. Helm and P. U. Jepsen,"Chemical recognition with broadband THz spectroscopy," *Proceedings of the IEEE*, vol. 95, no. 8, pp. 1592–1604, 2007.

[24] M. Nagel, P. H. Bolivar, M. Brucherseifer, H. Kurz, A. Bosserhoff and R. Bttner, "Integrated THz technology for label-free genetic diagnostics," *Appl. Phy. Lett.*, vol. 80, no. 154, pp. 154–156, 2002.

[25] B. M. Fischer, M. Hoffmann, H. Helm, R. Wilk, F. Rutz, T. Kleine-Ostmann, M. Koch, and P. Uhd Jepsen, "Terahertz time-domain spectroscopy and imaging of artificial RNA," *Opt. Express.*, vol. 13, no. 14, pp. 5205–5215, 2005.

[26] A. G. Markelz, A. Roitberg, E. J. Heilweil, "Pulsed terahertz spectroscopy of DNA, bovine serum albumin and collagen between 0.1 and 2.0 THz," *Chemical Physics Letters,*, vol. 320, no. 1, pp. 42–48, 2000.

[27] A. Rahman, A. K. Rahman, and B. Rao, "Early detection of skin cancer via terahertz spectral profiling and 3D imaging," *Biosensors and Bioelectronics*, vol. 82, no. 1, pp. 64–70, 2016.

[28] X. Yang, X. Zhao, K. Yang, Y. Liu, Y. Liu, W. Fu, Y. Luo "Biomedical Applications of Terahertz Spectroscopy and Imaging," *Trends in Biotechnology*, vol. 34, no. 10, pp. 810–824, 2016.

[29] T. Lffler, K. Siebert, S. Czasch, T. Bauer and H. G. Roskos, "Visualization and classification in biomedical terahertz pulsed imaging," *Phys. Med. Biol.*, vol. 47, 3847, 2002.

[30] D. Zimdars, J. S. White, "Terahertz reflection imaging for package and personnel inspection," *Proc. SPIE,, Terahertz for Military and Security Applications II,* 2004.

[31] M. R. Scarf, M. Roman, R. Di Pietro, O. Zeni, A. Doria, G.P. Gallerano, E. Giovenale, G. Messina, A. Lai, G. Campurra, D. Coniglio, M. D'Arienzo, "THz Exposure of Whole Blood for the Study of Biological Effects on Human Lymphocytes," *J. Biol Phys.*, vol. 29, no. 2–3, pp.171–176, 2003.

[32] R. H. Clothier and N. Bourne, "Effects of THz Exposure on Human Primary Keratinocyte Differentiation and Viability," *J. Biol Phys.*, vol. 29, no. 2–3, pp.179–185, 2003.

[33] G. Woyessa, A. Fasano, C. Markos, A. Stefani, H. K. Rasmussen, and O. Bang, "Zeonex microstructured polymer optical fiber: fabrication friendly fibers for high temperature and humidity insensitive Bragg grating sensing," *Opt. Mater. Express*, vol. 7, no. 1, pp.286–295, 2017.

[34] S. Rana, A. S. Rakin, H. Subbaraman, R. Leonhardt and D. Abbott, "Low loss and low dispersion fiber for transmission applications in the terahertz regime," *IEEE Photonics Technol. Lett.*, vol. 29, no. 10, pp. 830–833, 2017.

[35] M. S. Islam, J. Sultana, J. Atai, D. Abbott, S. Rana, and M. R. Islam, "Ultra low loss hybrid core porous fiber for broadband applications," *Applied Optics.*, vol. 56, no. 4, pp. 1232–1237, 2017.

[36] R. T. Bisen and D. J. Trevor, "Solgel-derived microstructured fibers: fabrication and characterization," *Optical Fiber Communication Conference, Technical Digest. OFC/NFOEC*, 2005. DOI: 10. 1109/OFC. 2005. 192772.

[37] S. Atakaramians, S. Afshar, H. Ebendorff-Heidepriem, M. Nagel, B. M. Fischer, D. Abbott, and T. M. Monro, "THz porous fibers: design, fabrication and experimental characterization," *Opt. Express*, 17, 14053–14062 2009.

[38] Fabrications of Photonic Crystal Fibers, Photonic Crystal Fibre Science, accessed on 9th October, (2017) [Online]. Available: http://www.mpl.mpg.de/en/russell/research/topics/fabrication.html.

[39] A. M. Cubillas, S. Unterkofler, T.G. Euser, B. J. M. Etzold, A. C. Jones, P. J. Sadler, P. Wasserscheid, P. St. J. Russell, "Photonic crystal fibres for chemical sensing and photochemistry," *Chem. Soc. Rev.*, vol. 42, no.22, pp. 8629–8648, (2013).

[40] H. Ebendorff-Heidepriem, J. Schuppich, A. Dowler, L. Lima-Marques, and T. Monro, "3D-printed extrusion dies: a versatile approach to optical material processing," *Opt. Mater. Express.*, vol. 4, no.8, pp. 1494–1504, (2014).

# Design of a Coarse Wavelength Demultiplexer Based on Simplified Semi-Objective Scheme

Mengwen Guan,[1] Weifeng Jiang,[1,2] and Xiaohan Sun[1,*]

[1]National Research Center for Optical Sensing/Communications Integrated Networking,
Department of Electronics Engineering, Southeast University, Nanjing 210096, China
[2]School of Electronic and Optical Engineering,
Nanjing University of Posts and Telecommunications, Nanjing 210023, China
[*]xhsun@seu.edu.cn

*Abstract*—**A simplified semi-objective scheme is proposed to optimally design a coarse wavelength demultiplexer (CDeMUX), based on the structure of multimode interference (MMI). The objective function of the CDeMUX is given as the difference between the desirable and actual output power. The conversion degree restriction (CDR) is defined as the upper limit of average permittivity difference in the multimode interference (MMI) region, which is divided into q × p conversion cells. The value of p or q increases alternately until the CDR is reached. The optimal design of CDeMUX with the insertion loss of 0.58 dB and 0.55 dB, extinction ratio of 26.3 dB and 27.6 dB is achieved for the quasi-TE mode at 1310 nm and 1550 nm, respectively. The scheme reduces the complexity of device structure and fabrication process.**

***Index Terms***—**Integrated optics devices, Wavelength division multiplexer, Multimode interference.**

## I. Introduction

Wavelength division multiplexing is an important strategy to improve the capacity of optical communication links, and on-chip wavelength demultiplexer is an essentially key component for realizing wavelength multiplexing systems [1]. Compared with other kinds of wavelength demultiplexer such as Y branch and Mach–Zehnder interferometers, wavelength demultiplexer based on multimode interference (MMI) shows advantages of low loss and large fabrication robustness [2]. Until now, most MMI-type wavelength demultiplexers are designed and fabricated on silicon-on-insulator (SOI) or InP/InGaAsP platform. However, due to large index difference between the waveguide and substrate, most of them are polarization-dependent and could be only used for one polarization state. A polarization-insensitive wavelength demultiplexer has been proposed on a sandwiched waveguide structure, but the fabrication progress is more complicated [3]. In addition, the performance inconformity between 1310nm port and 1550nm port is another problem, where the performance parameter at one wavelength obviously worse than at the other wavelength is often the case [4].

For the design of a wavelength demultiplexer, the structure and function of the device are limited by the designers' professional knowledge and intuition [5]. In order to eliminate this issue, several approaches, including the particle swarm optimisation, the genetic algorithm and level set method, have been reported [6]-[8]. Although a proposed structure can be optimised to achieve the best performance, it is not trivial to propose a novel and effective structure. Recently, a novel method named inverse design algorithm has been developed for nearly all linear photonic devices [9]. However, the optimised structures obtained by the algorithm are very complex, which are not trivial to be fabricated by the standard complementary metal–oxide–semiconductor (CMOS) process. Fabrication constraints are considered in a modified version of the direct-binary-search algorithm [10]. Nevertheless, the computation time is extremely long and the DBS algorithm may converge to local optimum. Therefore, an efficient optimisation algorithm which produces a device with high performance and achievable fabrication process is highly needed.

In this paper, we propose and develop a novel simplified semi-objective scheme so that can obtain the optimal design of a coarse wavelength demultiplexer (CDeMUX).

## II. Principle of Scheme

The CDeMUX with one input port and N output ports is designed to work at M wavelengths, as shown in Fig. 1. The MMI region between the input port and output ports is divided into q × p conversion cells, where p and q are positive integers. Suppose an unit power is injected into the input port, the desirable output power to the $i_{th}$ (i=1, 2, 3, …, N) output port is $a_{ij}$ while the actual output power is $b_{ij}$. Thus the characteristics of the device can be described with the power transfer efficiency between input port and output ports. In the design scheme, the objective function is defined as the difference between the desirable output power and the actual output power, which is

$$F = \frac{1}{MN}\sum_{i=1}^{M}\sum_{j=1}^{N}|\, a_{ij} - b_{ij}\,| \qquad (1)$$

where the coefficient M*N is a normalized factor. For two different device structures, the output power of each port is simulated and the values of objective function are calculated. The structure with lower value of objective is closer to the target device.

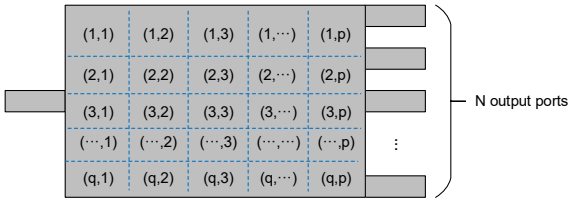


Fig. 1 Schematic of a CDeMUX with one input port and N output ports.

The simplified semi-objective scheme involves two iterations. In the initialization, the value of p and q equals one, which means the MMI region include only one conversion cell. For the inner iteration, each conversion cell is filled with one proper geometric component. The shape and dimension

parameter are optimized to obtain a smaller value of objective function. For the outer iteration, the value of p or q increases by one alternately. The MMI region is divided into more conversion cells as the values p and q increase, which results a more complicated device structure. In order to prevent the device structure from being too sophisticated to be fabricated, a conversion degree restriction is set in the scheme. The conversion degree is defined as the average of absolute permittivity difference of all conversion cells in the MMI region, which is normalized between 0 and 1. The value of conversion degree represents the geometry complexity of the device structure and it is noted that the MMI region with smaller value of conversion degree is easier to be fabricated. The conversion degree restriction (CDR) is defined as the upper limit of the conversion degree of the MMI region. When the CDR is reached, the values of p and q stop increasing and the outer iteration ends. Until now, the structure and parameter with the smallest value of objective function is obtained as the target.

## III. Design and Optimization

Following, the design of a 1×2 1310/1550 nm CDeMUX is taken as an example to prove the capability of the scheme. For the CDeMUX, the most crucial performance parameters are the insertion loss (IL) and the extinction ratio (ER). Considering these performance parameters, the objective function F is defined as

$$F = \frac{1}{4}(2 + a_{11} + a_{22} - a_{21} - a_{22}) \qquad (2)$$

where $a_{11}$ and $a_{21}$ is the normalized power at 1310 nm for output ports 1 and 2, respectively. While $a_{12}$ and $a_{22}$ is the normalized power at 1550 nm for output ports 1 and 2, respectively. Considering the standard CMOS process, the CDR of the MMI region is set to be 0.4. Thus the design and optimisation problem is reduced to search for a device structure with proper parameters that minimises F, which simultaneously satisfies the CDR condition.

The design of the CDeMUX is based on silica-on-silicon (SoS) waveguide, which is compatible with the CMOS process and with high coupling efficiency to the single mode fiber [11]. The refractive index of the silica buffer layer is taken as 1.4444 at the wavelength of 1550 nm and the relative index difference, Δ is taken as 1.5%. Before the scheme starts, a simple three-port structure with one input port, a rectangular MMI region and two output ports 1 and 2 is initialized. In the implementation of the scheme, the actual output power of the device is obtained by the three-dimensional full-vector beam propagation method [12]. The output power from the output port 1 is defined as the output power (OP) at 1310 nm, while the output power from the output port 2 is defined as the OP at 1550 nm.

The design and optimisation process last for about 120 h on an Intel Xeon CPU E5-2687W v2 @3.40GHz. After running the scheme, the MMI region of the CDeMUX is divided into 2 × 3 conversion cells as shown in Fig. 2a. The conversion cell (1, 1) and (2, 1) are bonded into a bulk rectangular waveguide MMW1. It can be noted that the length of the MMW2 mostly influences the output power at 1310 nm while has little effect on the output power at 1550 nm. The situation is converse for the length of MMW3. The coupling loss increases with an increase of the propagation mode difference between the multimode waveguide and the single mode waveguide [13]. The MMW2, MMW3 and MMW4 are mainly applied to reduce the width of the electric filed and confine the electric field intensity. Moreover, with these multimode waveguides, the ERs can be improved by filtering the power at undesirable wavelength. Finally, extinction ratios can be further improved by filling the conversion cell (2, 3) with a parallelogram single mode waveguide instead of a rectangular single mode waveguide as shown in Fig. 2a. The output power at 1310 and 1550 nm wavelengths is hardly influenced by the tilt, as illustrated in Fig. 2b. As the value of tilt changes from negative to positive, the ER at 1310 nm decreases monotonically, while the ER at 1550 nm firstly increases to the maximum point and then decreases. Therefore, the tilt value is chosen to be -3.5 μm, where the negative symbol represents the tilt is towards MMW4.

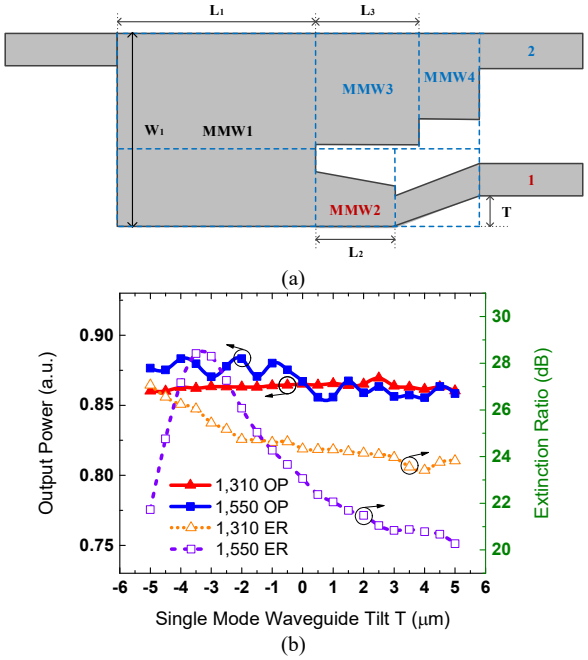


Fig. 2 (a) Structure of the CDeMUX. (b) Output power and extinction ratio change with tilt.

## IV. Results and Discussion

The simulated intensity distributions for the quasi transverse electric (quasi-TE) and quasi transverse magnetic (quasi-TM) polarised light at 1310 nm and 1550 nm are shown in Fig. 3(a). It can be observed that the input light for 1310 nm and 1550 nm is separated by the CDeMUX for both the polarisations. The optimal CDeMUX with the insertion loss of 0.58 dB and 0.55 dB, extinction ratio of 26.3 dB and 27.6 dB can be achieved for the quasi-TE mode at the wavelengths of 1310 nm and 1550 nm, respectively. With the identical structure, the insertion loss of 0.57 dB and 0.56 dB, extinction ratio of 28.7 dB and 22.3 dB are obtained for the quasi-TM mode at the wavelength of 1310 nm and 1550 nm, respectively.

The wavelength response of the CDeMUX for the both polarisations is shown in Fig. 3(b). It can be noted that the 1 dB bandwidth exceeds 60 nm and 70 nm at centre wavelength of 1310 nm and 1550 nm, respectively. Thus, the characteristics of the CDeMUX is tolerant to the wavelength variation. Besides, it can be noted that the polarisation dependent loss of the CDeMUX is lower than 0.01 dB. Hence, the CDeMUX has similar performances for the both polarisations. In the end, we consider the tolerance of the CDeMUX to the fabrication process. As the beat length of the multimode waveguide is positively related to its width, a

CDeMUX with a smaller width is more sensitive to the fabrication error [2]. It is found that the characteristics of the CDeMUX is the most sensitive to the change of MMW3 width. Within a derivation of ± 0.25 μm for the width of MMW3, the insertion loss is less than 1 dB and the ER is >23 dB at 1550 nm. Therefore, the CDeMUX can be fabricated easily by the standard CMOS process.

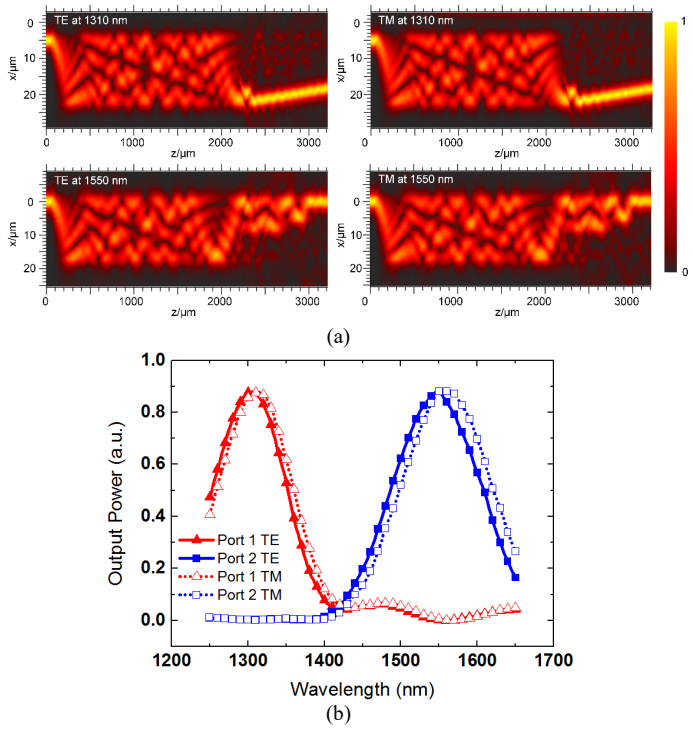


Fig. 3 (a) Intensity distributions at 1310 nm and 1550 nm. (b) Wavelength response at output ports 1 and 2.

## REFERENCES


[1] L. Luo, N. Ophir, C. P. Chen, et al., "WDM-compatible mode-division multiplexing on a silicon chip," *Nature Commun.*, vol. 5, pp. 3069, Jan. 2014.

[2] C. Yao, H. G. Bach, R. Zhang, et al., "An ultracompact multimode interference wavelength splitter employing asymmetrical multi-section structures," *Opt. Express*, vol. 20, pp. 18248-18253, Jul. 2012.

[3] Y. Shi, S. Anand, S. He, "A polarization-insensitive 1310/1550-nm demultiplexer based on sandwiched multimode interference waveguides," *IEEE Photon. Technol. Lett.*, vol. 19, pp. 1789-1791, Oct. 2007.

[4] Y. Ma, P. Magill, T. Baehr-Jones, M. Hochberg, "Design and optimization of a novel silicon-on-insulator wavelength diplexer," *Opt. Express*, vol. 22, pp. 21521-21528, Sept. 2014.

[5] J. Lu, J. Vučković, "Nanophotonic computational design," *Opt. Express*, vol. 21, pp. 13351-13367, Jun. 2013.

[6] J. Robinson, Y. Rahmat-Samii, "Particle swarm optimization in electromagnetics," *IEEE Trans. Antenn. Propag.*, vol. 52, pp. 397-407, Feb. 2004.

[7] S. Preble, M. Lipson, H. Lipson, "Two-dimensional photonic crystals designed by evolutionary algorithms," *Appl. Phys. Lett.*, vol. 86, pp.061111, Feb. 2005.

[8] C. Y. Kao, S. Osher, E. Yablonovitch, "Maximizing band gaps in two-dimensional photonic crystals by using level set methods," *Appl. Phys. B*, vol. 8, pp. 235-244, Jul. 2005.

[9] A. Y. Piggott, J. Lu, T. M. Babinec, et al., "Inverse design and implementation of a wavelength demultiplexing grating coupler," *Sci. Rep.*, vol. 4, pp. 7210, Nov. 2014.

[10] B. Shen, P. Wang, R. Polson, et al, "An integrated-nanophotonics polarization beamsplitter with 2.4× 2.4 μm2 footprint," *Nature Photon.*, vol. 9, pp. 378-382, May. 2015.

[11] W. Jiang, X. Sun, "TE-pass polarizer with cylinder array inserted in buffer layer of silica-on-silicon waveguide," *IEEE Photon. Technol. Lett.*, vol. 26, pp. 937-940, May. 2014.

[12] Z. Zhu, T. G. Brown, "Full-vectorial finite-difference analysis of microstructured optical fibers," *Opt. Express*, vol. 10, pp. 853-864, Aug. 2002.

[13] S. H. Fan, D. Guidotti, H. C. Chien, et al., "Compact polymeric four-wavelength multiplexers based on cascaded step-size MMI for 1G/10G hybrid TDM-PON applications," *Opt. Express*, vol. 16, pp. 12664-12669, Aug. 2008.

2017 IEEE International Conference on Telecommunications and Photonics (ICTP)
26-28 December, 2017, Dhaka, Bangladesh


# Performance Evaluation of MLD and ZFE in a MIMO OFDM System Impaired by Carrier Frequency Offset, Phase Noise and Timing Jitter

Ismat Jarin* and Satya Prasad Majumdar
Department of Electrical and Electronic Engineering
Bangladesh University of Engineering and Technology, Dhaka-1205, Bangladesh
*Corresponding author: ismatjarin16147@gmail.com

***Abstract*—In this paper performances of maximum likelihood detection (MLD) and zero forcing equalizer (ZFE) in MIMO OFDM systems are analyzed with the combined effect of phase noise, timing jitter and normalized CFO over Rayleigh fading channels. Results include the bit error rate (BER), power penalty and BER floor for different value of SNR, number of receiving and transmitting antennas, variance of phase noise and variance of timing jitter. It is observed that OFDM system suffers due to the presence of normalized CFO, phase noise and timing jitter. Significant improvements in this system can be obtained by using multiple antenna techniques. Results show that compare to ZFE the performance of MLD is better for a given parameter of power penalty at a given BER due to timing jitter. Also MLD gives lower BER floor over ZFE due to phase noise.**

***Index Terms*—Multiple input multiple output (MIMO), OFDM, Maximum likelihood detection (MLD), Zero forcing equalizer (ZFE), Bit error rate (BER), BER floor, Power penalty, timing jitter, phase noise.**

## I. Introduction

Multiple input multiple output (MIMO) system is rapidly popular in wireless communication system for robustness to fading, increasing data rate and efficient system capacity. For high data rate and high performance, a MIMO OFDM is an efficient feature to sustain with multiple antennas [1]. OFDM system is very much sensitive to synchronization errors such as carrier frequency offset, timing jitter and phase noise [2]–[4]. The performance of OFDM can be enhanced by using multiple antennas in both input and output. An MIMO OFDM system can be also under the loss of orthogonality and effected by ISI [5]. So such systems require efficient transmission and reception techniques.

Performance analysis of a MIMO OFDM system with efficient way of zero forcing (ZF), Minimum mean square error (MMSE), Vertical bell laboratory layered Space-Time (V-Blast) and maximum likelihood detection(MLD) methods are popular [6], [7]. Among them, MLD method is optimum for minimizing error, low order transmitting antenna and constellation [8]. Zero forcing equalizer or ZFE is a linear equalizer which reduce the system ISI (inter symbol interference) to zero and also very simple to implement. By MLD decoding, diversity order can be achieved by only receiving antenna where ZF demand both transmitting and receiving antenna scheme. MLD has also a SNR advantage with increasing number of transmit antennas [9].

BER performance of a Single input single output (SISO) OFDM system in the presence of CFO , phase noise and timing jitter are presented in [10]. BER performance of a single input multiple output (SIMO) system with diversity technique are presented in [11], [12]. Single input single output (SISO) and single input multiple output (SIMO) techniques due to normalized CFO, phase noise and timing jitter are analyzed by several authors.However a MIMO OFDM system with this error parameters should be analyzed. In this paper we evaluate the BER performance of the MIMO-OFDM systems with Zero forcing equalizer(ZFE) and maximum likelihood detection (MLD) in the presence of CFO, jitter and phase noise for BPSK modulation and also compare their performance .

## II. Theoretical Analysis

### A. OFDM

In OFDM system binary data scheme converter into serial to parallel (S/P) and modulated by BPSK modulation in our analysis. OFDM method is done by IDFT operation. The parallel to serial (P/S) is done by inserting of cyclic prefix. Though channel, OFDM system have to face Rayleigh and AWGN noise. At the receiver, demodulation scheme is done by the inversion system of modulation. The output signal at kth receiving subcarrier can be modeled as [1].

$$\begin{aligned} Y(k) &= \frac{1}{N}\sum_{n=0}^{N-1} y(n) e^{\frac{-j2\pi kn}{N}} \\ &= X(k)H(k) + W(k), 0 \le k \le N-1 \end{aligned} \quad (1)$$

Where, $W(k)$ is noise and $H(k)$ is the channel frequency response with transmitting data stream $X(k)$.

### B. MIMO OFDM System

MIMO OFDM system is multiple transmitting antenna and multiple receiving antenna in an OFDM system. We can assume the uncorrelated signal if there is enough space between transmitting and receiving antennas [1]. Let us assume an MIMO OFDM system which has $M$ number of transmitting antenna and $R$ number of receiving antenna. So the system is

978-1-5386-3374-8/17/$31.00 ©2017 IEEE

a $M \times L$ MIMO system. If $X$ is the transmitting vector stream, $Y$ is the receiving vector then this system can be presented as

$$Y = HX + W \tag{2}$$

Where, $H$ is the channel matrix or the channel transfer function which is a $L \times M$ matrix. Also $W$ is the noise vector which is $L \times 1$ matrix. Now the system can be presented as Eq. 3.

$$\begin{bmatrix} Y_1 \\ Y_2 \\ \vdots \\ Y_L \end{bmatrix} = \begin{bmatrix} H_{11} & \dots & H_{1M} \\ H_{21} & \dots & H_{2M} \\ \vdots & \vdots & \vdots \\ H_{L1} & \dots & H_{LM} \end{bmatrix} \begin{bmatrix} X_1 & X_2 & \dots & X_M \end{bmatrix} + \begin{bmatrix} W_1 \\ W_2 \\ \vdots \\ W_L \end{bmatrix} \tag{3}$$

### C. ZFE

Zero forcing equalizer or ZFE is a linear equalizer which has a transfer function of inverse of the channel. A ZF equalizer has the filter coefficients of $C(f)$ such that the filter response will be: $H(f) = \frac{1}{C(f)}$ or, $H(f) \times C(f) = 1$. A system with ZFE can be represented as

$$\upsilon = (H^H H)^{-1} H^H y \tag{4}$$

Where $H^H H$ is a $M \times M$, a square matrix and $(H^H H)^{-1} H^H$ is the left inverse matrix of $H$ which is applicable for different number of transmitting and receiving antenna such that $L$ can be greater than $M$ (no need to $L = M$). Which is flexible for multiple user. ZFE model is very simple to implement and it brings the ISI to zero. As it's implementation is easy, this technique is not optimum. BER performance of a ZFE depends on both the number of transmitting and receiving antennas.

### D. MLD

MLD is maximum likelihood detection in terms of minimizing total error with small number of transmitting antenna. Maximum likelihood method depends only on number of receiving antennas. MLD scheme has high computational complexity to find an optimum solution [13] But in our analysis we use low order constellation and perfect CSI to simplify the BER computation [14].

## III. System Model

### A. MIMO OFDM System with ZF

A MIMO OFDM system with BPSK modulation in Rayleigh fading channels gives similar BER as a SIMO OFDM system with MRC. The bit error probability for MIMO ZF with BPSK modulation can be obtained as Eq. 5.

$$P_b = \left(\frac{1}{4\overline{SINR}}\right)^{L-M+1} \times \binom{2L-2M+1}{L-M+1} \tag{5}$$

Where, $\overline{SINR}$ is average signal to interference plus noise ratio considering phase noise, timing jitter and normalized CFO obtained from [4]. And probability density function or PDF of Rayleigh channel with $L > M$ can be represented as

$$P_{\gamma,L,M}(x) = x^{L-M} \times \frac{e^{-x/\Gamma_C}}{(L-M)!\Gamma_C^{L-M+1}} \tag{6}$$

Where, $L$ is the number of receiving antenna and $M$ is the number of transmitting antenna. Here, $\gamma$ is the SNR per bit and $\Gamma_C = E(\gamma)$. For MIMO system with ZF value of $\Gamma_C$ can be expressed as Eq. 7 [10].

$$\Gamma_C = \frac{2\sigma_\alpha^2 \times \overline{SINR}}{L-M+1} \tag{7}$$

Where $\sigma_\alpha^2$ is the variance of fading parameter $\alpha$. Then BER for a BPSK OFDM system in Rayleigh fading channels considering normalized CFO, phase noise and timing jitter can be calculated as Eq. 8.

$$BER = \int_{-\infty}^{\infty}\int_{-\infty}^{\infty}\int_{0}^{\infty} P_b(e|\epsilon,\zeta,\gamma)P(\epsilon)P(\zeta)P(\gamma)d\epsilon d\zeta d\gamma \tag{8}$$

Where, $P(\zeta)$ and $P(\epsilon)$ are PDF for timing jitter and normalized CFO assumed Gaussian.

### B. MIMO OFDM System with MLD

MIMO MLD technique normally performs at receiver. MLD is optimum receiver scheme that will perform better than V-BLAST, ZFE and MMSE. With some restriction, BER performance of MIMO MLD system is described in [8]. MLD has high computational complexity but in our analysis with some assumptions and boundary we use a less complex MLD system. At perfect CSI and low order modulation, such as BPSK modulation which is assumed in this analysis, MIMO MLD bit error probability impaired by phase noise, timing jitter and normalized CFO can be calculated as

$$P_b = \left(\frac{L}{4\overline{SINR}}\right)^{L} \times \binom{2L-1}{L-1} \tag{9}$$

Where, $\overline{SINR}$ the average SINR considering normalized CFO, phase noise and timing jitter over Rayleigh fading channel obtained from [4].

It should be noted that the result is depend only on number of receiving antenna $L$ not on number of transmitting antenna $M$ [14]. Performance of Rayleigh fading channel of MLD system can be obtained from [8], [15]. From ML estimation of Rayleigh fading channel we obtain probability density function or pdf of channel will be as Eq. 10.

$$P(\mu) = \left(\frac{1}{2\pi\sigma^2}\right)^{L} \times e^{-\frac{\mu}{2\sigma^2}} \tag{10}$$

Where, $\sigma^2 = ||d||^2 + N_0$ and $d$ is the transmitted signal vector at a particular time instant and $N_0$ is single sided power spectral density for AWGN noise. $\mu$ can be expressed as Eq. 11.

$$\mu_L = \sum_{l=1}^{l=L} ||Y_l - H(\alpha)X_l||^2 \quad (11)$$

Where, $\alpha$ is the fading parameter so $\mu$ is the function of fading parameter and also depends on $L$. Now BER performance of BPSK MIMO OFDM system with MLD considering normalized CFO, timing jitter and fading parameter is

$$BER = \int_{-\infty}^{\infty}\int_{-\infty}^{\infty}\int_{0}^{\infty} P_b(e|\epsilon,\zeta,\alpha)P(\epsilon)P(\zeta)P(\mu)d\epsilon d\zeta d\mu \quad (12)$$

## IV. Results and Discussions

Following analytical approach presented in section III, we evaluate the BER performance results for MIMO OFDM systems using MLD and ZFE. System parameters used for this result section are shown in Table-I.

TABLE I: System parameters used in simulation.

| | |
|---|---|
| Modulation Type | BPSK |
| Channel Type | Rayleigh channel |
| Number of Subcarrier (N) | 64,1024 |
| SNR (dB) | 20 dB |
| Variance of phase noise $\sigma_u^2$ | .005 |
| Variance of timing jitter $\sigma_\zeta^2$ | .01 |
| Variance of normalized CFO $\sigma_\epsilon^2$ | .03 |

Fig. 1 shows BER performance of MIMO OFDM systems with ZFE and MLD without the presence of timing jitter, phase noise and normalized CFO. This plot shows that BER=$10^{-5}$ obtained at 10 dB SNR for 4 number of receiving antennas using MLD but at ZFE same BER value is obtained at higher value of SNR. So MLD with higher number of receiving antennas gives better performance. Fig. 1 also shows that at

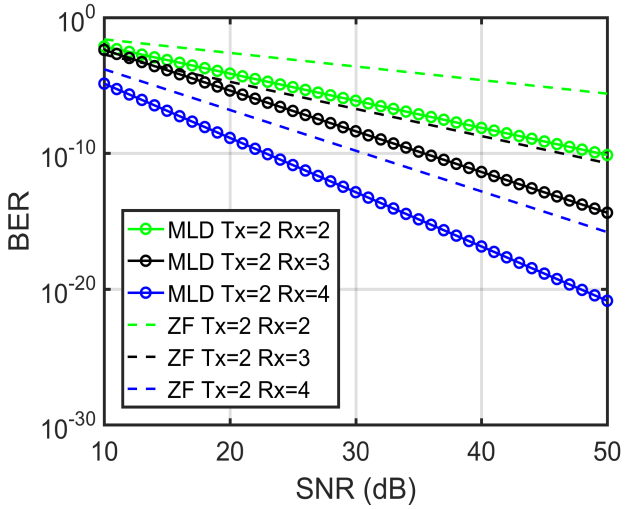


Fig. 1: BER vs. SNR (dB) without considering phase noise, timing jitter and normalized CFO for both MLD and ZFE for different number of Transmitters (Tx) and Receivers (Rx).

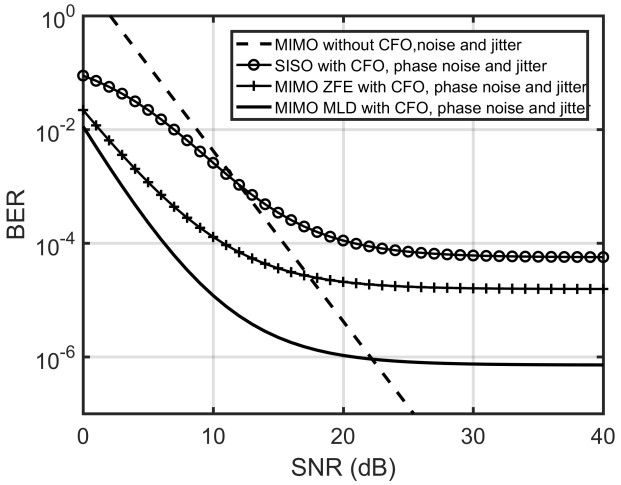


Fig. 2: BER vs. SNR(dB) for SISO OFDM, MIMO OFDM with MLD and ZFE detection for $\sigma_u^2$ =.005, $\sigma_\zeta^2$ =.01 and $\sigma_\epsilon^2$ =.03

Rx=2, 3, 4, MLD gives better BER performance than ZFE for equal number of receiving antennas. Without the presence of synchronization errors MLD gives better BER performance over ZFE.

Fig. 2 is for BER performance comparison between SISO and MIMO OFDM systems in presence of CFO, jitter and phase noise. BER=$10^{-3}$ obtained for the values of 4 dB, 6 dB and 13 dB input SNR for MLD method, ZFE detection and SISO system respectively. This represents that MIMO OFDM systems give better BER performance than SISO OFDM systems in presence of synchronization errors.

Fig. 3 and Fig. 4 show BER performance comparison between ZFE and MLD in MIMO OFDM systems. Fig. 4 shows that BER floor gives lowest value for MLD with higher number of receiving antennas. For example, Tx=2 and Rx=6 BER floor is $1.5\times10^{-8}$ for MLD where ZFE with equal Rx and Tx gives BER floor $1.5\times10^{-7}$. So, MLD gives better BER

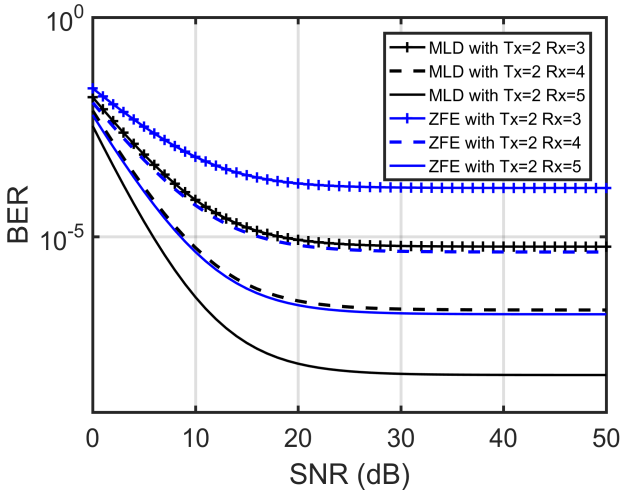


Fig. 3: BER vs. SNR (dB) for MLD and ZFE for $\sigma_u^2$ =.005, $\sigma_\zeta^2$ =.01 and $\sigma_\epsilon^2$ =.03 for different number of Receivers(Rx) and Transmitters(Tx).

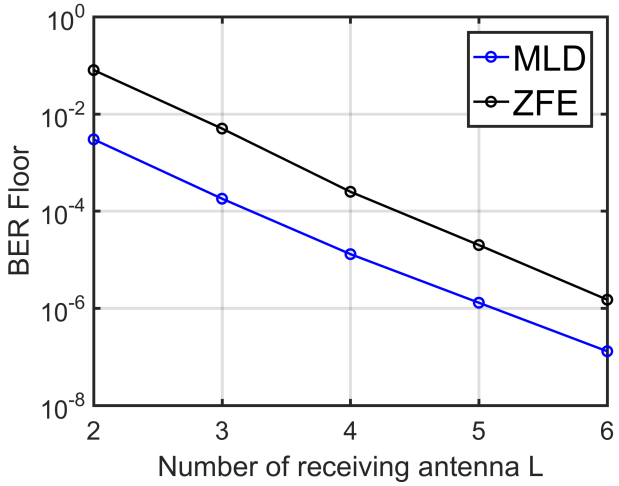


Fig. 4: BER floor vs. number of receiving antenna (L) for MIMO with MLD and ZFE for $\sigma_u^2$ =.005, $\sigma_\zeta^2$ =.01 and $\sigma_\epsilon^2$ =.03

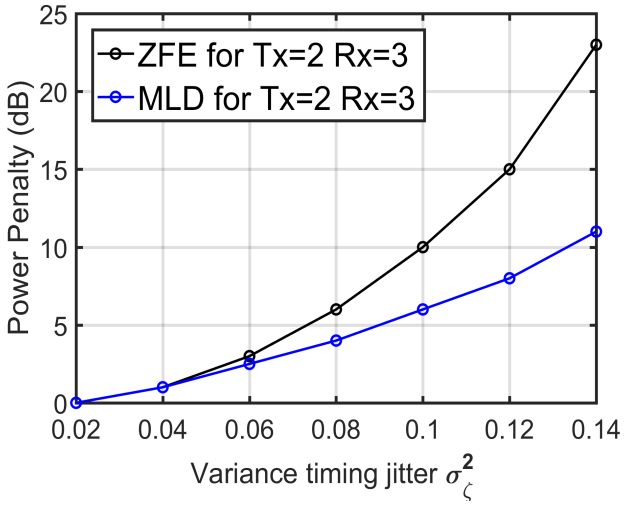


Fig. 6: Power penalty comparison for MIMO ML and ZF detection with respect to variance of timing jitter for $\sigma_u^2$ =.005 and $\sigma_\epsilon^2$ =.03

performance than ZFE with presence of CFO, jitter and phase noise.

Fig. 5 shows power penalty vs. timing jitter for MLD at BER=$10^{-3}$ varying number of receiving antennas in the presence of timing jitter, phase noise and CFO. It can be noticed that system is less effected by jitter for MLD if higher number of receiving antennas are used. For example at variance of timing jitter = 0.05 at L=5 penalty is 2dB where at L=2 penalty is 5 dB for BER=$10^{-3}$.

Fig .6 illustrates Power penalty vs. variance of timing jitter for both MLD and ZFE. This graph is plotted for 2 transmitting antennas and 3 receiving antennas. Fig. 6 shows that the system is less effected by jitter for MLD compared to ZFE. Power penalty is almost similar for lower value of jitter but for higher value of timing jitter, ZFE suffers more penalty compared to MLD.

Fig. 7 shows the effect of variance of phase noise for MLD and ZFE in MIMO OFDM systems. This plot is variance of phase noise vs. BER floor plot for ZFE and MLD in presence of CFO, jitter and noise for different value of receiving antennas and two transmitting antennas. Fig. 7 shows that MLD gives better BER floor performance than ZFE for equal number of receiving antennas. But ZFE with higher number of receiving antennas gives lower BER floor than MLD with lower number of receiving antennas. Also results show that BER floor is increasing with the increasing value of variance of phase noise. MLD with higher number of receiving antenna is suffered less by phase noise than ZFE. For example, at L=5 at variance of phase noise =0.03 , MLD gives BER floor = $10^{-5}$ where ZF at L=5 gives BER floor = $10^{-4}$ and ML L=3 gives BER floor = $10^{-3}$, where L is the number of receiving antenna.

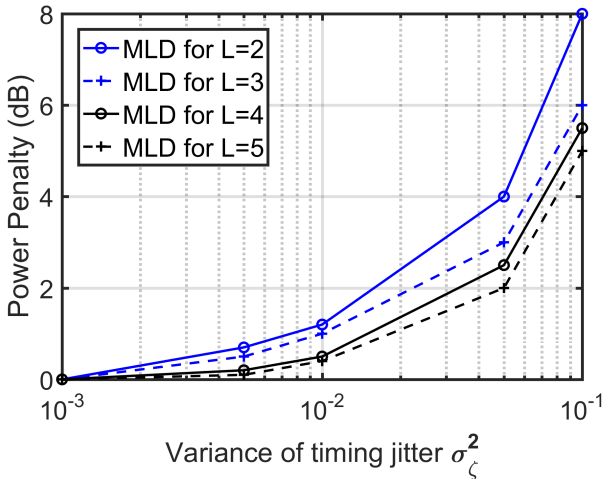


Fig. 5: Power Penalty (dB) vs. variance of timing jitter for MLD at BER=$10^{-3}$ considering $\sigma_u^2$ =.005 and $\sigma_\epsilon^2$ =.03 varying number of receiving antennas (Rx or L)

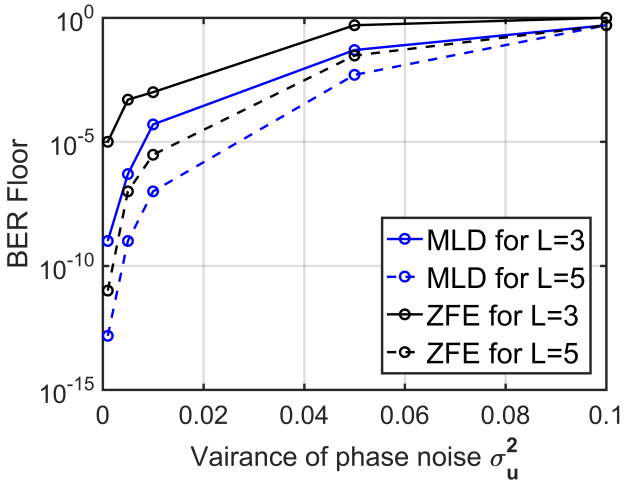


Fig. 7: BER floor vs. variance of phase noise for MIMO OFDM system with MLD and ZFE for different number of receiving antenna L considering $\sigma_\zeta^2$ =.01 and $\sigma_\epsilon^2$ =.03

## V. Conclusion

This paper proposes two multiple antenna techniques to improve OFDM channel performance and also compare their performances. Results show that MIMO OFDM systems with MLD and ZFE give better performance than SISO OFDM system in the presence of normalized CFO, phase noise and timing jitter. Again it is observed that MLD method suffers less penalty and gives lower value of BER floor due to timing jitter, phase noise and normalized CFO over ZFE. System suffers less penalty and BER loss due to phase noise, timing jitter and normalized CFO if higher number of receiving antennas are used. This analysis can be used in practical applications where fading, jitter and noise strongly exist.

## References


[1] N. Achra, G. Mathur, and R. Yadav, "Performance analysis of mimo ofdm system for different modulation schemes under various fading channels," *International Journal of Advanced Research in Computer and Communication Engineering*, vol. 2, no. 5, pp. 2098–2103, 2013.

[2] M. Tiwari and K. P. Kaur, "Analysis on lowering the effect of timing jitter in ofdm system using oversampling," *International Journal of Engineering and Advanced Technology (IJEAT)*, vol. 3, no. 5, 2014.

[3] J. Desai and S. Kulkarni, "Effect of noise on ber of bpsk, qpsk, dpsk, and qam modulation techniques," *International Journal of Research and Scientific Innovation (IJRSI)*, vol. 3.

[4] S. Mallick and S. P. Majumder, "Performance analysis of an ofdm system in the presence of carrier frequency offset, phase noise and timing jitter over rayleigh fading channels," in *Electrical and Computer Engineering, 2008. ICECE 2008. International Conference on*. IEEE, 2008, pp. 205–210.

[5] K. J. P. Pratibha Singh, "Ber performance comparison of mimo ofdm with channel equalizers," *INTERNATIONAL JOURNAL OF INNOVATIVE RESEARCH IN TECHNOLOGY*, vol. 2.

[6] B. A. Bjerke and J. G. Proakis, "Multiple-antenna diversity techniques for transmission over fading channels," in *Wireless Communications and Networking Conference, 1999. WCNC. 1999 IEEE*, vol. 3. IEEE, 1999, pp. 1038–1042.

[7] P. W. Wolniansky, G. J. Foschini, G. Golden, and R. A. Valenzuela, "V-blast: An architecture for realizing very high data rates over the rich-scattering wireless channel," in *Signals, Systems, and Electronics, 1998. ISSSE 98. 1998 URSI International Symposium on*. IEEE, 1998, pp. 295–300.

[8] X. Zhu and R. D. Murch, "Performance analysis of maximum likelihood detection in a mimo antenna system," *IEEE Transactions on Communications*, vol. 50, no. 2, pp. 187–191, 2002.

[9] R. Van Nee, A. Van Zelst, and G. Awater, "Maximum likelihood decoding in a space division multiplexing system," in *Vehicular Technology Conference Proceedings, 2000. VTC 2000-Spring Tokyo. 2000 IEEE 51st*, vol. 1. IEEE, 2000, pp. 6–10.

[10] T. H. Nipa and S. P. Majumder, "Impact of inter-carrier interference (ici) on simo ofdm system over rayleigh fading channel," in *Electrical and Computer Engineering (ICECE), 2010 International Conference on*. IEEE, 2010, pp. 598–601.

[11] M. Hasan and S. P. Majumder, "Performance limitations of a simo ofdm wireless link impaired by carrier frequency offset, phase noise and rayleigh fading," in *Communication Software and Networks, 2010. ICCSN'10. Second International Conference on*. IEEE, 2010, pp. 573–577.

[12] D. Lee, G. J. Saulnier, Z. Ye, and M. J. Medley, "Antenna diversity for an ofdm system in a fading channel," in *Military Communications Conference Proceedings, 1999. MILCOM 1999. IEEE*, vol. 2. IEEE, 1999, pp. 1104–1109.

[13] K. Letaief, E. Choi, J.-Y. Ahn, and R. Chen, "Joint maximum likelihood detection and interference cancellation for mimo/ofdm systems," in *Vehicular Technology Conference, 2003. VTC 2003-Fall. 2003 IEEE 58th*, vol. 1. IEEE, 2003, pp. 612–616.

[14] R. D. Murch and K. B. Letaief, "Antenna systems for broadband wireless access," *IEEE Communications Magazine*, vol. 40, no. 4, pp. 76–83, 2002.

[15] S. J. Grant and J. K. Cavers, "Performance enhancement through joint detection of cochannel signals using diversity arrays," *IEEE Transactions on Communications*, vol. 46, no. 8, pp. 1038–1049, 1998.

# Homodyne versus Self-Coherent Detection in Polarization Diversity Optical Transmission Systems

Kazi Abu Taher[1,*] and Satya Prasad Majumder[1]
[1]Department of EEE, Bangladesh University of Engineering and Technology (BUET), Dhaka, Bangladesh
[*]kataher@yahoo.com

***Abstract*—Analytical results of the performance of homodyne coherent detection (HCD) and self-coherent detection (SCD) schemes in a polarization division multiplexed (PDM)-quadrature phase-shift keying (QPSK) polarization diversity optical transmission system are discussed focusing to highlight their relative merits. Analytical results are compared for the two detection schemes for different parameters including the cross-polarization induced crosstalk, received signal power, data rate and ASE induced crosstalk of EDFA. It is found that the HCD receiver has more sensitivity than the SCD receivers under similar operating conditions. For BER of $10^{-9}$ and for the data speed of 100 Gbps, the requirement of received optical signal power in SCD receiver is 7.05 dB more than that in HCD receivers at mean misalignment of 40°. But SCD receiver has better resilience to mean misalignment at the polarization beam splitter (PBS) than HCD receivers.**

***Index Terms*— Polarization, self-coherent, homodyne coherent detection, misalignment.**

## I. Introduction

Higher receiver sensitivity of coherent detection emerged as the solution to support high speed optical fiber long haul transmission and to meet up the future demands for internet-based multimedia and data services [1,2]. Multilevel modulation schemes with higher spectral efficiency (SE) and coherent detection powered by efficient digital signal processing (DSP) algorithms have raised the data transmission speed even with existing legacy optical network systems that were designed initially for lower data rates [3].

When the high intensity waves propagate through the fiber, power dependent nonlinear effects inflect nonlinear changes in the refractive indices along the two modes. The refractive indices of the modes induce a nonlinear coupling giving rise to nonlinear birefringence causing nonlinear polarization rotation [4-6]. This nonlinear rotation causes the eigen-mode of the fiber to change randomly with respect to the eigen-mode of the PBS at the receiver causing misalignment [7,8]. This misalignment will have fading effect on the signal as well as inter-channel crosstalk. HCD receiver raises the system sensitivity by using LO which also remained as the source of complexity. Of late, the cross-polarization (XPol) induced cross-talk on the performance of a PDM-QPSK optical transmission system with HCD is reported in [9,10].

SCD system came up with lower complexity without the need for LO and related synchronization mechanism at the receiver. It is reported as the alternative to the HCD mainly for short range connectivity [11]. PDM-QPSK SCD receiver with lesser complexity without LO has emerged as an efficient scheme for supporting short range high-speed optical transmission. It combines the features of DD and HCD. In [12,13], the authors have reported simulation and experimental results of SCD system. Analytical results of BER performance of SCD system considering the XPol induced effects is reported in [14]. Since both HCD and SCD systems seem promising, a comparison between them is necessary.

We present a comparison for the first time, of the performance of optical PDM-QPSK polarization diversity HCD and SCD receivers taking account of the XPol induced crosstalk, received optical power and data rates in light of [10] and [14]. This paper is arranged as follows; the system model is explained in Section 2, the theoretical analysis of the models is given in Section 3, Section 4 contains the results and discussion. Finally, Section 5 concludes the paper.

## II. System Model

Transmitter and fiber section of PDM-QPSK self-coherent and coherent homodyne transmission systems are identical and its block diagram is shown Fig. 1. Four data streams $X_{I,k}$, $X_{Q,k}$, $Y_{I,k}$ and $Y_{Q,k}$ modulate the same laser by the two QPSK modulators. X and Y indicate the two orthogonal polarizations modes. The upper QPSK Mach-Zender modulator (MZMs) modulates the carrier using two input data streams $X_{I,k}$ and $X_{Q,k}$. Similarly the lower QPSK modulator modulates the same laser using two input data streams $Y_{I,k}$ and $Y_{Q,k}$. A PBS is used in at the transmitter to separate the orthogonal polarizations of the input laser which are used as input to the two optical QPSK modulators. Each of the QPSK modulators modulates the in- and quadrature-phase (IQ) of the laser by two input data streams. Output of the two QPSK modulators are combined at the polarization beam combiner (PBC) and generate the PDM-QPSK signal $E_t(t)$ as shown in Fig. 1(a). SMF of fixed length with EDFA form a span and the total link consists of number of spans. The attenuation of the fiber is just equal to the gain of the EDFA. The modulated signal $E_t(t)$ is fed into the fiber link and signal $E_s(t)$ is received at the receiver end after passing through N number of spans as shown in Fig. 1(b). The transmitter and fiber link of both HCD and SCD systems are identical.

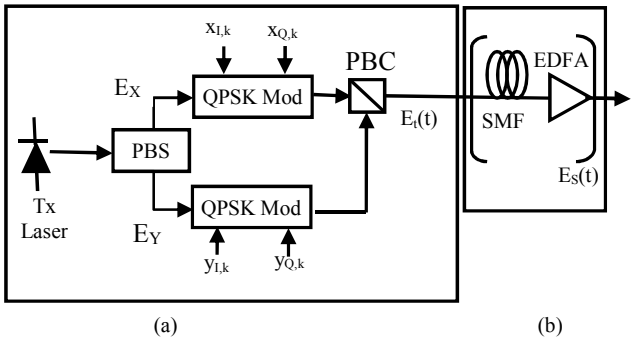


**Fig. 1.** Block diagram of (a) PDM-QPSK transmitter system and (b) optical fiber link with erbium doped fiber amplifier (EDFA).

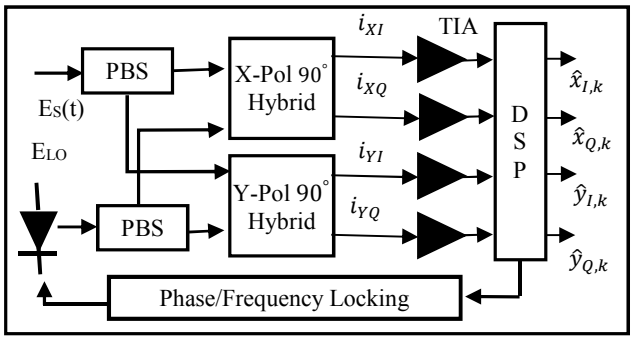


**Fig. 2.** Block diagram of a PDM-QPSK polarization diversity HCD optical receiver.

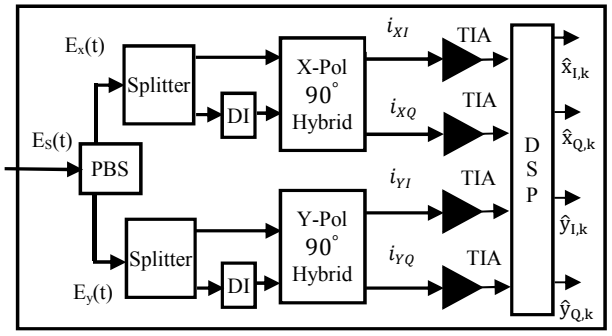


**Fig. 3**. Block diagram of self-coherent PDM-QPSK polarization diversity SCD optical receiver. DI: Delay interferometer

The block diagram of the receiver section of a HCD PDM-QPSK polarization diversity transmission system is shown in Fig. 2. The received signal $E_S(t)$ is fed to a PBS in the absence of PC which is the striking feature of polarization diversity technique. The PBS provides the X- and Y-polarized signals at the output. The X-polarized (X-Pol) signal is fed to the upper 90° hybrid and the Y-polarized (Y-Pol) signal is fed to the lower 90° hybrid. The output laser from the LO is linearly polarized at 45° with respect to the receiver polarization and is fed into the lower PBS. The outputs of the lower PBS are the local reference laser and are fed into the two 90° hybrids as shown in Fig. 2. The received signal is thus gets coupled with the LO laser in the 90° hybrids. The 3-dB couplers within the 90° hybrids beat the LO laser signal with the signal to generate the baseband signal following homodyne approach.

Fig. 3 depicts the block diagram of the receiver section of optical PDM-QPSK polarization diversity SCD receiver. Here the received signal at the receiver end is $E_s(t)$ which is passed to the PBS and there is no PC. The X-Pol signal $E_x(t)$ and Y-Pol signal $E_y(t)$ from the output of the PBS are fed into two splitters to split the signal into two halves. Outputs of each splitter are the two copies of the same signal. One of the outputs of each splitter is passed through a delay interferometer (DI) after introducing a delay of one symbol period. Thus one input of the X-Pol 90° hybrid is the X-Pol signal and the other input is the delayed version of the X-Pol signal. Similarly the Y-Pol 90° hybrid has inputs from Y-Pol signal and its delayed version. There is no local oscillator in this model. Delayed signal of the previous symbol period acts as the reference. The original signal and its delayed version gets coupled in the 90° hybrids and beat together to generate the data $i_{X,I}(k)$, $i_{X,Q}(k)$, $i_{Y,I}(k)$ and $i_{Y,Q}(k)$ of $k^{th}$ symbol.

## III. Theoretical Analysis

The signal entering the PBS of the HCD and SCD receiver section of Fig. 2 and Fig. 3 respectively, is given by [10,14]:

$$E_S(t) = E_{S,X}(t)\hat{x} + E_{S,Y}(t)\hat{y} \tag{1}$$

where

$$E_{S,X}(t) = E_{X,I}(t)\cos[\omega_0 t + \phi_{X,I}(t)] - E_{X,Q}(t)\sin[\omega_0 t + \phi_{X,Q}(t)] \tag{2}$$

$$E_{S,Y}(t) = E_{Y,I}(t)\cos[\omega_0 t + \phi_{Y,I}(t)] - E_{Y,Q}(t)\sin[\omega_0 t + \phi_{Y,Q}(t)] \tag{3}$$

where $E_{S,X}(t)\hat{x}$ and $E_{S,Y}(t)\hat{y}$ are the X-Pol and Y-Pol components of the received signal respectively, $E_{X,I}$, $E_{X,Q}$, $E_{Y,I}$ and $E_{Y,Q}$ are the IQ components of the X-Pol and Y-Pol components respectively, $\omega_0$ is the optical carrier frequency, $\phi_{X,I}, \phi_{X,Q}, \phi_{Y,I}$ and $\phi_{Y,Q}$ are the phase angles associated IQ components of the X-Pol and Y-Pol components respectively. Since the X-Pol and Y-Pol modes carry data independently and act as channels, they can be termed as subchannels $U_X$ and $U_Y$ respectively. Considering fading and crosstalk suffered by subchannel $U_x$ at the PBS due to nonlinear birefringence induced random rotations of the subchannel SOPs, the output signal at the X-Pol and Y-Pol are $E'_{SIG,X}(t)$ and $E'_{SIG,Y}(t)$ respectively, where

$$E'_{SIG,X}(t) = \varepsilon_F E_{S,X}(t) + \varepsilon_X E_{S,Y}(t) \tag{4}$$

$$E'_{SIG,Y}(t) = \varepsilon_F E_{S,Y}(t) + \varepsilon_X E_{S,X}(t) \tag{5}$$

where $\varepsilon_F$ and $\varepsilon_X$ are the fading and crosstalk coefficients respectively and $\varepsilon_F = \cos\frac{\theta}{2}$ and $\varepsilon_X = \sin\frac{\theta}{2}$ where $\theta$ represents the mean misalignment angle between the eigenmode of the received signal and eigenmode of the receiver PBS. The outputs of the PBS are the similar for both HCD and SCD receivers, but their subsequent processing are different as explained below.

### *A. HCD Receivers*

Instantaneous X-Pol input from the local oscillator to the X-Pol 90° hybrid of HCD as in Fig. 2 is given by

$$E_{LO,X}(t) = E_{LO,X}\cos\omega_0 t \tag{6}$$

Considering crosstalk and fading suffered by subchannel $U_x$ due to the random polarization rotation of the subchannel SOPs at the PBS, the signal at the upper input of the X-Pol 90° hybrid is:

$$E'_{SIG,X}(t) = \varepsilon_F E_{SIG,X}(t) + \varepsilon_X E_{SIG,Y}(t) \tag{7}$$

The instantaneous output signal at port C1 of X-Pol 90° hybrid is giver by

$$E_{X,C1}(t) = E'_{SIG,X}(t) - E_{LO,X}(t) = \varepsilon_F E_{SIG,X}(t) + \varepsilon_X E_{SIG,Y}(t) - E_{LO,X}(t) \tag{8}$$

Squaring both sides of (8), detail synthesis is carried out to separate the in-phase terms to get the baseband signals. The useful total photocurrent at the output of the single ended detector of port C1 is:

$$i_{X,C1} = R_{C1}\Big[\varepsilon_F^2(P_{SIG,X} + P_{LO,X}) - 2\varepsilon_F\sqrt{P_{X,I}P_{LO,X}}\cos\phi_{X,I} + \varepsilon_X^2 P_{SIG,Y} + 2\varepsilon_X\sqrt{P_{X,I}P_{LO,X}}\cos\phi_{X,I} + 2\varepsilon_X\varepsilon_F\sqrt{\tfrac{\kappa}{2}}P_{X,I}\sqrt{\tfrac{\kappa}{2}}P_{Y,I}\cos(\phi_{X,I} - \phi_{Y,I})\Big] \tag{9}$$

The total useful photocurrent at the output of the single ended detector of port C2 is:

$$i_{X,C2} = R_{C1}\Big[\varepsilon_F^2(P_{SIG,X} + P_{LO,X}) + 2\varepsilon_F\sqrt{P_{X,I}P_{LO,X}}\cos\phi_{X,I} + \varepsilon_X^2 P_{SIG,Y} + 2\varepsilon_X\sqrt{P_{X,I}P_{LO,X}}\cos\phi_{X,I} + 2\varepsilon_X\varepsilon_F\sqrt{\frac{\kappa}{2}}P_{X,I}\sqrt{\frac{\kappa}{2}}P_{Y,I}\cos(\phi_{X,I} - \phi_{Y,I})\Big] \quad (10)$$

Here, $R_{C1}$ and $R_{C2}$ are the effective responsivities of the PDs for $i_{X,C1}$ and $i_{X,C2}$ respectively. The output of the balanced detector is the differential photocurrents from the output ports C1 and C2 which can be obtained from (9) and (10) as $i_{X,C} = i_{X,C2} - i_{X,C1}$. Then the crosstalk term and the faded signal can be segregated to calculate the signal-to-noise (SNR). The faded signal is:

$$i_{SIG,X,C,HCD} = \varepsilon_F^2[R_{C2} - R_{C1}](P_{SIG,X} + P_{LO,X}) + 2\varepsilon_F[R_{C2} + R_{C1}]\sqrt{P_{X,I}P_{LO,X}}\cos\phi_{X,I} \quad (11)$$

The interchannel crosstalk term due to XPol is:

$$i_{Xtalk,X,C,HCD} = \varepsilon_X^2[R_{C2} - R_{C1}]P_{SIG,Y} + 2\varepsilon_X[R_{C2} + R_{C1}]\sqrt{P_{Y,I}P_{LO,X}}\cos\phi_{Y,I} + 2\varepsilon_X\varepsilon_F[R_{C2} + R_{C1}]\sqrt{\frac{\kappa}{2}}P_{X,I}\sqrt{\frac{\kappa}{2}}P_{Y,I}\cos(\phi_{X,I} - \phi_{Y,I}) \quad (12)$$

In HCD, the inline amplifiers and LO will contribute to the total noise. HCD receiver has a noise with variance $\sigma_n^2$ details of which is given at [10]. The output signal of the HCD receiver includes shot noise, thermal noise and amplified spontaneous emission (ASE) with noise variance $\sigma_n^2$:

$$\sigma^2_{Noise,HCD} = \sigma^2_{shot,HCD} + \sigma^2_{thermal,HCD} + \sigma^2_{ASE,HCD} \quad (13)$$

where

$$\sigma^2_{shot,HCD} \cong 2qR_{C1}(P_{LO} + P_{SIG})B\Big[1 + \delta - 2\sqrt{(1-\mu)\delta_X}\cos\emptyset_{X,I}\Big] + 2qR_{C2}P_{LO}B\Big[1 + \delta + 2\sqrt{(1-\mu)\delta}\,cos\emptyset_{X,I})\Big]$$

$$\sigma^2_{thermal,HCD} = 2(1 - r_{th})\,i_{th}^2 B$$

$$\sigma^2_{ASE,HCD} = \sigma^2_{ASE,shot} + \sigma^2_{s-sp} + \sigma^2_{sp-sp} = 2q\eta B(I_i G + I_{sp}) + 4G\eta^2 I_i I_{sp}\frac{B}{B_o} + \eta^2 I_{sp}^2\left(2 - \frac{B}{B_o}\right)\frac{B}{B_o}, \quad 0 < B \le \frac{B_o}{2}$$

where q is the electric charge, $R_{C1}$ and $R_{C2}$ are the effective responsivity of the PDs at the port $C_1$ and $C_2$ of $90^\circ$ hybrid, $P_{LO}$ is the LO power, $P_{SIG}$ is the received signal power, δ is the ratio of received signal power to the LO laser power, *B* is the transmitted data bandwidth, μ is the quadrature power imbalance ratio, and $\emptyset_{X,I}$ is the phase angle of the X-Pol in-phase signal considering no correlation between single ended noise current densities. Here, $r_{th}$ is the correlation coefficient of the differential thermal noise power, $i_{th}$ is the input equivalent noise current spectral density of the single ended input, $I_{sp}$ and $I_i$ are the photocurrent equivalent of the ASE noise power and the signal power respectively, η is the quantum efficiency of the detectors, G is the amplifier gain and $B_o$ is the optical band-width.

Adding X-Pol induced crosstalk to the $U_x$ subchannel for a particular mean misalignment angle $\theta_m$ and total noise, we can find the conditional signal to crosstalk plus noise ratio (SCNR) for HCD receiver as:

$$SCNR_{HCD}(\theta) = \frac{|i_{SIG,X,C,HCD}|^2}{|i_{Xtalk,X,C,HCD}|^2 + \sigma^2_{Noise,HCD}} \quad (14)$$

Using this SCNR, we can define conditional BER before the DSP as:

$$BER_{HCD}(\theta) = 0.5 * \text{erfc}\sqrt{SCNR_{HCD}(\theta)} \quad (15)$$

As the misalignment angle originates from the random rotation of the eigenmodes caused by nonlinear birefringence, the distribution of the misalignment angle is also considered have Maxwellian distribution and the probability density function (pdf) of the random phase angles is given by [11,12]:

$$P_\theta(\theta) = \frac{32}{\pi^2\langle\theta\rangle^3}\theta^2\exp\left(\frac{-(2\theta)^2}{\pi\langle\theta\rangle^2}\right) \quad (16)$$

where θ is the instantaneous misalignment angle and ⟨θ⟩ is the mean misalignment angle. Using this pdf, the average $BER_{HCD}$ can then be obtained as:

$$BER_{HCD} = \int_0^{\pi/2} BER_{HCD}(\theta)\,P_\theta(\theta)\,d\theta \quad (17)$$

*B. SCD Receivers*

The signal of (4) and (5) are processed by passing them through the splitter as shown in Fig. 3. Delay equal to one symbol period is introduced to one part of the signal by passing it through the DI. The direct signal $E_S(t)$ and its delayed version $E_D(t)$ delayed by one symbol period T, are given as the input of the $90^\circ$ hybrid and details of the $90^\circ$ hybrid is shown in [10]. Considering the crosstalk and fading suffered by subchannel $U_X$ due to subchannel $U_Y$, the input signal at the X-Pol $90^\circ$ hybrid of Fig. 3 is:

$$E_S(t) = \varepsilon_F E_{S,X}(t) + \varepsilon_X E_{S,Y}(t) \quad (18a)$$

$$E_D(t) = \varepsilon_F E_{S,X}(t - T) + \varepsilon_X E_{S,Y}(t - T) \quad (18b)$$

The instantaneous output of the signal at port C1 of X-Pol $90^\circ$ hybrid of Fig. 3 corresponding to the input signal of (18) is giver by [14]:

$$E_{X,C1}(t) = E_S(t) - E_D(t) = \varepsilon_F E_{S,X}(t) + \varepsilon_X E_{S,Y}(t) - \varepsilon_F E_{S,X}(t - T) - \varepsilon_X E_{S,Y}(t - T) \quad (19)$$

Detail synthesis is carried out by squaring both sides of (19) to separate the effective in-phase signal and interfering terms. Effective responsivities of the PDs are considered as $R_{C1}$ and $R_{C2}$ that are used to generate the currents at the output of the balanced detector as:

$$i_{X,C} = i_{X,C2} - i_{X,C1} = 2\varepsilon_F^2[R_{C2} - R_{C1}]P_X + 2\varepsilon_F^2[R_{C2} + R_{C1}]P_{XI}\cos\left(\phi_{X,I}(t) - \phi_{X,I}(t - T)\right) + 2\varepsilon_X^2[R_{C2} - R_{C1}]\,P_Y + 2\varepsilon_X^2[R_{C2} + R_{C1}]P_{YI}\cos\left(\phi_{Y,I}(t) - \phi_{Y,I}(t - T)\right) \quad (20)$$

After segregation, the crosstalk term and the signal are:

$$i_{X,C,SCD} = 2\varepsilon_F^2[R_{C2} - R_{C1}]P_X + 2\varepsilon_F^2[R_{C2} + R_{C1}]P_{XI}\cos\left(\phi_{X,I}(t) - \phi_{X,I}(t - T)\right) \quad (21)$$

$$i_{Xtalk,X,C,SCD} = 2\varepsilon_X^2[R_{C2} - R_{C1}]P_{S,Y} + 2\varepsilon_X^2[R_{C2} + R_{C1}]P_{YI}\cos\left(\phi_{Y,I}(t) - \phi_{Y,I}(t - T)\right) \quad (22)$$

In the absence of the LO in SCD system, the main source of the noise is the inline amplifier. Total noise variance is given as (16) but there is no LO related terms in SCD receiver [14].

$$\sigma^2_{\text{Noise,SCD}} = \sigma^2_{\text{shot,SCD}} + \sigma^2_{\text{thermal,SCD}} + \sigma^2_{\text{ASE,SCD}} \quad (23)$$

where

$$\sigma^2_{\text{shot,SCD}} \cong 2qR_{C1}P_{SIG}B\left[1 - 2\sqrt{(1-\mu)\delta_X}\cos\emptyset_{X,I}\right] + 2qR_{C2}P_{SIG}B\left[1 + 2\sqrt{(1-\mu)\delta}\cos\emptyset_{X,I}\right]$$

$$\sigma^2_{\text{thermal,SCD}} = 2(1-r_{th})\, i^2_{th}B$$

$$\sigma^2_{\text{ASE,SCD}} = \sigma^2_{\text{ASE,shot}} + \sigma^2_{s-sp} + \sigma^2_{sp-sp} = 2q\eta B(I_i G + I_{sp}) + 4G\eta^2 I_i I_{sp}\frac{B}{B_o} + \eta^2 I^2_{sp}\left(2 - \frac{B}{B_o}\right)\frac{B}{B_o}, \quad 0 < B \le \frac{B_o}{2}$$

Adding X-Pol induced crosstalk to the $U_x$ for a particular mean misalignment angle $\theta_m$ and total noise, we can find the conditional SCNR and BER for SCD receiver as:

$$\text{SCNR}_{SCD}(\theta) = \frac{|i_{X,C,SCD}|^2}{|i_{Xtalk,X,C,SCD}|^2 + \sigma^2_{\text{Noise,SCD}}} \quad (24)$$

$$\text{BER}_{SCD}(\theta) = 0.5 * \text{erfc}\sqrt{\text{SCNR}_{SCD}(\theta)} \quad (25)$$

Considering the Maxwellian distribution, the pdf of mean misalignment angle θ, $P_\theta(\theta)$ is used to calculate the average BER similar to (16). The average BER can then be obtained from the conditional BER as:

$$\text{BER}_{SCD} = \int_0^{\pi/2} \text{BER}_{SCD}(\theta)\, P_\theta(\theta) d\theta \quad (26)$$

## IV. Results and Discussions

Using the analytical expressions presented in Section III, we compare numerically the required signal power and penalty in power caused by X-Pol at the output of the HCD and SCD PDM-QPSK receivers for a particular mean misalignment $\theta_m$. The comparison between the HCD and SCD detection system is compared for different received signal powers, misalignment angles data rates and BER. The findings of this paper are post FEC values and no DSP algorithm is used. Different parameters and their values used in this simulation are shown in Table 1.

Table 1. Table of parameters used in numerical computation

| Parameter | Value |
|---|---|
| Effective responsivity at port C1 | 0.14 A/W |
| Effective responsivity at port C2 | 0.18 A/W |
| Phase of the X-Pol signal $\emptyset_{XI}$ | 22.5° |
| Phase of the Y-Pol signal $\emptyset_{YI}$ | 30° |
| Power split ratio between polarizations | 0.41 |
| LO power split ratio for HCD | 0.46 |
| SMF link length | 100 km |
| Attenuation loss | 0.2 dB/km |
| Optical carrier wavelength | 1550 nm |
| Spontaneous emission factor | 1.4 |
| Gain of the EDFA | 20 dB |
| Local oscillator power for HCD | 10 dBm |
| Optical filter bandwidth | 100 GHz |
| Photocurrent equivalent of the signal noise power, $I_i$ | 15.5 μA |
| Photocurrent equivalent of the ASE noise power, $I_{sp}$ | 4.22 μA |
| Input equivalent noise current density, n_th | 15 pA²/Hz |

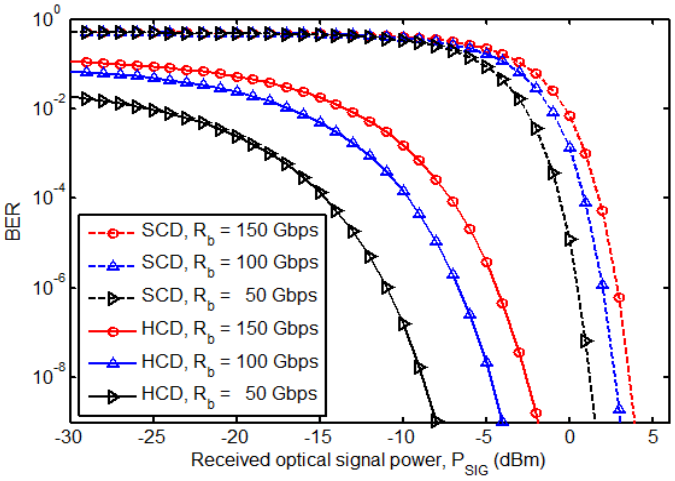


**Fig. 4.** BER versus received signal power for various data rates in HCD and SCD receivers.

Fig. 4 depicts the plots the BER as a function of received signal power $P_{SIG}$ of HCD and SCD receivers for mean misalignment of 40° and different data rates. It presents the BER performance of HCD and SCD receivers in one graph and thus can be compared easily.

It is clearly evident from the graph that at a particular BER and mean misalignment angle, the SCD receiver needs more signal power than HCD receiver. Moreover, in both the receivers, the required signal power increases with the increase of data rates. For BER of $10^{-4}$ and for data rates of 100 and 150 Gbps, SCD receiver needs 0.92 and 1.8 dBm but HCD receiver needs -9.65 and -7.1 dBm. Again, for BER of $10^{-9}$ and for the same data rate, SCD receiver needs 3.05 and 3.96 dBm but HCD receiver needs -4.0 and -1.95 dBm requiring an increase of required optical signal power in SCD receiver by 7.05 and 5.91 dB respectively.

Fig. 5 shows the plots of the required signal power $P_{SIG}$ for BER of $10^{-9}$ as a function of data rates for various mean misalignment angles in HCD and SCD receivers. The continuous lines show the plots of the required power of HCD receivers at LO power of 10 dBm and the dashed lines show the plots of the required power of SCD receivers. At higher misalignment angles, the need of required signal power increases comparing to the power requirement for no-

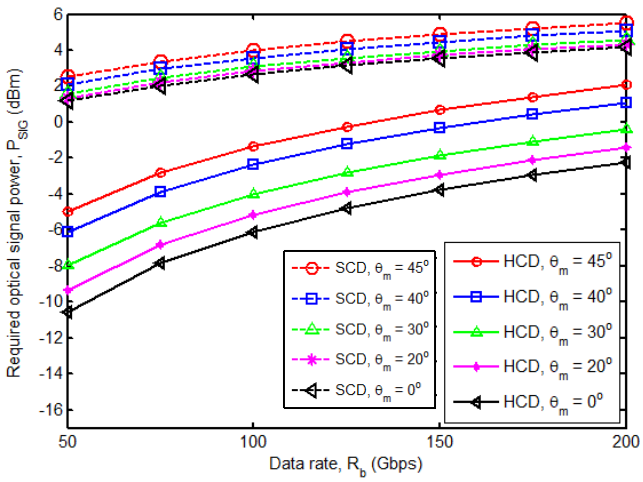


**Fig. 5.** Required optical signal power for BER of $10^{-9}$ versus data rate for different mean misalignment angles in HCD and SCD receivers.

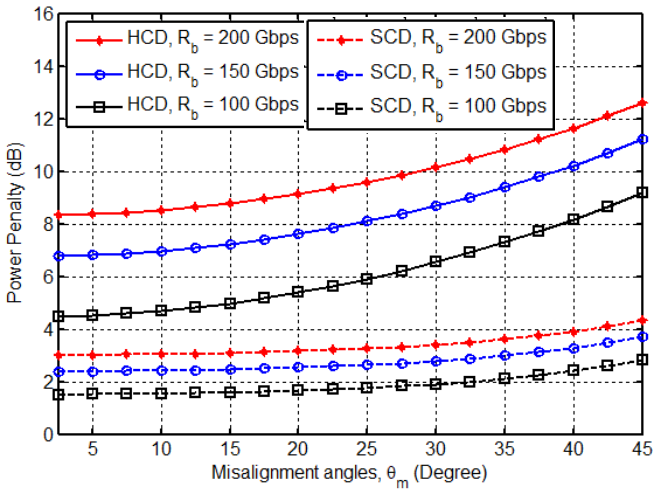


**Fig. 6.** Power penalty for BER of $10^{-9}$ versus mean misalignment angles in HCD and SCD receivers .

misalignment condition. Moreover, the requirement of the signal power increases with the increase of the data rate. The graph shows that in HCD receiver, the required signal power for BER of $10^{-9}$ at 100 Gbps and LO power of 10 dBm are -5.148, -3.994, -2.364 and -1.34 dBm for misalignment angle of $20^{\circ}, 30^{\circ}, 40^{\circ}$ and $45^{\circ}$ respectively.

The dashed lines of Fig. 5 show the plots the received optical signal power. At higher mean misalignment angles, the need for required signal power increases comparing to the power requirement for no-misalignment condition. Moreover, the requirement of the signal power increases with the increase of the data rate. The graph shows that for BER of $10^{-9}$ at 100 Gbps, SCD receiver 2.834, 3.083, 3.582 and 4.012 dBm received signal power for misalignment angle of $20^{\circ}, 30^{\circ}, 40^{\circ}$ and $45^{\circ}$ respectively. It is clear that the increase in signal power in HCD receiver is much larger than that of SCD receiver that is required for a particular rise in the mean misalignment angle. Thus it is clear that the changes in misalignment angles have very less effect in the power requirements of SCD receivers. The graph shows that to achieve a particular BER with the increase of specific mean misalignment angle, the amount of signal power requirement is much higher in HCD receivers. The requirement of signal power increases by 2.784 dB in HCD receiver when misalignment angle increases from $20^{\circ}$ to $40^{\circ}$ at data rate of 100 Gbps, but under the same condition the increment is only 0.748 dB in SCD receiver.

Fig. 6 plots the power penalty for BER of $10^{-9}$ versus mean misalignment angles in HCD and SCD receivers taking the signal power required at 50 Gbps setting mean misalignment angle at $0^{o}$. The continuous line graph represents power penalty in HCD receivers and the dashed lines represent that of SCD receivers. It is clear from the graph that SCD receivers have better tolerance to the change of mean misalignment angle than HCD receivers.

## V. Conclusions

Comparison of the performance of PDM-QPSK polarization diversity HCD and SCD receivers are presented considering standard fiber parameters. The performances are quantified in terms of BER, required signal power, misalignment angles and power penalty for both the systems. Results show that SCD and HCD suffer significant BER deterioration due to XPol induced crosstalk and significant amount of signal power penalty occurs at a particular BER. It is found that HCD receiver has more sensitivity over SCD receiver at a given BER and misalignment angle. HCD receiver has out-performed the SCD receivers in terms of better BER and higher sensitivity but SCD receiver has lower complexity and higher tolerance to misalignment angles. Further, HCD system suffers more power penalty compared to SCD system due to a particular misalignment angle. It is found that SCD receiver has higher tolerance to misalignment induced crosstalk than HCD receiver. The both the receivers will require robust DSP algorithms and advanced photonic integrated circuit to handle the nonlinear birefringence induced random misalignment of the eigenmodes of the fiber and that of the PBS that results in the misalignment. Results of this work can be used in designing high-speed optical PDM-QPSK polarization diversity transmission systems.

## ACKNOWLEDGMENT

The work is carried out as a part of Ph. D. dissertation in the Department of Electrical and Electronic Engineering of Bangladesh University of Engineering and Technology (BUET), Dhaka, Bangladesh.

## REFERENCES

[1] I. Ezra, P. T. L. Alan, J. F. B. Daniel, K. M. K. Joseph, Coherent detection in optical fiber system, Opt. Express 16(2) (2008) 753-791.

[2] S. Bottacchi, A. Beling, A. Matiss, M. L. Nielsen, A. G. Steffan, G. Unterb, A. Umbach, Advanced photoreceivers for high-speed optical fiber transmission systems, IEEE J. of Selected Topics in Quantum Electronics 16(5) (2010) 1099-1112.

[3] D. Sperti, P. Serena, A. Bononi, Optical solutions to improve PDM-QPSK resilience against cross-channel nonlinearities: a comparison, *IEEE Photonics Technol. Lett.* 23(11) (2011) 667-9.

[4] C. R. Menyuka, B. S. Marks, Interaction of polarization mode dispersion and nonlinearity in optical fiber transmission systems, J. of Lightwave Technol. 24(7) (2006) 2806-26.

[5] R. Dar, M. Feder, A. Mecozzi, M. Shtaif, Properties of nonlinear noise in long, dispersion-uncompensated fiber links, Opt. Express 21(22) (2013) 25685-25699.

[6] C. H. Holbrow, E. Galvez, M. E. Parks, Photon quantum mechanics and beam splitters, J. of Phys. 70(3) (2002) 260-265.

[7] J. Zweck, E. Minkoff, Modeling compensation for optical fiber communication systems, Society for Industrial and Applied Mathematics (SIAM) J. Optim 17(3) (2006) 738-775.

[8] M. Winter, C. A. Bunge, D. Setti, K. Petermann, A statistical treatment of cross-polarization modulation in DWDM systems, J. of Lightwave Technol. 27(17) (2009) 3739-51.

[9] S. S. Keerthika, A. Sivanantharaja, S. Selvendran, C. Mahendran, Analysis of cross polarization modulation in semiconductor optical amplifier for wavelength conversion, International J. of Computer Science and Information Technol. 5(1) (2014) 901-3.

[10] K. A. Taher, S. P. Majumder, Analytical evaluation of the effect of cross polarization induced crosstalk on the BER performance of a PDM-QPSK coherent homodyne optical transmission system, J. of Optical Commun. 38(2) (2017) 111-120.

[11] X. Liu, S. Chandrasekhar, A. Leven, Digital self-coherent detection, Opt. Express 16(7) (2008) 792-803.

[12] I. Tselniker, S. B. Ezra, J. Li, J. Leuthold, Self-coherent complex field reconstruction with in-phase and quadrature delay detection without a direct-detection branch, Opt. Express 20(14) (2012) 15452-73.

[13] J. Li, M. Nazarathy, C. S. Langhorst, S. B. Ezra, I. Tselniker, C. Koos, W. Freude, J. Leuthold, A self-coherent receiver for detection of PolMUX coherent signals, Opt. Express 20(21) (2012) 21413-33.

[14] K. A. Taher, S. P. Majumder, BER performance degradation of a PDM-QPSK self-coherent detection optical transmission system due to cross polarization effects, Proc. of the International IEEE Region 10 Conf. (TENCON) (2016) 2152-5.

2017 IEEE International Conference on Telecommunications and Photonics (ICTP)
26-28 December, 2017, Dhaka, Bangladesh


# Hybrid Diversity Combined OFDM for LiFi

M. Rubaiyat Hossain Mondal*, and Rumana Binte Faruque
Institute of Information and Communication Technology
Bangladesh University of Engineering and Technology
Dhaka, Bangladesh
*rubaiyat97@yahoo.com

***Abstract*—Orthogonal Frequency Division Multiplexing (OFDM) based light fidelity (LiFi) scheme provides the opportunity of high speed data transmission along with room illumination. This paper proposes *Hybrid Diversity Combined OFDM* (HDC-OFDM) for LiFi by combining the aspects of existing *diversity-combined asymmetrically clipped optical OFDM* (DACO-OFDM) and *direct current biased optical OFDM* (DCO-OFDM). The proposed HDC-OFDM has the benefits of power efficiency of DACO-OFDM and the dimming flexibility of DCO-OFDM. In HDC-OFDM transmitter, the lower subcarriers are modulated with DACO-OFDM, and the higher subcarriers with DCO-OFDM. In order to remove the impact of DCO-OFDM clipping noise on DACO-OFDM component, a high DC bias is applied on DCO-OFDM. On the other hand, the effect of DACO-OFDM clipping noise on DCO-OFDM element is reduced by estimating the DACO-OFDM clipping noise and then deducting the noise from the received signal of DCO-OFDM. In order to obtain the optimum bit error rate performance of HDC-OFDM, the percentage of subcarriers and the ratio of power levels for DACO-OFDM and DCO-OFDM components are varied. Simulation results show that the dimming flexible HDC-OFDM is 5 dB better than DCO-OFDM and only 1.5 dB inferior to DACO-OFDM in terms of optical power efficiency.**

***Index Terms*—LiFi, OFDM, diversity combined ACO-OFDM, DCO-OFDM, dimming.**

## I. Introduction

The demand for reliable and high-speed wireless data services is growing enormously. However, with the increase in bandwidth-intensive applications, the radio frequency (RF) spectrum is becoming more and more congested. RF communication is also experiencing issues like spectrum licensing, security, electromagnetic interference, etc. As a result, optical wireless communication (OWC) is regarded as a supplementary technique to RF communications [1]-[10]. Moreover, light fidelity (LiFi) systems, a subset of OWC, are having increasing attention to offload mobile data traffic along with existing RF based wireless fidelity (WiFi) solutions. In a generalized LiFi system, data are first modulated in the electrical domain and then converted to an optical signal by optical modulators. The transmitted signal is received by photodetectors. For such systems, laser diodes (LD) or LEDs are examples of optical modulators whereas positive-intrinsic-negative (PIN) and avalanche photodiodes are some examples of photodetectors [1]-[2].

LiFi has a number of advantages over WiFi [6]-[10]. Firstly, a huge unregulated optical bandwidth is available for communication in the optical spectrum. The optical signal in LiFi does not interfere with surrounding RF signals. In addition, optical signals are blocked by room walls and thus cannot be received by eavesdroppers. Optical signals can be made narrow and highly directional with the use of beam-shaping elements. Hence, information security is higher in LiFi than WiFi. However, the achievable data rates of LiFi are restricted by the modulation bandwidth of the optical modulators. For instance, white LEDs offer only 20 MHz bandwidth. Hence, the data rate in LiFi has to be increased by the application of the multiple-input multiple-output (MIMO) technique, which uses a number of transmitting and receiving elements [6]-[7].

LiFi uses arrays of white LEDs to provide wireless internet service and room lighting simultaneously. The lighting requirements for LiFi regulate the allowable transmitted optical power. For the case of LiFi, illumination or dimming the LEDs has always been a crucial problem to address because the lighting requirement may be different depending on time, location, weather and level of comfort to the human eye [10]. LiFi is based on intensity modulation and direct detection (IM/DD) where the signal is modulated onto light intensity. Hence, the data-carrying transmitted signals have to be only unipolar or positive-valued. Since LiFi uses orthogonal frequency division multiplexing (OFDM) [11]-[21] for encoding large volumes of data, the bipolar OFDM signal has to be converted to unipolar before transmission.

Several OFDM forms such as *asymmetrically clipped optical OFDM* (ACO-OFDM) [11]-[12], *diversity-combined ACO-OFDM* (DACO-OFDM) [18]-[21], *direct current biased optical OFDM* (DCO-OFDM) [11]-[15] and *asymmetrically clipped DC biased optical OFDM* (ADO-OFDM) [16]-[17] are developed for optical communication. In [12], it has been shown that for a specific DC bias level, ACO-OFDM is approximately 4.5 dB more efficient than DCO-OFDM in terms of optical power. The required bias level for DCO-OFDM has been demonstrated for a 2-D spatial channel [4]-[5]. The use of different bias levels is also shown for ADO-OFDM in [17]. With the selection of an optimum DC bias value, DCO-OFDM can have comparable performance as ACO-OFDM in terms of optical power. ADO-OFDM is shown to have slightly better BER performance than both ACO-OFDM and DCO-OFDM in some particular scenarios [17], but for many cases ADO-OFDM does not show comparable performance as ACO-OFDM and DCO-OFDM. It is shown in [18]-[19] that theoretically, DACO-OFDM can have a gain of approximately 3 dB with respect to ACO-OFDM. Therefore, DACO-OFDM has the potential to be more power efficient than its counterparts. However, when room illumination is considered, DCO-OFDM is much more flexible than other OFDM formats. Therefore, there is a need to develop a modulation scheme which has the benefits of power efficiency and illumination capacity. In order to achieve both of these benefits simultaneously, this research focuses on combining the aspects of DACO-OFDM and DCO-OFDM for forming a new modulation scheme termed as *hybrid diversity combined*

978-1-5386-3374-8/17/$31.00 ©2017 IEEE

*OFDM* (HDC-OFDM).

It can be noted that similar to the proposed HDC-OFDM, the existing ADO-OFDM [17] is also a combination of two modulation schemes. However, the basic difference between ADO-OFDM and HDC-OFDM is that for the case of ADO-OFDM, odd-index subcarriers carry ACO-OFDM and even-index subcarriers carry DCO-OFDM, whereas in HDC-OFDM, the lower-index (both odd and even) subcarriers carry DACO-OFDM and higher-index (both odd and even) subcarriers carry ACO-OFDM. In HDC-OFDM, the power and subcarrier proportions can be varied according to the requirements of the system. On the other hand, in ADO-OFDM, the proportion of subcarriers is not changeable, but the power proportion can be changed in this OFDM system.

The main contributions of this work are summarized in the following.

1) Firstly, a framework for the proposed HDC-OFDM modulation is developed combining the aspects of DCO-OFDM and DACO-OFDM. The merging of DCO-OFDM and DACO-OFDM is not straightforward. The DACO-OFDM is computed on low-index subcarriers while DCO-OFDM on high-index subcarriers. When these two signals are added, they interfere with one another. The clipping noise due to DCO-OFDM signal impairs the performance of DACO-OFDM element. This is reduced by using a high DC bias on DCO-OFDM which results in less clipping noise. On the other hand, when DACO-OFDM signal is generated in the transmitter side, a clipping noise is formed affecting the DCO-OFDM signal. At the receiver side, the DACO-OFDM clipping noise is estimated and then deducted from the received signal of DCO-OFDM.

2) Secondly, the proportion of DACO-OFDM and DCO-OFDM elements in HDC-OFDM that results in the best BER performance is investigated in this paper. It is shown in this work that the optimum BER result is achieved when half of the subcarriers are modulated by DCO-OFDM and the remaining ones by DACO-OFDM where the power levels on these two signals are set equal.

## II. PROPOSED HDC-OFDM MODEL

It has already been mentioned that the proposed HDC-OFDM system is a combination of the ideas of DACO-OFDM and DCO-OFDM. A typical HDC-OFDM scheme is described in the following.

### A. HDC-OFDM Transmitter

Fig. 1 shows the transmitter of an HDC-OFDM system. In the transmitter, serial data are first converted to parallel and then mapped to the constellation points being used. For M-QAM based HDC-OFDM, the binary data will be mapped to the M constellation points. The resultant complex signal is given by the input data vector $\mathbf{X}$ as follows

$$\mathbf{X} = [X_0, X_1, X_2, .....X_{N-1}] \tag{1}$$

where $N$ is the number of subcarriers. The $\mathbf{X}$ vector is constrained to have Hermitian symmetry and the values of $X_0$ and $X_{N/2}$ are kept zero. This symmetry is required to confirm that the resultant signal from the IFFT block has a real value. The Hermitian Symmetry condition is mathematically described as

$$X_k = X^*_{N-k} \ , \ 0 < k < N/2 \tag{2}$$

where $k$ is the subcarrier index and $X_k$ is an element of $\mathbf{X}$ . Next, the complex signal $\mathbf{X}$ given in (1) is divided into lower-index subcarriers, $\mathbf{X_L}$ , and higher-index subcarriers, $\mathbf{X_H}$. The terms $\mathbf{X_L}$ and $\mathbf{X_H}$ are to be transformed into DACO-OFDM and DCO-OFDM, respectively. When only the independent data-carrying subcarriers are considered (excluding the Hermitian Symmetry portion), $\mathbf{X_L}$ can be represented as follows:

$$\mathbf{X_L} = [X_0, X_1, X_2, .....X_{P-1}, 0, ....., 0] \tag{3}$$

where $P$ is a value of index $k$. Similarly, $\mathbf{X_H}$ can be written as

$$\mathbf{X_H} = [0, 0, 0, .....X_P, X_{P+1}.....X_{N-1}] \tag{4}$$

First, the case for $\mathbf{X_L}$ (the DACO-OFDM part) is considered. The complex signal $\mathbf{X_L}$ is input to an IFFT block resulting in a time domain real and bipolar signal $\mathbf{x_L}$. The negative portion of the signal $\mathbf{x_L}$ is removed by clipping the amplitude at zero. Next, the resultant unipolar signal $\mathbf{s_L}$ is transformed from parallel to serial (P/S) and then a digital to analog (D/A) operation is performed. After these conversions, the signals are filtered by low pass filters leading to $x_L(t)$ where $t$ represents time. This is the continuous time domain transmitted DACO-OFDM signal.

Now the case for $\mathbf{X_H}$ (the DCO-OFDM part) is considered. The complex signal $\mathbf{X_H}$ is input to an IFFT block resulting in a time domain real and bipolar signal $\mathbf{x_H}$ . The negative portion of the signal $\mathbf{x_H}$ is removed by adding a DC bias. The resultant unipolar signal $\mathbf{s_H}$ is then passed through the P/S and D/A blocks. After these conversions, low pass filtering is done on the analog signals resulting in $x_H(t)$ . This is the continuous time domain transmitted DCO-OFDM signal. Next, the DACO-OFDM and DCO-OFDM signals are added to form the HDC-OFDM transmitted signal $x(t)$:

$$x(t) = x_L(t) + x_H(t) \tag{5}$$

A cyclic extension known as cyclic prefix (CP) is appended to $x(t)$ and then the resultant signal is input to an optical transmitter to generate optical signals $p(t)$. This is the HDCO-OFDM transmitted signal in the optical domain.

## III. HDC-OFDM RECEIVER

Fig. 2 presents the receiver of an HDC-OFDM system. The received optical signal $q(t)$ is transformed into the electrical domain by the photodetecting elements. Like previous research papers, it is assumed that the channel noise modelled as additive white Gaussian noise (AWGN) is added to the received signal in the electrical domain. Next, the resultant electrical signal is low pass filtered and converted to digital from analog. After that the CP is removed and the signal is converted into parallel streams. The parallel signal is passed through a single step frequency domain equalizer. The equalized signal, $\mathbf{Y}$, is divided into lower-index subcarriers, $\mathbf{Y_L}$ , to perform DACO-OFDM demodulation, and higher-index subcarriers, $\mathbf{Y_H}$, to perform DCO-OFDM demodulation.

First consider the demodulation of DACO-OFDM component. By excluding the Hermitian Symmetry part, the term $\mathbf{Y_L}$ can be expressed as

$$\mathbf{Y_L} = [Y_0, \ Y_1, \ Y_2, \ Y_3, .....Y_{P-1}, 0, .....0] \tag{6}$$

Next, $\mathbf{Y_L}$ is divided into odd-index subcarriers $\mathbf{Y_{L,odd}}$ and even-index subcarriers $\mathbf{Y_{L,even}}$. The term $\mathbf{Y_{L,odd}}$ can be

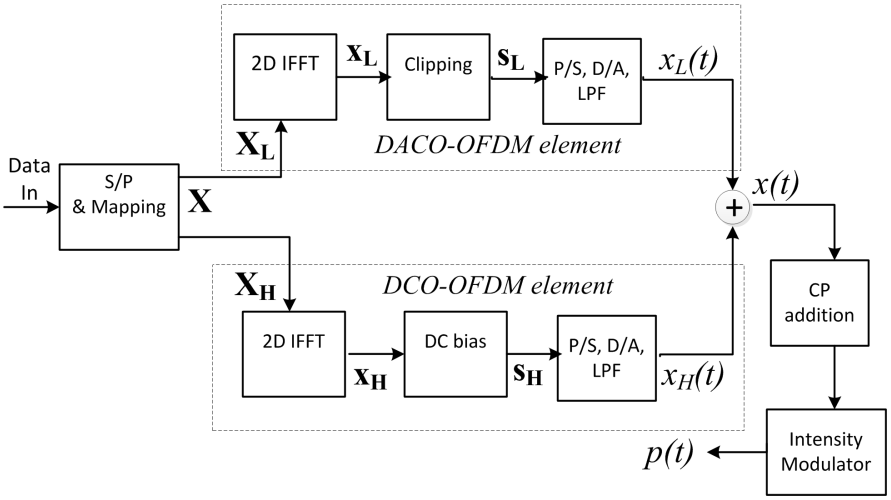


Fig. 1. Block diagram of a HDC-OFDM transmitter.

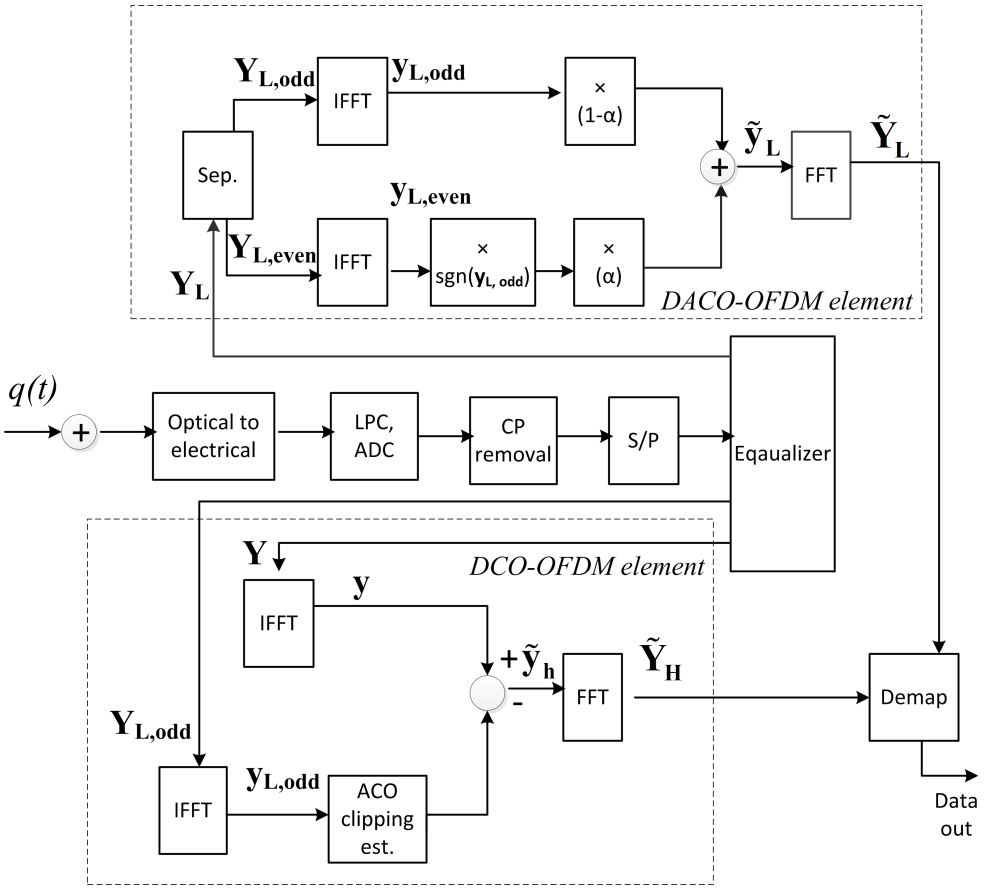


Fig. 2. Block diagram of a HDC-OFDM receiver.

expressed as

$$\mathbf{Y_{L,odd}} = [0,\, Y_1,\, 0,\, Y_3, 0.....Y_{P-1}, 0, .....0] \quad (7)$$

Similarly, $\mathbf{Y_{L,even}}$ can be written as

$$\mathbf{Y_{L,even}} = [Y_0,\, 0,\, Y_2,\, 0, Y_4.....Y_{P-2}, 0, 0.....0] \quad (8)$$

After that $\mathbf{Y_{L,odd}}$ and $\mathbf{Y_{L,even}}$ are converted to time domain signals by two IFFT operations. The terms $\mathbf{y_{L,odd}}$ and $\mathbf{y_{L,even}}$ are combined together to form an estimate of the time domain DACO-OFDM signal as follows:

$$\tilde{\mathbf{y_L}} = (1-\alpha) \times \mathbf{y_{L,odd}} + \alpha \times \mathrm{sgn}(\mathbf{y_{L,odd}}) \times \mathbf{y_{L,even}} \quad (9)$$

where $\alpha$ is a constant. An FFT is computed on $\tilde{\mathbf{y_L}}$ to form the frequency domain estimate of the DACO-OFDM signal, $\tilde{\mathbf{Y}}_\mathbf{L}$. The term $\tilde{\mathbf{Y}}_\mathbf{L}$ can be expressed as

$$\tilde{\mathbf{Y_L}} = [\tilde{Y}_0,\, \tilde{Y}_1,\, \tilde{Y}_2,\, \tilde{Y}_3, .....\tilde{Y}_{P-1,}\, 0, .....0] \quad (10)$$

It can be noted that the clipping noise generated on DCO-OFDM signal impairs the performance of DACO-OFDM element. This is reduced by using a high DC bias on DCO-OFDM which results in less clipping noise. Now, let us consider the DCO-OFDM demodulation. The combined signal, $\mathbf{Y_{L,odd}}$, obtained from the equalizer is converted to a time domain signal by an IFFT operation. On the other hand, the signal

obtained from the equalizer is converted to time domain by another IFFT operation. It can be noted that when DACO-OFDM signal is generated in the transmitter side, a clipping noise is formed affecting the DCO-OFDM signal. At the receiver side, the DACO-OFDM clipping noise is estimated and then deducted from the received signal of DCO-OFDM. This clipping noise estimation technique is the one described in for ADO-OFDM [17]. This is explained in the following. The signal is bipolar and thus is clipped at zero to estimate the DACO-OFDM clipping noise generated at the transmitter side. This resultant signal is deducted from the term $\mathbf{y}$ to form the time domain estimate of DCO-OFDM signal $\tilde{\mathbf{y}_\mathbf{h}}$. The frequency domain equivalence of $\tilde{\mathbf{y}_\mathbf{h}}$ is generated by an FFT operation forming $\tilde{\mathbf{Y}}_\mathbf{H}$. The term $\tilde{\mathbf{Y}}_\mathbf{H}$ can be expressed as

$$\tilde{\mathbf{Y}}_\mathbf{H} = [0, 0,\ 0, 0, .....\tilde{Y}_P, \tilde{Y}_{P+1}, .....\tilde{Y}_{N-1}] \tag{11}$$

Next, $\tilde{\mathbf{Y}}_\mathbf{L}$ and $\tilde{\mathbf{Y}}_\mathbf{H}$ are added to form an estimated signal $\tilde{\mathbf{Y}}$ as follows

$$\tilde{\mathbf{Y}} = \tilde{\mathbf{Y}}_\mathbf{L} + \tilde{\mathbf{Y}}_\mathbf{H} \tag{12}$$

The expression in (12) can be rewritten as

$$\tilde{\mathbf{Y}} = [\tilde{Y}_0, \tilde{Y}_1, \tilde{Y}_2, \tilde{Y}_3, .....\tilde{Y}_{P-1}, \tilde{Y}_P, \tilde{Y}_{P+1}.....\tilde{Y}_{N-1}] \tag{13}$$

The signal is demapped to recover the original binary data.

## IV. PERFORMANCE EVALUATION OF HDC-OFDM

In this section, the performance of HDC-OFDM based LiFi is evaluated in terms of BER. Both average electrical and average optical power are taken into consideration for the performance evaluation. For an electrical signal of $x$, the average optical power and average electrical power depend on $E\{x\}$ and $E\{x^2\}$, respectively, where $E(.)$ is defined as the expectation operator. In this paper, $E_{b(elec)}/N_o$ and $E_{b(opt)}/N_o$ are considered as performance metric where $E_{b(elec)}$ is the received energy (electrical) per bit, $E_{b(opt)}$ is the received energy (optical) per bit, and $N_o$ is the noise spectral density (single sided). With the use of MATLAB tool, simulation results have been presented for an ideal AWGN optical channel with no other distortion. Simulations were carried out considering 256 subcarriers $N$=256, a CP of 10% and constellation sizes $M$ of 4 and 16. It can be noted that in ACO-OFDM and DACO-OFDM, only the odd subcarriers are modulated, whereas in DCO-OFDM, both the odd and even subcarriers are modulated for data transmission. Similarly, for the case of DACO portion in HDC-OFDM, only the odd subcarriers carry data and the even subcarriers are kept unused; while for the DCO portion all the odd and even subcarriers transmit data. In order to take this variation in the spectral efficiency of different modulation forms, the total transmitted optical power is normalized to unity. The BER performance of HDC-OFDM is a function of the power level on DACO-OFDM and DCO-OFDM elements. Fig. 3 presents the plots for BER versus $E_{b(elec)}/N_o$ for 4-QAM HDC-OFDM for different percentage of power levels on DACO and DCO components. The percentage of subcarriers and the power level on DACO-OFDM is represented in the figure as $p_{DACO}$. For example, $p_{DACO}$=50% means the power on DACO and DCO components is the same and the number of subcarriers belonging to DACO is also the same as that of DCO-OFDM. Fig. 3 indicates that the BER performance degrades when the values of $p_{DACO}$ increase or decreases from the mid value $p_{DACO}$=50%. In other words, the best BER performance is achieved when $p_{DACO}$ reaches 50%. The degradation is about 2 dB when the $p_{DACO}$ value increases from 50% to 87.5%.

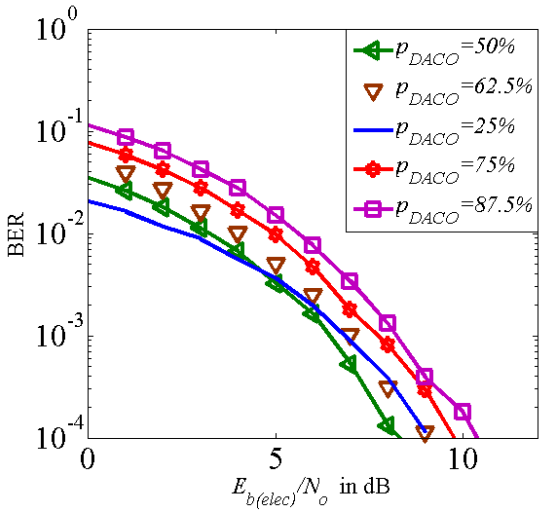


Fig. 3. BER versus $E_{b(elec)}/N_o$ for 4-QAM HDC-OFDM for different power levels on DACO element.

Now, the modulation forms are compared considering the same overall data rate. It can be noted that like ACO-OFDM, DACO-OFDM carries data by using only the odd subcarriers providing half data rate. Therefore, 16-QAM stand-alone DACO-OFDM and 16-QAM ACO-OFDM have the same data rate as 4-QAM DCO-OFDM. Similarly, the DACO component within HDC-OFDM has only the odd subcarriers to transmit data; however, the DCO-OFDM part has all the subcarriers useful. Therefore, to obtain the same data rate as 4-QAM stand-alone DCO-OFDM, the DACO component of HDC-OFDM should be mapped by 16-QAM and the DCO part by 4-QAM. The BER performance of ADO-OFDM depends on the levels of power on ACO-OFDM and DCO-OFDM elements within ADO-OFDM. It is shown in [17] that the BER performance for ADO-OFDM depends on the optical power loaded on ACO-OFDM component, constellation size and the level of DC bias used. When ADO-OFDM is considered in the simulations, it is assumed that 50% power is on ACO-OFDM element and 50% power on DCO-OFDM component. Fig. 4 shows the plots of BER versus $E_{b(elec)}/N_o$ for the same overall data rate that is the same bits/sec/Hz. The plots show that at a given BER of $10^{-4}$, the BER performance of HDC-OFDM is 5 dB better than ADO-OFDM. Moreover, HDC-OFDM is 3 dB better than 4-QAM DCO-OFDM, 2 dB better than 16-QAM ACO-OFDM, but only 1 dB inferior to DACO-OFDM. Therefore, HDC-OFDM is very close to DACO-OFDM in terms of electrical power efficiency.

Fig. 5 presents the plots of BER versus $E_{b(opt)}/N_o$ for different optical OFDM forms with the same overall data rate that is the same bits/sec/Hz. It can be seen that for a given data rate, HDC-OFDM (16QAM DACO and 4-QAM DCO) is only 1.5 dB less efficient than 16-QAM DACO-OFDM. However, this HDC-OFDM is now better than 16-QAM ACO-OFDM and 4-QAM DCO-OFDM by 1 dB and 5 dB, respectively. Moreover, for the cases considered, HDC-OFDM is almost 7 dB more optically power efficient than ADO-OFDM.

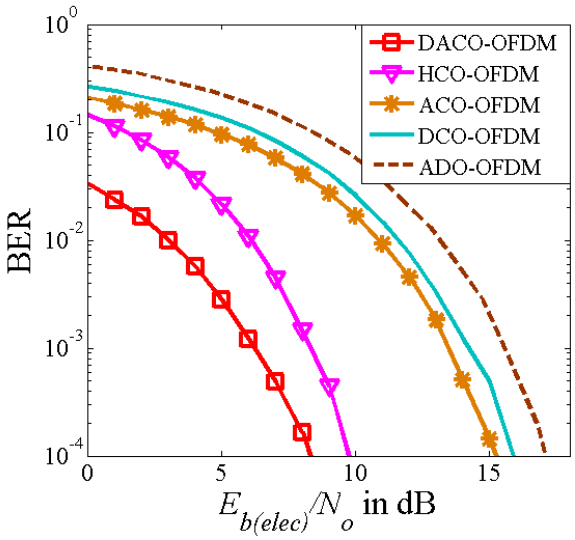


Fig. 4. BER versus $E_{b(elec)}/N_o$ for different OFDM forms.

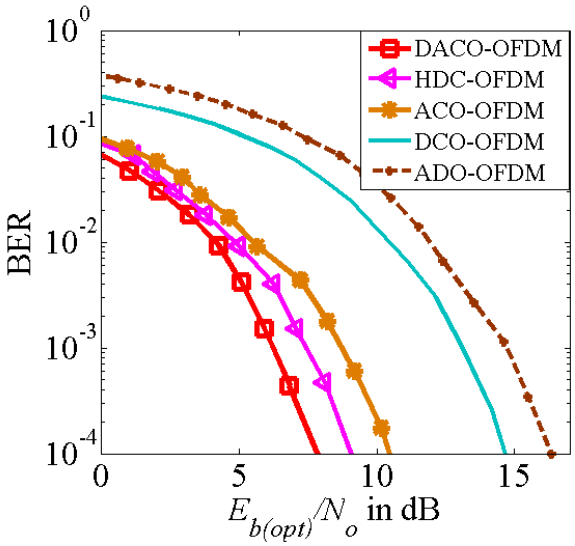


Fig. 5. BER versus $E_{b(opt)}/N_o$ for different OFDM forms.

## V. Conclusions

This paper proposes a new modulation format termed as HDC-OFDM. This HDC-OFDM is a combination of the aspects of existing DCO-OFDM and DACO-OFDM modulations. Simulation results indicate that the BER results of HDC-OFDM varies depending on the proportion of DACO-OFDM and DCO-OFDM components. Since the HDC-OFDM has a DCO-OFDM component, the dimming facility is easily achieved in HDC-OFDM by only increasing/decreasing the DC bias level without using any other additional system. It is also shown that the performance of HDC-OFDM is close to DACO-OFDM in terms of electrical and optical power efficiency. In HDC-OFDM, the lower subcarriers are modulated with DACO-OFDM and the higher subcarriers with DCO-OFDM. As long as a stand-alone AWGN channel is considered, the results will not change if the DACO-OFDM is mapped to higher subcarriers and DCO-OFDM at lower subcarriers. The BER performance results in this paper are illustrated for a target BER of $10^{-4}$. In a data communication scenario, a target BER of $10^{-9}$ is desirable. By the use of convolutional channel coding, the BER plots in this work can be extended to a BER of $10^{-9}$. In future, a multipath dispersive channel can be considered to evaluate the effectiveness of the proposed HDC-OFDM.

## References


[1] A. Jovicic, J. Li, and T. Richardson, Visible light communication: opportunities, challenges and the path to market, *IEEE Commun. Mag.*, vol. 51, no. 12, pp. 2632, 2013.

[2] S. Wu, H. Wang, and C. H. Youn, Visible light communications for 5G wireless networking systems: from fixed to mobile communications, *IEEE Netw.*, vol. 28, no. 6, pp. 4145, Nov. 2014.

[3] M. S. A. Mossaad, S. Hranilovic, and L. Lampe, Visible light communications using OFDM and multiple LEDs, *IEEE Trans. on Commun.* vol. 63, no. 11, pp. 43044313, 2015.

[4] M. R. H. Mondal, and K. Panta, "Performance analysis of spatial OFDM for pixelated optical wireless systems", *Transactions on Emerging Telecommunications Technologies*, vol. 28, no. 2, Feb. 2017.

[5] M.R.H. Mondal, "Impact of spatial sampling frequency offset and motion blur on optical wireless systems using spatial OFDM", *EURASIP Journal on Wireless Communications and Networking*, vol. 238, 2016.

[6] K. C. Hu, A. G. Armada, M. Snchez-Fernndez and A. Royo, "Prototyping and measurements for a LiFi system," *IEEE Sensor Array and Multichannel Signal Processing Workshop (SAM)*, Rio de Janerio, 2016, pp. 1-5.

[7] W. Abdallah and N. Boudriga, "Enabling 5G wireless access using Li-Fi technology: An OFDM based approach," *18th International Conference on Transparent Optical Networks (ICTON)*, Trento, 2016, pp. 1-6.

[8] Y. Wang, X. Wu and H. Haas, "Fuzzy logic based dynamic handover scheme for indoor Li-Fi and RF hybrid network," *IEEE International Conference on Communications (ICC)*, Kuala Lumpur, 2016, pp. 1-6.

[9] M. Ayyash et al., "Coexistence of WiFi and LiFi toward 5G: concepts, opportunities, and challenges," *IEEE Commun. Mag.*, vol. 54, no. 2, pp. 64-71, February 2016.

[10] H. Haas, L. Yin, Y. Wang, and C. Chen, "What is LiFi?", *J. Lightw. Technol.*, vol.34, pp.1533-1544, Mar. 2016.

[11] J. Armstrong, "OFDM for optical communications", *J. Lightw. Technol.*, vol. 27, no. 3, pp.189204, 2009.

[12] J. Armstrong and A. J. Lowery, "Power efficient optical OFDM," *Electron. Lett.*, vol. 42, pp. 370-372, 2006.

[13] J. Armstrong and B. J. C. Schmidt, "Comparison of asymmetrically clipped optical OFDM and DC-biased optical OFDM in AWGN," *IEEE Commun. Lett.*, vol. 12, pp. 343-345, 2008.

[14] Y. Yang, Z. Zeng, J. Cheng, and C. Guo, An enhanced DCO-OFDM scheme for dimming control in visible light communication systems, *IEEE Photon. J.*, vol. 8, no. 3, 2016.

[15] T. Mao, Z. Wang, Q. Wang, and L. Dai," Ellipse-based DCO-OFDM for visible light communications", *Optics Communications*, vol. 360, pp. 1-6, 2016.

[16] S. D. Dissanayake, K. Panta and J. Armstrong, A novel technique to simultaneously transmit ACO-OFDM and DCO-OFDM in IM/DD systems, *Proceedings of the IEEE Globecom Workshops*, pp. 782786, 2011.

[17] S. Dissanayake and J. Armstrong, "Comparison of ACO-OFDM, DCO-OFDM and ADO-OFDM in IM/DD systems," *J. Lightw. Technol.*, vol. 31, pp. 1063-1072, Apr. 2013.

[18] L. Chen, B. Krongold, and J. Evans, "Diversity Combining for Asymmetrically Clipped Optical OFDM in IM/DD Channels", *IEEE Global Telecommunications Conference*, pp. 1-6, 2009.

[19] S. D. Dissanayake and J. Armstrong, "Novel Techniques for Combating DC Offset in Diversity Combined ACO-OFDM," *IEEE Commun. Lett.*, vol. 15, pp. 1237-1239, 2011.

[20] M. Tahar, T. Q. Wang, M. F. G. Medina, O. Gonzlez, and J. Armstrong, "Experimental Demonstration of Diversity Combining for Asymmetrically Clipped Optical OFDM," *IEEE Commun. Lett.*, vol. 20, pp. 906-909, 2016.

[21] M. F. Sanya, C. Aupetit-Berthelemot, L. Djogbe and A. Vianou, "Diversity-Combining in asymmetrically clipped optical OFDM for PON IM/DD fiber link," *IEEE International Conference on Communications Workshops (ICC)*, Sydney, NSW, 2014, pp. 403-406.

[22] J. Dang, Z. Zhang and L. Wu, "Frequency-Domain Diversity Combining Receiver for ACO-OFDM System," *IEEE Photon. J.*, vol. 7, no. 6, pp. 1-10, Dec. 2015.

[23] T. Q. Wang, H. Li and X. Huang, "Diversity Combining for Layered Asymmetrically Clipped Optical OFDM Using Soft Successive Interference Cancellation," *in IEEE Commun. Lett.*, vol. 21, no. 6, pp. 1309-1312, Jun. 2017.

# Performance of Multi-Stage Threshold Decoding in MC-CDMA

Hasib-Al-Rashid,* Shafkat Islam, Muhammad Ahsan Ullah
Department of EEE, Chittagong University of Engineering and Technology
Chittagong, Bangladesh.
*hasib_eee_cuet@ieee.org

*Abstract*— **A decoding method, multi-stage threshold decoding for multicarrier code division multiple access (MTD/MC-CDMA) is proposed. Under two different channels, AWGN and Rayleigh fading (multipath), the comparative studies of BER performance between MTD/MC-CDMA and uncoded MC-CDMA is presented. Results show that MTD/MC-CDMA saves 5dB power under AWGN channel and 12dB power under Rayleigh fading channel (18-paths) for same process gain. MTD/MC-CDMA reduces BER to $10^{-6}$ at 20dB $E_b/N_o$ (fading channel) and 8dB $E_b/N_o$ (AWGN channel).**

***Index Terms***— **MTD, AWGN, MC-CDMA, BER, Rayleigh Fading.**

## I. Introduction

The wireless communication system is nowadays preceding to the highest peak of its efficiency. Wireless communication system will have Multi-carrier Code Division Multiple Access (MC-CDMA) as a popular candidate for having high spectral efficiency. Code division multiple access (CDMA) in combination with orthogonal frequency division multiplexing (OFDM) composes MC-CDMA. This combination helps to have robustness in opposition to inter-symbol interference.

High data rate broadcasting is a major issue for a communication system. The multi-carrier transmission has an advantage over all other techniques in high data rate broadcasting by reducing the signal processing complexity. In the mid-1960s, Chang presented the idea of multi-channel transmission in his paper [1], [2]. He had shown that single band limited channel can be used to simultaneously transmit data. This transmission method avoids inter channel and inter symbol interferences i.e. ICI and ISI respectively. This was the starting of orthogonal multi-carrier transmission. Further, Weinstein and Ebert had shown in [3] that multi-carrier transmission can be done in the frequency domain. To avoid ICI and ISI, they presented the idea of the guard time. In 1993, Fazel introduced a unique multiple access scheme combining OFDM and CDMA in [4]-[5]. Several other authors simultaneously came with similar ideas. It was then termed MC-CDMA.

Despite having a range of advantages of both OFDM and CDMA, MC-CDMA has some drawbacks of having high ratio of peak to average power i.e. PAPR. It also has multiple access interferences (MAI). These drawbacks can be overcome with the use of forward error correcting codes having high coding gain [6]. Authors of [5], [7], [8] used linear convolutional codes in the multi-carrier system. Several authors presented turbo coded MC-CDMA with different configurations in [9]-[12]. But being computationally complex, turbo code increases the system complexity. Recently, researchers are incorporating LDPC codes into MC-CDMA. Different researchers presented LDPC coded MC-CDMA systems in [6], [13], [14]. LDPC is less complex than turbo codes which reduces the system complexity but not completely.

Threshold decoding (TD) is considered less complex decoding techniques among all other codes presented before. The modified version of threshold decoding i.e. multi-stage threshold decoding (MTD) is presented in [15]-[18]. Authors of [19] employed MTD in optical communication. In this paper, MTD is incorporated with MC-CDMA and its performance is evaluated.

The paper is structured as follows. Section II gives idea of system architecture. Section III presents simulation environments and results in detail. At last, section IV concludes the paper.

## II. System Architecture

Fig. 1 shows the system architecture of the MTD/MC-CDMA. The stream of data is generated in the form of bits. The generated data are then MTD encoded. These encoded data are forwarded to the MC-CDMA transmitter. In the transmitter, data are modulated and multiplexed with the corresponding pilot symbols. Then it is forwarded to the channel after digital to analog converted. The analog signal is then received by the receiver. Then it is again converted to digital and demodulation is done. Pilot and reference symbols are derived from demodulated data which are used in channel estimation. After that data are sent to MTD decoder. Finally, data are received and estimated data are used along with generated data for BER calculation.

### *A. MC-CDMA transmitter*

The transmitter designed for MC-CDMA for j-th user with QPSK format is presented in Fig. 2. Here, QPSK modulated data is multiplexed with pilot data. These multiplexed data are converted from serial to parallel. They are then multiplied by the spreading code chip. Inverse Fast Fourier transform is performed for generating an orthogonal multi-carrier signal. Then finally, Guard interval (GI) is added to overcome ISI and ICI resulted from multi-path fading. The complex equivalent signal is represented as –

$$S(t) = \sum_{u=0}^{U-1} \sum_{p=0}^{P-1} \sum_{k=0}^{K-1} d_p^u \, C_k^u \, P_s(t - kT_s) e^{j\,2\pi\,(P.k+p)\,(t-kT_s)\,\Delta f} \quad (1)$$

978-1-5386-3374-8/17/$31.00 ©2017 IEEE

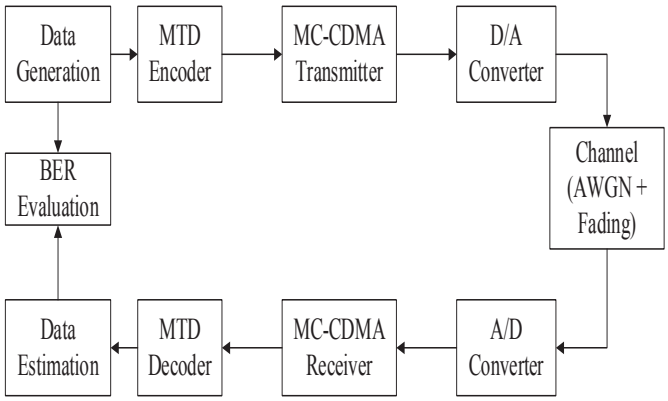


Fig. 1. System Architecture of proposed algorithm

Table-1 shows meanings of the symbols used in equation (1)

TABLE I
CORRESPONDING SYMBOLS' MEANING OF EQUATION (1)

| Symbols | Meanings |
|---|---|
| K | Processing Gain |
| U | User number |
| P | Transmitted bits per user |
| $d_p^u \in \{\pm 1\}$ | p-th bit of user U |
| $C_p^u \in \{\pm 1\}$ | k-th chip of u-th user's spreading sequence |
| $T_s$ | Symbol duration |
| $\Delta f$ | Separation of sub-carrier |
| $P_s(t)$ | Rectangular waveform of symbol pulse |

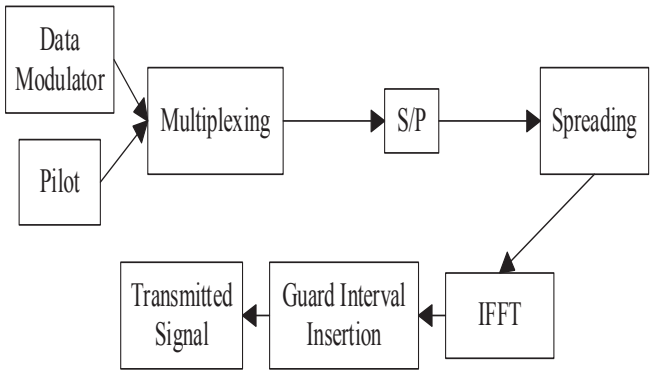


Fig. 2. MC-CDMA transmitter

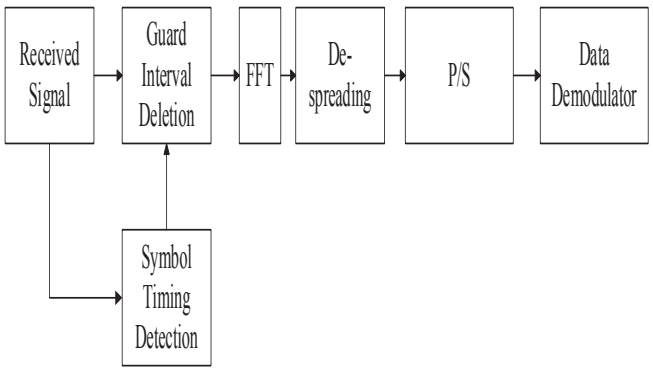


Fig. 3. MC-CDMA receiver

The transmitter of MC-CDMA is nearly similar to the OFDM transmitter. The main dissimilarity is that MC-CDMA transmits same symbol in parallel through different sub-carriers whereas OFDM transmits different symbols.

### *B. MC-CDMA Receiver*

The receiver of MC-CDMA is presented in Fig. 3. At first, the signal is received from the channel. Then the previously added guard interval is deleted. After that, Fast Fourier Transformation is done and the symbols are despread. Then the parallel symbols are converted into serial. Then they are demodulated. The received signal can be written as –

$$r(t) = \sum_{u=0}^{U-1} r_{MC}^{u}(t) + n(t) \tag{2}$$

Where,

$$r_{MC}^{u}(t) = \sum_{p=0}^{P-1}\sum_{k=0}^{K-1} Z_{p,k}^{u}(t)\ d_p^u\ C_k^u\ P_s(t - kT_s) e^{j\,2\pi\,(P.k+p)\,(t-kT_s)\,\Delta f} \tag{3}$$

In the equation (3), $Z_{p,k}^{u}(t)$ denotes received complex envelope at the $(P.k+p)$-th sub-carrier of the u-th user.

### *C. Walsh-Hadamard as spreading codes:*

In this proposed system, Walsh-Hadamard spreading codes are incorporated. They are orthogonal and easy to generate recursively by Hadamard transform. Hadamard transform is stated in [20] as –

$$\boldsymbol{H_1} = [0] \tag{4}$$

$$\boldsymbol{H}_{2n} = \begin{bmatrix} H_n & H_n \\ H_n & \overline{H_n} \end{bmatrix} \tag{5}$$

Here, Hadamard matrix, $H_n$ is only for $n = 2^i$ where $i \geq 1$. It is a square shaped matrix and symmetric in nature. Each row or column here corresponds to a n length Walsh code. Each row of $H_n$ is orthogonal to remaining all rows.

### *D. Multi-stage threshold decoding:*

Multi-stage threshold decoding is used in this paper as error correction code. It is an iterative bit flipping algorithm. The hamming distance between the decoded code word and received word becomes shorter when each information bit is flipped. Self-orthogonal convolutional code of type-2 (SOCC T-2) is considered in this paper. As stated in [17]-[18], in SOCC T-2, by using n information bit stream of N/n bits, multiple generating polynomials originate n parity bit streams.

In the threshold decoding technique, a syndrome bit sequence is generated by using received bit sequences. All the syndrome values are first checked and then summed by the comparator circuit used in threshold decoding. The result is called check-sum value. When this check-sum value exceeds the predefined threshold value, the comparator circuit holds '1' as its output. When this decision is taken, the syndromes are updated and register contents one position right shifted. As threshold decoding does not give satisfactory error performance, it is further modified as Multi-stage Threshold Decoding (MTD), keeping the main techniques same. MTD is described by the authors of [15]-[18]. Here iterations are done in each decoding

stage. Difference register (DR), an additional shift register, is introduced in MTD against an information shift register. The whole algorithm is thus called multi-stage threshold decoding with difference register (MTD-DR).

DR introduces a new specialty in MTD. The contents of the DR supplies the Hamming distance value of received word and decoded code word. At the very beginning of the process, DR possesses all the '0' bits because of the similarity of received word and decoded code word. Following the same process, as stated in [17]-[18], the checksum value of the MTD for SOCC T-2 is evaluated by,

$$L_j^{(b)} = \sum_{p=1}^{u} \sum_{a=1}^{J_p^{(b)}} S_{j+g_{p,a}^{(b)}}^{(p)} + d_j^{(b)} \tag{6}$$

The meanings of the symbols used in the equation (6) is mentioned in table II.

The threshold value is calculated by,

$$T_b = \frac{\sum_{p=1}^{n} J_p^{(b)} + 1}{2} \tag{7}$$

When the checksum value $L_j$ exceeds the threshold value $T_b$, the information bit, syndrome bit and related DR are inverted. If more than half of bits from difference register possesses '1', the bit is flipped. This decision also produces same number of bits. Following this process, the Hamming distance reduces after each bit flipping.

## III. Simulation & Results

### A. Simulation Parameters

To assess the performance improvement of MTD/MC-CDMA, simulation results are compared with un-coded MC-CDMA system. The simulation environment for both the systems is kept same. Table III shows the simulation parameters.

TABLE II
CORRESPONDING SYMBOLS' MEANING OF EQUATION (2)

| Symbols | Meanings |
|---|---|
| $a$ | Tap connection position |
| $p$ | Number of tap connection set |
| $b$ | Number of shift register |
| $J_p^{(b)}$ | Number of Taps |
| $S_j^{(p)} + g_{p,a}^{(b)}$ | $j + g_{p,a}^{(b)}$-th syndrome bit in the p-th syndrome register |
| $d_j^{(b)}$ | j-th bit in b-th difference register |

TABLE III
SIMULATION PARAMETERS

| | |
|---|---|
| No. of packet | 1000 |
| Symbol duration | 6.4 μ$s$ |
| Packet Length | 40000 |
| Baseband modulation | QPSK |
| Channel | AWGN & Rayleigh Fading |
| Channel Estimation | Pilot Based |
| MTD iterations | 15 |
| Minimum distance and code rate of code | 11 & 0.5 |
| Process Gain | 1 & 4 |
| No. of multi-paths | 18 |
| Spreading Code | Walsh-Hadamard |

### B. Results

Results of uncoded MC-CDMA is tabulated in table IV.

TABLE IV
TABLE FOR UNCODED MC-CDMA IN AWGN CHANNEL

| **$E_b/N_o$ (dB)** | **BER** |
|---|---|
| 12 | $6.1 \times 10^{-5}$ |
| 10 | $4.0 \times 10^{-4}$ |

Fig. 4 shows the simulation results of MTD/MC-CDMA in AWGN channel for process gain (PG) = 1. The MTD/MC-CDMA has a gain of 4 dB over MC-CDMA at BER level of $10^{-4}$ and 5dB at BER level of $10^{-5}$.

For Rayleigh Fading Channel of 18 paths, the results are summarized in table V and table VI. Here, flat fading is considered. Fig. 5 and Fig. 6 show the curve of MTD/MC-CDMA and MC-CDMA in Rayleigh fading channel for process gain 1 and 4 respectively. At BER level $10^{-3}$ the MTD/MC-CDMA system has a gain of 12dB over MC-CDMA system for PG=1. Increasing the process gain at 4, the MTD/MC-CDMA system has performance gain of 10dB over the MC-CDMA system at BER level $10^{-4}$. Thus, the use of MTD in MC-CDMA significantly improves the error correcting capability of the system. The error correcting capability of the MTD depends upon its minimum distance, $D_{min}$. In the MTD/MC-CDMA, $D_{min} = 11$ and Hard Decision MTD (HMTD) are used. The code rate is 0.5. Though HMTD has limitations in correcting error bits for a given code in error floor region, its performance in MC-CDMA system is promising both in AWGN and fading channel.

TABLE V
COMPARISON OF UNCODED AND MTD/MC-CDMA IN RAYLEIGH FADING CHANNEL AT PG = 1

| $E_b/N_o$ (dB) | MTD/ MC-CDMA | Un-coded MC-CDMA |
|---|---|---|
| 09 | $5.16 \times 10^{-3}$ | $3.50 \times 10^{-2}$ |
| 18 | $3.26 \times 10^{-4}$ | $5.30 \times 10^{-3}$ |
| 27 | $2.70 \times 10^{-5}$ | $7.60 \times 10^{-4}$ |

TABLE VI
COMPARISON OF UNCODED AND MTD/MC-CDMA IN RAYLEIGH FADING CHANNEL AT PG = 4

| $E_b/N_o$ (dB) | MTD/ MC-CDMA | Un-coded MC-CDMA |
|---|---|---|
| 09 | $9.90 \times 10^{-4}$ | $2.60 \times 10^{-2}$ |
| 18 | $7.50 \times 10^{-6}$ | $1.30 \times 10^{-3}$ |
| 27 | – | $4.30 \times 10^{-5}$ |

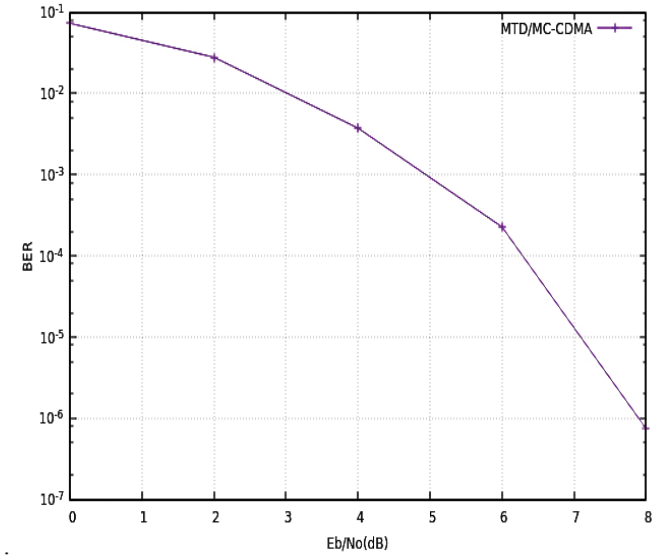


Fig. 4. BER vs. $E_b$/No for MTD/MC-CDMA in AWGN channel (PG=1)

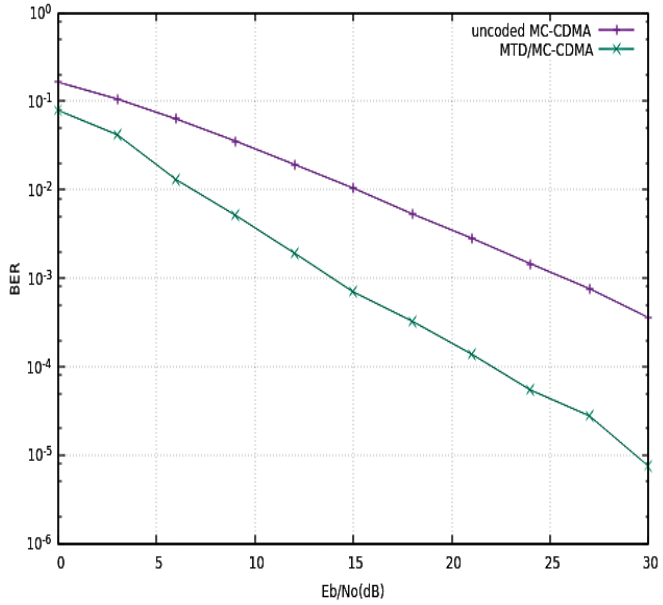


Fig. 5. BER vs. $E_b$/No for MTD/MC-CDMA and Un-coded MC-CDMA in 18 paths Rayleigh Fading channel (PG=1)

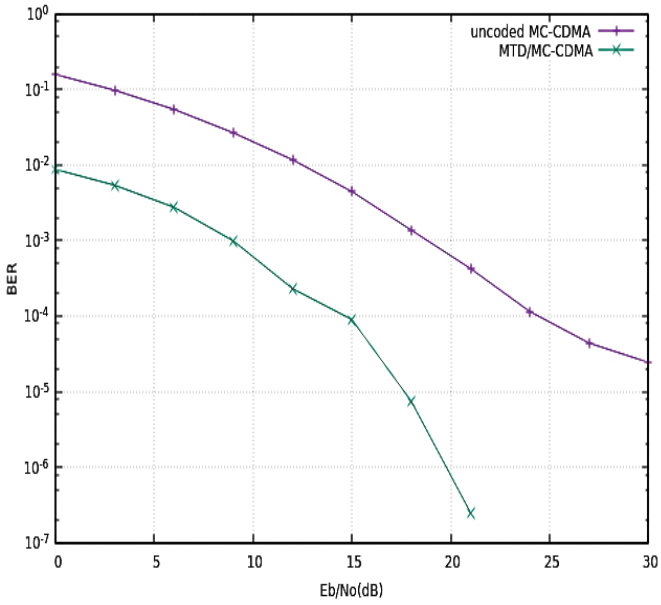


Fig. 6. BER vs. $E_b$/No for MTD/MC-CDMA, Un-coded MC-CDMA in 18 paths Rayleigh Fading channel (PG=4)

## IV. Conclusions

The MTD/MC-CDMA successfully reduces the number of error bits in the system. The MTD/MC-CDMA achieves BER level of $10^{-6}$ at 20dB $E_b/N_o$. MC-CDMA cannot achieve that level of BER in the simulation process.

The proposed system saves much power in fading channel compared to AWGN channel. The complexity of the MTD/MC-CDMA is less than LDPC coded MC-CDMA or Turbo coded MC-CDMA as MTD is itself a less complex decoding technique. The BER performance of MTD/MC-CDMA might be improved by using other advanced MTD techniques like Soft decision MTD or Combined MTD. Using advanced MTD techniques will increase system complexity and execution time. Though the time and complexity is less compared to other contemporary decoding techniques in MC-CDMA. So, MTD/MC-CDMA may be taken as a promising technique where lower BER is required in wireless communication.

## References

[1] R. W. Chang, "Synthesis of band-limited orthogonal signals for multi-channel data transmission," Bell Labs Technical Journal, no. 45, pp. 1775–1796, Dec. 1966.

[2] R. W. Chang and R. A. Gibby, "A theoretical study of performance of an orthogonal multiplexing data transmission scheme," IEEE Transactions on Communication Technology, vol. 16, pp. 529–540, Aug. 1968.

[3] S. B. Weinstein and P. M. Ebert, "Data transmission by frequency-division multiplexing using the discrete Fourier transform," IEEE Transactions on Communication Technology, vol. 19, pp. 628–634, Oct. 1971.

[4] K. Fazel, "Performance of CDMA/OFDM for mobile communications system," in Proc. IEEE International Conference on Universal Personal Communications (ICUPC '93), Ottawa, Canada, pp. 975–979, Oct. 1993.

[5] K. Fazel and L. Papke, "On the performance of convolutionally-coded CDMA/OFDM for mobile communications system," in Proc. IEEE International Symposium on Personal, Indoor and Mobile Radio Communications (PIMRC '93), Yokohama, Japan, pp. 468–472, Sept. 1993.

[6] K. Rasadurai, Parvathy S Kumar, N. Kumaratharan, " Performance Enhancement of MC-CDMA system using LDPC codes", Proceeding of 2013 IEEE International Conference of Informatics and Communication Technologies, pp. 395-399.

[7] D. N. Rowitch and L. B. Milstein, “Convolutional Coding for Direct Sequence Multicarrier CDMA,” MILCOM’95 Conf. Proc., pp.55-59, 1995.
[8] L. Meylani, N. Andini, I. Hidayat, “Performance of Coded Modulation in Multicarrier CDMA System,” Indonesian Journal of Electrical Engineering and Computer Science, vol. 1, no. 3, pp. 583-589, March 2016.
[9] V. Le Nir, M. H´elard, and R. Le Gouable, “Spacetime block coding applied to turbo coded multicarrier CDMA,” in Proceedings of VTC Spring’03, Jeju, Korea, pp. 577–581, May 2003.
[10] A. R. Enayati, P. Azmi, Y. Taghinia, A. Salahi, “A novel bandwidth efficient SOC-based turbo coding scheme mid reduced complexity MUD for SA-based MC-CDMA systems,” Springer Telecommun Syst, vol. 50, pp. 71-88, Dec. 2010.
[11] Q. Jun-wei, X. Rui and F. Fang, “Performance of MC-CDMA system based on turbo code in wideband shortwave channel,” 2011 IEEE 3rd International Conference on Communication Software and Networks, pp. 394-397, 2011.
[12] A. Marczak, “Performance analysis of data transmission in MC-CDMA radio interface with turbo codes”, Telecommunication Systems, Vol. 59, Issue 4, pp 501-507, August 2015.
[13] Z. Duan, M. Valkama, M. Renfors, “On the Design and Performance of LDPC Coded MC-CDMA Systems,” in Proc. 14th IST Mobile and Wireless Communications Summit, June 2005.
[14] I. Marcu, C. Voicu, R. Crăciunescu and S. Halunga, "LDPC performances in multi-carrier systems," 2016 International Conference on Communications (COMM), Bucharest, 2016, pp. 209-212.
[15] V.V. Zolotarev, “The multithreshold decoder performance in Gaussian channels”, 7th Int. Symp. on Commn. Theory and Applications (ISCTA’03), pp. 18-22, UK, July 2003.
[16] New Algorithm of Multithreshold Decoding of Noise Proof Codes Website. [Online]. Available: http://www.mtdbest.iki.rssi.ru
[17] M. A. Ullah, K. Okada and H. Ogiwara, "Multi-stage threshold decoding for self-orthogonal convolutional codes," IEICE Trans. Fundamentals, vol. E93-A, no.11, pp. 1932-1941, November 2010.
[18] M. A. Ullah and H. Ogiwara, “Performance improvement of multi-stage threshold decoding with difference register,” IEICE Trans. Fundamentals, vol. E94–A, no.6, pp. 1449-1457, June 2011.
[19] M.A. Ullah, R. Omura, T. Sato and H. Ogiwara, “Multi-Stage Threshold Decoding of High Rate Convolutional Codes for Optical Communications,” 7th Advanced Int. Conf. on Telecommunications (AICT2011), pp. 87-93, March 2011.
[20] L. Hanzo and T. Keller, *An OFDM and MC-CDMA Primer*. Piscataway, NJ: IEEE Press/Wiley, 2006, pp. 223.

# Performance Analysis of Crosstalk due to Inter-core Coupling in a Heterogeneous Multi-core Optical Fiber Communication System

Md Afzal Hossain* and S P Majumder**
Depart of Electrical and Electronic Engineering (EEE)
Bangladesh University of Engineering and Technology (BUET)
Dhaka, Bangladesh
*ayonarnab@yahoo.com, **spmajumder2002@yahoo.com

***Abstract*— Analysis of crosstalk due to inter-core coupling in a 7-core heterogeneous multi-core optical fiber (MCF) based optical communication system is presented. The analysis is further carried out to find crosstalk power at the output of any core with excitation to other core of an MCF. The expression for optical signal to crosstalk power ratio is developed at the output of the desired core. At the output of the excited core Signal to Crosstalk plus Noise Ratio (SCNR) is determined. Finally, Bit Error Rate (BER) performance results are evaluated for different system parameters. The power penalty due to crosstalk is determined for a given input power and data rate for various propagation distance and core parameter. It is noticed that power penalty due to crosstalk is significant and can be reduced by increasing the core-to-core separation (pitch). For example, the power penalty is found to be 57 dBm for a core pitch of 15 µm at a given BER of 10e-9 for a propagation distance of 135 km, where as it is found to be 37 dBm for the same distance and BER with a pitch of 30 µm.**

***Keywords*—Multi-Core Fiber, Coupling Coefficient, Coupling Length, Crosstalk, Mode Coupling, Strong Coupling, Weak Coupling**

## I. INTRODUCTION

Iintensive research works on Multi-core Optical fibers (MCFs) are being undertaken in order to explore their huge application in optical communications, fiber couplers, optical sensors, optical lasers, and microwave photonics etc. In the fields of optical communications, MCFs have the high potentials to be used in space-division multiplexing (SDM) or mode-division multiplexing (MDM) systems to overcome the limit of transmission capacity [1-4]. Performance analysis in terms of Bit Error Rate (BER) in MCF considering assumed crosstalk (Xtalk) has been done in [5-6]. Extensive research works have been done on MCFs for their use in optical communications and optical fiber sensors [7] etc. Reducing the inter-core Xtalk is the main issue in respect of the design, manufacture and use MCFs. In order to estimate the inter-core Xtalk in MCFs, Coupled-mode theory (CMT) and Coupled-power theory (CPT) have been introduced [8].

There are two types of Xtalk in MCF: intra-core and inter-core Xtalk. The inter-core Xtalk arises from the mode coupling between the neighboring cores. On the other hand, the coupling between the fiber modes within each core because of the fiber imperfections, like, index perturbations, bends, and twists etc cause the intra-core Xtalk. Generally, weak coupling among cores is required to overcome Xtalk, while strong coupling is essential for the application in MDM systems to form super-modes in the use of MCFs [1-4].

However, behavior of coupling coefficients based on various geometry and arrangements of the cores, and performance deterioration due to Xtalk caused by inter-core coupling in the MCF have not yet been analyzed. In this paper, we have analyzed the propagation dynamics of both optical signal and Xtalk power in heterogeneous MCFs. The performance deterioration in terms of Bit Error Rate (BER) has also been analyzed in this paper.

## II. SYESTEM MODEL

Fig. 1 shows the system model/schematic diagram or of a 7-core MCF optical communication link consisting of a 7-core MCF. Two Tapered Multi-core Connectors (TMC) are used to couple the individual signals in-and-out of the MCF. Seven commercially available un-coupled Distributed Feedback Fiber (DFB) transmitters are used as the stable light sources, and PIN Photo Diodes are used in the receivers. The DFB Laser Diodes (LDs) are considered to be set at 1550 nm and are directly modulated at 2.5 Gbit/sec message signal. All the cores are terminated via the second TMC and seven detectors to seven optical receivers to receive the data bits.

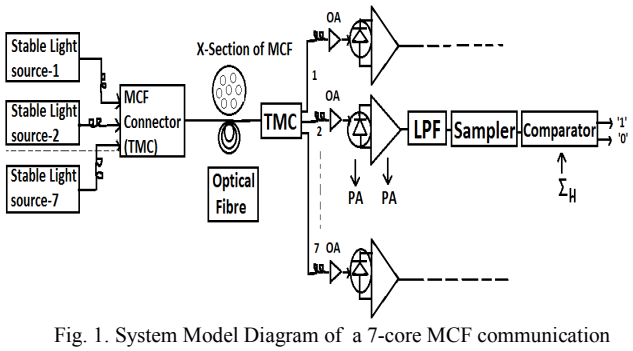


Fig. 1. System Model Diagram of a 7-core MCF communication Link

The MCF is made of seven cores arranged in a hexagonal array with a given core-to-core distance (pitch), and is assumed to be designed for operation in 1.55 µm window ( single-mode) when in isolation. The output optical signals of

978-1-5386-3374-8/17/$31.00 ©2017 IEEE

the MCF cores are pre-amplified by optical amplifiers and are given input to direct detection receivers via PIN photodiodes.

## III. THE COUPLED-MODE EQUATIONS

We consider the 7-core MCF made of a centre core (core 1) and 6 surrounding cores (core 2 to 7), as in Fig 1. The radius, $a_p$ and refractive index, $n_{1p}$ respectively identify the p$^{th}$ core. On the other hand, $n_2$ is the cladding refractive index. In order to apply the traditional coupled-mode theory for analyzing the mode coupling dynamics in the cores, the same are spatially placed to ensure relatively well isolation of the fields from each core [1], [4]. If the mode field of each core is

$$E_p = A_p \exp(-\mathrm{j}\beta_p \mathrm{z}), \quad \text{where}$$

$A_p$, amplitude of the field at the p$^{th}$ core and $\beta_p$, propagation constant of the single core in the absence of other cores [4].

To describe the propagation of the fields in every core, a set of Coupled Mode Equations (CME) are written in matrix form as [4]

$$\frac{dA(\mathrm{z})}{dz} = -CA(\mathrm{z}) \tag{1}$$

where, A(z) = [A1(z) A2(z)-------An(z)]$^T$ is a column vector, T is the transpose, z denotes direction of propagation, and C is a nxn matrix. $C_{pq}$ is the coupling coefficient between p$^{th}$ and q$^{th}$ core. As it defines, $C_{pq}$ is a measure of the spatial overlapping of the mode fields of core p and q over the cross-sectional area of core q [4]. In order to explain the mode field of core p with the help of the local coordinate system of core q, addition theorem is used. Using the eigenvalue equation for a step-index fiber $C_{pq}$ can be obtained as [4].

$$C_{pq} = \left\{ jC_{pq} \exp\left[ j\left(\beta_p - \beta_q\right) z \right], \mathrm{p} \neq \mathrm{q} \right. \tag{2}$$
$$= 0, \; p = q$$

where $\beta_p$ is the propagation constant for the $LP_{01}$ mode of core *p*. Analytically, $C_{pq}$ can be evaluated using the mathematical model as done in [4]

$$C_{pq} = \sqrt{2\Delta_q} W_q U_p K_0\left(\left(\frac{W_p d_{pq}}{a_p}\right)\right)\left[\begin{array}{l} a_p U_q J_1(U_q) I_0\left(\frac{W_p a_q}{a_p}\right) + \\ a_q W_p J_0(U_q) I_1\left(\frac{W_p a_q}{a_p}\right) \end{array}\right]\left[\begin{array}{l} V_p J_1(U_q) K_1(W_p) \\ \left(a_p^2 U_q^2 + a_q^2 W_p^2\right) \end{array}\right]^{-1} \tag{3}$$

where, $J_l$, $I_l$ and $K_l$ denote the Bessel function of the first kind and the modified Bessel functions of the first and second kinds of order *l* respectively. The pitch, $d_{pq}$ is the core-to-core distance. $U_p$ $V_p$ and $W_p$ are the normalized fiber parameters which are expressed as $U_p = a_p[(2\pi n_{1p}/\lambda)^2 - \beta_p^2]^{1/2}$, $V_p = a_p[(2\pi/\lambda)(n_{1p}^2 - n_2^2)^{1/2}$, $W_p = a_p[(\beta_p^2 - (2\pi n_2/\lambda)^2]^{1/2}$ with λ as the operating wavelength. The relative refractive index difference $\Delta_p = (n_{1p}^2 - n_2^2)/(2n_{1p}^2)$, approximated as $(n_{1p} - n_2)/n_{1p}$ [4]. For simplicity we shall take the normalized values of $C_{pq}$ for our analysis.

$E_p(z)$, the electric field of individual core is expressed as in [4]

$$E_p(z) = A_p(z) \exp(-\mathrm{j}\,\beta_p z) \tag{4}$$

Translating equation (4) to an eigenvalue problem using equation (1) we get

$$d\boldsymbol{E}(z)/dz = -\mathbf{R}\mathbf{E}(z) \tag{5}$$

where $\mathbf{E}(z) = [\mathrm{E1(z)\ E2(z)\ ----\ En(z)}]^T$ and $\mathbf{R}$ contains z-independent elements $r_{pq}$ given by

$$r_{pq} = \begin{cases} jC_{pq} & p \neq q \\ j\beta_p & p = q \end{cases} \tag{6}$$

To get the solution to equation (5) we use the substitution formula $\mathbf{E}(z) = \exp(-\mathbf{R}z)\mathbf{E}(0)$, as

$$\boldsymbol{E}(z) = \boldsymbol{V}[\exp(-\gamma_p z)\delta_{pq}]\, \boldsymbol{V}^{-1}E(0) \tag{7}$$

$$\text{and } \boldsymbol{V} = [\boldsymbol{v_1}\, \boldsymbol{v_2} - - - \boldsymbol{v_n}] \tag{8}$$

Where $\delta_{pq}$ denotes the Kronecker delta function, $\gamma_p$ represents the eigenvalue of $\mathbf{R}$, whose eigenvector is expressed as $\mathbf{v}_p$. Equation (7) provides a generalized solution for an n-core MCF describing the inter-modal power exchange between the modes of individual cores as the light signal propagates.

In this paper we shall analytically investigate the propagation dynamics of input signal power as well as Xtalk power in 7-core heterogeneous MCFs arranged in a triangular lattice as shown in Fig. 2.

## IV. ANALYSIS OF MODE COUPLING DYNAMICS FOR HETEROGENEOUS 7-CORE MCF

Let us consider the MCF with $\Delta_2 = \Delta_4 = \Delta_6$, $\Delta_3 = \Delta_5 = \Delta_7$, $\Delta_1 \neq \Delta_2 \neq \Delta_3$ as shown in Fig.2 below.

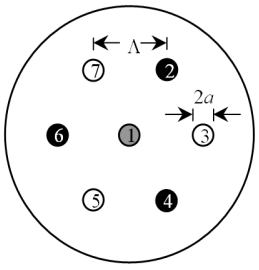


Fig. 2. Heterogeneous 7 core MCF with three types of cores, $\Delta_2 = \Delta_4 = \Delta_6$, $\Delta_3 = \Delta_5 = \Delta_7$, $\Delta_1 \neq \Delta_2 \neq \Delta_3$

For making a heterogeneous one, the 7-core MCF is made of a centre core along with 2 core groups. Each group has 3 similar cores. The matrix C is given as in [4]

$$C = j\times\begin{pmatrix} 0 & C_{12}e^{j\Delta\beta_2 z} & C_{13}e^{j\Delta\beta_3 z} & C_{12}e^{j\Delta\beta_2 z} & C_{13}e^{j\Delta\beta_3 z} & C_{12}e^{j\Delta\beta_2 z} & C_{13}e^{j\Delta\beta_3 z} \\ C_{21}e^{j\Delta\beta_2 z} & 0 & C_{23}e^{j\Delta\beta_3 z} & C_{24} & 0 & C_{24} & C_{23}e^{j\Delta\beta_3 z} \\ C_{31}e^{j\Delta\beta_2 z} & C_{32}e^{j\Delta\beta_2 z} & 0 & C_{32}e^{j\Delta\beta_2 z} & C_{35} & 0 & C_{35} \\ C_{21}e^{j\Delta\beta_2 z} & C_{24} & C_{23}e^{j\Delta\beta_3 z} & 0 & C_{23}e^{j\Delta\beta_3 z} & C_{24} & 0 \\ C_{31}e^{j\Delta\beta_2 z} & 0 & C_{35} & C_{32}e^{j\Delta\beta_2 z} & 0 & C_{32}e^{j\Delta\beta_2 z} & C_{35} \\ C_{21}e^{j\Delta\beta_2 z} & C_{24} & 0 & C_{24} & C_{23}e^{j\Delta\beta_3 z} & 0 & C_{23}e^{j\Delta\beta_3 z} \\ C_{31}e^{j\Delta\beta_2 z} & C_{32}e^{j\Delta\beta_2 z} & C_{35} & 0 & C_{35} & C_{32}e^{j\Delta\beta_2 z} & 0 \end{pmatrix} \tag{9}$$

where $\Delta\beta_{pq} = \beta_p - \beta_q$. The specific eigen values are obtained as

$$\gamma_1 = \gamma_6 = \left[ \bar{\alpha}_2 + \bar{\alpha}_3 + \sqrt{(\bar{\alpha}_2 - \bar{\alpha}_3)^2 + C_{23}C_{32}} + \beta_1 \right],$$

$$\gamma_2 = \gamma_7 = \left[ \bar{\alpha}_2 + \bar{\alpha}_3 - \sqrt{(\bar{\alpha}_2 - \bar{\alpha}_3)^2 + C_{23}C_{32}} + \beta_1 \right],$$

$$\gamma_3 = j(g + h + \frac{\overline{\alpha}_2 + \overline{\alpha}_3}{3} + \beta_1),$$

$$\gamma_4 = \frac{\sqrt{3}}{2}(g-h)) + j\left[-\frac{1}{2}(g+h) + \frac{\overline{\alpha}_2 + \overline{\alpha}_3}{3} + \beta_1\right],$$

$$\gamma_5 = -\frac{\sqrt{3}}{2}(g-h)) + j\left[-\frac{1}{2}(g+h) + \frac{\overline{\alpha}_2 + \overline{\alpha}_3}{3} + \beta_1\right],$$

Where,

$$\alpha_2 = \beta_2 - \beta_1 + 2C_{12} \qquad \alpha_3 = \beta_3 - \beta_1 + 2C_{35}$$

$$\overline{\alpha}_2 = \frac{\beta_2 - \beta_1 - C_{24}}{2}, \overline{\alpha}_3 = \frac{\beta_3 - \beta_1 - C_{35}}{2}$$

$$u = a_2 a_3 - 3(C_{12}C_{21} + C_{13}C_{31}) - 4C_{23}C_{32} - \frac{1}{3}(a_2 + a_3)^2$$

$$v = -\frac{2}{27}(a_2 + a_3)^3 + \frac{1}{3}(a_2 + a_3)[a_2 a_3 - 3(C_{12}C_{21} + C_{13}C_{31}) - 4C_{23}C_{32}]$$
$$+3(C_{13}C_{31}a_2 + C_{12}C_{21}a_3) - 6(C_{32}C_{13}C_{21} + C_{12}C_{23}C_{31}),$$

$$g = \left\{-\frac{v}{2} + \left[\left(\frac{u}{3}\right)^2 + \left(\frac{v}{2}\right)^2\right]^{\frac{1}{2}} + \right\}^{\frac{1}{3}}, h = \left\{-\frac{v}{2} + \left[\left(\frac{u}{3}\right)^2 + \left(\frac{v}{2}\right)^2\right]^{\frac{1}{2}} + \right\}^{\frac{1}{3}}$$

When core-2 is excited, the expressions for mode powers are calculated as in [4] :

$$|A_2(z)|^2 = \frac{1}{9} + \frac{8}{9}\cos^2\left[\frac{-j(\gamma_2 - \gamma_5)z}{2}\right], \quad (10)$$

$$A_4(z)|^2 = |A_6(z)|^2 = \frac{4}{9}\sin^2\left[\frac{-j(\gamma_2 - \gamma_5)z}{2}\right] for \Delta_2 \prec \Delta_1, \Delta_3$$

The propagation nature of the mode powers in the MCF ( $for \Delta_2 \prec \Delta_1, \Delta_3$ ) with core parameters as

$\Delta_1 = 0.37\%$, $\Delta_2 = \Delta_4 = \Delta_6 = 0.325\%$, and $\Delta_3 = \Delta_5 = \Delta_7 = 0.36\%$

and a = 4.5 μm, Λ= 30 μm are shown in Fig. 3.

The coupling length is obtained as in [4]:

$$L_{c2} = \frac{\pi}{|-j(\gamma_2 - \gamma_5)|} for \Delta_2 \prec \Delta_1, \Delta_3 \quad (11)$$

## V. Determination Of Crosstalk Power At The Output Of The MCF

When the center core is excited i.e. $A_1(0)=1$ and $A_p(0) = 0$ for $p \neq 1$ in the MCF, the expression for mode amplitude at distance z are obtained analytically as

$$A_1(z) = [\cos(\sqrt{7}C_{12}z) + \frac{j}{\sqrt{7}}\sin(\sqrt{7}C_{12}z)]\exp(-jC_{12}z) \quad (12)$$

$$A_p(z) = \frac{-j}{\sqrt{7}}\sin(\sqrt{7}C_{12}z)]\exp(-jC_{12}z) \qquad p \neq 1 \quad (13)$$

The signal obtained through equations (12) and (13) would be at the output of the MCF.

As a result of inter-core crosstalk, signal of $p^{th}$ core will also enter the other cores of the MCF. As such, the expression for the signal in $q^{th}$ core is given by

$$E_q(t,z) = e^{j\omega_c t}\, e - j\beta_p z,\ p \neq q \quad (14)$$

The signal passing through all $q^{th}$ cores will constitute the total crosstalk signal, and is obtained as

$$E_{CT} = \sum_{q=1}^{M} E_q(t,z); q \neq p \quad (15)$$

At a distance z, the signal in core 1 is given in [5- 6]

$$E_1(z) = E_1(0)Cos(\beta_1 z) + E_2(0)Cos(C_{21}z) + --+ E_7(0)Cos(C_{71}z) -$$
$$j\{E_1(0)Sin(\beta_1 z) + E_2(0)Sin(C_{21}z) + \ldots\ldots\ldots + E_7(0)Sin(C_{71}z)\} \quad (16)$$

So, upon launching the light into core 1, signal power ($P_{sig}$) and Xtalk power ($P_{CT}$) can be obtained as in [5-6]

$$P_{sig} = |E_1(0)|^2 \quad (17)$$

$$P_{CT} = \left|\begin{matrix} E_2(0)Cos(C_{21}z) + E_3(0)Cos(C_{31}z) + --- + \\ +E_2(0)Sin(C_{21}z) + \ldots.. + E_7(0)Sin(C_{71}z) \end{matrix}\right|^2 \quad (18)$$

using the two equations (17) and (18) the signal to Xtalk ratio for core 1 can be evaluated as

$$(SCR)_{optical} = \frac{P_{sig}}{P_{CT}} \quad (19)$$

At a distance z from the transmitter, the optical signal along with Xtalk received at the input of receiver's photo detector is obtained as

$$e_r(t,z) = \sqrt{2GP_{sig}(z)\,e^{j\omega_c t}} + \sqrt{2P_{CT}(z)\,e^{j(\omega_c t - \beta z)}} \quad (20)$$

where G denotes optical pre-amplifier gain. The photo current at the output of the photo detector is evaluated as

$$i_d = R_d E|R_e\{e_r(t,z)\}|^2 \quad (21)$$

The current at the output of pre amplifier is given by

$$I_0(t) = I_{sig}(z).G + I_{CT}(t) + I_{shot}(t) + I_{sig-CT}(t)$$
$$+ I_{ASE}(t) + I_{sig-ASE}(t) + I_{ASE-CT}(t) + I_{th}(t) \quad (22)$$

where $I_{th}(t)$ is the thermal noise caused due to preamplifier.

The variance of the noise components can be expressed as:

$$\sigma_{shot}^2 = 2.e.B\left(R_d.G.P_{sig} + R_d.P_{CT} + R_d.P_{ASE}\right)$$

$$\sigma_{CT}^2 = \left(R_d.P_{CT}\right)^2)$$

$$P_{ASE} = \sigma_{ASE}^2 = n_{sp}(G-1)\,h\,\gamma.B_0$$

$$\sigma_{Sig-CT}^2 = 4R_d^2.P_{sig}.P_{CT}.Cos^2\beta z$$

$$\sigma_{Sig-ASE}^2 = 2.R_d^2.P_{sig}.\left[n_{sp}(G-1)\,h\,\gamma.B_0\right]$$

$$\sigma_{CT-ASE}^2 = 2.R_d^2.P_{CT}.\left[n_{sp}(G-1)\,h\,\gamma.B_0\right]$$

$$\sigma_{th}^2 = \frac{4KT}{R_L}B$$

wherein the symbols $\sigma_{shot}$, $\sigma_{CT}$, $\sigma_{sig\text{-}CT}$, $\sigma_{th}$ denote the shot noise, Xtalk noise, spontaneous noise with Xtalk and thermal noises respectively. $R_d$, $n_{sp}$, γ symbolize the receiver responsivity, spontaneous emission factor and frequency of light wave respectively. $B_o$ denotes optical amplifier bandwidth and B is receiver's electrical bandwidth. Therefore,

the electrical signal to crosstalk plus noise ratio (SCNR) at the output of low pass filter is obtained as

$$SCNR = \frac{I_{sig}^{\ 2}.G2}{\sigma_{shot}^{\ 2} + \sigma_{CT}^{\ 2} + \sigma_{ASE}^{\ 2} + \sigma_{Sig-CT}^{\ 2} + \sigma_{Sig-ASE}^{\ 2} + \sigma_{CT-ASE}^{\ 2} + \sigma_{th}^{\ 2}} \quad (23)$$

where $I_{CT} = R_d P_{CT}$ and $Ir = R_d P_r$. For the given direct detection system the Bit Error Rate (BER) is evaluated as

$$BER = 0.5 erfc \frac{\sqrt{SCNR}}{2\sqrt{2}} \quad (24)$$

where erfc is the complementary error function.
Numerical computations are shown in Table 1.

**Table - 1: MCF Parameters**

| Parameter | Value |
|---|---|
| Core Index, $n_1$ | Varies with Δ |
| Cladding Index, $n_2$ | 1.444 |
| Core radius, a | 4.5e-6 m |
| Core-to-core distance, $d_{pq}$ | 30e-6 |
| Operating wave length, lamda | 1550 nm |
| Relative Index difference, Δ% | 0.37%, 0.325% and 0.36% |
| Data rate, $R_b$ | 2.5 Gbps |

## VI. Results And Discussions

The variation of mode power in a heterogeneous 7-core MCF as determined by using the equation (10) is shown in Fig. 3 with MCF parameters as, $\Delta_1 = 0.37\%, \Delta_2 = \Delta_4 = \Delta_6 = 0.325\%$, and $\Delta_3 = \Delta_5 = \Delta_7 = 0.36\%$ and a = 4.5 µm, Λ= 30 µm when core 2 is energized. The figure shows that the strong effect of core-2 on the coupling dynamics of cores 4 and 6.

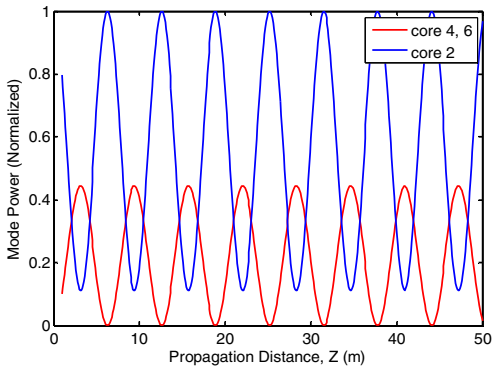


Fig. 3. Variation of mode power in a 7- core heterogeneous MCF with index contrast, $\Delta_1 = 0.37\%$; $\Delta_2 = \Delta_4 = \Delta_6 = 0.325\%$; $\Delta_3 = \Delta_5 = \Delta_7 = 0.36$ when core 2 is energized.

Fig. 4 shows the plot of coupling coefficient as a function of relative index difference of the cores. It is noticed that the coupling coefficient decreases with the increase of the relative index contrast in the core groups of the MCF.

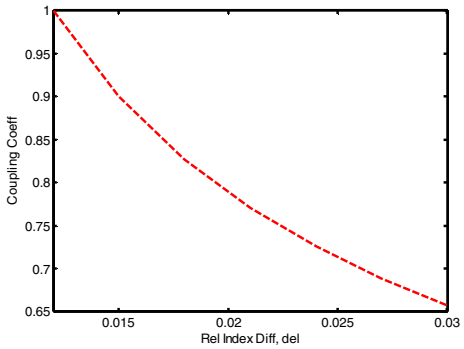


Fig. 4. Plot of coupling coefficient as a function of relative index diff in a 7 core heterogeneous MCF while light is launched into core 2.

Fig. 5 shows the variation of Xtalk power as expressed in equation (18) for heterogeneous 7-core MCF considering inter-core coupling with the geometry and parameter arrangement as , $\Delta_1 = 0.37\%, \Delta_2 = \Delta_4 = \Delta_6 = 0.325\%$, and $\Delta_3 = \Delta_5 = \Delta_7 = 0.360\%$ , identical radii, a = 4.5 µm, pitch Λ=30 µm when light is launched into core 2. It is found that the crosstalk occurs in a periodic manner, and there are maximum and minimum values of the crosstalk with increase of propagation distance. This pattern of variation may be due to the three distinct groups of cores with three separate index contrasts.

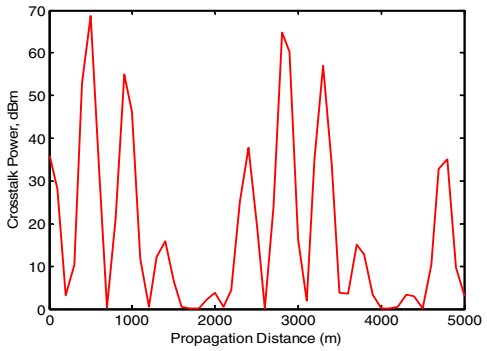


Fig. 5. Variation of crosstalk power as a function of propagation distance in a heterogeneous 7-core MCF when light is launched into core 2.

In Fig. 6 the BER performance are depicted as a function of input signal power at different propagation distance of the 7-core heterogeneous MCF. It is noticed that inter-core coupling induced crosstalk degrades the BER performance and system suffers power penalty due to crosstalk at a given BER. For example, input power, Pin with crosstalk at a distance of 10 km to achieve BER 10-9 is 26 dBm when the required Pin is found to be 32 dBm when the link distance is 100 km.

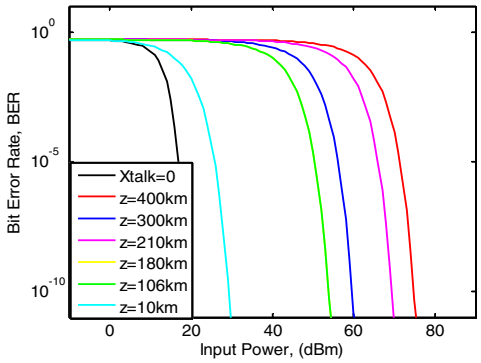


Fig. 6. BER performance as a function of input power (at diff propagation distance) and identical core radii for 7-core heterogeneous MCF considering Xtalk power

The variation of crosstalk induced power penalty with respect to propagation distance is shown in Fig.7. which depicts the relation of power penalty (PP) versus propagation distance. It is noticed that power penalty increases with the increase of propagation distance for maintaining the same BER value (say, 10e-9) for a given core-to-core distance (pitch).

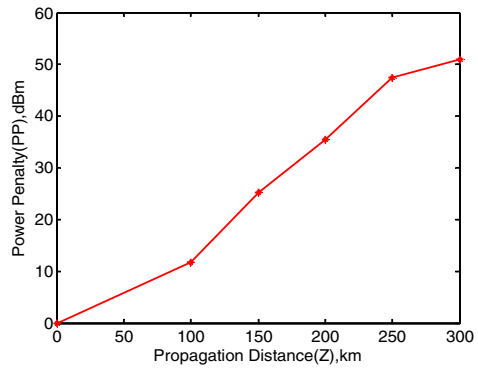


Fig. 7. Plot of power penalty as a function of propagation distance in a 7-core heterogeneous MCF

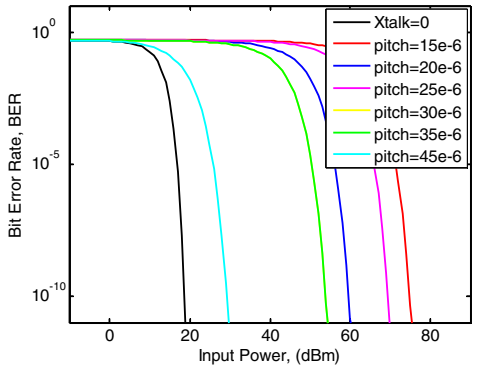


Fig. 8. BER performance as a function of input power with varying core-to-core pitch at fixed propagation distance, z=135 km for 7-core heterogeneous MCF considering crosstalk power

In Fig. 8 the BER curves shown as a function of input power at a given propagation distance (135 km) with respect to various core-to-core distance (pitch) of the 7-core heterogeneous MCF. It is noticed that input power needs to be increased to achieve the desired BER (say, 10e-9) for MCF with lower values of core-to-core distance, meaning the higher values of coupling coefficient, that is, for stronger coupling.

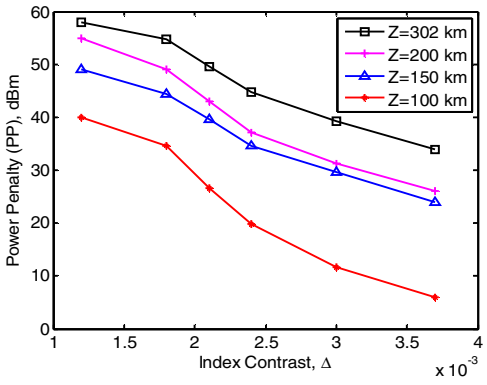


Fig. 9. Power Penalty as a function of relative index contrast () at varying propagation distance (z km) for 7-core heterogeneous MCF considering crosstalk power

The variation of crosstalk induced power penalty with respect to core-to-core distance is shown in Fig.9. which depicts the relation of power penalty (PP) versus core pitch. It is noticed that power penalty increases with the decrease of core-to-core distance for maintaining the same BER value (say, 10e-9) for a given propagation distance. It is also seen that power penalty due to crosstalk increases with the increase of propagation distance.

## VII. Conclusion

An analytical approach is developed to evaluate the amount of crosstalk due to inter-core coupling in a 7-core heterogeneous MCF based optical communication link. Dependence of the crosstalk power on the geometry and other parameters of the fiber in the MCF is investigated. Signal to crosstalk plus Noise Ratio (SCNR) at the output of the energized core of the MCF link is analytically determined. The performance analysis in terms of Bit Error Rate (BER) of the MCF link is carried out for a given input power and data rate for various propagation distance and fiber parameter. It is found that crosstalk is significant and deteriorates the BER performance and can be minimized by increasing the inter-core separation of the MCF. The outcome of this research work may find its application in designing and implementing optical communication systems using MCFs to enhance transmission channel capacity.

## Acknowledgements

The work is carried out as a part of Ph.D dissertation in the Dept of EEE, BUET. The authors would like to acknowledge with gratitude the support provided by the Dept of EEE, BUET.

## References

[1] Wenhua Ren, Zhongwei Tan, "A study on the coupling coefficients for multi-core fibers"; Optik - International Journal for Light and Electron Optics 127(6), DOI: 10.1016/j.ijleo.2015.12.021

[2] T. Hayashi, T. Sasaki, and E. Sasaoka, B "Multi-core fibers for high capacity transmission", [ presented at the Optical Fiber Communication Conference, OSA Technical Digest (CD) (Optical Society of America, 2012), paper OTu1D.4.

[3] K. Takenaga, S. Matsuo, K. Saitoh, and M. Koshiba, B "Characteristics of MC fibers: new techniques and challenges", presented at the Optical Fiber Communication Conference, OSA Technical Digest (CD) (Optical Society of America, 2012), paper OTu1D.5.

[4] F.Y.M. Chan, A.P T Lau, and H.Y Tam. "Mode coupling dynamics and communication strategies for multi-core fiber systems", Optics Express, vol. 20, no. 4, Feb 13, 2012.

[5] Md Jahangir Hossain1, S.P. Majumder. "Performance Limitations Due to Crosstalk in an Optical Transmission Link over Multi-Core Fiber" ; International Conference on Telecommunications and Photonics (ICTP), 2015, IEEE, Electronic ISBN**:** 978-1-4673-8688-3

[6] Md Al Amin Sajeeb, Farhat Tasnim Farin, Abdur Rahim, S P Majumder, "BER performance limitation of an optical link with multicore fiber (MCF) due to crosstalk caused by mutual coupling among the cores" ; 3rd International Conference on Electrical Engineering and Information Communication Technology (ICEEICT), 2016 , IEEE, Electronic ISBN: 978-1-5090-2906-8

[7] Y. Kokubun and M. Koshiba, "Novel multi-core fibers for mode division multiplexing: proposal and design principle," IEICE Electronics Express, vol 6, no. 8, pp. 522–528, Apr. 25, 2009.

[8] S. Zheng, G. Ren, Z. Lin, et al, "Mode coupling Analysis and Trench Design for Large mode area low cross talk Multi-core fiber", Appl. Opt, 52(2013).4541-4548

# Modeling of Photocurrent and Dark Count Probability of InGaAs/ InP Single Photon Avalanche Photodiode

Ahammed Mofasser,[1,*] Samprity Saha,[1] Khan Shaikhul Hadi,[1] Farseem M. Mohammedy,[1] and Yasser El-Batawy[2]

[1]Department of Electrical and Electronic Engineering, Bangladesh University of Engineering and Technology (BUET), Bangladesh

[2]Engineering Mathematics and Physics Dept., Faculty of Engineering, Cairo University, Egypt

[*]ahammedmofasser@gmail.com

*Abstract*—**Single photon avalanche detector is widely used for the optical detection of weak signals utilizing photocurrent multiplication mechanism beyond the breakdown voltage. In the present work, photocurrent characteristics of InGaAs/InP based SPAD device are analysed. The device in the model employs self-differencing method and operates in gated mode with 1GHz gating frequency in near infrared region. Dark count probabilities have been generated for varying single photon detection efficiency (SPDE). The results of current-voltage characteristics (for operating temperatures -50, -30, 0 and 20 degree Celsius) and dark count probability as a function of SPDE have been examined by comparing them with published experimental results. Error analysis shows that the deviation of the present model from the experimental results is low in room temperature and agrees with the experimental values within 3% range.**

***Index Terms*—Avalanche Photodiodes, Single Photon Avalanche Photodiode, Avalanche Probability, Dark count probability, Single photon detection efficiency**

## I. INTRODUCTION

Single Photon Avalanche Detector (SPAD) with low dark count rate has gained increasing interest in optical communication systems and optical quantum information applications in recent years. There is a widespread interest of the development of III-V based SPAD in near infrared range to exploit the advantage of low loss and low dispersion window at 1.3 and 1.55μm. SPAD has overcome operational limitations of other photon counting technologies like superconducting SPDs in practical applications [1]. Due to its special internal photoelectric effect mechanism beyond breakdown, they have higher detection efficiency than other photodetectors [2]. As the prerequisite for SPADs is to ensure high output signals in response to a single incident photon, to be processed by electronic circuits, therefore high multiplication gain is a prime necessity. Operation of SPAD beyond the breakdown voltage ensures higher multiplication gain characteristics than in conventional APDs.

These detectors find applications in fields where images are to be obtained in the shortest possible duration of time and in quantum information technologies where individual photons are encoded with information. SPADs have gained wide use for single photon counting and time correlated single photon counting. SPADs have versatile applications like quantum key distribution (QKD), light detection and ranging (LIDAR) [3], fluid velocimetry, optical time-domain reflectometry, single molecule detection, astronomy, distributed sensing [4].

Single photon detectors are basically p-n junction operating beyond the breakdown voltage resulting in high electric field in the depletion region for reliable detection of single photon excited carrier that triggers a self-sustaining avalanche in the multiplication region and the device provides output sensing the leading edge of avalanche current. As the triggered avalanche is self-sustaining, it needs to be quenched soon by resetting the SPAD to a lower voltage below the breakdown level for a while and then restored again to the operative level for detection of subsequent photons. Gated pulse biasing is one of the methods of quenching the avalanche and restoring the operation. A schematic cross-section of InGaAs/InP based SPAD has been presented in Fig. 1.

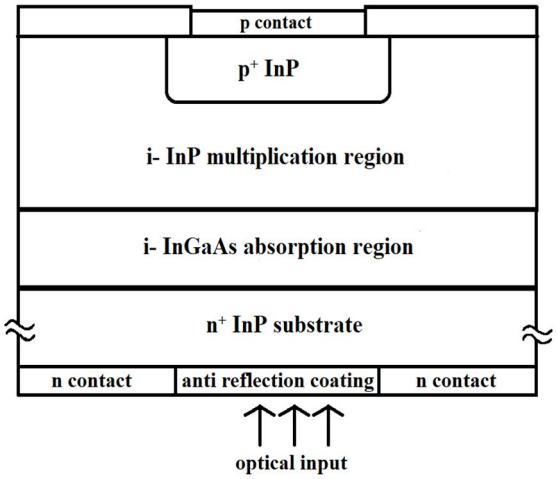


Fig. 1 Simplified schematic cross-section of InGaAs/InP based Single Photon Avalanche Diode (SPAD) structure.

In the present model, dark count probability as a function of single photon detection efficiency (SPDE) and current-voltage characteristics have been studied.

In the absence of illumination, the device may provide false counts or dark counts where carriers are generated by mechanisms other than photo excitation. Thermal excitation, tunneling excitation, trap assisted tunneling excitation are some of those mechanisms. These triggers result in false avalanche in the multiplication region which consequently leads to dark counts [1]. Dark counts may also be enhanced by after-pulsing effect. This phenomenon results from the release

978-1-5386-3374-8/17/$31.00 ©2017 IEEE

of carriers during a pulse which were trapped in previous pulses due to the defects and the impurity levels in the multiplication region of the material.

The trapped carriers require considerable time to get de-trapped which is denoted by de-trapping time ($\tau_d$). The time period for which the SPAD remains insensitive to incoming photon inputs and remains quenched, is called the hold off time. If the de-trapping process of trapped carriers takes longer time than the hold off time, release of previously trapped carriers during active operation time may trigger false avalanche later even in the absence of photons. So, the longer the hold off time is, the lower the afterpulse effect. However, this condition limits the maximum count rate. Increasing the operational temperature may shorten the de-trapping time but results in an increase of the dark count rate. As a result, it requires trade off with other performance parameters to acquire the desired afterpulsing performance.

In [5], Kang *et al.* established a physical model for dark count probability as a function of detection efficiency for single photon avalanche diode. Exploration of the experimental data presented by Comandar *et al.* [3] and later finding the congruence between the results and our theoretical model has been the target of our analysis. To check the validity of our presented model, it is compared with the experimental results in [3] and a good agreement has been obtained.

## II. Current-Voltage Model

The variation of multiplication with the biasing voltage is expressed as [6]-[7],

$$M = \frac{1}{1-\left(\frac{V}{Vbr}\right)^n} \tag{1}$$

where $M$ is the multiplication gain of the avalanche photodiode, $V$ is the biasing voltage, $V_{br}$ is the breakdown voltage and $n$ is an empirical parameter the data. $n$ is a function of temperature, device structure and wavelength of incident radiation. The breakdown voltage is a strong linear function of temperature that is expressed as [3],

$$V_{br}(T) = V_{br}(T_0) + \gamma(T - T_0) \tag{2}$$

where $\gamma$ is the temperature coefficient of $V_{br}$ that strongly depends on the semiconductor material properties.

The voltage at which the depletion region extends through the charge layer to the edge of absorption layer is referred as punch-through voltage. Before punch through occurs, most of the photo generated carriers of the absorption layer lack in sufficient energy to travel across heterojunction interfaces and therefore the photocurrent level is very low before punch-through voltage. This can be referred as unity gain reference point. Punch-through occurs before the electric field in the multiplication region is enough to produce gain and so the photocurrent after punch-through remains relatively constant [8]. Before punch through transition voltage, there is a very small dark current present in the device that is dominated by the primary dark current.

The total current $I_{out}$ in a photodiode comes from two different contributions namely photocurrent and dark current. Dark current has two components, unmultiplied dark currents and multiplied dark currents. The dark current, $I_d$ thus can be written as

$$I_d = MI_{dm} + I_{dum} \tag{3}$$

where $I_{dm}$ is multiplied dark current and $I_{dum}$ is unmultiplied dark current. Unmultiplied dark currents originate from surface contribution and from regions where multiplication is insignificant. Multiplied dark current originate before multiplication region and go through avalanche multiplication process.

Total current,$I_{out}$ in a photodiode is expressed as

$$I_{out} = MI_{pho} + I_d \tag{4}$$

Where $I_{pho}$ is the photogenerated current. This multiplied photocurrent is added with the dark current to get final contribution. $I_{pho}$ can be expressed as [3]

$$I_{pho} = \eta P_{opt} \frac{e\lambda}{hc} \tag{5}$$

where $\eta$ is the quantum efficiency, $P_{opt}$ is the incident optical power, $e$ is the elementary charge, $\lambda$ is the wavelength of the incident photons, $h$ is Planck's constant and $c$ is the speed of light.

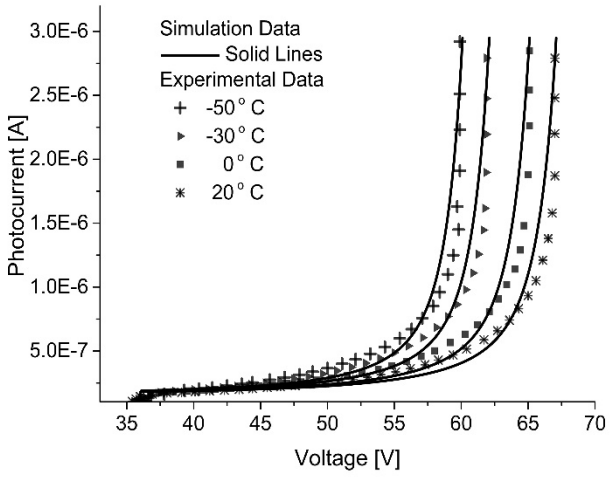


Fig. 2 Variation of photocurrent with applied voltages in different temperatures. Gate pulse width used in this calculation is 400ns.Punchthrough occurs around 36V.The lines (solid lines) indicate our simulation result while the bullet points represent plots obtained by Comandar *et al.* [3].

From Fig. 2 we can observe that before punch through, multiplication is negligible. As the biasing voltage increases, the multiplication gain also increases. Near breakdown voltage multiplication rises quickly. In real devices, at highly multiplied current levels, the maximum achievable multiplication is limited by several factors;(1) the voltage drop across the load resistor, across the contacts series resistance, and across the undepleted bulk material; (2) the space charge effects in which carriers drift through depletion region reducing electric field; (3) microscopic device defects which

limit the desired electric field in regions; (4) reduction of the electron and hole ionization coefficients and hence reduction of the electric field. This is caused by thermal resistance which results in heating of the junctions [8]. A fast photodetector should sense the onset of avalanche and provide an output proportional to it. After detection is made, the photodetector must be reset or quenched to detect photon again.

## III. Dark- Count Model

Single Photon Detection efficiency (SPDE), $\eta_{SPDE}$ can be expressed as [1]

$$\eta_{SPDE} = \eta_{EQE}\, P_{ava}\, P_{det} \tag{6}$$

where $P_{ava}$ is the avalanche probability which quantifies the probability that an avalanche event is to occur following an impact ionization event, $P_{det}$ is the detection efficiency of the photodetector and $\eta_{EQE}$ is the external quantum efficiency of the photodetector. External quantum efficiency, $\eta_{EQE}$ is expressed as,

$$\eta_{EQE} = P_{abs}\ P_{transit} \tag{7}$$

where $P_{abs}$ is the absorption efficiency of the photodetector, which is the ratio between number of photo-generated electron-hole pairs and incident photons and $P_{transit}$ is the transit probability which depends on the material of the absorption region of the SAGCM structure and the device architecture. The avalanche probability can be derived from the relationship between quantum efficiency (QE), $\eta$ and single photon detection efficiency (SPDE), $\eta_{SPDE}$.

In our analysis, we used avalanche probability, $P_{ava}$ as a parameter in finding different values of single photon detection efficiency and dark count probability. To understand the dark count phenomena, the mechanisms that create dark count have to be understood. One statistical model was proposed by Kang et al. [5]. Primary dark carriers can be generated inside multiplication region due to thermal processes even when the gate pulse is off. When the gate pulse is activated above break down voltage, trapped carriers in intermediate traps or defect states during previous pulses may get released to create dark counts [9].

Before the arrival of the pulses, thermally generated or de-trapped dark carriers can go through a series of impact ionizations with DC gain. Some of these released carriers from traps may also stay in the multiplication region when the pulse arrives. The probability of dark count $P_d$ can be expressed as

$$P_d = 1 - \exp(-N_d\, P_{ava}) \tag{8}$$

where $N_d$ is average number of dark carriers in multiplication region. When the photodiode circuit is on, there always remains the probability that a current pulse will be initiated in the photodiode by generated carriers. The probability that the current is triggered by photo generated carriers or dark carriers while the device is in active mode, namely combined probability $P_{on}$ can be written as

$$P_{on} = 1 - \exp(-N_{on}\, P_{ava}) \tag{9}$$

where $N_{on}$ is the number of total carriers that includes photon-generated carriers along with previously stated dark carrier. Using values of $P_{on}$ and $P_d$, we can calculate $\eta_{SPDE}$ as,

$$\eta_{SPDE} = \frac{P_{on} - P_d}{P_{ph}} \tag{10}$$

where $P_{ph} = 1 - \exp(-N_0)$ is the probability of whether an incident optical pulse contains any photon or not and $N_0$ is number of incident photon per pulse. The dark count probability $P_d$ and Combined carrier (i.e. dark and photo generated) generation probability $P_{on}$ are calculated respectively as following,

$$P_d = 1 - exp\left\{-P_{ava}\left[\frac{I_{DM}\,\tau}{q} + \frac{I_{DM}{M_0}^2}{2\pi q\beta} + P_d N_{tr}\,\frac{exp\left(\tau/\tau_d\right)-1}{exp\left(\Delta T/\tau_d\right)-1} + P_d N_{tr}\,\frac{exp\left({\tau_{tr}}^*/\tau_d\right)-1}{exp\left(\Delta T/\tau_d\right)-1}\right]\right\} \tag{11}$$

$$P_{on} = 1 - exp\left\{-P_{ava}\left[\frac{I_{DM}\,\tau}{q} + \frac{I_{DM}{M_0}^2}{2\pi q\beta} + P_{on} N_{tr}\,\frac{exp\left(\tau/\tau_d\right)-1}{exp\left(\Delta T/\tau_d\right)-1} + P_{on} N_{tr}\,\frac{exp\left({\tau_{tr}}^*/\tau_d\right)-1}{exp\left(\Delta T/\tau_d\right)-1} + \eta N_0\right]\right\} \tag{12}$$

where $\tau$ is the gate pulse width, $\tau_d$ is the de-trapping time of the carrier, ${\tau_{tr}}^*$ is effective transit time of dark carriers in the multiplication region, $\Delta T$ is the gating bias period, $N_{tr}$ is average number of carrier trapped after a pulse, $\beta$ is gain bandwidth product, $M_o$ refers DC gain, $\eta$ is quantum efficiency and $I_{DM}$ is the primary multiplied dark current [5].

Relations among the variables $P_{on}$, $P_d$, $\eta_{SPDE}$ and $\eta$ are implicit functions and does not have any conventional algorithm to solve them. Hence, we pursued an iterative method to solve them.

## IV. Results and Discussions

To check the validity of the presented model, its results have been compared with the experimental results reported in [3]. While carrying out the analysis, iteration procedure was employed to get more accurate values of $P_{on}$ and $P_d$. For temperatures of -30℃, 0℃, 20℃, $I_{DM}$ was considered as 0.1fA, 1fA and 10fA, respectively. In the presented calculations, a gating frequency of 1 GHz and effective gate pulse with of 400 ps were used. DC gain was selected between 5 and 20. In Fig. 3, the dark current probability $P_d$ of SPAD has been plotted for different single photon detection efficiency for different operating temperatures. In this figure,

the results of the presented model have been compared with experimental results reported in [3].

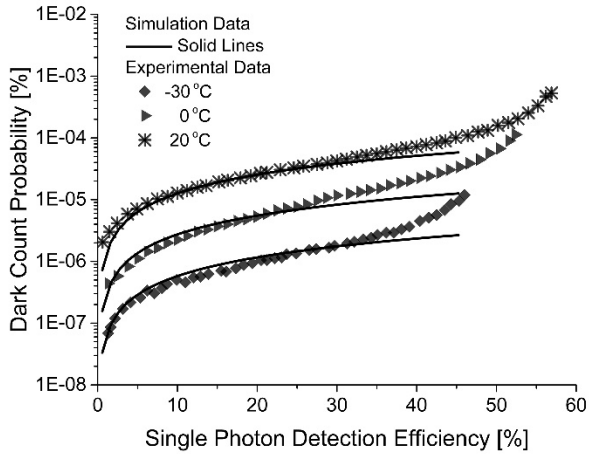


Fig. 3 Dark count probability ($P_d$) as a function of SPDE calculated by the iteration method (solid lines) and experimental values measured by Comandar *et al.* [3] (bullet points) for different temperatures.

As shown in Fig. 3, the results of present calculations are in good agreement with the experimental results especially within the range of 10% to 30% single photon detection efficiency region, which is the region of operation for most commercial SPADs [10]. Among the curves, 20℃ curve has the best match in this region. As the temperature rises, breakdown voltage increases due to increase of non-ionizing collisions.

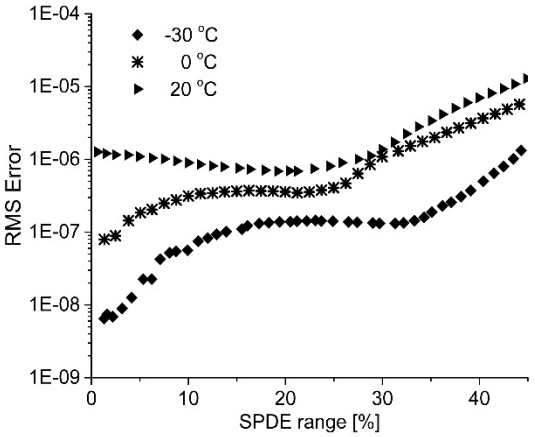


Fig. 4 RMS error (mismatch) between simulated and experimental results plotted against SPDE range for different temperatures.

To check the accuracy of the calculated results in comparison with the experimental results reported in [3], Root Mean Square (RMS) errors of the calculated $P_d$ in comparison to those of the measured values for different SPDE range have been calculated and are plotted in of Fig. 4.

The RMS error is found to be within the order of $10^{-6}$ in 10% to 30% SPDE range. Since the assumption of the multiplication gain being constant with the variation of the biasing voltage does not remain valid for higher SPDE values, our simulated results deviate significantly from the experimental results above 35% SPDE range. The dependency of $M_o$ on the biasing voltage should be studied more thoroughly and taken into consideration to have more accurate results. As the avalanche gain is actually a function of ionization coefficient, hence it is also a function of electric field in the multiplication region. So, the effects of doping, thickness of the photodetectors' dead space width region and the related parameters are needed to be analyzed to predict the values of dark count probability $P_d$ for higher SPDE regions in Fig. 3.

Most commercial self-differencing InGaAs SPADs reported to have efficiencies around 10% at operating temperature 240K [11]. To find the congruence of the experimental and the simulated data obtained by our simulation model, the standard deviation for the extrapolated values of $P_d$ has been calculated in the range of 10% to 30% single photon detection efficiency (SPDE). We found that the calculated values of dark count probabilities vary around 18%, 12%, 15% and 3% from the experimentally measured values in the limited range of SPDE for operating temperature -50°, -30°, 0° and 20°C, respectively. For room temperature condition the physical model is in good agreement with the experimental results resulting in a low percentage of deviation.

The shorter the gate pulse, the more improvement in after-pulse behavior is expected because of larger hold off time. As our analysis has been mainly focused on dark count probability, $P_d$ and SPDE relationship excluding the dark counts generated by afterpulsing, therefore afterpulsing effect must be considered negligible here. If the gate pulse period is denoted with $\Delta T$ , we justify this by making the de-trapping time $\tau_d << \Delta T$ so that afterpulse effect is minimized.

## V. Conclusions

In this paper, we have presented a semi numerical iterative model of the photocurrent and the dark count probability for single photon avalanche detector (SPAD). At punch through voltage, the electric field starts to penetrate the absorption layer. Multiplication before this voltage is negligible and hence current is dominated by dark current mainly. After punch through, the output current is dominated by photocurrent. This model has been validated by comparing the simulated values with experimental results and a good agreement has been found. In room temperature range around 20˜ C and within 10% to 30% SPDE range, our model shows good match with the experimental data and has only 3% mismatch. RMS errors between the experimental data and simulated data are in the order of $10^{-6}$ in this SPDE region.

## References

[1] J. Zhang, M. Itzler, H. Zbinden and J. Pan, "Advances in InGaAs/InP single-photon detector systems for quantum communication", *Light: Science & Applications*, vol. 4, no. 5, p. e286, 2015.

[2] M. Ghioni, A. Gulinatti, I. Rech, F. Zappa and S. Cova, "Progress in Silicon Single-Photon Avalanche Diodes", *IEEE Journal of Selected Topics in Quantum Electronics*, vol. 13, no. 4, pp. 852-862, 2007.

[3] L. Comandar, B. Fröhlich, J. Dynes, A. Sharpe, M. Lucamarini, Z. Yuan, R. Penty and A. Shields, "Gigahertz-gated InGaAs/InP single-photon detector with detection efficiency exceeding 55% at 1550 nm", *Journal of Applied Physics*, vol. 117, no. 8, p. 083109, 2015.

[4] A. Spinelli and A. Lacaita, "Physics and numerical simulation of single photon avalanche diodes", *IEEE Transactions on Electron Devices*, vol. 44, no. 11, pp. 1931-1943, 1997.

[5] Y. Kang, H. Lu, Y. Lo, D. Bethune and W. Risk, "Dark count probability and quantum efficiency of avalanche photodiodes for single-

photon detection", *Applied Physics Letters*, vol. 83, no. 14, pp. 2955-2957, 2003.
[6] S. Miller, "Avalanche Breakdown in Germanium", *Physical Review*, vol. 99, no. 4, pp. 1234-1241, 1955.
[7] S. Miller, "Ionization Rates for Holes and Electrons in Silicon", *Physical Review*, vol. 105, no. 4, pp. 1246-1249, 1957.
[8] H. Liu, H. Pan, C. Hu, D. McIntosh, Z. Lu, J. Campbell, Y. Kang and M. Morse, "Avalanche photodiode punch-through gain determination through excess noise analysis", *Journal of Applied Physics*, vol. 106, no. 6, p. 064507, 2009.
[9] W. Shockley, "Problems related to p-n junctions in silicon", *Solid-State Electronics*, vol. 2, no. 1, pp. 35-67, 1961.
[10] R. Hadfield, "Single-photon detectors for optical quantum information applications", *Nature Photonics*, vol. 3, no. 12, pp. 696-705, 2009.
[11] M. Itzler, r. Ben-Michael, C. Hsu, K. Slomkowski, A. Tosi, S. Cova, F. Zappa and R. Ispasoiu, "Single photon avalanche diodes (SPADs) for 1.5 μm photon counting applications", *Journal of Modern Optics*, vol. 54, no. 2-3, pp. 283-304, 2007.

# Modelling of Carrier Transport in Non-polar, M-plane III-nitride Quantum Cascade Detectors

Sumit Saha,* and Jitendra Kumar

Department of Electronics Engineering, Indian Institute of Technology (Indian School of Mines)
Dhanbad-826004, Jharkhand, India
*sumitahas@gmail.com

***Abstract*— In this work, two different designs of mid-infrared (IR) quantum cascade detectors (QCDs) based on non-polar, m-plane III-nitride material system have been presented and the temperature dependent detector characteristics have been investigated. The carrier transport in these QCD structures is modelled using a simplified rate equation approach. The major carrier scattering mechanisms responsible for the intersubband transitions of carriers in non-polar, m-plane III-nitride quantum cascade structures have been identified and included in the rate equation model. The carrier scattering rates are calculated using Fermi's golden rule approximation. The detector performance characteristics have been predicted through the evaluation of current responsivity. It is observed that the resonant tunnel design gives higher responsivity performance compared to the scattering tunnel design whereas the thermal stability of current responsivity of the scattering tunneling design is much better than the resonant tunneling transport design. Both the structures show thermal stability of detection wavelength.**

***Index Terms*— Quantum cascade detector, m-plane III-nitrides, carrier transport, scattering rates, resonant tunneling, rate equations.**

## I. Introduction

Semiconductor quantum cascade detectors (QCDs) [1], [2] are stealing attention of the researchers due to their performance advantages compared to other detectors. QCDs are semiconductor heterostructure photon detector that works on the principle of cascaded transport of carriers through a quantum cascade structure. After their first demonstration [1], QCDs have gone through lot of improvements in their design to get better performance characteristics. Presently, QCDs are able to detect radiations in the whole infrared (IR) spectral region even in terahertz (THz) region with high responsivity and detectivity performances at moderate temperatures. Apart from the design of QCDs, use of different material systems improves the performance of the detector greatly. Use of III-nitride material system for QCD design enables them for high temperature near- and far-IR optoelectronic applications. c-plane III-nitride materials are mostly used for the design of optoelectronic devices. This material system shows strong internal polarization fields due to presence of spontaneous and piezoelectric polarizations [3]. Polarization induced strong internal electric field in polar III-nitrides decreases the intersubband optical transition strength and bounds the accessible wavelength range and also makes the device design more complicated. Non-polar, m-plane III-nitrides [4] are free from internal polarization fields which makes the device design using this material system much easier and extends the range of accessible wavelengths while maintaining the other advantages of III-nitrides. In the last few years, lots of studies have been carried out on non-polar, m-plane III-nitride quantum well structures both theoretically and experimentally [4]-[12]. However, in those researches, major focuses have been made on the structural and optical properties of quantum wells of this material system. There has no such research in literature describing the carrier transport in non-polar, m-plane III-nitride heterostructures.

Here, in this research work, we have designed two QCD structures using non-polar, m-plane III-nitride material system for the mid-IR detection applications and the carrier transport in these structures has been modelled theoretically. For the transport modelling, most of the important carrier scattering mechanisms are identified and calculated using Fermi's golden rule approximations. For the device design, it is very important to know the electronic band structure of the m-plane III-nitride heterostructure. Conduction band profile, electron energies and corresponding wave functions are calculated by solving coupled Schrödinger-Poisson equation self-consistently. Carrier transport in the designed QCD structures has been modelled using simplified rate equations formulation. Finally, the responsivity performances of the QCDs have been evaluated and the effect of temperature on the current responsivity has been investigated.

## II. Design of non-polar, m-plane III-nitride QCD structures

To model the carrier transport and investigate the output characteristics of the detector, we have presented two separate designs for the QCD using non-polar, m-plane III-nitrides.

### *A. Scattering tunneling transport design*

The energy band diagram of the two consecutive periods of the QCD structure along with eigen energies and corresponding wave functions is shown in Fig. 1. The layers thicknesses of a period of the QCD are as follows: 3.12/**1.56**/1.35/**1.17**/1.9/**1.17 (nm)**. The quantum wells in the QCD structure are of GaN material. The barrier layers ($Al_{0.6}Ga_{0.4}N$) are represented in bolded font. The first layer is the active quantum well which is doped intentionally with n-type dopants. The doping concentration is $7x10^{18}$ $cm^{-3}$. n-type doping of the active well provides free electrons which occupy the ground energy state of the active well at equilibrium. Upon incidence of the optical radiation on the QCD structure, electrons in the ground energy state in the active well get excited and jump to the excited energy state in the active well. The photoexcited electrons then extracted from the active well by scattering tunneling transport mechanism and transported to the active well of the next

978-1-5386-3374-8/17/$31.00 ©2017 IEEE

period. To achieve the scattering tunneling transport, the extractor wells are designed in such a way that the ground energy states of the extractor wells and the excited energy state of the active well together form a phonon ladder. The photoexcited carriers get transported to the next period by phonon scattering mechanism.

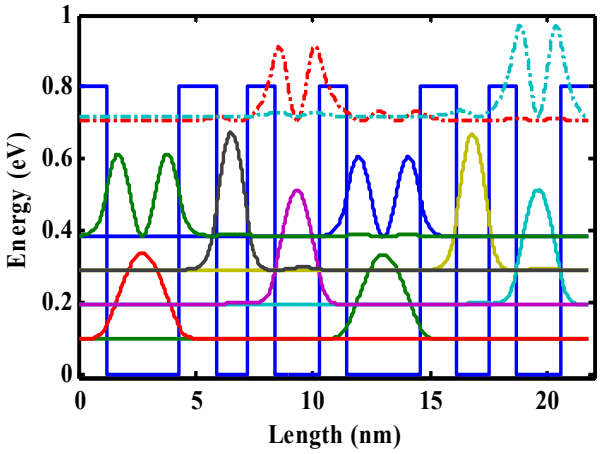


Fig. 1 Conduction band diagram of two consecutive periods of scattering tunneling transport QCD design.

### *B. Resonant tunneling transport design*

To make the extraction of the photoexcited carriers more efficient, a narrow quantum well has been inserted between the active well and the extractor period. The dimension of the inserted potential well is adjusted in such a way that the ground energy state of the well will be in resonance with the excited energy state of the active well. As the condition for energy resonance satisfies, the photoexcited carriers will first undergo through a resonant tunneling process and gets extracted from the active well, and then they will again undergo scattering tunneling process and will be transported to the next QCD period. The successive layer dimensions of a period of the QCD are as follows: 3.12/**2.6**/1.04/**1.17**/1.35/**1.17**/1.9/**1.17 (nm)**. A similar doping arrangement has been used for the both structures. The energy band diagram of the two consecutive periods of the designed detector is shown in Fig. 2.

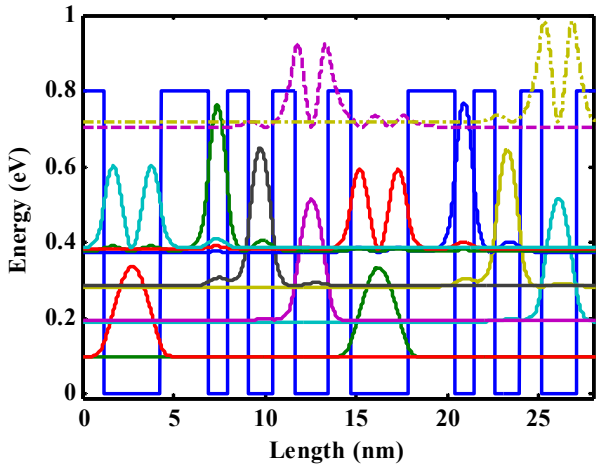


Fig. 2 Conduction band diagram of two consecutive periods of resonant tunneling transport QCD design.

Both the structures are designed for the detection of optical radiations mainly in mid-IR spectral region. The detection wavelengths of the designed detectors are around 4.3 µm. This wavelength is very important because one of the most important environmental gas carbon dioxide has its fingerprint spectrum at this wavelength. Carbon dioxide shows strong optical absorption at this wavelength. Therefore, for the environmental gas sensing, specifically for carbon dioxide sensing, these QCDs are very useful.

## III. Band Solution and Carrier Transport Modelling

The conduction band diagrams, eigen energies and the corresponding wave functions associated with non-polar, m-plane III-nitride QCD structures have been calculated by solving coupled Schrödinger-Poisson equation self-consistently [4], [13]. The conduction band nonparabolicity is considered in the process of band solution through energy dependent electron effective masses. Temperature dependent band solution has been obtained by incorporating temperature variation of the band parameters according to Varshni equation. The dimensions of the quantum wells are adjusted in such a way that the designed QCDs shall be able to detect 4.3 µm wavelength radiations and the successive extractor well energies will be at phonon resonance with the preceding well energies. The carrier transport in these QCDs will be predominantly along the growth direction due to design of the structures and the transport will be assisted by different carrier scatterings. There are many scattering mechanisms that influence the carrier dynamics in semiconductor heterostructures. For III-V semiconductor heterostructures, electron-phonon and electron-interface roughness interactions are identified as the dominating source of carrier scatterings. The major carrier scattering processes responsible for the intersubband carrier transitions in the QCD structure are electron-phonon scattering, electron-interface roughness scattering, alloy scattering and ionized impurity scattering. The electron-phonon scattering is caused by optical and acoustic phonons in the material. Among different optical phonons, polar longitudinal-optical (LO) phonons and non-polar transverse optical (TO) phonons play the dominating roles. The acoustic phonon scattering is due to deformation potential coupled acoustic phonons and piezoelectric potential coupled acoustic phonons. The LO-phonon scatterings, interface roughness scatterings and ionized impurity scatterings are calculated using the formulas presented in [3] whereas the TO-phonon scatterings, alloy scatterings and deformation potential coupled acoustic phonon scatterings are calculated according to Jirauschek and Kubis [14]. For the calculation of alloy scatterings, the unit cell volume of the zinc-blende structure in the alloy scattering rate equation is replaced by the unit cell volume of the wurtzite crystal structure. The piezoelectric potential coupled acoustic phonon scattering rate is calculated according to [15]. The value of the mean interface roughness height is taken as 0.1 nm and the correlation length is taken as 5 nm according to [8] for the interface roughness scattering rate calculation. The carrier scatterings due to polarization induced line-charges and dislocation densities [16] play major role in controlling the in-plane movements of carriers in bulk III-nitrides. However, for the present study, as we mainly focus on the intersubband transport of carriers in m-plane III-nitride QCD structures, the above mentioned scatterings (polarization induced line-charge scattering and dislocation scattering) can be neglected.

The current responsivity of the QCD is given as [2], [3]

$$R = \left(J_{photo} / P_{in}\right), \tag{1}$$

where the input optical power density ($P_{in}$) is considered as 1 mW/cm$^2$ and the output photocurrent density ($J_{photo}$) is calculated as [2], [3]

$$J_{photo} = e \sum_{i \in A,\, j \in A^+} \left( \frac{n_i}{\tau_{ij}} - \frac{n_j}{\tau_{ji}} \right). \tag{2}$$

The current through the QCD structure is calculated by considering a reference plane between two consecutive periods of the QCD structure and taking difference between the number of charge carriers crossing the plane in the forward direction and in the backward direction per unit time interval. The current density calculated under illumination condition gives the photocurrent density. Here, $A$ denotes the first period and $A^+$ is the next period at the right of the first period. $n$ is the subband electron population density. The carrier dynamics in the excited state of the active well of the QCD can be described using the following rate equation [2]

$$\frac{dn_i}{dt} = -\left(\frac{J_{tunnel}}{q}\right) + \sum_{j=1,\, j\neq i}^{N} \frac{n_j}{\tau_{ji}} - n_i \sum_{j=1,\, j\neq i}^{N} \frac{1}{\tau_{ij}} + \sum_{j=1,\, j\neq i}^{N} n_j \left( \frac{1}{\tau_{ji^+}} + \frac{1}{\tau_{j^+ i}} \right) - n_i \sum_{j=1,\, j\neq i}^{N} \left( \frac{1}{\tau_{ij^+}} + \frac{1}{\tau_{i^+ j}} \right), \tag{3.a}$$

and for the first extractor well state, it is given as [2]

$$\frac{dn_i}{dt} = \left(\frac{J_{tunnel}}{q}\right) + \sum_{j=1,\, j\neq i}^{N} \frac{n_j}{\tau_{ji}} - n_i \sum_{j=1,\, j\neq i}^{N} \frac{1}{\tau_{ij}} + \sum_{j=1,\, j\neq i}^{N} n_j \left( \frac{1}{\tau_{ji^+}} + \frac{1}{\tau_{j^+ i}} \right) - n_i \sum_{j=1,\, j\neq i}^{N} \left( \frac{1}{\tau_{ij^+}} + \frac{1}{\tau_{i^+ j}} \right), \tag{3.b}$$

where for other energy states in the QCD structure, rate equation will take the following form [2]

$$\frac{dn_i}{dt} = \sum_{j=1,\, j\neq i}^{N} \frac{n_j}{\tau_{ji}} - n_i \sum_{j=1,\, j\neq i}^{N} \frac{1}{\tau_{ij}} + \sum_{j=1,\, j\neq i}^{N} n_j \left( \frac{1}{\tau_{ji^+}} + \frac{1}{\tau_{j^+ i}} \right) - n_i \sum_{j=1,\, j\neq i}^{N} \left( \frac{1}{\tau_{ij^+}} + \frac{1}{\tau_{i^+ j}} \right). \tag{3.c}$$

In the above equations, $J_{tunnel}$ represents the resonant tunneling current density [2], [3] and $N$ is the number of states in a QCD period. Resonant tunneling current density will be significant only for the resonant tunneling transport QCD design and can be omitted for the case of scattering tunneling transport design.

The total intersubband scattering rate between two subbands $i$ and $j$ is given as

$$\tau_{ij}^{-1} = \left(\tau_{rad}^{-1} + \tau_{non-rad}^{-1}\right). \tag{4}$$

In the above equation $\tau_{rad}^{-1}$ is the radiative scattering rate [3] and $\tau_{non-rad}^{-1}$ is the total nonradiative scattering rate which is given as

$$\tau_{non-rad}^{-1} = \tau_{phonon}^{-1} + \tau_{roughness}^{-1} + \tau_{impurity}^{-1} + \tau_{alloy}^{-1}, \tag{5}$$

where $\tau_{roughness}^{-1}, \tau_{alloy}^{-1}$ and $\tau_{impurity}^{-1}$ are the electron scattering rates caused by the interface roughness, alloy disorder and ionized impurities present in the structure, respectively and the term $\left(\tau_{phonon}^{-1}\right)$ is the phonon scattering rate which is mainly due to the interaction of electrons with optical and acoustic phonons in the material. The total electron-phonon scattering rate is given as

$$\tau_{phonon}^{-1} = \tau_{LO}^{-1} + \tau_{TO}^{-1} + \tau_{acoustic}^{-1}, \tag{6}$$

where $\tau_{LO}^{-1}$ is the LO-phonon scattering rate, $\tau_{TO}^{-1}$ is the TO-phonon scattering rate and $\tau_{acoustic}^{-1}$ is the acoustic phonon scattering rate. The acoustic phonon scattering rate has two components and is given as

$$\tau_{acoustic}^{-1} = \tau_{def-acoustic}^{-1} + \tau_{piezo-acoustic}^{-1}, \tag{7}$$

where $\tau_{def-acoustic}^{-1}$ is the deformation potential coupled acoustic phonon scattering rate and $\tau_{piezo-acoustic}^{-1}$ is the piezoelectric potential coupled acoustic phonon scattering rate.

## IV. Results and Discussion

We have obtained the conduction band diagrams, confined electron energies and corresponding wave functions of the non-polar, m-plane III-nitride QCDs presented in this work by solving coupled Schrödinger-Poisson equation self-consistently. The intersubband transition rates of electrons are obtained by using these energies and wave functions in the scattering rate equations under Fermi's golden rule approximations. The calculated intersubband transition lifetimes of electrons are then used in the rate equations to determine the steady state subband carrier distributions. Then, using these carrier profiles and the intersubband transition rates, photocurrent generated in these QCD structures are calculated for a fixed incident optical power density and the current responsivity of the detectors have been anticipated. This is the first time in literature to study the carrier transport in non-polar, m-plane III-nitride QCDs.

Fig. 3 shows the variation of the current responsivity of the non-polar, m-plane III-nitride QCD structures reported in this work with temperatures. Fig. 3(a) shows the current responsivity behaviour for the scattering tunneling transport design and Fig. 3(b) shows the current responsivity behaviour for the resonant tunneling transport design. It is observed that the responsivity of the QCD decreases with the increase of temperature for both of the designs. It is mainly due to the decrease in output photocurrent density at higher temperatures which is caused by the decreased absorption efficiency and increased nonradiative scattering rates. The current responsivity for resonant tunneling transport design is much higher than the scattering tunneling transport design as seen in the figures. This proves that the resonant tunneling transport design gives much efficient carrier extraction and transport than that of the scattering tunneling transport design. However, the percentage variation of current responsivity for a temperature variation of 250 K (from 50 K to 300 K) for the scattering tunneling transport design is 50.8 % which is smaller than the percentage variation of current responsivity for resonant tunneling transport design which is 60.6%.

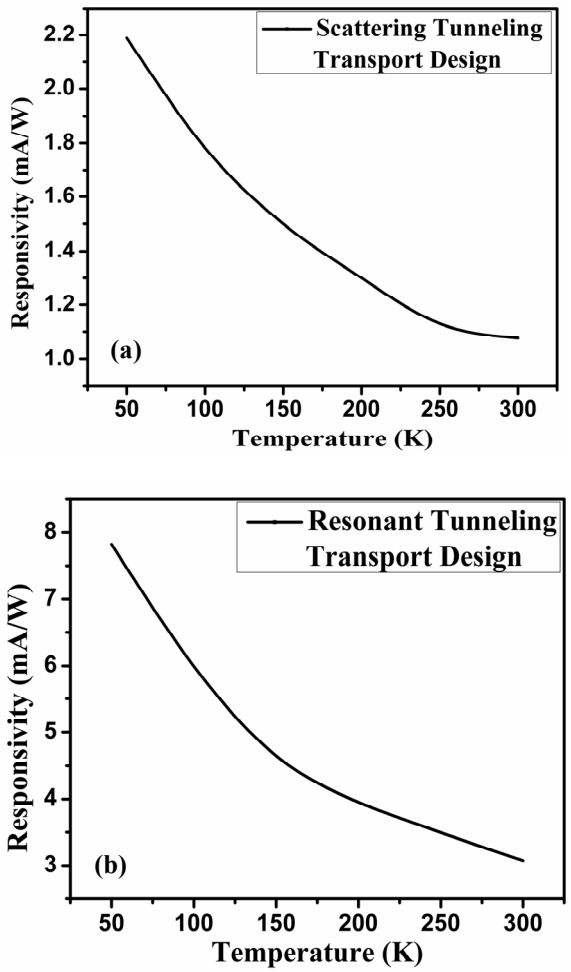


Fig. 3 Tempearture variation of current responsivity of (a) scattering tunneling transport QCD design and (b) resonant tunneling transport QCD design.

Therefore, in terms of thermal stability of the responsivity performance, scattering tunneling transport design is much better than that of the resonant tunneling transport design. Both of the designs are superior in their respective ways and must be utilized depending on the application requirement.

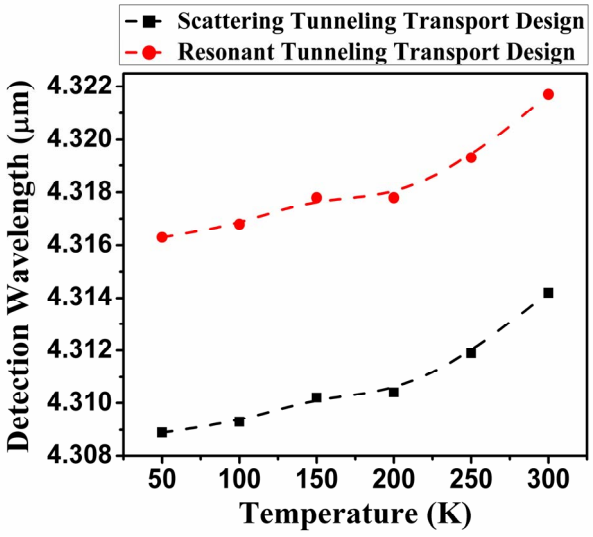


Fig. 4 Temperature variation of the detection wavelengths.

The temperature dependent detection wavelengths of the two designs are plotted in Fig. 4. It is observed that the detection wavelengths for both of the designs are nearly temperature insensitive.

Detectivity performances of these QCD structures need to be evaluated in future to get the idea of noise performances of these detectors. Further optimization can be done for these two structures for optimized device performance keeping the design concepts in mind.

## V. Conclusions

Carrier transport in the non-polar, m-plane III-nitride QCDs has been modelled theoretically for the first time. Major intersubband carrier scattering mechanisms responsible for carrier dynamics in the QCD structure are identified. Band solution of the QCD structure has been obtained by solving coupled Schrödinger-Poisson equation and the intersubband carrier scattering rates are calculated using Fermi's golden rule approximation. Responsivity performance of the QCD has been obtained by using a simplified rate equation model and the thermal behaviour has been evaluated. Two different QCD designs have been presented and their advantages are highlighted.

## References

[1] L. Gendron, M. Carras, A. Huynh, V. Ortiz, C. Koeniguer, and V. Berger, "Quantum cascade photodetector," *Appl. Phys. Lett.,* vol. 85, pp. 2824-2826, 2004.

[2] S. Saha, and J. Kumar, "Rate equation modelling and investigation of quantum cascade detector characteristics," *Superlattices and Microstructures*, vol. 98, pp. 70-77, 2016.

[3] S. Saha, and J. Kumar, "Role of interface roughness scattering, temperature, and structural parameters on the performance characteristics of III-nitride quantum cascade detectors," *J. Appl. Phys.*, vol. 121, pp. 053104-1-053104-9, 2017.

[4] S. Saha, B. Ch. Mech, S. Hussain, and J. Kumar, "Optical analysis of non-polar, m-plane GaN/AlGaN quantum cascade structures," in *Proc. IEEE*, 2017, pp. 153-154.

[5] D. Feezell, Y. Sharma, and S. Krishna, "Optical properties of nonpolar III-nitrides for intersubband photodetectors," *J. Appl. Phys.*, vol. 113, pp. 133103-1-133103-7, 2013.

[6] T. Kotani, M. Arita, and Y. Arakawa, "Observation of mid-infrared intersubband absorption in non-polar m-plane AlGaN/GaN multiple quantum wells," *Appl. Phys. Lett.,* vol. 105, pp. 261108-1-261108-4, 2014.

[7] C. Edmunds, J. Shao, M. Shirazi-HD, M. J. Manfra, and O. Malis, "Terahertz intersubband absorption in non-polar m-plane AlGaN/GaN quantum wells," *Appl. Phys. Lett.,* vol. 105, pp. 021109-1-021109-4, 2014.

[8] T. Kotani, M. Arita, and Y. Arakawa, "Doping dependent blue shift and linewidth broadening of intersubband absorption in non-polar m-plane AlGaN/GaN multiple quantum wells," *Appl. Phys. Lett.,* vol. 107, pp. 112107-1-112107-4, 2015.

[9] C. B. Lim, M. Beeler, A. Ajay, J. Lahnemann, E. Bellet-Amalric, C. Bougerol, and E. Monroy, "Intersubband transitions in nonpolar GaN/Al(Ga)N heterostructures in the short- and mid-wavelength infrared regions," *J. Appl. Phys.*, vol. 118, pp. 014309-1-014309-8, 2015.

[10] C. B. Lim, A Ajay, C Bougerol, B Haas, J Schörmann, M Beeler, J Lähnemann, M Eickhoff, and E Monroy, "Nonpolar m-plane GaN/AlGaN heterostructures with intersubband transitions in the 5–10 THz band," *Nanotechnology*, vol. 26, pp. 435201-1-435201-6, 2015.

[11] C. B. Lim, A. Ajay, C. Bougerol, E. Bellet-Amalric, J. Schormann, M. Beeler, and E. Monroy, "Effect of Al incorporation in nonpolar m-plane GaN/AlGaN multi-quantum-wells using plasma-assisted molecular beam epitaxy," *Phys. Status Solidi A,* doi:10.1002/pssa.201600849 (2016).

[12] T. Kotani, M. Arita, K. Hoshino, and Y. Arakawa, "Temperature dependence of mid-infrared intersubband absorption in AlGaN/GaN multiple quantum wells," *Appl. Phys. Lett.,* vol. 108, pp. 052102-1-052102-5, 2016.

[13] S. Saha, and J. Kumar, "Fully self-consistent analysis of III-nitride quantum cascade structures," *J Comput. Electron.*. vol. 15, pp. 1531–1540, 2016.
[14] C. Jirauschek, and T, Kubis, "Modeling techniques for quantum cascade lasers," *Appl. Phys. Rev.,* vol. 1, pp. 011307-1-011307-51, 2014.
[15] Z. Li, P. Wang, J. He, H. Chen, and J. Cheng, "Effect of polarization on the performance of ZnO/MgZnO quantum cascade detector," *Superlattices and Microstructures,* doi:10.1016/j.spmi.2017.07.046 (2017).
[16] A. Konar, A. Verma, T. Fang, P. Zhao, R. Jana, and D. Jena, "Charge transport in non-polar and semi-polar III-V nitride heterostructures," *Semicond. Sci. Technol.,* vol. 27, pp. 024018-1-17, 2012.

# Analysis of Dark Current and Detectivity of Quantum Dot Infrared Photodetectors under the effect of microscale and nanoscale transport mechanisms

Sweta Rani,* Saddam Hussain, Sumit Saha, and Jitendra Kumar
Department of Electronics Engineering, Indian Institute of Technology (Indian School of Mines) Dhanbad
Jharkhand-826004, India
*rani.sweta32@gmail.com

*Abstract*— **An analysis has been done for the dark current and detectivity of quantum dot infrared photodetectors (QDIPs). Dark current being the most influential factor in the performance of QDIPs has been studied with utmost importance. The effect of drift velocity on the dark current model for QDIPs has been taken into consideration. The effect of variation of electric field on dark current at different temperature values has been analyzed. Detectivity, which is an important figure of merit for measuring the performance of the device, has also been analyzed in accordance with the change in electric field. The effect of the change in the area of the photodetector on the dark current has also been analyzed. This analysis has been done by considering the drift velocity of electrons along with two electron transport mechanisms – the microscale and nanoscale transport and the mobility.**

***Index Terms*** **– dark current, mobility, drift velocity, detectivity**

## I. INTRODUCTION

Quantum dot infrared photodetectors (QDIPs) have made significant progress in the field of detection in recent years. The performance of QDIPs has significantly enhanced over decades by using improved architecture. QDIP is an important topic of research with various advantages such as high temperature operation, sensitivity to normal incident infrared radiation, longer carrier lifetimes [1] etc. However, the performance of QDIPs gets significantly reduced due to the presence of unwanted parameters such as dark current [2]. The study of dark current leads to optimization of the device and can be useful for the device designers [3].

The dark current consideration of QDIPs is different from other type of detectors [4]. Different models have been devised earlier for the calculation of dark current which utilized the thermal generation rate and capture probability of the system [5]. The direct band gap semiconductor devices give a close competition to the QDIPs but the characterization of the dark current in these detectors is different from other detectors [6-8]. By considering the count of mobile carriers in the barrier, we can develop a new model for dark current. Dark current also leads to noise, thus, dark current needs to be very cleverly analyzed.

This work focuses on the calculation and analysis of dark current under the influence of drift velocity and the effects of microscale and nanoscale transport mechanisms. The dark current flowing across the potential barrier of the QDIP is considered to be equal to the dark current of the total photodetector.

## II. THEORETICAL FORMULATION

The dark current density is estimated by getting the measure of carrier density in the potential barrier and then multiplying it with the drift velocity.

$$\langle J_{dark} \rangle = q n_{3d} v_d \quad , \tag{1}$$

where q is charge of electron, $n_{3d}$ is three-dimensional density [9] and $v_d$ is drift velocity of the electrons. Earlier, the three-dimensional density was estimated as

$$n_{3d} = 2\left(\frac{m^* kT}{2\pi\hbar^2}\right)^{1.5} \exp\left(-\frac{E_a}{kT}\right) \quad , \tag{2}$$

where $m^*$ is the electron's effective mass and $E_a$ is the thermal activation energy [10]. The thermal activation energy is equal to the energy difference between the Fermi levels in the dot and the top of the barrier. In this model, only the thermal activation energy was considered but in our model we will be considering other transport mechanisms like microscale and nanoscale transport. So the three-dimensional density now becomes

$$n_{3d} = 2\left(\frac{m^* kT}{2\pi\hbar^2}\right)^{1.5} \exp\left(-\frac{E_{micro}\exp(-E/E_0) + E_{nano} - \beta E}{kT}\right), \tag{3}$$

and thus the dark current can be written as:

$$I_{dark} = 2qv_d A \times \left[\frac{m^* kT}{2\pi\hbar^2}\right]^{1.5} \exp\left[-\frac{E_{micro}\exp(-E/E_0) + E_{nano} - \beta E}{kT}\right], \tag{4}$$

where $k$ is the Boltzmann constant, $T$ is the temperature taken into consideration, $\hbar$ is the reduced Planck's constant, $E$ is applied electric field, $A$ is the area of the photodetector, $E_{nano}$ and $E_{micro}$ are the activation energies under nanoscale and microscale electron transport, respectively, at no bias applied whereas $E_0$ and $\beta$ are the rate of change of the activation energies under microscale and nanoscale transport energy, respectively. As devices shrink

978-1-5386-3374-8/17/$31.00 ©2017 IEEE

to microscale and nanoscale levels, the transmission of heat and energy takes place in a different form as compared to macroscale levels. This model shows the effect of miniaturization of devices on performance of QDIPs.

The drift velocity of electrons depends upon electric field applied to the device, mobility of the electrons and saturation velocity of electrons. The drift velocity can be obtained as:

$$v_d = \mu E\left(1+\left(\frac{\mu E}{v_{sat}}\right)^2\right)^{-0.5}, \qquad (5)$$

where $\mu$ is trap controlled mobility and $v_{sat}$ is the saturation velocity of electrons. The trap controlled mobility plays an important role and is calculated using trap free band mobility, volume concentration of the traps and effective trap energy which is equal to the nanoscale transport energy under no bias. Traps are caused due to the presence of defects in the device. Increase in the trap energy and trap concentration can deteriorate the performance of the photodetector devices.

Mobility can be obtained using these parameters and can be calculated through the given equation:

$$\mu = \mu_0 \times \frac{\left[\dfrac{e^{\frac{E_{te}}{kT}} - e^{\frac{\varsigma E_{te}^{1.5}}{qEa}} e^{-\varsigma E_{te}^{1.5}} e^{\frac{qEa}{kT}}}{1-e^{-\varsigma E_{te}^{1.5}} e^{\frac{qEa}{kT}}}\right]}{\underbrace{\left[c+\dfrac{e^{\frac{E_{te}}{kT}} - e^{\frac{\varsigma E_{te}^{1.5}}{qEa}} e^{-\varsigma E_{te}^{1.5}} e^{\frac{qEa}{kT}}}{1-e^{-\varsigma E_{te}^{1.5}} e^{\frac{qEa}{kT}}}\right]}_{=x}}, \qquad (6)$$

where $\mu_0$ is the trap free band mobility, $E_{te}$ is the single effective trap energy which is taken as equal to $E_{nano}$, $a$ is the radius of the quantum dot, $c$ is the volume concentration of traps, $\varsigma$ is a constant that is related to carrier which can be obtained as

$$\varsigma = a\left(\frac{2m^* q}{\hbar^2}\right)^{0.5}. \qquad (7)$$

In this paper, $c$ is assumed to be 0.1 and $\mu_0/c$ =1.

Substituting (5) and (6) in (4), we can now get the equation for dark current as

$$I_{dark} = 2q(\mu_0 x)A \times E\left(1+\left(\frac{(\mu_0 x)E}{v_{sat}}\right)^2\right)^{-0.5} \times \left(\frac{m^* kT}{2\pi\hbar^2}\right)^{1.5} \exp\left(-\frac{E_{micro}\exp(-E/E_0)+E_{nano}-\beta E}{kT}\right), \qquad (8)$$

Using above equation we can calculate dark current for QDIPs. In this model, QDIPs are considered to be fabricated using GaAs or InGaAs as these are the most commonly used materials for the fabrication of QDs [9].

There is a large dependence on electric field for drift velocity. Thus, dark current also depends on the intensity of applied electric field. Thus the calculations of dark current have been made with respect to applied electric field with the variation in temperature and area of the photodetector.

The normalized dark current, $I_{dark} = G_{th}q$ can be directly used to determine thermal detectivity as

$$D = \frac{\eta}{2\hbar\vartheta\sqrt{G_{th}}}. \qquad (9)$$

Detectivity is a parameter that is directly proportional to the performance of the detector. It is the detector's signal-to-noise ratio at 1 watt of input radiation to a detector of unit bandwidth and a unit area [11]. This figure of merit is used to characterize the performance of QDIPs.

## III. Results and Discussion

To fully demonstrate the potential of QDIPs, we need to be accurate and specific with our theoretical investigation. Earlier, only thermal activation energy was considered for the calculation of dark current. There are various new parameters involved in this model which makes the calculations more accurate. The values considered for the calculations are $\beta$ = 2.79 meVcm/kV, $E_0$ = 1.62 kV/cm, $E_{micro}$ = 34.6 meV, $E_{nano}$ = 224.7 meV, $v_{sat}$ = 5x10$^7$ cm/s, $a$ = 10.5 nm and $m^*$=0.023$m_e$. A range of applied electric field is considered for the calculations.

This model is used to estimate the influence of few structural parameters on the performance of the photodetectors under un-illuminated condition and paves a way for optimization of QDIP architecture.

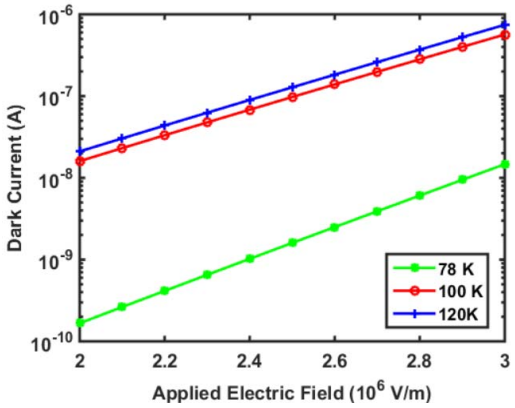


Fig. 1. Dark current of QDIP on varying electric field (at the temperature 78 K, 100 K and 120 K)

The plot in Fig. 1 shows the variation of dark current within 2x10$^6$ – 3x10$^6$ V/m of the applied electric field. The value of dark current goes on increasing with the increase in applied electric field. However, at 78 K the value of dark current is lower than the value of dark current at 120 K.

With a slight increase in temperature value, the value of dark current also increases slightly. There is a large difference in the values of dark current at 78 K and 100 K but small difference in the values of dark current at 100 K and 120 K.

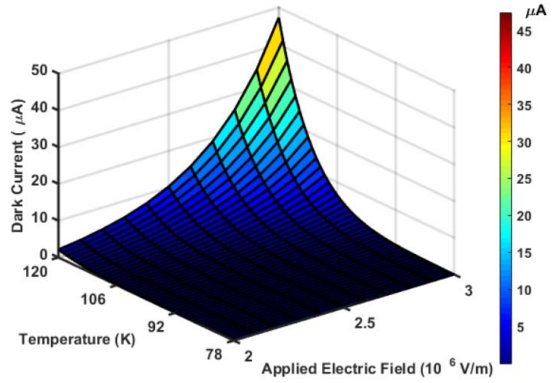


Fig. 2. Dark current of QDIP on varying temperature and electric field

A simultaneous increase in applied electric field and temperature leads to increase in dark current significantly as shown in Fig. 2. This increasing pattern of the dark current density shows the contributions of the temperature and applied electric field to the dark current of the QDIP. Dark current is an unwanted parameter that deteriorates the device performance. Lower dark current leads to higher sensitivity of detector.

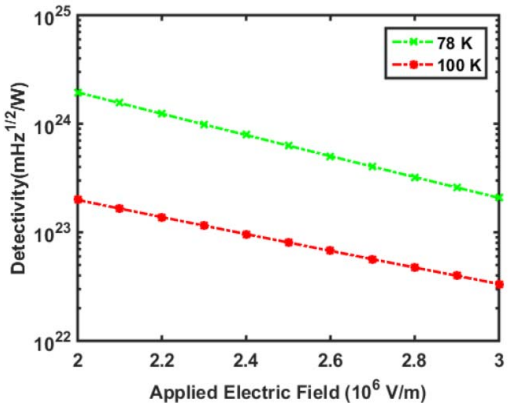


Fig. 3. Detectivity of QDIP on varying electric field (at the temperature 78 K, 100 K and 120 K)

One more parameter is detectivity which is a measure of the level of performance of the photodetector. The size of the QDs and the area of the photodetector affect the optical absorption of the device and thus affect the detectivity of the QDIPs. By optimizing the effective area of the QDIP, we can achieve lower dark current and higher detectivity. Detectivity gets reduced due to noise produced originating through trapping mechanism in QDs due to the defects. We can find out a comparison between detectivities at different temperatures from Fig. 3. With the increase in applied electric field, detectivity goes on decreasing. One important factor which contributes to the reduction in the detectivity is the presence of trap energy which forms the basis of this model.

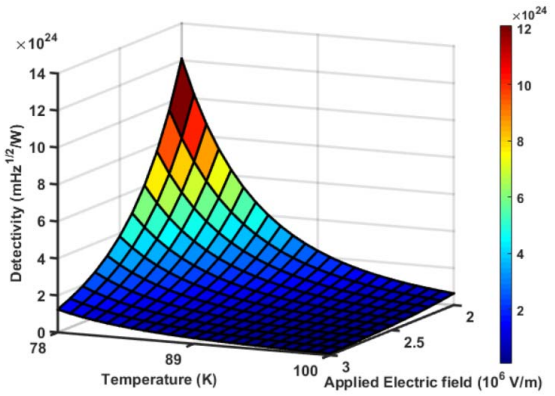


Fig. 4. Detectivity of QDIP on varying temperature and electric field

Detectivity is high at low electric field and keeps decreasing at higher values of electric fields as can be seen from Fig. 4. As temperature is increasing, the detectivity is also decreasing exponentially and becomes very low around 100 K. Increase in temperature and electric field has adverse effect on detectivity of the photodetector.

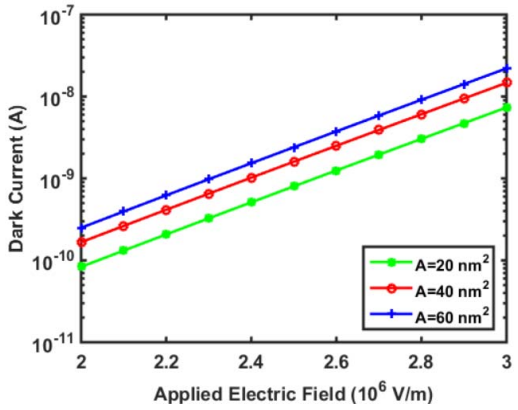


Fig. 5. Dark current of QDIP on varying electric field (at different values of area of photodetector)

Increase in the area of the photodetector leads to increase in dark current. In Fig. 5, we can see that dark current increases with the increase in electric field. The dark current is low for small area of photodetector as compared to larger area.

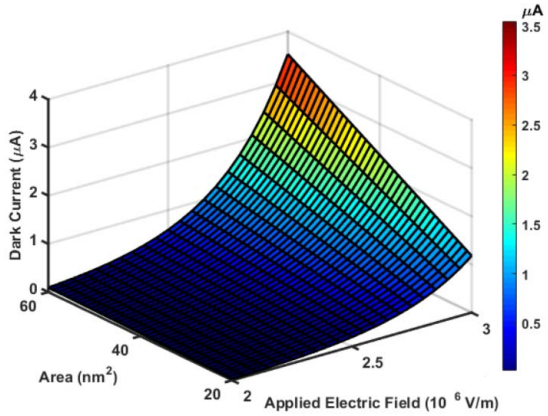


Fig. 6. Dark current of QDIP on varying area of photodetector and electric field

The increase in dark current is gradual at low values of area of detector. With the increase in area, the increase in dark current becomes prominent as it can be seen in Fig. 6. Thus, it can be said that the size of the detector should be kept optimum to avoid unwanted effects within the device.

## IV. Conclusion

In this model, a more accurate formulation has been done considering activation energy under micro and nanoscale transport. The mathematical model is derived to explicitly represent the performance of the structure. The dark current increases with the increasing temperature and electric field. The parameters of mathematical model are used in such a way that optimum results are achieved. Proposed model which gives a relation between dark current, mobile carrier concentration and drift velocity is deduced. It is important to have low dark current and this model predicts the amount of dark current produced. The area of the detector should also be maintained such that it does not affect the performance of the detector adversely.

This model can be used in optimizing and estimating the performance of the device. This model can be extended to calculate dark current for different quantum structures. This formulation can be taken as basis for further developments in the field of quantum structure photodetection. These results show large dependence on electric field intensity which can provide ways to optimize the performance of QDIPs. This will help in wide application of QDIPs such as defense, commercial fields etc. [12].

## References


[1] A. D. Stiff Roberts, "Quantum-dot infrared photodetectors: a review," *Journal of Nanophotonics*, vol. 3, pp. 031607-1-031607-17, 2009.

[2] H. Liu, and J. Zhang, "Dark current and noise analysis of quantum dot infrared photodetectors," *J. Opt. Soc. Am*., vol. 51, pp. 2767-2771, 2012.

[3] P. Martyniuk and A. Rogalski, "Quantum-dot infrared photodetectors: Status and outlook," *Progress in Quantum Electronics*, vol. 32, pp. 89-120, 2008.

[4] M. A. Kinch, "Fundamental Physics of Infrared Detector materials," *Journal of Electronic Materials*, vol. 29, pp. 809-817, 2000.

[5] P. Martyniuk and A. Rogalski, "Insight into performance of quantum dot infrared photodetectors," *Bulletin of the Polish Academy of Sciences: Technical Sciences*, vol. 57, pp. 103-116, 2009.

[6] P. Martyniuk, S. Krishna and A. Rogalski, "Assessment of quantum dot infrared photodetectors for high temperature operation," *Journal of Appled Physics*, vol. 104, pp. 034314-1-034314-6, 2008.

[7] J. Phillips, "Evaluation of the fundamental properties of quantum dot infrared detectorss," *Journal of Applied Physics*, vol. 91, pp. 4590-4594, 2002.

[8] A. Mahmoodi, H. D. Jahromi and M. H. Sheikhi, "Dark current modeling and noise analysis in Quantum Dot Infrared Photodetectors," *IEEE Sensors Journal*, vol. 15, pp. 5504-5509, 2015.

[9] H. Liu, and C. Yang, "Dark current model of quantum dot infrared photodetectors based on the influence of the drift velocity of the electrons," *Applied Mechanics and Materials*, vols. 556-562, pp. 2141-2144, 2014.

[10] H. C. Liu, "Quantum dot infrared photodetector," *Opto-electronics Review*, vol. 11, pp. 1-5, 2003.

[11] H. Liu, and J. Zhang, "Performance investigations of quantum dot infrared photodetectors," *Infrared Physics & Technology*, vol. 55, pp. 320-325, 2012.

[12] I. I. Mahmoud, H. S. Konber and M. S. El_Tokhy, "Performance improvement of quantum dot infrared photodetectors through modeling," *Optics & Laser Technology*, vol. 42, pp. 1240-1249, 2010.

# Suppression of Excess Noise in Polarization Enhanced Back Illuminated AlGaN Solar-Blind SAM APDs with Modified Multiplication Layer

Muhammad Navid Anjum Aadit,[1] Shamima Nasrin Juthi,[2] and Ummay Sumaya Khan[3]
Department of Electrical and Electronic Engineering
Bangladesh University of Engineering and Technology
Dhaka-1205, Bangladesh
[1]navidanjumaadit@gmail.com, [2]juthishamimanasrin@gmail.com, and [3]ummay.sumaya@gmail.com

***Abstract*—In this paper, we propose a novel and improved structure of a solar-blind back illuminated AlGaN separate absorption and multiplication avalanche photodiode (SAM APD) with a modified multiplication layer. It is shown that the excess noise factor can be suppressed at about 35% due to the higher threshold impact ionization energy of wide bandgap AlN layer inserted on both sides of the conventional avalanche layer. The enhanced polarization at the layer interface improves the photocurrent and the reduced excess noise limits the dark current. We use an in-house built simulator to investigate device characteristics of both the conventional and the proposed APDs. Some important figures of merit of the proposed solar-blind SAM APDs have been compared with the conventional ones and found to be superior in all aspects. With improved photocurrent, reduced dark current, low excess noise factor, excellent responsivity, and increased efficiency, the proposed device offers optimized solar-blind applications that can be useful in advanced optical fiber communication.**

***Index Terms*—Avalanche, Back Illumination, Excess noise, Polarization, Solar-blind.**

## I. Introduction

A photodiode is an opto-electronic device which takes photon as input and generates electron-hole pair as well as photocurrent as output [1]. Avalanche photodiode (APD) is an improved photodiode in which a built-in first step gain is achieved through avalanche multiplication [2]. APDs show an internal current gain due to avalanche effect [3]. In order to achieve higher gain and better responsivity, separate absorption and multiplication (SAM) APDs are designed. In SAM APDs, the multiplication process starts with only one type of carrier as the absorption and the multiplication regions are separated [4]. It is an avalanche photodiode in which the light-absorbing area consists of a low-bandgap material and the multiplication area consists of a high-bandgap material, reducing dark current and increasing gain [5]. The multiplication factor depends on the excess noise generated from impact ionization [6]. SAM APDs generate noise from randomness in the number and position of arrived photons and photogenerated carriers [7]. Although noise is undesirable in any device as dark current increases with it, reduction of noise reduces the device gain. Therefore, there exists a trade-off between gain and excess noise in SAM APDs. Excess noise factor is considered to be a figure of merit for APD devices that must be reduced. One common technique to reduce the excess noise factor is to decrease the width of the multiplication region [8]. Thin multiplication layer has increased dead space which is the minimum distance that the generated carriers have to cross in order to gain sufficient energy for impact ionization. Monte-Carlo studies confirm that the excess noise factor reduces with dead space [9]. However, the limitation of this technique is poor tunneling which results in unacceptable amount of dark current. The other conventional ways to reduce the excess noise factor include the use of impact ionization engineering, designing centered-well (CW) multiplication layer, and the use of different materials [8]. Staircase and superlattice APDs with heterostructure in the multiplication region are also designed to generate low noise but with limited performance [10]. New approaches to suppress the excess noise factor are required to ensure enhanced device performance.

Solar-blind SAM APD is a solid-state device that is transparent to the wavelength of the solar spectrum but is responsive to the ultraviolet (UV) ray ($\lambda < 280$ nm). III-Nitrides act as semiconductors of direct and wide bandgaps from deep ultraviolet (6.2 eV) to near infrared (0.7 eV) range [11]. AlGaN compounds with more than 40% Al composition and intrinsic solar-blind characteristics to remove natural background radiation from sunlight, are attracting a great deal of attention [12]. As a result, UV detectors based on Nitride compounds with the capability of detecting very weak UV signals under intense background radiation, have massive applications in biological and chemical agent detection, missile detection and interception, national defense, and scientific research [13], [14]. Many variations like GaN/SiC APDs, AlGaN solar-blind SAM APDs are designed for various purposes which override the basic structure of SAM APDs designed by Pau *et al.* [15]. To improve the carrier ionization, a low Al-content multiplication layer along with a photonic-crystal structure as an optical window is employed in a solar-blind AlGaN APD [16]. The avalanche ionization can be improved further by replacing AlGaN homogeneous multiplication region with a high/low Al content layer which exhibits 51% higher gain than conventional APDs [17]. Shao *et al.* reported that applying a photo-electrochemical experimental process can recover etching defects and the leakage current of the fabricated devices [18]. Moreover, Dong *et al.* proposed an AlGaN/GaN heterostructure SAM APD to combine the solar-blind UV absorption properties of AlGaN with the better avalanche characteristics of GaN [19]. To enhance the performance of solar-blind APDs, a new design scheme of device is also proposed by introducing polarization electric field in the multiplication region [11].The polarization electric field induced in the multiplication region reduces the reverse-bias

978-1-5386-3374-8/17/$31.00 ©2017 IEEE

breakdown voltage and enhances the multiplication gain of device [20]. Chang *et al.* suggested that a moderated gain should be adopted keeping the noise minimum to get a higher signal to noise ratio [21]. Although most of these works focus on lowering the breakdown voltage and increasing the gain, excess noise factor is still a common problem in all these new propositions. Unlike other SAM APDs, very few engineering works on the conventional AlGaN/GaN APD structures to reduce the excess noise factor are found in literature [22].

In this paper, an improved back illuminated solar-blind SAM APD design is presented which suppresses excess noise significantly with the use of three layered multiplication region. Impact ionization is limited by the higher impact ionization threshold energy of the AlN layers placed on two sides of the conventional AlGaN multiplication layer. The AlGaN layer still allows impact ionization with low impact ionization threshold energy but within optimum limit so that high gain as well as low excess noise can be achieved. Moreover, photocurrent and other optical properties of the device have been improved with enhanced polarization and reduced noise.

The rest of the paper includes device structure and modeling in Section II and detailed analysis of the findings of this study in Section III. The proposed design is proved to be superior to the conventional ones by comparing photocurrent, dark current, excess noise factor, responsivity and quantum efficiency under optimum simulation conditions.

## II. Device Structure and Modeling

### A. Device Structure

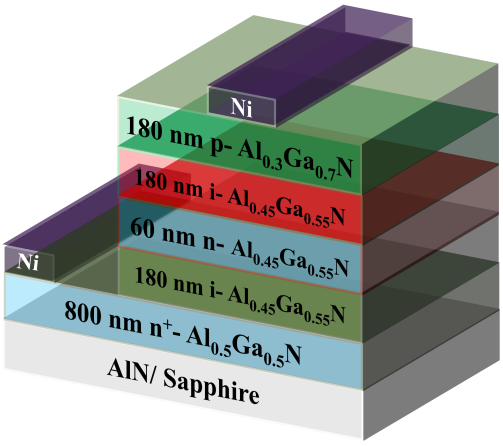


Fig. 1. Schematic model of a conventional back illuminated AlGaN solar-blind SAM APD

The conventional structure of an AlGaN back illuminated solar-blind SAM APD is shown in Fig. 1. In this structure, there are alternating AlGaN layers with different doping concentrations placed on AlN templates or c-plane sapphire substrates [18]. From bottom to top, the AlGaN APD consists of $n^+$-$i$-$n$-$i$-$p$ layers of AlGaN. The two unintentionally doped $i$-$Al_{0.45}Ga_{0.55}N$ layers work as the absorption and the multiplication layers with the same thickness of 180 nm as shown in the figure. The thickness of $n^+$-$Al_{0.5}Ga_{0.5}N$ layer is 800 nm and that of $n$-$Al_{0.45}Ga_{0.55}N$ layer is 60 nm. It is well-known that Al composition greater than 40% exhibits outstanding solar-blind (UV) properties [23]. With reverse bias applied at the $Ni$ contacts, this conventional structure works well with back illumination for solar-blind applications. However, like other SAM APDs, back illuminated AlGaN solar-blind APDs also suffer from excess noise generated due to impact ionization in the avalanche process.

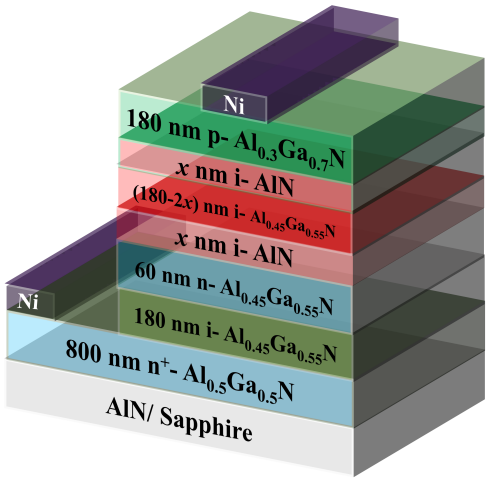


Fig. 2. Schematic model of the proposed back illuminated AlGaN solar-blind SAM APD

In order to overcome this limitation, we are proposing a novel device structure as shown in Fig. 2 to reduce the excess noise factor by modifying the multiplication region where impact ionization takes place. The proposed structure is also designed to be illuminated from the back side and similar to the conventional one except the multiplication layer only. We have divided the multiplication layer into three sections with different bandgaps and ionization threshold energies. At the two sides of the multiplication layer, higher bandgap material $i$-AlN ($E_g$ = 6.02 eV) with thickness of $x$ nm and in the middle, a comparatively lower bandgap material $i$-$Al_{0.45}Ga_{0.55}N$ ($E_g$ = 4.57 eV) with thickness of (180 - 2$x$) nm are placed. In this study, we have considered two 60 nm $i$-AlN layers placed on both sides of a 60 nm $i$-$Al_{0.45}Ga_{0.55}N$ layer to ensure symmetry in the multiplication layer. Therefore, $x$ = 60 has been assumed for the simulation. For both APD structures, the electron doping concentrations for the $n$-$Al_{0.45}Ga_{0.55}N$ and $n^+$-$Al_{0.5}Ga_{0.5}N$ layers are $10^{18}$ $cm^{-3}$ and $2 \times 10^{18}$ $cm^{-3}$ respectively and for the $p$-$Al_{0.3}Ga_{0.7}N$ layer, the hole doping concentration is $2 \times 10^{17}$ $cm^{-3}$. The doping concentration of residual electron in the unintentionally doped intrinsic layers is $10^{16}$ $cm^{-3}$ [17].

### B. Modeling

2D numerical simulations for both the conventional and the proposed AlGaN/GaN back illuminated solar-blind SAM APDs are performed in APSYS software [24] in order to solve the Poisson's equation and the continuity equations self-consistently to investigate carrier transport [25]. The Poisson's equation can be expressed as,

$$\left(\frac{d^2}{dx^2} + \frac{d^2}{dy^2} + \frac{d^2}{dz^2}\right)U = -\frac{\rho}{\varepsilon}, \tag{1}$$

where,

$U$ is the device potential,
$\rho$ is the density of charge, and
$\varepsilon$ is the dielectric constant.

Piezoelectric and spontaneous polarization effects contribute largely to the electric field in AlGaN/GaN solar-blind SAM APDs to reduce breakdown voltage and enhance gain. Incorporating polarization vector, (1) becomes,

$$\left(\frac{d^2}{dx^2}+\frac{d^2}{dy^2}+\frac{d^2}{dz^2}\right)U=-\frac{\rho}{\varepsilon}+\frac{\overrightarrow{P}}{\varepsilon}, \tag{2}$$

where,
$\overrightarrow{P}$ is total i.e. piezoelectric and spontaneous polarization vector.

After the convergence of the self-consistent solver, the photocurrent and the dark current of the the device are calculated [26]. The multiplication factor or gain, $M$ can be expressed as,

$$M=\frac{I_M}{I_0}, \tag{3}$$

where, $I_M$ is the multiplied photocurrent and $I_0$ is the mean unmultiplied photocurrent.

After that, responsivity of the simulated APD is calculated as follows,

$$R=\frac{I_0}{P}, \tag{4}$$

where, $P$ is the input power for the back illuminated APD.

Next, the quantum efficiency of the solar-blind SAM APD is obtained by,

$$\eta=\frac{Rh\nu}{q}, \tag{5}$$

where, $h$ is Planck's constant and $\nu$ is frequency of the illuminating light.

The ratio of ionization coefficient of hole and that of electron is denoted as $k$, and determined as following,

$$k=\frac{\beta}{\alpha}, \tag{6}$$

where, $\beta$ is hole ionization coefficient and $\alpha$ is electron ionization coefficient which are extracted from [27].

Finally, the figure of merit, excess noise factor, F, which is the point of interest in this study is calculated as,

$$F=M[1+\left(\frac{1-k}{k}\right)\left(\frac{M-1}{M}\right)^2], \tag{7}$$

These APD equations are shown in details with derivation in [28].

## III. Results and Discussions

At first, we simulate the device using the 2D solver to find the transport characteristics of both the conventional and the proposed AlGaN APDs. The device is a back illuminated solar-blind SAM APD, and so for simulation, light illumination is specified to be directed from the bottom with a solar-blind wavelength of 275 nm. The simulated dark current and the photocurrent of the conventional and the proposed devices with variation of reverse voltages are shown in Fig. 3. It is obvious that the photocurrent is significantly improved for the proposed device. At low reverse voltage of 20 V, the conventional APD shows a photocurrent of $1.06\times10^{-8}$ A and the proposed one shows a photocurrent of $1.62\times10^{-8}$ A. Therefore, photocurrent is increased about 52%. However, at this voltage, dark current decreases from $1.53\times10^{-12}$ A to $1.45\times10^{-12}$ in the proposed device which indicates a change of 5% only. The opposite direction of change in the photocurrent and that in the dark current suggests that enhanced polarization has increased

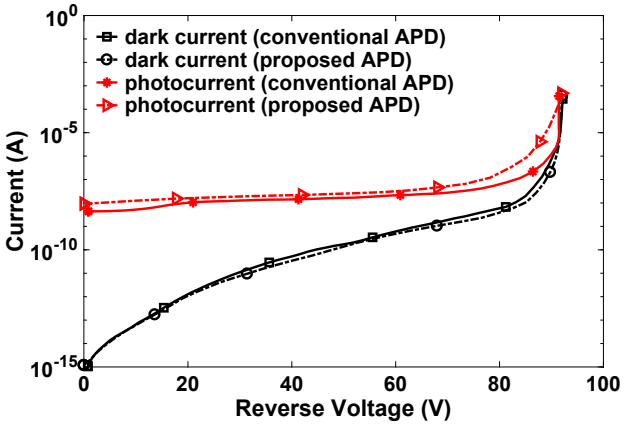


Fig. 3. Variation of photocurrent and dark current of both the conventional and the proposed devices with change in reverse voltage

the photocurrent, whereas low excess noise has decreased the dark current in the proposed APD. Both these changes indicate improvement in APD characteristics. Before the high breakdown voltage region, this improvement becomes more significant. For example, at 80 V reverse voltage, photocurrent increases from $7.73\times10^{-8}$ A to $3.41\times10^{-8}$ A in the proposed device with a rate of change of 126%, which is almost double compared to the case of 20 V. Also, the dark current at high reverse voltage (80 V) decreases rapidly from $5.5\times10^{-9}$ A to $3.77\times10^{-9}$ A in the proposed device indicating a rate of change of 45%. High reverse voltage enhances the polarization charge density in the proposed device even more to make photocurrent rise rapidly. On the other hand, the conventional device suffers more from impact ionization generated excess noise at high reverse voltage which is a strong function of applied reverse voltage and the resultant electric field. Since the proposed device shows more improvement (decrease) in dark current at high reverse voltage, it indicates that the proposed device has significant immunity to excess noise.

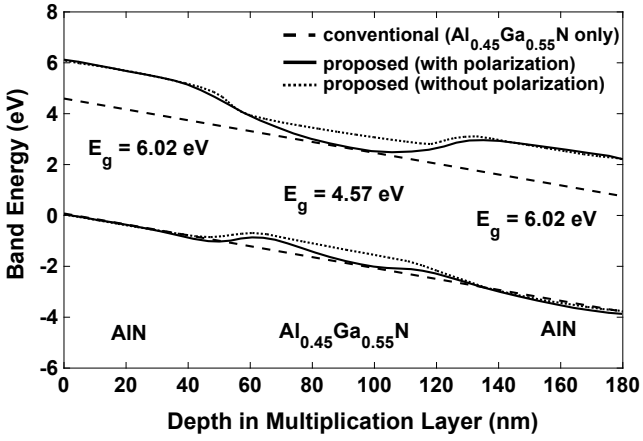


Fig. 4. Simulated energy band diagram of the conventional and the proposed devices under equilibrium condition

To investigate the physics behind the two-way performance improvement as indicated in Fig. 3, the energy band diagram of the multiplication layer of the back illuminated AlGaN APD simulated at zero bias is shown in Fig. 4. For the conventional device, the band diagram is nothing but a homogeneous bandgap of 4.57 eV without any discontinuity. The proposed

APD is designed with an $i$-$Al_{0.45}Ga_{0.55}N$ layer sandwiched between two $i$-AlN layers. It is well known that AlGaN/AlN heterostructure provides strong spontaneous and piezoelectric polarization at the interface. The $p$-$Al_{0.3}Ga_{0.7}N$ layer at the top provides negative polarization sheet charge at its interface to align the polarization electric field in the same direction as the applied reverse bias field. The proposed device is simulated with and without polarization effect by keeping and dropping the $\overrightarrow{P}$ term of (2) respectively and the results are shown in the figure simultaneously. When polarization is considered, the band diagram becomes much steeper with polarization sheet charge density of $6 \times 10^{-12} cm^{-2}$ at the interface. As a result, holes find easier path of transport and the resultant photocurrent increases. Increasing the reverse bias increases the steepness as polarization electric field is enhanced which is in the same direction of the applied reverse bias field. Thus, inserting AlN in the multiplication layer in order to reduce excess noise has a substantial benefit of enhanced polarization charge which increases photocurrent in the proposed design.

Moreover, the energy band diagram indicates that there is a quantum well formed in the multiplication layer due to the difference in the bandgaps of AlN and $Al_{0.45}Ga_{0.55}N$ layers. The well has a lower impact ionization threshold energy [8] with respect to its side layers and so impact ionization occurs in this well which ensures optimum multiplication. On the other hand, restricted impact ionization in the AlN side layers with higher impact ionization threshold energy ensures low excess noise in the proposed AlGaN solar-blind SAM APD.

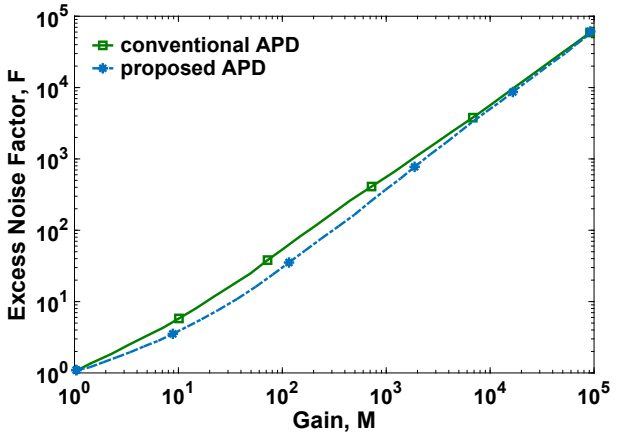


Fig. 5. Comparison of excess noise factor in the conventional and the proposed devices at 3 MV/cm electric field ($k$ = 75)

To demonstrate the efficacy of the proposed APD in reducing excess noise, using (7), a plot of excess noise factor, $F$ with respect to multiplication gain, $M$ is shown in Fig. 5. The characteristics impact ionization ratio, $k$ = 75 is considered in the simulation for the conventional device which is defined for $Al_{0.45}Ga_{0.55}N$ at the critical electric field (3 MV/cm) for breakdown [22]. The figure depicts that the proposed device successfully reduces the excess noise exploiting the higher impact ionization threshold energy of the side layers. For example, for gain, $M$ = 1000, the excess noise factor reduces from $F$ = 577 to $F$ = 375 at a decrease rate of about 35%. At very high gain, however, the difference tends to diminish as it indicates a large amount of impact ionization in the multiplication layer.

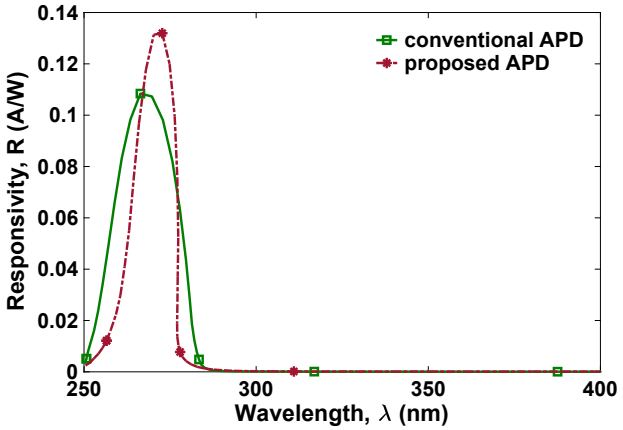


Fig. 6. Comparison of responsivity with respect to the wave length of back illumination in the conventional and the proposed devices

The proposed solar-blind AlGaN SAM APD is superior to the conventional ones in terms of responsivity and quantum efficiency. The responsivity of an APD represents how much photocurrent is generated using a certain amount of input power and is a figure of merit that should be increased. Fig. 6 shows the simulated responsivity of the conventional and the proposed APDs with respect to the wavelength of back illumination. The conventional APD shows maximum responsivity of 0.1084 A/W at the wavelength of 266 nm. On the other hand, the proposed APD shows maximum responsivity of 0.1319 A/W at a wavelength of 270 nm. Thus the proposed AlGaN SAM APD retains solar-blind property with about 22% better responsivity.

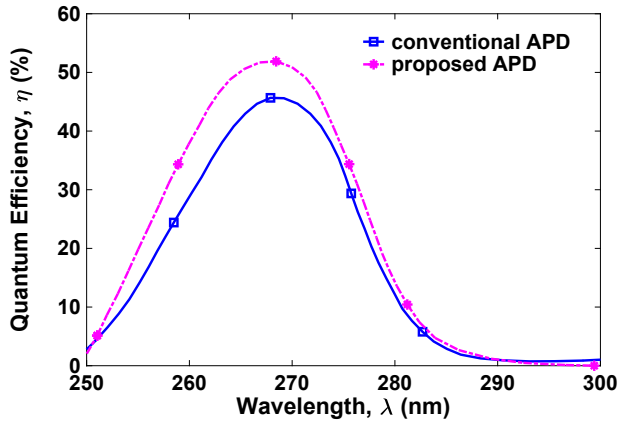


Fig. 7. Comparison of quantum efficiency with respect to the wave length of back illumination in the conventional and the proposed devices

Fig. 7 shows another important figure of merit, quantum efficiency with respect to the wavelength of back illumination. The simulated conventional APD works most efficiently ($\eta$ = 45.66%) at a wavelength of 268 nm. A better efficiency ($\eta$ = 51.88%) is obtained in the proposed APD at a wavelength of 268 nm. Therefore, the proposed AlGaN SAM APD is a better solar-blind APD than the conventional one with higher efficiency.

## IV. Conclusion

We have presented how excess noise factor in a solar-blind back illuminated AlGaN separate absorption and multiplication avalanche photodiode (SAM APD) can be suppressed

using multiplication layer engineering. It is shown that the excess noise can be minimized to a great extent by using high band gap material as side layers in the multiplication region. Exploiting the polarization charge induced at the layer interface, photocurrent is improved in the proposed device. Moreover, reduced excess noise ensures low dark current. Excellent solar-blind property is retained with better responsivity and higher efficiency. The proposed device would be helpful in further research to design more improved AlGaN solar-blind SAM APDs for UV applications.

## REFERENCES


[1] A. K. Ganguly, A. Ganguly, M. Bhoumic, and A. Ganguly, "High-Speed Metal-Semiconductor-Metal Photo diode," in *Industrial and Information Systems, 2008. ICIIS 2008. IEEE Region 10 and the Third international Conference on*. IEEE, 2008, pp. 1–4.

[2] H. W. Ruegg, "An optimized avalanche photodiode," *IEEE Transactions on Electron Devices*, vol. 14, no. 5, pp. 239–251, 1967.

[3] Wikipedia. (2017) Avalanche photodiode. [Online]. Available: https://en.wikipedia.org/wiki/Avalanche_photodiode

[4] N. Susa, H. Nakagome, H. Ando, and H. Kanbe, "Characteristics in InGaAs/InP avalanche photodiodes with separated absorption and multiplication regions," *IEEE Journal of Quantum Electronics*, vol. 17, no. 2, pp. 243–250, 1981.

[5] M. N. A. Aadit and U. S. Khan, "Stark effect on InP-InGaAs separate absorption and multiplication avalanche photodiodes," in *Informatics, Electronics and Vision (ICIEV), 2016 5th International Conference on*. IEEE, 2016, pp. 703–707.

[6] F. Osaka and T. Mikawa, "Excess noise design of InP/GaInAsP/GaInAs avalanche photodiodes," *IEEE journal of quantum electronics*, vol. 22, no. 3, pp. 471–478, 1986.

[7] N.-F. Shih, "Excess noise analysis of separate absorption multiplication region superlattice avalanche photodiodes," *IEEE Transactions on Electron Devices*, vol. 48, no. 6, pp. 1075–1081, 2001.

[8] F. Emami and M. F. Tehrani, "Noise reduction and simulation in Avalanche Photodiodes," *Int. J. Commun.*, vol. 2, no. 1, pp. 17–26, 2008.

[9] M. M. Hayat, Z. Chen, and M. A. Karim, "An analytical approximation for the excess noise factor of avalanche photodiodes with dead space," *IEEE Electron Device Letters*, vol. 20, no. 7, pp. 344–347, 1999.

[10] S. Wang, F. Ma, X. Li, R. Sidhu, X. Zheng, X. Sun, A. L. Holmes, and J. C. Campbell, "Ultra-low noise avalanche photodiodes with a "centered-well" multiplication region," *IEEE journal of quantum electronics*, vol. 39, no. 2, pp. 375–378, 2003.

[11] Z. Shao, D. Chen, Y. Liu, H. Lu, R. Zhang, Y. Zheng, L. Li, and K. Dong, "Significant performance improvement in AlGaN solar-blind avalanche photodiodes by exploiting the built-in polarization electric field," *IEEE Journal of Selected Topics in Quantum Electronics*, vol. 20, no. 6, pp. 187–192, 2014.

[12] E. Cicek, Z. Vashaei, R. McClintock, C. Bayram, and M. Razeghi, "Geiger-mode operation of ultraviolet avalanche photodiodes grown on sapphire and free-standing GaN substrates," *Applied Physics Letters*, vol. 96, no. 26, p. 261107, 2010.

[13] M. Razeghi, "Short-wavelength solar-blind detectors-status, prospects, and markets," *Proceedings of the IEEE*, vol. 90, no. 6, pp. 1006–1014, 2002.

[14] P. Kung, A. Yasan, R. McClintock, S. Darvish, K. Mi, and M. Razeghi, "Future of $Al_xGa_{1-x}N$ materials and device technology for ultraviolet photodetectors," in *Proc. SPIE*, vol. 4650, 2002, pp. 199–206.

[15] J. Pau, C. Bayram, R. McClintock, M. Razeghi, and D. Silversmith, "Back-illuminated separate absorption and multiplication GaN avalanche photodiodes," *Applied Physics Letters*, vol. 92, no. 10, p. 101120, 2008.

[16] Q. Cai, M. Ge, J. Xue, L. Hu, D. Chen, H. Lu, R. Zhang, and Y. Zheng, "An Improved Design for Solar-Blind AlGaN Avalanche Photodiodes," *IEEE Photonics Journal*, vol. 9, no. 4, pp. 1–7, 2017.

[17] H. You, Z. Shao, Y. Wang, L. Hu, D. Chen, H. Lu, R. Zhang, and Y. Zheng, "Fine Control of the Electric Field Distribution in the Heterostructure Multiplication Region of AlGaN Avalanche Photodiodes," *IEEE Photonics Journal*, vol. 9, no. 3, pp. 1–7, 2017.

[18] Z. G. Shao, D. J. Chen, H. Lu, R. Zhang, W. J. Luo, Y. D. Zheng, L. Li, Z. H. Li *et al.*, "High-gain AlGaN solar-blind avalanche photodiodes," *IEEE Electron Device Letters*, vol. 35, no. 3, pp. 372–374, 2014.

[19] K. X. Dong, J. Wang, Y. Y. Zhang, X. C. Cheng, and M. Y. Ou, "Back-illuminated GaN/AlGaN solar-blind avalanche photodiodes," *IEEE Photonics Technology Letters*, vol. 27, no. 3, pp. 272–275, 2015.

[20] K. X. Dong, D. J. Chen, H. Lu, B. Liu, P. Han, R. Zhang, and Y. D. Zheng, "Exploitation of polarization in back-illuminated AlGaN avalanche photodiodes," *IEEE Photonics Technology Letters*, vol. 25, no. 15, pp. 1510–1513, 2013.

[21] C. Chang, J. Xu, and X. Li, "Noise characteristic of AlGaN-based solar-blind UV avalanche photodiodes," in *Selected Proceedings of the Photoelectronic Technology Committee Conferences held August-October 2014*. International Society for Optics and Photonics, 2015, pp. 952 225–952 225.

[22] M. Hou, Z. Qin, C. He, L. Wei, F. Xu, X. Wang, and B. Shen, "Study on AlGaN P-I-N-I-N solar-blind avalanche photodiodes with AlGaN multiplication layer," *Electronic Materials Letters*, vol. 11, no. 6, pp. 1053–1058, 2015.

[23] V. Kuryatkov, A. Chandolu, B. Borisov, G. Kipshidze, K. Zhu, S. Nikishin, H. Temkin, and M. Holtz, "Solar-blind ultraviolet photodetectors based on superlattices of AlN/AlGa(In)N," *Applied physics letters*, vol. 82, no. 9, pp. 1323–1325, 2003.

[24] C. S. Inc. (2017) Crosslight Apsys. [Online]. Available: http://crosslight.com/products/apsys/

[25] X. Wang, B. Wang, L. Hou, W. Xie, X. Chen, and M. Pan, "Photoresponse simulation for separate absorption and multiplication GaN/AlGaN avalanche photodiode," in *Numerical Simulation of Optoelectronic Devices (NUSOD), 2014 14th International Conference on*. IEEE, 2014, pp. 31–32.

[26] B. Van Zeghbroeck, "Principles of semiconductor devices," *Colarado University*, 2004.

[27] E. Bellotti, F. Bertazzi, S. Shishehchi, M. Matsubara, and M. Goano, "Theory of carriers transport in III-Nitride materials: State of the art and future outlook," *IEEE Transactions on Electron Devices*, vol. 60, no. 10, pp. 3204–3215, 2013.

[28] G. Keiser, *Optical Fiber Communications*. John Wiley and Sons, Inc., 2003.

# Highly Confined Plasmon Modes in a Finite Nonplanar Hybrid Structure

Md. Abdullah-Al-Noman Sarker, K. B. M. Rakib Hasan, and M. Shah Alam†

Department of Electrical and Electronic Engineering
Bangladesh University of Engineering and Technology (BUET)
Dhaka-1205, Bangladesh

†Corresponding author (shalam@eee.buet.ac.bd)

***Abstract*—The full vectorial numerical analysis of finite non-planar hybrid structure reveals that both highly confined bound surface plasmon modes and leaky surface plasmon modes are supported in such structure. The extremely low effective mode area associated with highly confined mode makes the waveguide a hotspot source and the tunable antenna mode which is a subdivision of leaky mode is useful for both beam steering devices and free space coupling. The dispersion propertiy, propagation length, and the confinement factor of these plasmon modes have been analyzed and presented in this study.**

***Index Terms*—Surface plasmon polariton (SPP), hybridness, metal-insulator-metal (MIM) structure, propagation length, free-space radiation coupling.**

## I. Introduction

Recently, the transverse magnetic (TM) polarized surface plasmon (SP) mode propagating along the dielectric-metal interfaces with evanescent fields in both sides is being investigated extensively. The sub-wavelength mode confinement property of plasmonic waveguides has made it a promising alternative to conventional dielectric waveguides. Insulator-metal-insulator (IMI) multilayer structure has been reported as long-range SP waveguides previously [1]. Also, finite planar and metal-insulator-metal (MIM) SP waveguides have been studied numerically and found to offer higher confinement factor at the expense of relatively high loss [2]-[5].

In this work, a finite, nonplanar hybrid waveguide consisting of gold and zinc oxide as metal and insulator, respectively, has been studied. Both gold and zinc oxide operate in the visible, near visible and telecom range of spectrum. This hybrid structure has been analyzed exhaustively to find modal confinement, bound and leaky modes, effective area, propagation length and loss using full vectorial method. The analysis shows that this structure excites antenna like mode that allows angle dependent free space interaction with plasmonic devices, suggesting steerable input-output coupling functions, and consequently, the waveguide will interact with the free space without the prism and grating. The extremely low effective area of this waveguide can be exploited to create a plasmonic hotspot [6]-[8].

## II. Waveguide Structure And Analysis Technique

The schematic of the multilayer cylindrical structure comprising with gold-zinc oxide-gold (Au-ZnO-Au) is shown in Fig. 1. The radius of central gold nanowire is $r_1$, while the zinc oxide coating has an outer radius, $r_2$, and the z axis has been considered as the direction of wave propagation. The full vector finite element method (VFEM) formulation correctly employing the boundary condition at the dielectric interfaces has been used here as the optical modes in such structure are usually hybrid modes offering polarization mixing and all the components of **E** and **H**-fields are existing. To terminate the computational window, a cylindrical perfectly matched layer (PML) has been considered around the gold boundary.

The dispersion relation, describing the effect of dispersion on the properties of a wave traveling in a medium, is one of the factors determining the modal properties of the waveguide. The complex refractive index of gold versus the operating wavelength is shown in Fig. 2. The dispersion here has been obtained by an analytical formula that incorporates the Lorentz-Drude Model. The effect of finite cross section affecting the mean free path of free electron in the nanowire has been taken into account by including the damping frequency [9]-[10]. The complex refractive index of the

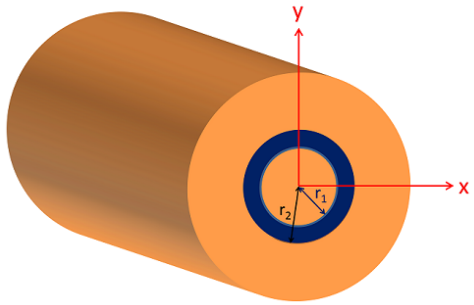


Fig.1: Schematic diagram of gold nanowire with ZnO coating.

978-1-5386-3374-8/17/$31.00 ©2017 IEEE

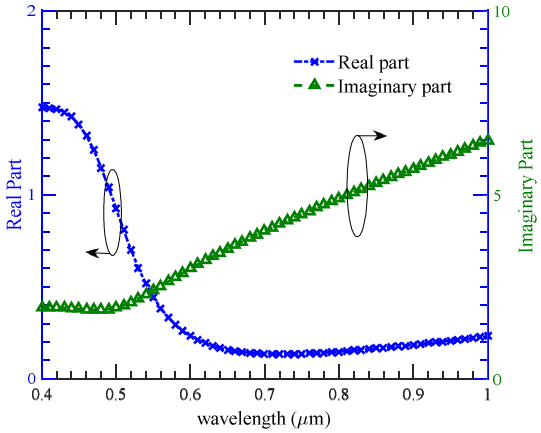


Fig. 2: Refractive index of gold.

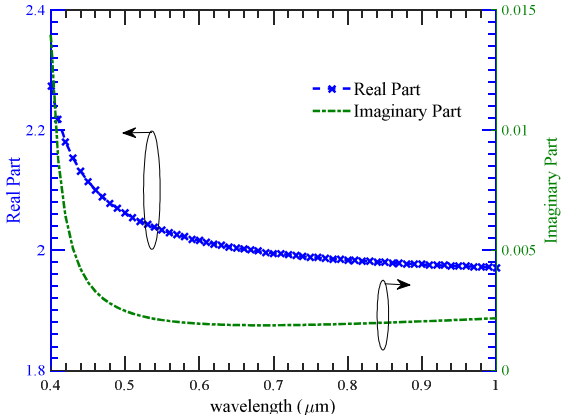


Fig. 3: Refractive index of ZnO.

interlayered oxide semiconductor (ZnO) has been calculated using the formulation as given in [11] and the fitting parameters has been obtained from [12]-[13]. As shown in Fig. 3, the index of ZnO varies from 2.2 to 2.0 in the wavelength range of 0.4 to 1.0 μm. Although the imaginary part of the index is nearly zero, it has been considered in this work.

## III. Results And Discussion

### A. Hybrid Mode Index

The effective index of Plasmon mode of a waveguide structure depends on the dispersion relation of the guiding materials. The real part of effective index of plasmonic modes of the MIM structure of Fig. 1 is shown in Fig. 4, where $r_1$= 50 nm and $r_2$= 65 nm, has been shown. The quasi TM polarized modes excited in this structure are either even or odd [14]-[15] and we have limited our discussion to the fundamental odd $H_{11}^{y}$, fundamental even $H_{11}^{y}$ and hybrid even $H_{21}^{y}$ modes. It has been noticed that at around λ = 0.50 μm, the effective index exceeds the refractive index of ZnO and the modes propagate as bound SPP. The effective index of different surface plasmon modes follow almost identical trends having the resonant peak at around λ = 0.56 μm. This phenomenon can be explained by constructing a single interface gold-zinc oxide waveguide and looking at the maxima of the polarizability

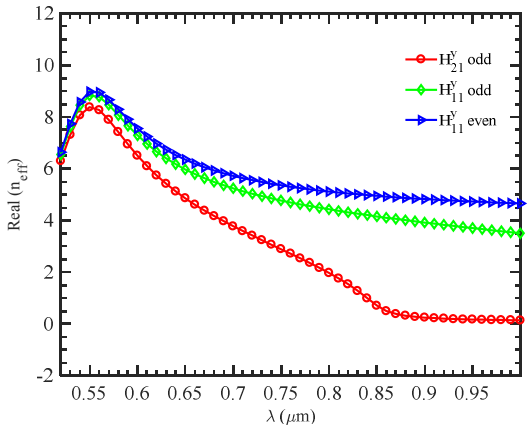


Fig. 4: Effective index of different modes.

function at Au-ZnO interface as an MIM structure can be viewed as a cascaded form of two metal-insulator single interfaces where modes of the two interfaces couple together [14], [16].

To explain the relation between effective index and polarizability factor, a gold nanowire having cross sectional area, A, has been considered, where the z-axis is parallel to its axis, the dielectric function is $\varepsilon_{mr}+j\varepsilon_{mi}$, and the wire is coated with ZnO having dielectric constant $\varepsilon_d$. The electric polarizabilities along the x, y and z-directions are calculated using the equations [2], [15],

$$\alpha_x = \alpha_y = 2A\frac{\varepsilon_{mr} + j\varepsilon_{mi} - \varepsilon_d}{\varepsilon_{mr} + j\varepsilon_{mi} + \varepsilon_d} \tag{2}$$

and

$$\alpha_z = A\left(\varepsilon_{mr} + j\varepsilon_{mi} - \varepsilon_d\right). \tag{3}$$

Using eqns. (2) and (3), the components of polarizability function with unit cross sectional area have been found for different wavelengths. The transverse components $\alpha_x$ or $\alpha_y$ show a maximum value at around λ = 0.56 μm. The transverse polarizabilities $\alpha_x$ and $\alpha_y$ correspond to the larger effective mode index around the value of λ = 0.56 μm.

### B. Power Distribution and Confinement

The power distribution of different plasmon modes in the MIM nanowire is shown in Fig. 5. Part (a) shows the power distribution of the odd $H_{11}^{y}$ plasmon mode at λ = 0.56 μm. It is seen that the power is confined only in the dielectric material, ZnO, having the peak at the inner interface and this profile is very common for fundamental mode. For fundamental $H_{11}^{y}$even mode, interestingly power is divided into two lobes and this is because of the even symmetric field distribution of the mode and this is shown in Fig. 5(b). It is clear from the figure that the peak is located on the inner interface and confined in the dielectric material and decreases monotonically towards *y* direction. The power distribution $S_z$ along z axis for odd $H_{21}^{y}$ is shown in Fig. 5(c). The power is confined in the dielectric material having the peak at the inner

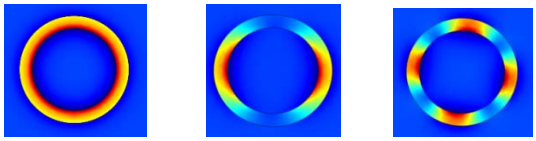

(a) (b) (c)

Fig. 5: $S_z$ for (a) $H_{11}^y$ odd, (b) $H_{11}^y$ even, (c) $H_{21}^y$odd.

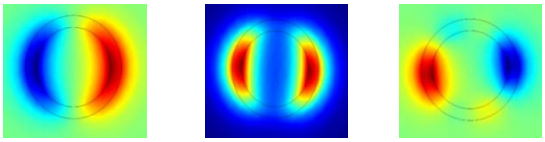

(a) (b) (c)

Fig. 6: $H_y$ field distribution for (a) $H_{11}^y$ odd, (b) $H_{11}^y$ even, (c) $H_{21}^y$odd.

interface and divided into four lobes. Fig. 6 shows the corresponding $H_y$ field patterns of the plasmon modes for the *y* polarized modes.

The percentage of power confined in metal region at different wavelengths is shown in Fig. 7. The confinement depicted in this figure represents portions of the total power present inside the metal, as the real part of the complex index of ZnO is larger than that of the gold. A larger portion of power remains in the interlayered dielectric in the lower wavelength region. Previously it has been shown that at around λ = 0.56 μm, the highest polarizability is obtained and thus the confinement factor shows the pattern of the plasmonic resonance [16]. Following the resonant peak, the confinement factor reduces monotonically for fundamental mode as a function of the wavelength. In case of hybrid $H_{21}^y$ mode the effective index shows slight transition that contributes to the transition of confinement factor at λ = 0.85 μm.

### C. *Effective Modal Area*

The effective modal area of an optical waveguide can be defined as the equivalent cross-sectional area through which electromagnetic power propagates. It is calculated by using the following equation,

$$A_{eff} = \frac{(\iint_s E_{norm}^2 ds)^2}{\iint_s E_{norm}^4 ds}, \qquad (4)$$

where, $E_{norm}$ is the normalized electric field intensity and $\iint(.)ds$ indicates integration over the cross sectional area. Fig. 8 shows the effective area of different modes with respect to wavelength. It is clear from the figure that effective area decreases with increasing wavelength. This extremely low effective area can be exploited to make plasmonic hotspot and high confinement solar devices [17].

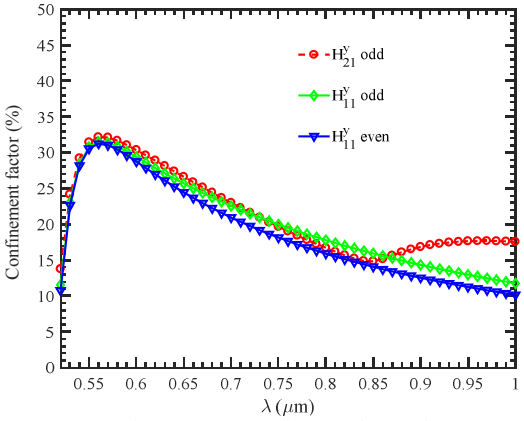


Fig. 7: Power confinement in metal.

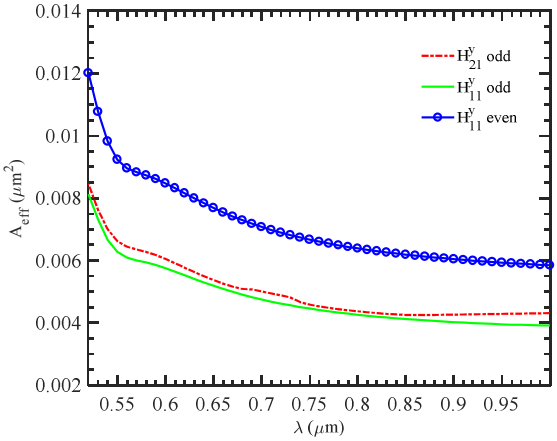


Fig. 8: Effective area of plasmonic modes.

### D. *Attenuation Characteristics and Figure of Merits*

The attenuation of the waveguide is quantified by calculating the loss as,

$$loss = -(2 \times k_0 \times \kappa_{eff}), \qquad (5)$$

where, $k_0 = 2\pi/\lambda_0$ and $\kappa_{eff}$ is the imaginary part of the mode effective index. As mentioned previously that the confinement factor obtains a peak value at around λ = 0.56 μm, the loss also show resonance peaks around this same wavelength.

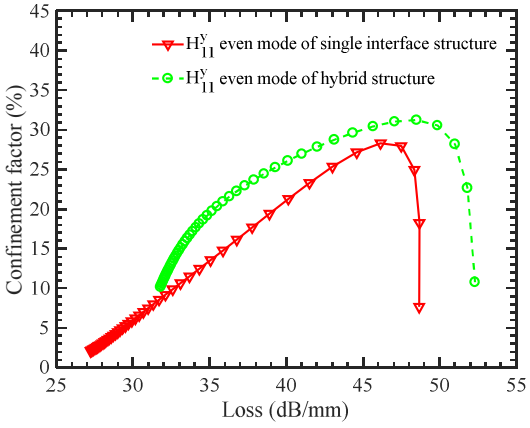


Fig. 9: Representative figure of merit (confinement versus loss).

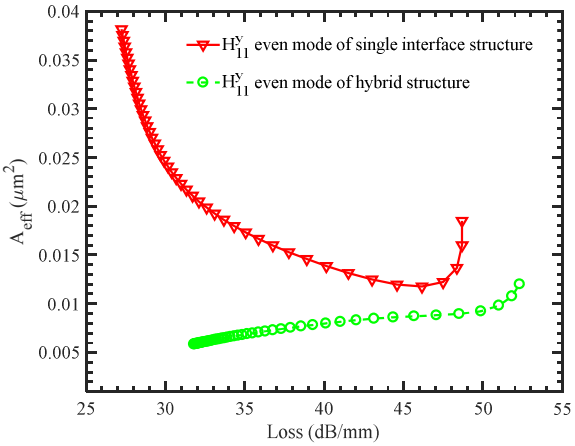


Fig. 10: Figure of merit on the basis of mode area versus loss.

Fig. 9 shows that this hybrid structure offers higher confinement at the same loss with respect to single interface gold nanowire as proposed in [16] and other structures also. Fig. 10 shows that this hybrid structure also tenders extremely low effective area suggesting that it can be used where extremely high confinement is required.

Leaky mode which has been reported to exist in planar MIM structure [14] has also been found in this nonplanar geometry. The exponential increment of fields in the bounding media makes leaky modes mathematically valid, however, the improper solution of the problem used to find guided mode as explained in [2]. The physical existence of proper or improper solution is obtained by the real part of the solution of effective index and the index of outermost bounding material and this gives rise to spectral gap in dispersion. Thus, when the $H_{21}^y$ mode crosses the light line, it is changed into a leaky mode from bound mode and a spectral gap is resulted and this spectral gap can be tuned by simple thickness manipulation of ZnO. Also, the antenna mode, a subdivision of leaky mode region, exists when $\mathrm{Re}\{n_{eff}\}>\mathrm{Im}\{n_{eff}\}$ and is characterized by propagation of energy out of the guide. By manipulating the outer gold layer thickness it has been found that this structure supports the existence of antenna mode also.

## IV. Conclusion

The modal analysis of gold nanowire based MIM structure with zinc oxide as insulating intermediate layer have been carried out by using a full-vectorial FEM. The lower order modes have been studied and illustrated. Below the wavelength of 0.48 μm, the magnitude of the dielectric function of zinc oxide is larger than that of the gold and with the increase in wavelength the negative part of dielectric constant of gold increases exhibiting a resonance peak at around $\lambda = 0.56$ μm and leads the transverse polarizability to a maximum value. Also, the effective indices of fundamental and lower order hybrid modes show resonant peak around this wavelength. In case of MIM structures, the modes generated at the inner and outer interfaces couple and give rise to the highly confined plasmon modes. Though this nonplanar structure suffers from a relatively higher loss, its confinement in the metallic gold layer is way more than other structures like a planar MIM structure. Furthermore, the structure can excite localized plasmonic mode in a moderately wide frequency range that falls in the visible light wavelength range and infrared region. So, the structure can be used in high confinement solar cell design. The extremely low effective area offers the chance of creating plasmonic hotspot at lower loss.

## References


[1] R. Charbonneau, N. Lahoud, G. Mattiussi, and P. Berini, "Demonstration of integrated optics elements based on long-ranging surface plasmon polaritons," *Opt. Expr*., vol. 13, no. 3, pp. 977-984, Feb. 2005.

[2] J. Chen, G. A. Smolyakov, S. R. J. Brueck, and K. J. Malloy, "Surface plasmon modes of finite, planar, metal-insulator-metal plasmonic waveguide," *Opt. Expr.,* vol. 16, no. 19, pp. 14902–14909, Sep. 2008.

[3] R. Hao, E. Li, and X. Wei, "Two-dimensional light conf nement in cross-index-modulation plasmonic waveguides," *Opt. Lett.,* vol. 37, pp. 2934–2936, 2012.

[4] G. Veronis, Z. Yu, S.E. Kocabas, D.A.B. Miller, M. L. Brongersma, and S. Fan, "Metal-dielectric-metal plasmonic waveguide devices for manipulating light at the nanoscale," *Chin. Opt. Lett*., vol. 7, no. 4, Apr. 2009.

[5] M. Z. Alam, J. S. Aitchison, and M. A. Mojahedi, "Marriage of convenience: Hybridization of surface plasmon and dielectric waveguide modes," *Laser Phot. Rev.,* vol. 8, no. 3, pp. 394–408, May 2014.

[6] R. F. Oulton, V. J. Sorger, D. A. Genov, D. F. P. Pile, and X. Zhang, "A hybrid plasmonic waveguide for sub-wavelength confinement and long-range propagation," *Nature Photon*., vol. **2**, pp. 496 – 500, Aug. 2008.

[7] R. F. Oulton, G. Bartal, D. F. P. Pile, and X. Zhang, "Confinement and propagation characteristics of sub-wavelength plasmonic modes," *N. J. of Phy.,* vol. 10, Oct. 2008.

[8] W. Yao, C. Sun, Q. Gong, and Jianjun, "Controlling surface-plasmon-polaritons launching with hot spot cylindrical waves in a metallic slit structure," Nanotech. , vol. 27, no. 38, Aug. 2016.

[9] P.G. Etchegoin, E.C.L. Ru, and M. Meyer, "An analytic model for the optical properties of gold," *Jour. of Chem. Phy*., vol. 125, no. 16, Nov. 2006.

[10] P.G. Etchegoin, E. C. L. Ru, and M. Meyer, "Erratum: An analytic model for the optical properties of gold," *Jour. of Chem. Phy*., vol. 127, no. 18, Nov. 2007.

[11] T. Holden, P. Ram, F. H. Pollak, J. L. Freeouf, B. X. Yang, and M. C. Tamargo, "Spectral ellipsometry investigation of $Zn_{0.53}Cd_{0.47}Se$ lattice matched to InP," *Phys. Rev. B*, vol. 56, no. 7, pp. 4037– 4046, Aug. 1997.

[12] G. E. Jellison and L. A. Boatner, "Optical functions of uniaxial ZnO determined by generalized ellipsometry," *Phys. Rev. B*, vol. 58, no. 7, pp. 3586–3589, Aug. 1998.

[13] G. E. Jellison, "Erratum: optical functions of uniaxial ZnO determined by generalized ellipsometry," *Phys. Rev. B*, vol. 65, no. 4, Jan. 2002.

[14] S. A. Maier (2007), Plasmonics: Fundamentals and Applications, (Springer).

[15] S. Aldawsari, L. Wei, and W. K. Liu, "Theoretical study of hybrid guided modes in a multilayer symmetrical planar plasmonic waveguide," *J. Lightwave Technol*., vol. 33, pp. 3198–3206, 2015.

[16] K. Namassivayane, H. Tanvir, A. Quadir, B. M. A. Rahman, and K.T.V. Grattan, "Study of modal properties in gold nanowire with ZnO cladding by using the finite element method," *Appl. Opt.*, vol. 50, no. 25, pp. E177-E183, Sept. 2011.

[17] D. Daoxin, W. Hao, and W. Zhang, "Utilization of Field Enhancement in Plasmonic Waveguides for Sub-wavelength Light-Guiding, Polarization Handling, Heating, and Optical Sensing," *Materials,* vol. 8, pp. 6772-6791, Oct. 2015.

# Study of Surface Plasmon Polariton Mode in Coupled Elliptical Nanowires

K. B. M. Rakib Hasan, Md. Abdullah-Al-Noman Sarker, and M. Shah Alam†

Department of Electrical and Electronic Engineering
Bangladesh University of Engineering and Technology (BUET)
Dhaka-1205, Bangladesh

†Corresponding author ( shalam@eee.buet.ac.bd)

***Abstract*—Modal solutions of surface plasmon polariton mode in a coupled structure containing two identical elliptical gold nanowires at close vicinity embedded in ZnO dielectric have been obtained by using full-vectorial finite element method on the basis of E field. The tight confinement found here reveals the characteristics of MIM structure and large propagation length exhibits the property of IMI waveguide. Modal properties like the effective index, polarizabilities, field and power confinement, effective mode area and propagation length of some lower order plasmon modes have been analyzed to find potential applications.**

***Index Terms*—Coupled plasmon structure, hybrid mode, plasmon hotspot, effective area.**

## I. Introduction

Traditional electronic interconnects are not capable of meeting the colossal data carrying capacity requirement of a typical modern microprocessor that contains a legion of transistors. An apparent solution to this problem is to replace the electronic interconnects by conventional optical waveguides but the diffraction limit of light stanches that due to size mismatch of these two technologies at chip level. Scientists and researchers suggest sub-diffraction limited plasmonic waveguide integration with electronics and evolvement of hybrid chips able to take full advantage of both electronics and photonics [1]-[4]. Plasmonic waveguide thus renders a potential solution to this problem as it offers high speed data carrying capability along with some other interesting phenomena.

In high contrast optical sensing, surface enhanced Raman spectroscopy and to manipulate the SPP propagation of nearby waveguides strongly localized electromagnetic fields, generally known as plasmonic hotspots, are necessary [3], [5]. Thus the waveguide structures having sharp edges like metallic corners have been proposed so far as they can also form plasmon hotspots [5]-[12]. But sharp-edged waveguide fabrication at nanometer range requires very intricate technologies and hence they are cost inefficient. In this paper a smooth cornered metallic structure has been investigated and proposed to generate strongly localized mode. The designed structure tenders high confinement and extremely small effective area with comparatively large propagation length giving us the opportunity to propagate the SPP at substantial length with high confinement and also offers us the possibility of making plasmon hotspot exploiting its extremely low effective area. The significant modal properties like effective index, effective area, propagation length, mode size and loss associated with a coupled nanowire structure have been obtained in a full-vectorial finite element method.

## II. Design of the Coupled Structure

The coupled structure with two identical elliptical gold nanowires embedded in direct bandgap ZnO material is shown in Fig. 1. Each of the gold nanowire has a major axis length of 2a parallel to x direction and minor axis length of 2b parallel to y direction. d is the distance between the centers of the nanowires and the z axis has been regarded as the wave propagation axis. In order to calculate the modal solutions accurately full-vectorial formulation correctly employing the boundary condition at the metal-dielectric interfaces has been used here to study the waveguide. To terminate the computational window, a cylindrical perfectly matched layer (PML) has been considered around the cladding region.

The dispersion relation of conventional plasmonic material gold used in this study shows inter-band transition and to incorporate this transition an analytic formula considering Lorentz-Drude model has been used and obtained from [13]-[14]. Also, the damping frequencies arising from the comparable nanowire cross section with the mean free path of electron have been included in this model[13]-[15].The complex index of the dielectric medium (ZnO) has been found using the analysis presented in [16]and the fitting parameters has been obtained from [17]-[18].

## III. Results And Discussion

### A. Effective Index and Polarizabilities

The effective mode indices of plasmon waveguides depend on the operating wavelength since the comprising materials have a wavelength dependence of dielectric functions. The

978-1-5386-3374-8/17/$31.00 ©2017 IEEE

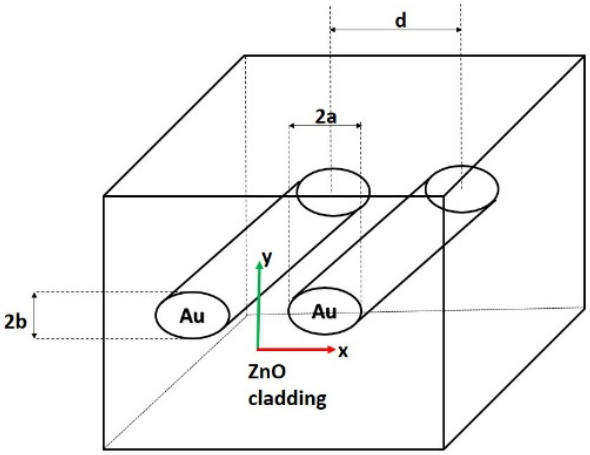


Fig.1: The schematic representation of the coupled nanowire.

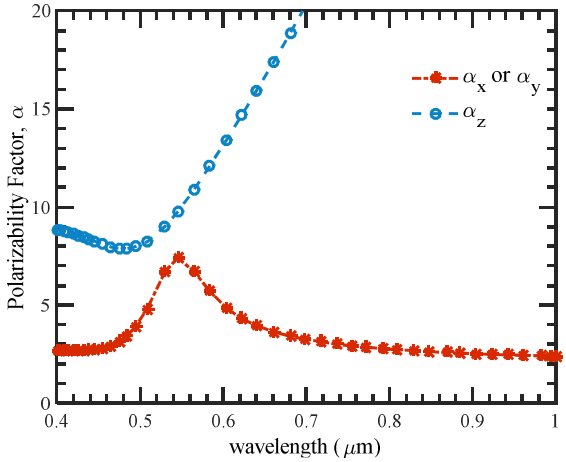


Fig. 3: Polarizability factor along different axes.

real part of complex effective mode index of plasmonic modes in the structure depicted in Fig. 1 with a= 120 nm b= 100 nm and d= 270 nm has been demonstrated in Fig. 2.The horizontally as well as vertically polarized modes excited in a single elliptical waveguide are non-degenerate in nature as the electromagnetic interactions between the surface charges along the x and y axes are not identical and this is unlike to a circular optical waveguide. When two elliptical nanowires are in close vicinity to each other the plasmon modes of the two single nanowires couple to generate coupled modes with intriguing modal properties that are not possible to generate in a single nanowire. To analyze the effect of coupling the effective mode index of the coupled structure has been compared with the $H_{11}^{y}$ odd mode which is fundamental mode for a single elliptical nanowire in ZnO cladding. In this coupled structure, it has been found that for λ> 0.52 μm the real part of effective index of all the modes exceeds the real part of refractive index of the surrounding dielectric medium and propagates as SPP mode [19].

Each of the SPP modes finds their resonant peak at around λ= 0.56μm and after the resonant peak mode indices reduces monotonically following the trend of the real part of index of

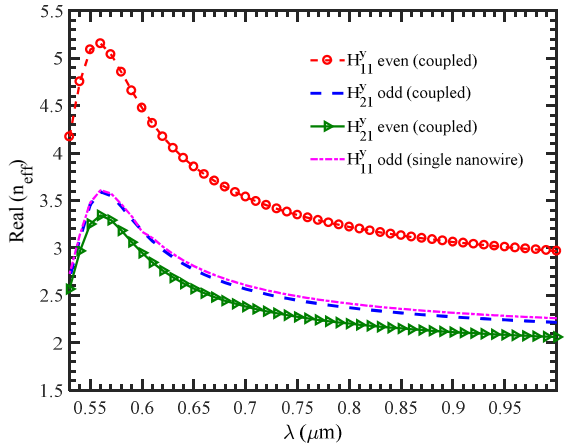


Fig. 2: Effective index of different modes.

ZnO. The resonant peak at 0.56μm wavelength can be attributed to the location of the maxima of transverse polarizability function for gold-ZnO interface [19]. The effective index of y polarized quasi-TM surface mode is linked to its polarizability factor. The electric polarizabilities along the transverse directions and longitudinal direction for a single circular nanowire is obtained from [15] and depicted in Fig. 3. From the figure it is clear that transverse polarizability component, $\alpha_y$ achieves its resonant maxima at around0.55μm which clearly points to the surface plasmon resonance at λ=0.56μm.

### *B. Field and Power Confinement*

Fig. 4 shows the transverse H-field patterns of different plasmon modes in the coupled structure as well as single nanowire. It has been found that this nonplanar coupled structure excites odd and even symmetric modes like planar MIM or IMI structures [4], [11]. The odd and even symmetric modes are the result of mode coupling of the adjacent interfaces [9]. One of the advantages of this coupled structure over planar structure is that it can excite odd and even modes even for a comparatively large separation between the nanowires due to the adjacent mode coupling like a planar MIM structure, but it cannot excite leaky plasmon modes.

Fig. 5 shows the Poynting vector along the z axis ($S_z$) of different plasmon modes at resonant frequency. Around the surface plasmon resonance, power confinement is more in the metallic region than in the dielectric cladding region and this is because of the significantly larger value of mode effective index than the refractive index of cladding in the smaller wavelength regime. With increasing wavelength, the mode index decreases monotonically resulting in less amount of power in the metal.

The effective index of plasmon mode quantifies surface confinement and is inversely proportional to the evanescent field decay length in the dielectric region from the interface [4]. The more the decay length, the less the surface confinement. Previously it has been shown in Fig. 4 that the

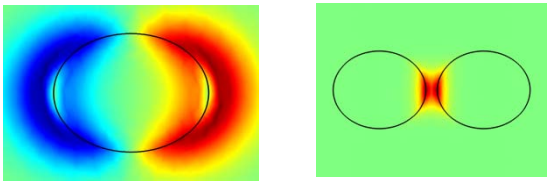

(a) (b)

Fig. 4: $H_y$field for (a)$H_{11}^{y}$ odd mode in single nanowire, (b) $H_{11}^{y}$even mode in coupled structure at λ=0.56μm.

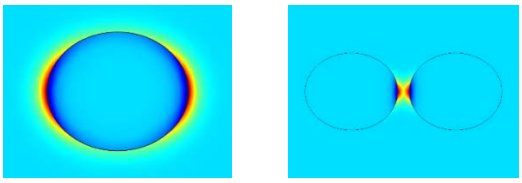

(a) (b)

Fig. 5: $S_z$ for (a)$H_{11}^{y}$ odd mode in single nanowire, (b)$H_{11}^{y}$even mode in coupled structure at λ=0.56μm.

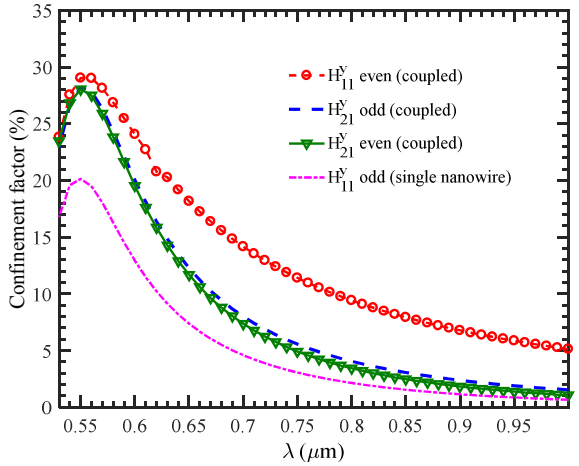


Fig. 6: Power confinement in metal.

coupled $H_{11}^{y}$even mode has the highest mode index and hence the most tightly confined SPP mode in the coupled structure. The power confinement factor curve shown in Fig. 6 is also in congruent to this. From the figure it is seen that fraction of power in the metal region is much larger than that of a single nanowire.

### *C. Effective Mode Area and Propagation Characteristics*

The effective mode area is the equivalent cross-sectional area through which electromagnetic power propagates. This parameter is calculated by,

$$A_{eff} = \frac{(\iint_s H_{norm}^2 ds)^2}{\iint_s H_{norm}^4 ds}, \quad (1)$$

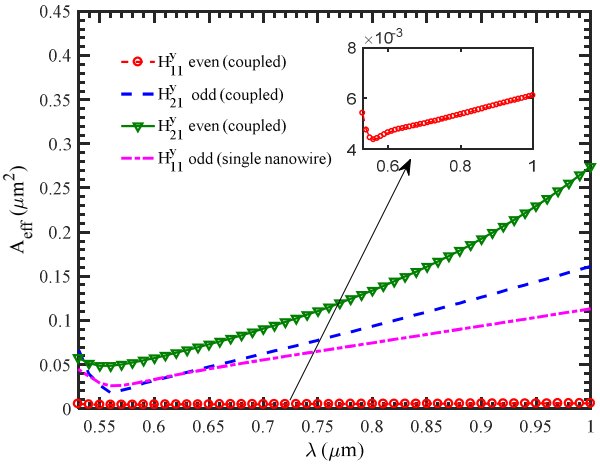


Fig. 7: Effective area of plasmonic modes.

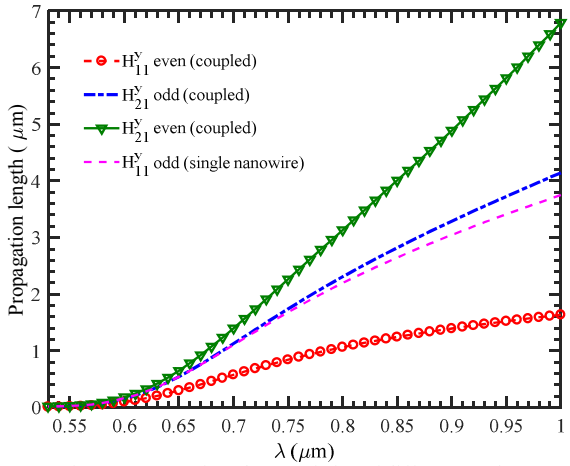


Fig. 8: Propagation characteristics of different modes.

where, $H_{norm}$ is the normalized magnetic field intensity and the $\iint(.)ds$ indicates integration over the cross sectional area. Fig. 7 shows the effective area of different modes with respect to wavelength. In conventional plasmonic waveguides the mode effective area is the minimum at SPP resonance wavelength as the modes are tightly confined. Plasmon modes achieve higher effective area at higher wavelength as the modes evolves into loosely bound nature at higher wavelength. One of the advantages of this elliptical structure is that it offers very small effective area for a large bandwidth and this has been shown in Fig. 7. The$H_{11}^{y}$even mode has a very small gradient, $\frac{d(A_{eff})}{d\lambda}$,as such it results into smallereffective area than that of the other modes excited in single nanowire waveguide structure. The reason behind this extremely low mode size is that in this case modes of two identical elliptical nanowires completely couple with each other in the tiny gap region and there is no power present elsewhere.

One of the novelties of this structure is that this structure working as nonplanar MIM structure offers high confinement [12] and working as two IMI structure coupled with each other

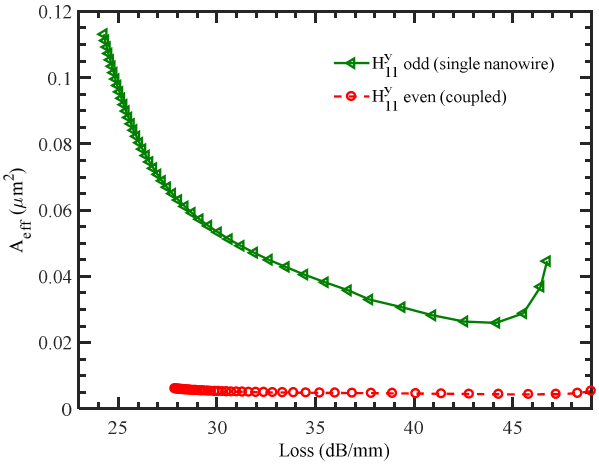


Fig. 9: Figure of merit.

tenders long propagation length [20]. The propagation length characteristics of this waveguide have been shown in Fig. 8. From the figure it is seen that propagation length is substantially larger than planar MIM and other coupled structures [10]-[11].

One way to compare different waveguide is to analyze their figure of merits. Fig. 9 depicts the figure of merit on the basis of effective area versus loss. The $H_{11}^{y}$ even mode in the coupled structure has noticeably smaller effective area at lower loss which is an evident of tight surface confinement of the mode unlike the single nanowire generated SPP modes. This is attributed by their much higher effective mode area at the same level of lower loss.

## IV. Conclusion

The coupled structure comprising of two gold nanowires embedded in zinc oxide dielectric medium has been investigated by means of E field based full VFEM to find the modal properties of some lower order SPP modes. The modal properties reveal that the fundamental $H_{11}^{y}$ even mode supported by this structure has very small effective mode area with a very small gradient of effective area dispersion. In the infrared regime the $H_{11}^{y}$ even mode of the coupled structure has more than 85% of total propagating power in the dielectric region having tight surface confinement with very small effective area resulting in a highly localized electromagnetic field. Therefore, this simple structure can be suggested to generate plasmonic hotspot in infrared and telecommunication window. For lower propagation length of the fundamental $H_{11}^{y}$ even mode, the structure is not suitable for waveguiding considering the modal properties of the gap mode although proper geometric modification may lead to be a plasmonic hotspot source for the higher order modes.

## References


[1] R. Zia, J. A. Schullar, A. Chandran, and M. L. Brongersma, "Plasmonics: The Next Chip-Scale Technology," *Materialstoday,* vol. 9, no. 7-8, pp. 20-27, Jul-Aug. 2006.

[2] G. Chen, H. Chen, M. Haurylau, N. N. Philippe, M. Fauchet, E. G. Friedman, and D. Albonesi, "Predictions of CMOS Compatible On-Chip Optical Interconnect," *Integ. the VLSI Jour., Elsevier*, vol. 40, no. 4, pp. 434-446, Jul. 2007.

[3] W. Yao, C. Sun, Q. Gong, and Jianjun, "Controlling surface-plasmon-polaritons launching with hot spot cylindrical waves in a metallic slit structure," *Nanotech.* , vol. 27, no. 38, Aug. 2016.

[4] S. A. Maier (2007), Plasmonics: Fundamentals and Applications, (Springer).

[5] R. F. Oulton, G. Bartal, D. F. P. Pile, and X. Zhang, "Confinement and propagation characteristics of sub-wavelength plasmonic modes," *N. J. of Phy.,* vol. 10, Oct. 2008

[6] D. Daoxin, W. Hao, and W. Zhang, "Utilization of Field Enhancement in Plasmonic Waveguides for Sub-wavelength Light-Guiding, Polarization Handling, Heating, and Optical Sensing," *Materials,* vol. 8, pp. 6772-6791, Oct. 2015.

[7] Y. Bian, Z. Zheng, X. Zhao, L. Liu, Y. Su, J. Liu, J. Zhu, and T. Zhou, "Hybrid Plasmon polariton guiding with tight mode conf nement in a V-shaped metal/dielectric groove," *J. Opt*. vol. 15, 2013.

[8] R. F. Oulton, V. J. Sorger, D. A. Genov, D. F. P. Pile, and X. Zhang, "A hybrid plasmonic waveguide for sub-wavelength confinement and long-range propagation," *Nat. Phot*., vol. 2, pp. 496 – 500, Aug. 2008.

[9] M. Z. Alam, J. S. Aitchison, and M. A. Mojahedi, "Marriage of convenience: Hybridization of surface plasmon and dielectric waveguide modes," *Laser Phot. Rev.,* vol. 8, no. 3, pp. 394–408, May 2014.

[10] R. Hao, E. Li, and X. Wei, "Two-dimensional light conf nement in cross-index-modulation plasmonic waveguides," *Opt. Lett.,* vol. 37, pp. 2934–2936, 2012.

[11] S. Aldawsari, L. Wei, and W. K. Liu, "Theoretical study of hybrid guided modes in a multilayer symmetrical planar plasmonic waveguide," *J. Lightwave Technol*., vol. 33, pp. 3198–3206, 2015.

[12] G. Veronis, Z. Yu, S. E. Kocabas, D. A. B. Miller, M. L. Brongersma, and S. Fan, "Metal-dielectric-metal plasmonic waveguide devices for manipulating light at the nanoscale," *Chin. Opt. Lett*., vol. 7, no. 4, Apr. 2009.

[13] P. G. Etchegoin, E. C. L. Ru, and M. Meyer, "Erratum: An analytic model for the optical properties of gold," *Jour. of Chem. Phy*., vol. 127, no. 18, Nov. 2007.

[14] J. A. Gordon and R. W. Ziolkowski, "The design and stimulated performance of a coated nano-particle laser," *Opt. Expr*., vol. 15, no. 5, pp. 2622–2653, Feb. 2007.

[15] T. Holden, P. Ram, F. H. Pollak, J. L. Freeouf, B. X. Yang, and M. C. Tamargo, "Spectral ellipsometry investigation of $Zn_{0.53}Cd_{0.47}Se$ lattice matched to InP," *Phys. Rev. B*, vol. 56, no. 7, pp. 4037– 4046, Aug. 1997.

[16] G. E. Jellison and L. A. Boatner, "Optical functions of uniaxial ZnO determined by generalized ellipsometry," *Phys. Rev. B*, vol. 58, no. 7, pp. 3586–3589, Aug. 1998.

[17] G. E. Jellison, "Erratum: optical functions of uniaxial ZnO determined by generalized ellipsometry," *Phys. Rev. B*, vol. 65, no. 4, Jan. 2002.

[18] S. Albaladejo, R. Gómez-Medina, L. S. Froufe-Pérez, H. Marinchio, R. Carminati, J. F. Torrado, G. Armelles, A. García-Martín, and J. J. Sáenz, "Radiative corrections to the polarizability tensor of an electrically small anisotropic dielectric particle," *Opt. Expr*., vol. 18, no. 4, pp. 3556–3567, Feb. 2010.

[19] K. Namassivayane, H. Tanvir, A. Quadir, B. M. A. Rahman, and K.T.V. Grattan, "Study of modal properties in gold nanowire with ZnO cladding by using the finite element method," *Appl. Opt.*, vol. 50, no. 25, pp. E177-E183, Sept. 2011.

[20] L. Chen, T. Zhang, X. Li, and W. Huang, "Novel hybrid plasmonic waveguide consisting of two identical dielectric nanowires symmetrically placed on each side of a thin metal f lm," *Opt. Express,* vol. 20, pp. 20535–20544, 2012.

# Graphene Based High Gain and Small Size Grounded Coplanar Waveguide Feed Patch Antenna for Millimeter Wave Applications

Liton Chandra Paul*, Md. Sohel Rana, Md. Rashedul Islam, Md. Saiful Islam

Dept. of Electronic & Telecommunication Engineering
Pabna University of Science & Technology, Pabna-6600
*litonpaulete@gmail.com, sohel120522@gmail.com, rashed.ru11@gmail.com, msislam0701@gmail.com

***Abstract*— Graphene based array antennas are becoming more popular for wireless applications due to their ultra slim structure, versatile nature, flexibility, robustness and other advantages as compared to conventional patch antennas. Small size and high gain coplanar waveguide (CPW) feed single element microstrip patch antenna (MPA), 16 elements array antenna and 32 elements array antenna for millimeter wave applications are presented in this paper. The proposed antenna configurations have been designed and simulated using computer simulation technology (CST). Kapton is used as the dielectric substrate having dielectric constant of 3.5 and thickness of 0.075 mm. Graphene is used in the radiating patch as well as ground plane of the antennas whose electrical conductivity is of $1.4286 \times 10^6$ S/m$^2$. The thickness of patch and ground plane are of 0.025 mm and 0.05 mm respectively. Each single element antenna has dimension of $1.75 \times 1.5 \times 0.075$ mm$^3$ and each array configuration consist of corresponding number of same dimensional single elements. The results of all the proposed antenna configurations have been analyzed in terms of return loss, bandwidth, gain, VSWR and radiation efficiency. Among all the proposed antennas and analyzed feeding methods, the grounded coplanar waveguide (GCPW) feed 32 elements array antenna shows the best performance.**

***Keywords—RMPA; Graphene; CPW; High gain; CST-MWS;***

## I. INTRODUCTION

Day by day, the demand for wireless communication technology is increasing all over the world. Graphene has drawn a great concentration of the researchers because of numerous distinct physical features of it [1]. Graphene is nothing but a single molecular stratum of graphite. It possesses very tenuous atomic thickness as well as $sp^2$ hybridization. It has also very attractive intrinsic properties as well as zero-overlap semimetal with very high electrical conductivity. It is the strongest material of world with tensile strength (TS) of 130 Gpa which is 200 times stronger than steel. Graphene also shows excellent electrical and thermal conductivity with optical and transparent properties [2]. The use of Graphene in the patch of microstrip patch antenna (MPA) offers extreme miniaturized [3], high operating frequency [4] and high gain [5] antenna. Graphene is such a promising material which helps to rule the radiation from the patch and enhance the performance of an antenna [6].

In [7], author has explained the coplanar waveguide (CPW) feed Graphene array antenna which is designed and simulated by using computer simulation technology - microwave studio (CST-MWS) for three dielectric substrates (Kapton, A4 paper and RT Duroid) at the operating frequency ranging about 13-17 GHz and the bandwidth is of 1.89 GHz for kapton, 2.12 GHz for A4 paper and 1.74 GHz for RT duroid substrate. The obtained simulated gain for the array antennas having substrate width of 10.8 mm and length of 8.8 mm are 7.62 dBi, 7.09 dBi and 7.19 dBi respectively. The thickness of Kapton ($\varepsilon_r$=3.5), A4 paper ($\varepsilon_r$=3.2) and RT Duroid ($\varepsilon_r$=2.2) were of 0.075, 0.05 and 0.254 mm respectively.

A Graphene based miniaturized array antenna provides significant gain which was observed and reported in [8]

This paper reports the analysis of Graphene based single element, 16 elements and 32 elements array antennas. All of these antennas were designed and analyzed for the same dielectric substrate material, length, width, thickness using the CST software version 2011. Due to some distinct feature of Graphene we were motivated to analyze Graphene based high gain array antenna. The simulated results represent various plots and figures of the antenna performance parameters that facilitate to measure and calculate the bandwidth, return loss, gain, directivity, radiation efficiency, VSWR and radiation pattern.

## II. DESIGN AND SIMULATION

This section presents the design and physical specifications of all the proposed antennas as well as simulation results of them from which bandwidth, gain, directivity, return loss, radiation efficiency of the proposed antennas can be estimated. For all configurations, Kapton is used as dielectric substrate having dielectric constant of 3.5 and height of the substrate is of 0.075 mm and Graphene is used in the radiating patch and ground plane of the antennas. The thickness of patch and ground plane are 0.025 mm and 0.05 mm respectively.

### *A. Single Element GCPW Feed Antenna*

Fig. 1 shows the proposed single element grounded coplanar wave guide (GCPW) feed rectangular microstrip patch antenna (RMPA) configuration. All the necessary dimensions of the GCPW feed RMPA are listed in table I.

978-1-5386-3374-8/17/$31.00 ©2017 IEEE

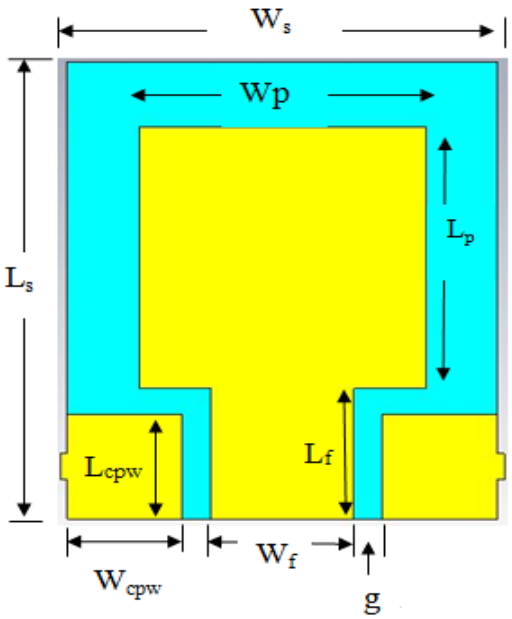


Fig. 1 Single element GCPW feed RMPA

TABLE I PHYSICAL DIMENSIONS OF SINGLE ELEMENT GCPW FEED RMPA

| Parameter | Value (mm) |
|---|---|
| Width of substrate ($W_s$) | 1.5 |
| Length of substrate ($L_s$) | 1.75 |
| Thickness of substrate (h) | 0.075 |
| Width of patch($W_p$) | 1 |
| Length of patch ($L_p$) | 1 |
| Thickness of patch ($t_p$) | 0.025 |
| Thickness of ground plane ($t_g$) | 0.05 |
| Width of feed line ($W_f$) | 0.5 |
| Length of feed line ($L_f$) | 0.5 |
| Width of CPW ($W_{cpw}$) | 0.4 |
| Length of CPW ($L_{cpw}$) | 0.4 |
| Gap between CPW and feed line (g) | 0.1 |

In the proposed single element antenna, Kapton is used as dielectric substrate having dielectric constant of 3.5 and Graphene is used as the radiating element (patch) and ground plane with electrical conductivity of $1.4286\times10^6$ S/m. The length and width of the ground plane is same as the substrate. In this model coplanar waveguide (CPW) is grounded i.e. it is attached with ground plane. The proposed single element RMPA is simulated by using CST-MWS. The magnitude of $S_{11}$ parameter of the antenna with respect to frequency is shown in Fig. 2.

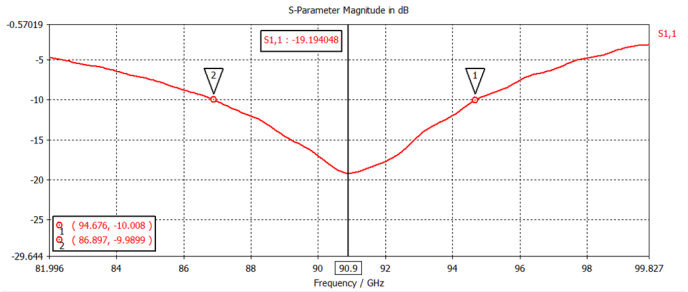


Fig. 2 $|S_{11}|$ parameter of single element GCPW feed RMPA

From the above curve, it is seen that the proposed single element antenna operates at 90.9 GHz with return loss of -19.19 dB and bandwidth of 7.779 GHz. The gain (IEEE), VSWR and total efficiency of the single elements antenna are 14.59 dB, 1.24 and 12.74 dB. The VSWR and 3D gain are presented in Fig. 3 and 4 respectively.

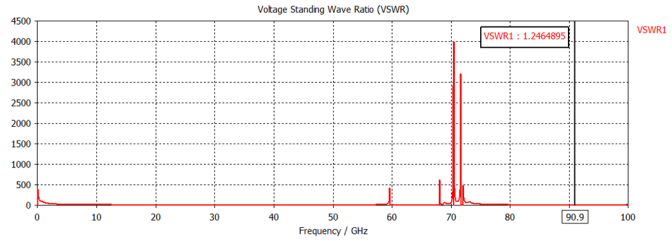


Fig. 3 VSWR of single element GCPW feed RMPA

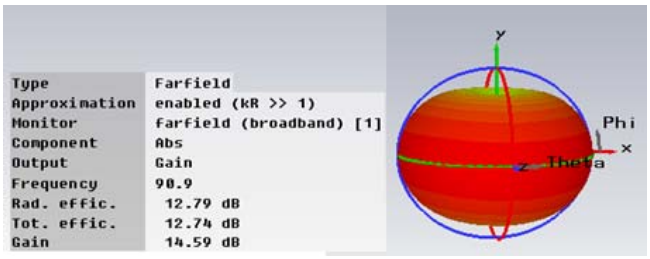


Fig. 4 3D gain of single element GCPW feed RMPA

TABLE II PERFORMANCE SUMMARY OF SINGLE ELEMENT RMPA FOR GROUNDED CPW AND WITHOUT GROUNDED CPW FEED

| Name of Parameter | Grounded CPW feed single element RMPA | Without grounded CPW feed single element RMPA |
|---|---|---|
| Center operating Frequency | 90.9 GHz | 93.3 GHz |
| Bandwidth | 7.779 GHz | 6.79 GHz |
| return loss | -19.19 dB | -24.89 dB |
| IEEE gain | 14.59 dB | 13.20 dB |
| Realized gain | 14.54dB | 13.19 dB |
| Power pattern | 2.018 dBW/$m^2$ | 0.2476 dBW/$m^2$ |
| Radiation efficiency | 12.79 dB | 11.02 dB |
| Total efficiency | 12.74 dB | 11.00 dB |
| VSWR | 1.24 | 1.12 |

The proposed Graphene based single element grounded CPW feed RMPA is also simulated and estimated the performance parameters without attaching CPW to ground plane. The estimated performance parameters of without

grounded CPW feed RMPA are listed and prepared a comparison scenario with grounded CPW feed RMPA in the table II.

### *B. 16 Elements GCPW Feed Array Antenna*

A 16 elements Graphene based GCPW feed array antenna has been presented in Fig. 5. This antenna consists of 16 individual RMPA elements which has been presented and discussed in the immediate previous subsection.

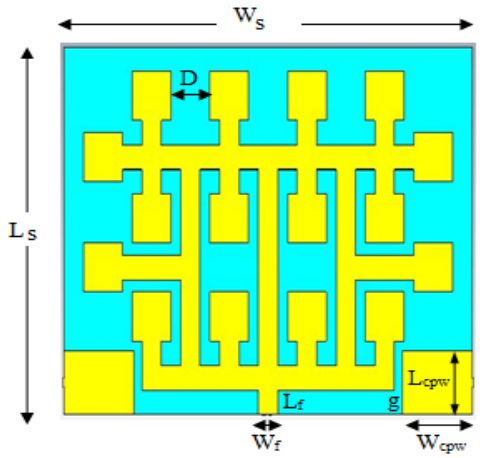


Fig. 5 16 elements GCPW feed array antenna

Distance between two single elements (D) is of 2 mm. The proposed 16 elements antenna is fed by coplanar waveguide. The coplanar wave guides are attached with ground plane. The gap (g) between CPW and feeder of adjacent antenna element is of 0.2 mm. All the dimensions of the 16 elements are listed in table III. Dimensions of every single element of the array are same with the single elements GCPW feed RMPA proposed in subsection A.

TABLE III PHYSICAL DIMENSIONS OF 16 ELEMENTS GCPW FEED ARRAY ANTENNA

| Name of parameter | Value (mm) |
|---|---|
| Width of substrate ($W_s$) | 10.5 |
| Length of substrate ($L_s$) | 7.5 |
| Thickness of Substrate (h) | 0.075 |
| Width of feed line ($W_f$) | 0.5 |
| Length of feed line ($L_f$) | 0.5 |
| Width of CPW ($W_{cpw}$) | 1.8 |
| Length of CPW ($L_{cpw}$) | 1.3 |
| Thickness of patch ($t_p$) | 0.025 |
| Thickness of ground ($t_g$) | 0.05 |
| Gap (g) | 0.2 |
| Distance (D) | 2 |

Fig. 6 shows return loss curve of 16 elements GCPW feed array antenna. From the curve, it is noticed that the proposed 16 elements GCPW feed array antenna operates at center frequency of 92.2 GHz. This antenna possesses return loss of-22.97 dB and bandwidth of 2.309 GHz.

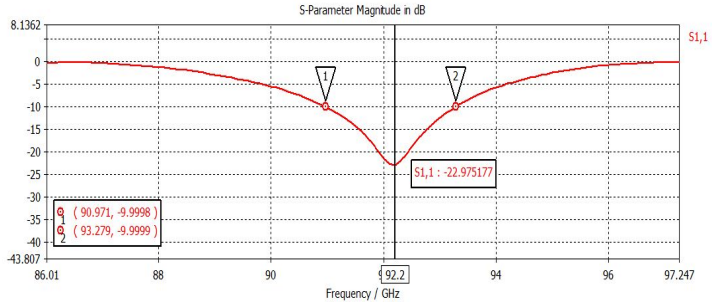


Fig. 6 $|S_{11}|$ parameter of 16 elements GCPW feed array antenna

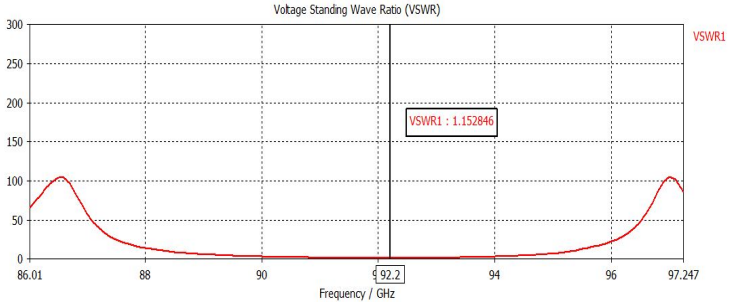


Fig. 7 VSWR of 16 elements GCPW feed array antenna

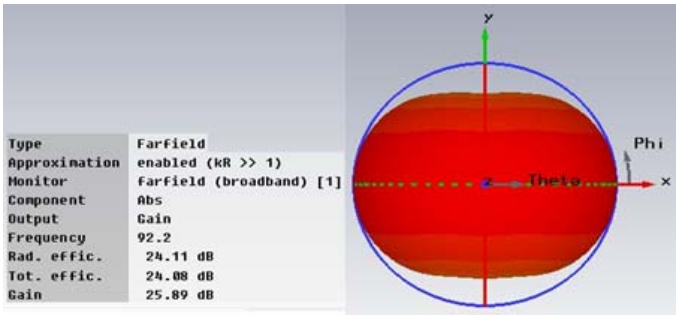


Fig. 8 3D gain of 16 elements GCPW feed array antenna

TABLE IV PERFORMANCE SUMMARY OF 16 ELEMENTS ARRAY ANTENNA FOR GCPW, WITHOUT GROUNDED CPW AND MICROSTRIP LINE FEED

| Parameter | 16 elements GCPW feed Array | 16 elements without grounded CPW feed array | 16 elements microstrip line feed array |
|---|---|---|---|
| Frequency | 92.2 GHz | 92.2 GHz | 92.4 GHz |
| Bandwidth | 2.309 GHz | 2.305 GHz | 1.057 GHz |
| Return loss | -22.97 dB | -22.99 dB | -14.55 dB |
| IEEE gain | 25.89 dB | 25.82 dB | 19.61 dB |
| Realized gain | 25.86 dB | 25.80 dB | 19.45 dB |
| Power pattern | 14.01 dBW/$m^2$ | 13.95 dBW/$m^2$ | 7.878 dBW/$m^2$ |
| Radiation Efficiency | 24.11 dB | 24.03 dB | 17.42 dB |
| Total Efficiency | 24.08 dB | 24.01 dB | 17.27 dB |
| VSWR | 1.15 | 1.15 | 1.46 |

The proposed 16 element GCPW feed array antenna shows VSWR of 1.15 dB as shown in Fig. 7 and the high gain of 25.89 dB as presented in Fig. 8.The proposed Graphene based 16 elements grounded CPW feed array antenna is also

simulated as well as the performance parameters of the antenna are estimated for without attaching coplanar waveguide (CPW) to ground plane and for microstrip line feed method. The estimated performance parameters of without grounded CPW feed and simple microstrip line feed array antenna are listed and prepared a comparison scenario with GCPW feed array antenna in the following table IV.

### *C. 32 Elements GCPW Feed Array Antenna*

Fig. 9 shows the proposed 32 elements GCPW feed array antenna configuration including all the dimensions. The proposed 32 elements array antenna comprised of 32 single element RMPAs which has been presented and discussed in the previous subsection A.

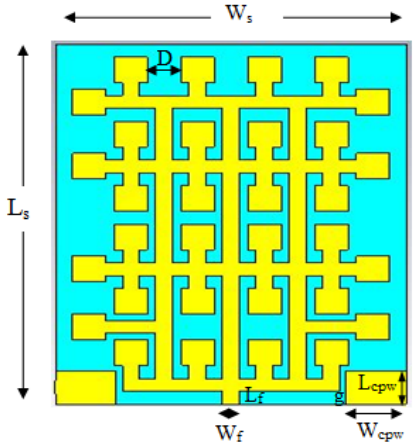


Fig. 9 32 elements GCPW feed array antenna

The substrate length of 32 elements GCPW feed array antenna is 14 mm whereas the length of 16 elements GCPW feed array antenna is 7.5 mm. Only the substrate length of 32 elements array antenna differs from the 16 elements array antenna, moreover, all others physical dimensions of 32 elements are same with the 16 elements array. The proposed 32 elements array antenna has also been simulated by CST-MWS 2011.

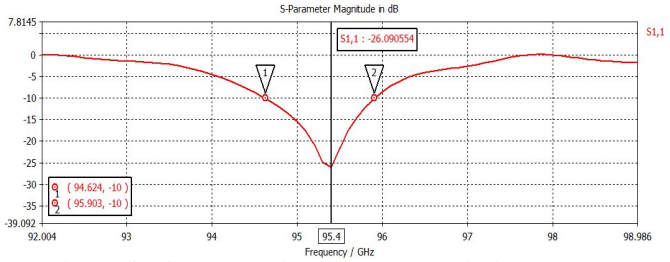


Fig. 10 $|S_{11}|$ parameter of 32 elements GCPW feed array antenna

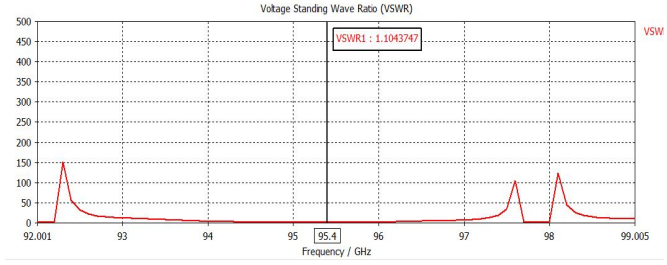


Fig. 11 VSWR of 32 elements GCPW feed array antenna

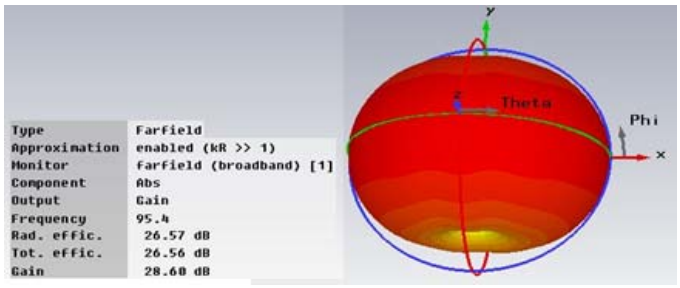


Fig. 12 3D gain of 32 elements GCPW feed array antenna

The simulated return loss curve, VSWR and 3D gain of 32 elements GCPW feed microstrip array antenna are depicted in Fig. 10, 11 and 12 respectively. The proposed 32 elements array antenna operates at center operating frequency of 95.4 GHz with bandwidth of 1.279 GHz and return loss of -26.09 dB. The antenna has VSWR of 1.10 and high gain of 28.68 dB. It is clear that the 32 elements array shows high gain and better VSWR, return loss as well as radiation efficiency. The proposed antenna also analyzed for without grounding the CPW feed and for microstrip line feed. For both feeding method, we estimated the performance parameter like return loss, gain, efficiency, VSWR etc. Those parameters are listed and prepared a comparison scenario by putting in a single table V.

TABLE V PERFORMANCE SUMMARY OF 32 ELEMENTS ARRAY ANTENNA FOR GCPW, WITHOUT GROUNDED CPW AND MICROSTRIP LINE FEED

| Parameter | 32 elements GCPW feed array antenna | 32 elements without grounded CPW feed array antenna | 32 Elements microstrip line feed array antenna |
|---|---|---|---|
| Frequency | 95.4 GHz | 95.4 GHz | 96.2 GHz |
| Bandwidth | 1.279 GHz | 1.28 GHz | 0.825 MHz |
| Return loss | -26.09 dB | -26.09 dB | -20.98 dB |
| IEEE gain | 28.60 dB | 22.76 dB | 19.13 dB |
| Realized gain | 28.59 dB | 22.75 dB | 19.10 dB |
| Power pattern | 16.69 dBW/m$^2$ | 10.85 dBW/m$^2$ | 7.06 dBW/m$^2$ |
| Radiation Efficiency | 26.57 dB | 20.09 dB | 17.25 dB |
| Total Efficiency | 26.56 dB | 20.08 dB | 17.21 dB |
| VSWR | 1.10 | 1.10 | 1.19 |

## III. PERFORMANCE COMPARISON AND SUMMARY

We have designed and simulated Graphene based different antenna (single element, 16 elements array, 32 elements array) configuration by using CST-MWS 2011. These antennas have been able to provide very high gain covering the millimeter wave wireless communication. All the proposed array configurations have been designed to provide better performance than conventional patch antenna. All of the proposed antennas both single element antenna and array antennas offers improved performance than the antennas mentioned in reference section. For example, the [7] have

designed array antennas using three different substrates and it obtained maximum gain of 7.62 dB and [9] has simulated gain of 18 dB but consists of large number of elements (256). In [10] the simulated gain is of 16.3 dB for dense dielectric microstrip patch antenna array configuration by using EM band gap structure and dielectric superstrate. But our designed and proposed Graphene based GCPW feed single element, 16 elements array and 32 elements array antennas offer better performance like gain (IEEE) of 14.59 dB with return loss of -19.19 dB covering bandwidth of 7.779 GHz for single element, gain (IEEE) of 25.89 dB with return loss of -22.97 dB covering bandwidth of 2.309 GHz for 16 elements, gain (IEEE) of 28.60 dB with return loss of - 26.09 dB covering bandwidth of 1.279 GHz for 32 elements array. Not only simulated performance parameters but also according to the size of the array, our proposed array configurations are better than [7]. All the simulated performance parameters of single element, 16 elements and 32 elements array antennas for grounded CPW (GCPW) feed, without grounded CPW feed and microstrip line feed are summarized in the following table VI. From the table VI, it is seen that among three analyzed feeding method of the proposed antennas shows comparative better performance for grounded waveguide feed. And among all the proposed antennas, 16 elements array shows better performance than single elements antenna and 32 elements array shows better performance than the 16 elements array antenna.

TABLE VI PERFORMANCE SUMMARY OF GRAPHENE BASED PROPOSED ANTENNAS

| Proposed antenna | Feeding | Center frequency (GHz) | Return loss (dB) | -10 dB BW (GHz) | Gain (dB) | Radiation Efficiency (dB) |
|---|---|---|---|---|---|---|
| Single Element | GCPW | 90.3 | -19.19 | 7.779 | 14.59 | 12.79 |
| | NGCPW | 93.3 | -24.89 | 6.79 | 13.20 | 11.02 |
| 16 Elements | GCPW | 92.2 | -22.97 | 2.309 | 25.89 | 24.11 |
| | NGCPW | 92.2 | -22.99 | 2.30 | 25.82 | 24.03 |
| | ML | 92.4 | -14.55 | 1.05 | 19.61 | 17.42 |
| 32 Elements | GCPW | 95.4 | -26.09 | 1.279 | 28.60 | 26.57 |
| | NGCPW | 95.4 | -26.09 | 1.28 | 22.76 | 20.09 |
| | ML | 96.2 | -20.98 | 0.825 | 19.13 | 17.25 |

*GCPW= Grounded CPW, NGCPW= Not grounded CPW, ML= Microstrip line feed

## IV. Conclusion and Future Plan

In this work, Graphene based three small sized high gain microstrip patch antennas have been designed and analyzed, first one is single element rectangular microstrip patch antenna, second and third are 16 elements and 32 elements array antennas. All the antennas are also simulated and analyzed using different feeding methods such as ground coplanar waveguide feed, without grounded coplanar waveguide feed and microstrip line feed. Among all the proposed antennas and analyzed feeding methods, the grounded coplanar waveguide feed 32 elements microstrip array antenna shows best performance. The proposed antennas are suitable for millimeter wave applications such as 5G, high speed mobile communication, most modern radar, satellite communication, radio astronomy, high speed data transmission, directed energy weapons etc. In future, we are highly interested to fabricate the proposed antennas to buttress the simulated results.

## References


[1] A. K. Geim and K. S. Novoselov, "The rise of graphene," *Nature Materials*, vol. 6, pp. 183–191, 2007.

[2] R. Atif, I. Shyha and F. Inam, "Mechanical, Thermal and Electrical Properties of Graphene-Epoxy Nanocomposites-A Review," *Polymers*, vol. 8, no. 8, pp. 1-37, 2016,

[3] J. Perruisseau-Carrier, "Graphene for Antenna Applications: Opportunities and Challenges from Microwaves to THz," *IEEE Loughborough Antennas & Propagation Conference*, Loughborough, UK, pp.1-4,12 - 13 Nov. 2012,

[4] I. Llatser, C. Kremers, A. Cabellos-Aparicio, J. M. Jornet, E. Alarcon and D. N. Chigrin, "Graphene-based nano-patch antenna for terahertz radiation," *Photonics and Nanostructures - Fundamentals and Applications*, Elsevier, vol. 10 , pp. 353–358, 2012.

[5] B. L. Larsen,"Graphene antennas for THz radiation," MS thesis, Dept. of Photonics Engineering, Technical University of Denmark (DTU), pp. 1-39, 4 June 2013.

[6] A. Radwan, V. Verri, M. D. Amico and G. G. Gentili, "THz Nano-Array Antenna Based on a Monolayer Reflector Graphene Surface," *1st URSI AtlanticRadio Science IEEE Conference (URSI AT-RASC)*, Las Palmas, Spain, pp. 1-5, 16-24 May 2015.

[7] S. N. H. Sadon, M. R. Kamarudin, F. Ahamed, M. Jusoh and H. A. Majid, "Graphene array antenna for 5G applications," *Applied Physics A: Materials Science and Processing*, vol. 123, no. 2, Springer, pp. 1-4, 2017.

[8] L. Zakrajsek, E. Einarsson, N. Thawdar, M. Medleyand J. M. Jornet, "Design of graphene-based plasmonic nano-antenna arrays in the presence of mutual coupling", *11th European Conference onAntennas and Propagation (EUCAP)*, IEEE, Paris, France, pp. 1-5, 19-24 March 2017.

[9] X. Pang, W. Hong, T. Yang and L. Li, "Design and implementation of an active multibeam antenna system with 64 RF channels and 256 antenna elements for massive MIMO application in 5G wireless communications", *China Communication*, vol. 11, no. 11, pp. 16–23, Nov. 2014.

[10] O. M. Haraz, A. Elboushi, S. A. Alshebeili and A. R. Sebak, "Dense dielectric patch array antenna with improved radiation characteristics using EBG ground structure and dielectric superstrate for future 5G cellular networks", *IEEE Access*, vol. 2, pp. 909-913, 2014.

# Terahertz Switch Based on Reconfigurable Subwavelength Metallic Ring Apertures

Sanaz Zarei[1,*]

[1] Photonics Research Laboratory, School of Electrical and Computer Engineering, College of Engineering, University of Tehran, Tehran, Iran

[*] szarei@ut.ac.ir

*Abstract*—**A polarization-sensitive terahertz switch is presented in this work. The device works passively in the transmission mode and shows different transmission behaviors for the two orthogonal polarizations. The operation central frequency and bandwidth of the switch are 926GHz and 140GHz, respectively. The switching contrast of the device is 9.3dB for y-polarization and 28.5dB for x-polarization at its center frequency. The impact of the geometrical parameters of the switch on its performance is briefly discussed.**

***Index Terms***—**Terahertz switch; on/off ratio; subwavelength metallic ring apertures.**

## I. INTRODUCTION

Due to small electromagnetic interaction of terahertz waves with natural materials and the practical difficulties in scaling the existing optical and infrared design dimensions, devices to control and manipulate terahertz wave propagation such as switches, filters, modulators and polarizers still hinder the technology development. Metamaterials, due to their ability in alleviating the severe materials issues, have turned into the most promising approaches for manipulating terahertz waves.

Inspired by realization of tunability or switching ability, the focus on metamaterials has been extended from the structural design of a specific electromagnetic response to reconfigurable terahertz metamaterial devices. Several researches have recently conducted on geometrical reconfiguration of metamaterials by using micro-electro-mechanical system (MEMs) techniques. For instance, a reconfigurable RF-MEMs capacitor switch within a split-ring resonator (SRR) on a low-loss quartz substrate is proposed in [1-2], reconfigurable metallic slits are employed in [3-5] for broadband terahertz switching and terahertz MEMs switches based on metallic mesh filters are presented in [6-8].

On the other hand, extraordinary optical transmission through subwavelength metallic apertures due to the resonance excitation of surface plasmons has been of great interest in manipulation of electromagnetic waves below the wavelength scale. Several terahertz switches/modulators based on subwavelength metallic apertures have been demonstrated including those using Graphene material [9-10], those based on metallic hole array on vanadium dioxide film [11] or on gallium arsenide based substrates [12], complementary plasmonic arrays [13], electrically transmission-tunable subwavelength hole arrays [14].

Important parameters to characterize a terahertz switch are switching contrast, insertion loss, and a designable resonance frequency and bandwidth. In this article, we propose a MEMs-actuated reconfigurable dual-layered array of subwavelength metallic ring apertures on a low-loss substrate to demonstrate broadband switching of terahertz waves at room-temperature with tailored operation frequency and large on/off ratio. Each layer consists of a periodic arrangement of metallic holes or metallic pillars. Similar configuration to ours, with silicon as the constituent material, has formerly been used in [15] by Hadzialic et. al. for displacement sensing in the optical frequency band.

## II. DESIGN AND SIMULATION

The switch considered in this work consists of a metal film perforated with a periodic array of holes, suspended above the polystyrene foam substrate. The membrane is attached to a MEMs actuator for lateral positioning. In the center of each hole, there is a metal pillar that is fixed to the substrate. Before actuating the MEMs, which is the switch OFF-state, the pillars are located exactly at the center of the holes. In this case, the unit cell of the structure is reduced to a coaxial waveguide, which its response to incident terahertz waves can be obtained straightforwardly due to its well-known mode fields and their cut-off frequencies [16-21]. After actuating the MEMs, which is switch ON-state, the suspended metal membrane shifts laterally and the holes and pillars are in contact with each other. Therefore, the transmission spectrum of terahertz waves through the structure changes as the geometry of the structure varies. The schematic diagram and operation principle of our switch is depicted in fig. 1.

The electromagnetic modeling of the structure is performed using a commercial FEM electromagnetic solver. The pillars were modeled as perfect electric conductor (PEC) with radius ($r_i$) of 54um and the membrane which is perforated with holes is also modeled as PEC with the holes' radii ($r_o$) of 60um. The thickness of membrane ($H_1$) is 5um and the periodicity of the periodic structure ($\Lambda$) is 200um.

We analyzed the structure for two perpendicular polarizations (x and y). The transmission spectrum of terahertz light through the switch, for both polarizations, are shown in fig. 2. For both polarizations, when the switch is OFF, we have a transmission peak with the transmission frequency of 0.926THz and transmission bandwidth of 140GHz. As the holes are displaced laterally in the x-direction with an amount of 6um and become in contact with the pillars (switch ON-state), a spectrum shift appears in the transmission peak of transmitted light and this can be used to switch the terahertz light. For y-polarized light, this spectrum shift is 225GHz towards higher frequencies. The on/off ratio of the switch at its resonance frequency of 0.926THz is 0.9 for this polarization. The spectrum shift for x-polarized incident terahertz light is 351GHz towards lower frequencies and the on/off ratio at its resonance frequency is 0.98.

As is seen, when the holes are displaced by an amount of 6um, the transmission at 0.926THz changes by more than 90% for both polarizations.

978-1-5386-3374-8/17/$31.00 ©2017 IEEE

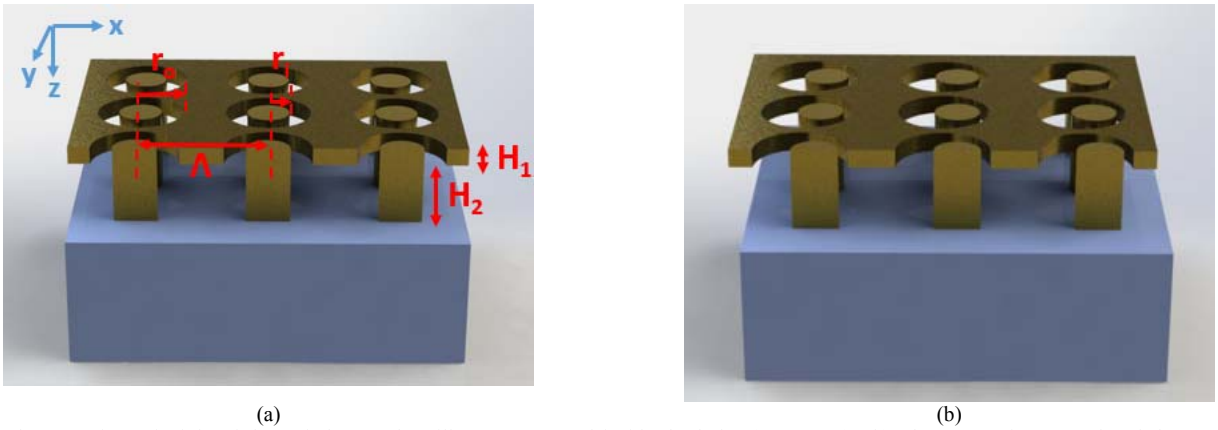


(a) (b)

Fig. 1 The operation principle of the switch. (a) The pillars are centered inside the holes (OFF state). (b) The MEMs is actuated and the membrane displaces laterally and the holes are in contact with the pillars (ON state).

However, the transmission behavior of switch in ON-state is different for the two polarizations. The difference in the spectrum shift for two polarizations is due to the excitation of different modes according to different structural symmetry in ON-state.

The device shows a high switching contrast of 28.5dB at its maximum transmission frequency of 926GHz for x-polarized terahertz light. However, for y-polarized light, this contrast is only 9.3dB. The isolation diagram of the switch for the whole transmission bandwidth is shown in fig. 3.

At zero bias voltage, which is the switch OFF-state, the insertion loss at the resonance frequency is 0.07dB. When a bias voltage is applied and the switch goes to ON-state, the transmission band shifts and the insertion loss reaches the value of 9.3dB for y-polarization and 28.5dB for x-polarization at the resonance frequency of 926GHz. The insertion loss diagram of the switch for both states is depicted in fig. 4.

Figure 5 (left side) shows the amplitude transmission of the switch at 926GHz (OFF-state resonant frequency) for different displacement values of the inner cylinder in the x direction for both polarizations. Figure 5 (right side) shows the resonance frequency of switch versus the displacement of the inner cylinder.

It is observed that the amplitude transmission value is decreased when the displacement of inner cylinder is increased to 6um. Also it is inferred from fig. 5 that the resonance frequency of switch varies conversely for different polarizations as the displacement is increased.

It is of great importance to choose a proper substrate for the designed structure, as it will certainly affect the performance of the switch. In this work, polystyrene foam is used as the substrate, which has a remarkable low refractive index of 1.017 to 1.022 and very small losses in the terahertz range between 0.2 and 4THz [22]. This makes the polystyrene foam a suitable material for transmitting terahertz radiation.

It is assumed that the height of pillars beneath the membrane and above the substrate ($H_2$) is zero in all the presented results. Our investigations show that nonzero value of $H_2$ leads to more insertion loss. Complete representation of this issue will be done in future.

## III. DISCUSSION

Compared to previous works, the presented terahertz switch offers some interesting advantages. This switch shows switching capability for both polarizations, although with a significant difference in switching contrast. Moreover, the operation frequency of this switch is near 1THz, which is highly matched with the center frequency of terahertz waves generated by optical methods such as difference frequency generation and optical rectifications.

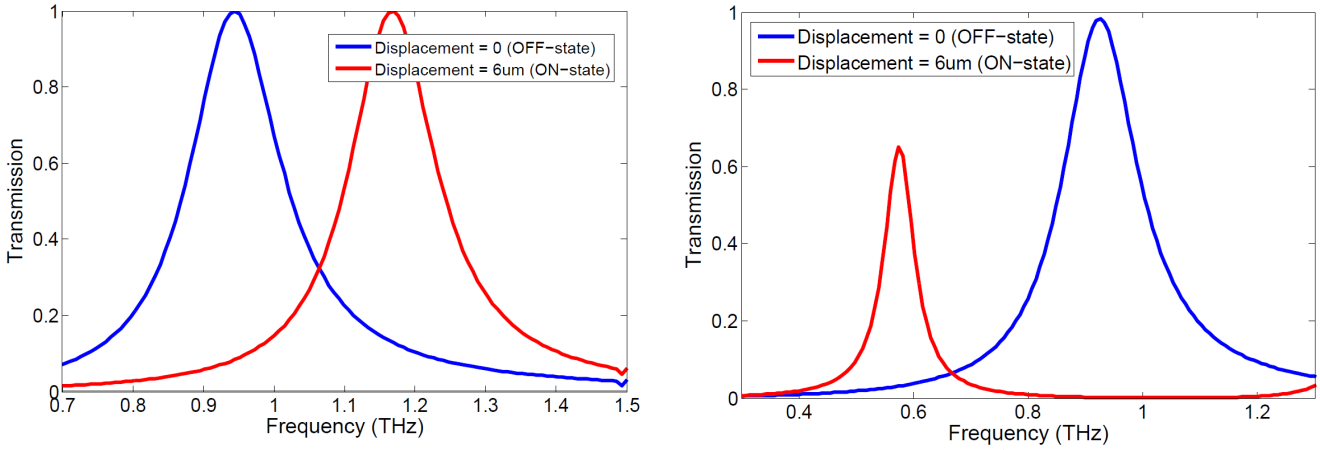


(a) (b)

Fig. 2 (a) The modulation characteristics of the designed terahertz switch for incident terahertz light polarized perpendicular to the moving axis (y-polarized) (b) for incident terahertz light polarized along the moving axis (x-polarized). The blue curve shows the device transmission in OFF state and the red curve shows the device transmission in ON state.

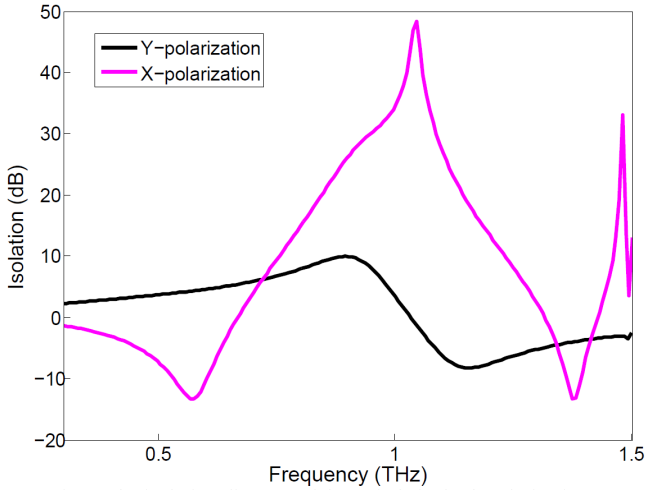


Fig. 3 The isolation diagram of the switch for both polarizations.

The switching contrast for x-polarization is 28.5dB, which comparing to [1] that proposed a switch with contrast of 16.5dB at 480GHz, and [2] with a contrast ratio of 26.2dB at 602GHz, shows a relatively improved switching performance. In [7-8], a reconfigurable meta-surface switch/modulator is proposed with less than 10dB modulation index, which its main advantage is its broad operation bandwidth. Other works offer modulation depths of less than 10dB in their modulation bandwidth, although they propose some novelties in their designs which lead to high modulation speeds [9-14].

Due to scaling properties of metamaterials, it is apparent that the switch resonance frequency, bandwidth and isolation can be tailored by varying the geometry and dimension of the structure. For the purpose of analyzing the effects of structural parameters on the transmission properties of switch, we changed the inner and outer radius of the cylinders, the membrane's height and the periodicity of the structure.

For a fixed outer radius of the rings ($r_o$), as far as the inner rod's radius ($r_i$) is increased, the resonance frequency and bandwidth are decreased and the isolation through the whole transmission band is increased. Also as the period of structure ($\Lambda$) is decreased, while reserving the ratio of inner to outer radii of the rings, it is found that the transmission resonance frequency and bandwidth, as well as isolation are increased.

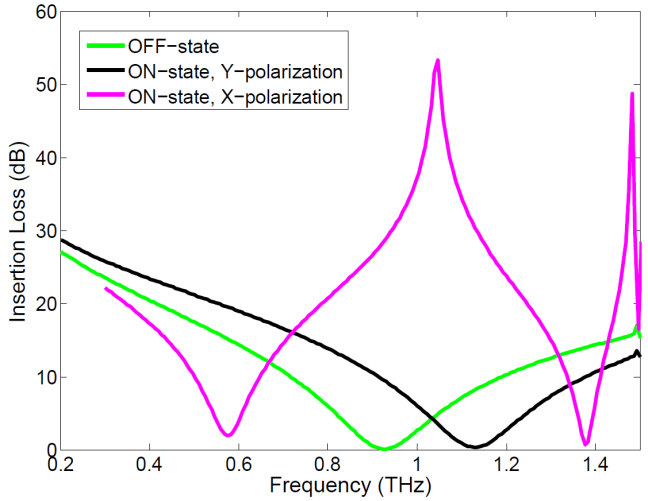


Fig. 4 The insertion loss of the switch for OFF-state which is the same for both polarizations (green curve), and the ON-state for y-polarized terahertz light (black curve) and x-polarized terahertz light (purple curve).

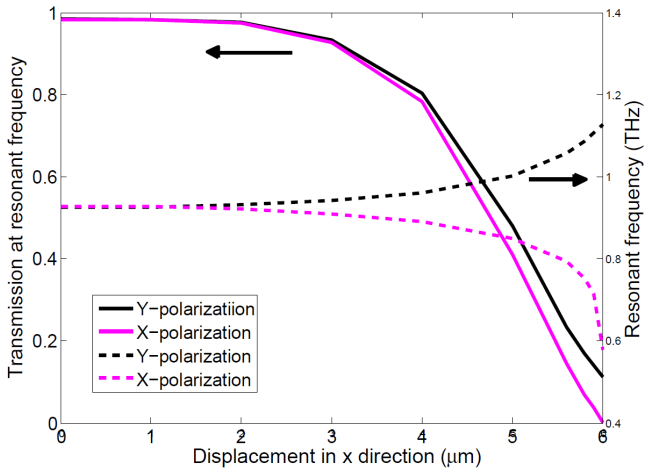


Fig. 5 (Left side) Amplitude transmission of the switch at OFF-state resonance frequency for different displacement values of membrane for y-polarized (black curve) and x-polarized (purple curve) terahertz light, (Right side) Variation of the resonant frequency versus displacement of membrane for both polarizations.

Furthermore, by increasing the height of the membrane ($H_1$), moderate decrement in transmission bandwidth and slight decrement in transmission frequency appears and the isolation enhances through the bandwidth. Therefore, the performance parameters of the switch can be enhanced significantly by further optimization of the device geometry.

## IV. CONCLUSION

A low-loss MEMs actuated terahertz switch, consists of dual-layered array of subwavelength metallic ring apertures is proposed in this paper. Lateral displacement of metallic membrane perforated with a periodic arrangement of holes with respect to metallic pillars is used to control ON/OFF operation of the switch. A high switching contrast of 28.5dB for x-polarized light and moderate contrast of 9.3dB for y-polarized light is demonstrated at 926GHz which is the center band-pass frequency of the switch. The operation bandwidth is 140GHz. Further improvement of the device performance is possible through additional optimization of the geometrical parameters of the design.

## ACKNOWLEDGMENT

The author would like to thank Mr. Ebrahim Panahpoori from University of Tehran for his help to sketch the device configurations.

## REFERENCES

[1] Z. Han, K. Kohno, H. Fujita, K. Hirakawa, and H. Toshiyoshi, "MEMS reconfigurable metamaterial for terahertz switchable filter and modulator," *Opt. Express*, vol. 22, no. 18, p. 21326, Aug. 2014.

[2] Z. Han, K. Kohno, H. Fujita, K. Hirakawa, and H. Toshiyoshi, "Tunable Terahertz Filter and Modulator Based on Electrostatic MEMS Reconfigurable SRR Array," *IEEE J. Select. Topics in Quantum Electron.*, vol. 21, no. 4, pp.114-122, Aug. 2015.

[3] S. Zarei, M. Jarrahi, "Broadband terahertz modulation based on reconfigurable metallic slits", *Proc. IEEE Photonics Society Winter Topicals*, 30, Majorca, Spain, Jan. 2010.

[4] M. Jarrahi, "Broadband terahertz modulators based on reconfigurable metamaterials and their potential application in terahertz imaging", *Proc. International Symposium on Electromagnetic Theory (EMTS)*, 640, Berlin, Germany, Aug. 2010.

[5] C. Berry, J. Moore, and M. Jarrahi, "Design of reconfigurable metallic slits for terahertz beam modulation," *Opt. Express*, vol. 19, no. 2, p.1236, Jan. 2011.

[6] S. Zarei, "polarization-independent Broadband Terahertz Modulator," Munich, Germany, May 2011.

[7] M. Unlu, M. Hashemi, C. Berry, S. Li, S. Yang, and M. Jarrahi, “Switchable Scattering Meta-Surfaces for Broadband Terahertz Modulation,” *Sci. Rep.*, vol. 4, no. 1, July 2014.

[8] M. Unlu, and M. Jarrahi, “Miniature multi-contact MEMS switch for broadband terahertz modulation,” *Opt. Express*, vol. 22, no. 26, p.32245, Dec. 2014.

[9] W. Gao, J. Shu, K. Reichel, D. Nickel, X. He, G. Shi, R. Vajtai, P. Ajayan, J. Kono, D. Mittleman and Q. Xu, "High-Contrast Terahertz Wave Modulation by Gated Graphene Enhanced by Extraordinary Transmission through Ring Apertures", *Nano Lett.*, vol. 14, no. 3, pp. 1242-1248, 2014.

[10] X. He, T. Li, L. Wang, J. Wang, J. Jiang, G. Yang, F. Meng and Q. Wu, "Electrically tunable terahertz wave modulator based on complementary metamaterial and graphene", *J. Appl. Phys.*, vol. 115, no. 17, pp. 17B903, 2014.

[11] J. Dong, Y. Li, L. Chen, C. Sun, L. Chai and C. Wang, "Tunable terahertz plasmonic filter based on a substrate of photo-induced phase-transition vanadium dioxide film", *International Symposium on Photonics and Optoelectronics 2014*, 2014.

[12] F. Fan, M. Chen, S. Chen, X. Wang and S. Chang, "Complementary Plasmonic Arrays for Extraordinary Transmission and Modulation of Terahertz Wave", *IEEE Photon. Technol. Lett.*, vol. 27, no. 23, pp. 2485-2488, 2015.

[13] A. Azad, H. Chen, S. Kasarla, A. Taylor, Z. Tian, X. Lu, W. Zhang, H. Lu, A. Gossard and J. O’Hara, "Ultrafast optical control of terahertz surface plasmons in subwavelength hole arrays at room temperature", *Appl. Phys. Lett.*, vol. 95, no. 1, p. 011105, 2009.

[14] Y. Zhang, Y. Liu and J. Han, "Electrically tunable resonant terahertz transmission in subwavelength hole arrays", *Chinese Physics B*, vol. 23, no. 6, p. 067301, 2014.

[15] S. Hadzialic, S. Kim, A. Sarioglu, A. Sudbo and O. Solgaard, "Displacement Sensing With a Mechanically Tunable Photonic Crystal", *IEEE Photon. Technol. Lett.*, vol. 22, no. 16, pp. 1196-1198, 2010.

[16] F. Baida, D. Van Labeke, G. Granet, A. Moreau and A. Belkhir, "Origin of the super-enhanced light transmission through a 2-D metallic annular aperture array: a study of photonic bands", *Appl. Phys. B*, vol. 79, no. 1, pp. 1-8, 2004.

[17] F. Baida, "Enhanced transmission through subwavelength metallic coaxial apertures by excitation of the TEM mode", *Appl. Phys. B*, vol. 89, no. 2-3, pp. 145-149, 2007.

[18] W. Fan, S. Zhang, B. Minhas, K. Malloy and S. Brueck, "Enhanced Infrared Transmission through Subwavelength Coaxial Metallic Arrays", *Phys. Rev. Lett.*, vol. 94, no. 3, 2005.

[19] A. Moreau, G. Granet, F. Baida and D. Van Labeke, "Light transmission by subwavelength square coaxial aperture arrays in metallic films*", Opt. Express*, vol. 11, no. 10, p. 1131, May 2003.

[20] F.I. Baida and D. Van Labeke, “Light transmission by subwavelength annular aperture arrays in metallic films,” *Opt. Commun.*, vol. 209, pp. 17–22, Aug. 2002.

[21] V. Lomakin,S. Li, and E. Michielssen, “Transmission through and wave guidance on metal plates perforated by periodic arrays of through-holes of subwavelength coaxial cross section,” *Microw. Opt. Tech. Lett.*, vol. 49, no. 7, pp. 1554-1558, July 2007.

[22] G. Zhao, M. T. Mors, T. Wenckebach, and P. C. M. Planken, “Terahertz dielectric properties of polystyrene foam,” *J. Opt. Soc. Am. B*, vol. 19, no. 6, 2002.

# 3D Double S-Shaped Unidirectional Antenna for Microwave Imaging

Md. Atikur Rahman[1,*], Md. Samsuzzaman[1], Md. Naimur Rahman[2], Md. Tarikul Islam[1], Tariqul Islam[2]
[1]Dept. of Computer and Communication Engineering
Patuakhali Science and Technology University, Patuakhali, Bangladesh
[2]Dept. of Electrical Electronic and Systems Engineering,
Universiti Kebangsaan Malaysia, Malaysia
[*]atikur11@cse.pstu.ac.bd

*Abstract* - **A concise 3D wideband antenna with direction is exposed to microwave imaging application. The proposed prototype has a low profile and a three dimensional folded structure is the main geometry of the antenna. To attain uni-directionality and resonance at a lower frequency, a special S-shaped along with a 3D technique is used. The dimension of the proposed antenna is 0.11×0.279×0.044 $\lambda^3$ at 1.1 GHz which has fed with 50Ω microstrip transmission line. The antenna has a capability of covering the frequency of 1.1 GHz to 2.2 GHz with an average gain 5.5 dBi at 2.0 GHz. The proposed antenna accomplishes 66% fractional bandwidth (1.1 – 2.2) GHz. This prototype is designed and simulated in HFSS and CST Microwave Studio software.**

***Keywords*—3D; Dual; High gain; Microwave imaging; S-shaped; Unidirectional.**

## I. INTRODUCTION

Microwave imaging is an innovative technique in recent few decades which attracts a huge interest in medical diagnostic applications such as brain tumor detection, health monitoring etc. owing to its low profile, low cost, portability, side impact reducing properties. Some premature deaths are occurred due to various brain disease which is undetected at the beginning of the phase. Some existing techniques those are standard for brain tumor detection such as Magnetic Resonance Imaging (MRI), Biopsy and Computerized Tomography (CT) scan. But due to their heavy weight and static structure, they are not available in outside of the hospital[1-3].

The resonance frequency right from 1 - 4 GHz is the specified band with regard to head imaging application [4-6]. The most challenging task is to design a compact three-dimensional patch antenna with direction and operates at a lower frequency when it is applied in a most vulnerable portion of the human physique (brain). For head imaging, it is said that the antenna must be unidirectional. Because directivity makes the imaging technique easier and simpler. Some efforts have been made recently in antennas to realize high gain and directivity for microwave imaging [7-9]. Even so, the directivity of the antenna seriously isn't very acceptable for the Human Head Imaging [10]. The gain is 4 dBi and not highly directive of the radiation pattern. Another paper which gain and radiation pattern are not perfect for head imaging [11]. The antenna achieves 3.5 dBi average gain with 63% fractional bandwidth [10]. The antenna reaches 6-8 front to back ratio with 53% fractional bandwidth which is not appropriate for microwave imaging [9]. The low-cost FR4 substrate is used to construct the antenna, but its peak is approximately 2.8 dBi which provides low directivity [8].

In this paper, a compact 3D double S-shaped wideband antenna is introduced. The dimension of the prototype is 0.11×0.279×0.044 $\lambda^3$ at 1.1 GHz. The frequency band which is covered by the antenna is 1.1 GHz to 2.2 GHz. CST and HFSS simulator are used to simulate the proposed antenna. The prototype antenna is small dimensions, cost lessen and have decent features which make it suitable for easy use in the sector of microwave imaging.

## II. ANTENNA CONFIGURATION

The structure of the antenna elements generally starts with the fundamental equations for finding width and length of the microstrip antenna. To realizing the dimensions of the patch is first to determine the width and length using the following equation:

$$W = \frac{c}{2f_0}\sqrt{\frac{\varepsilon_r + 1}{2}} \quad \ldots\ldots\ldots\ldots \quad 1$$

$$L = \frac{c}{2f_0\sqrt{\varepsilon_r}} - 2\Delta l \quad \ldots\ldots\ldots\ldots \quad 2$$

The final design of the prototype is demonstrated in Fig 1. The antenna is comprised of Roger RT/Duroid 5880 substrate which breadth is 1.6 mm. The permittivity of the substrate is 2.2. In this letter, only one substrate is used instead of this paper [12]. The dimension of the proposed antenna is 70×30×13.4 $mm^3$. The patch is situated on both sides of the substrate which size is 36.5 × 15 $mm^2$. A 13.4 × 4 $mm^2$ feeding line is branded on the top most side of Roger RT. The patch is S-shaped. A parasitic reflector and two copper walls are added at the bottom of the substrate, in order to give a 3D structure of the antenna. To attain uni-directional radiation pattern and the lower operating band a folded parasitic structure is used. The proposed antenna insures the bandwidth 1.1 - 2.2 GHz with an average gain 5.5 dBi at 2.0 GHz, which is acceptable for microwave imaging. The size of the parameters are presented in Table I.

978-1-5386-3374-8/17/$31.00 ©2017 IEEE

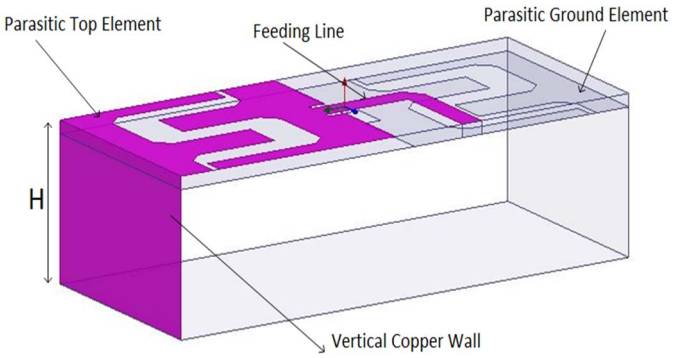


Figure 1. Geometric layout of the proposed Antenna

TABLE ˜ PARAMETERS SIZE OF THE ANTENNA

| Parameters | mm | Parameters | mm |
|---|---|---|---|
| *W* | 30 | *L5* | *3* |
| *L* | 70 | *L6* | *6* |
| $L_p$ | 33.5 | *W1* | 4 |
| *L1* | 20 | *W2* | 6 |
| *L2* | 6 | *W3* | 4 |
| *L3* | 13.4 | *h* | 1.6 |
| *L4* | 7.5 | | |

## III. RESULT AND DISCUSSION

Computer Simulation Technology (CST) and High-Frequency Structural Simulator (HFSS) software both are used to observed the performances and got the simulated result of proposed antenna. Typically the particular antenna is fed by 50 Ω microstrip transmission line. In order to get high gain and lower frequency, we change the initial design in a different way and simulate those design. The final s11 comes out in three conditions such as a) Only S-shaped without a cutter, b) Double S-shaped without copper wall and parasitic reflector and c) the complete design. At first, we simulate only S-shaped without a cutter. The result was not satisfactory. Then change it respectively single S-shaped on the top side and Double S-shaped without copper walls and parasitic reflector. At last design, the proposed antenna and got the proper gain at lower frequency shown in Fig 2. Designing the patch different shaped are applied to the substrate those are H-shape, V-shape, and L-shape. But applying s-shape on the top and bottom part of the Roger RT, make the proposed antenna working at the desired frequency with high gain and efficiency. By developing this way, the proposed antenna is perfect for microwave imaging. The s11 result and simulated peak gain are presented respectively in Fig 4 and Fig 5. The maximum appreciated gain is 5.5 dBi at 2 GHz. Fig. 4 demonstrates the simulated s11 result against frequency for the proposed antenna in both HFSS and CST. The efficiency is expressed in Fig 6. The surface current distribution is shown in Fig 7 where the maximum radiating area is feed line and then the edge of S-shape. At lower frequency upper S-shape radiating most but at a higher frequency, the lower S-shape radiates larger than the upper side. The 2D radiation pattern is displayed in Fig 8 which indicates that antenna has unidirectional characteristics. In table 2 the proposed antenna is compared with some existent antenna to verify its performance. For the head imaging, high directivity is essential characteristics which are not followed in the following referenced paper. But the proposed antenna is small in size and high directivity. So the proposed antenna is perfect in using of head imaging application.

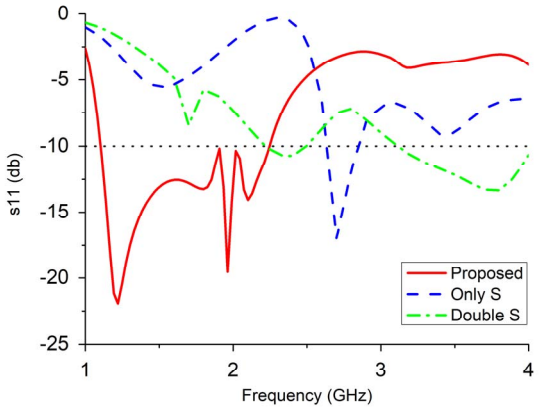


Figure 2. Simulated s11 at various conditions of antenna

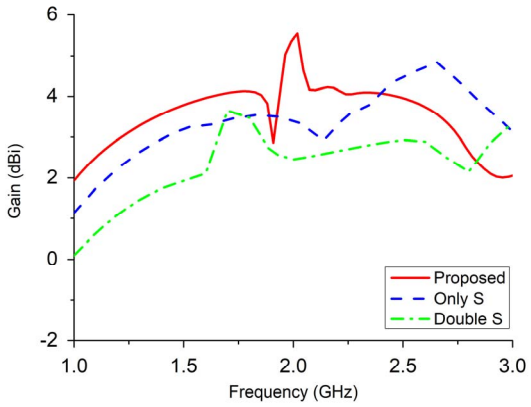


Figure 2. Simulated peak gain at different conditions

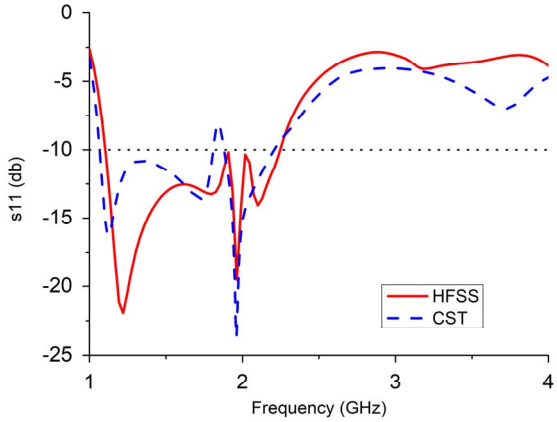


Figure 4. Simulated s11 in HFSS and CST

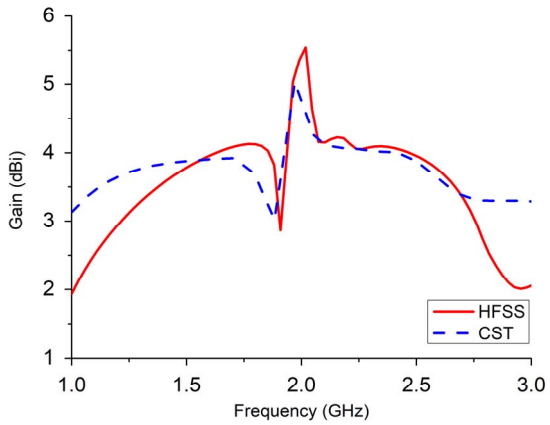


Figure 5. Simulated peak gain of the antenna

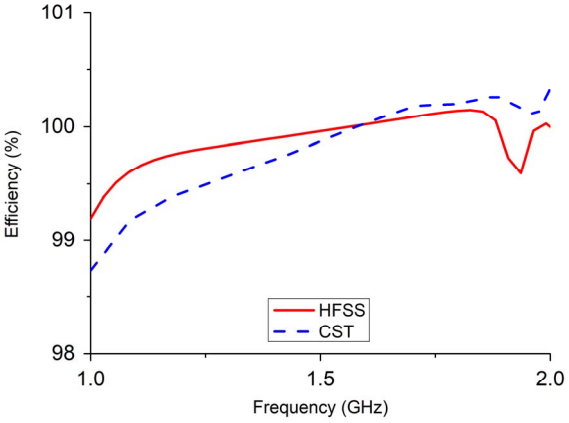


Figure 6. Simulated efficiency in HFSS and CST

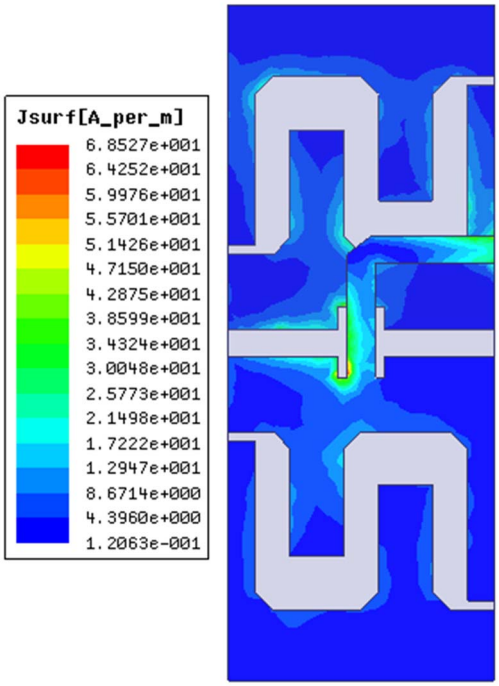


Figure 7. Current distribution of the surface

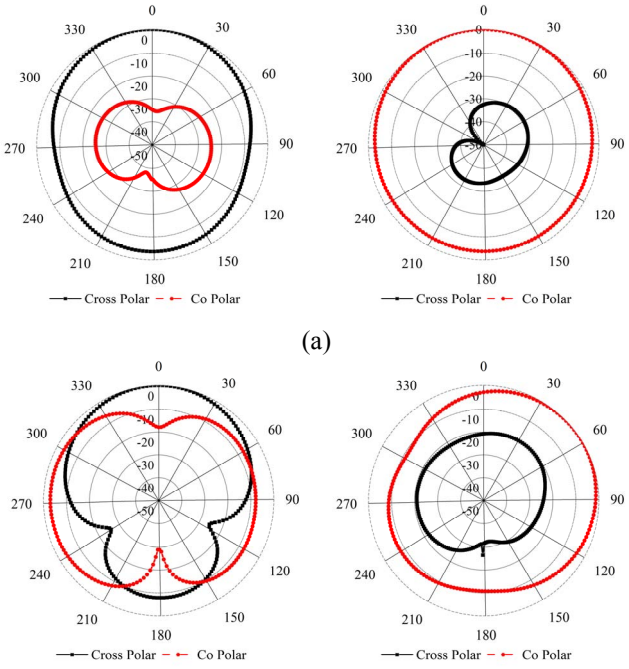


(a)

(b)

Figure 8. 2D measured radiation pattern at (a) 1 GHz & (b) 2 GHz

TABLE II COMPARISON WITH OTHER WORKS

| Antennas | BW GHz(-10dB) | Dimension | Gain (dBi) |
|---|---|---|---|
| [10] | 1.03 - 1.85 | 0.24 λ × 0.10 λ × 0.05 λ | 4 |
| [13] | 1.41 - 3.57 | 0.11 λ × 0.23 λ × 0.05 λ | 2.5 |
| [14] | 0.5 - 1 | 0.29 λ × 0.08 λ ×.08 λ | 3-5 |
| [15] | 1.25 – 2.4 | 0.29 λ × 0.12 λ× 0.06 λ | 3.5 |
| Proposed | 1.1 – 2.2 | 0.11 λ × 0.279 λ × 0.044 λ | 5.5 |

## IV. CONCLUSION

The structure of a wideband patch antenna with direction is presented. The antenna consists of double S-shaped on Roger RT substrate on both sides. The overall dimension of the prototype is 0.11 λ × 0.279 λ × 0.044 λ3 at 1.3 GHz which has fed with 50Ω microstrip transmission line. The antenna insures the frequency band from 1.1 - 2.2 GHz and obtains an average gain 5.5 dBi at 2.0 GHz. The proposed antenna defines 66% fractional bandwidth (1.1 – 2.2) GHz. The geometric design of the antenna is simple enough and is very easy to be implemented with microwave imaging applications.

## REFERENCES

[1] M. Mahmud, M. T. Islam, M. Samsuzzaman, S. Kibria, and N. Misran, "Design and parametric investigation of directional antenna for microwave imaging application," *IET Microwaves, Antennas & Propagation,* vol. 11, pp. 770-778, 2016.

[2] M. M. Islam, M. T. Islam, M. Samsuzzaman, M. R. I. Faruque, N. Misran, and M. F. Mansor, "A miniaturized antenna with negative index metamaterial based on modified SRR and CLS unit cell for UWB microwave imaging applications," *Materials,* vol. 8, pp. 392-407, 2015.

[3] M. Mahmud, M. Islam, and M. Samsuzzaman, "A high performance UWB antenna design for microwave imaging system," *Microwave and Optical Technology Letters,* vol. 58, pp. 1824-1831, 2016.

[4] J. M. Beada'a, A. M. Abbosh, S. Mustafa, and D. Ireland, "Microwave system for head imaging," *IEEE Transactions on Instrumentation and Measurement,* vol. 63, pp. 117-123, 2014.

[5] M. Rokunuzzaman, M. Samsuzzaman, and M. T. Islam, "Unidirectional Wideband 3-D Antenna for Human Head-Imaging Application," *IEEE Antennas and Wireless Propagation Letters,* vol. PP, pp. 1-1, 2016.

[6] S. Mustafa, B. Mohammed, and A. Abbosh, "Novel preprocessing techniques for accurate microwave imaging of human brain," *IEEE Antennas and Wireless Propagation Letters,* vol. 12, pp. 460-463, 2013.

[7] A. Sabouni and A. A. Kishk, "Dual-Polarized, Broadside, Thin Dielectric Resonator Antenna for Microwave Imaging," *IEEE Antennas and Wireless Propagation Letters,* vol. 12, pp. 380-383, 2013.

[8] M. Z. Mahmud, M. T. Islam, M. N. Rahman, T. Alam, and M. Samsuzzaman, "A miniaturized directional antenna for microwave breast imaging applications," *International Journal of Microwave and Wireless Technologies,* pp. 1-6, 2017.

[9] X. Li, M. Jalilvand, Y. L. Sit, and T. Zwick, "A compact double-layer on-body matched bowtie antenna for medical diagnosis," *IEEE Transactions on Antennas and Propagation,* vol. 62, pp. 1808-1816, 2014.

[10] A. T. Mobashsher and A. Abbosh, "Slot-loaded folded dipole antenna with wideband and unidirectional performance for L-band applications," *IEEE Antennas and Wireless Propagation Letters,* vol. 13, pp. 798-801, 2014.

[11] A. Mobashsher, P. Nguyen, and A. Abbosh, "Detection and localization of brain strokes in realistic 3-D human head phantom," in *Microwave Workshop Series on RF and Wireless Technologies for Biomedical and Healthcare Applications (IMWS-BIO), 2013 IEEE MTT-S International*, 2013, pp. 1-3.

[12] A. T. Mobashsher, A. M. Abbosh, and Y. Wang, "Microwave system to detect traumatic brain injuries using compact unidirectional antenna and wideband transceiver with verification on realistic head phantom," *IEEE Transactions on Microwave Theory and Techniques,* vol. 62, pp. 1826-1836, 2014.

[13] S. A. Rezaeieh, A. Zamani, and A. Abbosh, "Three Dimensional Wideband Antenna for Head Imaging System with Performance Verification in Brain Tumor Detection," 2014.

[14] S. A. Rezaeieh, A. Abbosh, and Y. Wang, "Wideband unidirectional antenna of folded structure in microwave system for early detection of congestive heart failure," *IEEE Transactions on Antennas and Propagation,* vol. 62, pp. 5375-5381, 2014.

[15] A. T. Mobashsher and A. Abbosh, "Development of compact directional antenna utilising plane of symmetry for wideband brain stroke detection systems," *Electronics Letters,* vol. 50, pp. 850-851, 2014.

# Slotted-Microstrip Antenna with Modified Ground Plane for Performance Parameters Enhancement

Chandan Roy[1,*] and Taimoor Khan[2]

[1]Department of Electrical and Electronic Engineering
Khulna University of Engineering and Technology, Khulna-9203, Bangladesh
[2]Department of Electronics and Communication Engineering
National Institute of Technology, Silchar-788010, India
[*]croy68957@gmail.com

***Abstract*— This paper presents a compact slotted rectangular microstrip antenna with modified ground plane. Performance advancements with simple modifications of a reference antenna has been carried out in the entire work. The radiating patch and the ground surface has been loaded by two asymmetrical slots and two symmetrical slots respectively. This slight change in antenna shape makes the microstrip antenna more compact. In addition, the directivity, gain, and radiation efficiency have been enhanced significantly. The overall antenna size is 41.3 mm × 48.5 mm × 1.6 mm. The proposed antenna provides 19.8% of the compactness along with 2.9dB of gain enhancement, directivity boost of 2.5dB and radiation efficiency improvement of 25%, approximately. An acceptable relationship is observed between co and cross polarization from achieved patterns which imply the antenna structure as a qualified radiator in terms of polarization purity. A prototype is fabricated with proper characterization. The measured results have a good agreement with simulated results.**

***Index Terms*—Microstrip antenna, rectangular patch, symmetrical slots, asymmetrical slots, performance parameters.**

## I. INTRODUCTION

In the era of modern wireless communication, microstrip antennas are commonly used because of their several attractive features like low cost, low profile, light weight, ease of fabrication, etc. However, the microstrip antennas are having the laminations of narrow bandwidth and poor radiation characteristics inherently [1]-[2]. These antennas work efficiently near the resonance frequency due to the narrow bandwidth problem. Thus, precise determination of the resonant frequency of the antenna is mandatory. Patch dimension, effect of fringing field as well as the effective dielectric permittivity are the major issues which are required to take account on determining the resonance frequency of the antenna accurately [3].

Antenna gain enhancement is advantageous for increasing the transmission distance and for reducing the transmitter power consumption as well. Different techniques [4]-[12] have been employed to overcome the low gain problem of microstrip antennas. Multiple patches in an array have been used to enhance the antenna gain [4]. Slotted patch has removed the overall gain characteristics [5]. Laminated conductors have been implemented in order to increase the gain [6]. Adding parasitic patch as well as different types of feeding techniques have also been used to improve the gain [7]. A circular headed dumbbell shaped defected ground plane with peak realized gain of 9 to 9.5dBi and impedance bandwidth of 22% has been proposed in [8]. In [9], a high gain dual band resonance cavity antenna has been designed with orthogonal polarization using slotted patch over the ground plane. An antenna consisting of planer and vertical patches has been designed for gain improvement [10]. A wideband high gain antenna has been designed using the square patch on air substrate [11]. Antenna without external filtering circuit consists of both driven patch and stacked patch have been designed for gain enhancement [12].

In this communication, a high gain, compact and directive microstrip antenna has been designed with higher radiation efficiency. The performance parameters of the designed rectangular microstrip antenna are improved by two asymmetrical slots embedded on the radiating surface along with two symmetrical slots inserted the ground plane. The paper is summarized as follows: section II describes the antenna geometry. Section III describes the results with validation. Conclusion is given in section IV. Acknowledgment followed by references is then included at the ending of the paper.

## II. ANTENNA GEOMETRY

The top-view and the bottom view of the proposed antenna are shown in Fig. 1(a) and Fig. 1(b), respectively. A rectangular patch having the dimensions of 41.3 mm × 48.5 mm has been designed by employing two stacked Rogers Duroid 5880 ($\varepsilon_{r1} = \varepsilon_{r2} = 2.2$ and $h_1 = h_2 = 0.762$mm) substrates sheets which have the dimensions of 70 mm × 70 mm. For excitation, a 50Ω microstrip feed line of dimensions 14.35 mm × 1.20 mm is used. For improving the performance parameters of the patch antenna, the radiating patch is loaded by slot-1 and slot-2 (having the same dimension) are inserted in the ground surface as illustrated in Fig. 1.

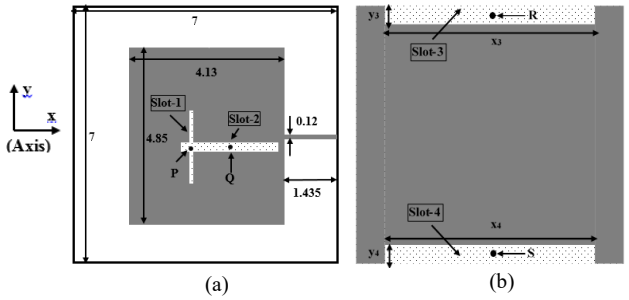


(a) (b)

(Center coordinates of the slots are indicated by P, Q, R and S. here, cm is used as unit in the complete geometry)

Fig. 1 Geometry of proposed antenna. (a) Top view and (b) Bottom View

Positions and dimensions of the slots on radiating patch and ground surface are optimized respectively to enhance the performance parameters of the antenna for the frequency range of 1.75 GHz to 2.50 GHz. The antenna geometry is designed using finite element method based HFSS (high-frequency structure

simulator) software [13]. Dimensions of the inserted slots are mentioned in Table I. Here, the positions of the slots indicates the center location of the respective slots.

TABLE I
PARAMETERS OF INSERTED SLOTS

| Slot Parameters | Value |
|---|---|
| Position of slot-1 | P ($x_1$ = -3.0 mm, $y_1$ = -7.832 mm) |
| Position of slot-2 | Q ($x_2$ = 6.8 mm, $y_2$ = -6.982 mm) |
| Position of slot-3 | R ($x_3$ = 0 mm, $y_3$ = 32.5 mm) |
| Position of slot-4 | S ($x_4$ = 0 mm, $y_4$ = -32.5 mm) |
| Dimensions of slot-1 | 20 mm × 1.0 mm |
| Dimensions of slot-2 | 26 mm × 2.5 mm |
| Dimensions of slot-3 | 55 mm × 5.0 mm |
| Dimensions of slot-4 | 55 mm × 5.0 mm |

## III. RESULTS AND VALIDATION

Fig. 2(a) and Fig. 2(b) illustrates the top view and bottom view of the fabricated antenna, respectively.

(a) (b)

Fig. 2 Snapshots of fabricated antenna (a) Top view and (b) Bottom view.

Fig. 3 depicts the $S_{11}$ values comparison between the simulated and measured results of the slotted optimized antenna with the reference antenna where there is no slots in either of the patch or the ground plane. The Agilent N5230A network analyzer is used during the $S_{11}$ parameters measurement of the fabricated prototype.

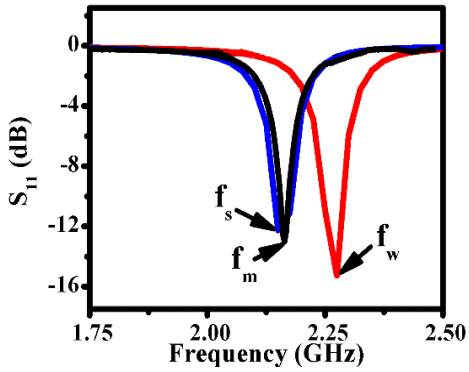


Fig. 3 $S_{11}$ vs. Frequency comparison.

2.275 GHz of the simulated resonance frequency has been observed for the reference antenna (without slots). In case of the slotted optimized antenna, the simulated resonant frequency has been found as $f_s$ = 2.15 GHz while measured resonance frequency of the fabricated prototype, $f_m$ =2.155 GHz. Consequently, the measured and the simulated resonant frequency are observed as close enough.

The resonant frequency of the designed antenna has been reduced by 0.125 GHz by inserting the slots on both of the radiating patch and the ground plane. Slots on the antenna structure generally lengthens the surface current path which enhance the antenna length. As a result, the operating frequency of the designed antenna is dropped by 5.49% with respect to the reference antenna (no slots). This operation results in 19.8% (approximately) of the patch size reduction for an expected resonance frequency design. Thus, the optimized prototype displays a good compactness in size.

Fig. 4 depicts the contrast of simulated gain for reference antenna and the slotted optimized antenna. Numerically, 4.555dB of gain has been observed at the resonant frequency of the reference antenna. Slot insertion in the patch and ground surface has enhanced the gain 7.44 dB at the particular operating frequency (2.155 GHz) while simulation result shows 7.02 dB of gain at the operating frequency of 2.15 GHz. Thus, a significant betterment in case of gain has been achieved by employing the slots on both of the radiating patch and ground plane.

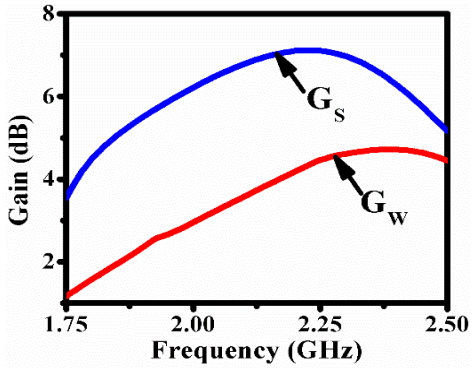


Fig. 4 Gain vs. Frequency comparison.

Friis formula of transmission is used to calculate the gain of the optimized slotted antenna as follows:

$$P_R = \frac{P_T G_T G_r \lambda^2}{(4\pi R)^2} \quad (1)$$

The experimental setup gives us $P_T$ = Cable Loss = -8.5 dB, $P_R$ = Received Power (Max. at $0^0$) = -36.56 dB and R = distance between the testing antenna and the horn antenna = 200cm.

Now the wavelength, λ is computed as:

$$\lambda = \frac{c}{f} = 13.92cm \quad (2)$$

The intermediate factor used in (1) is computed as follows:

$$k = \left(\frac{\lambda}{4\pi R}\right)^2 = \left(\frac{13.92}{4\times 3.14\times 200}\right)^2 = -45dB \quad (3)$$

Now, finally the gain (dB) is computed as follows:

$$G_r = P_R - P_T - G_T - K = 7.44dB \quad (4)$$

The simulated directivity and the radiation efficiency comparison between reference antenna and slotted optimized antenna are presented in Fig. 5(a) and Fig. 5(b), respectively. The directivity of the patch antenna is observed as 5.06 dB whereas for optimized antenna it is observed as 7.5578 dB. Similarly, the

radiation efficiency of the reference antenna and the slotted optimized antenna is calculated as 70% and 95%, respectively.

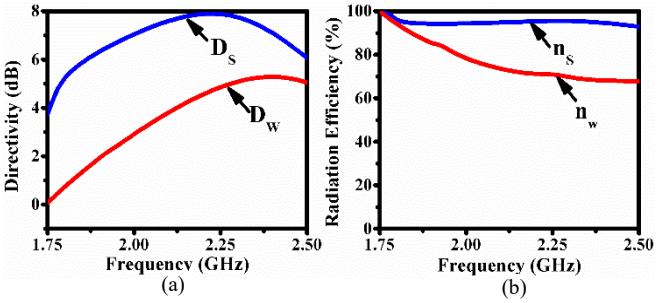


Fig. 5 Comparison of (a) Directivity and (b) Radiation Efficiency.

The achieved radiation patterns of the designed antenna are shown in Fig. 6. Fig. 6(a) and Fig. 6(b) illustrates co and cross polarization for E- plane respectively. A good agreement between simulated and measured patterns is observed. Likewise, Fig. 6(c) and Fig. 6(d) illustrates co and cross polarization for H-plane, respectively. Nearly 20 dB of difference between co and cross polarization is observed. Thus, the designed microstrip antenna having the polarization purity up to the mark.

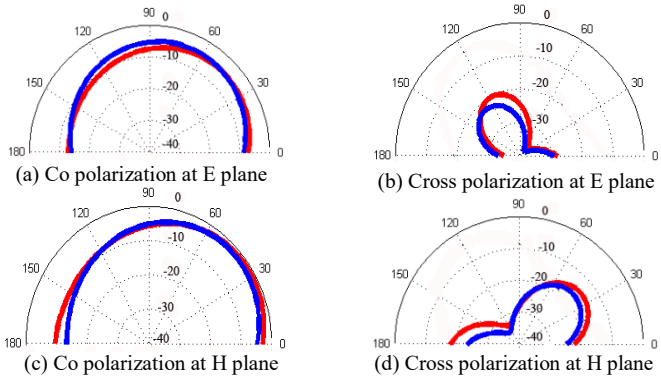


Fig. 6 Achieved Radiation Patterns (Red lines indicate simulated patterns and Blue lines indicate measured patterns).

Hence, an excellent improvement is found in the slotted optimized antenna as compared to the reference antenna for different performance parameters such as operating frequency, directivity, gain, and radiation efficiency. In addition, the optimized antenna structure is more compact than the reference antenna. Furthermore, a good agreement has been found between the simulated and measured results. A slight deviation is noticed between the simulated and measured results. This error might take place due to staking of two same substrates during fabrication. Besides, effect of soldering in PCB board and connector has not taken under the consideration during the simulation work.

## IV. Conclusions

A novel slotted-microstrip antenna has been demonstrated with a defected-ground plane to improve antenna performance such as compactness, gain, directivity and radiation efficiency. These parameters are improved in designed antenna compared to the reference antenna, which has no slots in both radiating patch and ground surface.

A prototype of the proposed antenna design has been fabricated with proper characterization for validation. An excellent convergence has been observed between the measured and the simulated results. A significant improvement in different performance parameters gain has been noticed by employing two slots on the radiating patch and another two slots in the ground surface. This encouraging amount of enhancement in four various performance parameters has made the proposed antenna an excellent alternative for enhanced radiation characteristics applications for wireless communications.

## Acknowledgment

The author is grateful to Indian Council of Cultural Relations (ICCR) Fellowship for financial assistance. We are also thankful to Prof. Binod Kumar Kanaujia for providing antenna fabrication and testing facility in the lab of IIT-Delhi, India.

## References

[1] K.F. Lee, K.F. Tong, et al. (2012). Microstrip patch antennas-basic characteristics and some recent advances. *Proceedings of the IEEE*. 100(7), 2169-2180.

[2] G. Angiulli, M. Versaci, et al. (2003). Resonant frequency evaluation of microstrip antennas using a neural-fuzzy approach, *IEEE Transactions on Magnetics*. 39(3), 1333-1336.

[3] P. Mythili, A. Das, et al. (1998). Simple approach to determine resonant frequencies of microstrip antennas. *IEEE Proceedings Microwave Antennas Propagation*. 145(2), 159-162.

[4] H.D. Chen, C.Y.D. Sim, J.Y. Wu, T.W. Chiu, et al. (2012). Broadband high-gain microstrip array antennas for WiMAX base station. *IEEE Transactions on Antennas and Propagation.* 60(8), 3977-3980.

[5] Q. Rao, R.H. Johnston, T.A. Denidni, A.R. Sebak, et al. (2005). A new high gain-slot antenna, *IEEE Microwave and Wireless Component Letters.* 15(10), 633-634.

[6] S.I. Latif, L. Shafai, C. Shafai, et al. (2011). Gain and efficiency enhancement of compact and miniaturized microstrip antennas using multi-layered laminated conductors. *IET Microwave Antennas and Propa*gation. 5(4), 402–411.

[7] Nasimuddin, K.P. Esselle, A. K. Verma, et al. (2008). Wideband high-gain circularly polarized stacked microstrip antennas with an optimized C-type feed and a short horn. *IEEE Transactions on Antennas and Propa*gation. 56(2), 578-581.

[8] S. Chakraborty, S. Chattopadhyay, et al. (2016). Substrate fields modulation with defected ground structure: a key to realize high gain, wideband microstrip antenna with improved polarization purity in principal and diagonal planes. *International Journal on RF Microwave CAD Engineering*. 26(2), 174-181.

[9] H. Moghadas, M. Daneshmand, P. Mousavi, et al. (2012). Dual-band high-gain resonant cavity antenna with orthogonal polarization using slotted patch partially reflective superstrate. *Electronic Letters*. 48(15), 897-899.

[10] H. Zhai, Q. Gao, C. Liang, R. Yu, Sheng Liu, et al. (2014). A dual-band high-gain base-station antenna for WLAN and WiMAX applications. *IEEE Antennas Wireless Propagation Letters*. 13, 876-879.

[11] D. Guha, C. Sarkar, S. Dey, C. Kumar, et al. (2015). Wideband high gain antenna realized from simple unloaded Single Patch. *IEEE Transactions on Antennas and Propagation*. 63(10), 4562-4566.

[12] X.Y. Zhang, W.D., Y.M. Pan, et al. (2015). High-gain filtering patch antenna without extra circuit, *IEEE Transactions on Antennas and Propagation*. 63(12), 5883-5888.

[13] Ansoft HFSS 14.0, Ansoft Corporation, Pittsburgh, PA.

# A Flexible Polymer Substrate Based Wideband Antenna for WBAN Applications

[1]Emranul Haque,[2]Subaha Mahmuda and [3]Feroz Ahmed
Department of Electrical and Electronic Engineering
[1,3]Independent University, Bangladesh
[2]Primeasia University
[1]emran1612@gmail.com, [2]subaha2007@yahoo.com and [3]fahmed@iub.edu.bd

***Abstract*—A compact and broadband wearable antenna is presented in this paper. The coplanar waveguide (CPW) feed antenna is composed of a modified rectangle patch with truncated top and bevelled bottom corners which operates from 3.2 to 14 GHz frequency band. The proposed antenna is employed on flexible Liquid Crystal Polymer (LCP) substrate and has a compact dimension of 37.91×28.39×0.88 mm³. The fractional bandwidth of the antenna is about 125.58% by taking -10dB reflection coefficient into consideration. The performance of the antenna under structural deformation, humid condition and on-body placement are also evaluated. The wideband operation, compact size, resilient to frequency de-tuning in on-body configuration with low specific absorption rate make the proposed antenna suitable for the wireless body area network (WBAN) applications.**

***Keywords— WBAN; Wearable antenna; wideband;LCP***

## I. INTRODUCTION

An antenna is the requisite part of the WBAN system which demands light weight, compact size, mechanical robustness, directivity and physical comfort for excellent operations. For narrowband operation, such antennas show a shift of resonant frequency when in close contact with human body [1-4]. Simultaneously, antenna may experiences different bending situations when human body moves. Therefore maintaining balanced electrical and mechanical features under distinct bending situations are also the major discretions in the study of the wearable antenna. On the other hand, computing the impact of these antennas on the human body regarding maximum allowable specific absorption rate (SAR) is important too [5].

Various low-profile antennas along textile substrates are investigated in [6,7, 8]. Disrupted substrate material of an antenna can be easily affected by the humidity. Thus an expensive substrate is used to fabricate a miniacape-like monopole antenna in [9]. In [10] and [11], a dual band circular radiator antenna is designed with area size of 3846 mm$^2$ on the Roger Duriod 5870 substrate and 2500 mm$^2$ on expensive velcro substrate respectively. A 931 mm$^2$ coplanar waveguide (CPW)-fed tri-band antenna of 3-GHz, 5-GHz and UWB upper band on FR4 substrate has been introduced in [12] where bending conditions are ignored. A complex structured textile based dual band coplanar antenna is proposed in [13] on an electromagnetic bandgap (EBG) substrate.

The demand of liquid crystal polymer (LCP) is increasing day by day as a powerful high-performance microwave substrate and packaging material [10-12]. Several antennas on LCP substrate have been studied in [14-18]. Considering different bending conditions, a LCP based patch antenna is proposed in [15] whereas, the effect of human body on the antenna radiation is overlooked. Besides in [17], SAR analysis has not been done in the modeling of the mentioned multi frequency antenna.

In this paper, a compact wideband flexible antenna which fulfills the requirement of WBAN applications such as compact size, resilient under humid and different bending conditions, human body loading effect and low SAR is proposed. By using a modified rectangle patch with truncated top and bevelled bottom corners, the developed antenna can operate from 3.2 to 14 GHz frequency band for VSWR $\leq$ 2.These features of the designed antenna make it a well-fitted candidate for various WBAN applications.

## II. ANTENNA DESIGN AND PARAMETER STUDY

The framework of the presented antenna is shown in Fig. 1. The 50 ohm coplanar waveguide (CPW) feed antenna is composed of a modified rectangle patch with truncated top and bevelled bottom corners which ensure broadband impedance transitions. This antenna is printed on a 37.91×28.39mm$^2$ flexible LCP substrate with tangent loss of 0.009, relative permittivity of 2.9 and thickness of 0.88mm. Partial ground planes are printed on the front face of the antenna which are lying symmetrically on each side of the feed line with 0.21mm gap. CST microwave studio is used to simulate and analyze the proposed antenna. The optimized values of some parameters are tabulated in Table I.

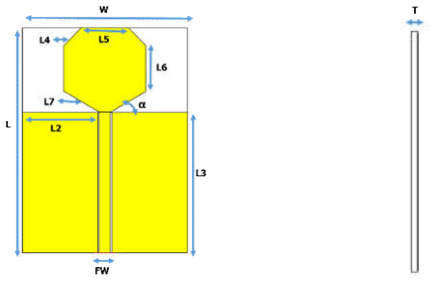


(a) (b)

Fig. 1. Structure of the antenna (a) front view, (b) side view.

TABLE I. PARAMETERS OF THE PROPOSED ANTENNA

| Parameter | Value [mm] | Parameter | Value [mm] |
|---|---|---|---|
| W | 28.39 | $L_4$ | 4.24 |
| L | 37.91 | $L_5$ | 8.20 |
| T | 0.88 | $L_6$ | 7.66 |
| $L_2$ | 13.01 | $L_7$ | 7.07 |
| $L_3$ | 23.66 | α | $30^0$ |

## III. RESULT ANALYSIS, PERFORMANCE EVALUATION AND COMPARISON WITH OTHER RELATED WORK

### *A. Return loss and VSWR of the proposed antenna*

The return loss and VSWR of the simulated antenna are given in Fig. 2 and 3 respectively. Considering -10 dB level, the antenna covers from 3.2 to 14 GHz frequency band. From Fig. 3, it is clearly seen that VSWR≤ 2 in the operating band.

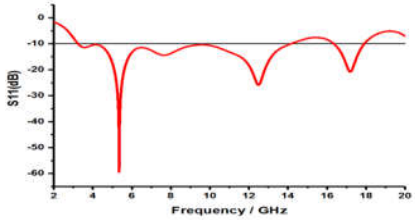


Fig. 2. The return loss of the flat antenna.

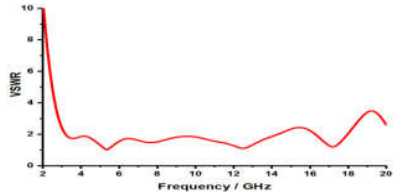


Fig. 3. VSWR of the flat antenna.

### *B. Current distribution of the proposed antenna*

It can be noticed from Fig. 4(a) that for lower frequency band, the electric current is concentrated mostly on the edge of the bottom corner of the radiating patch, edge of the ground and feed line. In Fig. 4(b), currents are concentrated mostly on the edge of top and bottom corners of the radiating patch, edge of the ground and feed line for higher frequency band. So ground plane and feed line also have effects on both the lower and higher frequency bands. Current distribution on the antenna at 4 GHz and 13 GHz is shown in Fig. 4 (a,b).

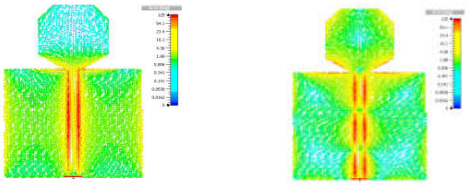

(a) (b)

Fig. 4. Current distribution at (a) 4 GHz, (b) 13 GHz.

### *C. Bending the antenna*

Considering human body shape and movement, holding the body worn antenna in a flat position is quite challenging. Hence it is necessary to study the wearable antenna's performance under different bending conditions for WBAN applications. The proposed antenna is bended with three radii of curvature values, namely, $60^0$, $40^0$ and $20^0$ along the x-axis for horizontal and y-axis for vertical bending. Fig. 5 (a,b,c,d,e,f) presents the six bended antenna.

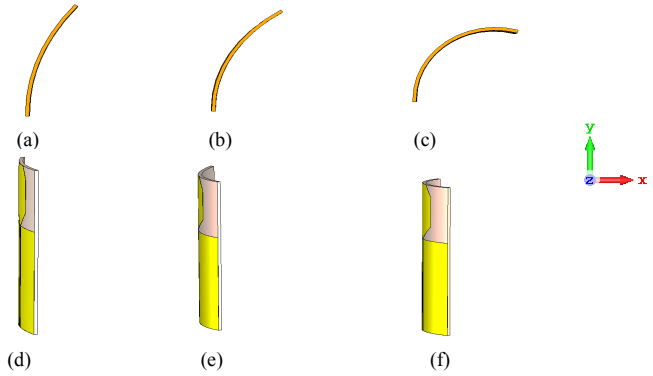


Fig. 5. Different bending at (a) $60^0$ horizontal, (b) $40^0$ horizontal (c) $20^0$ horizontal (d) $60^0$ vertical, (e) $40^0$ vertical, (f) $20^0$ vertical.

Fig. 6 (a, b) displays the simulated return loss and VSWR of the antenna under the four radii bending values. From Fig. 6(a), it is examined that the antenna maintains its resonant frequency by exhibiting -10dB return loss for the entire operating frequency bands. However, at extreme 20 degree bending condition the starting of the lower frequency band has been shifted to 3.17 GHz from 3.2 GHz due to the change in the impedance path of the antenna. Besides, Fig. 6(b) shows that VSWR≤ 2 in the operating frequency band.

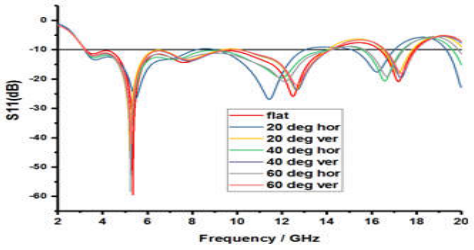


(a)

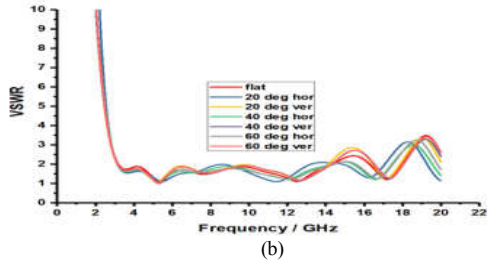


(b)

Fig. 6. (a) Return loss under different bending conditions. (b)VSWR under different bending conditions.

### D. Human body loading and humid condition

Human body can degrade the performance of the worn antenna due to presence of the biological tissues beneath the antenna [19].Therefore, the wearable antenna should be resilient to human body loading effects and withstand the degrading factors. To evaluate the human body loading effect, the proposed antenna is placed on the right arm and leg of the realistic human Hugo voxel model shown in Fig. 7 provided by CST microwave studio [21]. Moreover, to analyze the performance under humid condition, the proposed antenna (except the waveguide port area) is submerged in the water vapor environment as shown in Fig 8 to simulate humid environment.

The simulated free space as well as on-body and humid condition reflection co-efficient and VSWR of the antenna are presented in Fig. 9 (a,b).

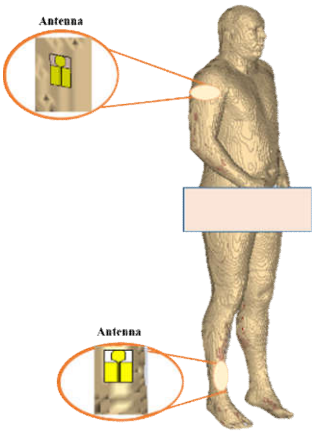


Fig. 7. Antenna on human voxel model (HUGO).

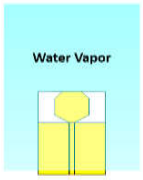


Fig. 8. Antenna in the water vapor .

It can be depicted from Fig. 9(a) that the resonant frequency of the suggested antenna remain unchanged by maintaining -10dB return loss. However, depth of the return loss has been deceased due to presence of the human tissue and water vapor. On the other hand, Fig. 9(b) shows VSWR is also in the acceptable range.

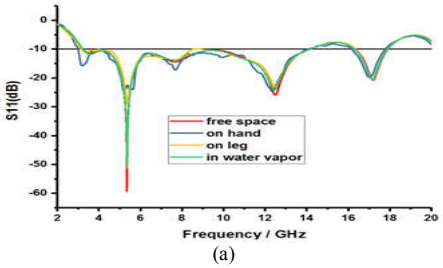


(a)

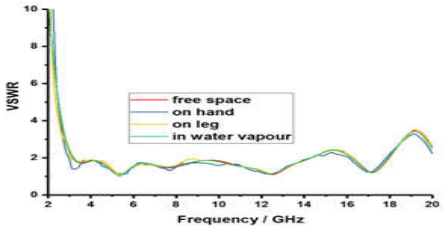


(b)

Fig. 9. Effect of human body and humidity on (a) Return loss (b) VSWR.

### E. Specific Absorption Rate Analysis

Since wearable antennas operate in the proximity of the human body, it is important to consider the amount of radiation absorbing by the body. According to the specifications of FCC, maximum SAR value can be 1.6 W/kg averaged over 1 g of tissue [4]. To investigate the SAR, the antenna is placed on a single layer muscle phantom model (400x400x80m$^3$) maintaining a distance of 5 mm. The SAR value is found to be less than 1.6 W/Kg at different frequencies. The computed value of SAR at 13 GHz is depicted in Fig. 10 as an example.

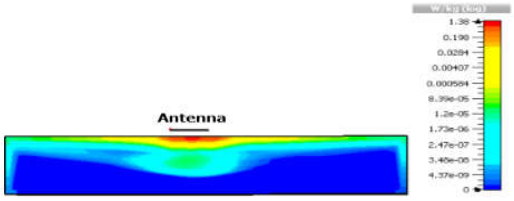


Fig. 10. SAR at 13 GHz

### F. Radiation pattern analysis

The radiation pattern of the presented antenna is also evaluated in different situations. These include free space, different bending radii curvature, humid condition and on human body placement. The simulated radiation pattern is calculated in the E and H plane for different frequencies.

*1) free space (flat and bended condition):* Fig. 11 and 12 show E and H plane radiation patterns respectively, for 4 GHz, 8 GHz and 12 GHz. From figure 11 it is seen that in the E plane quasi-omnidirectional pattern is seen at 4 GHz and 12 GHz for both flat and bended conditions. Dipole like radiation pattern is seen at 8 GHz. A small distortion is visible at 12 GHz when the antenna is being bended by 20 degree.

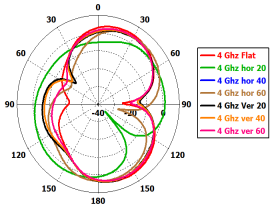


(a)

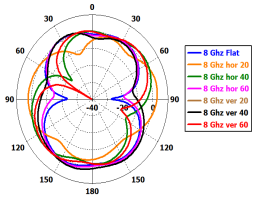


(b)

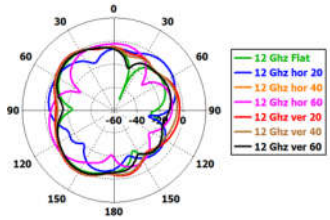


(c)

Fig. 11. E plane at (a) 4 GHz, (b) 8 GHz, (c) 12 GHz.

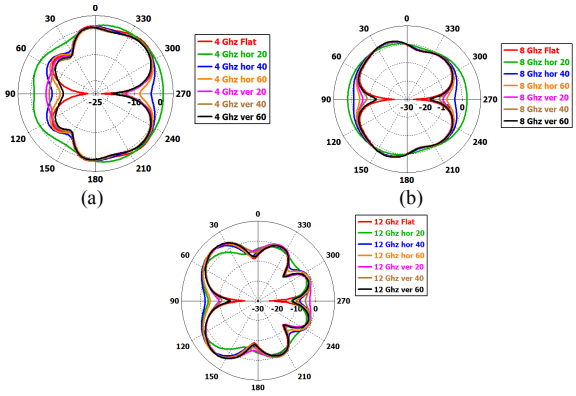


(a) (b)

(c)

Fig. 12. H plane at (a) 4 GHz, (b) 8 GHz, (c) 12 GHz.

Figure 12 represents that in the H plane, the radiation pattern is nearly omnidirectional under all conditions. However, a discrepancy is seen when the antenna is 20 degree bended at 12 GHz

*2) On-body placement:* It is realized from the Fig. 13(a) that the on-body configuration has degraded the radiation pattern in E plane by means of changing the quasi-omnidirectional radiation pattern of the antenna into directional pattern. This is happened due to radiation from human body and superposition of the back radiation [12]. In the H plane, the radiation pattern is still nearly omnidirectional for the on-body configuration which is given in Fig 13 (b).

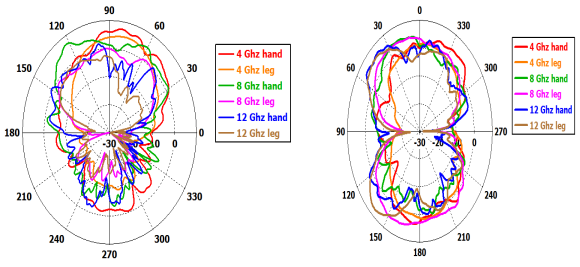


(a) (b)

Fig. 13.On-body placement (a) E plane, (b) H plane

*3) humid condition:* It is seen from the figure 14 that the radiation pattern is nearly omnidirectional for both the E and H plane under humid condition. A small discrepancy is visible at 4 GHz for both E and H plane.

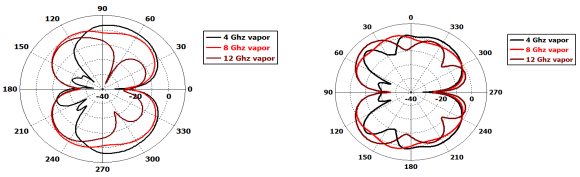


(a) (b)

Fig. 14. Humid condition (a) E plane, (b) H plane

## G. Gain and Radiation Efficiency analysis

TABLE II. GAIN AND EFFICIENCY OF THE PROPOSED ANTENNA IN FREE SPACE

| Bending & Moisture Conditions | Gain (dB) | | | Efficiency | | |
|---|---|---|---|---|---|---|
| | 4 GHz | 8 GHz | 12 GHz | 4 GHz | 8 GHz | 12 GHz |
| $0^0$ | 4.73 | 2.33 | 5.25 | 94% | 90% | 96% |
| $20^0$ Vertical | 4.81 | 2.29 | 4.97 | 96% | 89% | 95% |
| $20^0$ Horizontal | 2.94 | 2.92 | 5.71 | 93% | 82% | 89% |
| $40^0$ Vertical | 4.71 | 2.46 | 5.16 | 97% | 90% | 95% |
| $40^0$ Horizontal | 4.26 | 2.35 | 5.57 | 98% | 85% | 92% |
| $60^0$ Vertical | 4.56 | 2.4 | 5.28 | 97% | 90% | 95% |
| $60^0$ Horizontal | 3.72 | 2.68 | 5.72 | 98% | 88% | 93% |
| Humid condition | 3.96 | 2.26 | 5.26 | 87% | 89% | 94% |

Table II represents antenna gain and radiation efficiency for 4 GHz, 8 GHz and 12 GHz frequency under different bending and moisture conditions. Maximum and minimum gains are found at 12 GHz with $60^0$ horizontal bending and at 8 GHz in humid condition, respectively. Gain is decreased at mid frequency band, perhaps due to the mismatched impedance which could be improved by optimizing the impedance matching technique for mid frequency bands. On the other hand, highest efficiency can be examined at 4GHz with $40^0$ and $60^0$ horizontal bending. At 8GHz frequency, lowest efficiency is noticed under all conditions.

Higher frequencies (5, 10, 14 GHz) are considered for computing gain and efficiency of the antenna on the human body. Human body back scatters high amount of energy at higher frequencies which leads to change in directivity and induced current on the antenna [20].

TABLE III. GAIN AND EFFICIENCY OF THE PROPOSED ANTENNA ON THE HUMAN BODY

| Frequency | Hand | | | | Leg | | | |
|---|---|---|---|---|---|---|---|---|
| | On Body Placement | | Free Space | | On Body Placement | | Free Space | |
| | Gain (dB) | Efficiency | Gain (dB) | Efficiency | Gain (dB) | Efficiency | Gain (dB) | Efficiency |
| 5 GHz | 6.88 | 70% | 3.5 | 92% | 5.59 | 71% | 3.5 | 92% |
| 10 GHz | 7.34 | 72% | 4.02 | 86% | 6.71 | 70% | 4.02 | 86% |
| 14 GHz | 7.73 | 62% | 4.49 | 83% | 7.67 | 63% | 4.49 | 83% |

It can be seen from Table III that the proposed antenna shows high gain on both hand and leg placement case at 14 GHz due to the reflection of the signal by the human tissues [12]. Efficiency seems to be decreased for on-body placement due to the high tissue absorption [12].

### *H. Comparison with other related work*

In order to demonstrate the novelty of this work, the proposed antenna is compared with the recent works in terms of dimension, gain, efficiency and the bands covered by the antenna. From Table IV, it can be noticed that the suggested antenna has a wide multiband operation while maintaining a small dimension with high efficiency.

TABLE IV. COMPARISON OF THE PROPOSED ANTENNA WITH OTHERS IN TERMS OF ANTENNA SIZE AND FREQUENCY BAND

| Ref. | Antenna Size $(l \times w \times h)\, mm^3$ | Max Gain (dBi) | Max Efficiency | Frequency Band |
|---|---|---|---|---|
| [4] | 68 × 38 × 1.57 | 6.88 at 2.45 GHz | ----- | Single band (2.45 GHz) |
| [12] | 26.6 × 35 × 1.6 | 5.50 at 3.8 GHz | 92% at 7.8 GHz | Tri-band-WiMAX (3.3–3.8 GHz), WLAN 5 GHz, and UWB upper bands (6–10 GHz) |
| [18] | 132 × 132 × 2.2 | 3.4 | ----- | Dual band, ISM-2.45 GHz and ISM-5.8 GHZ |
| [17] | 40 × 26 ×1 | 4.6 at 6.2 GHz | 94.56% at 5.2 GHz | Multi-band-WLAN bands (lower band of 2.40 GHz-2.48 GHz and upper band of 5.15 GHz-5.80 GHz) and WiMAX bands (2.4 GHz– 2.6 GHz and 3.4 GHz –3.6 GHz, and 5.25 GHz –5.85GHz) |
| [10] | 3846 | 6.8 at 5.8 GHz | ----- | Dual band |
| [11] | 2500 | ----- | ----- | Dual band |
| [7] | 120 × 120 ×2.2 | 7.6 at 5.8 GHz | ----- | Dual band |
| [19] | 96.65 × 98.2 × 3 | 9.90 at 7.05 GHz | 91% at 4.65 GHz | Multi-band-Wi-Fi (5.1 GHz) and C band (4.0/4.65/6.22.7.05 GHz) |
| This work | 37.91 × 28.39 × 0.88 | 5.2 at 12 GHz | 96% at 12 GHz | Multi-band-3.2 GHz to 14 GHz (WiMAX 3.3–3.8 GHz, WLAN 5 GHz, C band 4.0/4.65/6.22.7.05 GHz, upper UWB bands 6–10 GHz, X band 8-12 GHz) |

## IV. CONCLUSION

In this paper, a flexible wideband wearable antenna has been presented for WBAN application. Modified rectangle patch with truncated top and bevelled bottom corners and partial ground ensure broadband impedance bandwidth of 10.8 GHz ranging from 3.2 to 14 GHz frequency band for VSWR ≤ 2. Considering -10dB bandwidth, the antenna maintains its resonant frequency and sustains in humid and different bending conditions as well as on-body placement. Besides, low SAR confirms its competence for WBAN application.

## V. REFERENCES


[1] P. S. Hall and Y. Hao, "Antenna and Propagation for Body-Centric Wireless Communications", Norwood, MA, USA: Artech House, 2012.

[2] C. Roblin et al., "Antenna design and channel modeling in the BAN context—Part I: Antennas," Ann. Telecommun., vol. 66, no. 3, pp. 139–155, Jan. 2011.

[3] P. S. Hall and Y. Hao, Antenna and Propagation for Body-Centric Wireless Communications. Norwood, MA, USA: Artech House, 2006.

[4] Muhammad Ali Babar Abbasi, Symeon (Simos) Nikolaou, Marco A. Antoniades, Marija Nikoli´c Stevanovi´c, and Photos Vryonides "Compact EBG-Backed Planar Monopole for BAN Wearable Applications", IEEE Trans. Antennas Propag. , vol.65, no. 2, Feb. 2017.

[5] Evaluating Compliance With FCC Guidelines for Human Exposur to Radiofrequency Electromagnetic Fields Supplement C, Federal Commun. Commission Office Eng., Technol., Washington, DC, USA, 2001.

[6] B. Sanz-Izquierdo, F. Huang, and J. C. Batchelor, "Convert dual band wearable button antenna," IET Electron. Lett., vol. 42, no. 12, pp. 668–670, Jun. 2006.

[7] S. Zhu and R. Langley, "Dual-band wearable textile antenna on an EBG substrate," IEEE Trans. Antennas Propag., vol. 57, no. 4, pp. 926–935, Apr. 2009.

[8] C. Hertleer, A. Tronquo, H. Rogier, and L. Van Langenhove, "An aperture coupled patch antenna for integration into wearable textile systems," IEEE Antennas Wireless Propag. Lett., vol. 6, pp. 392–395, Aug. 2007.

[9] D. Chun-Ping, L. Xiong-Ying, Z. Zhen-Kun, and M. M. Tentzeris, "A miniascape-like triple-band monopole antenna for WBAN applications,"IEEE Antennas Wireless Propag. Lett., vol. 11, pp. 1330–1333, Nov. 2012.

[10] Z. G. Liu and Y. X. Guo, "Dual band low profile antenna for body centric communications," IEEE Trans. Antennas Propag., vol. 61, no. 4, pp. 2282–2285, Dec. 2012.

[11] B. Sanz-Izquierdo, J. A. Miller, J. C. Batchelor, and M. I. Sobhy, "Dualband wearable metallic button antennas and transmission in body area networks," IET Microw., Antennas Propag., vol. 4, no. 2, pp. 182–190, Feb. 2010.

[12] Mohammed Nazmus Shakib, Mahmoud Moghavvemi and Wan Nor Liza Binti Wan Mahadi,"Design of a Tri-Band Off-Body Antenna for WBAN Communication", IEEE antenna and wireless propag., vol. 16, pp. 210 – 213, May 2016.

[13] Shaozhen Zhu and Richard Langley, "Dual-Band Wearable Textile Antenna on an EBG Substrate", IEEE Trans. Antennas Propag. , Volume: 57, no. 4, Apr. 2009.

[14] Penirschke, A., S. Muller, P. Scheele, C. Weil, M. Wittek, C. Hock, and R. Jacoby, "Cavity Perturbation Method for Characterization of Liquid Crystals up to 35 GHz", 34th European Microwave Conference, vol. 2, pp. 545-548., 14 Oct. 2004.

[15] Dane C. Thompson, O. Tantot, H. Jallageas, George E. Ponchak, Manos M. Tentzeris, and J. Papapolymerou, "Characterization of Liquid Crystal Polymer (LCP) Material and Transmission lines on LCP Substrates from 30 to 110 GHz", IEEE Transactions on Microwave Theory and Techniques, vol. 52, no. 4, pp. 1343-1352, Apr. 2004.

[16] Andy C. Chen, Morgan J. Chen and Anh-Vu Pham, "Design and Fabrication of Ultra-Wideband Baluns Embedded in Multilayer Liquid Crystal Polymer Flex", IEEE Transactions on Advanced Packaging, Vol. 30, No. 3, pp. 533-540, Aug. 2007.

[17] Md Shaad Mahmud and Fawwaz Jinan Jibrael Jabri, "Wideband Microstrip Patch Antenna for WLAN and WiMAX Applications on Liquid Crystal Polymer Substrate", International Conference on Informatics, Electronics & Vision (ICIEV), May 2013.

[18] Fuheng Zhang , Guo-Min Yang and Ya-Qiu Jin, "Dual-band wearable antenna on liquid crystalline polymer based metasurface", Asia Pacific Microwave Conference (APMC), 2015.

[19] Waqas Farooq , Masood Ur-Rehman, Xiaodong Yang and Qammer Hussain Abbasi, "Study of a novel multi-band antenna for body-centric wireless networks" IEEE 11th International Conference on Wireless and Mobile Computing, Networking and Communications (WiMob), 2015.

[20] Masood Ur-Rehman,Qammer Hussain Abbasi, Muhammad Akram, Clive Parini, "Design of band-notched ultra wideband antenna for indoor and wearable wireless communications" IET Microw., Antennas Propag., vol. 9, iss. 3, pp. 243–251, Feb. 2015.

[21] https://www.cst.com/Applications/Article/HUGO+Human+Body+Model. Accesed on Apr. 2017.

# Compact Planar UWB Antenna with 3.5/5.8 GHz Dual Band-Notched Characteristics for IoT Application

Sayed Amirul Hassan[1,*], Md. Samsuzzaman[2], Mohammad Jamal Hossain[3], Md. Akhtaruzzaman[4], Tariqul Islam[5]
Faculty of Computer Science and Engineering [1, 2, 3]
Patuakhali Science and Technology University, Bangladesh
Solar Energy Research Institute[4]
Dept. of Electrical Electronic and System Engineering[5]
Universiti Kebangsaan Malaysia, Malaysia
[*]sayedamirulhassanapon@gmail.com

*Abstract*— **Today's frontier demands ease in daily tasks and interaction with regular devices. This paper proposes an ultra-wideband (UWB) planar antenna with a close-fitting size of 24mm×26mm. The structure of this antenna contains micro-strip line-fed circular ring radiator. The semi-circular slot that produces 5.8GHz of WLAN, and an annular circular slot that produces 3.5GHz of WiMAX. The dual-notched characteristics reduce interference among the already existing UWB operating devices as antenna shows a negative gain at notched bands. Antenna acquires a wide impedance bandwidth of 117.67% from 3.11GHz to more than 12 GHz for s11< -10dB except for two frequency notched bands 3.28-3.85GHz and 5.11-6.4GHz for WiMAX and WLAN respectively. It has an omnidirectional radiation, high efficiency of 98.585%, radiation characteristics of the proposed antenna shows good stability and time domain behavior. All the observations make this antenna fit for IoT applications.**

***Keywords*** — **IoT; compact; notched band; UWB antenna.**

## I. INTRODUCTION

In embedded technology every object, every module, every device is wirelessly connected to a mesh network, this is the Internet of things (IoT). Wireless communication technologies will want to function at more than one frequency without increasing size of the antenna. Fast and reliable wireless communication for the IoT devices need task specifically optimized antenna. UWB is a radio technology which can be used for high bandwidth for short-range communication purposes covering large portion radio spectrum. Applications of IoT involves sensor data collection, precision locating, remote monitoring, security, wireless communication and tracking applications. These applications involve short-range communication with radio frequency, availability of lots of bandwidth for usage, cost management, optimization and the greatest challenge, i.e. the size of the component needs to decrease significantly. These are the prime features and reasons that make UWB the perfect candidate for IoT application. The operating range from 3.1 to 10.6 GHz is permitted by Federal Communication Commission (FCC) as the unlicensed band for radio transmission.

Now a day's many research has been focused on the UWB planar antenna for IoT applications and create notch band for rejecting some frequency bands [1]. IoT will represent an important preamble in the contemporaneous communication networks. In IoT applications for the antennas are required to achieve three important characteristics [2].Application and acceptance of UWB technology have grown so rapidly because of its broad bandwidth, decent radiation characteristics, high-speed data rate, portable size, etc. [3, 4].UWB antennas with notched characteristic for the Internet of Things (IoT) [5].Since the working band of UWB communication is astoundingly large and an inevitable overlap of working frequency with some other already operating frequency band like (WiMAX) ranging from 3.3 to 3.8 GHz and (WLAN) in 5.15 to 5.825 needs to be taken care of, the filtering of frequency bands 3.3–3.7 and 5.15–5.825 GHz, respectively, is required. Hence, we abide to reconfigure the structural part of the antenna to achieve the notched characteristics for the two frequency bands i.e., at WLAN(5.15 to 5.825GHz) and WiMAX(3.3 to 3.8 GHz) bandwidths [6].A paper has proposed of 5.15-5.35 GHz and 5.725-5.825 for notching at two different points for WLAN and one at 3.3 to 3.7GHz for WiMAX [7, 8].The problem is any useful information in this range of WiMAX and WLAN will be interfered by our antenna if the dual band characteristics are not achieved but to achieve this characteristic from our UWB antenna we need a modification at the intrinsic level [9].

This antenna doping the UWB band with dual band-notched characteristics is proposed. The proposed antenna shapes a circular ring patch and a partial ground. Two partial slots are inserted in the circular ring radiating patch to create dual notched frequency bands centered at 3.5 and 5.5 GHz. The bandwidth and center frequency of the notched bands can be controlled by manipulating the size and location parameters of this notch structure (slots). It is found that with a compact dimension of 24mm×26mm, the proposed antenna achieves an operating bandwidth ranging from 3.111 to more than 12 GHz with two notched frequency bands of 3.28–3.85 and 5.11–6.4 GHz. It is possible to generate dual-notched bands and minimizing the interference simultaneously.

## II. ANTENNA STRUCTURE

Fig 1(a) shows the structure and configuration of the proposed compact microstrip patch antenna. It is constructed on a 1.6-mm thick, low-cost FR4 substrate which is easy for fabrication. A dielectric loss tangent of 0.02 and relative permittivity of 4.4. The total area of the antenna is 24mm×26mm which is consisted by a circular ring radiator with 8 mm of outer radius, 3mm of inner radius, and a partial ground surface. The area of ground is 7.5 mm×26 mm. The distance between the feed line and the substrate on the left edge is 7.5 mm. It is chosen for its compact size, simplicity and stable radiation. One of the smallest and highly configured compact planner antennae which has a full UWB with dual notched characteristics antenna is proposed. The proposed antenna is fabricated on FR4 material which is low

978-1-5386-3374-8/17/$31.00 ©2017 IEEE

cost and having loss tangent is 0.02 and dielectric constant of 4.4. An SMA connector with the input impedance of 50 ohms is used for matching.

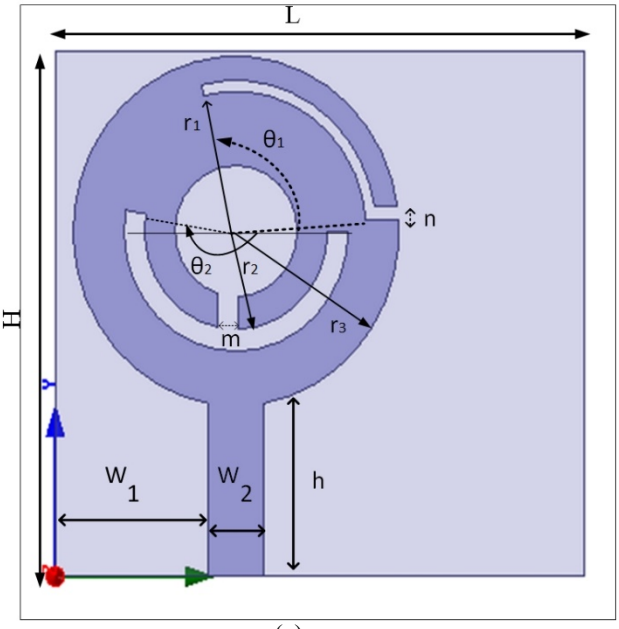


(a)

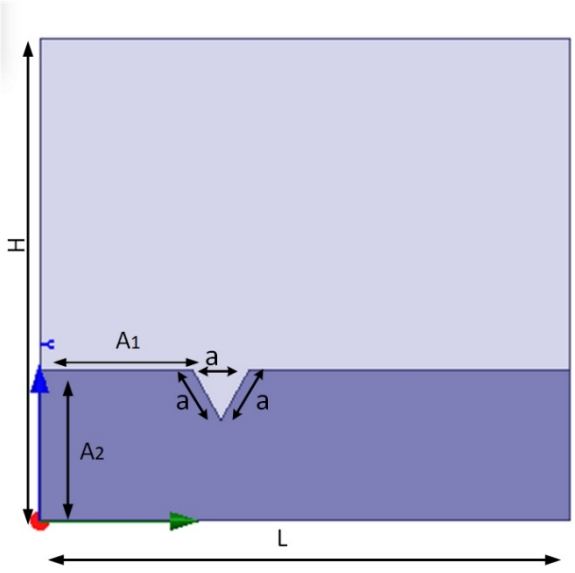


(b)

Fig. 1 Proposed antenna structure (a) Top view (b) Bottom view

Table 1. Different Optimized Parameters

| Parameter | mm | Parameter | mm | Parameter | mm |
|---|---|---|---|---|---|
| *L* | 26 | $r_1$ | 6.5 | $W_1$ | 7.5 |
| *H* | 24 | $r_2$ | 5.5 | $W_2$ | 2.75 |
| $A_1$ | 6 | $r_3$ | 8 | $\theta_1$ | 100° |
| $A_2$ | 7.5 | *m* | 1 | $\theta_2$ | 190° |
| *h* | 8 | *n* | .5 | *a* | 2.85 |

A parametric study has been conducted to explore the effects of partial annular and semi-circular slots on band-notched characteristics. It has been found in simulation that the center frequency, as well as the bandwidth of notched bands, is critically dependent on the flare angle of annular slot $\theta_1$ and flare angle of semi-circular slot $\theta_2$ widths of the rectangular slots b4 and b2 that is $\theta_1, \theta_2$, m and n are the most susceptible parameters for band-notch function. In the simulations, except for the parameter of interest, the other parameters are kept constant.

Fig 2 shows the results from the simulation from S11 software for the antenna as $\theta_2$ (Y-axis flare angle of the semi-conductor slot). Value of fare angle corresponding to $\theta_2$ = 180 degree shows poor band-notch capability for WLAN. On the other hand, for $\theta_2$ = 200 cannot totally reject the WLAN band. Hence, the value $\theta_2$ = 190 degrees is selected as an optimal value for $\theta_2$. Fig 3 shows the results from the simulation from S11 software for the antenna as $\theta_1$ (flare angle of the annular-circular slot). Value of $\theta_1$ = 115 has relatively poor band-notched characteristics for WiMAX, on the other hand, the curve for $\theta_1$ = 110 cannot totally reject the operating frequency bandwidth of WiMAX. Hence, Value of $\theta_1$ = 100 is chosen as an optimal value of flare angle of the annular-circular slot. Fig 4 shows the results from the simulation software S11 for the antenna as n (Y-axis as return loss). A value of n = 1mm results in notching at 3.1 to 3.7 GHz. On the other hand n = .50mm results in notching at 3.25-3.85 GHz and the desired frequency. Hence, n = 0.50mm is taken as the optimal result. Fig 5 shows the results from the simulation from S11 software for the antenna as m (Y-axis for return loss). It is noted that for a value of m = 1.5mm the notching starts at 3.3 to 3.8GHz, again for m = 0.75 the notching just starts. But, for m = 1mm a perfect notching is found for WiMAX band i.e., 3.28 – 3.8 GHz. Hence, m = 1mm is taken as suitable value.

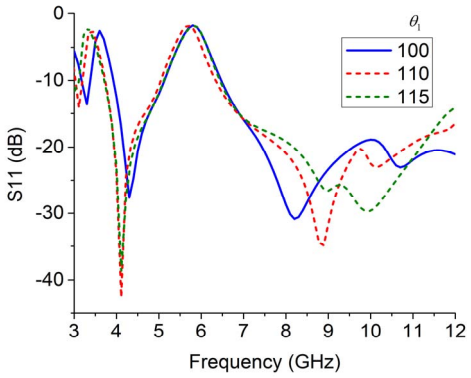


Fig. 2 Simulated return loss curve for $\theta_1$ in HFSS

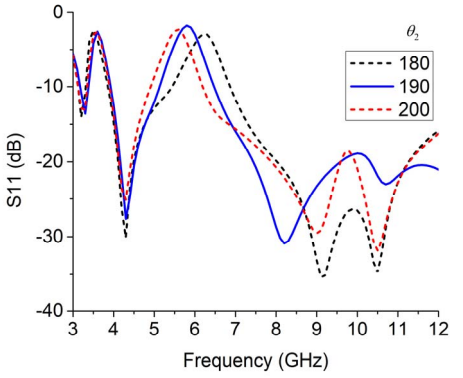


Fig. 3 Simulated return loss curve for $\theta_1$ in HFSS

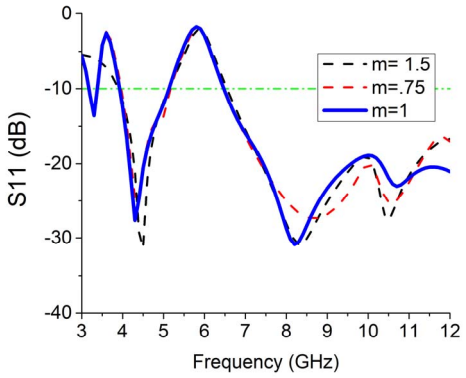


Fig. 4 Simulated return loss curve form in HFSS

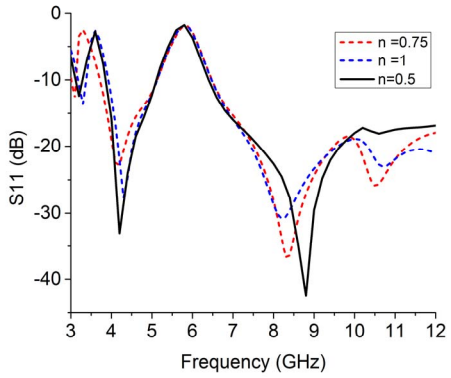


Fig. 5 Simulated return loss curve for n in HFSS

The typical current distributions on the radiating patch at center frequencies of the notched bands are plotted in Fig 6 (i) displays the current near the center frequency of first notched band at 3.6 GHz. Thus, high attenuation near this frequency produces notch frequency band for WiMAX. From Fig 6(ii), which depict the current distribution at 5.8 GHz, Hence, high attenuation near this frequency produces notch frequency band for WLAN. Fig 7 represents the input impedance of the antenna Zin with the operating frequency. The input reactance is around 0 Ω and the input resistance is around 50 Ω at the passbands while the antenna is operating and indicating UWB characteristics of this antenna. Obvious impedance mismatch occurs at the stop bands because of values deviating largely from the nominal values.

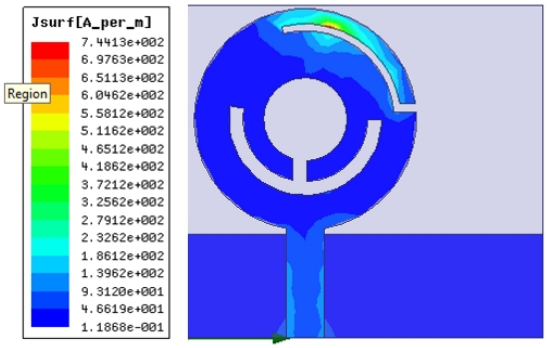


(i)

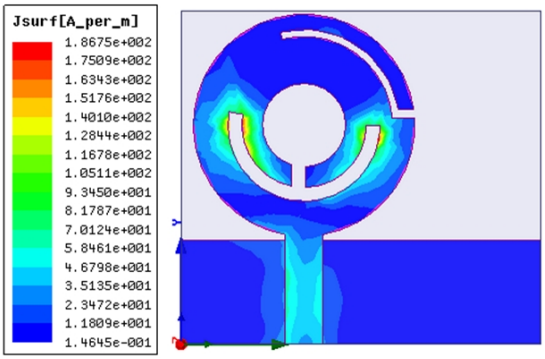


(ii)

Fig. 6 Simulated Surface Current Distributions Results at (i) 3.6 and (ii) 5.8 GHz

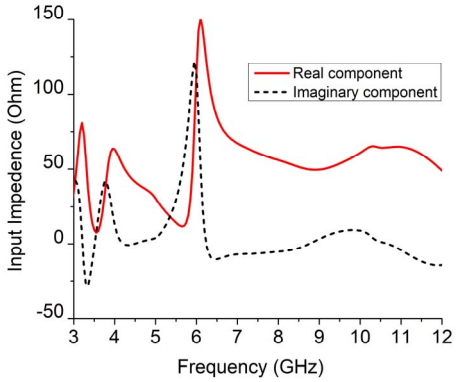


Fig. 7 Input impedance *Z* of the frequency versus antenna

## III. Result And Discussion

Fig 8, a dual band-notched structure with an optimal design with HFSS and CST software, that is 1= 100°, 2 = 190°, n = 0.50mm and m=1 mm, is tested using far-field antenna measurement system .Notching at two frequency bands 3.28-3.85GHz and 5.11-6.4GHz for WiMAX and WLAN is achieved respectively. From the graph, we conclude that this UWB antenna is capable of operating on a wide range of bandwidth, i.e., 3.1 to 12 GHz. The proposed antenna covers the full operating bandwidth from 3.1 to 10.6 GHz range which is used for UWB applications. Fig. 9 shows the gains for HFSS and CST respectively. The observed maximum gain is 5.1dBi. Gain under UWB is 11.5dBi and an average gain of 3.9dBi is also observed. In Fig. 10, the efficiency is confined between 95.84% and 98.85% for lower and higher band respectively. The gain and efficiency are affected by the dielectric substrate. Avoiding the use of cheap FR4 and using more dedicated dielectric can enhance the efficiency and gain of this proposed antenna.

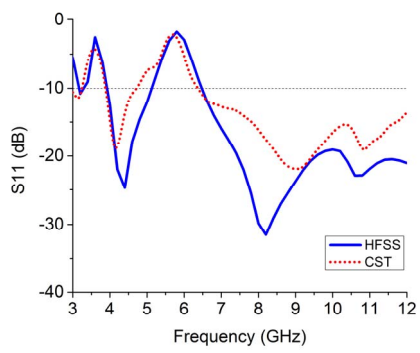


Fig. 8 Return loss curve in HFSS and CST Software.

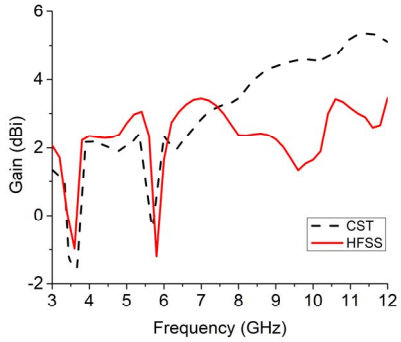


Fig. 9 Simulated gain in HFSS and CST Software

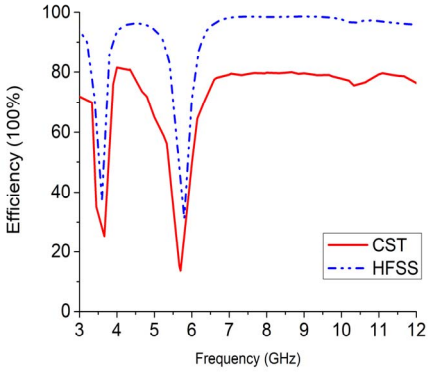


Fig. 10 Simulated efficiency in HFSS and CST Software.

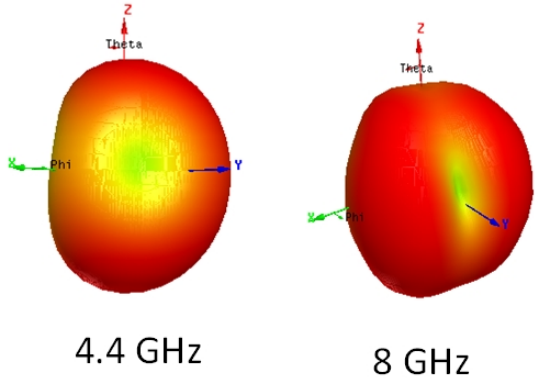


Fig. 11(a) 3D measured radiation pattern

Fig. 11(a) describe the simulated 3D radiation patterns at (a) 4.4GHz and (b) 8 GHz. The red color in the radiation patterns indicates the strongly radiated E-field and the weakest ones is indicated by blue color. At a low frequency of 4.4 GHz, the radiation pattern has a red color, indicating strongly radiated E-Field and the weakest are blue colored. In this case, the radiation is weak in the z-direction. Finally, the purposed antenna at a high frequency of 8GHz is a suitable candidate. Caring an ability to radiate 3-D omnidirectional patters. Fig. 11(b) shows the simulated radiation patterns of the proposed antenna in –XZ and –YZ planes for two resonant frequency of 4.4 and 8 GHz. The radiation pattern is found to be omnidirectional for the lower frequency of 4.4GHz.For, the higher frequency of 8GHz the radiation pattern is approx. omnidirectional to yz plane. We can figure out that the radiation patterns are remarkably stable during ultra-wideband.

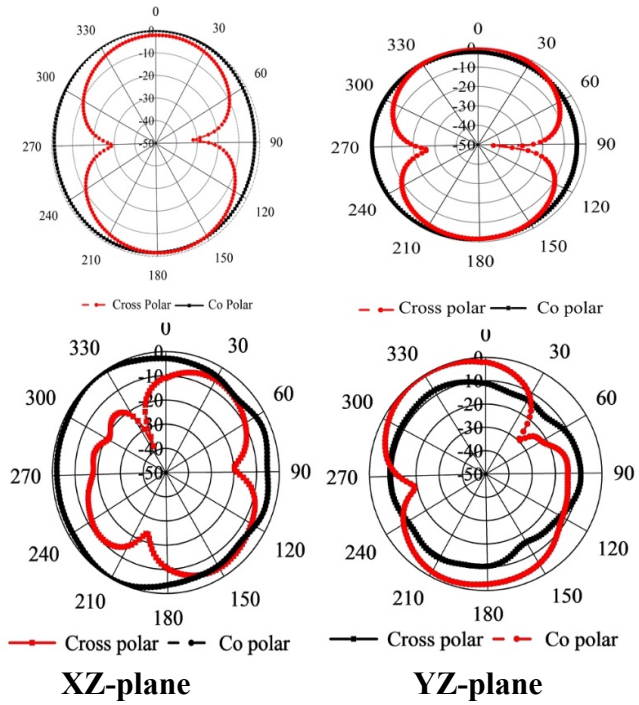


Fig. 11(b) 2D measured radiation pattern at 4.4 and 8 GHz

Table 2 : Comparison between the reported antennas with the proposed dual band-notched UWB antenna

| References | Antenna Size mm) | Operating Bandwidth(GHz) | Notched Band (GHz) |
|---|---|---|---|
| [6] | 30×22 | 2.9-11 | 3.26-3.71, 5.15-5.37, 5.78-5.95 |
| [10] | 30×25 | 2.9-11 | 5.1-5.5, 5.72-5.9 |
| [11] | 40.4×44 | 3-11 | 5.15-5.35, 5.725-5.85 |
| [12] | 35×30 | 3-11 | 4.91-5.9 |
| Proposed Antenna | 24×26 | 3.11-12 | 3.28-3.85, 5.1-6.4 |

This antenna size was not compact and incomplete rejecting for 3.30–3.80 and 5.15–5.85 bands. The proposed antenna sharply notched at two frequency bands 3.28-3.85GHz and 5.11-6.4GHz for WiMAX and WLAN respectively. The size of the antenna is finally finalized to be 24 mm × 26 mm with a microstrip line-fed circular ring radiator with a semi-circular slot for WLAN and an annular slot for WiMAX. And perform wider operation bandwidth, sufficient, complete band-notched function and compact size, and. This antenna may be suitable for IoT applications.

\

## IV. Conclusions

As per the discussion and analysis above we find the antenna is able to produce radiation characteristics of dual notched UWB spectrum. Sharply notched at two frequency bands 3.28-3.85GHz and 5.11-6.4GHz for WiMAX and WLAN respectively. The size of the antenna is finally finalized to be 24 mm × 26 mm with a microstrip line-fed circular ring radiator with a semi-circular slot for WLAN and an annular slot for WiMAX. Operating bandwidth of 117.67% is achieved. This simple design brings the manufacturing cost down without compromising the efficiency wiz. 98.585%. Considering the small size and greater operating bandwidth with such sharp frequency notch characteristics it perfect for IoT applications.

## References


[1] M. M. Islam, M. T. Islam, M. Samsuzzaman, and M. R. I. Faruque, "Five band‐notched ultrawide band (UWB) antenna loaded with C‐shaped slots," *Microwave and Optical Technology Letters,* vol. 57, pp. 1470-1475, 2015.

[2] M. A. Khan, M. A. ul Haq, and S. ur Rehman, "A practical miniature antenna design for future internet of things enabled smart devices," in *Signal Processing and Communication Systems (ICSPCS), 2016 10th International Conference on*, 2016, pp. 1-6.

[3] J. Zhang, P. V. Orlik, Z. Sahinoglu, A. F. Molisch, and P. Kinney, "UWB systems for wireless sensor networks," *Proceedings of the IEEE,* vol. 97, pp. 313-331, 2009.

[4] M. M. Islam, M. T. Islam, M. Samsuzzaman, M. R. I. Faruque, N. Misran, and M. F. Mansor, "A miniaturized antenna with negative index metamaterial based on modified SRR and CLS unit cell for UWB microwave imaging applications," *Materials,* vol. 8, pp. 392-407, 2015.

[5] J. Dong, Q. Li, and L. Deng, "Compact Planar Ultrawideband Antennas with 3.5/5.2/5.8 GHz Triple Band-Notched Characteristics for Internet of Things Applications," *Sensors,* vol. 17, p. 349, 2017.

[6] R. Azim, M. T. Islam, J. Mandeep, and A. Mobashsher, "A planar circular ring ultra-wideband antenna with dual band-notched characteristics," *Journal of Electromagnetic Waves and Applications,* vol. 26, pp. 2022-2032, 2012.

[7] J. Yang, H. Wang, Z. Lv, and H. Wang, "Design of miniaturized dual-band microstrip antenna for WLAN application," *Sensors,* vol. 16, p. 983, 2016.

[8] M. Samsuzzaman, T. Islam, N. Abd Rahman, M. R. I. Faruque, and J. Mandeep, "Compact modified swastika shape patch antenna for WLAN/WiMAX applications," *International Journal of Antennas and Propagation,* vol. 2014, 2014.

[9] M. Rotaru and J. Sykulski, "Compact electromagnetic bandgap structures for notch band in ultra-wideband applications," *Sensors,* vol. 10, pp. 9620-9629, 2010.

[10] R. Azim, M. T. Islam, and A. T. Mobashsher, "Dual band-notch UWB antenna with single tri-arm resonator," *IEEE Antennas and Wireless Propagation Letters,* vol. 13, pp. 670-673, 2014.

[11] A. A. Gheethan and D. E. Anagnostou, "Dual band-reject UWB antenna with sharp rejection of narrow and closely-spaced bands," *IEEE Transactions on Antennas and Propagation,* vol. 60, pp. 2071-2076, 2012.

[12] B. Li, J. Hong, and B. Wang, "Switched band-notched UWB/dual-band WLAN slot antenna with inverted S-shaped slots," *IEEE Antennas and Wireless Propagation Letters,* vol. 11, pp. 572-575, 2012.

# Circularly Polarized S Band Patch Antenna for Small Satellite Application

Syed Mahathir Hasan[1,*], Md.Samsuzzaman[1] ,Masud Rana[1] ,Taohidul Islam[1] ,and Tariqul Islam[2]

[1]Faculty of Computer Science and Engineering
Patuakhali Science and Technology University, Patuakhali, Bangladesh
[2]Dept. of Electrical Electronic and Systems Engineering
Universiti Kebangsaan Malaysia, Malaysia
[*]hasanrian014@gmail.com

***Abstract*— The main purpose of this invention is to design an S-band patch antenna which is basically highly directional and circularly polarized. In this paper this type of antenna is proposed which includes those characteristics. This antenna has a ground which is in a shape of square. On the upper portion, there is a patch which is also a square but two corner of that patch was slotted equally. Connection between patch and ground has been established by a coaxial probe. The patch of this antenna is fed through this probe. Creation of resonance is done by those slots which is created straightway of secondary diagonal of the patch. As this design is too simple so it'll be easier to integrate it on the satellite body. Those slots on the secondary diagonal side which is the modification of the patch, help to achieve resonance in the expecting frequency. Resonance is basically excited by these slots. Experimental and simulated results of proposed design are desirable. In operating band, its axial ratio is less than 3 dB. In 2.40 GHz frequency, the gain of this prototype is 7dBi. In small satellite implementation and also in application, this prototype is adjustable because of its properties like CP i.e. circular polarization, high gain and directional radiation pattern.**

***Keywords— CubeSat applications, High gain, circularly polarized and Directional antenna.***

## I. INTRODUCTION

For making a small satellite but without changing its performance and capabilities, "Miniaturization" is the best technique. This technique was started to be used from a recent decade ago. There are many types of a satellite including small, mini, micro and Pico-satellites. Now a day's small satellite is in an increasing number. The most attractive characteristics of small satellites are that the investments it needs and the mass production cost is too low. Although the investments and production cost is too low, it provides higher reliability, low lunching cost and also higher lunch flexibility. These characteristics make the small satellite more attractive. It's used involving in earth observation such as testing of different components, the system of communication and educational purpose [1]. Generally, for overcoming the physical limitations and also all types of restrictions, the subsystems which constitute the small satellite should have to design. In fact, here the high precision attitude determination systems are not used in this satellite. As a result, the pointing mechanisms which are expensive can't be implemented. This type of limitations like physical and the restriction of cost together makes it impossible to use a high directive antenna. If there is a shortage of reliable control systems, it will lead certain antenna point in a direction which is totally wrong. It'll be then a critical issue on that consequences. Another side, in omnidirectional antennas- there is a limitation of the data rate in the link between ground stations. On the basis of above discussion, the antennas which are highly directional are the most useful for certain goals, minimizing the complexity of the instruments, handling a huge quantity of data related to science, a huge rate of data transfer links and for the best ratio of signal to noise. The standard dimension of the Cube-Sat small satellite is 10x10x10 $cm^3$, it's weight is less than one kg, and it uses those components which are commercially off-shelf [2]. Nowadays, there are three types of Cube-Sat which are being used all over the world in the communication of small satellite. Here in this research, 3-unit Cube-Sat which dimension is 30x10x10 $cm^3$ is used. For satisfying the P-pod launcher dimensional restrictions, the profile of the antenna will be low [3], size will be reduced, directivity will be moderated and performances of gain must be increased. The standard dimension of the Cube-Sat small satellite is 10x10x10 cm3, it's weight is less than one kg, and it uses those components which are commercially off-shelf [2]. Nowadays, there are three types of Cube-Sat which are being used all over the world in the communication of small satellite. Here in this research, 3-unit Cube-Sat which dimension is 30x10x10 cm3 is used. For satisfying the P-pod launcher dimensional restrictions, the profile of the antenna will be low [3], size will be reduced, directivity will be moderated and performances of gain must be increased. Another side, for the communication of high speed, S-band is used in general. Especially for earth orbit small satellite which is low with respect to the surface. Video or high-resolution image transfer can be an example. But stability requirement is the basic problem of S-band patch antenna which is useful on the sector of cube satellite and on the other hand micro-strip arrays are able to handle the gain and directivity which is mainly high. High gain antennas band beam-width is too much narrow which makes the satellite stable as long as it is possible. In such a way we get an enhanced communication. Recently in satellite communication, radio frequency identification (RFID) readers, mobile to mobile communication compact patch microstrip antennas have got popularity as it has a good orientation of transmitter and

978-1-5386-3374-8/17/$31.00 ©2017 IEEE

receiver which is much more flexible[4-6]. It works both like as receiver and transmitter. It provides cross polarization and multipath propagation. This antenna is light weighted, smaller and its gain is too low which is required here. This type of problem has been investigated [7-9] and huge number of antenna designs have been published all over the years in technical literature. Gain enhancement methods have been proposed here [10]. But it requires a certain dielectrics which has a thick layer. This thick layer makes the antenna a little bit heavy. Configuration of stacked patch has been studied and got a gain around 9 dB which has two patches, in 3 layer configuration the gain is 10 dB [9] and parasitic patches of 2x2 array has a gain of 10.5 dB. For solving this problem we can use helical antenna as like as single element which is mainly a larger gain radiator. Here, we can easily obtain a gain which is more than 10 dB, here patch configuration is smaller than the structure. As a result, microstrip patch antennas impedance bandwidth has been improved. are used, increases the overall loss of that antenna, and for obtaining circular polarization, there is a feed network which feeds the patch through 2 shorting pins [11]. When the shorting pin numbers are increased, the function of patch is similar to the annular patch [12, 13]. It is compared with a circular patch for a given frequency, where annular-ring geometry is in smaller size. In the CP antenna, annular ring is employed for both requirements- compactness [14] and the dual- frequency operation [15]. There are two layers in dual-frequency circularly polarized antenna.

In this paper, a high gain CP antenna which has a compact concentric single annular ring patch is designed and verified. By a single feed, the antenna is fed. By the tuning, the rectangular slot ring and also the feed position CP is achieved. As the dielectric loss tangent is low here so the loss of the antenna is also low. A higher is achieved by making the patch size slightly larger than the conventional one. The antenna has fulfilled the mechanical properties of the low profile, robust, lightweight, good emissivity, and thermal properties. The main advantages of this antenna are- it is well suited fully for space application.

## II. Antenna Geometry

In Fig.1, the geometrical structure of this proposed antenna is shown. This is basically a square shape antenna. This antenna consists of two portions. The upper portion is a patch and the lower portion is ground. The distance between patch and ground is 1.575 mm. Both patch and ground are in square shape. In this antenna, we have used Rogers RT/ duroid 5880(TM) substrate. Though it's not cost effective but only for its high efficiency we've chosen this. In small satellite application, efficiency is a major requirement. Its relative permittivity is 2.2, relative permeability is 1 and dielectric loss tangent is 0.0009. Here, the patch is smaller than ground plane. Length of the patch is defined by L1 which is 40.421 mm. The ground plane is also in a square shape. Its length is defined by L which is 46.683 mm. On the upper portion that means on the patch, there is two triangular shape slot. Length of that slot is L3 which is 3.7 mm. These slots are straightway on the secondary diagonal of the patch. In between patch and ground, there is a 50 Ω coaxial probe. The required power is supplied through this probe. The outer diameter of the probe is 1.5 mm and the inner diameter is 0.5 mm. This is a cylindrical shape probe which has attached the patch and the ground plane. After performing a good number of parametric studies then we have fixed the dimensions.

## III. Results and Discussion

### *3.1 Parametric Study*

For designing a highly directional circularly polarized S-band patch antenna at 2.40 GHz for the purpose of satellite application, the parametric analysis is done which is comprehensive to it. In Fig.2 and 3, it also shows the reflection coefficient's result according to various types of dielectric size and about feed location. On that figure, slop which is marked by red color shows the proposed prototype's S11 result. Fig.4 and 5 also show the S11 outcome but on the basis of different sizes of patch measurement. When both slots are present in the layout architecture, it effects hugely not only on the reflection coefficient but also to the gain. In Fig.6 and 7, the outcome of the gain is depicted on the measurement of the different size of dielectric i.e. L and also on L1. When the dielectric size is 46.683 mm then it provides a gain of 7 dB which is satisfying. In small satellite application, the gain isn't a major factor. In this type of application, it never needs a high gain. This proposed prototype has fulfilled this requirement almost. In Fig.7, the gain is showed on the basis of the different size of L1. This figure also shows the same quantity of gain like L.

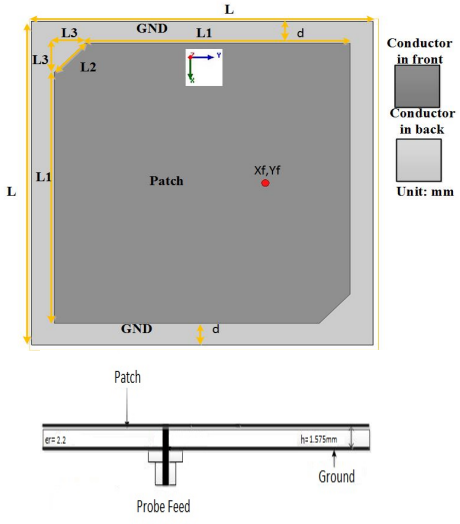


Figure 1. Geometry of proposed antenna

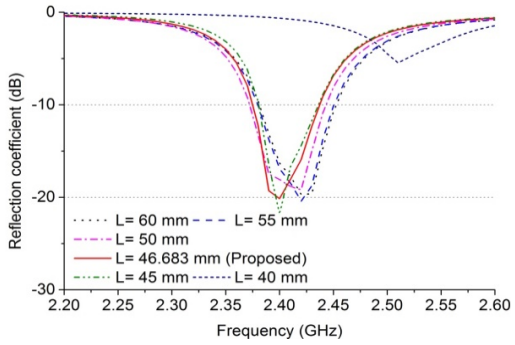


Figure 2. $S_{11}$ in various size of dielectric substrate

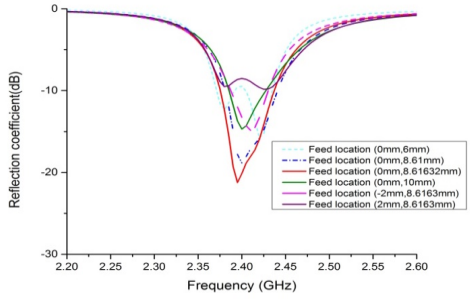


Figure 3. S11 in various feed location

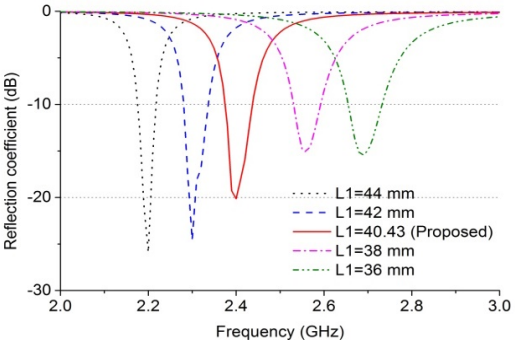


Figure 4. S11 in various L1 size

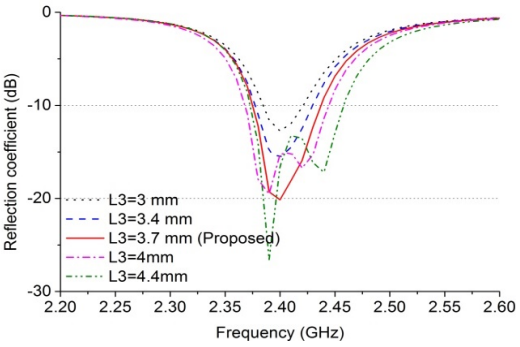


Figure 5. S11 in various L3 size

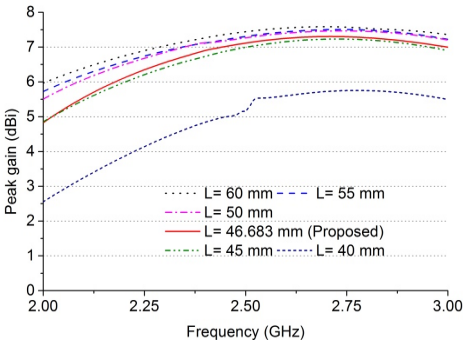


Figure 6. The gain of various dielectric size L.

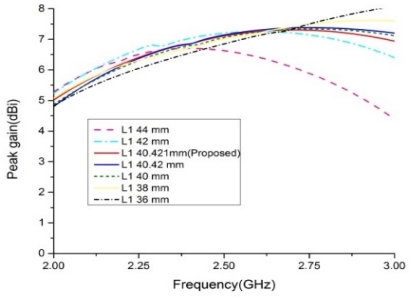


Figure 7: Gain of various L1

In this type of application, it never needs a high gain. This proposed prototype has fulfilled this requirement almost. In antenna design architecture, the current distribution is also an important field. Surface current distribution's magnitude on the patch at 2.40 GHz is depicted in Fig.8. In this figure, we have seen that It's phase shift is from $0^0$ to $270^0$. At first at $0^0$, surface current's phase shift is in the +X direction. At $90^0$, radiating current dominates in the +Y direction. When phase shift changes to $180^0$ then current's direction also changes. At $180^0$ it's direction is toward –X-axis. At last, when $270^0$ arrives, it goes through –Y axis. These directions prove that this prototype has an RHCP (Right Hand Circular Polarization) dominated polarization. Electromagnetic fields are examined carefully in between square shape patch and ground which are resonating. In Fig.9,10,11 and 12 axial ratios of the proposed prototype is shown in different measurement. E field's orthogonal components ratio is basically known as an axial ratio. In circularly polarized patch antenna, it's axial ratio is < 3dB. Axial ratio < 3dB means, the deviation from circular polarization is less than 3 dB over the specified angular range. 0 dB is the ideal magnitude of the axial ratio for circular polarization. In Fig.9 and 10, axial ratio is shown on the basis of L and different feed location. In both figures, axial ratio is less than 3dB. In Fig.11 and 12, L1 and L3 are used to find the axial ratio graph. L1 and L3 are 40.43 mm and 3.7 mm for the proposed design structure. These results are also less than 3dB. The antenna will show circular polarization on that bandwidth which is beneath 3dB and rest of the

bandwidth which is above 3dB, it will show the linear polarization.

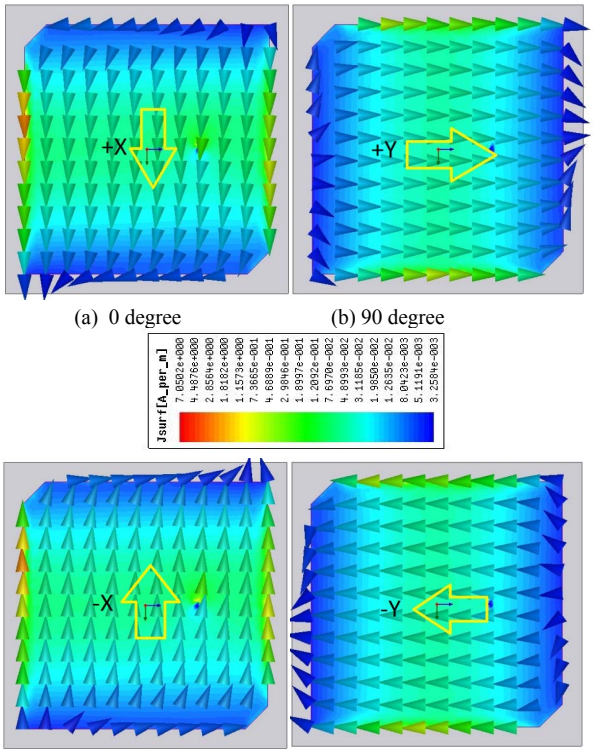


(a) 0 degree (b) 90 degree

(c) 180 degree. (d) 270 degree

Figure 1: Surface current distribution at 2.42 GHz a) $0^0$ b) $90^0$ c) $180^0$ d) $270^0$

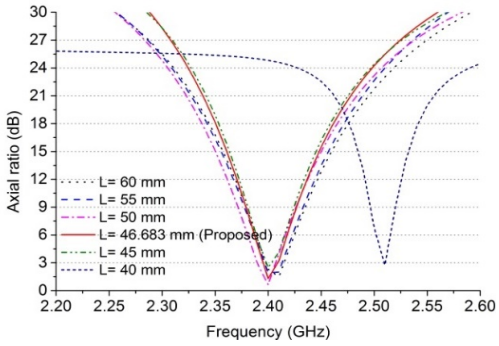


Figure 9: Axial ratio for various dielectric size (L)

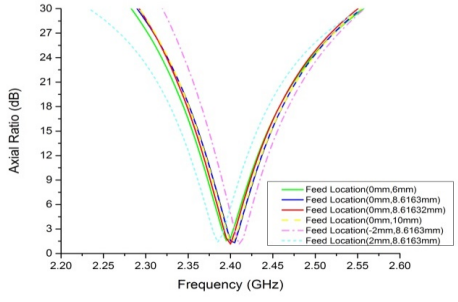


Figure 10: Axial ratio for various feed location

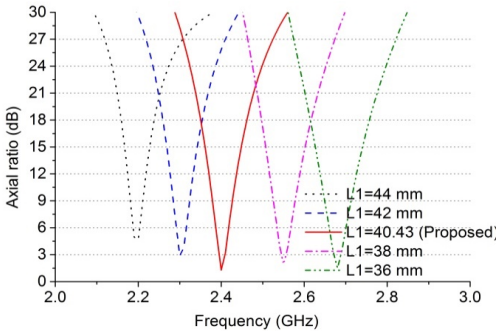


Figure 11: Axial ratio for various patch

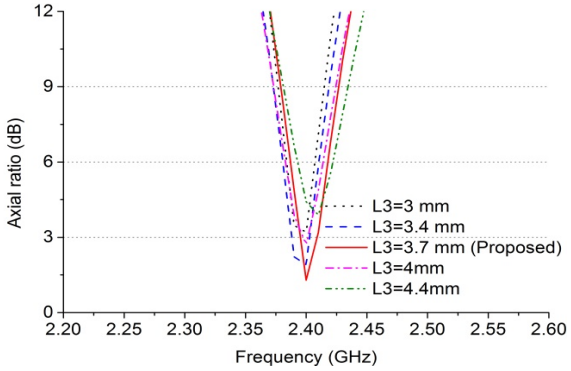


Figure 12: Axial ratio for various slot size (*L3*)

### *3.2 Experimental validation*

Fabricated antenna design is depicted in Fig.13. The dimension of the proposed antenna is 46.683 mm x 46.683 mm x 1.575 mm. Its patch size is 40.42 $mm^2$. There is a coaxial probe in between patch and ground plane. The inner and outer diameter of the coaxial probe is 0.5 mm and 1.5 mm. Here, Rogers RT/ Duroid 5880 (TM) is the substrate which is highly dielectric and copper is used as a conductor. Measured and simulated S11 of the final prototype indicates that it's bandwidth is in between 2.37 GHz to 2.43 GHz. This bandwidth is measured with respect to -10dBi. In this bandwidth, resonance frequency lies at 2.40 GHz. For covering the S-band characteristics, resultant bandwidth is sufficient. In this frequency band, the gain is almost 7 dBi and the worst case gain is near about 7.5 dBi. Proposed antenna has a directional radiation pattern. In Fig.14, 2D view of the radiation pattern is depicted. Black and red line show the LHCP Phi 0 and Phi 90.On the other hand, green and blue show the RHCP Phi 0 and Phi 90. Here, blue one dominates other i.e this radiation pattern is RHCP dominated in Phi 90. This comparison shows that the performance of the antenna is almost same in both simulation software. $S_{11}$ and gain curve is almost adjacent to each other. This means the design of the antenna is done in a proper way. As a result, we have got a desirable feedback. HFSS and CST results of S11 are almost in a similar shape. Measured results are shown here in Fig 15

Figure 13. Fabrication of proposed prototype

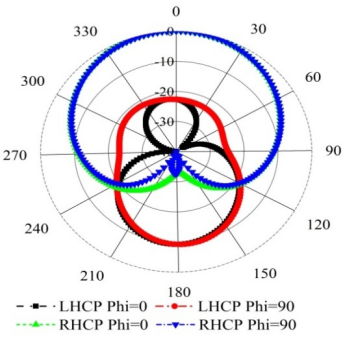


Figure 14. 2D view of Radiation Pattern

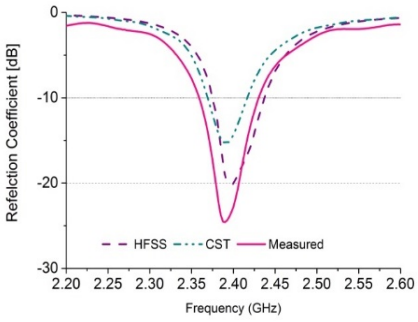


Figure 15. Comparison of $S_{11}$ in HFSS and CST

## IV Conclusion

The final prototype is basically a highly directional and circularly polarized S-band patch antenna. As the antenna has a single feed line, so it's loss is too low. There is a small square size patch which is fed by a coaxial probe of 1.5 mm. Antenna fabrication is done on a 1.575 mm thick substrate. Simulated result is in good agreement. Its gain is about 7 dBi at 2.40 GHz. Proposed prototype is low profile, circularly polarized and highly directional design structure which is able to cope up with the challenge of small satellite application.

## References

[1] W. Marchant and E. R. Taylor, "Status of CHIPS: A NASA university explorer astronomy mission," *Journal of Reducing Space Mission Cost,* vol. 1, pp. 277-287, 1998.

[2] H. Heidt, J. Puig-Suari, A. Moore, S. Nakasuka, and R. Twiggs, "CubeSat: A new generation of picosatellite for education and industry low-cost space experimentation," 2000.

[3] J. Puig-Suari, C. Turner, and R. Twiggs, "CubeSat: the development and launch support infrastructure for eighteen different satellite customers on one launch," 2001.

[4] M. T. Islam, M. Cho, M. Samsuzzaman, and S. Kibria, "Compact Antenna for Small Satellite Applications [Antenna Applications Corner]," *Antennas and Propagation Magazine, IEEE,* vol. 57, pp. 30-36, 2015.

[5] G. Liu, L. Xu, and Z. Wu, "Miniaturized Circularly Polarized Microstrip RFID Antenna Using Fractal Metamaterial," *International Journal of Antennas and Propagation,* vol. 2013, 2013.

[6] H. El Misilmani, M. Al-Husseini, K. Kabalan, and A. El-Hajj, "Compact circularly polarized multiband antennas for RFID applications," *International Journal of Antennas and Propagation,* vol. 2014, 2014.

[7] R. Q. Lee and K.-F. Lee, "Experimental study of the two-layer electromagnetically coupled rectangular patch antenna," *IEEE transactions on antennas and propagation,* vol. 38, pp. 1298-1302, 1990.

[8] M. Samsuzzaman, M. T. Islam, S. Kibria, and M. Cho, "A compact circularly polarized high gain S˜ band nanosatellite antenna using ramped convergence particle swarm optimization," *Microwave and Optical Technology Letters,* vol. 57, pp. 1503-1508, 2015.

[9] S. Egashira and E. Nishiyama, "Stacked microstrip antenna with wide bandwidth and high gain," *IEEE transactions on antennas and propagation,* vol. 44, pp. 1533-1534, 1996.

[10] M. H. Ullah, M. T. Islam, and M. R. I. Faruque, "A near-zero refractive index meta-surface structure for antenna performance improvement," *Materials,* vol. 6, pp. 5058-5068, 2013.

[11] S. F. Mahmoud and A. R. Al-Ajmi, "A novel microstrip patch antenna with reduced surface wave excitation," *Progress In Electromagnetics Research,* vol. 86, pp. 71-86, 2008.

[12] M. Samsuzzaman and M. T. Islam, "Dual frequency circularly polarized cross˜ shaped slotted patch antenna with a small frequency ratio," *Microwave and Optical Technology Letters,* vol. 56, pp. 2711-2719, 2014.

[13] D. Jackson, J. Williams, A. K. Bhattacharyya, R. L. Smith, S. J. Buchheit, and S. Long, "Microstrip patch designs that do not excite surface waves," *IEEE transactions on antennas and propagation,* vol. 41, pp. 1026-1037, 1993.

[14] M. Samsuzzaman, M. Islam, M. Nahar, J. Mandeep, F. Mansor, and M. Islam, "Circularly polarized high gain S band antenna for nanosatellite," *International Journal of Applied Electromagnetics and Mechanics,* 2015.

[15] J.-S. Row, "Dual-frequency circularly polarised annular-ring microstrip antenna," *Electronics Letters,* vol. 40, pp. 153-154, 2004b.

# Design and Optimization of Optical Interconnect Using Vertically Grown Periodic III-V Nanowires on Silicon

Dip Joti Paul[1] and Md. Zunaid Baten[1,*]
[1]Department of Electrical and Electronic Engineering, Bangladesh University of Engineering and Technology
Dhaka-1205, Bangladesh
*mdzunaid@eee.buet.ac.bd

***Abstract*—In this work, we study light propagation and coupling in a system of III-V nanowire array arranged vertically on a planer silicon waveguide, using two-dimensional (2D) and three-dimensional (3D) Finite-Difference Time-Domain (FDTD) techniques. We have considered waveguide comprising GaAs and GaN nanowires and shown that efficient light coupling can be achieved by optimizing the lateral and longitudinal dimensions, heights and spacings of the nanowires. The results of 2D analysis show that 82% light can be extracted from a waveguide of GaAs nanowire array, whereas the value is 40% for GaN nanowire array because of the lower refractive index of this material system. In the presence of a coherent source, the efficiency of light coupling from nanowire array to waveguide becomes 80% for GaAs and 57% for GaN nanowires. We also find that for efficient light coupling in both directions, less amount of material will be required in GaAs-based system due to the smaller-diameter-nanowire requirement for GaAs than for GaN. In order to study a more practical system, the performance characteristics are further analyzed using 3D FDTD simulation technique and the results are in good agreement with the results of 2D analysis.**

***Index Terms*—III-V nanowire array, waveguide, optical interconnect, silicon photonics.**

## I. Introduction

The use of vertical array of semiconductor nanowires for light generation, detection and propagation has gained considerable attention over the recent years because of the viability of this material system for light generation, transmission and detection [1], [2]. Recent advances in nanoscale fabrication have made it possible to grow nanowires on precise locations on cheap substrates, particularly on silicon. Moreover, because nanowires can be grown by radial strain relaxation on lattice mismatched substrates, the constraints on lattice constant are significantly relaxed in nanowire based systems, compared to the case of bulk and quantum well-based devices. Hence nanowire based photonic systems have gained huge applications in different areas of photonics and optoelectronics, for example in photovoltaics, photodetectors, optical data communication and photo-emitters [3]–[6].

With the recent developments in optoelectronic and photonic integrated circuits and systems, it is quite obvious that low-bandwidth electrical interconnects will not be able to meet the future demands of fast on-chip and intra-chip data transfer rates [7]. Since silicon dominates the microelectronic industry, different optical components like light sources, photodiodes, photo-collectors and waveguide are expected to be grown on silicon substrate. Though silicon can be used for guiding light, a standalone silicon photonic system is not sufficient to achieve active optical components like photodiode, nanolaser etc. because of the indirect bandgap nature of this material system. To this end, the integration of III-V materials in the form of III-arsenide and III-nitride nanowires on silicon substrate is being considered as an effective means of realizing efficient and scalable optoelectronic integrated circuits and systems [8]. Though GaAs nanowire array has shown excellent performance in light extraction from silicon waveguide due to its high refractive index, organized growth of GaAs on Si(111) substrate is challenging as small changes in surface roughness can make it difficult to reproduce similar GaAs nanowire array under different substrate conditions [9], [10]. On the other hand, though GaN nanowires, free of extended defects, can be grown on silicon, the light collection capability of GaN nanowires from silicon waveguide is poor due to its lower refractive index than silicon. Though a numerical simulation of GaAs nanowire array has already been reported [11], there has not been a comparative study between GaAs and GaN nanowires grown on identical silicon platform.

In this work, we investigate the optical response of vertically grown periodic GaAs and GaN nanowires on silicon waveguide and design the array spacing, nanowire diameter and height in order to get the maximum optical coupling between the waveguide and nanowire array. The performance characteristics of these two systems have been studied and compared using 2D and 3D FDTD techniques. To the best of our knowledge, this is the first reported comparative study of similar GaAs- and GaN-based vertically assembled nanowire arrays on silicon for the purpose of light propagation and coupling in photonic and optoelectronic integrated circuits.

## II. Device Geometry

A schematic representation of the periodic vertical array of III-V nanowires grown on silicon waveguide is shown in Fig. 1. The lateral dimension of the waveguide is sufficient to house three parallel rows of nanowires and its thickness ($t_{WG}$) is 0.5 um. The longitudinal (along X-axis) and lateral (along Z-axis) spacing of nanowires are denoted as $\Lambda_a$ and $\Lambda_b$, respectively. In accordance with the dimension of experimentally grown/fabricated III-V nanowires, the height of the nanowires is kept fixed at 1 $\mu$m throughout this study. The diameter ($d_{nw}$) of nanowire, along with their longitudinal spacing ($\Lambda_a$) and lateral spacing ($\Lambda_b$), are chosen carefully in order to enable efficient light-coupling between waveguide and nanowires for the wavelength of 1.3 $\mu$m. This wavelength is suited for III-V nanowire based optical interconnect applications due to lower propagation loss (0.3 dB/cm) [12]. Moreover, this wavelength

978-1-5386-3374-8/17/$31.00 ©2017 IEEE

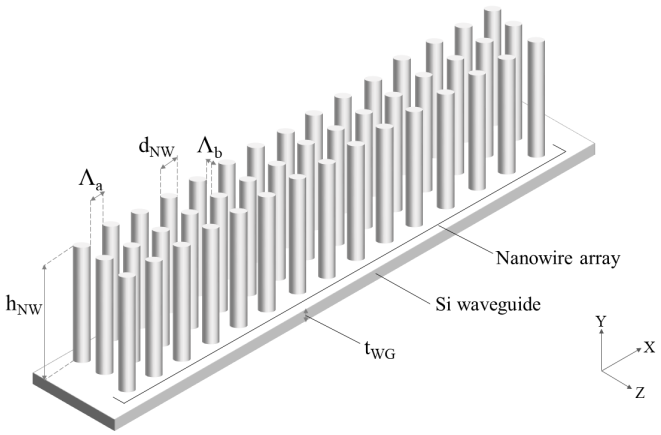


Fig. 1: Schematic showing periodic array of cylindrical NWs on top of a silicon waveguide, which is fabricated from a SOI wafer.

is a standard for fiber-optic communication along with 1.5 $\mu$m because of its low dispersion in standard silica fiber.

## III. Simulation Method

The numerical simulations are carried out using an open-source finite-difference time-domain (FDTD) program MEEP [13]. Perfectly matched layers (PMLs) are placed surrounding the computational region to truncate simulating wave equations. The materials are defined by their respective refractive indices at the wavelength of 1.3 $\mu$m: $n_{Si}$ = 3.504, $n_{GaAs}$ = 3.406, and $n_{GaN}$ = 2.324 [14]. Frequency dependent refractive index (material dispersion) is considered to account the actual spectral bandwidth of light-coupling. To reduce computational complexity, at first we have converted the 3D structure to a 2D model by taking a cross-section along X-Y plane and determined the optimum longitudinal spacing and nanowire diameter. Then keeping the values of these parameters unaltered, full 3D simulation is performed to determine the optimum spacing between the nanowires.

## IV. Results and Discussion

In this study, we have considered both out-coupling of light from the waveguide by the nanowires and in-coupling of light from the nanowires into the waveguide. We have considered an array of fifteen nanowires for both cases.

### A. Out-coupling of light

The 2D model for light out-coupling is shown in Fig. 2. The source, located 2 $\mu$m away from the first nanowire, generates TE-polarized plane wave (with transverse $E_Z$ component) which propagates along the X-direction through the waveguide. The input flux plane is situated in front of the source and output flux plane is placed on the top of the NW array. The output flux is calculated such that it comprises only the transmitted plane wave that is guided by the nanowires. This out-coupled light power normalized to the input flux gives the out-coupling ratio.

Fig. 3 depicts the out-coupling ratio as a function of the nanowire diameter ($d_{nw}$) and longitudinal spacing ($\Lambda_a$) for a fixed nanowire height of $h_{nw}$ = 1 $\mu$m. For GaAs NWs, light out-coupling is higher for nanowire spacing of 0.65 $\mu$m to 0.8 $\mu$m and for diameters between 290 nm and 330 nm, as shown in Fig. 3(a). The maximal out-coupling power is achieved at a value of $\Lambda_a$ = 0.69 $\mu$m and $d_{nw}$ = 310 nm. Because of photonic crystal effects, GaAs nanowires with 310 nm diameter and 1 $\mu$m longitudinal period exhibit the highest vertical out-coupling ratio of 80%. These are consistent with the values for the nanowire structure presented in [11]. Fig. 3(b) shows that the maximum light extraction occurs for nanowire spacing in the range of 0.34-0.4 $\mu$m and for diameters between 600 nm and 670 nm for GaN NWs. The peak extraction occurs at $\Lambda_a$ = 0.35 $\mu$m and $d_{nw}$ = 650 nm, with an extraction efficiency of ~40%. Hence the optimum longitudinal period of GaN nanowire array is 1 $\mu$m, which similar to that of GaAs NWs. The low extraction efficiency of the GaN NW arrays is attributed to the lower refractive index of this material system compared to GaAs.

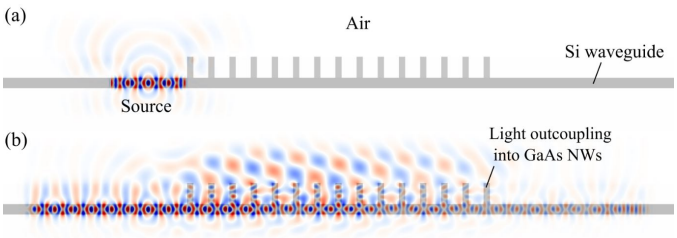


Fig. 2: MEEP simulation of the light propagation from silicon waveguide to the nanowire array (2D-model).

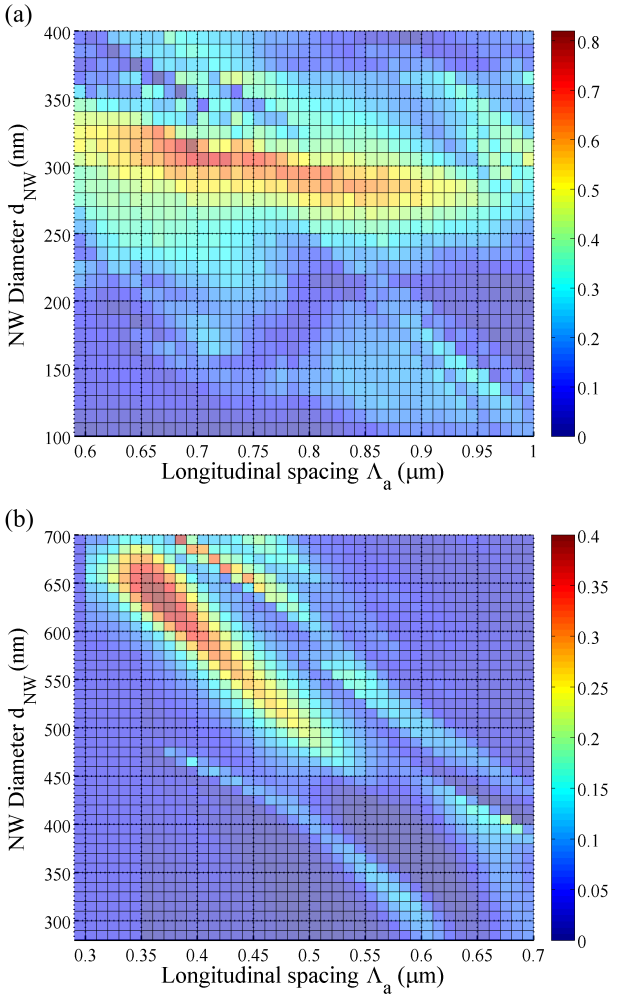


Fig. 3: Dependence of normalized out-coupled light power on array spacing and nanowire diameter for a fixed nanowire height, for (a) GaAs nanowires (b) GaN nanowires.

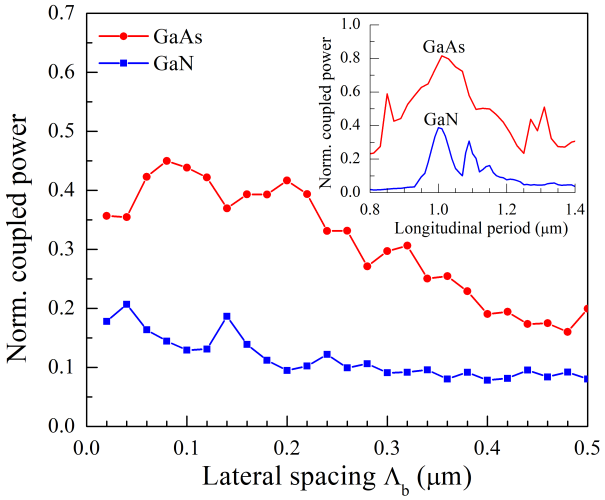


Fig. 4: Normalized out-coupled power as a function of lateral spacing of NWs for a fixed height ($h_{nw}$ = 1 $\mu$m) and fixed diameter, $d_{nw}$ = 310 nm for GaAs and 650 nm for GaN (3D-case). Dependence of out-coupled power on longitudinal period of NW array is shown in the inset.

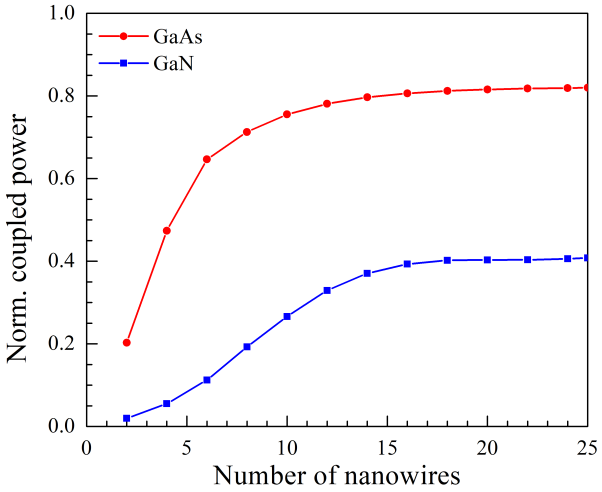


Fig. 6: Effect of the number of nanowires in the longitudinal direction on the normalized coupled optical power.

The effect of lateral spacing ($\Lambda_b$) on the coupling ratio is shown in Fig. 4. Without changing the values of $\Lambda_a$ and $d_{nw}$ for maximum out-coupling condition in 2D simulation, we have performed 3D analysis by varying only the lateral spacing of nanowires. For GaAs NW array, a maximum extraction ratio of 45% is obtained for a lateral spacing of 0.08 $\mu$m. Therefore, for a practical GaAs nanowire based system, the optimized values for maximum out-coupling are as follows: $d_{nw}$ = 310 nm, height = 1 $\mu$m, longitudinal spacing = 0.69 $\mu$m and lateral spacing = 0.08 $\mu$m. For GaN NW array, a peak extraction ratio of 21% is obtained for a lateral spacing of 0.04 $\mu$m. Therefore for the GaN-based system, resonance occurs for $d_{nw}$ = 650 nm, height = 1 $\mu$m, longitudinal spacing = 0.35 $\mu$m and lateral spacing = 0.04 $\mu$m. We also find that normalized coupled power of 3D simulation is almost half that of the 2D model for both cases, since light scattering in lateral direction is not considered in the 2D calculation.

Fig. 5 displays the spectral bandwidth of the out-coupling for both the GaAs and GaN based systems. Since the dimensions of the nanowire array have been optimized with respect to 1.3 $\mu$m transmission wavelength, distinct resonant peaks are observed at this wavelength for both the GaAs and GaN based systems. It is noteworthy that a second resonant peak is observed for the GaAs based system at around 1.18 $\mu$m. Hence, by properly tailoring the geometry of NW array, it is possible to design interconnects which can operate at different desired wavelengths. The effect of increasing the number of nanowires along the longitudinal direction is showed in Fig. 6. As expected, the coupled power increases linearly with the number of nanowires and then saturates for fifteen nanowires in both material systems.

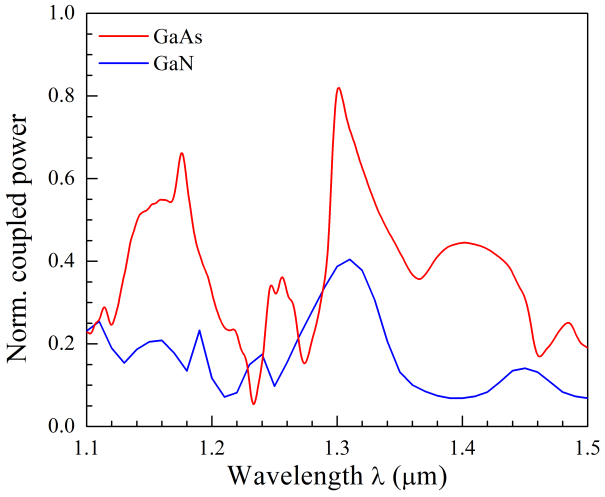


Fig. 5: Spectral bandwidth for light out-coupling at the optimized geometry of GaAs and GaN nanowire array (2D-model).

### B. *In-coupling of light*

In order to evaluate the light insertion performance from NW array into the silicon waveguide, we have performed FDTD simulation by placing light sources in the middle of the nanowires without considering the effect of nanowire doping profiles and heterostructures. In processing and fabrication, it is quite customary to passivate nanowires with suitable dielectric materials for reducing surface passivation and also for making top electrical contacts. In this regard, we studied the nanowire arrays by embedding them in $SiO_2$. In practice, two types of light sources can be achieved from nanowires: incoherent emission (as in LEDs) and coherent emission (as in LASERs) [15]–[17]. Only coherent emission source has been considered in this analysis because of its better performance characteristics in optical data communication.

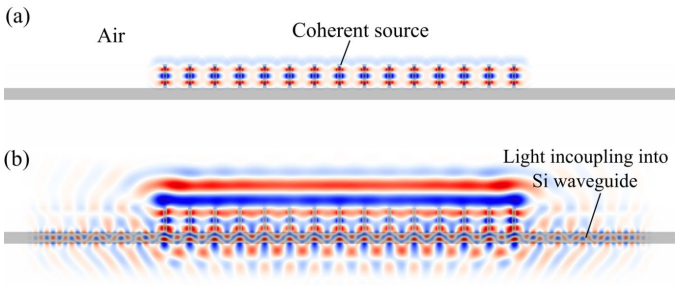


Fig. 7: MEEP simulation of the coherent light propagation from nanowire array to the silicon waveguide (2D-model).

A schematic of the 2D model for light in-coupling is shown in Fig. 7 where the emitters are embedded in the middle of the nanowires. The light is TE-polarized (with transverse $E_Z$ component) and propagates along the Y-direction. When this is coupled with the waveguide mode, it propagates along the X-direction through the waveguide. The ratio of the power of the guided light in the waveguide to the source power gives the normalized in-coupling power.

In Fig. 8, the in-coupling power is shown as a function of the nanowire diameter ($d_{nw}$) and longitudinal spacing ($\Lambda_a$) for a fixed nanowire height ($h_{nw}$) of 1 $\mu$m. Maximum coupling occurs for nanowire spacing in the range of 0.83-0.89 $\mu$m and for diameters between 160 nm and 210 nm for GaAs NW array. According to Fig. 8(b), the maximum in-coupling condition for GaN NWs occurs for longitudinal spacing of 0.65-0.72 $\mu$m and diameters between 340-400 nm. A maximum coupling efficiency of 57% is obtained in the GaN-based system at a spacing ($\Lambda_a$) of 0.69 $\mu$m and diameter of 350 nm whereas in GaAs NW arrays, the peak in-coupling efficiency is 80% for $\Lambda_a$ = 0.86 $\mu$m and $d_{nw}$ = 180 nm. As can be seen, the in-coupling efficiency for GaN NWs is lower than for GaAs NWs, similar to the case of out-coupling.

Longitudinal period is calculated by adding the longitudinal spacing ($\Lambda_a$) to the nanowire diameter ($d_{nw}$). Although the optimal longitudinal spacing and nanowire diameter are different for GaAs and GaN NWs, the respective longitudinal period remain constant for both material systems. In Fig. 9, we find that the maximum in-coupling occurs for a longitudinal period of 1.04 $\mu$m. As had been shown in Fig. 4, the optimized value of longitudinal period is 1 $\mu$m for maximum out-coupling condition for both GaAs and GaN based systems. Hence the nanowire array acts like a grating coupler on the Si waveguide at the longitudinal periodicity of about 1 $\mu$m for the light coupling in both directions, regardless of the material system.

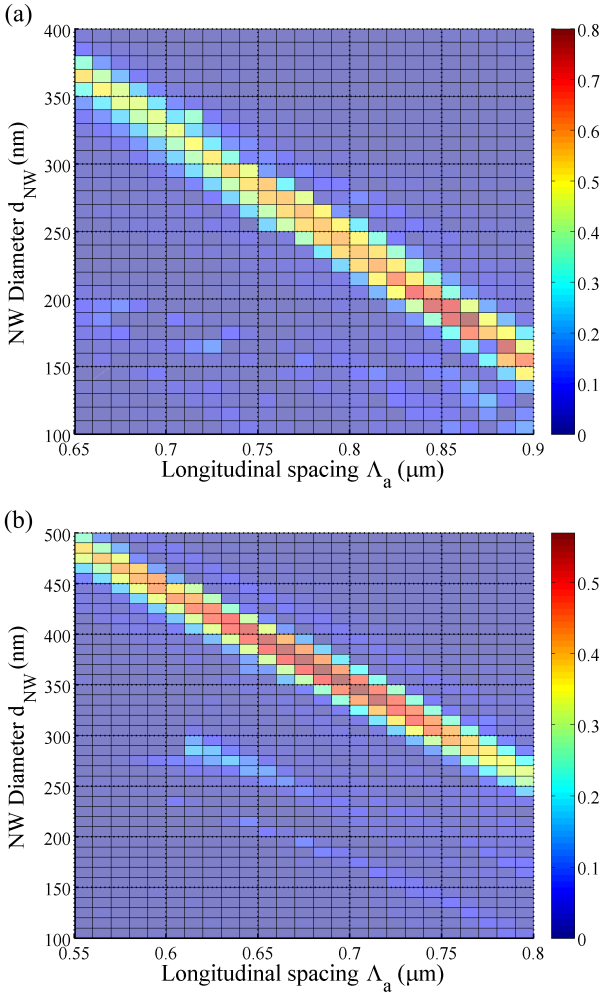


Fig. 8: Dependence of normalized in-coupled light power on array spacing and nanowire diameter for a fixed nanowire height, for (a) GaAs nanowires (b) GaN nanowires.

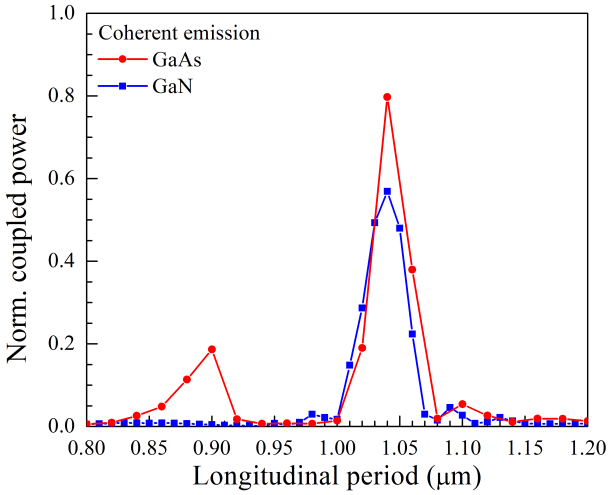


Fig. 9: Normalized in-coupled power as a function of longitudinal period of NWs for a fixed height ($h_{nw}$ = 1 $\mu$m).

## V. Conclusions

In conclusion, we have studied a nanowire array based optical waveguide and explored the ideal nanowire array configuration for maximum light coupling between the planer silicon waveguide and vertical III-V nanowires. This photonic platform can be organized in such a way that nanowires can work as an efficient photodetector and photo-collector, and therefore allow both detection and collection of light from the waveguide. In this work, we have observed that because of the higher refractive index, GaAs NWs yield better efficiency than GaN NW based systems with respect to both in- and out-coupling. Even though smaller diameter nanowires are required for GaAs, the optimum total length of the nanowire array is almost the same for both materials due to the larger nanowire spacing for GaAs. Hence, both material systems can produce a fairly compact optical interconnect device, and therefore can be used as a medium of future ultra-fast on-chip and intra-chip data communication.

## References

[1] J. Kupec, R. L. Stoop, and B. Witzigmann, "Light absorption and emission in nanowire array solar cells," *Optics express*, vol. 18, no. 26, pp. 27 589–27 605, 2010.

[2] N. Anttu and H. Xu, "Coupling of light into nanowire arrays and subsequent absorption," *Journal of nanoscience and nanotechnology*, vol. 10, no. 11, pp. 7183–7187, 2010.

[3] M. Tchernycheva, A. Messanvi, A. de Luna Bugallo, G. Jacopin, P. Lavenus, L. Rigutti, H. Zhang, Y. Halioua, F. Julien, J. Eymery *et al.*, "Integrated photonic platform based on InGaN/GaN nanowire emitters and detectors," *Nano letters*, vol. 14, no. 6, pp. 3515–3520, 2014.

[4] G. Roelkens, L. Liu, D. Liang, R. Jones, A. Fang, B. Koch, and J. Bowers, "III-V/silicon photonics for on-chip and intra-chip optical interconnects," *Laser & Photonics Reviews*, vol. 4, no. 6, pp. 751–779, 2010.

[5] Y. Zhang, J. Wu, M. Aagesen, and H. Liu, "III–V nanowires and nanowire optoelectronic devices," *Journal of Physics D: Applied Physics*, vol. 48, no. 46, p. 463001, 2015.

[6] R. Chen, T.-T. D. Tran, K. W. Ng, W. S. Ko, L. C. Chuang, F. G. Sedgwick, and C. Chang-Hasnain, "Nanolasers grown on silicon," *Nature Photonics*, vol. 5, no. 3, pp. 170–175, 2011.

[7] K. Gallo and G. Assanto, "All-optical diode based on second-harmonic generation in an asymmetric waveguide," *JOSA B*, vol. 16, no. 2, pp. 267–269, 1999.

[8] M. Hocevar, G. Immink, M. Verheijen, N. Akopian, V. Zwiller, L. Kouwenhoven, and E. Bakkers, "Growth and optical properties of axial hybrid III-V/Si nanowires," *arXiv preprint arXiv:1210.8350*, 2012.

[9] S. Plissard, K. A. Dick, G. Larrieu, S. Godey, A. Addad, X. Wallart, and P. Caroff, "Gold-free growth of GaAs nanowires on silicon: arrays and polytypism," *Nanotechnology*, vol. 21, no. 38, p. 385602, 2010.

[10] S. Plissard, G. Larrieu, X. Wallart, and P. Caroff, "High yield of self-catalyzed GaAs nanowire arrays grown on silicon via gallium droplet positioning," *Nanotechnology*, vol. 22, no. 27, p. 275602, 2011.

[11] I. Giuntoni, L. Geelhaar, J. Bruns, and H. Riechert, "Light coupling between vertical III-As nanowires and planar Si photonic waveguides for the monolithic integration of active optoelectronic devices on a Si platform," *Optics express*, vol. 24, no. 16, pp. 18 417–18 427, 2016.

[12] S. K. Selvaraja, W. Bogaerts, P. Absil, D. Van Thourhout, and R. Baets, "Record low-loss hybrid rib/wire waveguides for silicon photonic circuits," *Group IV Photonics*, vol. 2010, 2010.

[13] A. F. Oskooi, D. Roundy, M. Ibanescu, P. Bermel, J. D. Joannopoulos, and S. G. Johnson, "MEEP: A flexible free-software package for electromagnetic simulations by the FDTD method," *Computer Physics Communications*, vol. 181, no. 3, pp. 687–702, 2010.

[14] E. D. Palik, *Handbook of optical constants of solids*. Academic press, 1998, vol. 3.

[15] R. Wang, H. P. Nguyen, A. T. Connie, J. Lee, I. Shih, and Z. Mi, "Color-tunable, phosphor-free InGaN nanowire light-emitting diode arrays monolithically integrated on silicon," *Optics express*, vol. 22, no. 107, pp. A1768–A1775, 2014.

[16] P. Bhattacharya, A. Hazari, and S. Jahangir, "InGaN/GaN Dot-in Nanowire Monolithic LEDs and Lasers on (001) Silicon," in *Proc. of SPIE Vol*, vol. 10124, 2017, pp. 101 240H–1.

[17] A. Hazari, M. Zunaid Baten, L. Yan, J. M. Millunchick, and P. Bhattacharya, "An InN/InGaN/GaN nanowire array guided wave photodiode on silicon," *Applied Physics Letters*, vol. 109, no. 19, p. 191102, 2016.

# Phase-Tunable N-Cascaded Mach-Zehnder Interferometers Using External Adjustor

Weifeng Jiang[1,2*] and Xiaohan Sun[2]

[1]School of Electronic and Optical Engineering,
Nanjing University of Posts and Telecommunications, Nanjing 210023, China
[2]National Research Center for Optical Sensing/Communications Integrated Networking,
Department of Electronics Engineering, Southeast University, Nanjing 210096, China
[*]jwf@njupt.edu.cn

*Abstract*—**Phase-tunable N-cascaded Mach-Zehnder interferometers (N-CMZIs) are presented and demonstrated experimentally. The theoretical model of the N-CMZIs is established by using the coupled-mode theory and the transfer matrix method. The optimization of single and three-CMZIs based on the Silica-on-Silicon (SoS) are given. The CMZIs based on three-CMZIs and single-MZI are fabricated, respectively, by using the SoS processing and their characteristics are measured. The testing results show single-CMZIs with the insertion loss of less than 5.6 dB and the extinction ratio in output spectrum of 19 dB under the FSR of 0.8 nm and three-CMZIs with the channel spacing of 100 GHz have the top width of ~0.35nm under the wavelength jitters of 0.9 dB, respectively.**

***Index Terms***—**Phase-tunable, cascaded Mach-Zehnder interferometers, external adjustor.**

## I. Introduction

Mach-Zehnder Interferometer (MZI) is one of the most useful wavelength-shaping components applied in dense wavelength division multiplexing (DWDM), which can significantly increase the capacity of optical systems by providing flexible signal multiplexing/demultiplexing [1]. Hence, the considerable attention has been recently focused on the optimal design and fabrication technologies of the optical interleaver, in which many approaches have been reported [2-4].

Technologies of the CMZIs can be classified into two categories: all-fiber and planar lightwave circuit (PLC) based CMZIs. In ref. [5], all-fiber based CMZIs with high extinction ratio (ER) of 25dB are demonstrated. However, they need to suffer from various perturbations in actual communication systems, and also have instability owing to the lack of compactness. PLC based CMZIs can overcome these disadvantages and enable the compact devices with low costs and high performances. In ref. [6], PLC based CMZIs chip can be designed to achieve high temperature-stability. But its central wavelength is constant so that it cannot be reconfigurable. Although, dynamically reconfigurable CMZIs could be yielded by using electro-optic effect or thermo-optic effect [7-8], these approaches significantly increase the cost, complexity and extra loss.

In this paper, we present and demonstrated the N-CMZIs Compared with the previous CMZIs in ref. [9], the key advantage of this structure is that a reconfigurable CMZIs with a flat-top pass-band can be implanted by using monolithic integration and a more comprehensive theoretical model is presented. As a result, this structure saves costs and increases the capacity. The scheme of the N-CMZIs based interleaver is proposed and the output characteristics for the single-MZI and N-CMZIs are studied by using the coupler mode theory (CMT) and transfer matrix method (TMM). In order to verify the theoretical results, one and three-CMZIs have been fabricated by using SoS processing line and tested experimentally.

## II. Results

The principle of the N-CMZIs based interleaver is shown in Fig. 1. The whole structure consists of N-CMZIs based interleaver, in which each MZI consists of upper arms (including external adjustor and internal two arms), lower arm and two 3dB coupler. For MZI 1, the arm A1 is the fixed lower-arm and the upper arm consists of external adjustor 1, external arm A4, internal arms A2 and A3, in which the arm A4 is chosen to be a single mode fiber (SMF) as a connector between external adjustor 1 and the internal MZI 1 chip. Connected with MZI 1 by 3dB coupler 2, the MZI 2 is also composed of fixed lower-arm B1 and the upper arm, in which the upper arm consists of external arm B4 and adjustor 2, internal arms B2 and B3. The arm B4 is also chosen to be a SMF as a connector between external adjustor 2 and the internal MZI 2 chip. Similarly, the MZI N is composed of fixed lower-arm N1 and upper arms, in which upper arm consists of external adjustor N and arm N4, internal arms N2 and N3. External adjustor N is connected with the MZI N chip by using the external arm N4 chosen as SMF. It can be noted that the phase of the N-CMIZs can be easily and precisely tuned by adjusting the phase of the external adjustors. As a result, a flat-top pass-band can be achieved by synthetic adjusting the phases of the all external adjustors. In the following, we study the output characteristics for the N-CMZIs based interleaver by using CMT and TMM.

Firstly, the characteristic of the CMZIs based interleaver with single-stage is analyzed by choosing MZI 1 as an example. For a single-MZI, optical signal can be excited on either of port 1 or 2, in which port 1 is chosen as input port for this case. The input signal is split into the lower arm and upper arms by 3dB coupler 1. Following that, the signals are merged together and interference occurs at 3dB coupler 2. The output electrical intensity of the single-MZI 1 can be derived by using TMM as:

$$\begin{bmatrix} E_3 \\ E_4 \end{bmatrix} = \begin{bmatrix} c_2 & -js_2 \\ -js_2 & c_2 \end{bmatrix} \begin{bmatrix} 1 & 0 \\ 0 & \exp(j\Delta\varphi) \end{bmatrix} \begin{bmatrix} c_1 & -js_1 \\ -js_1 & c_1 \end{bmatrix} \begin{bmatrix} E_1 \\ E_2 \end{bmatrix} \quad (1)$$

where $\sqrt{k_i}$ is the optical power coupling ratio of 3dB coupler.

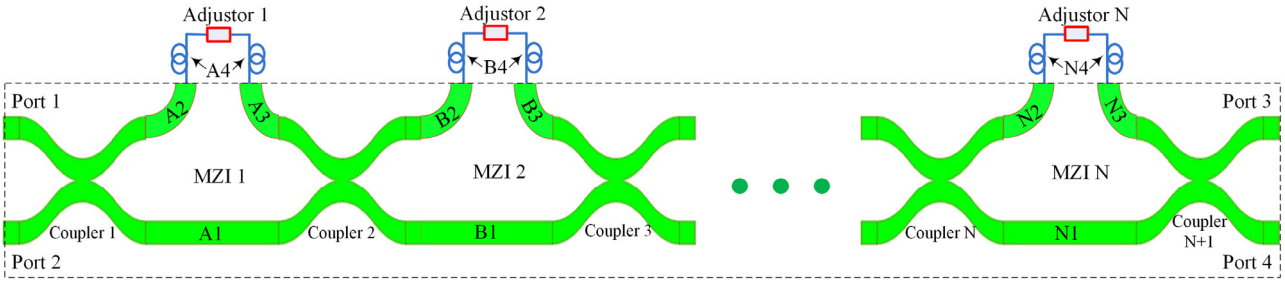


Fig. 1. Scheme of the N-CMZIs.

$c_i = \sqrt{1-k_i}$ and $s_i = \sqrt{k_i}$ are the meaning of transmissions at through and cross status, respectively. The subscript $i$ = 1, 2, respectively.

As shown in Fig. 1, the MZI 1 consists of lower arm A1 and upper arms. It can be observed that the phase shift should be the difference of the optical path between the lower and upper arms. Therefore, the phase shift of the single-MZI 1 is adjusted by:

$$\Delta\varphi = \Delta\varphi_2 + \Delta\varphi_3 + \Delta\varphi_4 + \Delta\varphi_{ad1} - \Delta\varphi_1 = \frac{2\pi(n_{A2}L_{A2}+n_{A3}L_{A3}+n_{A4}L_{A4}+n_{ad1}L_{ad1}-n_{A1}L_{A1})}{\lambda} \quad (2)$$

where $n_{An}$ and $L_{An}$ denote effective refractive index and the length of internal arms A1, A2, A3 and external arm A4, and the subscript $n$ = 1, 2, 3, 4, respectively. $n_{ad1}$ and $L_{ad1}$ are on behalf of the length and the effective refractive index of the external adjustor 1, respectively. It can be noted from the Eq. (2) that the phase of the single-MZI 1 can be changed by tuning the optical path of the external adjustor 1.

As the output performance of the single MZI and N-CMZIs based interleaver are obtained, we choose SoS-PLC based CMZIs as examples. The SoS waveguide is with the size of $w \times h_{co}$ and the depths of the buffer layer and deep etching are shown as $h_b$ and $h_{et}$, respectively. The refractive indices of the Si and $SiO_2$ are taken as 3.455 and 1.445, respectively. The relative refractive index difference $\Delta$ of 0.4% may be considered as a typical representative of the SoS waveguide, in which the core size of $w = h_{co} = 8$ μm is chosen on the basis of the single mode condition. In order to obtain a regular morphological SoS waveguide, we use a deep etching process, in which the deep etching depth is taken as $h_{et}$ = 0.5 μm. The height of the buffer layer of $h_b$ =13 μm are chosen to isolate the core layer and substrate.

In order to get the output transmission, 3dB coupler based on SoS waveguide need to be designed. 3 dB coupling ratio can be obtained when the coupling length and the separation between two coupling waveguides are chosen to be 3296 μm and 4.5 μm, respectively, by using 2D beam propagation method (BPM). For the input/output ports 1, 2, 3 and 4, the pitch between the input two ports or output two ports should be 127 μm. Hence, the separation between the upper and lower waveguide of 3dB coupler can be enlarged to be 127μm by using bending waveguides. External adjustors are chosen to be SMF as typical representative, which is a phase-sensitive component with good tunability. After giving the optimal design for 3dB coupler and the parameters of the SoS waveguide and external adjustor, the output characteristics of the single and N-CMZIs can be calculated.

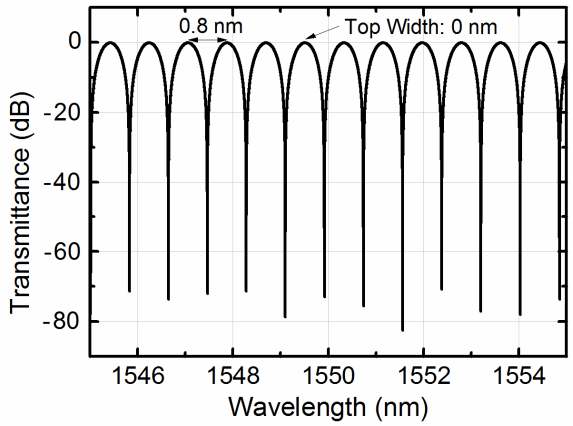


Fig. 3. Transmission spectra on port 3 with $L_{A4}+L_{ad1}$ = 3 mm.

At first, the transmission spectra on port 3 of the single-MZI with the wavelength spacing of 0.8 nm are calculated respectively, as shown in Fig. 3. By tuning the total length of the external arm and adjustor to be 3 mm, the free spectral range (FSR) of 100 GHz can be achieved corresponding to a wavelength spacing of 0.8 nm centered at ITU wavelength grids.

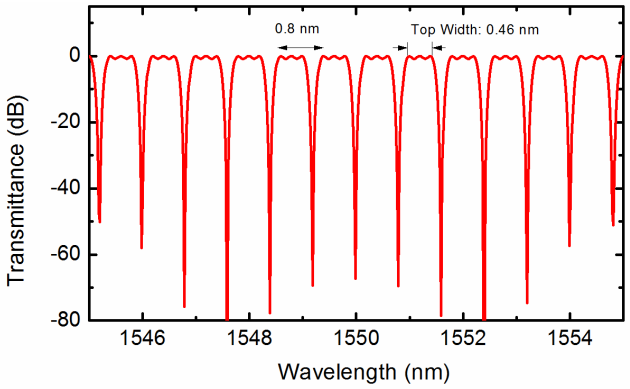


Fig. 4. Transmission spectra on port 3 of tree-CMZIs based interleaver. The wavelength spacing is 0.8 nm (100 GHz).

Next, the analysis of the transmission spectrum for the three-CMZIs is presented. Compared with the single-MZI, the N-CMZIs is composed of many MZIs which can provide a broad top width. In order to get a broad top width, optimization simulations for each external adjustor need to be studied. The transmission spectra of 100GHz three-CMZIs are given and shown in Fig. 4, in which a broad top width and large ER can be attained at the wavelength between 1530 nm and 1650 nm. For 100GHz interleaver based on three-CMZIs, the total length of the external arm A4 and adjustor 1 is 3.16 cm, the total length of the external arm B4 and adjustor 2 is 3.76 cm, and the total length of the external arm C4 and adjustor 3 is 2.76 cm, respectively. It can also be noted that the wavelength jitter at the top region of the spectrum is 0.72

dB. The top width are 0.55 nm under the wavelength jitter of 3 dB, respectively.

Following that, the single and three-CMZIs are fabricated and tested experimentally. Input 3dB coupler 1 and output 3 dB coupler 4 are shown in Fig. 5(a) and (b), respectively. The picture of the three-CMZIs based interleaver chip is shown in Fig. 5(c).

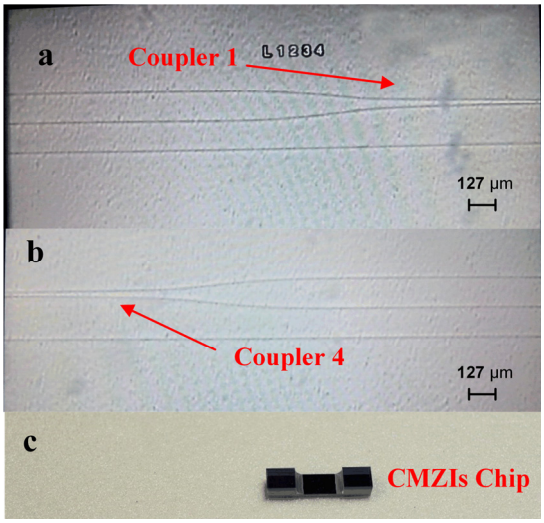


Fig. 5. Picture of input 3 dB coupler 1. (b) Picture of output 3 dB coupler 4. (c) Picture of three-CMZIs based interleaver chips.

In order to compare the transmission spectrum of the N-CMZIs based interleaver with the single-MZI, we tested the single-MZI by using a motorized variable optical delay line (MDL) based adjustor. The transmission spectrum of the single-MZI is shown in Fig. 6(a). It can be noted that the top width of the transmission spectrum is not good enough. The single-CMZI is with the insertion loss of less than 5.6 dB and the extinction ratio in output spectrum of 19 dB under the FSR of 0.8 nm. The measured transmission spectra for three-CMZIs based interleaver with wavelength spacing of 0.8 nm (100GHz) is shown in Fig. 6(b). For 100GHz interleaver, $L_{A4} + L_{adjustor1} \approx$ 3.16 cm, $L_{B4} + L_{adjustor2} \approx$3.76 cm, and $L_{C4} + L_{adjustor3} \approx$ 2.76 cm, respectively. It can be observed from Fig. 6(b) that the transmission spectrum of the 100GHz interleaver with the ER of about 27dB and the insertion loss varying between 2.5 dB and 7.5 dB. The top width is ~0.35 nm under the wavelength jitter of 0.9 dB at the top region of each channels. Compared experimental results in Fig. 6(b) with theoretical results in Fig. 4, the wavelength spacing and the central wavelengths are consistent and the insertion loss is larger than that of the latter. The increased wavelength-dependent insertion loss and the decreased flatness of three-CMZIs based interleaver are mainly because the match between the optimal design and the SoS process line is inadequate, which can induce phase error of the internal arms based on SoS waveguides. It can also be proved from Fig. 6 that the transmission spectra can be tuned by adjusting the lengths of the external arms and adjustors. Especially, the broad top width can be further increased by using N-CMZIs with more stages.

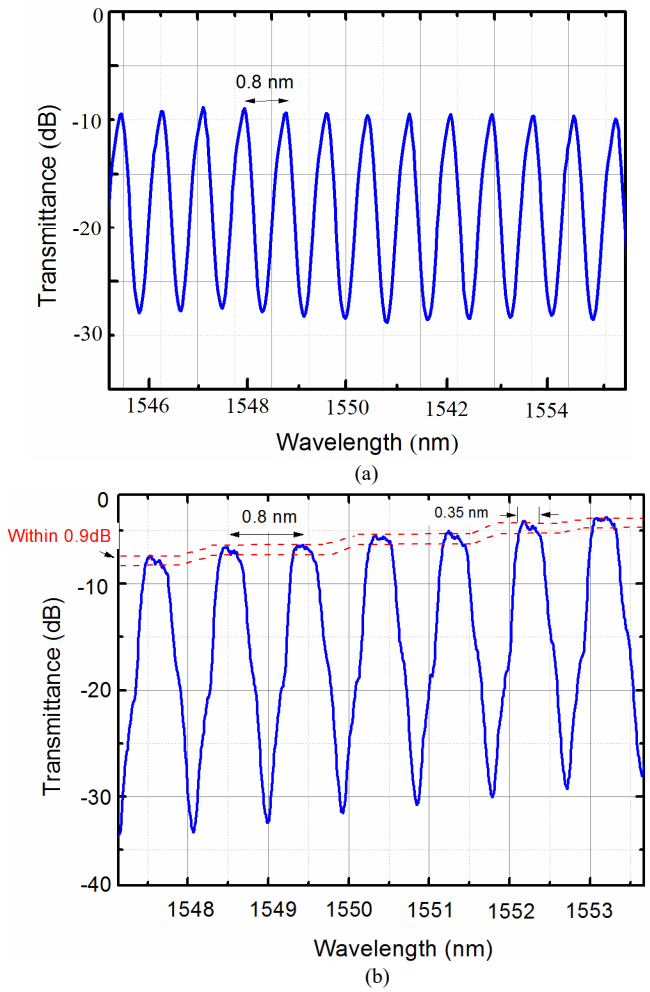


Fig. 6. Testing transmission spectra for (a) the single-CMZIs and (b) the three-MZI with the wavelength spacing of 0.8 nm.

## III. Conclusions

In conclusion, the N-CMZIs integrated by external adjustors have been presented. The characteristics of the single and three-CMZIs have been numerically investigated using the CMT and TMM. The experimental results show the 100 GHz three-CMZIs has high performance with the top widths of ~0.35nm under the wavelength jitters of 0.9 dB, the insertion loss of less than 7.5 dB, the high ER of 25 dB, respectively. Comparing with the testing results of single-MZI based interleaver, the top width of three-CMZIs based 100GHz interleaver could be dramatically improved from 0 nm to 0.35 nm and the ER can be increased from 19 dB to 27 dB.

## References

[1] K. X. Chen, H. P. Chan, and W. Y. Chan, "Design and Fabrication of a Polarization Independent Tunable Interleaver," *J. Lightw. Technol.*, vol. 31, no. 23, pp. 3694-3699, Dec. 2013.

[2] S. Cao, J. Chen, J. N. Damask, C. R. Doerr, L. Guiziou, G. Harvey, Y. Hibino, H. Li, S. Suzuki, K. Y. Wu, and P. Xie, "Interleaver technology: Comparisons and applications requirements," *J. Lightw. Technol.*, vol. 22, pp. 281-289, 2004.

[3] C. W. Lee, R. B. Wang, P. C. Yeh, and W. H. Cheng, "Sagnac interferometer based flat-top birefringent interleaver," *Opt. Exp.*, vol. 14, pp. 4636-4643, 2006.

[4] M. Gad, J. Ackert, D. Yevick, L. Chrostowski, and P. E. Jessop, "Ring resonator wavelength division multiplexing interleaver," *J. Lightw. Technol.*, vol. 29, no. 14, pp. 2102-2108, Jul. 2011.

[5] Y. Q. Wang, H. Zhu, and B. J. Li, "Cascaded Mach-Zehnder Interferometers Assembled by Submicrometer PTT Wires," *IEEE Photon. Tech. L.*, vol. 21, no. 16, pp. 1115-1117, Aug. 2009.

[6] W. Y. Chan, K. X. Chen, H. P. Chan, B. P. Pal, R. K. Varshney, “A flattop PLC polymer waveguide interleaver based on folded two-stage-cascaded Y-junction Mach-Zehnder interferometers,” *Opt. Commun.,* vol. 282, no. 5, pp. 883-886, Mar. 2009.

[7] J. X. Li and K. X. Chen, “An Interleaver With Arbitrary Passband Width Ratio Based on Hybrid Structure of Microring and Mach-Zehnder Interferometer,” *J. Lightw. Technol*., vol. 31, no. 10, pp. 1538-1543, May 2013.

[8] P. P. Sahu, “Polarization independent thermally tunable erbium-doped fiber amplifier gain equalizer using a cascaded Mach-Zehnder coupler,” *Appl. Opt*., vol. 47, no. 5, pp. 718-724, Feb. 2008.

[9] W. F. Jiang and X. H. Sun, “Mach-Zehnder Interferometers Cascaded and Tunable Interleaver Based on Silica-on-Silicon Waveguide,” in *Proc. ACP*, 2014, Paper ATh4A.2.

# Design of Compact and Easy-fabricated Polarization Splitter-rotator Based on Slotted Waveguide

Tao Lv,[1] Weifeng Jiang,[1,2] and Xiaohan Sun[1,*]

[1]National Research Center for Optical Sensing/Communications Integrated Networking,
Department of Electronics Engineering, Southeast University, Nanjing 210096, China
[2]School of Electronic and Optical Engineering,
Nanjing University of Posts and Telecommunications, Nanjing 210023, China
[*]xhsun@seu.edu.cn

*Abstract*—**A compact and easy-fabricated polarization splitter-rotator (PSR) using $SiO_2$ top-cladding directional coupler with a slotted waveguide is proposed and characterized. The proposed device can be easily fabricated with CMOS technology as only one regular slot needs to be etched on a silicon nanowire. Compact size of 42 μm device length at 1.55 μm is realized after the optimizing process while the maximum power conversion efficiency is achieved as high as 94%. With the length variation of ± 5 μm, the conversion efficiency is still larger than 91%, which shows a large fabrication tolerance. The influence of the slot center deviation on conversion efficiency and the bandwidth of the device are also investigated.**

***Index Terms***—**Silicon photonics, Polarization-splitter-rotator, Slotted waveguide**

## I. Introduction

In recent years, silicon photonic has attracted many researchers' attention due to its ultra-small size and CMOS-compatible processing, and therefore it is also regarded as one of promising candidates of next generation of photonic integration [1]. With the advantage of high index contrast, the dimension and bending radius of SOI strip waveguide can be reduced to as small as about 0.088μm$^2$ and 1μm respectively. However, high index contrast also results in the problem of high polarization-sensitivity in SOI-based devices. For example, fundamental transverse electric (TE) mode and transverse magnetic (TM) mode have quite different behaviours in Si nanowire, which brings about polarization mode dispersion and polarization dependent loss. Therefore, polarization diversity scheme is necessary in SOI-based photonic circuits to overcome the problem caused by different polarization modes.

Several approaches have been proposed to achieve polarization diversity scheme, such as polarization beam splitter (PBS) [2, 3], polarization rotator (PR) [4, 5] and polarization splitter-rotator (PSR) [6-9]. PBS is used to divide the wave of different polarization into different output ports and then they can be handled separately with other photonic devices designed for specific polarization mode (e.g., grating coupler for coupling between Si nanowire and fiber, whose design rely on the polarization of light), which will make the design of the whole integrated chip rather complicated. Different from the PBS, PR have only one output port, but the polarization of the output light depends on the input light. And if the input is a combination of light with different polarization, the PR would be useless. As a combination of PBS and PR, PSR avoid these problems and provide a better approach for polarization issues.

Here, we propose and optimize a compact and easy-fabricated PSR based on a novel directional coupler using a regular silicon nanowire and a slotted waveguide with $SiO_2$ cladding. Maximum polarization conversion efficiency (94%) is achieved with a device length of 42μm through the optimization of the height and width of the slot and the gap between the two waveguides. The fabrication tolerance and operating bandwidth are also investigated.

## II. Device Design

### A. Proposed Design

The cross-section view of the proposed PSR is schematically shown in Figure 1, which consists of a regular silicon nanowire and a slotted silicon nanowire with silica substrate and cladding. Considering the connection between the output ports and other photonic devices for further light signal process, the width (W) and height (H) of two waveguides are the same with the regular silicon nanowire, which are 400nm and 220nm, respectively. In order to realize the high conversion efficiency of the fundamental TM mode in one waveguide and the fundamental TE mode in the other, the phase matching condition must be satisfied, which means the propagation constants of the modes in two waveguides should be the same. It was found that introducing a slot in a regular waveguide will reduce the effective index of modes, therefore it is possible to realize the phase matching condition between the TM mode in regular waveguide and the TE mode in slotted waveguide. At the same time, due to the large difference between the fundamental TE mode and TM mode in regular waveguide, the TE mode in regular waveguide will not be coupled into the other waveguide.

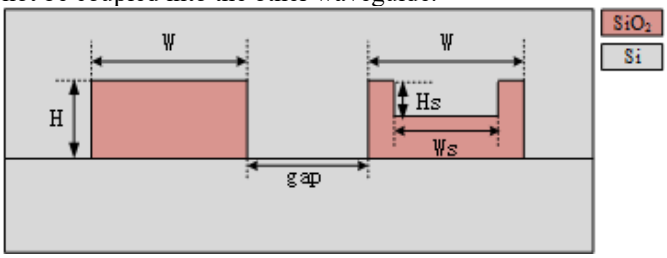


Fig. 1 Cross-section view of the proposed PSR

### B. Optimum Structure Design

Due to the strong polarization dependence of SOI devices, vector finite element method is used to calculate the propagation constants of two supermodes in the coupler and thus we can find the optimum parameters for phase matching

978-1-5386-3374-8/17/$31.00 ©2017 IEEE

condition, which are mainly the gap between the waveguides (g), the width of the slot (Ws) and the height of the slot (Hs). The refractive indices of the silicon is 3.45 and that of the silica substrate and cladding is 1.45 at 1550nm. It is found that the power of TE mode in slotted waveguide is mainly constrained under the slot, which means the mode can be easily affected by the height of the slot.

For three different gap values (100, 200, 300nm), the variation of the effective indices of the supermodes are investigated as a function of the slot width Ws and the results are shown in Fig. 2. It is noted that the phase difference between supermodes decreases firstly and then rises up again with the increase of the Ws, reaching the minimum at the phase matching condition. And for larger gap, the lines get closer and the smallest $\Delta\beta$ will be lower due to the weaker interactions between two waveguides. Coupling length *Lc* is another important parameter to investigate the supermodes in a coupler structure, which can illustrate the results intuitionally. The Fig. 3 shows the variation of *Lc* with Ws for different gap, from which we can straight find that the peak *Lc* become larger as gap increases. Although wide gap will results in long coupling length, which implies a large device, it can also help to increase the coupling efficiency because the supermodes is close to a linear combination of isolated modes due to weak coupling in large gap case. As 55μm is not a relative long length compared with other PSR based on directional couplers, 300nm gap is finally chosen for high conversion efficiency.

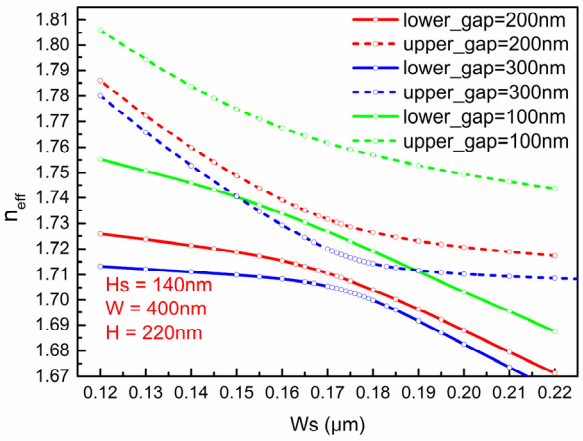


Fig. 2 Variation of effective indices with Ws

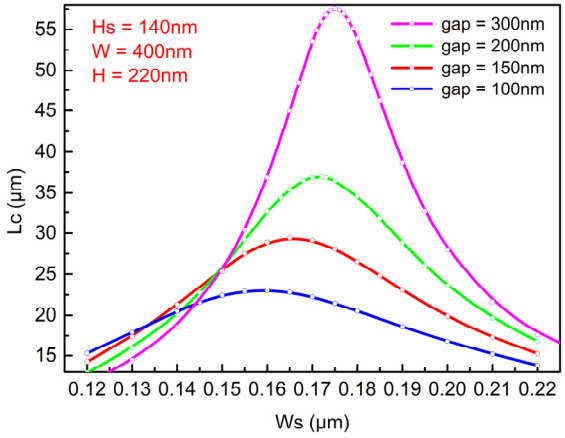


Fig. 3 Variation of *Lc* with Ws in different gap

## C. *Propagation Analysis*

Mode propagation in the device is analysed with FDTD method by inputting TE mode and TM mode in the regular silicon nanowire respectively. The variation of intensity of dominant field component in TE mode (Ex) and dominant field component in TM mode (Ey) are shown in Fig. 4 and Fig. 5. It can be found that the TM mode in regular waveguide is transferred to TE mode in slotted waveguide. Although in the figure we can still find Ey component in the two sides of the slotted waveguide, it is negligible because its power is relative small. The polarization conversion efficiency, which is defined as the ratio of the power of the output TE mode in slot waveguide and input power, is illustrated in the Fig. 6 with the variation of the device length. The maximum polarization conversion efficiency reaches as high as about 94% when *Lc* is 42μm and the PCE is larger than 90% when *Lc* ranges from 37μm to 47μm, which shows a large tolerance for device length.

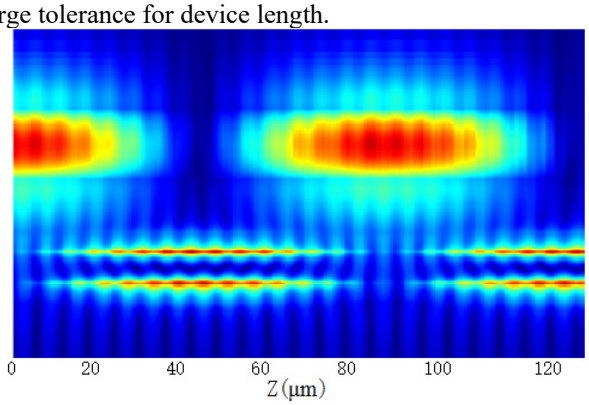


Fig. 4 Variation of Ex component along the Z direction

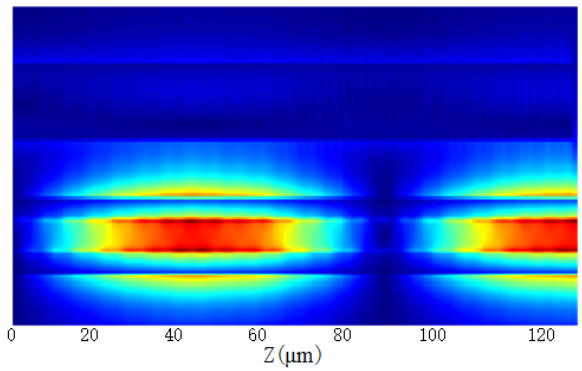


Fig. 5 Variation of Ey component along the Z direction

The influence of the slot center deviation on conversion efficiency and the bandwidth of the device are also investigated and shown in Fig. 7 and Fig. 8. As the effective index is sensitive to wavelength, the phase matching condition will be destroyed when the operating wavelength changes, which results in less efficient conversion and the unconverted TM mode will keeps propagating in the regular waveguide. It can also be inferred from the figure that the phase matching condition changes dramatically when the operating wavelength is reduced, compared to the small variation when the operating wavelength is increased. As for the lateral deviation of the slot, it can be found that the tolerance need to be controlled within 6nm to make the PCE higher than 90%.

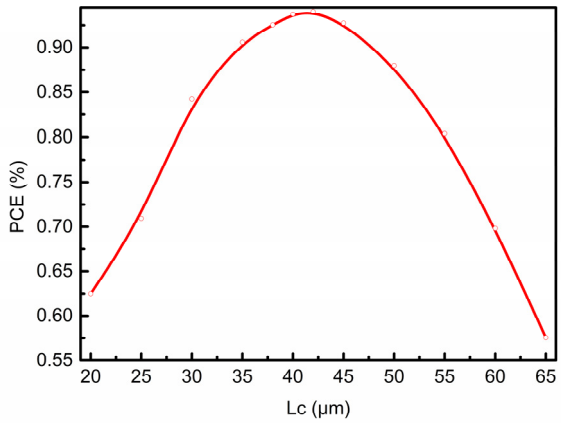


Fig. 6 Variation of PCE with coupling length

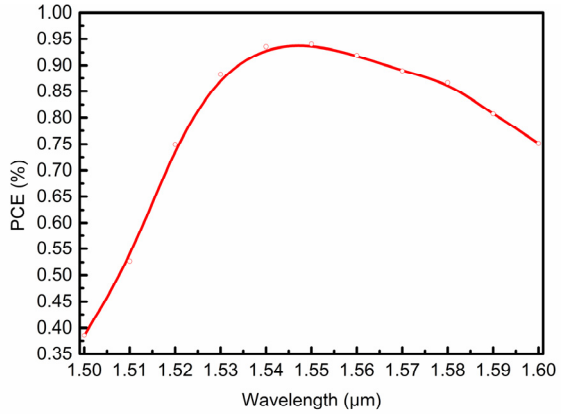


Fig. 7 Variation of PCE with wavelength

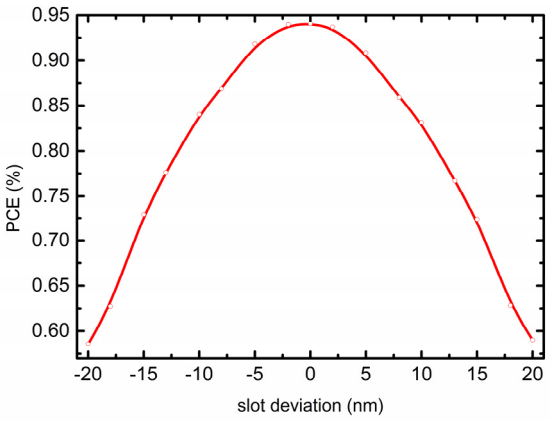


Fig. 8 Variation of PCE with slot deviation

## III. Conclusions

Through the numerical analysis, a compact and easy-fabricated polarization splitter-rotator with $SiO_2$ top and bottom cladding is presented here by combining a slotted waveguide and regular waveguide. The optimized slot height, slot width and gap are obtained through the analysis of phase matching condition with full-vectorial FEM and the corresponding coupling length obtained from the FDTD method is 42μm, where the polarization conversion efficiency reaches 94%. And ±5μm deviation of the coupling length is available for high polarization conversion efficiency ( > 90%), which indicates a large fabrication tolerance. The operating wavelength also has a wide range from 1535nm to 1565nm to keep the polarization conversion efficiency higher than 90%. In addition, only two masks are needed to fabricate the simple structure with CMOS technology and the top $SiO_2$ cladding and the same cross section size with silicon nanowire enable it to integrate with other SOI devices, which also always have a $SiO_2$ cladding. With advantages of small footprint, high polarization conversion efficiency, large tolerance and simple fabrication process, the proposed structure is a potential design for the polarization diversity scheme in photonic integrated circuit.

## References

[1] D. Dai, J. Bauters, and J. E. Bowers, “Passive technologies for future large-scale photonic integrated circuits on silicon: polarization handling, light non-reciprocity and loss reduction,” *Light: Science and Applications*, pp. 1-14, Jan. 2012.

[2] A. Hosseini, S. Rahimi, X. Xu, D. Kwong, J. Covey, and R. T. Chen, "Ultracompact and fabrication-tolerant integrated polarization splitter,” *Opt. Lett,* vol.36, pp.4047–4049, Oct. 2011.

[3] Y. Xu, J. Xiao, and X. Sun, “Compact polarization beam splitter for silicon-based slot waveguides using an asymmetrical multimode waveguide,” *J. Lightwave Technol*, vol. 32, pp. 4884–4890, Dec. 2014.

[4] J. N. Caspers, J. S. Aitchison, and M. Mojahedi, “Experimental demonstration of an integrated hybrid plasmonic polarization rotator,” *Opt. Lett*, vol 38, pp. 4054–4057, Oct. 2013.

[5] Y. Xu, J. Xiao, and X. Sun, “A compact hybrid plasmonic polarization rotator for silicon-based slot waveguides,” *IEEE Photon. Technol. Lett*, vol. 26, pp. 1609–1612, Aug. 2014.

[6] L. Liu, Y. Ding, K. Yvind, and J. M. Hvam, “Silicon-on-insulator polarization splitting and rotating device for polarization diversity circuits,” *Opt. Express,* vol. 19, pp.12646–12651, Jun. 2011.

[7] Y. Ding, L. Liu, C. Peucheret, and H. Ou, “Fabrication tolerant polarization splitter and rotator based on a tapered directional coupler,” *Opt. Express*, vol. 20, pp. 20021–20027, Aug. 2012.

[8] Y. Ding, H. Ou, and C. Peucheret, “Wideband polarization splitter and rotator with large fabrication tolerance and simple fabrication process,” *Opt. Lett*, vol. 38, pp. 1227–1229, Apr. 2013.

[9] Y. Fei, L. Zhang, T. Cao, Y. Cao, and S. Chen, “Ultracompact polarization splitter-rotator based on an asymmetric directional coupler,” *Appl. Opt*, vol. 51, pp. 8257–8261, Dec. 2012.

# Numerical Investigation of a Hybrid Plasmonic Waveguide for Subwavelength Confinement of Light

Raufur Rahman Khan, and Md Zahurul Islam*

Department of Electrical and Electronic Engineering, Bangladesh University of Engineering and Technology
Dhaka-1205, Bangladesh

*mdzahurulislam@eee.buet.ac.bd

*Abstract*— **We investigate the properties of the modes supported by a hybrid plasmonic waveguide. The variation of effective mode indices, field profiles and other properties of the hybrid modes for various choices of the waveguide dimensions are examined in this work by Finite-Difference Eigen-mode method. It is found that the guided mode is like a combination of a surface plasmon polariton mode and a dielectric slab mode. The field of the guided hybrid mode is confined more in the low index dielectric gap region. Thus the propagation loss is found to be significantly reduced. In ultra-high density integrated photonic circuits, coupling between two closely spaced similar waveguides occurs. This phenomenon is also investigated in this work. An optimization of the waveguide dimensions for the minimum propagation loss is performed and a comparative discussion among waveguides of similar topologies is presented.**

***Index Terms***—**Hybrid plasmonic waveguide; finite-difference eigen-mode; effective mode index**

## I. Introduction

Surface Plasmon (SP), a hybrid surface wave that results from the coupling of an electromagnetic wave and free electrons in a metal, has attracted a lot of interest in recent years for its unique properties and great potential for practical applications [1,2]. Plasmonic waveguides based on surface plasmon polaritons (SPP) have received a great attention for their ability to confine light below the conventional diffraction limit not possible by other guiding approaches [3]. However, their performance is limited by the large propagation loss. In the optical region of interest, metals are highly lossy and SP is strongly affected by this loss. As an alternative to purely plasmonic waveguides, a hybrid plasmonic waveguide has been proposed [4], which consists of a high-index dielectric slab separated from a metal surface by a low-index spacer layer. The power in this hybrid structure is mostly confined in the low-index layer, thereby improving the propagation loss suffered by pure plasmonic guides. Numerous topologies of such hybrid plasmonic waveguides have been proposed with many choices of metals and dielectrics since the first proposal of hybrid plasmonic waveguides[5-8]. In this work, we analyze a metal nanowire based hybrid plasmonic waveguide and its optical characteristics at the telecommunication wavelength of 1.55 micron. The numerical investigation was carried out by Finite- Difference Eigen-mode method [9].

## II. Waveguide Architecture

The architecture of the proposed hybrid plasmonic waveguide is illustrated in Fig. 1. The structure is based upon [10] and [11]. The metal (Ag) cylindrical nanowire of diameter d is separated from a square high-index dielectric (Ge) strip of width *w* by a nanoscale low-index dielectric gap (Silica) of h. In this study, we vary the Ge dielectric strip width, the dielectric gap width and the cylinder diameter to control the propagation distance, $L_m$, mode area, $A_m$, and electromagnetic field distribution of a single hybrid mode at 1550 nm wavelength. In our numerical investigation, for simplicity both the high and low-index dielectrics are assumed to be loss-less and dispersion-less (not a bad assumption for a highly n-doped and properly pumped Ge layer). Since only the TM modes are supported by a surface plasmonic structure, the hybrid modes will be TM-like or quasi-TM and only those modes are considered.

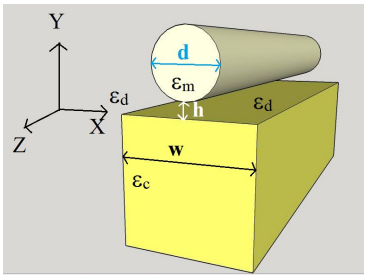


Fig. 1 **The schematic of the proposed hybrid plasmonic waveguide** . A metal cylindrical nanowire of permittivity $\varepsilon_m$ and diameter *d* is separated from a dielectric block of permittivity $\varepsilon_c$ and width (and height) *w* by a nanoscale low-index dielectric of permittivity $\varepsilon_d$.$\varepsilon_c$ = 18.2756 (Germanium) and $\varepsilon_d$ = 2.25 (Silica). The metal (Silver) permittivity $\varepsilon_m$ = -129 + 3.3i. The center of the cylinder defines the origin ($x = y = 0$). Light propagation occurs in the z direction.

## III. Methods, Results and Discussion

### A. Mode profiles

Fig. 2 shows the $E_y$ field profile for different scenarios of the structure. In absence of the high-index block, the silver (Ag) wire and its surrounding silica guide a pure SPP mode, as shown in Fig. 2(a). On the other hand, in the absence of the metal wire, the high-index block and the low-index dielectric (silica) in its surrounding guide a pure dielectric strip mode (Fig. 2(b)),where energy is tightly confined within the high index core region. For relatively large *d* (400 nm), and small *w* (100 nm), guided mode, which is more SPP-like, is observed (Fig. 2 (c)). On the other hand, with a relatively large *w* (450 nm) and small *d* (100 nm), we see a mode that is more strip-like (Fig. 2 (d)). Lastly, with comparable *d* and *w*, we see the hybrid mode (e), where the SPP-like mode and strip-like mode get coupled and the energy is confined within the low-index dielctric nanoscale gap region *h*.

### B. Effective Indices, Confinement and Propagation

Fig. 3 shows the variation of the real part of the effective indices with different strip width *w* for different gap height *h*,

with $d$ fixed at 200 nm. It also shows the effective index for SPP (cylinder) mode and strip mode. It can be seen that in any case, effective mode index of the hybrid mode is higher than that of pure plasmonic mode or pure dielectric mode. Mode index depends on $w$ primarily, increases with increasing $w$.

Fig. 4 shows the effective index variation for different $d$ with $w$ and $h$ fixed at 250 nm and 10 nm, respectively. Metal diameter seems to have very little effect on the effective mode index.

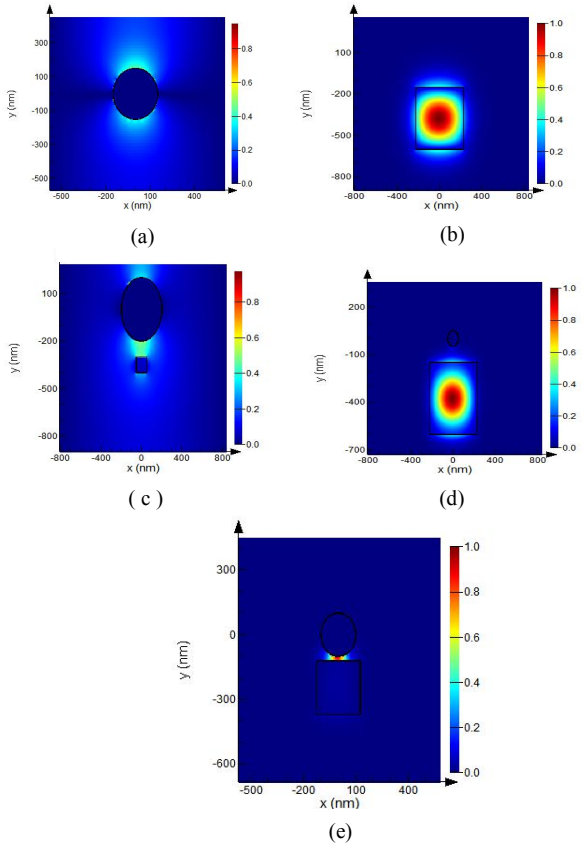


Fig. 2 Field profile of the hybrid plasmonic waveguide structure for different combinations of $d$ and $w$.

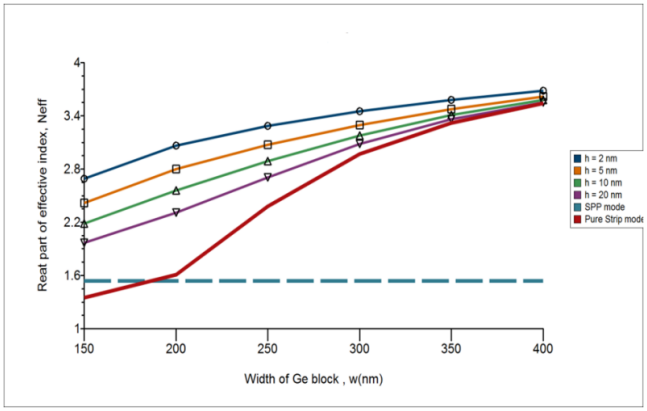


Fig. 3 Variation of effective mode index for different $w$ and $h$.

To measure confinement of a mode, we normalize the mode area, $A_m$, as defined in [12]. We plotted normalized mode area for different $w$ and $h$ in Fig. 5. A smaller value of normalized mode area indicates better mode confinement.

Another index of mode confinement for a given mode can be defined. In this definition, we focus on how much of the total electromagnetic energy is confined within the gap region. We define the low index spacer gap area in the following manner. we take a rectangular section in the low index gap region the length of which is the diameter of the metal wire and the height of which is $h$, the gap height.

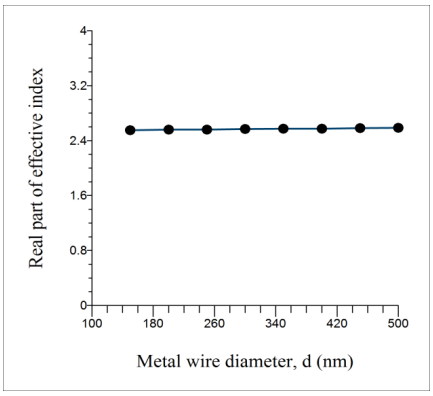


Fig. 4 Variation of effective mode index with metal wire diameter $d$.

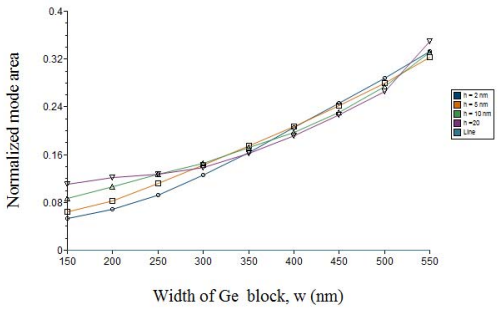


Fig. 5 Variation of normalized mode area with different $w$ and $h$.

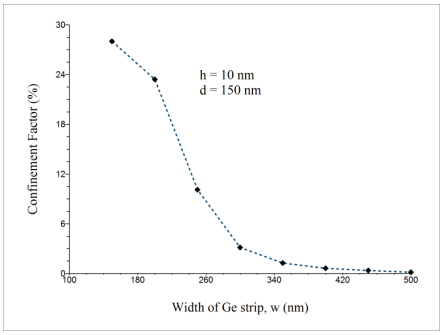


Fig. 6 Variation of confinement factor with $w$.

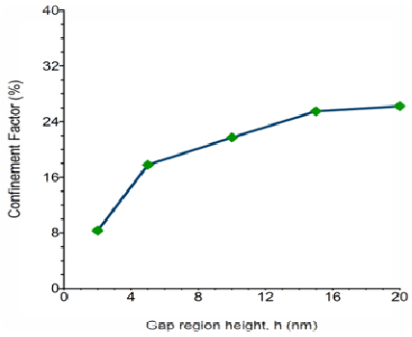


Fig. 7 Variation of confinement factor with $h$.

Then the ratio of power in this region and the total power, found by numerical integration, referred to as ‘Confinement

Factor' is plotted in Fig. 6, Fig. 7, and Fig. 8 for variation in *w, h* and *d*, respectively. This factor falls sharply with increase in *w*, rises slowly with increase of *h*, and shows little variation with *d,* as expected. This way of defining mode confinement can be a simple yet effective method of measuring waveguide performance.

Propagation length, $L_p$, is another important parameter for a plasmonic waveguide [13]. There happens to be a trade-off between moderate propagation length and better mode confinement. $L_p$ is defined as the distance in a waveguide over which the guided power reduces to $e^{-1}$ of its initial magnitude. In case of plasmonic waveguides, this length is given by an equation given in [13]. In Fig. 9, it is interesting to note that at lower values of *h,* propagation distance seems to increase with decreasing *w*. This is because, at small *w* and small *h* at the same time, fields tend to push out of the high index dielectric block into the surrounding silica. So, loss due to metal damping decreases a little and as a result, propagation length increases.

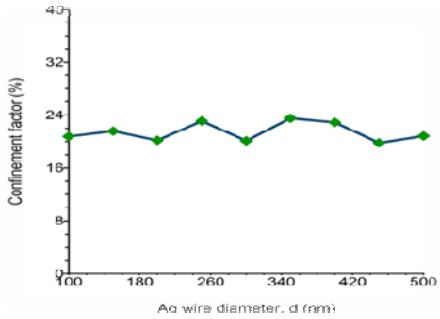


Fig. 8 Variation of confinement factor with *d*.

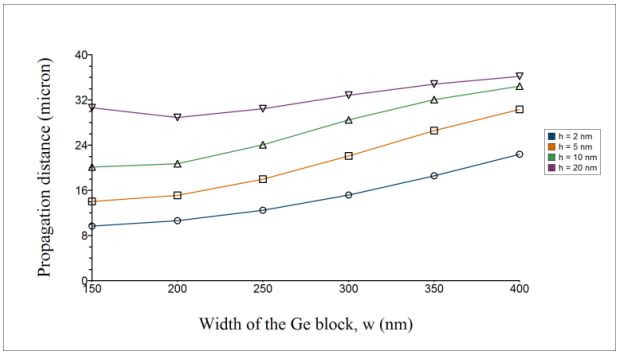


Fig. 9 Variation of propagation distance with *w*.

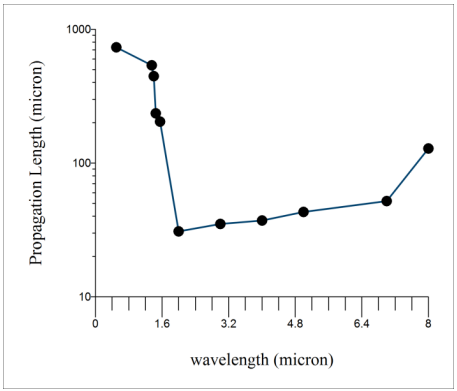


Fig. 10 Propagation length as a function of wavelength.

The propagation distance as a function of wavelength is shown in Fig. 10. As the wavelength increases from 0.5 µm, the propagation distance rapidly decreases from very high values. This is contrary to the pure plasmonic case. As a matter of fact, at shorter wavelength, the absolute value of the real part of the permittivity of the metal is very low, $\varepsilon_m$=7.57 at λ= 0.4 µm and 12.3987 at λ=0.5 µm. Since $\varepsilon_c > \varepsilon_m$, at these wavelengths the fraction of power in the high-index dielectric region is very high which results in long propagation. When wavelength increases, $|\mathrm{Re}(\varepsilon_m)|$ increases, so will the fraction of power in the metal which results in higher loss and lower propagation length. After around 4 µm, the propagation length again increases. This is because after a certain wavelength, the modal index is close to that of the surrounding (silica), so the power begins to radiate away from the gap and loss due to damping of metal decreases and propagation length increases.

### *C. Analysis of hybrid modes*

Using the coupled-mode theory, we can express the hybrid mode, to a first approximation, as a superposition of the strip waveguide modes and the SPP waveguide modes [8],

$$\Psi(w, h) = a(w, h)\,\Psi_{strip}(w) + b(w, h)\,\Psi_{spp} \qquad (1)$$

where $\Psi(w, h)$ is the strength of the hybrid mode, $a(w, h)$ is the amplitude of the constituent strip mode, $\Psi_{strip}(w)$ and $b(w, h)$ is that of the SPP mode $\Psi_{spp}(d)$ of the nanowire and they are related by $|a(w,h)|^2 + |b(w,h)|^2 = 1$. As plotted in Fig. 11 , after the critical strip width, near approximately 200 nm, the coupled mode is more dielectric strip mode and below the critical width its more SPP-like mode. The narrower the gap, the more 'middle' the mode character stays. This means that as *h* approaches 0, the mode approaches SPP mode.

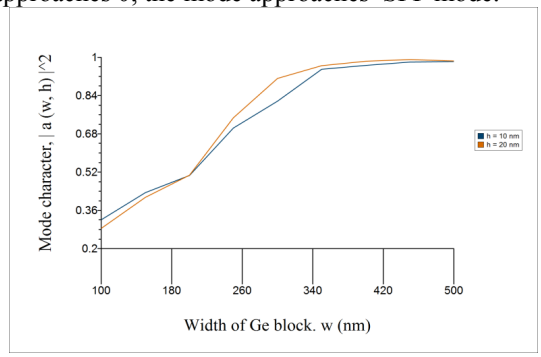


Fig. 11 Mode character variation with *w*.

### *D. Figure of Merit (FOM)*

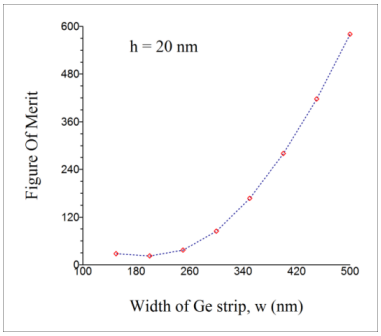


Fig. 12 Single-valued FOM variation with *w* of Ge strip.

A single-valued FOM for a plasmonic waveguide can be defined as the ratio of normalized propagation distance ($L_p/\lambda_0$) and normalized mode area ($A_m/A_0$) [12] . The larger this value, the better performance of the waveguide it represents. The value of this single-valued FOM will eventually depend on the dimensions of the particular waveguide. In Figs. 12 and

13, FOM variation for the Ge-Ag waveguide for different *w* and two different sets of *h* are shown. It is evident that both *w* and *h* affect the performance of the waveguide differently. So a single valued figure of merit is not a very reliable parameter of comparison while comparing waveguides of different dimensions. In this regard, a graphical figure of merit is helpful where we plot normalized propagation distance versus normalized mode area while continuously varying a particular dimension of the waveguide.

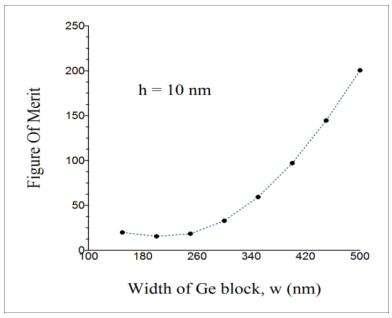


Fig. 13 Single-valued FOM variation with *w* of Ge block.

*E. Coupling between two waveguides*

We examined how closely two such waveguides can be placed so that they suffer negligible crosstalk. The expression for the crosstalk is given by [14],

$$XT = 10\log_{10}[\sin(\pi/2L_p/L_c)] \quad (2)$$

where $L_c$ is defined as the coupling length and $L_p$ is the propagation distance as defined in [13]. Coupling length is given by,

$$L_c = \pi.(\beta_e - \beta_o)^{-1} \quad (3)$$

where $\beta_e$ and $\beta_o$ are wavevectors in the propagating direction for even and odd supermodes, respectively. When fields of the confined mode in the waveguides are in the same direction then the modes are defined as the even supermodes and when the fields are in the opposite direction the modes are called odd supermodes.

In Fig. 14, we plotted the coupling length as a function of separation between two parallel waveguides, *s*. We can see that $L_c$ increases almost exponentially with *s*, as it should.

In Fig. 15, we plotted the calculated coupling lengths as a function of strip width *w* for different separations between waveguides, *s*. It can be seen that, for a given *s*, there is a *w* where coupling length is maximum. Larger coupling length is better for ultra high density integration.

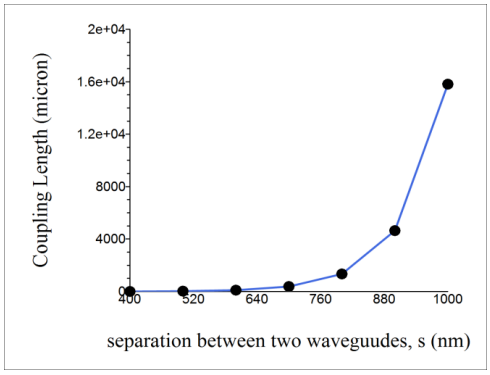


Fig. 14 Coupling length as a function of separation between two waveguides.

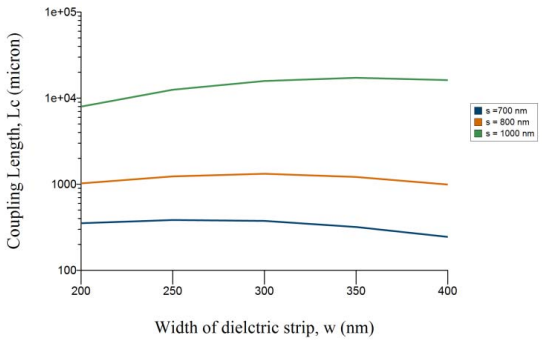


Fig. 15 Coupling length as a function of *w*.

The coupling length should be large enough so that cross talk $XT < XT_o$. If we set the maximum tolerable crosstalk $XT_0$ = -25 dB, the required coupling distance is approximately 27.9 times $L_p$. The separation which provides the minimum coupling length to avoid cross talk is known as the decoupling separation. If we take $L_p$ to be around 25 μm, then minimum coupling length becomes approximately 700 nm. This is helpful to achieve very high density of integration.

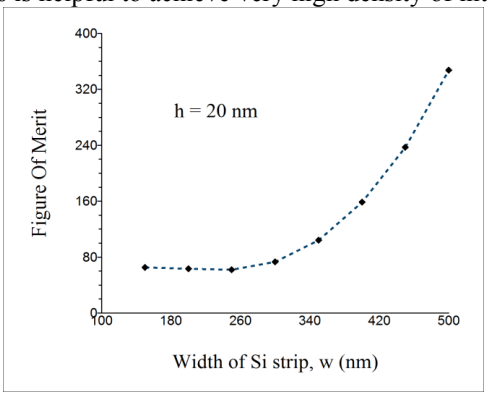


Fig. 16 Single-valued FOM as a function of width of Si strip.

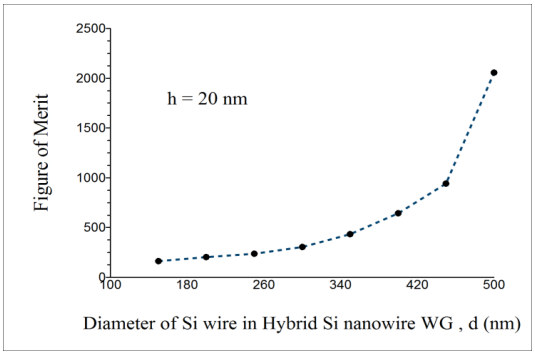


Fig. 17 Single-valued FOM as a function of Si wire diameter.

*F. Comparative Analysis*

We compared the waveguide with other waveguide topologies and configuration based on the single valued *FOM* discussed earlier. We consider two other hybrid plasmonic waveguides. For the first case, we replace the Ge strip of the Ge-Ag waveguide by a Si strip (more conventional choice). Secondly, we consider a waveguide with a cylindrical nanowire of Si with diameter d separated from a silver surface by the distance *h* (Hybrid Si Nanowire waveguide). The gap and the surrounding are filled with low index dielectric silica. In Figs. 16 and 17, we show the FOM of these waveguides as a function of one of the structural parameters. Although the

mode confinement of these latter waveguides are almost the same as the Ge-Ag waveguide considered so far, they are superior in case of propagation length and so their FOM values are much higher. But, the Ge-Ag waveguide shows its advantage when we compare them on the basis of graphical figure of merit (Fig. 18). Then it is evident that for the same amount of mode confinement, Ge-Ag waveguide shows more propagation length than the hybrid Si nanowire waveguide.

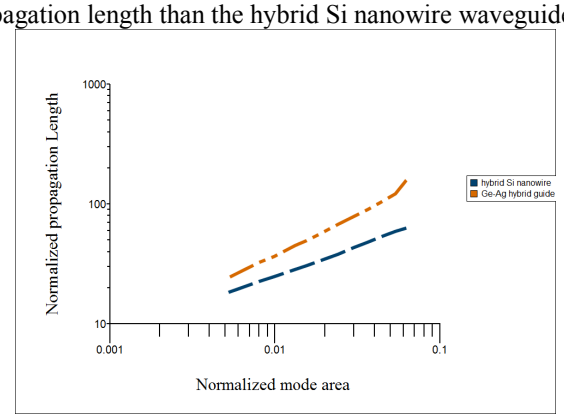


Fig. 18 Graphical Figure of Merit based comparison between Ge-Ag waveguide and Hybrid Si Nanowire waveguide.

## IV. Conclusions

In this work, we numerically analyzed, using Finite-Difference Eigen-mode method, the hybrid plasmonic mode generated as a result of the coupling between a pure plasmonic mode and a pure dielectric waveguide mode in a waveguide structure consisting of germanium block, silver nanowire and silica substrate. We investigated how the variation of the structural parameters influences the important properties of the guided modes. We also evaluated and thereby compared, the structure's performance as a plasmonic waveguide and analyzed the phenomenon of power coupling that occurs between two such closely placed waveguides which will be useful for future reference and for choosing suitable geometric dimensions that offer certain better performance traits for a particular application.

## References

[1] S. A. Maier, *Plasmonics: Fundamentals And Applications*, Springer 2007.

[2] L. Novotny and B. Hecht, *Principles of Nano-optics,* Cambridge University Press, 2006.

[3] B. Zhang, Y. Bian, L. Ren, F. Guo, S. Y. Tang, Z. Mao, X. Liu, J. Sun, J. Gong, X. Guo and T. J. Huang, "Hybrid Dielectric-loaded Nanoridge Plasmonic Waveguide for Low-loss Light Transmission at the Subwavelength Scale", *Scientific Reports 7,* 2017.

[4] M.Z. Alam, J. Meier, J.S. Aitchison and M. Mojahedi, "Super mode propagation in low index medium" *CLEO/QELS.* [Online]. Available: http://www.opticsinfobase.org/abstract.cfm?uri=CLEO-2007-JThD112.

[5] D. Dai and S. He, *Opt. Exp.* 17(19), 16646-16653, 2009.

[6] P. D. Flammer, J. M. Banks, T. E Furtak, C. G. Durfee, R. E. Hollingsworth, and R. T. Collins, *Opt. Exp.* 18(20), 21013-21023, 2010.

[7] Y. Bian, Z. Zheng, Y. Liu, J. Liu, J. Zhu and T. Zhou, *Opt. Exp.* 19(23), 22417-22422, 2011.

[8] J. Xiao, Q. Q. Wei, D. G. Yang, P. Zhang, N. He, G. Q. Zhang, T. L. Ren and X. P. Chen, "A CMOS-Compatible Hybrid Plasmonic Slot Waveguide with Enhanced Field Confinement ",*IEEE Electron Device Letters,* 37(4), 2016.

[9] C. P. Yu and H. C. Chang, "Yee-mesh-based Finite Difference Eigenmode Solver with PML absorbing Boundary Conditions for Optical Waveguides and Photonic Crystal Fiber", *Optics Express,* 2004.

[10] R. F. Oulton, V. J. Sorger, D. A. Genov, D. F. P. Pile and X. Zhang, "A hybrid plasmonic waveguide for subwavelength confinement and long-range propagation", *Nature Photonics,* 2:496-500, 2008.

[11] Y. Chowdhury, "Plasmonic Waveguides : Design and Comparative Study" , Master's Degree Project, Royal Institute of Technology, Sweden, 2011.

[12] R. F. Oulton, G. Bartal, D. F. P. Pile and X. Zhang, "Confinement and Propgation Characteristics of Subwavelength Plasmonic Modes", *New Journal of Physics,* 10, 105018, 2008.

[13] Y. Zhang, L. Cheng, Y. Liu, Z. Yu, R. Ma and H. Ye, "Hybrid Plasmonic Waveguide consisting of two identical semiconductor nanowires and metal film with semi-cylinder ridges", *IOP Publishing,* 2016.

[14] D. Dai and Y. Shi, "Comparative study of the integration density for passive linear planar light wave circuits based on three different nanophotonic waveguide", *Applied Optics,* 46, 1126-1131, 2007.

[15] D. Dai, "Low loss hybrid plasmonic waveguide with double low index nano slots", *Opt. Express,* 18, 17958-17966, 2010.

# Performance Analysis of a Coherent Free Space Optical System With Different Modulation Schemes

Nazia Mehnaz,[1,*] and M. S. Islam[1]

[1]Institute of Information and Communication Technology,
Bangladesh University of Engineering and Technology,
Dhaka-1000, Bangladesh.
[*]araninazia82@gmail.com

*Abstract*— **Free space optical (FSO) system is gaining more and more attention as this technology is one of the most promising alternative scheme for addressing the 'last mile' bottleneck and meets the increasing bandwidth demand of emerging applications and end users. When the optical signal is transmitted through the atmospheric channel, the performance could be severely degraded due to turbulence. Data modulation technique is one of the primary ways to enhance link sustainability. In this paper, a coherent FSO system is analyzed and evaluated with different modulation techniques like OOK, L-PPM, BPSK, DPSK and QPSK using Gamma-Gamma turbulence channel model. The analytical result shows that 8-PPM modulation scheme demonstrates better bit error rate (BER) in terms of signal to noise ratio among the modulation schemes. On the other hand, QPSK and BPSK scheme also provide better performance in terms of both spectral efficiency and BER.**

***Index Terms***— **Free Space optics, Gamma-Gamma distribution, bit error rate, modulation techniques.**

## I. INTRODUCTION

FSO communication systems have been developed for the growing demand for bandwidth demand in mobile communication. The technology is useful where the installation of buried fiber optic cable to provide a high speed network is impractical. FSO systems support diverse applications such as satellites, aircrafts, deep-space probes, ground stations and can also be used as last mile solutions to efficient deployment in densely populated urban areas or in unstructured environment such as disaster prone areas. FSO is gaining popularity due to its advantage over radio frequency communication (RF) includes immunity to electromagnetic interference, high data rate, low power consumption, more compact equipment, less cost and low BER.

FSO technology can provide data rates from hundreds of Mbps to several Gigabits and commercially available systems reports data rates as high as 100 Mbps to 2.5 Gbps [1]. Spectrum congestion in RF systems increases the bandwidth requirement exponentially which is the biggest challenge in expansion of network. The most efficient solution of the problem would be deploying FSO systems which guarantee abundant bandwidth. FSO systems operate in infrared range of spectrum .It desires an unobstructed line-of-sight between transmitter and receiver. FSO operates around 850 nm to 1550 nm wavelengths. The wavelength of 1550 nm is preferred because of more eye safety and reduced solar background radiation [2].

The free-space medium is utilized by FSO system for the transmission of data. As a result, atmospheric conditions inherently affect the transmission, among which turbulence has the most significant effect. It effects the propagation of optical beam by fluctuation of refractive index due to temperature, pressure and wind variation. Turbulence causes phase shift of propagating optical signals causing distortions in wave front as well as causes intensity distortion which is termed as scintillation. It also greatly reduces the receiver sensitivity and detection efficiency which results in the degradation of link performance. It is always an interesting problem to analyse the degradation of signal strength due to scintillation of optical signals as well as link performance against atmospheric turbulence channel. Many researchers have intensively researched and analysed several implementation techniques of FSO to improve the link performance. Advanced data modulation schemes can compensate the transmission impairments caused by atmospheric turbulence and enhance link sustainability significantly.

Many modulation formats are in use in FSO system. Pulse position modulation (PPM) is commonly used in FSO system because it is more energy efficient than on-off keying (OOK) and other modulation formats [3]. The ability to resist atmospheric turbulence for OOK modulation is particularly weak. Phase modulation techniques have higher sensitivity and excellent properties that is better suited for FSO system. In this paper, several modulation techniques includes OOK, Binary Phase Shift Keying (BPSK), Differential Phase Shift Keying (DPSK) , Quadrature phase Shift Keying (QPSK) and L-PPM have been studied and compared in a coherent FSO environment. There are many channel models but Gamma-Gamma model is most frequently used due to its large operating region which includes both weak and strong turbulence [4].

The rest of the paper is organized as follows. Section 2 describes the system model. The channel model is explained in Section 3. In Section 4, different modulation schemes and their bit error rate expressions are discussed. In section 5, the expression of average BER and spectral efficiency is discussed. In Section 6, the performance of different modulation technique under Gamma-Gamma turbulence model is compared. The conclusion is given in section 7.

## II. SYSTEM MODEL

A typical FSO coherent system consists of a laser source, transmitter, receiver and a continuous wave local oscillator beam before it strikes the photo-detector. The output signal of the modulator is is transmitted via atmospheric channel. The overall architecture of coherent system is shown in Fig.1. In

978-1-5386-3374-8/17/$31.00 ©2017 IEEE

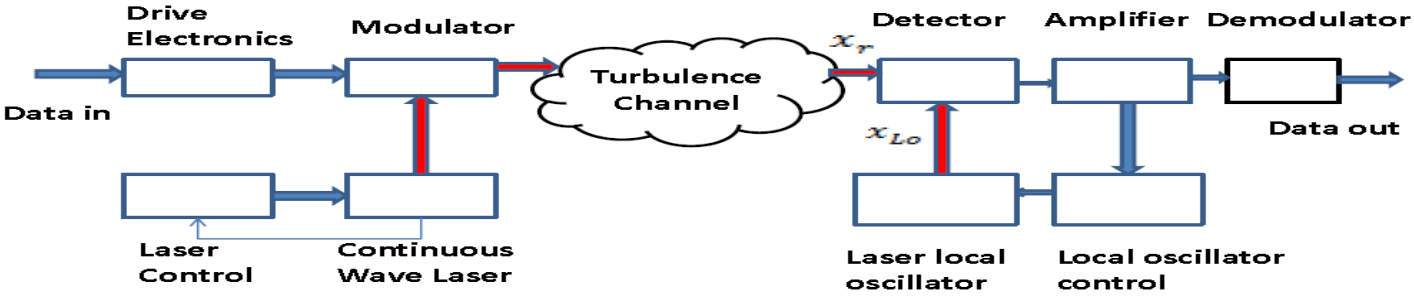


Fig 1.: Block diagram of a coherent FSO system

this section, the basic model of coherent receiver is explained and this could be adapted to other modulation receiver.

The electric field of the received optical and the local oscillator's signals are [5]:

$$x_r(t) = E_r \mathrm{I} e^{(2\pi f_c t + \frac{a\pi}{2})} \quad (1)$$

$$x_{Lo}(t) = E_{Lo} e^{2\pi f_c t} \quad (2)$$

where, $E_r$ and $E_{Lo}$ are the electric field of the received signal and the local oscillator laser respectively, I is the intensity fading coefficient, a=±1 is the information, $f_c$ is the optical carrier frequency. The total power of the received signal and local oscillator laser is:

$$P_T=|IE_r+E_{Lo}|^2=I^2E_r{}^2+E_{Lo}{}^2+2IE_rE_{Lo}$$
$$=I^2P_r+P_{Lo}+2I\sqrt{(P_rP_{Lo})} \quad (3)$$

where $P_s$ and $P_{Lo}$ are the power of the received signal and local oscillator respectively. Additionally, the output current of the photo-detector is:

$$i_p(t)=RP_T+i_{sh}(t)+i_{th}(t) \quad (4)$$

where R is the responsitivity of the receiver, $i_{sh}(t)$ is the shot noise and $i_{th}(t)$ is the thermal noise.

The noise power at the output is given by [6]:

$$\sigma_n^2 = \sigma_{th}^2 + \sigma_{sh}^2$$
$$= 2eB < i_{Lo} > + \frac{4kTB}{RL} = 2eBRP_{Lo} + \frac{4kTB}{R_L} \quad (5)$$

where $R_L$ is the load resistance.

The instantaneous SNR is given by:

$$SNR(I) = \frac{Signal\ Power}{Noise\ Power\ (=Thermal\ noise + Shot\ noise)}$$
$$= \frac{(2IRE_rE_{Lo})^2}{2eBRP_{Lo} + \frac{4kTB}{R_L}}$$
$$= \frac{(2IR)^2 \times P_rP_{Lo}}{2eBRP_{Lo} + \frac{4kTB}{R_L}} \quad (6)$$

If the Local oscillator power is large, the second part of the denominator can be ignored.

## III. Channel Model

The Gamma-Gamma turbulence model has been widely used to study the turbulent behaviour of the atmosphere. This model is suitable for both weak and strong turbulence regime. The beam intensity fluctuation probability density of Gamma-Gamma model is given by [7]:

$$f(I) = \frac{2(\alpha\beta)^{\frac{\alpha+\beta}{2}}}{\Gamma(\alpha)\Gamma(\beta)} I^{\left(\frac{\alpha+\beta}{2}-1\right)} K_{\alpha-\beta}(2\sqrt{\alpha\beta I}) \quad (7)$$

where, I>0 is the received signal irradiance, α and β are the parameters of probability density function, is the Gamma function and $K_a$ is the modified Bessel function of second kind of order a. Here, α and β are the effective number of small scale and large scale eddies of turbulent environment, which are given by [6]:

$$\alpha = \{exp\left[\frac{0.49\sigma_R{}^2}{(1+1.1\sigma_R{}^{\frac{12}{5}})^{\frac{7}{6}}}\right] - 1\}^{-1} \quad (8)$$

$$\beta = \{exp\left[\frac{0.51\sigma_R{}^2}{1+1.1\sigma_R{}^{\frac{12}{5}})^{\frac{5}{6}}}\right] - 1\}^{-1} \quad (9)$$

where, $\sigma_R{}^2 = 1.23C_n{}^2k^{7/6}L^{11/6}$ is called the Rytov variance which represents the variance of log-intensity fluctuation. $C_n{}^2$ is the refractive-index structure parameter and its value ranges from $10^{-13}$ to $10^{-17}$, k is the wave number and L is the distance between transmitter and receiver. When $\sigma_R{}^2<1$, it means the light intensity fluctuation is weak and $\sigma_R{}^2 > 1$ means strong intensity fluctuation.

## IV. Modulation Schemes

In recent times, one of the main goal of modulation is to squeeze as much data into the least amount of possible spectrums. Moreover, advanced data modulation technique can compensate the impairments caused by atmospheric turbulence. Selecting the more appropriate modulation scheme will depend on certain system requirement criterion. For optical wireless systems, the two main criterions are: power and bandwidth efficiency.

Since the average optical power emitted by an optical transmitter is always limited, the performance of modulation techniques is often compared in terms of BER at a given data rate but this is however not the only deciding factor is the choice of modulation technique. Different kinds of modulation schemes are suitable for FSO communication systems. In this article, we have focused on OOK, BPSK, L-PPM, DPSK and QPSK.

### *A. On-Off Keying (OOK)*

Most commercially launched FSO system has been implemented using OOK modulation scheme due to its simplicity. OOK modulation scheme uses either NRZ or RZ. In NRZ-OOK, a digital symbol of 0 is represented by an optical pulse of peak power $\alpha_e P_T$ while transmission of an optical peak power $P_T$ represents 1. The range of the optical source extinction ratio ($\alpha_e$) is $0 \leq \alpha_e \geq 1$. The finite duration of optical pulse is same as symbol duration T. The conditional bit error rate ($P_{e\text{-}OOK}$) for NRZ coded optical data with no

turbulence taken into consideration, can be expressed as a function of SNR as follows:

$$P_{b\_OOK} = \frac{1}{2} erfc(\frac{1}{2\sqrt{2}}\sqrt{SNR}) \quad (10)$$

### B. Pulse Position Modulation(L-PPM)

In this modulation scheme, each pulse of a laser can be used to represent one or more bits of information by its position in time relative to the start of a symbol whose duration is identical to that of information bits it contains. Bits in block encoding are transmitted in blocks instead of one at a time. To achieve optical block encoding, each word of $K_1$ bits is converted into one of $L=2^{K1}$ optical fields for transmission. Since L is the possible pulse positions code for $K_1$ bits of information in PPM scheme, and the bit rate is expressed as follows [8]:

$$R_b = B\frac{log_2\ L}{L} \quad (11)$$

For Gaussian noise, the BER for L-PPM scheme can be expressed as:

$$P_{e\_PPM} = \frac{1}{2} erfc(\frac{1}{2\sqrt{2}}\sqrt{(SNR\ \frac{L}{2} log_2\ L)} \quad (12)$$

### C. Binary Phase Shift Keying(BPSK)

BPSK is the simplest form of phase shift keying (PSK) which uses two different phases for data modulation such that phases are 180 degrees apart hence it can be termed as 2 PSK. This technique is more robust to resist noise than OOK. The conditional BER equation of BPSK is:

$$P_{b\_BPSK} = \frac{1}{2} erfc(\sqrt{SNR}) \quad (13)$$

In case of equal BER, the power requirement ratio of BPSK and OOK is:

$$\frac{P_{BPSK}}{P_{OOK}} = \frac{1}{2\sqrt{2}} \quad (14)$$

Theoretically, the NRZ-OOK requires as much as $2\sqrt{2}$ times power than BPSK to achieve particular BER performance.

### D. Differential Phase Shift Keying(DPSK)

In DPSK, when $\Delta\emptyset$ equals 0, this means two adjacent symbol signals are equal. When using differential decoding, the phase of modulated signal is shifted 180 degree relative to the previous phase of the signal while transmitting the information bit 1. And bit 0 will be transmitted without shifting the phase of modulated signal relative to previous state of modulated signal. The conditional BER of DPSK is without turbulence is as follows:

$$P_{b\_DPSK} = \frac{1}{2} erfc(\frac{\sqrt{(SNR)}}{\sqrt{2}}) \quad (15)$$

The average power requirement of DPSK normalized to OOK can be expressed as $\frac{P_{BPSK}}{P_{OOK}} = \frac{1}{2\sqrt{2}}$.Under the same BER condition, the average power of NRZ-OOK is twice than DPSK.

### E. Quadrature Phase Shift Keying(QPSK)

Different from BPSK and QPSK, the QPSK scheme uses two bits which are grouped together to form signals. When signals are transmitted there are four particular phases. Therefore, BER for QPSK can be considered as two orthogonal of BPSK combined. BER for QPSK can be described as:

$$P_{b\_QPSK} = erfc(\sqrt{SNR}) \quad (16)$$

Consequently, the average power requirement by QPSK normalized to NRZ-OOK can be expressed as:

$$\frac{P_{QPSK}}{P_{OOK}} = \frac{1}{2\sqrt{2}} \frac{erfc^{-1}(BER)}{erfc^{-1}(2BER)} \quad (17)$$

Therefore the average power requirement of QPSK is almost equal to BPSK, only a few amount of power more than BPSK is required. QPSK is bandwidth efficient than any other modulation schemes.

## V. Average BER and Bandwidth Efficiency Calculation

In this section, we have discussed how average BER and bandwidth efficiency of various modulation techniques are calculated.

### A. Average BER

The average BER of the coherent system, considering the atmospheric turbulence channel:

$$\overline{P_b} = \int_0^\infty P_b(I)\, f(I)\, dI \quad (18)$$

here, $f(I)$ is the PDF of Gamma-Gamma distribution. For different modulation technique $P_b(I)$, the conditional BER would be different. We have calculated average BER for different modulation techniques, varying the required received power as well as SNR.

### B. Bandwidth Efficiency

Bandwidth efficiency is another prime metric which is used to compare different modulation techniques performance. The bandwidth efficiency $\eta_b$ can be defined as [6]:

$$\eta_b = \frac{R_b}{B} \quad (19)$$

Where $R_b$ is the achievable bit rate and B is the required bandwidth. For OOK, BPSK and DPSK schemes, bandwidth efficiency is 1 [9]. QPSK is very spectrally efficient since each carrier phase represents two bits of data. The spectral efficiency is 2 bits/Hz, meaning twice the data rate can be achieved in the same bandwidth as OOK, BPSK and DPSK. The band width efficiency of QPSK is $\eta_{QPSK} = \frac{R_b}{0.5R_b} = 2$. For L-PPM, the required bandwidth is [9]:

$$B_{L-PPM} = \frac{LR_B}{Log_2 L} \quad (20)$$

The theoretical bandwidth efficiency of 2-PPM, 4-PPM and 8-PPM is 0.5, 0.5 and 0.375 respectively. The higher the PPM order, the lower the bandwidth efficiency.

## VI. Results

Following the above derivations, simulation has been carried out using MATLAB.

Fig. 2 shows probability density curves for gamma-gamma model with different values of turbulence strength. The strength of the atmospheric turbulence is indicated by different values of Rytov variance ($\sigma_R^2$).

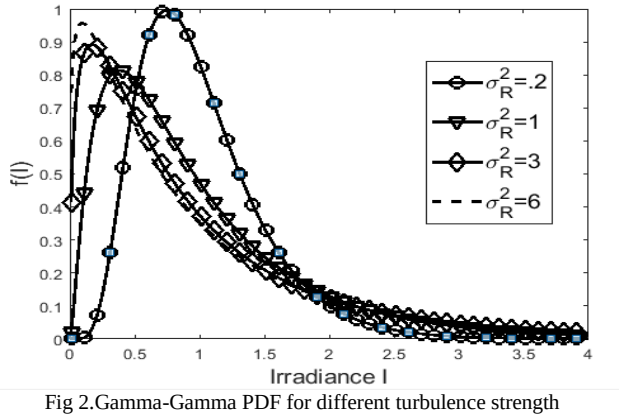


Fig 2.Gamma-Gamma PDF for different turbulence strength

Fig.3 represents the results of average BER, $P_b(I)$ as a function of average SNR for the different modulation techniques like OOK, BPSK, DPSK, QPSK, L-PPM for ${\sigma_R}^2 = 1$ . From the figure, it is observed that higher order PPM (8-PPM) gives better BER performance. BPSK and QPSK give overlapping performance after 20 dB SNR. Before that the BER values of BPSK is slightly higher than QPSK.

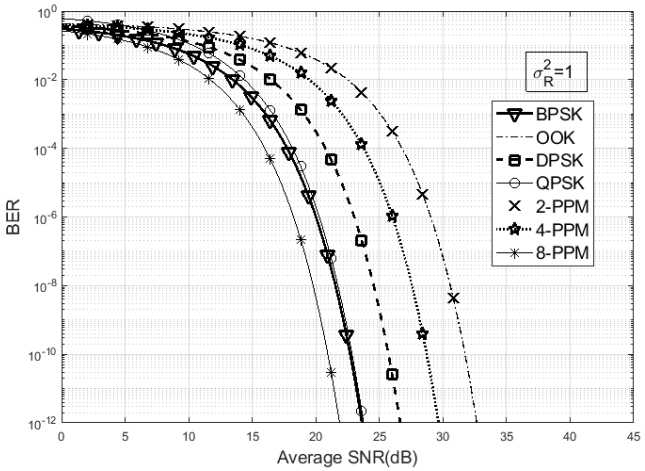


Fig 3: Comparison of BER performance as a function of average SNR in dB for ${\sigma_R}^2$=1

From Fig 4, it is clearly evident that the required received power is also lower for 8-PPM. It can be inferred from the figure that after 8-PPM, BPSK and QPSK gives better performance than other modulation technique in terms of BER vs.SNR and also average required received power. The BER performance of any modulation scheme cannot be the only metric to measure the performance of a modulation scheme. Bandwidth efficiency is also another prime metrics to evaluate the performance of a modulation technique.

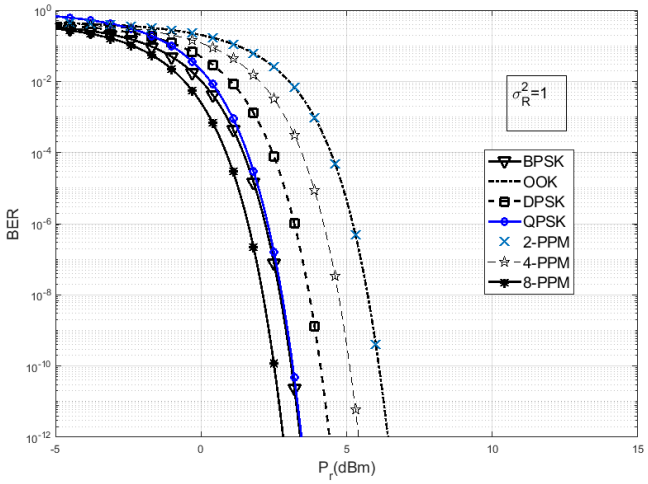


Fig 4. Plots of BER vs Received optical power for different modulation technique

The Fig.5 indicates that the band width efficiency of OOK, BPSK and DPSK is 1, for QPSK, the value is 2 which is highest among other modulation schemes. This suggests that QPSK modulation scheme can make full use of the system spectrum improving the transmission rate of the system. The spectral efficiency for different values of L is less than equal to 0.5 ($\eta_{L-PPM} \leq 0.5$).In L-PPM, the bandwidth expansion is severe for large values of L and ultimately limiting the information throughput of the system.

From the figure, it is found that power efficiency and spectral efficiency both into account QPSK and BPSK performed far better than the power efficient 8-PPM or more higher levels of L-PPM technique.

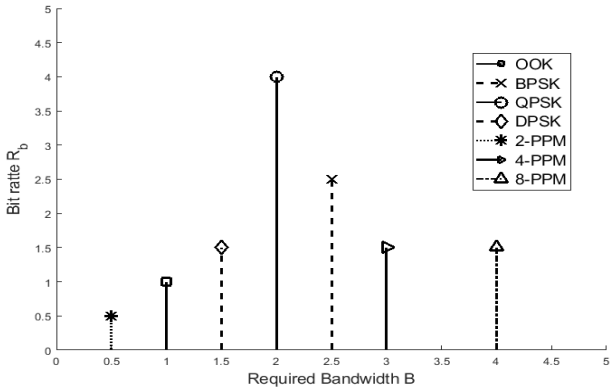


Fig 5. Bit rate vs. Bandwidth for different modulation techniques.

Fig.6 shows the BER performance of BPSK and QPSK for different levels of scintillation. The power requirement for QPSK is slight higher than BPSK.

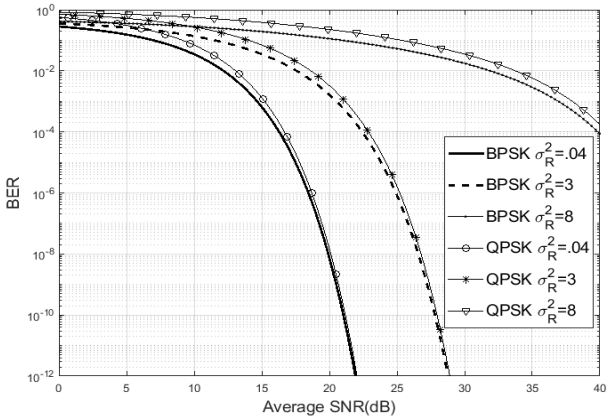


Fig 6. Plots of BER vs average SNR for BPSK and QPSK for different turbulence strength

In Fig.7, BPSK scheme is simulated for different levels of turbulence. For different values of Rytov variance (${\sigma_R}^2$) i.e 0.4, 1, 3, 6 ,the SNR values will be 21.4dB, 23.7dB, 27.6dB and 40.5dB for keeping the BER value $10^{-10}$ .Higher the value of ${\sigma_R}^2$, the more power is needed to achieve the same BER performance.

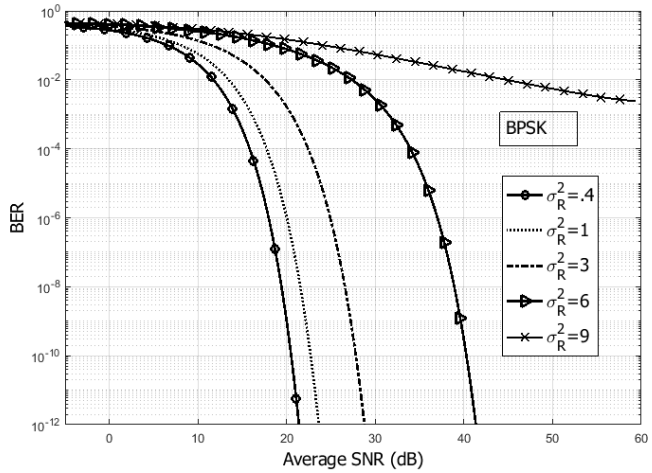


Fig 7.BER performance of BPSK for different turbulence strength

## VII. CONCLUSIONS

The performance evaluation of five modulation schemes for a turbulent FSO channel is presented in this paper. Analysis shows that 8-PPM gives higher BER performance than BPSK and QPSK. Though 8-PPM modulation scheme gives superior BER and SNR performance among the modulation schemes but it has poor spectral efficiency than BPSK and QPSK. If both spectral efficiency and BER performance is taken into account, QPSK and BPSK provide better performance. Again the BER performance of BPSK is slight better than QPSK. Consequently, among QPSK, PPM and BPSK, BPSK is thought to be the most suitable modulation scheme for FSO communication system.

## REFERENCES


[1] Henniger H. and Wilfert O., "An introduction to free space optical communication", Journal of Radio Engineering, vol.19, no.2, pp.203-212, pp.301-305, June 2010.

[2] Kaur A. and Panchal R. K., "Analysis of effect of atmosphere turbulence in free space optical (FSO) communication system", International Journal of Engineering and Innovative Technology, vol. 3, no.11, pp.301-305, May 2014.

[3] Sing J., Kapoor V. and Kumar N., "Performance evaluation of high speed optical wireless communication system", International Journal of Computer Application, vol.4, no.5, pp.11-14, 2012.

[4] Prokes A., "Modeling of atmospheric turbulence effect on terrestrial FSO link", Journal of Radio Engineering, vol.18, no.1, pp.42-47, 2009.

[5] Lim W., "BER analysis of coherent free space optical systems with BPSK over Gamma-Gamma Channels", Journal of the Optical Society of Korea, vol.19, no.3, pp. 237-240, June 2015.

[6] Ghassemlogy Z., Popoola W. and Rajbhandari S., "Optical Wireless Communication", CRC Press, 2013

[7] Shah D., Nayak B. and Jethawani D., "Study of different atmospheric channel models", International Journal of Electronics and Communication Engineering and Technology, vol.5, no.1, pp.105-112, 2014.

[8] Elaganimi T. U., "Performance comparison between OOK, PPM and PAM Modulation schemes for free space optical (FSO) communication", International Journal of Computer Applications, vol.79, no.11, pp.22-27,2013.

[9] Zhang H., Li H., Dongya X. and Chao C.,'' Performance analysis of different modulation techniques for free-space optical communication system", Telkomnica, vol.13, no.3, pp.880-888, September 2015.

# Effectiveness of LED Index Modulation and Non DC Biased OFDM for Optical Wireless Communication

Md. Imran Khan* and M. Rubaiyat Hossain Mondal
Institute of Information and Communication Technology (IICT)
Bangladesh University of Engineering and Technology (BUET)
Dhaka 1205, Bangladesh
*imrankhankuet@gmail.com

*Abstract*—**Optical wireless communication (OWC) can be classified into visible light communication (VLC) and pixelated communication. The multicarrier modulation schemes for VLC and pixelated OWC are *orthogonal frequency division multiplexing* (OFDM) and spatial OFDM, respectively. In the literature, two power-efficient forms of OFDM termed as *light emitting diode (LED) index optical OFDM* (LIM-OFDM) and *non DC biased optical OFDM* (NDC-OFDM) are developed only for VLC. This paper, for the first time, considers the spatial domain forms of LIM-OFDM and NDC-OFDM in the context of pixelated OWC. For pixelated communication, four and two consecutive image frames are used to realize spatial LIM-OFDM and spatial NDC-OFDM, respectively. Simulation results show that for both VLC and pixelated OWC, LIM-OFDM and NDC-OFDM show equal electrical power efficiency in the presence of stand-alone channel noise. Moreover, for the above-mentioned conditions, LIM-OFDM shows 1.3 dB better optical power efficiency than NDC-OFDM at a target uncoded bit error rate (BER) of $10^{-4}$. However, for a pixelated OWC affected by spatial impairments of defocus, linear fractional misalignment, vignetting and channel noise, NDC-OFDM is 3 dB electrically and 4 dB optically power efficient than LIM at a BER of $10^{-4}$.**

***Keywords*- visible light communication, pixelated systems, optical wireless communication, OFDM, LED index modulation, non DC biased OFDM.**

## I. INTRODUCTION

Optical wireless communication (OWC) is a supplementary technique to radio frequency (RF) scheme for the next generation of wireless communications. This is because the bandwidth offered by RF spectrum is not enough [1] for high data rate demanding applications like voice over IP, video streaming, etc. Furthermore, unlike RF spectrum, OWC has no spectrum licensing and electromagnetic interference issues [2-5]. OWC provides more directivity and higher security than RF communications [6-7]. The data rates in OWC can be further increased by arranging multiple-input multiple-output (MIMO) configuration [8-10]. Some examples of OWC are visible light communication (VLC) and pixelated communication. In VLC, the light emitting diode (LED) transmitter is used for data transmission and for room illumination. The fully networked version of VLC, termed as light fidelity (LiFi), is considered as a complementary solution to RF based WiFi. On the other hand, a pixelated OWC is an image transfer based data communication scheme where the screens of smart phones/tablets/laptops are used as transmitters and cameras of smartphones as receivers [11-15]. Unlike VLC systems, a pixelated system are susceptible to different spatial impairments such as defocus blur, linear fractional misalignment (LFM) and vignetting [13].

For encoding data in VLC [16], orthogonal frequency division multiplexing (OFDM) is used [17]. OFDM provides high data rates and is robust to intersymbol interference (ISI). OFDM symbols are bipolar. So, OFDM must be converted to unipolar to make it usable for intensity modulation and direct detection (IM/DD). Some of the unipolar forms of OFDM are *direct current* (DC) *biased optical OFDM* (DCO-OFDM), *asymmetrically clipped optical OFDM* (ACO-OFDM) [17], *non-DC biased optical OFDM* (NDC-OFDM) [18], *asymmetrically clipped DC biased optical OFDM* (ADO-OFDM) [19] and *LED index modulation optical OFDM* (LIM-OFDM) [20]. For DCO-OFDM, to make bipolar OFDM signal to unipolar, a DC bias is added. In ACO-OFDM, data are carried only by the frequency domain odd-index subcarriers, and the time domain OFDM signal is clipped at zero amplitude level. In ADO-OFDM, the odd-index frequency domain subcarriers are used to transmit ACO-OFDM signal, while the even-index subcarriers carry DCO-OFDM signal concurrently. Therefore, in case of ADO-OFDM, by clipping the negative part the data-carrying odd subcarriers are converted to unipolar ACO-OFDM signals, and the data-carrying even subcarriers are transformed to unipolar DCO-OFDM signals by using a DC bias. In NDC-OFDM [18], the positive and negative portions of OFDM symbols are transmitted by two different optical transmitting units where the index of the transmitting unit modulates the polarity of the symbol. On the other hand, LIM-OFDM transmits the negative, positive, real and imaginary elements of the time domain symbols by four optical modulators without using a DC bias [20]. Both NDC-OFDM and LIM-OFDM do not use any DC bias and thus provide more electrical power efficiency than DCO-OFDM. However, better power efficiency in NDC-OFDM and LIM-OFDM is obtained with compared to DCO-OFDM at the expense of using additional optical modulators and optical detectors.

978-1-5386-3374-8/17/$31.00 ©2017 IEEE

Note that VLC uses conventional OFDM in the time domain. However, pixelated systems encode data using *spatial OFDM,* an extension of the concept of OFDM to 2D space. The spatial OFDM frames are transformed to a sequence of optical domain image frames. The spatial domain forms of ACO-OFDM and DCO-OFDM are termed as *spatial ACO-OFDM* (SACO-OFDM) and *spatial DCO-OFDM* (SDCO-OFDM) when applied in pixelated systems [12-15]. Although NDC-OFDM and LIM-OFDM are developed for VLC, in the context of pixelated systems the effectiveness of these modulation schemes is yet to be evaluated.

This work considers, for the first time, NDC-OFDM and LIM-OFDM in the context of pixelated systems in the presence of spatial impairments. The main contributions of this paper are summarized below:

1. Comparing electrical and optical power efficiency of LIM-OFDM, NDC-OFDM, DCO-OFDM and ACO-OFDM for VLC.
2. Extending the concepts of LIM-OFDM and NDC-OFDM to the spatial domain to form spatial LIM-OFDM (SLIM-OFDM) and spatial NDC-OFDM (SNDC-OFDM) for pixelated communication systems.
3. Comparing both the electrical and optical power efficiency of SLIM-OFDM, SNDC-OFDM, SACO-OFDM as well as SDCO-OFDM for pixelated communication for the case of stand-alone channel noise.
4. Comparing both the electrical and optical power efficiency of SLIM-OFDM, SNDC-OFDM, SACO-OFDM and SDCO-OFDM for pixelated systems in the joint presence of vignetting, linear fractional misalignment (LFM), defocus blur and channel noise.

The paper is structured as follows. Section II describes the idea of LIM-OFDM and NDC-OFDM in the context of VLC and pixelated systems. Section III discusses the practical impairments in a pixelated communication system. Section IV gives a comparative study of the performance of different OFDM forms for both VLC and pixelated OWC. Finally, Section V provides concluding observations.

## II. LIM-OFDM AND NDC-OFDM SYSTEMS

This section describes LIM-OFDM and NDC-OFDM for VLC and then extends these concepts for pixelated OWC.

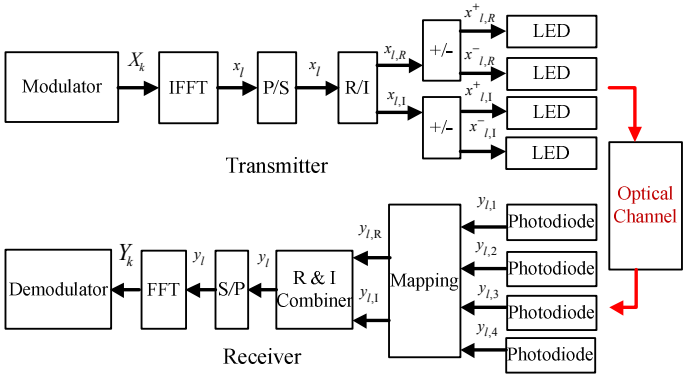


Fig. 1. System architecture of LIM-OFDM [20]

First consider LIM-OFDM. The system architecture of LIM-OFDM [20] for VLC is shown in Fig.1. Note that conventional OFDM signal is complex in nature and Hermitian symmetry is required to make it real valued. As a result, complexity increases to achieve compatibility to IM/DD systems. In LIM-OFDM, Hermitian symmetry is not required like other OFDM formats. At first, message data bits which are to be send are fed to the modulation block for M-array quadrature amplitude modulation (QAM) where M is the modulation order. After modulation frequency domain signal $X_k$ is converted to time domain signal $x_l$ using $N$ point inverse fast Fourier transform (IFFT). If the data size is N then

$$x = [x_0, x_1, x_2, \ldots\ldots x_{N-1}] \tag{1}$$

After parallel to serial conversion, each complex symbol $x_l$ is obtained where $l = [0,1,2\ldots\ldots N-1]$.

Next, the complex OFDM signal is separated into its real and imaginary parts. After that polarity is checked for its real and imaginary components. For a single OFDM complex symbol, at least four LEDs are required where the first two LEDs are responsible to transmit real part, and the other two are responsible to transmit imaginary part. The first LED will be in 'on state' if the real part of complex symbol is positive, and in that case the second LED will be in 'off state'. The reverse case will happen if the real part of complex symbol is negative. Similarly, the third LED will be in 'on state' if the imaginary part of complex OFDM symbol is positive and in that case the fourth LED will be in 'off state'. Again the reverse case will take place if the imaginary part is negative. In any circumstances, two LEDs will be in off state as real or imaginary part of a complex symbol cannot be bipolar at a time.

With this consideration, $x_l$ is separated into its real ($x_{l,R}$) and imaginary ($x_{l,\mathrm{I}}$) parts such that $x = x_{l,R} + jx_{l,\mathrm{I}}$. The sign is then checked for both real and imaginary parts as LED index modulates the sign information of symbols. The positive and negative portions of $x_{l,R}$ can be expressed by $x^+_{l,R}$ and $x^-_{l,R}$, respectively, as shown below:

$$x^+_{l,R} = \begin{cases} x_{l,R}, & \text{if } x_{l,R} > 0 \\ 0, & \text{if } x_{l,R} < 0 \end{cases} \tag{2}$$

$$x^-_{l,R} = \begin{cases} 0, & \text{if } x_{l,R} > 0 \\ -x_{l,R}, & \text{if } x_{l,R} < 0 \end{cases} \tag{3}$$

Similarly, the positive and negative portions of $x_{l,\mathrm{I}}$ can be expressed by $x^+_{l,\mathrm{I}}$ and $x^-_{l,\mathrm{I}}$, respectively, as shown below:

$$x^+_{l,\mathrm{I}} = \begin{cases} x_{l,\mathrm{I}}, & \text{if } x_{l,\mathrm{I}} > 0 \\ 0, & \text{if } x_{l,\mathrm{I}} < 0 \end{cases} \tag{4}$$

$$x^-_{l,\mathrm{I}} = \begin{cases} 0, & \text{if } x_{l,\mathrm{I}} > 0 \\ -x_{l,\mathrm{I}}, & \text{if } x_{l,\mathrm{I}} < 0 \end{cases} \tag{5}$$

Next, the four components of $x_l$ are used to illuminate four different LEDs.

In the receiver section, four photodiodes convert the light emitted by four transmitting LEDs in to the electrical domain. Similar to the literature [19], in the electrical domain additive white Gaussian noise (AWGN) is considered as channel noise. The four components of the noisy electrical signal are mapped by the mapping block to estimate the real, $y_{l,\mathrm{R}}$, and imaginary portion, $y_{l,\mathrm{I}}$. Next, the complex time domain signal $y_l$ is obtained as follows

$$y_l = \pm y_{l,\mathrm{R}} \pm y_{l,\mathrm{I}} \tag{6}$$

After serial to parallel conversion, and FFT operation, the frequency domain signal $Y_k$ is obtained. Finally, demodulation is performed for data recovery.

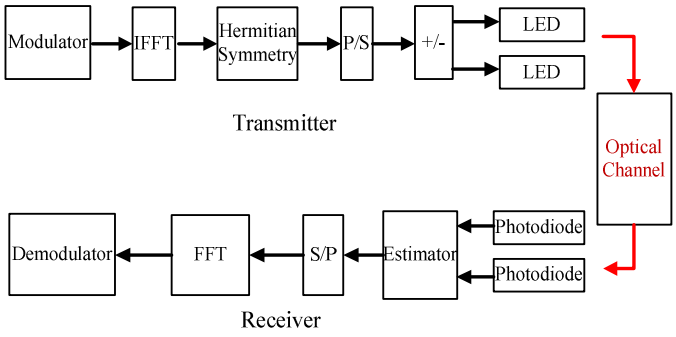


Fig. 2. System architecture of NDC-OFDM biased modulation [18]

Now consider NDC-OFDM. Fig. 2 shows the block diagram of NDC-OFDM [18]. The main difference between LIM-OFDM and NDC-OFDM modulation is that NDC-OFDM does not need real and imaginary separator blocks because NDC-OFDM uses Hermitian symmetry block which converts complex number into real. In NDC-OFDM, two different LEDs are used to transmit the positive and negative valued symbols and in the receiver section, an estimator is used to estimate the sign and magnitude of the symbols. Note that both LIM-OFDM and NDC-OFDM based VLC take advantage of the spatial domain by using multiple LEDs which increases infrastructure cost.

For the case of pixelated OWC, the above descriptions of LIM-OFDM and NDC-OFDM are extended to 2D spatial domain termed as SLIM-OFDM and SNDC-OFDM, respectively. In VLC, an LED is the smallest transmitting unit, whereas in pixelated communication, a pixel within an image is the smallest transmitting unit. In pixelated communication, four different image frames are required to represent the symbols for SLIM-OFDM: two frames for real valued positive and real-valued negative, while two others for imaginary-valued positive and imaginary-valued negative. Similarly, for SNDC-OFDM, two different image frames are used to carry positive and negative symbols. It is assumed in this paper that there is no timing synchronization error within the consecutive four or two image frames of SLIM-OFDM or NDC-OFDM. Unlike LIM-OFDM and NDC-OFDM based VLC which take advantage of spatial domain, the SLIM-OFDM and SNDC-OFDM based pixelated systems take advantage of the temporal domain by using multiple image frames.

## III. Impairments In Pixelated Communication

The most common channel impairments for pixelated communication are defocus blur, LFM and vignetting [12]-[13]. In a practical system, perfect alignment between transmitting device's screen and receiving device's camera is not possible which results in misalignment of received images. For LFM, the extent of misalignment is equal to fractional number of pixels. Due to LFM, some portion of image is not captured by receiver camera lens leading to high bit error rate (BER). If the receiver is not at a fixed distance from the transmitter, defocus blur occurs as the transmitting device is out of focus of the receiver lens. LFM and defocus blur cause attenuation of high frequency subcarriers resulting in incorrect data recovery. Vignetting is the imaging phenomenon of illumination falling-off gradually from the center to corner of the received images. This causes intercarrier interference and attenuation resulting in incorrect data recovery.

## IV. Performance Evaluation

In the following, the performance of different OFDM forms is evaluated in terms of BER. For this, both average electrical and average optical power are considered. It can be noted that the average optical power and average electrical power depend on $E\{x_l\}$ and $E\{x_l^2\}$, respectively for an electrical signal of $x_l$, where $E\{\bullet\}$ is the expectation operator [19]. To obtain a better BER, a modulation scheme with a higher electrical to optical power ratio $E\{x_l^2\}/E\{x_l\}$ is required for a fixed $E\{x_l\}$. In other words, the BER is better for systems that efficiently transform optical power into electrical power at the receiver. In this paper, $E_{b(opt)}/N_0$ is the optical energy in a bit to noise density (single sided spectal density), and $E_{b(elec)}/N_0$ is the electrical energy for a bit to noise density. In general, $E_{b(opt)}/N_0$ is more useful performance metric as it considers the optical to electrical domain conversion efficiency [19]. Howerver, both are taken as metrics in this work.

For VLC, simulation results are presented for an ideal AWGN channel with no other distortion. In case of pixelated communication system, a stand-alone AWGN channel, and a channel with joint spatial impairments are considered. Simulation results are obtained with the help of MATLAB tool. For simulations, 256 number of OFDM subcarriers, M-QAM constellations, constellation sizes of 4 and 16, and a cyclic prefix (CP) of 10 % are considered. It can be noted that in ACO-OFDM, data are encoded using only the odd subcarriers, whereas in DCO-OFDM, NDC-OFDM and LIM-OFDM, data are modulated using both the odd and even subcarriers. For the simulations, the total transmitted optical power is normalized to unity.

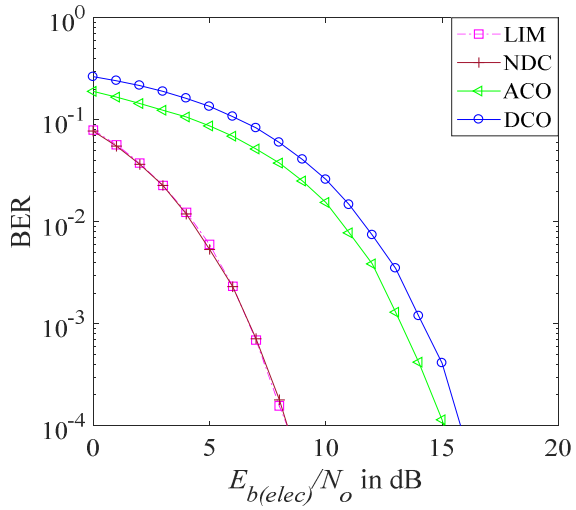


Fig. 3. BER vs. $E_{b(elec)}/N_0$ curve for VLC and pixelated systems for stand-alone AWGN channels.

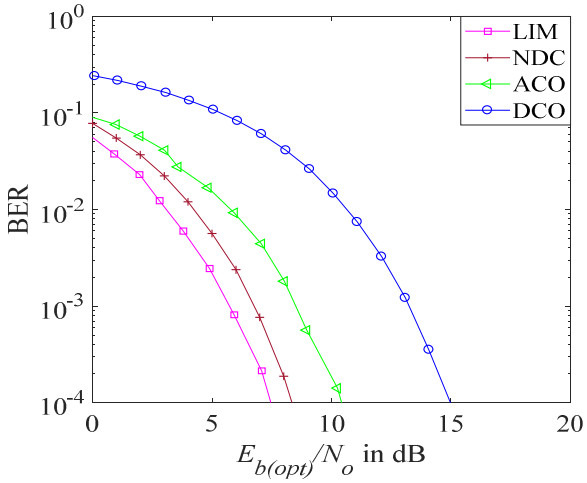


Fig. 4. BER vs. $E_{b(opt)}/N_0$ for VLC and pixelated systems for stand-alone AWGN channels.

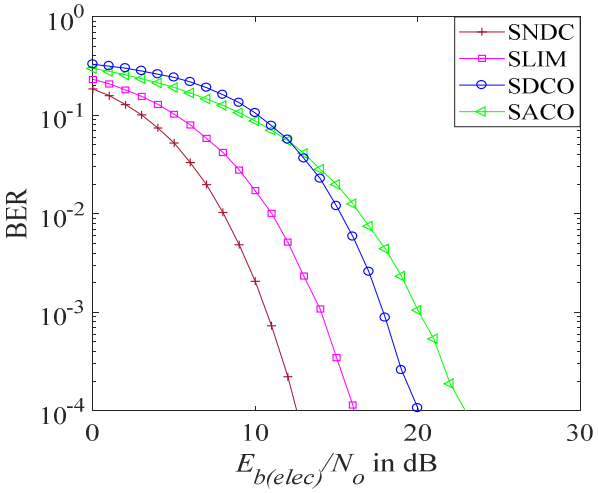


Fig. 5. BER vs. $E_{b(elec)}/N_0$ curves for pixelated systems with different impairments.

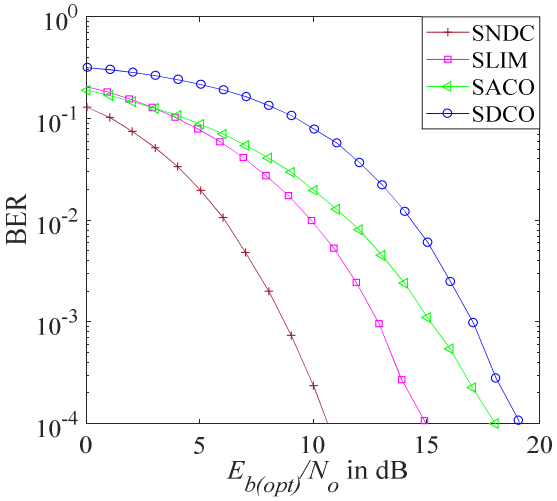


Fig. 6. BER vs. $E_{b(opt)}/N_0$ curves for pixelated systems with different impairments.

Next, the BER performance of LIM-OFDM modulation is compared with NDC-OFDM, DCO-OFDM and ACO-OFDM. Since the spectral efficiency of ACO-OFDM is half of DCO-OFDM, 16-QAM ACO-OFDM is comparable to 4-QAM DCO-OFDM, 4-QAM NDC-OFDM and 4-QAM LIM-OFDM. The plots of BER versus $E_{b(elec)}/N_0$ for AWGN channel for VLC and pixelated systems are shown in Fig. 3. The plots show that at a given BER of $10^{-4}$, the BER performance of both LIM-OFDM and NDC-OFDM are 7 dB better than 16-QAM ACO-OFDM and 8 dB better than 4-QAM DCO-OFDM. It is clear that the performance of NDC-OFDM is very close to LIM-OFDM when electrical power efficiency is considered. The same result is found for pixelated system where it is assumed that there is no other impairment except AWGN.

Fig. 4 illustrates the plots of BER versus $E_{b(opt)}/N_0$ for AWGN channels in case of VLC and pixelated systems. It can be seen that for the cases considered, LIM exhibits the best optical power efficiency. For example, for a given BER of $10^{-4}$, the BER performance of LIM-OFDM is 8.3 dB, 3.3 dB and 1.3 dB better than 4-QAM DCO-OFDM, 16-QAM ACO-OFDM and 4-QAM NDC-OFDM, respectively. So, Fig. 3 and Fig. 4 jointly indicate that compared to NDC-OFDM, LIM-OFDM has equal electrical power efficiency but better optical power efficiency. In other words, LIM-OFDM provides higher optical to electrical conversion than NDC-OFDM.

Next, the BER performances are evaluated for different spatial OFDM based pixelated systems in the presence of joint impairments of defocus, LFM, vignetting and AWGN. The effects of defocus and LFM are overcome by equalizing the received signal usign a single step equalizer in the frequency domain. Furthermore, $N/2$ number of higher-index subcarriers are kept null, where $N$ is the total number subcarriers. Fig. 5 demonstrates the BER versus $E_{b(elec)}/N_0$ for pixelated system for the combined case of impairments.

From Fig. 5 it can be seen that for pixelated communication, SNDC-OFDM provides 3 dB better electrical power efficiency than SLIM-OFDM. Moreover, for a BER of $10^{-4}$, the required $E_{b(elec)}/N_0$ for SNDC-OFDM is 8dB and 11 dB less than 4-QAM DCO-OFDM and 16-QAM SACO-OFDM, respectively. The plots of ACO-OFDM with 16-QAM and DCO-OFDM with 4-QAM shown in Fig. 3 and Fig. 5 indicate that ACO-OFDM outperforms DCO-OFDM in the presence of AWGN alone, and DCO-OFDM performs better for the case of impairments. Therefore, 16-QAM ACO-OFDM is more vulneable to impairments than 4-QAM DCO-OFDM. This is because for a given power level, higher order constellations (16-QAM) are more prone to joint impairments compared to lower constellations (4-QAM). Fig. 6 shows the BER as a function of $E_{b(opt)}/N_0$ for pixelated system with impairments. Unlike VLC where LIM-OFDM has a better optical power efficiency than NDC-OFDM, SNDC-OFDM based pixelated scheme has approximately 4 dB better optical power efficiency than SLIM-OFDM.

## V. Conclusion

This work extends the concepts of LIM-OFDM and NDC-OFDM to the 2D space to form SLIM-OFDM and SNDC-OFDM suitable for pixelated OWC. For SLIM-OFDM, four consecutive image frames are used to transfer the real/imaginary and positive/negative symbols, whereas for SNDC-OFDM two consecutive image frames transfer positive/negative symbols. However, the use of multiple image frames to encode a single spatial OFDM frame, makes the data rates of SLIM-OFDM and SNDC-OFDM to be lower than other spatial OFDM forms such as SDCO-OFDM. Simulation results indicate that when only AWGN is present, LIM-OFDM is more optically power efficient than NDC-OFDM for both VLC and pixelated OWC. However, for pixelated communication affected by different impairments of defocus, LFM, vignetting and AWGN, SNDC-OFDM outperforms SLIM-OFDM in terms of electrical as well as optical power efficiency. This indicates that compared to SLIM-OFDM, SNDC-OFDM is more robust to spatial impairments. It can be noted that in this paper an uncoded target BER of $10^{-4}$ is considered which can be reduced to $10^{-9}$ by using channel coding.

## References


[1] D. Karunatilaka, F. Zafar, V. Kalavally and R. Parthiban, "LED Based Indoor Visible Light Communications: State of the Art," in *IEEE Communications Surveys & Tutorials*, vol. 17, no. 3, pp. 1649-1678, 2015.

[2] M. Leba, S. Riurean and A. Lonica, "LiFi — The path to a new way of communication," *12th Iberian Conference on Information Systems and Technologies (CISTI)*, Lisbon, 2017, pp. 1-6.

[3] H. Burchardt, N. Serafimovski, D. Tsonev, S. Videv, and H. Haas, "VLC: beyond point-to-point communication," *IEEE Commun. Mag*., vol. 52, no. 7, pp. 98–105, Jul. 2014.

[4] L. Grobe, A. Paraskevopoulos, J. Hilt, D. Schulz, F. Lassak, F. Hartlieb, C. Kottke, V. Jungnickel, and K.-D. Langer, "High-speed visible light communication systems," *IEEE Commun. Mag.*, vol. 51, no. 12, pp. 60–66, Dec. 2013.

[5] M. Mukherjee, "Wireless communication-moving from RF to optical," *2016 3rd International Conference on Computing for Sustainable Global Development (INDIACom)*, New Delhi, 2016, pp. 788-795.

[6] H. Marshoud, P. C. Sofotasios, S. Muhaidat and G. K. Karagiannidis, "Multi-user techniques in visible light communications: A survey," *2016 International Conference on Advanced Communication Systems and Information Security (ACOSIS)*, Marrakesh, 2016, pp. 1-6.

[7] S. Wu, H. Wang, and C. H. Youn, "Visible light communications for 5G wireless networking systems: from fixed to mobile communications," *IEEE Netw.*, vol. 28, no. 6, pp. 41–45, Nov. 2014.

[8] Z. Lubin, D. O'Brien, M. Hoa, G. Faulkner, L. Kyungwoo, J. Daekwang, et al., "High data rate multiple input multiple output (MIMO) optical wireless communications using white led lighting," *IEEE Journal on Selected Areas in Communications*, vol. 27, pp. 1654-1662, 2009.

[9] T. Fath and H. Haas, "Performance comparison of MIMO techniques for optical wireless communications in indoor environments," *IEEE Transactions on Communications*, vol. 61, pp. 733-742, 2013.

[10] D. O'Brien, "Optical Multi-Input Multi-Output systems for short-range free-space data transmission," *7th International Symposium on Communication Systems, Networks & Digital Signal Processing (CSNDSP 2010)*, Newcastle Upon Tyne, UK, 2010, pp. 517-521.

[11] S. Kuzdeba, A. M. Wyglinski and B. Hombs, "Prototype implementation of a visual communication system employing video imagery," *2013 IEEE 10th Consumer Communications and Networking Conference (CCNC)*, Las Vegas, NV, 2013, pp. 184-189.

[12] M. R. H Mondal, J Armstrong, "Analysis of the effect of vignetting on MIMO optical wireless systems using spatial OFDM,". *J. Lightw. Technol*., vol. 32, no. 5, pp. 922–929, Mar. 2014.

[13] M. R. H. Mondal, and K. Panta, "Performance analysis of spatial OFDM for pixelated optical wireless systems," *Transactions on Emerging Telecommunications Technologies*, vol. 28, no. 2, pp. 1-13, Feb. 2017.

[14] N. Tazin and M. R. H. Mondal, "Optimal biased spatial OFDM for peak power limited optical wireless channels," *2016 10th International Conference on Signal Processing and Communication Systems (ICSPCS)*, Gold Coast, QLD, 2016, pp. 1-6.

[15] M. R. H. Mondal, "Impact of spatial sampling frequency offset and motion blur on optical wireless systems using spatial OFDM" in *EURASIP Journal on Wireless Communications and Networking,* vol. 238, pp.1-12, 2016.

[16] Y. Tanaka, T. Komine, S. Haruyama and M. Nakagawa, "Indoor visible communication utilizing plural white LEDs as lighting," *IEEE International Symposium on Personal, Indoor and Mobile Radio Communications. PIMRC 2001. Proceedings (Cat. No.01TH8598)*, San Diego, CA, 2001, pp. F-81-F-85 vol.2.

[17] J. Armstrong and A. J. Lowery, "Power efficient optical OFDM," in *Electronics Letters*, vol. 42, no. 6, pp. 370-372, Mar. 2006.

[18] Y. Li, D. Tsonev and H. Haas, "Non-DC-biased OFDM with optical spatial modulation," *2013 IEEE 24th Annual International Symposium on Personal, Indoor, and Mobile Radio Communications (PIMRC)*, London, UK, 2013, pp. 486-490.

[19] S. D. Dissanayake and J. Armstrong, "Comparison of ACO-OFDM, DCO-OFDM and ADO-OFDM in IM/DD systems," in *Journal of Lightwave Technology*, vol. 31, no. 7, pp. 1063-1072, Apr. 2013.

[20] A. Yesilkaya, E. Basar, F. Miramirkhani, E. Panayirci, M. Uysal and H. Haas, "Optical MIMO-OFDM with generalized LED index modulation," in *IEEE Transactions on Communications*, vol. 65, no. 8, pp.3429-3441, Aug. 2017.

# Performance Analysis of Multi-Wavelength Optical CDMA System over Atmospheric Turbulence FSO Channel using SIK Receiver

A. K. M. Nazrul Islam,[1,*] S. P. Majumder,[2]
[1] Dept of EECE, MIST, Dhaka-1216, Bangladesh
[2]Dept of EEE, BUET, Dhaka-1205, Bangladesh
[*]nazrul_4620@yahoo.com

*Abstract*— **An analytical study is carried out for evaluating the effect of atmospheric turbulence (AT) on the bit error rate (BER) performance of a multi-wavelength optical code division multiple access (CDMA) free space optical (FSO) system using optical domain encoder and Sequence Inverse Keying (SIK) balanced photodetector receiver. The analysis is represented to derive the expression of the signal current, multi-access interference (MAI) current and cross-talk current at the output of the SIK receiver considering the effect of AT due to FSO channel. The expression of average BER is found out by averaging the conditional BER over the effect of probability density function (PDF) of the AT. The numerical performance results are evaluated for different code length, number of simultaneous user, link distance and other system parameters. It is found that, the performance of a multi-wavelength optical CDMA system with a SIK receiver is degraded significantly due to AT effect and suffers considerable amount of power penalty at a given BER. The penalty is found to be 1 dB to 9.5 dB for link distance ranges from 500 m to 4000 m with user number 16 and code length 1024 at BER=$10^{-9}$.**

***Index Terms— Atmospheric turbulence (AT), Gamma-Gamma PDF, Multiple Access Interference (MAI), Multi-wavelength optical CDMA, Rytov variance and Sequence Inverse Keying (SIK).***

## I. INTRODUCTION

FSO communications have gained sufficient interests in recent years as an alternative to radio frequency (RF) links for transferring data at high rates over short distances. FSO also have enormous bandwidth compared to RF communication systems. Performance of an optical CDMA system is limited by multi-access interference and also by channel impairments. The capacity of optical CDMA system can be increased with a hybrid multiple access technique like multi-wavelength optical CDMA system and can be implemented by assigning a numbers of wavelength to optical CDMA user along with wavelength division multiplexing (WDM).

Numerous research works have been carried on the effect of different types of AT's and pointing error on multi-wavelength optical CDMA communications, FSO communications and optical CDMA FSO communications. A detail study has been presented on the effect of AT and pointing error on FSO communication system with mathematical model for AT and pointing error [1]. A theoretical study is represented to evaluate the effect of AT on optical CDMA over the FSO channel using polarization shift key (PolSK) modulation format [2]. The intensity fluctuation on the multi-wavelength pulse position modulation (MWPPM) signal due to the presence of AT has been studied in [3]. Passive optical network (PON) for fiber at home (FTTH) and optical CDMA over WDM are reported in [4, 5]. Remarkable advantages achieved by using hybrid optical CDMA WDM for different access network [6]. The benefit of high spectral efficiency of WDM/DWDM system is reported by theoretical analysis with experimental verification in [7, 8]. Multi-wavelength optical CDMA is the effective way to increase the channel capacity and to reduce the cross talk as discussed in [9]. Recently, the authors have presented analytical approaches on the performances of optical CDMA FSO link and Multi-wavelength optical CDMA system in presence of pointing error in [10, 11] using SIK receiver.

In this paper, analysis is carried out to evaluate the BER performance results of a Multi-wavelength optical CDMA FSO communication system using optical encoder and SIK decoder. The BER performance results are numerically evaluated to determine the capacity enhancement of a multi-wavelength optical CDMA system [7, 8] over atmospheric turbulent channel. The BER performance results are evaluated numerically based on the number of simultaneous users, numbers of wavelength, different link distances and code lengths, and the AT parameters using Gamma-Gamma distribution. Power penalties are also numerically evaluated for a given BER as a function of link distances and wavelengths in presence of AT.

This paper is presented as follow: multi-wavelength optical CDMA FSO system model and PDF of Gamma-Gamma channel model is presented is presented in section II and in section III respectively. In section IV, analysis on BER performance with AT is represented. Finally, numerical evaluations and conclusion are presented in section V and VI respectively.

## II. MULTI-WAVELENGTH-OPTICAL CDMA FSO SYSTEM MODEL

The block diagram for a multi-wavelength optical CDMA transmitter and multi-wavelength optical CDMA dual photodetectors SIK receiver system is shown in Fig 1. The serial input bit stream from $i^{th}$ channel is converted to N number of parallel bit streams. The optical input to the optical CDMA encoder is the modulated output of $i^{th}$ parallel data stream from the laser diode (LD) with wavelength $\lambda_i$. The optical CDMA encoder generates optical output with the help of a code generator (CG). The WDM multiplexes N numbers of wavelengths of optical CDMA encoders. The output of

978-1-5386-3374-8/17/$31.00 ©2017 IEEE

WDM multiplexer is the combined optical multi-wavelength CDMA signal. The combined signal from WDM multiplexer is then transmitted through the atmospheric turbulent FSO channel.

The optical signal received from the FSO atmospheric turbulent channel is amplified and then de-multiplexed by the WDM de-multiplexer. The outputs of WDM de-multiplexer are given to the optical CDMA decoder to decode by the CG. The SIK dual photodetector receivers receive the output of each optical CDMA decoder. The decision for data is taken on each data channel and then, the parallel data streams are converted to serial bit streams for the respective users [11].

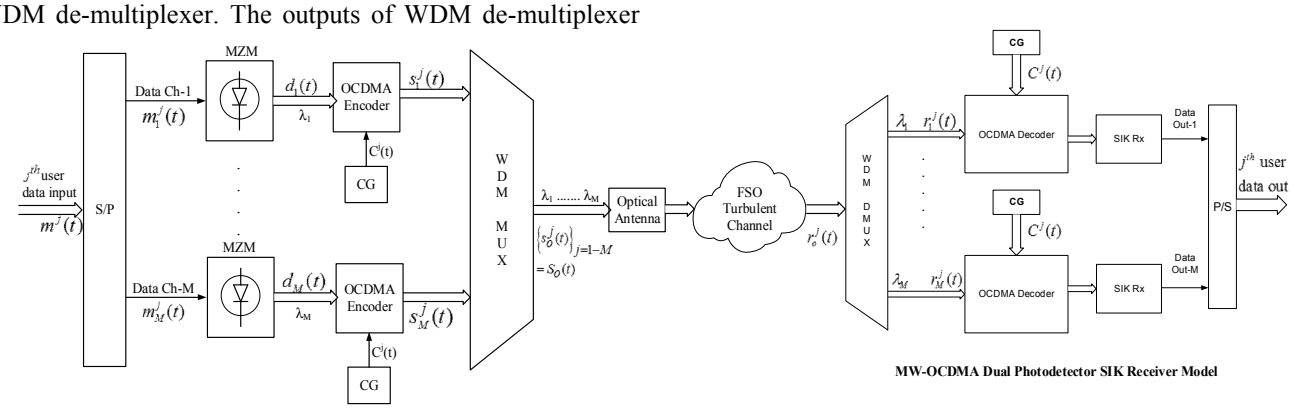


Fig. 1: Block diagram of optical CDMA transmitter and multi-wavelength optical CDMA SIK dual photodetector receiver.

## III. Multi-wavelength Optical CDMA FSO Channel Model

Performance of FSO system is adversely affected by the presence of AT in the channel. Gamma-Gamma distribution for strong turbulence is the proposed form of the intensity variation due to AT at the receiver of the optical link. The small scale and the large scale fluctuations of the atmospheric turbulent channel are describe by Gamma-Gamma PDF model as [1]:

$$p(I_S/\rho)=\frac{2(\alpha(\rho)\beta(\rho))^{(\alpha(\rho)+\beta(\rho))/2}}{\gamma\bar{I}(\sqrt{\rho})\Gamma(\alpha(\rho))\Gamma(\beta(\rho))}x\left(\frac{I_S}{\gamma\bar{I}(\sqrt{\rho})}\right)I^{((\alpha(\rho)+\beta(\rho))/2)-1}$$
$$x\,K_{(\alpha(\rho)-\beta(\rho))}\left(2\sqrt{(\alpha(\rho)\beta(\rho))I_s/\gamma\bar{I}(\sqrt{\rho})}\right) \quad (1)$$

where, the intensity of the signal is $I_s$, mathematical Gamma function is $\Gamma(.)$ and modified Bessel function of the second kind of order $\alpha(\rho)$-$\beta(\rho)$ is presented by $K_{\alpha(\rho)-\beta(\rho)}$. The effective number of small sale eddy $\alpha(\rho)$ and large scale eddy $\beta(\rho)$ of the scattering environment are related to atmospheric conditions according to [1] as:

$$\alpha(\rho)=\left[\exp\left(\frac{0.49\sigma_x^2}{\left(1+1.11\sigma_x^{12/5}\right)^{(7/6)}}\right)-1\right]^{-1} \quad \text{and}$$

$$\beta(\rho)=\left[\exp\left(\frac{0.51\sigma_x^2}{\left(1+0.69\sigma_x^{12/5}\right)^{(7/6)}}\right)-1\right]^{-1} \quad (2)$$

where, $\sigma_x^2=1.23C_n^2K^{7/6}L^{11/6}$ represents the Rytov variance, $C_n^2$ presents the refractive index constant, $L$ represents the propagation link distance and $K$ is the wave number.

## IV. Multi-wavelength Optical CDMA System Analysis

The serial input information bits are converted to parallel bit streams and the bit stream of $i^{th}$ branch for the $j^{th}$ user modulates the Laser Diode (LD) using the Mach-zehnder modulator (MZM) at a wavelength of $\lambda_i$. The output of the MZM of $\lambda_i$ can be represented as:

$$d_i^j(t)=\sqrt{2P_T}\,m_i^j(t)\cos\left[\frac{2\pi c}{\lambda_i}t\right] \quad (3)$$

The optical CDMA encoded signal for $j^{th}$ user to $i^{th}$ wavelength $\lambda_i$ can be written as:

$$s_i^j(t)=d_i^j(t).c^j(t)=\sqrt{2P_T}\sum_{l=0}^{L_c-1}m_i^j(t)c_l^j(t)p(t-lT_c)\cos\left[\frac{2\pi c}{\lambda_i}t\right] \quad (4)$$

where data of $i^{th}$ branch of the $j^{th}$ user is $m_i^j(t)$, wavelength of $i^{th}$ optical carrier is $\lambda_i$, $j^{th}$ user code is $c_j(t)$ consists of $L_c$ chips of duration $T_c$, the $l^{th}$ chip of the $j^{th}$ code is $c_l^j(t)$.

The $j^{th}$ user multi-wavelength optical CDMA signal transmitted can be expressed by:

$$S_o^j(t)=\sum_{i=1}^{M}s_i^j(t)=\sum_{i=1}^{M}\sqrt{2P_T}\sum_{l=0}^{L_c-1}m_i^j(t)c_l^j(t)\,p(t-lT_c)\cos\left[\frac{2\pi c}{\lambda_i}t\right] \quad (5)$$

Considering the effect of AT on the optical CDMA signal Is, then the optical CDMA signal received by K$^{th}$ user receiver can be expressed as:

$$r_o^K(t)=\sum_{j=1}^{K}S_o^j(t).I_se^{-\alpha d}.h_a\otimes h_c(t)$$
$$=\sum_{j=1}^{K}\sum_{i=1}^{M}\sqrt{2P_T}.I_se^{-\alpha d}.\sum_{l=0}^{L_c-1}m_i^j(t)c_l^j(t)p(t-lT_c)\cos\left[\frac{2\pi c}{\lambda_i}t\right].h_a\otimes h_c(t)$$
$$=\sum_{j=1}^{K}\sqrt{2P_r}.I_s\sum_{i=1}^{M}\sum_{l=0}^{L_c-1}m_i^j(t)c_l^j(t)p_{out}(t-lT_c).h_a\cos\left[\frac{2\pi c}{\lambda_i}t\right]$$
$$=\sum_{i=1}^{M}\sqrt{2P_r}.I_s\sum_{i=1}^{K}\sum_{l=0}^{L_c-1}m_i^j(t)c_l^j(t)p_{out}(t-lT_c).h_a\cos\left[\frac{2\pi c}{\lambda_i}t\right] \quad (6)$$

where the attenuation due to AT is $h_a$, normalized channel fading coefficient is $h_c(t)$, link distance is $d$, chip power is $p(t)$ and average optical received power is $P_r$ which is expressed as:

$$P_r = P_T.e^{-\alpha d} \text{ and } p_{out}(t) = p(t) \otimes h_c(t) \quad (6)$$

The $p^{th}$ wavelength signal for $j^{th}$ user receiver at the output of WDM de-multiplexer can be expressed by:

$$r_p^j(t) = \sqrt{2P_r}.I_s \sum_{j=1}^{K} \sum_{l=0}^{L_c-1} m_p^j(t) c_l^j(t) p_{out}(t-lT_c).h_a + \sqrt{2P_r}.I_s \sum_{\substack{i=1 \\ i\neq p}}^{M} x_i \sum_{l=0}^{L_c-1} m_i^j(t) c_l^j(t) p_{out}(t-lT_c) h_a \quad (8)$$

where the cross talk parameter is represented by $x_i$ for $i^{th}$ WDM channel for the use of WDM multiplexer and de-multiplexer.

The output of the SIK receiver for the $p^{th}$ wavelength channel for the $j^{th}$ user is expressed by:

$$Z_i(t) = \frac{R_d P_r I_s}{2} \int_0^{T_s} \sum_{j=1}^{K} h_a \sum_{l=0}^{L_c-1} m_p^j(t).p_{out}(t-lT_c).\left\{C^j(t-lT_c) - \overline{C^j(t-lT_c)}\right\} dt + \frac{R_d P_r I_s}{2} \int_0^{T_s} \sum_{\substack{j=1 \\ i\neq p}}^{M} x_i \sum_{j=1}^{K} h_a \sum_{l=0}^{L_c-1} m_i^j(t).p_{out}(t-lT_c).\left\{C^j(t-lT_c) - \overline{C^j(t-lT_c)}\right\} dt + i_n(t) \quad (9)$$

where $T_s = M.T_b$ and $T_c = T_s/L_c$

The proto-current, $Z_i(t)$ can also be expressed by (10) and (11) as [10, 11]:

$$Z_i(t) = \frac{R_d P_r I_s}{2} \int_0^{T_s} \sum_{j=1}^{K} h_a \sum_{l=0}^{L_c-1} m_p^j(t).p_{out}(t-lT_c).\left\{\frac{1+b^l(t-lT_c)c^l(t-lT_c)}{2}\right\} dt + \frac{R_d P_r I_s}{2} \int_0^{T_s} \sum_{\substack{j=1 \\ i\neq p}}^{M} x_i \sum_{j=1}^{K} h_a \sum_{l=0}^{L_c-1} m_i^j(t).p_{out}(t-lT_c).\left\{\frac{1+b^l(t-lT_c)c^l(t-lT_c)}{2}\right\} dt + i_n(t) \quad (10)$$

$$Z_i(t) = \frac{R_d P_r h_a I_s}{4} \int_0^{T_s} \sum_{j=1}^{K} \sum_{l=0}^{L_c-1} m_p^j(t).p_{out}(t-lT_c).\left\{\frac{1+b^l(t-lT_c)c^l(t-lT_c)}{2}\right\} dt + \frac{R_d P_r x_i h_a I_s}{2} \int_0^{T_s} \sum_{\substack{j=1 \\ i\neq p}}^{M} \sum_{j=1}^{K} \sum_{l=0}^{L_c-1} m_i^j(t).p_{out}(t-lT_c).\left\{\frac{1+b^l(t-lT_c)c^l(t-lT_c)}{2}\right\} dt + i_n(t) \quad (11)$$

The simplified form of (11) is given below [10, 11]:

$$Z_i(t) = \frac{R_d P_r h_a I_s}{4} \int_0^{T_s} \sum_{l=0}^{L_c-1} \left\{p_{out}^k(t-lT_c)c^l(t-lT_c).dt\right\} + \frac{R_d P_r h_a I_s}{4} \int_0^{T_s} \sum_{l=0}^{L_c-1} \left\{p_{out}^i(t-lT_c)b^i(t-lT_c)\left|c^l(t-lT_c)\right|^2 dt\right\} + \frac{R_d P_r h_a I_s}{2} \int_0^{T_s} \sum_{j=1}^{K} \sum_{l=0}^{L_c-1} p_{out}^k(t-lT_c)\left\{b^k(t-lT_c)c^k(t-lT_c).c^l(t-lT_c).dt\right\} + \frac{R_d P_r x_i h_a I_s}{4} \int_0^{T_s} \sum_{j=1}^{K} \sum_{l=0}^{L_c-1} \left\{p_{out}^m(t-lT_c)c^i(t-lT_c).dt\right\} + \frac{R_d P_r x_i h_a I_s}{4} \int_0^{T_s} \sum_{\substack{i=0 \\ i\neq p}}^{M} \sum_{j=1}^{K} \sum_{l=0}^{L_c-1} \left\{p_{out}^i(t-lT_c)b^i(t-lT_c)\left|c^l(t-lT_c)\right|^2 dt\right\} + i_n(t) \quad (12)$$

For a given value of $h_a$, the mean value of photo current $Z_i(t)$ can be expressed as:

$$U(I_s.h_p) = \frac{R_d P_r}{4T_s} \int_0^{T_s} \sum_{l=0}^{L_c-1} I_s.h_p(t).p_{out}(t-lT_c)dt \quad (13)$$

$$\text{And, } \overline{U^2(h_a)} = \int_0^{\infty} U^2(I_s, h_p) p(I_s) d(I_s) \quad (14)$$

The variance of noise current $i_n(t)$ can be expressed as:

$$\sigma_n^2 = \sigma_{th}^2 + \sigma_{shot}^2 = \frac{4K_bTB}{R_L} + 2eB(I_{sig} + I_x + I_b) \quad (15)$$

where $I_{sig}=R_dI_o$ and $I_b=R_dP_b$, $I_x = R_dP_x$, $P_x = P_r.\sum_{i=1}^{M}\left|x_i^2\right|$,

Boltzmann constant is $K_b$, temperature of the receiver in Kelvin is $T$, bandwidth of the receiver is $B$, receiver load resistance is $R_L$, the background radiation is presented by $P_b$ and $e$ is the electron charge.

The variance of MAI can be expressed by:

$$\sigma_{MAI}^2(I_s) = U^2(I_s, h_a) \quad (16)$$

For a given value of $I_s$, the variance of MAI is given by [11]:

$$\sigma_{MAI}^2(I_s) = U^2(I_s, h_a).\frac{2(K-1)}{3L_c} \quad (17)$$

The variance of MAI in presence of the cross talk parameter [9] $x_i$ can be presented by:

$$\sigma_{MAI/x_i}^2(I_s) = U^2(I_s, h_a).x_i^2.\frac{2(K-1)}{3L_c} \quad (18)$$

The signal to noise plus interference ratio (SNIR) for $h_a$=1.0, is then expressed by:

$$\xi(I_s) = \frac{U^2(I_s)}{\sigma_{th}^2 + \sigma_{shot}^2 + \sigma_{MAI}^2(I_s) + \sigma_{MAI/x_i}^2(I_s)} \quad (19)$$

For a given value of channel coefficient $h_a$, the conditional BER can be presented by:

$$P_b(I_s) = \frac{1}{2} erfc\left[\sqrt{\xi(I_s)} / 2\sqrt{2}\right] \quad (20)$$

The unconditional BER can be presented by:

$$BER = \frac{1}{2} \int_{-\infty}^{\infty} erfc\left[\sqrt{\xi(I_s)} / 2\sqrt{2}\right] p(I_s) d(I_s) \quad (21)$$

## V. Results and Discussions

We evaluate the average BER for a dual photodetector SIK receiver at a bit rate of 1Gbps considering strong AT. Numerical evaluations are carried out in terms of BER for the number of wavelengths, number of simultaneous user, code length and link distances. Finally, power penalties are evaluated for number of wavelengths and link distances. The system parameters used for numerical computations are presented in Table I.

TABLE I
SYSTEM PARAMETERS

| *Parameter* | *Symbol* | *Value* |
|---|---|---|
| Bit rate | $R_b$ | 1 Gbps |
| Bandwidth of the receiver | $B$ | 1 GHz |
| Responsivity | $R_d$ | 0.85 A/W |
| Temperature of the receiver | $T$ | 300 $^0$K |
| Receiver load resistance | $R_L$ | 50 Ω |
| Boltzmann's constant | $K_b$ | 1.38x10$^{-23}$ W/K/Hz |
| Charge of Electron | $e$ | 1.6x10$^{-19}$ C |
| Transmitter effective beam radius | $W_t$ | 20 cm |
| Receiver effective beam spot radius | $W_r$ | 50 cm |
| Aperture radius of detector | $r$ | 20 cm |
| wavelength | $\lambda$ | 1550 nm |
| Link distance | $L$ | 500-4000 m |
| Rytov variance for strong AT | $\sigma_x^2$ | 0.0559-3.8081 |
| Index of refraction structure | $C_n^2$ | 10$^{-14}$ |
| Number of user | $M$ | 1 – 64 |
| Code length | $L_c$ *(Gp)* | 64 –1024 |
| Power penalty measured at a BER | - | 10$^{-9}$ |
| Cross talk current | $I_x$ | 1 nA |
| Background current | $I_b$ | 10 nA |
| Cross talk parameter | $x_i$ | 0.01 |

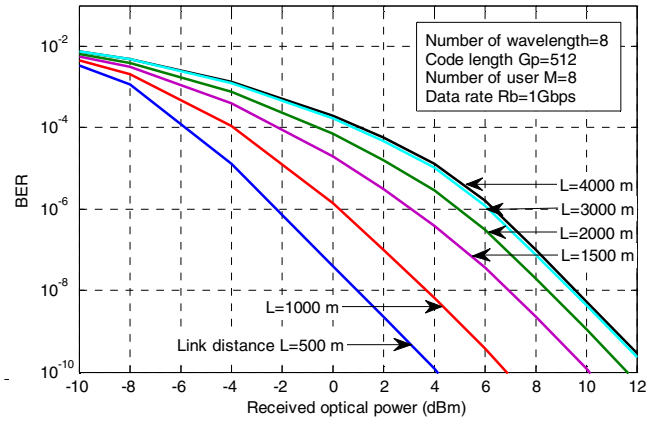


Fig. 2: BER as a function of average received optical power for number of wavelength=8, number of users $M$=8 and code length $Gp$=512 using link distance $L$ as a parameter.

It is noticed from Fig. 2 and Fig. 3 that, the BER performance results improves with the increase of code length from 512 to 1024 but degrades with the increase of link distances from 500 m to 4000 m. The effect of MAI and presence of AT in the channel are the cause of this degradation. Comparison of the figures reveals that, the BER performance results depends on the number of channel, number of simultaneous user and code length.

It is noticed from Fig. 4 that, the BER performance results improves satisfactorily due to the increase of number of wavelengths. The BER performance results are improved significantly since the bandwidth of each of the sub-channels are reduced with the increase of number of wavelength. This result is similar to the multi-carrier CDMA (MC-CDMA) system.

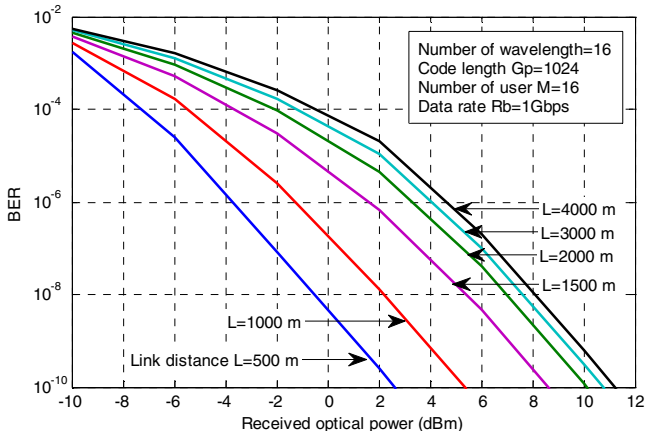


Fig. 3: BER as a function of average received optical power for number of wavelength=16, number of users $M$=16 and code length $Gp$=1024 using link distance $L$ as a parameter.

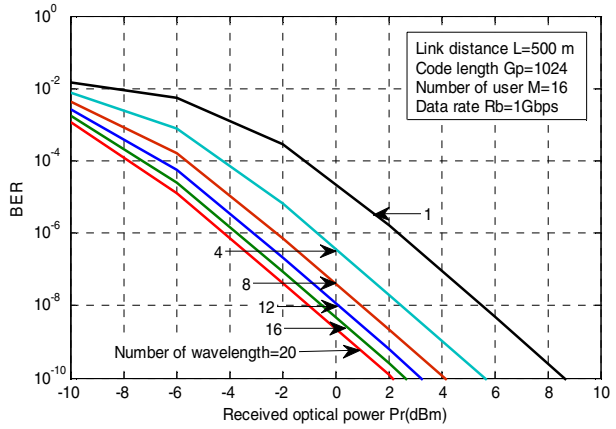


Fig. 4: BER as a function of average received optical power for number of user $M$=16, code length $Gp$=1024 and link distance $L$=500 m using number of wavelength as a parameter.

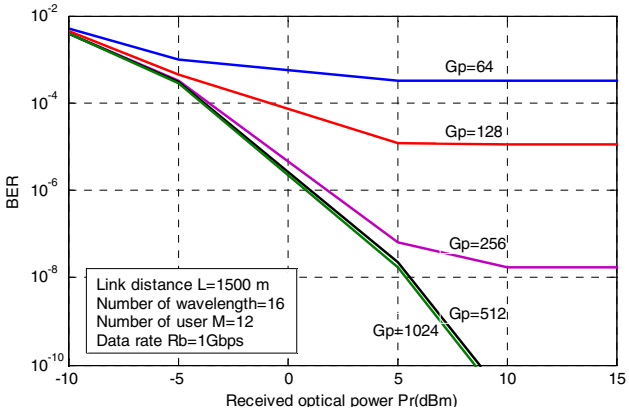


Fig. 5: BER as a function of average received optical power for link distance $L$=1500 m, number of wavelength=16 and number of simultaneous users $M$=12 using code length Gp as a Parameter.

It is found from Fig. 5 that, the BER performance results of the multi-wavelength optical CDMA FSO system predominantly depends on the code lengths (Gp). It is also found from the same Fig that, since the code length increases from 64 to 1024 the BER performance results improves significantly. The flooring of BER starts to occur at a code lengths lower than 256 due to the impact of MAI and cross talk present in the channels. Thus, the performance of a multi-wavelength optical CDMA FSO system can be greatly improved using higher code length.

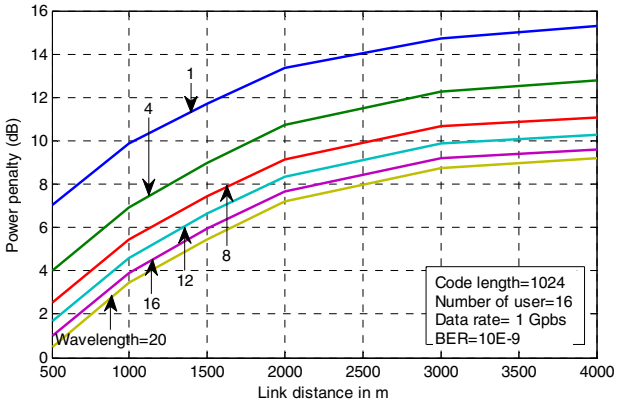


Fig. 6: Power penalty as a function of link distance with number of simultaneous users $M$=16, code length $Gp$=1024 and at a BER=$10^{-9}$ using number of wavelengths as a parameter.

It is noticed from Fig. 6 that, remarkable improvement of power penalty could be achieved by increasing the wavelength even the AT effect increases with the increases of link distances. It is seen from the figure that, the power penalty improves from 14 dB to 8 dB since the number of wavelength increase from 1 to 20 at a link distance 2500 m in presence of pointing error. Similar improvement could be achieved in Fig. 7 even the link distances increases from 500 m to 3000 m in presence of AT. It is also seen from the figure that, the power penalty improves approximately form 8.75 dB to 0.5 dB when wavelength number increases from 1 to 20 once link distance decreases from 3000 m to 500 m.

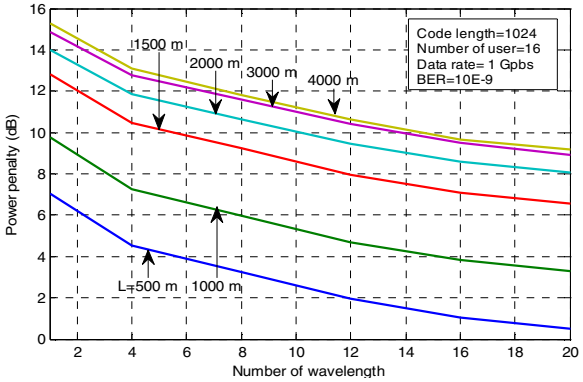


Fig. 7: Power penalty as a function of number of wavelength with number of simultaneous user $M$=16, code length $Gp$=1024 and at a BER=$10^{-9}$ using link distance as a parameter.

Experimental results are reported in [4, 6] for 3-wavelength multi-wavelength optical CDMA system using 511-chip, 640 Gchips/s superstructured fiber Bragg grating (SSFBG) with the central wavelength of 1550.8 nm and repetition rate 10 GHz. In the experiment, maximum number of active user was 16 at a BER of $10^{-9}$ without considering AT. We have numerically evaluated the system performance results using SIK dual photodetector receiver at a bit rate of 1 Gbps, wavelength of 1550 nm for wave number of 1 to 20 using the other system parameters of Table I considering the presence of AT in the channel. The results are very much comparable with the experimental result which validates the analytical approach.

## VI. Conclusions

In this paper, the BER performance results of a multi-wavelength optical CDMA communication system is evaluated analytically under the effect of strong AT using dual photodetector SIK receiver. Results are numerically evaluated at the data rates of 1 Gbps using different system parameters considering strong AT present in the channel. It is noticed that, the system suffers from considerable amount of power penalties due to the effects AT's, link distance and different numbers of user using the channel simultaneously. It is also observed that, these power penalties on BER performance results could be significantly improved using higher code length and also by higher number of wavelengths per user. Thus, the capacity of an optical CDMA system can be largely enhanced by using multi-wavelength optical CDMA system over atmospheric optical channel.

## Acknowledgment

The research work is a part of PhD Dissertation carried out in the EEE department of BUET, Dhaka-1205, and in the EECE department of MIST, Dhaka-1216, Bangladesh.

## References

[1] D.K. Borah and D.G. Voelz, "Pointing Error Effects on Free-Space Optical Communication Links in the Presence of Atmospheric Turbulence," *Journal of Lightwave Technology*, vol. 27, no. 18, pp. 3965-3973, 12 May 2009.

[2] F. Bai, Y. Su and T. Sato, "Performance Analysis of Polarization Modulated Direct Detection Optical CDMA Systems over Turbulent FSO Links Modeled by the Gamma-Gamma Distribution," *Photonics*, vol. 2, no. 1, pp. 139-155, 29 January 2015.

[3] N. T. Dang and A. T. Pham, "Performance improvement of FSO/CDMA systems over dispersive turbulence channel using multi-wavelength PPM signaling," *Optics Express,* vol. 20, no. 24, pp. 26786-26797, 2012.

[4] K. Kitayama, X. Wang and N. Wada, "OCDMA Over WDM PON-Solution Path to Gigabit-Symmetric FTTH," *Journal of Lightwave Technology*, vol. 24, no. 4, pp. 1654-1662, 2006.

[5] X. Wang, N. Wada, T. Hamanaka, T. Miyazaki, G. Cincotti, and K. Kitayama, "OCDMA over WDM transmission," *Transparent Optical Networks Conference (ICTON)*, pp. 110-113, 2007.

[6] N. Ahmed, S. A. Aljunid, A. Fadil, R. B. Ahmad, and M. A. Rashid, "Hybrid OCDMA/WDM system using complementary detection technique for FTTH access networks," *IEEE Symposium on Industrial Electronics and Applications (ISIEA)*, pp. 227-230, 2011.

[7] R. Banos, D. Pastor, V. Garcia-Munoz, and W. Amaya, "Spectral efficiency in WDM-OCDMA Coherent Direct Sequence encoder/decoder devices based on fiber Bragg gratings," *15th International Conference on Transparent Optical Networks (ICTON)*, pp. 1-4, 2013.

[8] R. Vij and N. Sharma, "One bit/s/Hz Spectrally Efficient Transmission for an Eight-Channel NRZ-Modulated DWDM System," *Journal of Optical Communications,* vol. 36, pp.1-7, 2015.

[9] H. Keang-Po and J. M. Kahn, "Methods for crosstalk measurement and reduction in dense WDM systems," *Journal of Lightwave Technology,* vol. 14, pp. 1127-1135, 1996.

[10] A. K. M. N. Islam and S. P. Mjumder, "Effect of Pointing Errror on the BER Performance of an Optical CDMA FSO Link with SIK Receiver," *Journal of Optical Communications,* vol. 36, no. 2, pp. 161-168, July 2016.

[11] A. K. M. N. Islam and S. P. Mjumder, "Effect of Pointing Error on BER Performance of a Multi-wavelength OCDMA FSO System with SIK Dual Dectector Receiver," *Journal of Optical Communications,* Ahead of print, Online published September 2017.

# Analytical Performance Evaluation of a Multiple Subcarrier Modulated FSO Communication System with Coherent Optical Receiver under Strong Atmospheric Turbulence

Bobby Barua* and S. P. Majumder

Department of EEE, Bangladesh University of Engineering and Technology, Dhaka, Bangladesh

*bobby@aust.edu

*Abstract*- **Optical communication through Free-Space termed as FSO system became popular in recent days as a possible alternative to solve the bottleneck of connectivity problem. But atmospheric turbulence induced fading may severely degrade the performances of FSO communication system. We developed an analytical approach here to evaluate the performances of FSO communication system in respect of carrier to noise ratio and bit error rate with RF subcarrier modulation considering the strong atmospheric turbulence effect and the effect is modeled as gamma-gamma distribution. An analytical expression is developed to find carrier to noise ratio (CNR) by considering the turbulence effect at the coherent optical receiver output. Results are analyzed inform of average CNR, BER and power penalty taking into account the turbulence effect for a certain BER for different system parameters like variance of turbulence, link distance, local oscillator power etc. It is found that at a data rate of 10 Gbps with number of subcarrier 4, the power penalty at a BER of $10^{-9}$ is 6dB for a link distance of 3.6 Km.**

*Index Terms*- *Coherent optical receiver, carrier to noise ratio (CNR), free space optical (FSO) communication, gamma-gamma channel model, subcarrier multiplexer.*

## I. INTRODUCTION

Free-space optical communication (FSO) systems have developed to meet the growing demand for high-speed communication systems [1-2]. FSO is suggested as an alternative to the fiber network in recent days. The success of FSO link is completely depends on clear Line Of Sight (LOS) between transmitting and receiving end.

Unfortunately, the propagation of optical wave through free space provides fluctuation in phase and amplitude due to the effect of the atmospheric turbulence [3]. Atmospheric turbulence induced fading produce intensity fluctuation which may degrade the performances of FSO communication system even under clear sky condition.

Significant amount of researches have already been reported in literature to find the atmospheric turbulence effect on the performance on FSO link [5-11]. Most of works are based on computer simulation [5-10]. Even in Ref [6-8] researcher performed their simulation work only for 2 subcarriers where the effects of inter modulation distortion is not considered. In ref [11] analysis for 64 subcarriers is presented considering the effects of inter-modulation distortions (IMD) but the analyses have not considered the effect of link distance, data rate and turbulence variance. Some analytical works are also reported on direct detection optical receiver with limited number of subcarrier [7, 9] and there is no clarification of choosing the detection scheme. Some experimental works are also reported [9-10] to analysis the performance of FSO communication for direct detection scheme. So the development of analytical approach of a RF over FSO communication system is very limited.

We provide an analysis here to find the BER performance of a free space link over strong atmospheric turbulence using ASK RF modulation scheme with coherent optical receiver. RF demodulation is carried out using a synchronous demodulator. Analytical approaches are presented inform of BER and power penalty of the system. Results are evaluated at a data rate of 10 Gbps over link distance of 1 to 3.6 Km for various turbulence variances.

## II. SYSTEM MODEL:

The input data stream is converted to parallel first then the output of the parallel bits are transmitted using N subcarriers. ASK modulator is used to modulate each data channel and the outputs of the modulators are combined using subcarrier multiplexer. The output of the multiplexer is transferred to the optical intensity modulator to produce intensity modulated signal. Now the optically modulated signal is passes through free space. The optical signal is detected by coherent detection system at the receiver and the output current of the photo detector is amplified by preamplifier. The output of the preamplifier is the combined RF signal which is filtered by a RF band pass filter to reduce the effect of the noise due to photo detector and preamplifier. Now the signal output of the RF demodulator mixed with the signal of the local oscillator and demodulated through intermediate frequency (IF) demodulator to get the original data stream at the output.

978-1-5386-3374-8/17/$31.00 ©2017 IEEE

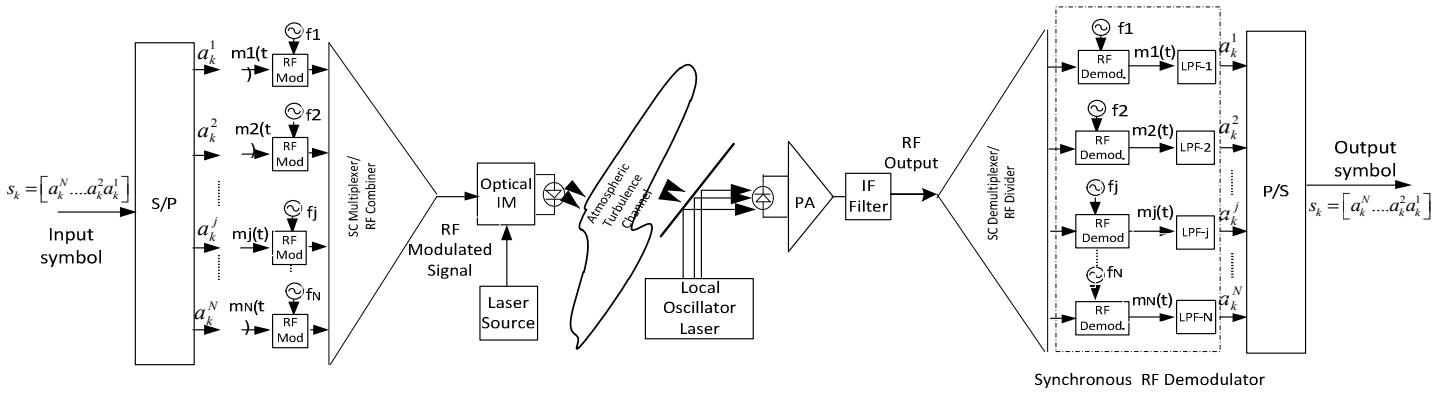


Fig. 1: RF Subcarrier Modulated Optical FSO System with Optical Coherent Receiver followed by RF Synchronous Demodulator.

## III. CHANNEL MODELLING:

To develop a high-performance FSO communication link, it is important to define the channel property properly. Different probability density functions (PDFs) of the channel have been reported in literature to demonstrate the effect of intensity fluctuation. The most reliable channel model for atmospheric turbulence is the Gamma-gamma model. This model can be expressed mathematically and can be characterized by the Rytov variance $\sigma_R^2$ is given by [12],

$$\sigma_R^2 = 1.23 C_n^2 k^{7/6} L^{11/6} \tag{1}$$

$C_n^2$ is the strength of the turbulence, $k = 2\pi/\lambda$ is the optical wave number and propagation distance is represented by L.

The intensity fluctuation PDF for gamma-gamma model is represented by [12]

$$p(I) = \frac{2(\alpha\beta)^{(\alpha+\beta)/2}}{\Gamma(\alpha)\Gamma(\beta)} I^{\frac{(\alpha+\beta)}{2}-1} K_{(\alpha-\beta)}(2\sqrt{\alpha\beta I}), I > 0 \tag{2}$$

I represents the fluctuation of light intensity due to atmospheric turbulence, gamma function is represented by Γ(.) and the modified Bessel function of the second order αβ is given by $K_{(\alpha-\beta)}$ .where α and β are PDF parameters describing the scintillation are given by [12]

$$\alpha = \frac{1}{\exp\left[\frac{0.49\sigma_R^2}{(1+0.18d^2+0.56\sigma_R^{12/5})^{7/6}}\right]-1} \tag{3}$$

$$\beta = \frac{1}{\exp\left[\frac{0.51\sigma_R^2\left(1+0.69\sigma_R^{12/5}\right)^{-5/6}}{(1+0.9d^2+0.62d^2\sigma_R^{12/5})^{5/6}}\right]-1} \tag{4}$$

where $d=(kD^2/4L)^{1/2}$ and the diameter of the receiver collecting lens aperture is given by D.

## IV. THEORETICAL ANALYSIS:

*Let,* $S_k$ represents the *k-th* input data symbol consisting of *N* number of bits ranging from $a_k^1$ *to* $a_k^j$. The symbol is given input to a serial to parallel converter and output parallel bits $\{a_k^j, j=1 : N\}$ are transmitted using N subcarriers. Thus $a_k^j$ is the *j-th* bit of the *k-th* symbol and is used to modulate the *j-th* subcarrier.

Let $m^j(t)$ represents the message at the *j-th* branch of the serial to parallel converter. Then $m^j(t)$ can be given as:

$$m^j(t) = \sum_k a_k^j p(t - kT_s) \tag{5}$$

where $T_s=N\,T_b$, $T_b$ represents the bit period while $T_s$ represents the symbol period.

The output electrical field of the *j-th* subcarrier modulator can be expressed as:

$$e_k^j(t) = \sum_k a_k^j p(t - kT_s) A_j Cos(\omega_j t) \tag{6}$$

where $\omega_j$ is the angular frequency of the *j-th* RF subcarrier and the amplitude of the *j-th* subcarrier is given by $A_j$.

The output of the subcarrier multiplexer (RF combiner) corresponding to *k-th* symbol can be expressed as:

$$\begin{aligned} e_k(t) &= \sum_{j=1}^{N} e_k^j(t) \\ &= \sum_{j=1}^{N} \sum_k a_k^j p(t - kT_s).A_j \cos(\omega_j t) \end{aligned} \tag{7}$$

The multiplexed RF signal is then intensity modulated (IM) with the laser diode output through an electro optic intensity modulator.

The intensity modulated optical carrier output as electric field can be derived as:

$$e_{opt}(t) = \sqrt{2P_T}\left[1 + k_a.e_k(t)\right]e^{j\omega_c t} \tag{8}$$

where the transmitted laser power is represented by $\boldsymbol{P_T}$ and $\boldsymbol{k_a}$ represents the optical modulation index and angular frequency of optical carrier is given by $\boldsymbol{\omega_c}$. The optical signal the is received by the photodetector can be expressed as:

$$r(t) = \sqrt{2P_R.I}\left[1 + k_a e_k(t)\right]e^{j\omega_c t} + n_b(t) \tag{9}$$

where $\boldsymbol{P_R=P_T}\, e^{-\alpha L}$ is the received optical power, α represents the atmospheric channel attenuation coefficient, L is the distance of the optical link, the background radiation is $n_b$ and the turbulence induced fading is represented by I.

The output signal of the optical local oscillator is given by,

$$e_{LO_{opt}} = \sqrt{2P_{LO_{opt}}}\, e^{j\omega_{LO}t} \tag{10}$$

where $P_{LO}$ represents the optical power of the local oscillator and $\omega_{LO}$ represents the angular frequency of the local oscillator.

The output current of the photo detector can be expressed as,

$$\begin{aligned} i_d(t) &= R_d \left| r(t) + e_{LO_{opt}}(t) \right|^2 \\ &= R_d \left| \sqrt{2P_R I}\left[1 + k_a e_k(t)\right] e^{j\omega_c t} + \sqrt{2P_{LO_{opt}}}\, e^{j\omega_{LO}t} \right|^2 \end{aligned} \tag{11}$$

The RF power output of the *j-th* subcarrier is given by,

$$\begin{aligned} C_j(I) &= R_d \left| \frac{\sqrt{2P_R I}\left[1 + k_a A_j \cos\omega_j t\right] e^{j\omega_c t} + \sqrt{2P_{LO_{opt}}}\, e^{j\omega_{LO}t}}{2} \right|^2 \\ &\cong R_d \left| \frac{\sqrt{2P_R I}\left[k_a A_j \cos\omega_j t\right] e^{j\omega_c t} + \sqrt{2P_{LO_{opt}}}\, e^{j\omega_{LO}t}}{2} \right|^2 \end{aligned} \tag{12}$$

If $\omega_{LO}=\omega_j$, then the j-th subcarrier output is given by,

$$\begin{aligned} C_j(I) &= R_d \left| \frac{\sqrt{2P_R I}k_a A_j \cos\omega_j t + \sqrt{2P_{LO_{opt}}}}{2} \right|^2 \\ &= R_d \left( \frac{\sqrt{2P_R I}k_a A_j \cos\omega_j t + \sqrt{2P_{LO_{opt}}}}{2} \right)^2 \\ &= R_d \left( P_R I k_a{}^2 A_j{}^2 \cos^2\omega_j t + P_{LO_{opt}} + 2\sqrt{P_R I}\sqrt{P_{LO_{opt}}}\, k_a A_j \cos\omega_j t \right) \end{aligned} \tag{13}$$

The output power of the band pass filter for j-th subcarrier, ignoring the second order term is given by,

$$P_j(t) = 2R_d \sqrt{P_R I}\sqrt{P_{LO_{opt}}}\, k_a A_j \cos\omega_j t \tag{14}$$

The output signal of the local oscillator is given by,

$$e_{LO} = A_{LO_{RF}} \cos\omega_{LO_{RF}} t = \sqrt{2P_{LO_{RF}}} \cos\omega_{LO_{RF}} t \tag{15}$$

where $P_{LORF}$ represents the power of the local oscillator and $\omega_{LORF}$ is the angular frequency of the local oscillator.

The synchronous RF demodulator output of j-th subcarrier is given by,

$$\begin{aligned} S_j(t) &= 2R_d\sqrt{P_R I}\sqrt{P_{LO_{opt}}}\, k_a A_j \cos\omega_j t \sqrt{2P_{LO_{RF}}} \cos\omega_{LO_{RF}} t \\ &= 2R_d\sqrt{P_R I}\sqrt{P_{LO_{opt}}}\sqrt{2P_{LO_{RF}}}\, k_a A_j \cos\omega_j t \cos\omega_{LO_{RF}} t \\ &= R_d\sqrt{P_R I}\sqrt{P_{LO_{opt}}}\sqrt{2P_{LO_{RF}}}\, k_a A_j \left[\cos\left(\omega_j + \omega_{LO_{RF}}\right) + \cos\left(\omega_j - \omega_{LO_{RF}}\right)\right] \end{aligned} \tag{16}$$

We can filter out the sum terms in equation. Then we have,

$$S_j(t) = R_d \sqrt{P_R I}\sqrt{P_{LO_{opt}}}\sqrt{2P_{LO_{RF}}}\, k_a A_j \cos\left(\omega_j - \omega_{LO_{RF}}\right) \tag{17}$$

If we consider $\omega_{LO}= \omega_j$ , then

$$S_j(t) = R_d \sqrt{P_R I}\sqrt{P_{LO_{opt}}}\sqrt{2P_{LO_{RF}}}\, k_a A_j \tag{18}$$

The total output of the synchronous RF demodulator for N number of subcarrier is given by,

$$\begin{aligned} S(I) &= \sum_{j=1}^{N} S_j(I) \\ &= R_d \sqrt{P_R I}\sqrt{P_{LO_{opt}}}\sqrt{2P_{LO_{RF}}}\, k_a A N \end{aligned} \tag{19}$$

The noise power produced by the band pass filter can be expressed as:

$$\begin{aligned} \sigma_n{}^2 &= \sigma_{sh\_sig}{}^2 + \sigma_{th}{}^2 + \sigma_{sh\_LO}{}^2 \\ &= 2eB[I_s] + \frac{4kT}{R_L}B + 2eB[I_{LO}] \\ &= 2eB[R_d P_0(t) \times k_a . e_{sc}(t) + R_d P_{LO} \times k_a . A_{LO}] + \frac{4kT}{R_L}B \end{aligned} \tag{20}$$

where B is the band width of the band pass filter, the shot noise variance is $\sigma_{sh}^2$, and $\sigma_{th}^2$ is the thermal noise variance.

However, performances of multiple subcarriers modulated (MSM) FSO communication system may be perceptible degraded due to the nonlinearity of laser diode, mixing of subcarriers and inter-modulation distortions (IMD). If we consider that the transmission band is limited to single octave then the second-order IMD (IMD2) can be designed out and the third-order IMD (IMD3) provides the interference between the carriers [11]. So the IMD3 term which falls between the N numbers of subcarriers is given by [11]

$$\sigma_{IMD}^2 = \frac{1}{2}\left(\frac{3}{4}a_3 m_n^3 D_2(N,n) + \frac{3}{2}a_3 m_n^3 D_3(N,n)\right)^2 I \tag{21}$$

where

$$D_2(N,n) = \frac{1}{2}\left\{N - 2 - \frac{1}{2}\left[1 - (-1)^N\right](-1)^n\right\} \tag{22}$$

$$D_3(N,n) = \frac{n}{2}(N-n+1) + \frac{1}{4}\left((N-3)^2 - 5\right) - \frac{1}{8}\left(1 - (-1)^N\right)(-1)^{N+n} \tag{23}$$

Now the CNR with the IMD considering the fading effect introduced by the turbulence can be expressed as

$$CNR(I) = \frac{(R_d\sqrt{P_R I}\sqrt{P_{LO_{opt}}}\sqrt{2P_{LO_{RF}}}\, k_a AN)^2}{2eB[R_d P_r I \times k_a . e_{sc}(t) + R_d P_{LO} \times k_a A_{LO}] + \frac{4kT}{R_L}B + \sigma_{IMD}^2} \tag{24}$$

So, the BER conditioned is given by [10],

$$BER(I) = \frac{1}{2} erfc\left(\frac{\sqrt{CNR(I)}}{2\sqrt{2}}\right) \tag{25}$$

Finally the average BER is given as:

$$BER = \int BER(I).p(I)\,dI \tag{26}$$

*p(I)* represents the PDF of gamma-gamma condition.

## V. Results and Discussion

Following the analysis presented in previous section, we verify the performance results of subcarrier modulated optical free space link. The parameters that are include for computation are given in table below.

**Table1: System Parameters used for computation**

| Parameters | Values |
|---|---|
| Data rate | 10 Gbps |
| Number of the Subcarriers | 1, 2, 4, 8,16,32 and 64 |
| Wavelength of the Laser, λ | 1550nm |
| Responsivity of PIN photodetector, R | 0.85 |
| RF modulation index, k | 0.5 and 1 |
| Link distance, L | 1000 m - 3600 m |
| Subcarrier Power, $P_s$ | 0.5 W and 1 W |
| Optical local oscillator power, $P_{LOOPT}$ | 1 W |
| RF Local Oscillator power, $P_{LORF}$ | 1mW and 5mW |
| Received power | -30 to 30 dBm |
| Subcarrier power | 1.0 watt and 0.5 watt |
| Turbulence strength, $C_n^2$ | $1*10^{-14}m^{-2/3}$and $1*10^{-15}m^{-2/3}$ |

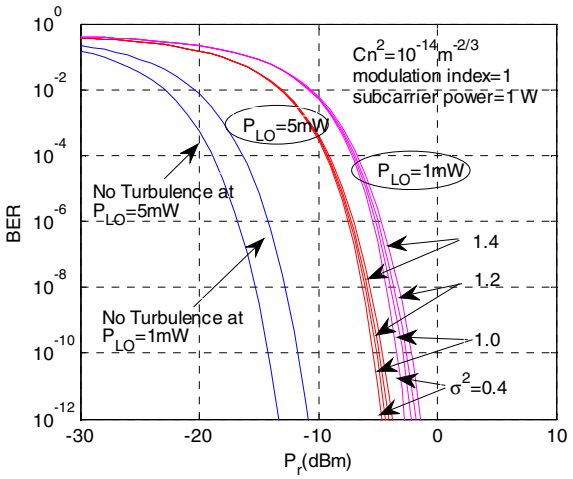


Fig 2: BER performances with respect to the Received optical power with turbulence variance with two different value of local oscillator power.

Fig.2 includes the plots of BER vs. Received optical power with local oscillator power of 1mW and 5mW respectively. From the close analysis of the figure it is clear that the high amount of received power is required to get a desired BER and the BER increases with the atmospheric turbulence level. It is also found that the error performance improves with the increasing the local oscillator power.

The effect of turbulence is depicted in Fig.2 by plotting power penalty as a function on turbulence variance is shown in Fig.3.

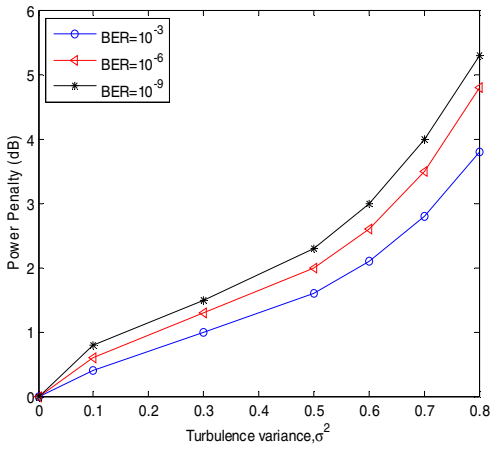


Fig 3: Plots of Power Penalty with respect to the Turbulence variance for different condition of BER with 1mW local oscillator power.

From the close analysis of the figure it is observed that with the variance of the turbulence the power penalty increases irrespective of the BER. It is also noticed for higher BER the power penalty is maximum at same turbulence level. For example, when the turbulence variance is 0.5 the penalty due to turbulence is are ~ 1.8 dB, 2 dB and 2.3 dB at a BER of $10^{-3}$, $10^{-6}$ and $10^{-9}$, respectively.

The link distance, L dependence of the system is illustrated in Fig. 4,. It is noticed that the error performance gradually decreases as L increases from L = 1000m to L = 3600m. It is also noticed that the length increases from 3200m to 3600m shows more critical performance deterioration than in the case where length increases from 1000m to 3200m.

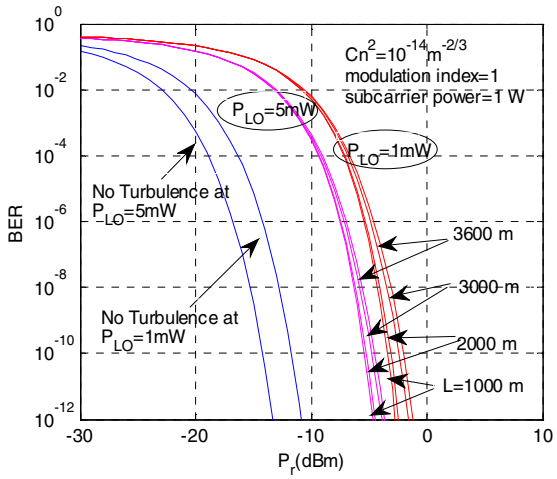


Fig 4: BER performances with respect to the Received power for variable link distance (m) with two different value of local oscillator power.

It is also noticed that if we maintain the similarity in aperture configurations then the BER performances remain unchanged. But increase the power of local oscillator demands lower received power.

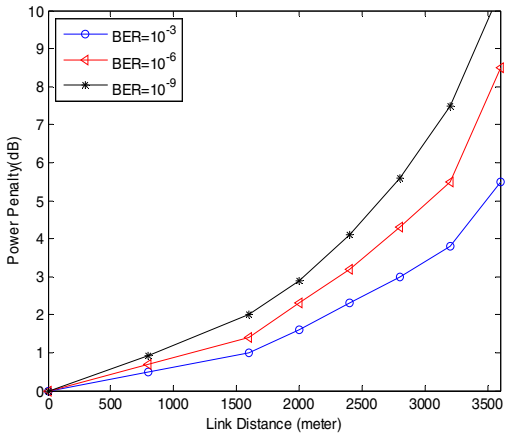


Fig 5: Power Penalty performance of the system with respect to the Link distance under different BER Condition with local oscillator power is 1mW.

The power penalty performances of the system at BER $10^{-3}$, $10^{-6}$ and $10^{-9}$ with respect to the link distance are shown in Fig.5.

Fig. 6 shows the BER performances with respect to the received optical power considering effect of the turbulence strength. Figure demonstrates that the changing effect of turbulence strength is not so impressive on BER performances.

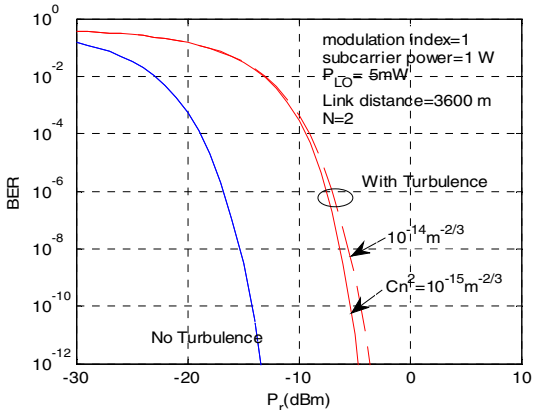


Fig. 6 Plots of BER vs. Received optical power with different Refractive index structure parameter.

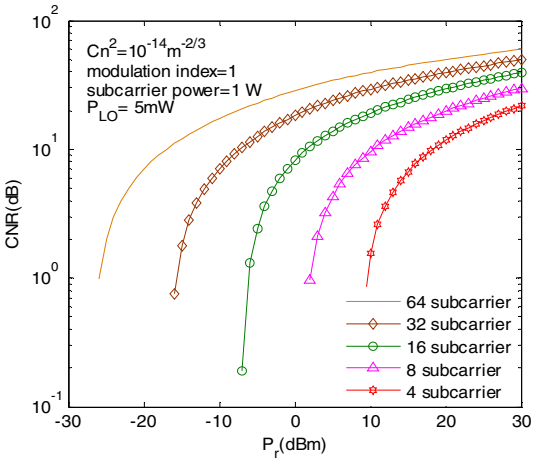


Fig7: CNR performance with respect to the Received power with variable number of subcarriers.

The plots of CNR vs. received power under strong turbulence with variable number of subcarriers are shown in Fig.7. It is noticed that there are improvement in CNR with increasing the number of subcarrier.

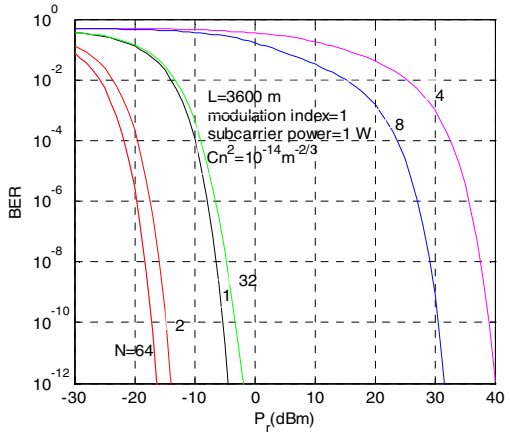


Fig. 8 Plots of BER vs. Received power for variable combinations of subcarriers under turbulent condition.

Fig 8 shows the different combination of subcarriers under turbulent conditions to realize the improvement of the link.

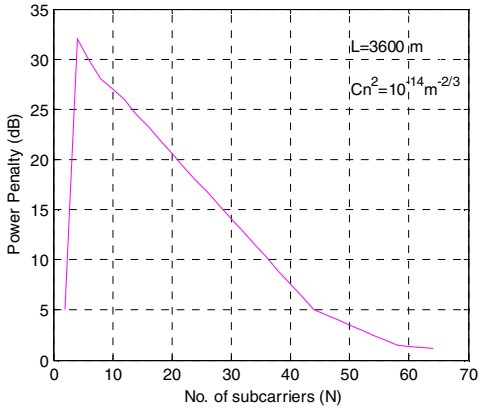


Fig. 9 Plot of power penalty vs. subcarrier number under turbulent condition.

The power penalty vs. different number of subcarriers is included in Fig.9. Figure shows that, due to increasing the number of subcarrier from 4 to further the value of IMD decreases and the overall performance gradually improves.

## VI. Conclusions

We have provided a novel analytical approach for error performance analysis for a FSO link with multiple RF subcarriers considering strong turbulence with gamma-gamma distribution as channel model. In this analysis we use ASK modulation technique for subcarrier modulated FSO communication systems with coherent optical receiver. It is also reported that for unchanged configurations of apertures, the error performance deteriorates as link distance increases and increasing the value of local oscillator power can improve the overall performances. It is found that at a data rate of 10 Gbps with number of subcarrier 4, the power penalty at a BER of $10^{-9}$ is 6dB for the link distance of 3.6 Km.

## Acknowledgements

This work is carried out as a part of Ph.D dissertation in the Dept. of EEE, BUET. The authors would like to acknowledge with gratitude the support provides the Dept. of EEE, BUET.

## References

[1] V. W. S. Chan, "Free-space optical communications," J. Light wave Tech., vol. 24, no. 12, pp. 4750–4762, 2006.

[2] H. Henniger, O. Wilfert," An Introduction to Free-Space Optical Communications'" Journal of Radio Engineering vol. 19, no. 2, June 2010.

[3] Barua, Bobby, and S. P. Majumder. "Performance analysis of a LDPC coded multiple input/multiple output free-space optical system with Q-ary pulse-position modulation", International Conference on Electrical & Computer Engineering (ICECE 2010), 2010.

[4] E. Lee, Z. Ghassemlooy, W. P. Ng, and M. A. Khalighi, "Joint optimization of a partially coherent Gaussian beam for free-space optical communication over turbulent channels with pointing errors," *Optics Letters*, vol. 38, no. 3, pp. 350–352, Feb. 2013.

[5] Belmonte and J. M. Kahn, "Performance of synchronous optical receivers using atmospheric compensation techniques," *Optics Express*, vol. 16, no. 18, pp. 14151–14162, Sept. 2008.

[6] B.T. Vu, N.T. Dang, T.C. Thang, and A.T. Pham, "Bit error rate analysis of rectangular QAM/FSO systems using an APD receiver over atmospheric turbulence channels". *IEEE/OSA Journal of Optical Communications and Networking* 2013; 5(5): 437–448.

[7] W. O. Popoola, Z. Ghassemlooy, J. I. H. Allen, E. Leitgeb, and S. Gao, "Free-space optical communication employing subcarrier modulation and spatial diversity in atmospheric turbulence channel" *Optoelectronics, IET,* vol. 2, pp. 16 - 23, February 2008.

[8] W. G. Alheadary, K. H. Park and M. S. Alouini, "Performance analysis of subcarrier intensity modulation using rectangular QAM over Malaga turbulence channels with integer and non-integer" Journal of Wirel. Commun. Mob. Comput. (2016)

[9] J. Libich, M. Kmanec, S. Zvanovec, P. Pesek, W. O. Popoola, and Z. Ghassemlooy, "Experimental verification of all – optical dual-hop 10 Gbit/s free-space optics link under turbulence regimes" *Optics Letters,* 40(3) (2015).

[10] H. Samimi,; P. Azmi, Performance analysis of adaptive subcarrier intensity-modulated free-space optical systems. IET Optoelectron. 2011, 5, 168–174.

[11] X. Tang, S. Rajbhandari; W. O. Popoola, Z. Ghassemlooy, S.S. Muhammad, E. Leitgeb, and G. Kandus, "Performance of BPSK Subcarrier Intensity modulation Free-space optical communications using a Lognormal Atmospheric Turbulence Model" *IEEE Conference* , pp. 17 - 20, July 2010.

[12] M. A. Al-Habash, L. C. Andrews, and R. L. Phillips, "Mathematical model for the irradiance probability density function of a laser beam propagating through turbulent media," Opt. Eng. 40, 1554–1562 (2001).

# BER Performance Analysis of an Optical M-ary PPM over FSO Turbulent Channel with Pointing Error using PIN Receiver

Israt Ara*, Meherunnesa Mira, Subah Fairooz and A.K.M. Nazrul Islam Department of EECE, Military Institute of Science & Technology
Mirpur Cantonment, Dhaka, Bangladesh
*isratmist@gmail.com

***Abstract*—Analytical approach for evaluating the performance of bit error rate (BER) of an optical M-ary Pulse Position Modulation (M-PPM) scheme using a PIN receiver and considering the effect of pointing error through a strong atmospheric turbulent channel is presented. The expression of conditional and unconditional BER is developed over the probability density functions (pdf) of atmospheric turbulence strength and the normalized pointing error. Numerical evaluations were conducted for 10 Gbps data rate considering the effect of normalized pointing error through atmospheric turbulence with PIN receiver for a different M-PPM order. The evaluation showed that significant BER degradation occurs when the effects of pointing error and atmospheric turbulence increases and significant performance improvement is achieved using higher order PPM. It is also noticed that power penalty of the system suffers significantly for both pointing error and atmospheric turbulence.**

***Index Terms*—** *Bit Error Rate, Optical M-PPM, Pointing Error, Gamma-Gamma distribution, Atmospheric turbulence strength, PIN photodiode.*

## I. INTRODUCTION

Free Space Optical (FSO), commonly referred as Wireless Optical Communication (WOC) is a popular way of communications due to its advantages over RF communication providing higher bandwidth, secure transmission, low cost and easy deployment. However, FSO systems are sensitive to fog, cloud, rain, haze, dust, snow, atmospheric turbulence and this causes significant bit errors in the received data. Change in temperature changes the refractive index of the channel hence, changing the atmospheric turbulence which can be classified into weak and strong turbulence [1-3]. The degradation caused by atmospheric turbulence can be analytically evaluated by Log-normal and Gamma-Gamma distribution models on terrestrial FSO links with IM/DD modulation [1, 2] and [4-7]. Pointing error also bears tremendous importance in the performance of a FSO system. BER of the received data will be high if there is pointing error and turbulence; which degrades the entire aim of FSO communication system.

Numerous research works have been done on FSO link for finding BER and pointing error applying intensity modulation and direct detection (IM/DD). But Optical M-PPM is a much more energy efficient modulation format than On-Off Keying or other modulation techniques. The performance of BER of a FSO system using Log-normal and negative exponential distribution with error correction coding and without coding has been evaluated in [8]. The authors in [9-10] have reported atmospheric turbulence effects, timing jitter and pointing error on the bit error rate performance of an optical PPM FSO link using PIN and APD receivers. Investigation in [11-14] shows that for future optical communications, OCDMA (Optical Code Division Multiple Access) along with optical PPM (OPPM) schemes are emerging as more promising communication scheme.

In this paper, an evaluation of the impact of pointing error along with atmospheric turbulence on optical M-PPM FSO system with PIN receiver is conducted analytically. The entire analysis is carried out for finding out the effect of pointing error that strong turbulent channel has on the performance of BER in an optical M-PPM FSO communication system. Power penalty due to several cases of turbulence is determined against pointing errors for a given BER on optical M-PPM FSO communication system.

This paper is arranged as follows: System model, model of atmospheric turbulence and pdf of pointing error are represented in Section II, III and IV respectively. BER performance analysis using PIN photodetector receiver is presented in Section V. At the end, section VI holds the evaluation of BER performance and conclusion is given in section VII.

## II. SYSTEM MODEL

M-OPPM FSO system block diagram with PIN photodiode is presented in Fig. 1 In the transmission end serial to parallel binary data bits are given as input to the M-PPM. The PPM modulated data bits are then transmitted by laser transmitter in channel.

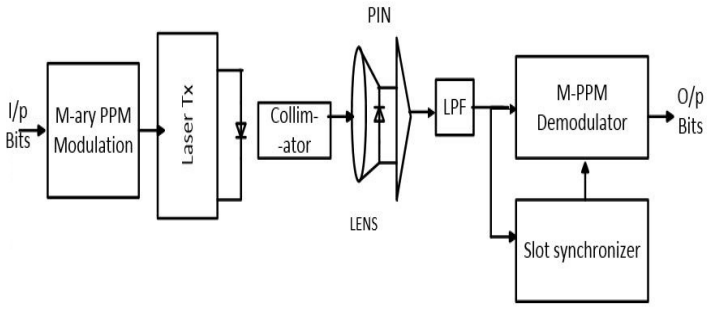


Fig.1. Block diagram of M-PPM FSO system using PIN photodiode

At the receiving end, a PIN receiver is present to receive the modulated optical data beam. An opto-electrical conversion takes place and then data is fed to low pass filter to remove the effects of channel noise. The output obtained is a pulse position modulated data which is passed through a PPM demodulator and as it is required to match the position of the input bits and the output bits, hence a slot synchronizer is used to synchronise the transmitted and received data stream.

978-1-5386-3374-8/17/$31.00 ©2017 IEEE

## III. ATMOSPHERIC TURBULENCE MODEL

Assuming strong turbulent channel, the intensity distribution is given using Gamma-Gamma distribution model by [2]:

$$p(I_s/\rho)=\frac{2(\alpha(\rho)\beta(\rho))^{(\alpha(\rho)+\beta(\rho))/2}}{\bar{\gamma I}(\sqrt{\rho})\Gamma(\alpha(\rho))\Gamma(\beta(\rho))}\times\left(\frac{I_s}{\bar{\gamma I}\sqrt{\rho}}\right)^{(\alpha(\rho)+\beta(\rho))/2-1}\times K_{\alpha(\rho)-\beta(\rho)}\left(2\sqrt{\alpha(\rho)\beta(\rho)I_s/\bar{\gamma I}(\sqrt{\rho})}\right) \quad (1)$$

Here, $\rho$ is a function of fluctuation by which optical field is defined, $\Gamma(.)$ represents Gamma function, $K_{\alpha(\rho)-\beta(\rho)}(.)$ is modified Bessel function of second order $\alpha(\rho)-\beta(\rho)$. $\alpha$ and $\beta$ are connected to atmospheric conditions as follows [16]:

$$\alpha=\left[\exp\left(0.49\sigma_R^2/\left(1+1.11\sigma_R^{12/5}\right)^{7/6}\right)-1\right]^{-1} \quad (2)$$

$$\beta=\left[\exp\left(0.51\sigma_R^2/\left(1+0.69\sigma_R^{12/5}\right)^{5/6}\right)-1\right]^{-1} \quad (3)$$

and $\sigma_R^2$ is Rytov variance and is described as:

$$\sigma_R^2=1.23\left(2\pi/\lambda\right)^{7/6}*C_n^2L^{11/6} \quad (4)$$

here $\lambda$ denotes wavelength, $L$ defines link distance, and the strength of atmospheric turbulence is denoted by the parameter $C_n^2$.

## IV. PDF OF POINTING ERROR

Pointing error takes place when the received optical beam is incident imperfectly on the photodetector. Assuming that $h_p$ is the attenuation occurred by pointing error, pdf of $h_p$ can be represented as [15]:

$$f_{hp}(h_p)=\frac{\gamma^2}{A_0{}^{\gamma^2}}h_p{}^{\gamma^2-1},0\le h_p\le A_0 \quad (5)$$

here $\gamma=\omega_{zeq}/2\sigma_s$ and it defines the ratio among beam radius (equivalent) and standard deviation of pointing error at the receiver side. The parameter $\omega_{zeq}$ can be defined by the equation [15]:

$$v=\frac{\sqrt{\pi}r}{\sqrt{2}\omega_z},\omega_{zeq}^2=\omega_z^2\frac{\sqrt{\pi}erf(v)}{2v\exp(-v^2)},A_0=\left[erf(v)\right]^2$$

here $\omega_z$ is the radius measured from z distance from the transmitter.

## V. SYSTEM ANALYSIS

We consider the effect of atmosphere on the optical signal in terms of $h_{oc}(t)$, which represents the overall impulse response of the atmosphere which also includes the effect of both pointing error and atmospheric turbulence and $h_{oc}(t)$ can be represented as [4]:

$$h_{oc}(t)=h_ah_p \quad (6)$$

here, $h_p$ is pointing error and atmospheric turbulence is represented by $h_a$.

The M-ary optical PPM signal transmitted over the atmospheric channel is given by:

$$S(t)=2P_Te^{j\omega_ct}.a_k \quad (7)$$

here, $a_k$ is the $k^{th}$ bit which is either 1 or 0, average transmitted optical power is denoted by $P_T$ and angular optical carrier frequency is presented by $\omega_c$. The received signal at n[th] receiver aperture is given by:

$$r_n(t)=R_dS(t)\sum_{m=i}^{M}h_{mn}e^{-\alpha L}+n(t),n=1,.....,N \quad (8)$$

where, $M$ is the number of transmitter and $N$ is the number of receiver photodetector, $\alpha$ represents path loss coefficient, $L$ is the link distance, $R_d$ is detector responsivity, $n(t)$ represent the photodetector shot noise, preamplifier thermal noise and zero mean Gaussian noise with variance $\sigma_n^2$. Parameter $h_{mn}$ is the normalized fading channel coefficient which models the effect of turbulence in the channel from the $m^{th}$ transmit aperture to the $n^{th}$ receive aperture.

The output of the photodetector can be expressed as:

$$i_d(t)=R_d.r_n(t)=2R_dI_s\sum_{m=1}^{M}h_{mn}.a_k+i_n(t) \quad (9)$$

where, $I_s$ is the received optical irradiance with atmospheric turbulence.

Mean value of photo current for a given value of $\rho$, $I_s$ and $h_{oc}$ can be expressed as:

$$R(\rho,I_s,h_{oc})=2R_dI_s(\rho)\sum_{m=1}^{M}[h_{mn}.a_k+i_n(t)] \quad (10)$$

$$R^2(I_s,h_{oc})=\int_0^{\infty}R^2(\rho,I_s,h_{oc})p(\rho)d\rho \quad (11)$$

Here, noise variance, $\sigma_n^2$ where,

$$\sigma_n^2=2eB(R_dI+I_b)+\frac{4k_bT}{R_L}B \quad (12)$$

Here, charge of electron is $e$, responsivity is denoted by $R_d$ and $R_L$ here defines load resistance of receiver, $I_b$ is the background radiation intensity, $\beta$ is receiver bandwidth and $T$ is the temperature of receiver in Kelvin.

Now the signal to noise ratio (SNR) for PPM order $K$ and bit rate $R_b$ is given by:

$$\xi(I_s,h_{oc})=\frac{R^2(I_s,h_{oc})}{\sigma_n^2}\times K\log_2K \quad (13)$$

The conditional BER conditioned on a given value of channel coefficient $h_{oc}$ is then given by:

$$P_b(I_s,h_{oc})=\frac{1}{2}erfc[\sqrt{\xi(I_s,h_{oc})}/2\sqrt{2}] \quad (14)$$

The average bit error rate (BER) for a given $I_s$ is given by:

$$P_b(I_s)=\int P_b(I_s,h_{oc})P(h_{oc})dh_{oc} \quad (15)$$

The unconditional BER is obtained as:

$$BER=\int P_b(I_s)P(I_s)dI_s \quad (16)$$

Finally, the equation for unconditional BER can be written as:

$$BER=\int\int 0.5erfc[\sqrt{\xi(I_s,h_{oc}}/2\sqrt{2}].P(I_s)P(h_{oc})dI_sdh_{oc} \quad (17)$$

## VI. RESULTS

In accordance with the approach shown analytically estimating a bit rate of 10 Gbps and considering the effect of

pointing error in presence of atmospheric turbulence in the channel for different values of MPPM order.

The parameters that were used for this system are given below in Table 1.

TABLE 1

**System parameters**

| Parameter | Symbol | Value |
|---|---|---|
| Data rate | $R_b$ | 10 Gbps |
| Wavelength | $\Lambda$ | 1550 nm |
| Responsivity | $R_d$ | 0.85 A/W |
| Bandwidth of receiver | $B$ | 10 Gbps |
| Temperature of receiver | $T$ | 300 K |
| Load resistance of receiver | $R_l$ | 50 Ω |
| PPM order | $K$ | 2 to 128 |
| Background current | $I_b$ | 10nA |
| Standard BER for power penalty | - | $10^{-10}$ |
| Pointing error | $\sigma_s/r$ | 0.2 to 2.5 |

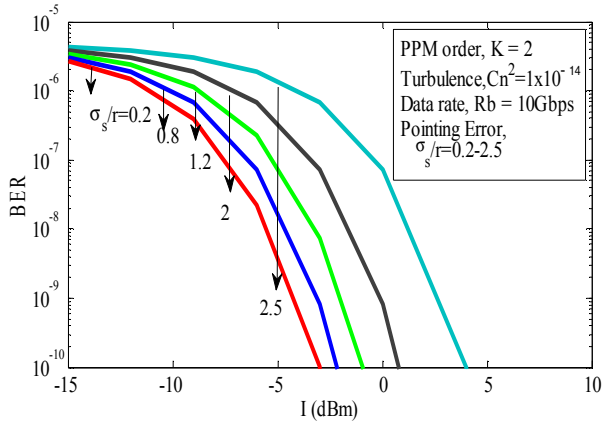


Fig. 2. Plot of BER vs. received optical signal intensity $I$ (dBm) for PIN receiver using pointing error as a parameter at a data rate $R_b$= 10 Gbps when atmospheric turbulence strength, $C_n^2 = 1\text{x}10^{-14}$.

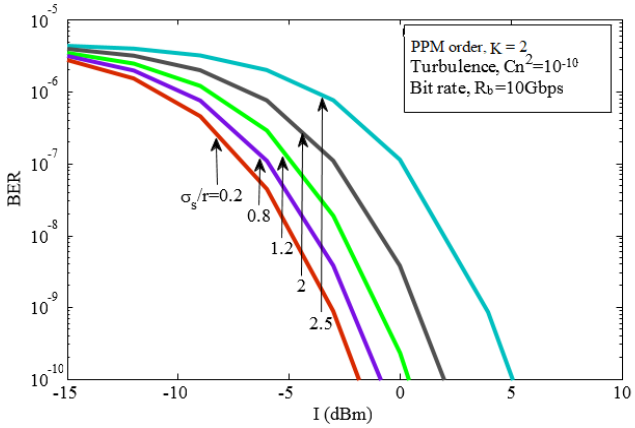


Fig. 3. Plot of BER vs. received optical signal intensity *I (dBm)* for PIN receiver using pointing error as a parameter at a data rate $R_b$= 10 Gbps when atmospheric turbulence strength, $C_n^2 = 1\text{x}10^{-10}\ \text{m}^{-2/3}$

Plot of BER vs. signal intensity $I$ (dBm) are shown in Fig.2 and Fig.3 for pointing error $(\sigma_s/r)$ from 0.2 to 2.5 and data rate 10 Gbps in presence of atmospheric turbulence strength, $C_n^2$ equals to $1\text{x}10^{-14}\ \text{m}^{-2/3}$ and $1\text{x}10^{-10}\ \text{m}^{-2/3}$ respectively. Fig. 2 and Fig. 3 shows that FSO system suffers because of atmospheric turbulence and imperfect normalized pointing error. It is also noticed from the Figures that as the atmospheric turbulence strength increases, BER is also degrades significantly. The results of BER performance improve notably when the normalized pointing error $(\sigma_s/r)$ decreases from 2.5 to 0.2 keeping the other system parameters (turbulence strength, data rate) constant.

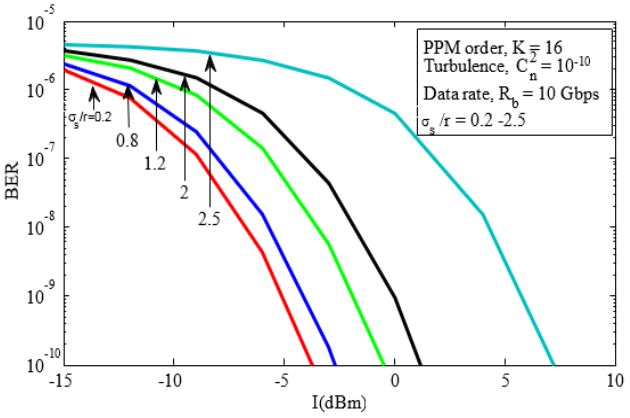


Fig. 4 Plot of BER vs. $I$(dBm) for PIN receiver while PPM order,$K$= 16, atmospheric turbulence,$C_n^2$= $1\text{x}10^{-10}$ at data rate equals to 10 Gbps.

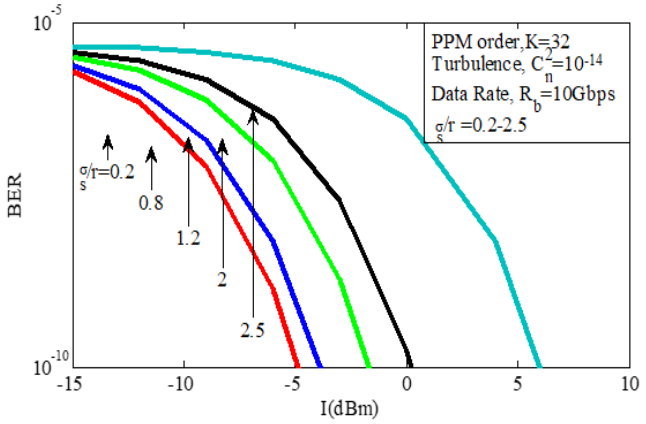


Fig. 5. Plot of BER vs. $I$(dBm) for PIN receiver while PPM order,$K$= 32, atmospheric turbulence,$C_n^2$= $1\text{x}10^{-14}$ at data rate equals to 10 Gbps .

Comparing Fig. 3 and Fig. 4 it is observed that, for the same normalized pointing errors and at $C_n^2$=$1\text{x}10^{-10}$, BER performance improves significantly for low pointing error such as 0.2, 0.8, 1.2, 2 when PPM order was increased from 2 to 16 but degraded for high pointing error of 2.5 which also proves the degrading effect of pointing error on BER performance. Similarly, difference of Fig. 2 and Fig. 5 shows that, if PPM order is increased from 2 to 32, BER performance improves significantly for the same $C_n^2$ value of $10^{-14}$ when pointing error is less and for high pointing error that is $\sigma_s/r$ = 2.5, BER performance degrades. So, it can be concluded that even if FSO communication occurs in atmospheric turbulent channel and pointing error is present, by increasing the PPM order BER performance can be improved.

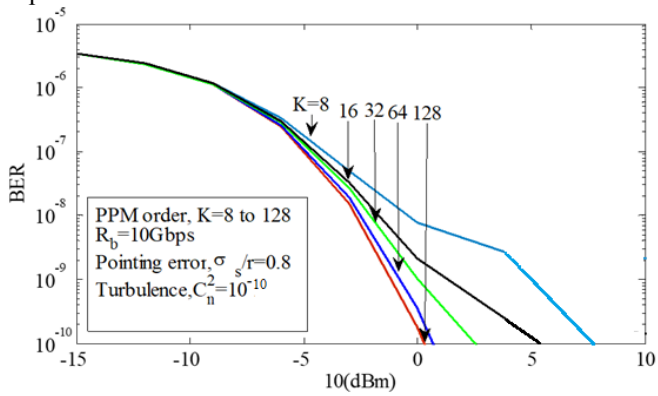


Fig. 6. Plot of BER vs. received optical signal intensity *I (dBm)* for PIN

receiver using PPM order as a parameter varying from 8 to 128 and at a data rate $R_b$ = 10 Gbps when atmospheric turbulence, $C_n^2$ = 1x10$^{-10}$ and at pointing error, $\sigma_s/r$ = 0.8.

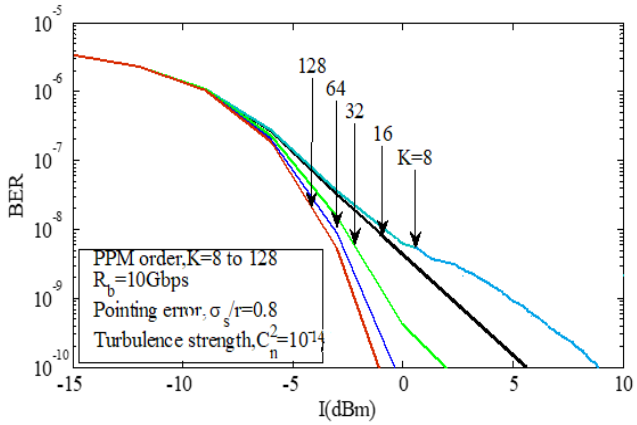


Fig. 7. Plot of BER vs. received optical signal intensity *I (dBm)* for PIN receiver using PPM order as a parameter varying from 8 to 128 and at a data rate $R_b$ = 10 Gbps when atmospheric turbulence, $C_n^2$ = 1x10$^{-14}$ and at pointing error, $\sigma_s/r$ = 0.8.

The plots of BER vs. signal intensity $I$ (dBm) are shown in Fig. 6 and Fig. 7 when the parameter PPM order, $K$ is varied from 8 to 128 for normalized pointing error $\sigma_s/r$=*0.8,* data rate of 10 Gbps in presence of atmospheric turbulence, $C_n^2$ equals to 10$^{-14}$ m$^{-2/3}$ and 10$^{-10}$ m$^{-2/3}$ respectively. It is noticed from Fig. 6 and Fig. 7 that BER increases at a higher atmospheric turbulence, $C_n^2$ and BER performance results significantly improves with the increase of MPPM order from 8 to 128.

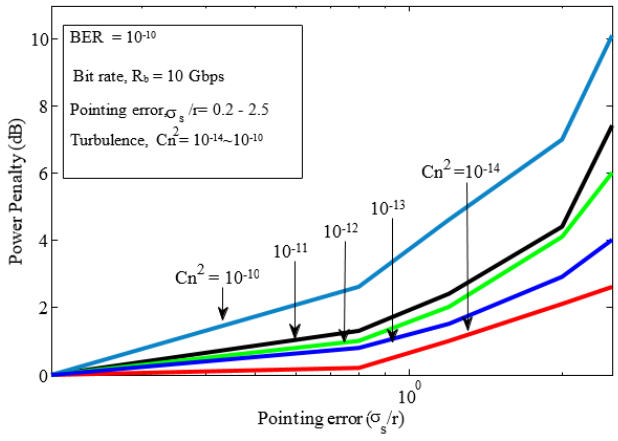


Fig. 8. Plot of power penalty (dB) vs. pointing error($\sigma_s/r$) at BER= 10$^{-10}$, data rate, $R_b$= 10 Gbps as a parameter of atmospheric turbulence strength, $C_n^2$ for PIN receiver.

The plots of power penalty (dB) vs. normalized pointing error $\sigma_s/r$ for atmospheric turbulence strength, $C_n^2$ equals to 1x10$^{-14}$ m$^{-2/3}$, 1x10$^{-13}$ m$^{-2/3}$ ,1x10$^{-12}$ m$^{-2/3}$, 1x10$^{-11}$ m$^{-2/3}$ and 1x10$^{-10}$ m$^{-2/3}$ respectively are shown in Fig.8 at BER equals to 10$^{-10}$, data rate, $R_b$= 10 Gbps as a parameter of for PIN receiver. It can be observed that penalty is significant and higher for stronger atmospheric turbulence and lower for lower atmospheric turbulence strength. So, by decreasing atmospheric turbulence strength ($C_n^2$), power penalty in dB can be decreased for given pointing errors ($\sigma_s/r$). For instance, the power penalty improves from 9.7 dB for $C_n^2$ = 1x10$^{-10}$ to 2 dB for $C_n^2$ =1x10$^{-14}$ at a normalized pointing error 2.5.

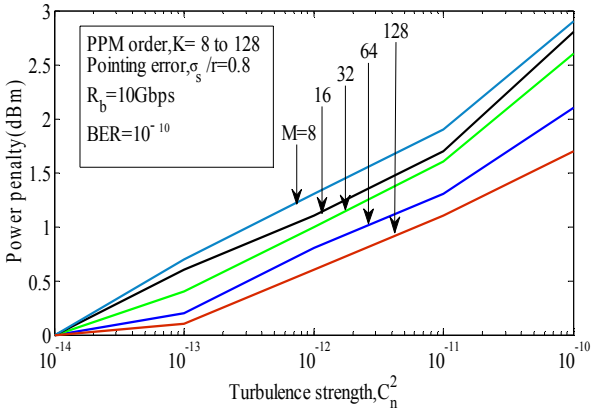


Fig. 9. Plot of power penalty (dB) vs. atmospheric turbulence strength, $C_n^2$ at BER= 10$^{-10}$, data rate, $R_b$= 10 Gbps as a parameter of PPM order, $K$ for PIN receiver.

The plots of power penalty in dB due to atmospheric turbulence, $C_n^2$ at a given BER of 10$^{-10}$ for PPM order of 8, 16, 32, 64 and 128 respectively are shown in Fig. 9 at a data rate of 10 Gbps. It can be noticed that, penalty is significant and is higher for lower order PPM order. Thereby, it can be depicted that, higher order of PPM is required to maintain the same BER performance as well as to reduce atmospheric turbulence and pointing error effects.

From Fig. 9, it is observed that for data rate, $R_b$ = 10 Gbps, pointing error, $\sigma_s/r$=0.8, BER = 10$^{-10}$ Gbps and turbulence strength, $C_n^2$ = 10$^{-10}$ m$^{-2/3}$; when PPM order, $K$=128 power penalty is the lowest and the value is 1.8(dBm) whereas for $K$=8, power penalty is the maximum and the value is 2.8(dBm). As with the increase of PPM order, bandwith requirement also increases drastically, an optimum value of PPM order was chosen for our system which is K=32 for which power penalty is 2.6(dBm).

## VII. CONCLUSIONS

An analytical formulation is presented, providing evaluation of atmospheric turbulence effects, normalized pointing error and MPPM order in the BER performance results on the FSO link using a PIN receiver. It was observed clearly that, significant increase in BER occurred for increasing effect of normalized pointing errors and also of atmospheric turbulence. Power penalty suffered by the system due to pointing error and turbulence could be reduced significantly using higher order MPPM. The analysis can be proved useful and applied in designing a high data rate optical M-PPM FSO communication system using PIN receiver.

## ACKNOWLEDGEMENT

This work was conducted as a part of undergraduate thesis work in EECE department of Military Institute of Science & Technology.

## REFERENCES

[1] D.K Borah and D.G. Voelz,'Pointing error effects on Free-space Optical communication links in the presence of atmospheric turbulence, Lightwave Technology, 27, (18), pp.3967-3973, 12, May 2009.

[2] A.G. Zambrana, B.C. Vazquez, C. C. Vazquez, and R. B. Ruiz, "Bit detect and forward relaying for FSO links using equal gain combinig over gamma-gamma atmospheric turbulence channels with pointing errors",Optical Express,20,(15),pp. 16394-16409, 17, July 2012.

[3] T.A. Tsiftsis, H.G. Sandalidis, G.K. Karagiannisdis and M. Uysal, "BER performance of FSO Links over strong atmospheric turbulence channels

with pointing errors', IEEE Communication Letters, 12,(1), pp.44-46, January 2008.

[4] A. Garcia-Zambrana, B. Castillo- Vazquez, and C. Castillo- Vazquez, "Asympotic error-rate analysis of FSO links using transmit laser selection over gamma-gamma atmospheric turbulence channels with pointing error", Optics express, 20,(3), pp.2096-2109, 30 January 2012.

[5] L. L. Cao, M. Sheng, and X. X. Xie, "BER performance of free-space optical communication in strong turbulence with pointing errors", International Conference on Wireless Communication and Signal processing(WCSP),pp. 1-5, ,25-27 October 2012.

[6] F. Yang, J. Cheng, T. Tshifsts, "Fress-space optical communication with nonzero boresight pointing errors", IEEE Trascations on communications, 62, (2) pp.713-725, February 2014.

[7] W. Gappmair, S. Harnilovic and E. Leitgeb, "Performance of PPM terrestrial FSO links with turbulence and pointing errors", IEEE Communication Letters, 14,(5),pp. 468-470, May 2010.

[8] M.R. Abaza, N.A. Mohammed and M.H. Aly, "BER performance of M-ary PPM free space optical communications with channel fading', IEEE 8th international Symposium on High Capacity Optical Networks and Enabling Technologies, (HONET 2011),Ryadh,saudi Arabia,pp. 111-115, 19-21 December 2011.

[9] A.K.M.N. Islam and S.P.Majumdar, "Effect of timing jitter on the BER performance of a MPPM FSO link over atmospheric turbulence channel", IEEE 8th ICECE 2014, Dhaka, Bangladesh,pp. 409-412,20-22 December 2014.

[10] A.K.M.N Islam and S.P. Majumdar, "Impact of timing jitter on the BER performance of an M-PPM Free Space Optical link in the presence of atmospheric turbulence", IEEE 2nd ICEEICT 2015, Savar, Dhaka, Bangladesh, pp. 1-4, 21-23 May 2015.

[11] T. Ohtsuki, "Performance analysis of atmospheric optical PPM CDMA systems", Journal of Lightwave technology, 21, (2), pp. 406-411, 15 April 2003.

[12] J. Hossen and S.P. Majumdar, "Performance analysis of an atmospheric Optical M-PPM CDMA system with optical orthogonal code and partial modified prime code", Computer Science and Engineering Research Journal,12/2008;5. (Available in ResearchGate. 10 0ct 2014).

[13] H.M.H. Shalaby, "Performance analysis of SAC-OCDMA systems adopting overlapping PPM schemes", Journal of Lightwave Technology, 31(12), pp 1856-1866, June 15, 2013.

[14] X. Zhou, X. Zhamg, R. Zhang, L. Hanzo, 'Chip-interleaved optical code division multiple access relying on a photon-counting iterative successive iterference canceller for free space optical channel', Optics Express, 21, (13), pp. 15926-15937, 1 July 2013.

[15] A.K.M.N. Islam and S.P. Majumdar, "Effect of pointing error on the BER performance of an optical CDMA FSO link with SIK receiver", Journal of Optical Communications, pp-2, July 2016.

[16] A.K. Majumdar, "Advanced Free space optics(FSO) : A system approach", Springer Series in Optical Sciences, 3.35, p. 85, 2015.

2017 IEEE International Conference on Telecommunications and Photonics (ICTP)
26-28 December, 2017, Dhaka, Bangladesh


# Performance Analysis of a Multi-hop Free Space Optical Link over Weak Atmospheric Turbulence Channel for M-Ary PPM Modulated Signal

Mohammad Asaduzzaman[1,*], Mohammad Asif Ibna Mustafa[1], Anika Tasnim Primula[1] and Md. Khorshed Alam[1], S.P. Majumder[2]
[1]Department of EECE, Military Institute of Science and Technology (MIST)
Mirpur-12, Dhaka, Bangladesh
[2]Department of EEE, Bangladesh University of Engineering and Technology (BUET)
Dhaka-1000, Bangladesh
*m.asaduzzaman.29@gmail.com

***Abstract*—In this paper, the performance of multi-hop free-space-optical (FSO) communications systems over atmospheric turbulence fading channel along with pointing error effects is analyzed considering Pulse Position Modulation (PPM). The analysis is done under weak atmospheric turbulence i.e. Lognormally distributed and transmission using multi-hop which is established on amplify-and-forward relays. We illustrate combined probability density function for multi-hop FSO system. The numerically found results show that the multihop transmission along with M-ary PPM is a good solution for obtaining desired Bit Error Rate (BER) under the effects of weak turbulence and pointing error.**

***Index Terms*—Free space optics (FSO), multi-hop relaying, weak turbulence, PPM modulation, pointing error, relay assisted FSO, energy over a PPM bit.**

## I. Introduction

An FSO communication is a system that uses visible or infrared rays to transmit data over a distance, applying the line of sight (LOS) technology. In recent days FSO is frequently used in designing communication channel models due to its significant advantages over radio wave and micro wave like last-mile access, fiber backup etc. [1].

Like any other system using FSO has its pros and cons, atmospheric turbulence effects the system severely and deteriorates its performance. Atmospheric turbulence creates fluctuation of received optical signal specially for link ranges longer than 1 km. Another drawback of using FSO is the effect of pointing error on its performance. To solve the turbulence related problem, as well as to broaden the coverage of the system multihop transmission technique is considered as an effective option [2-4].

The main idea of multi-hop is to relay signal from transmitter or receiver that is from source to destination. Types of relaying that are generally used : decode-and-forward (DF) and amplify-and-forward (AF). DF implies to a technique in which the received signal is demodulated and decoded before it is remodulated and retransmitted at each hop or relay. Whereas AF is the system in which the received signal is amplified before it is retransmitted at each hop, amplification can be done by electrical or optical means.

As FSO is very popular now-a-days, studies related to FSO channel link performances are quite common. Many studies have been made in this field including BER vs. SNR for multi-hop FSO channel [12]. Popular models such as Gamma-Gamma distributions and Log-Normal channel models have been studied for investigating the effects of turbulence [1], [13]. Other papers have investigated the outage probability of a multi-hop FSO communication system in the weak turbulence region and pointing error induced fading [6].

We have analyzed the BER of a multi-hop free space optical link. The type of modulation used here is PPM and pointing error has been taken into account in our analysis. The required receiver sensitivity for different PPM order has been included in our analysis. Maximum allowable transmission distance that is the distance within which we get desired BER has been computed for a particular hop length. We have also calculated the energy over a PPM bit.

## II. System Model

An FSO system consisting of a source terminal (S) with one transmitter aperture for transmitting data to the $1^{st}$ hop), seven hops with one receiver aperture (for receiving the tx data sent from the source or from the $(k-1)^{th}$ hop) and one transmitter aperture (for transmitting signals to the receiver or to the next hop) and one destination node (D) with one receiver aperture (for receiving the tx data by the seventh hop) is assumed. Type of modulation used is OPPM and aforementioned system model is portrayed in Fig. 1. Transmitter consists of an Optical PPM (OPPM) modulator. An FSO system with OPPM modulation direct detection with loss between any two hops or nodes due to atmospheric turbulence and pointing error is assumed between $(k-1)^{th}$ and $k^{th}$ hops. There are N+1 nodes

978-1-5386-3374-8/17/$31.00 ©2017 IEEE

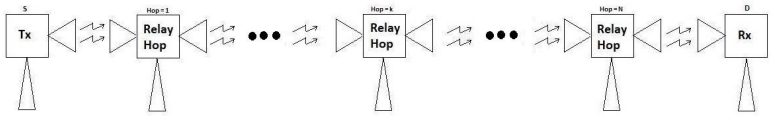


Figure 1: An FSO link with Multiple Hops

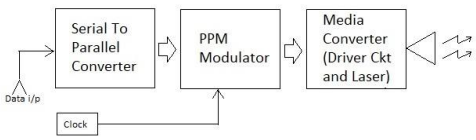


(a) Diagram of a Optical PPM Transmitter

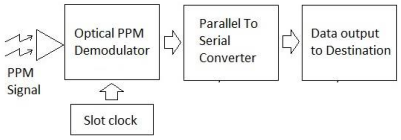


(b) Diagram of a Optical PPM Receiver

Figure 2: Transmitter and Receiver Block

for N hops.

In the source terminal, there is a PPM modulator which consists of a serial to parallel converter followed by a PPM modulator. A laser diode is driven by this OPPM modulator output for media conversion. Then the PPM modulated optical signal is transmitted.

The transmitted optical signal is received by a relay node which amplifies the signal and retransmits to the next relay node. Finally, the optical signal is received by the optical receiver at the destination and demodulation is carried out by optical PIN Photo Diode (PD) and PPM demodulator.

## III. FSO Channel Fading Model

One of the main challenges of FSO channel model is turbulence induced fading (TIF), which occurs due to changes of temperature and pressure. For distance dependent turbulence fading, there are some popular channel models. We have considered pointing error and weak turbulence. Since The property of each of the hops is considered same, the PDF of each hop is considered same.

### A. Atmospheric turbulence-induced fading

Due to variation of refractive index, the optical signal is affected severely due to inhomogeneities the performance of the signal is degraded. We here discuss weak turbulence with popular distribution model of log normal distribution [7].

$$f^a_{h_{k-1,k}}(h^a_{k-1,k}) = \frac{1}{2h^a_{k-1,k}\sqrt{2\pi\sigma_x^2}} exp(-\frac{(ln(h^a_{k-1,k})+2\sigma_x^2)^2}{8\sigma_x^2}) \tag{1}$$

where $\sigma_x^2$ is the turbulence induced variance and can be calculated by [10]:

$$\sigma_x^2 = 1.33k^{7/6}C_n^2(L)z^{11/6} \tag{2}$$

### B. Pointing Error

We consider a model of misalignment fading in which the receiver radial displacement is Rayleigh distributed. The probability density function (PDF) then can be written as [7]:

$$f_{h^p_{k-1,k}}(h^p_{k-1,k})=\frac{\gamma^2}{A_0^{\gamma^2}(h^a_{k-1,k})^{\gamma^2-1}} \tag{3}$$

where $\gamma = w_{zeq}/2\sigma_s$ is the ratio between equivalent beam radius $w_{zeq}$ and pointing error displacement standard deviation $\sigma_s$ at the receiver [7].

$$A_0 = [erf(v)^2] and \qquad w^2_{zeq}=w_z^2\frac{\sqrt{\pi}erf(v)}{2vexp(-v^2)} \tag{4}$$

Here $v = \sqrt{\pi}a/\sqrt{2}w_z$. $w_z$ is the Gaussian beam radius at a distance z and $z = L_{k-1,k}$

### C. Channel Statistical Model

Considering both the PDF of weak turbulence and pointing error we generalize $h_{k-1,k}$ as the channel state (for single hop). where $h_{k-1,k} = h^a_{k-1,k} \times h^p_{k-1,k}$. So the probability distribution function is expressed as [7]:

$$f_{h_{k-1,k}}(h_{k-1,k}) = \int f_{h_{k-1,k}|h^a_{k-1,k}}(h_{k-1,k} \mid h^a_{k-1,k}) \times f^a_{h_{k-1,k}}(h^a_{k-1,k})dh^a_{k-1,k} \tag{5}$$

where $h^a_{k-1,k}$ is turbulence state, $f_{h_{k-1,k}}(h_{k-1,k})$ is the PDFs of parameter and $f^a_{h_{k-1,k}}(h^a_{k-1,k})$ is the PDF of weak atmospheric turbulence and $f_{h_{k-1,k}|h^a_{k-1,k}}(h_{k-1,k} \mid h^a_{k-1,k})$ is the conditional PDF. This is the equation for single hop. Here, $f_{h_{k-1,k}|h^a_{k-1,k}}(h_{k-1,k} \mid h^a_{k-1,k}) = \frac{1}{h^a_{k-1,k}} f^p_{k-1,k}(\frac{h_{k-1,k}}{h^a_{k-1,k}})$

$$= \frac{\gamma^2}{A_0^{\gamma^2}}(h^a_{k-1,k})(\frac{h_{k-1,k}}{h^a_{k-1,k}})^{\gamma^2-1}; 0 \le h \le A_0 h^a_{k-1,k} \tag{6}$$

Substituting Equation (5) and (6) we get,

$$f_{h_{k-1,k}}(h_{k-1,k}) = \frac{\gamma^2}{A_0^{\gamma^2}}(h_{k-1,k})^{\gamma^2-1} \int_{(h_{k-1,k})A_0}^{\infty} f^a_{h_{k-1,k}} (h^a_{k-1,k}) \frac{1}{2h^a_{k-1,k}\sigma_x\sqrt{2\pi\sigma_x^2}} exp(-\frac{(ln(h^a_{k-1,k}) + 2\sigma_x^2)^2}{8\sigma_x^2}) \tag{7}$$

Considering weak turbulence $\sigma_x^2 \leq 0.3$, $f^a_{h_{k-1,k}}(h^a_{k-1,k})$ is Log-Normally Distributed. So, finally from equation (7) we can write,

$$f_{h_{k-1,k}}(h_{k-1,k}) = \frac{\gamma^2}{2A_0^{\gamma^2}}(h_{k-1,k})^{\gamma^2-1} \times erfc(\frac{ln\frac{(h_{k-1,k})}{A_0} + \mu}{\sqrt{8}\sigma_x}) e^{(2\sigma_x^2\gamma^2(1+\gamma^2))} \tag{8}$$

where $\mu = 2\sigma_x^2(1 + 2\gamma^2)$ is the mean. Finally, for calculating overall PDF, we convolute the combined PDF, $f_{h_{k-1,k}}(h_{k-1,k})$, k times for $(k+1)^{th}$, $(1 \leq k+1 \leq N)$ hop as,

$$f_{h_{0,k}}(h_{0,k}) = f_{h_{0,k-1}}(h_{0,k-1}) \circledast f_{h_{0,k-1}}(h_{0,k-1}) \tag{9}$$

where $f_{h_{0,k-1}}(h_{0,k-1})$ can be found as:

$$f_{h_{0,k-1}}(h_{0,k-1}) = f_{h_{0,k-2}}(h_{0,k-2}) \circledast f_{h_{0,k-2}}(h_{0,k-2}) \tag{10}$$

Similarly $f_{h_{0,k-2}}(h_{0,k-2})$ can also be found in aforementioned method of reconvolving upto k times.

## IV. Performance Analysis

### A. Signal To Noise Ratio

For PPM of M order modulation the transmitted signal is [8]:

$$s(t) = \sqrt{2P_t}e^{j\omega_c t} \times a_k \tag{11}$$

where $P_t$ is the transmitted signal power. $\omega_c$ is the carrier frequency of optical signal and $a_k$ is the $k^{th}$ bit. Due to randomness of nature (variation of refractive index) the signal does not remain same while transmitting through $(k-1)^{th}$ hop to $k^{th}$ hop. We here consider Shot noise and Thermal noise both as noise factors. $I_s$ is defined as the output signal of the photocurrent from the photo-diode in the $k^{th}$ node [9].

$$\begin{bmatrix} I_k \end{bmatrix} = \begin{bmatrix} I_k^s \\ I_k^n \end{bmatrix} = \begin{bmatrix} R_d P_r h_{k-1,k} + n_k^s \\ n_k^n \end{bmatrix} \tag{12}$$

where $I_k^s$ is the received signal and $I_k^n$ is denoted as non signal parameter i.e. on time and off time of PPM modulation time slots. The power received by the photo diode is not as same as transmitted power due to atmospheric attenuation. So we calculate SNR as the ratio of signal power to noise power, If the signal power is $I_s^2$ then [9] ,

$$I_s^2 = (R_d P_r h_{k-1,k})^2 \tag{13}$$

where $R_d$ is the receiver sensitivity ; $P_r$ is the received optical power;

The Shot noise is given by [8] :

$$\sigma^2_{shot} = 2qR_d P_r h_{k-1,k}\Delta f \tag{14}$$

where $\Delta f = Be/2$ is the effective electrical Bandwidth; q depicts electron charge ;

And Thermal noise is expressed by [8] :

$$\sigma^2_{thermal} = \frac{8K_B T}{R_L}\Delta f \tag{15}$$

where $K_B$ is Boltzman Constant ; T signifies absolute temperature and $R_L$ denotes load resistor. Combining these two noise from Equation (15) and (16), we get the total noise given by [8] :

$$\sigma_n^2 = \sigma^2_{shot} + \sigma^2_{thermal} \tag{16}$$

So finally we calculate SNR by the expression:

$$SNR(h_{k-1,k}) = \frac{I_s^2}{\sigma_n^2} \tag{17}$$

### B. Energy over a Bit

We assume L number of bits are sent in a word with the Pulse Position Modulation where pulse width $T_b = L/(2^L Br)$ [14]. Here $L = log_2 M$ and Br = Bit Rate. We can now calculate the energy over a PPM bit, $E_b$ by the equation:

$$E_b = P_r \times T_b \tag{18}$$

where $P_r$ is defined as received power and $T_b$ denotes bit period.

### C. Bit Error Rate

So the conditional BER can be calculated [11] :

$$BER_{PPM}(h_{k-1,k}) = \frac{1}{2}erfc(\frac{1}{2\sqrt{2}}\sqrt{SNR(h_{k-1,k})\frac{M}{2}log_2 M}) \tag{19}$$

where PPM modulation order, $M = 2^L$, and L is the number of bits per transmission word and $SNR(h_{k-1,k})$ can be shown as (17):

$$SNR(h_{k-1,k}) = \frac{(R_d P_r h_{k-1,k})^2}{2qR_d P_r h_{k-1,k}\Delta f + \frac{8K_B T}{R_L}\Delta f} \tag{20}$$

So the average BER can be calculated by integrating Equation (19):

$$BER_{PPM} = \int BER_{PPM}(h_{k-1,k}) \times f_{h_{k-1,k}}(h_{k-1,k}) dh_{k-1,k} \tag{21}$$

where $f_{h_{k-1,k}}(.)$ represents the combined PDF for Lognormal distribution and Pointing Error PDF for single hop according to Equation (8).

For multiple hop:

$$BER_{PPM} = \int BER_{PPM}(h_{0,k}) \times f_{h_{0,k}}(h_{0,k}) dh_{0,k} \tag{22}$$

where $f_{h_{0,k}}(h_{0,k})$ is from Equation (9):

$$f_{h_{0,k}}(h_{0,k}) = f_{h_{0,k-1}}(h_{0,k-1}) \circledast f_{h_{0,k-1}}(h_{0,k-1}) \tag{23}$$

## V. Results and Discussion

This section deals with our findings of performance evaluation by numerically computing the aforementioned mathematical models and equations from Section 3 and 4. We have evaluated the bit error rate and some other results derived from these curves using MATLAB. At first, we considered the total transmission distance is fixed to 14 km. Then we assumed a fixed hop distance of 4 km. For both case multi-hop transmission is analyzed. Parameters those we assumed are shown in the Table below:

| Parameters | Values |
|---|---|
| PIN Photodiode Responsivity, $R_d$ | 0.85 A/w |
| Received Power, $P_r$ | -35 dBm to 5 dBm |
| Electron Charge, q | $1.6 \times 10^{-19}$C |
| Frequency Deviation ,$\Delta f$ | 5 GBps |
| Jitter Standard Deviation, $\sigma_s$ | 30cm |
| Beam Radius , $w_z$ | 2.5 m |
| Refractive Index variation, $C_n^2$ | $10^{-13}m^{-2/3}$ |
| PD Load Resistance, $R_L$ | 100 Ω |
| Laser Wavelength , $\lambda$ | 1550nm |
| Total link Distance, L | 14 km |
| Log Normal Variance, $\sigma_x^2$ | $0.1 \leq \sigma_x^2 \leq 0.7$ |

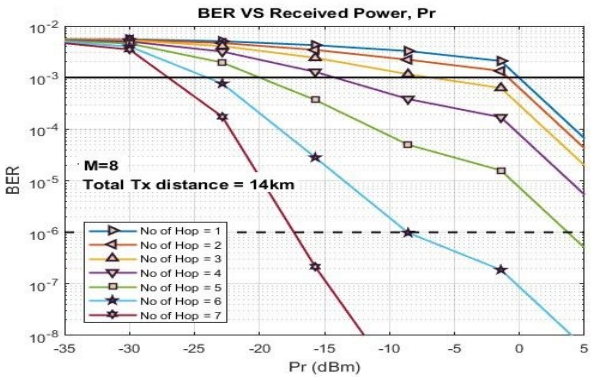


Figure 3: BER vs Rx Optical Power with various no. of Hops

Fig.3 shows the bit error rate (BER) vs Received optical power for various number of hops. It is found that, if the number of hop increases, then the BER decreases (i.e. the BER curve shifts to left) considerably for transmission distance 14 km with PPM modulation order 8. For maximum number of hops the best performance is found in Fig.3.

From this curve, we can derive the required receiver sensitivity for a fixed BER value. We have derived for BER =$10^{-3}$ and also for BER = $10^{-6}$ depicted in Fig.4 and Fig.5.

In Fig.4 and Fig.5 it is found that for lower PPM oder higher receiver sensitivity is required. In case of acquiring BER =$10^{-3}$ considering PPM order 4, required receiver sensitivity 0 dBm, -1 dBm, -5 dBm and -26.57 dBm for single hop,double hop,third hop and seventh hop accordingly.Thus, the required receiver sensitivity for other PPM modulation order can be found from the Fig.4 for BER= $10^{-3}$.Similarly from Fig.5, It

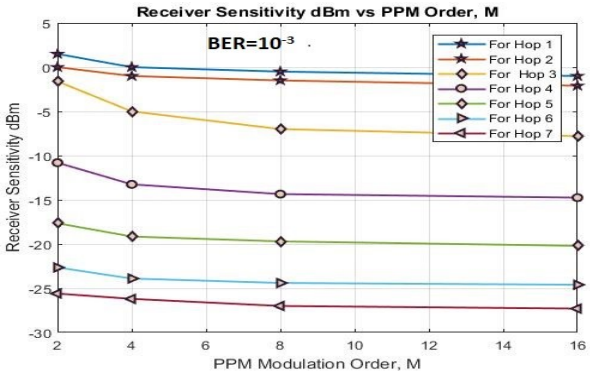


Figure 4: Receiver Sensitivity vs Order of PPM Modulation of BER $10^{-3}$

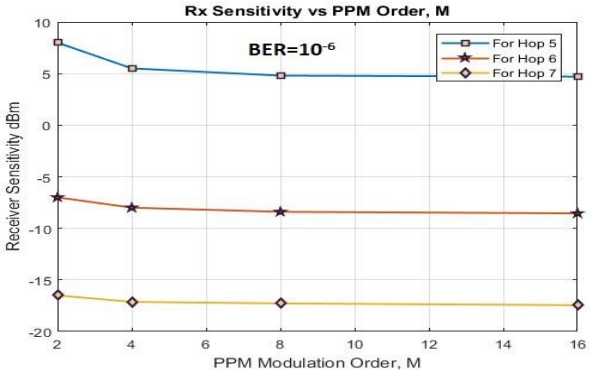


Figure 5: Receiver Sensitivity vs Order of PPM Modulation for BER $10^{-6}$

is found that in order to acquire BER =$10^{-6}$ required receiver sensitivity is 5 dBm, -7.66 dBm and -16.89 dBm for fifth and sixth hop and seventh hop respectively.

We also calculated the energy over a PPM bit which is

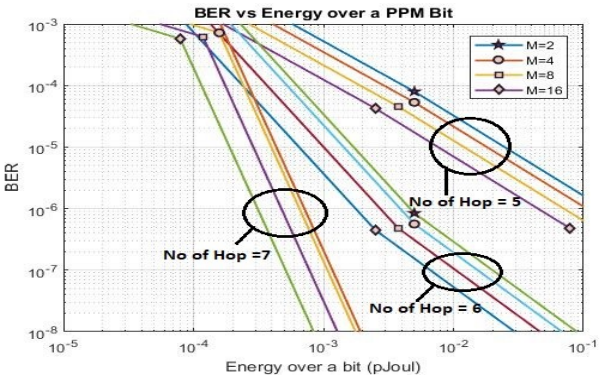


Figure 6: BER vs Energy over a PPM bit

depicted in Fig.6 which shows the plot of BER vs Energy over a PPM bit. It is found that, for any hop with the increase in PPM order BER curve shifts left and BER decreases. It is also shown from Fig.6 that for a lower BER, the required energy over a bit is high.

Now keeping the Hop distance, $d_{k-1,k}$ fixed to 4 km we see

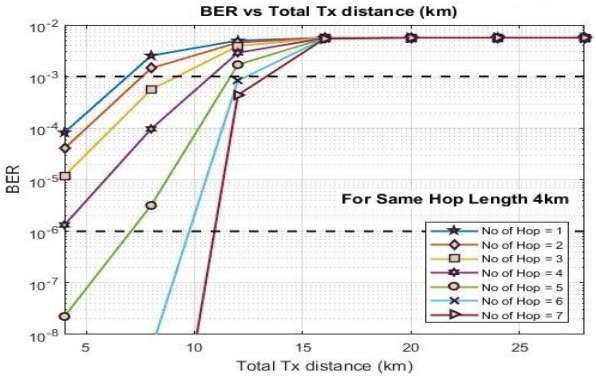


Figure 7: BER vs Total Tx distance (km)

that in Fig.7, the BER increases with the increase in total Tx distance.

From these curves and for a fixed BER = $10^{-3}$ we have derived maximum transmission distance, depicted in Fig.8, and found that with the increase in number of hops the maximum allowable Tx distance can be increased also results for various PPM orders are shown. When no. of hops $n_h$ =4 and PPM order, M=2 for keeping BER= $10^{-3}$ max 14 km can be transmitted. If we increase PPM order 2 to 4,8,16 we can transmit maximum 14.76 km, 15.34 km and 16 km respectively for BER= $10^{-3}$. Thus using seventh hop , we can transmit maximum 20 km for BER= $10^{-3}$ from our derived curves.

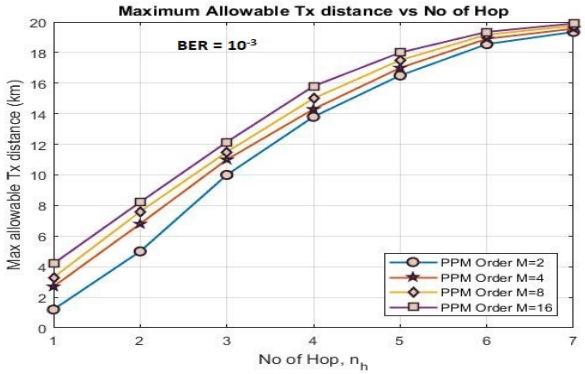


Figure 8: Max allowable Tx distance vs No of Hop for BER = $10^{-3}$

## VI. Conclusion

An analytical approach is presented to find the Bit Error Rate (BER) performance of a multiple-hop FSO link in presence of weak atmospheric turbulence and pointing errors, which is Log Normally distributed. The results show that better performance can be achieved by using more number of hops than no hop considering higher PPM order of modulation. The maximum allowable distance that reported in this paper and also other results can be used for designing multiple-hop FSO link.

## Acknowledgment

The authors would like to acknowledge with gratitude the support provided by the Dept. of EECE, MIST as a part of B.Sc. thesis under the supervision of Dr. S.P. Majumder, Dept of EEE, BUET.

## References

[1] M.Safari and M.Uysal, *"Relay-Assisted Free-Space Optical Communication,"* IEEE Transactions on Wireless Communications,vol.7, no.12. Dec.2008.

[2] H.G.Sandalidis and T.A.Tsiftsis, *"Optical Wireless Communications with Heterodyne Detection Over Turbulence Channels With Pointing Errors,"* Journal of lightwave technology, vol. 27, no. 20, pp. 4440-4445. Oct.2009.

[3] D.K.Borah and D.G.Voelz, *"Pointing Error Effects on Free-Space Optical Communication Links in the Presence of Atmospheric Turbulence,"* Journal of Lightwave Technology,vol.27,no.18, pp.3965-3973. Sep.2009.

[4] Karimi, M., Nasiri-Kenari, M. , *Outage analysis of relay-assisted freespace optical communications,* Communications, IET, vol. 4, no. 12, pp. 1423 - 1432, August, 2012..

[5] Thanh V. Pham, Truong C. Thang and Anh T. Pham, *"Performance Analysis of Multihop FSO System Using APD Receivers Over Log-Normal Channels."*, 9th International Conference on Optical Communications and Networks (ICOCN), 2010.

[6] Yuan Jiao, Jun-Bo Wang, Xiaoyu Dang, Ming Chen, Wen Hu and Yu-Hua Huang, *"Performance Analysis of Multi-Hop Free Space Optical Communications With Pointing Errors."*, 9th International Conference on Optical Communications and Networks (ICOCN). 2010.

[7] A. A. Farid and S. Hranilovic, *"Outage capacity optimization for free space optical links with pointing errors,"*,Journal of Lightwave Technology, 2007, 25(7): .

[8] A. K. M. Nazrul Islam and S. P. Majumder , *"Performance Analysis of an FSO Link in Presence of Pointing Error using Multiple PIN Photodetectors with Equal Gain Combiner"*, 18th International Conference on Computer and Information Technology(ICCIT) 21-23 December,2015.

[9] Ngoc T. Dang , Hien T. T. Pham and Anh T. Pham, *"Average BER Analysis of Multihop FSO Systems over Strong Turbulence and Misalignment Fading Channels"*, 2nd IEEE/CIC International Conference on Communications in China (ICCC): Optical Communication Systems (OCS) 2013.

[10] M. Uysal, J. Li and M. Yu, *"Error rate performance analysis of coded Free-Space Optical links over Gamma-Gamma atmospheric turbulence channels,"*, IEEE Trans. on Wireless Communications, Vol. 5, No. 6, pp. 1229-1233, 2006.

[11] Taissir Y. Elganimi, *"Studying the BER Performance, Power- and Bandwidth- Efficiency for FSO Communication Systems under Various Modulation Schemes,"*, IEEE Jordan Conference on Applied Electrical Engineering and Computing Technologies (AEECT) 2013.

[12] J. Akella M. Yuksel, and S. Kalyanaraman , *"Error Analysis of Multihop free space optical communication,"*, proc. of IEEE international conference on commun, pp. 1777-1781, 2005.

[13] C. K. Datsiks, K. P. Peppas, N. C. Sagias and G. S. Tombras, *"Serial Free- Optical Relaying Communications over Gamma-Gamma Atmospheric Turbulence Channel,"*, J. Opt. Commun. Netw, vol2, no 8, August 2010.

[14] JAMES B. ABSHIRE , *"Performance of OOK and Low-Order PPM Modulations in Optical: Communications When Using APD-Based Receivers,"*, IEEE TRANSACTIONS ON COMMUNICATIONS, VOL. COM-32, NO. 10, OCTOBER 1984.

# Strain Induced Enhancement of Photoluminescence of $Er^{3+}$-$Yb^{3+}$ co-doped $Al_2O_3$ Films

Zhengying Xu, Ningfeng Bai, and Xiaohan Sun*

National Research Center for Optical Sensing/Communications Integrated Networking,
Department of Electronics Engineering, Southeast University, Nanjing 210096, China
*xhsun@seu.edu.cn

***Abstract*—$Er^{3+}$-$Yb^{3+}$ co-doped $Al_2O_3$ thin films were sputtered on $SiO_2$ substrate at 350℃ in argon-oxygen conditions by magnetron sputtering method. Thermal annealing was performed at high temperatures, ranging from 750℃ to 950℃. The films annealed at different temperatures were characterized by Scanning Electron Microscopy, X-ray diffraction, Raman spectra and photoluminescence. The results show the smooth surface morphology of $Er^{3+}$-$Yb^{3+}$ co-doped $Al_2O_3$ thin films fabricated with magnetron sputtering method. With increasing annealing temperature, the as-grown amorphous films became gradually crystallized. Sample annealed at 850℃ is shown to provide the highest photoluminescence intensity, which indicated that the formation of strained Er-O or Yb-O clusters will enhance the photoluminescence intensity.**

***Index Terms*—Magnetron sputtering, $Er^{3+}$-$Yb^{3+}$ co-doped $Al_2O_3$ film, Annealing temperature**

## I. Introduction

Optical devices such as amplifiers, optical couplers, splitters as well as optical detectors are widely used in optical telecommunication system. There is an urged for new material and new fabrication process to achieve devices of cheap price, high efficiency for integrated system [1][2]. Erbium is used as an optically active element in optical devices because of its intra-4f transitions at 1.54um, which involving wavelengths of interest for telecommunications [3][4] However, the $Er^{3+}$ doped materials performance is not very efficient because of its small absorption cross-section, one possible solution is co-doping with $Yb^{3+}$. The $Yb^{3+}$ optical absorption cross-section is much larger than $Er^{3+}$ with about 975nm exciting photons. The $Yb^{3+}$ has also a high efficiency of energy transfer to $Er^{3+}$ [5][6][7][8]. It has been reported very wide range of materials suitable for $Er^{3+}$/$Yb^{3+}$ doping such as polymer and nanocrystals[9]. Among them, $Al_2O_3$ is considering to be an efficient host medium for $Er^{3+}$-$Yb^{3+}$ co-doped waveguide amplifiers for its small absorption in the wavelength region [1] and host of high concentrations of $Er^{3+}$ and $Yb^{3+}$ ions, $Er_2O_3$ and $Yb_2O_3$ is thought to be incorporated in $Al_2O_3$[10]. However, the optical properties of $Er^{3+}$ or $Yb^{3+}$ doped $Al_2O_3$ waveguide is not robust enough for vast device application because of the difficulties in the material fabrication process, i.e., with the magnetron sputtering method the material fabrication suffering from the tricky in gas flow ratios, the influences of annealing temperature and even the working power. The annealing process will enhance or degrade the performance of material in many aspects like crystal size, surface morphology, vacancies. In this work, we report the influences of annealed temperature on the crystal structure of $Er^{3+}$-$Yb^{3+}$ co-doped $Al_2O_3$ thin films sputtered on $SiO_2$ substrate and their influence on the optical properties.

## II. Experimental

The $Er^{3+}$-$Yb^{3+}$ co-doped $Al_2O_3$ film was deposited on a $SiO_2$ substrate by magnetron sputtering of Er/Yb/Al composite target. The atom number ratio of the metallic Er, Yb and Al in the composite target was 0.8:3.2:96, this atomic ratio had been calculated by numerical simulation using Optical System software. Before the deposition, the substrate was ultrasonic cleaned by acetone and isopropanol to remove the surface particle, then it was cleaned with deionized water then used nitrogen gas to dry the it and finally placed it on the holder-plate inside the sputtering chamber. The gas pressure of chamber achieved before deposition was $5x10^{-4}$pa. The temperature of the substrate was stay 350℃. the airflow ratios of oxygen and argon was 15sccm:35sccm, the sputtering was kept for 2.5 hours and the thickness of the deposited films were measured to be about 680 nm.

To study the co-doped film's micro-structure highly related crystallization characteristics and the photoluminescence, the film samples were annealed in $N_2$ ambient at 750℃, 850℃, 950℃ (both elevating and cooling rate is about 5℃/min) for 1h, respectively. SEM measurements were carried out to study the surface morphology of the films and XRD were performed to evaluate the crystallization of the films annealed at different temperature. Raman spectra has been measured to study the vibration mode and local structure of the samples. Photoluminescence (PL) measurement were taken at Suzhou Institute of Nano-Tech and Nano-Bionics. All the above-mentioned measurements were carried out at room temperature.

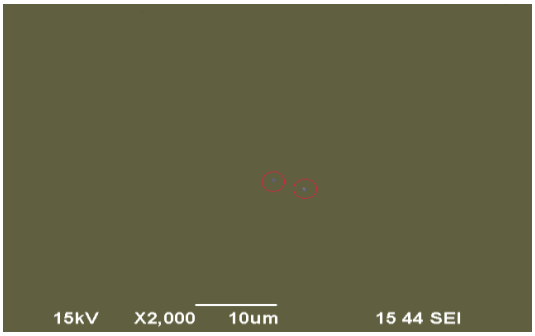


Fig. 1 SEM images of $Er^{3+}$-$Yb^{3+}$ co-doped $Al_2O_3$ film

## III. Results and Discussion

Fig.1 show the SEM images of a typical $Er^{3+}$-$Yb^{3+}$ co-doped $Al_2O_3$ film. The uniform distribution of the image pixels (expect for several 'hot point' indicated with red circles) reveal

the smooth morphology (with the resolution of 10um) of $Er^{3+}$-$Yb^{3+}$ co-doped $Al_2O_3$ thin films fabricated with magnetron sputtering method. Several 'hot point' may be due to the defects on the surface of the $SiO_2$ subtract which can lead to thermal inhomogeneous during the sputtering process.

The XRD patterns of the samples annealed at various temperatures were shown in figure 2, with an indicate the $SiO_2$ subtract data as a reference. It is shown that for annealed temperature of 750℃, there is a small peak located around 35 degrees appeared, which could be indexed as the (1,0,4) peak of $Al_2O_3$ crystal. The very small intensity of the peak and the coexisted of a bump indicated the crystalized phase hosted in a amorphous mother phase. When the annealed temperature increase to 850℃, the intensity of the peak increasing, showing the crystalized process, which increasing annealed temperature. The location of the peak shifted a little to lower angle comparing with XRD database mainly due to the strain in the film. When the annealed temperature goes up to 950℃, this peak moves a little to higher angle indicated the relax of the strain when annealed temperature goes higher.

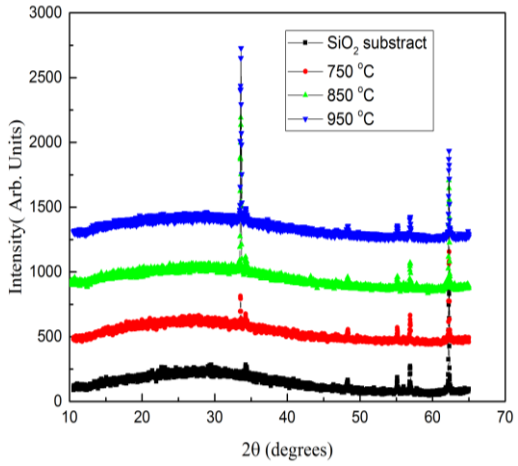


Fig.2 Measured XRD patterns of samples annealed at various temperatures

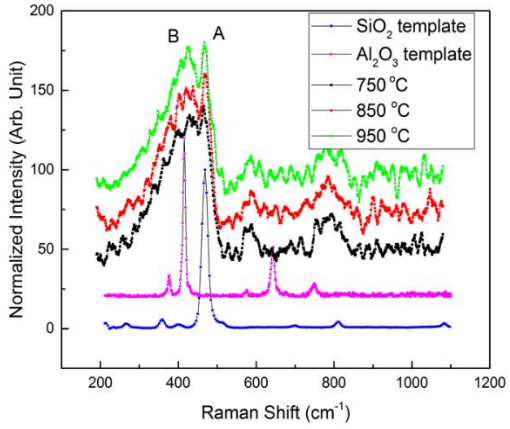


Fig.3 The Raman shifts of the samples annealed at various temperature. The data of crystalized $SiO_2$ and $Al_2O_3$ are also shown in the figure as references.

The Raman spectra of the samples annealed at 750ºC, 850ºC and 950ºC are shown in figure 3. The most intensity peak (A) is assign to the strongest $A_1$ mode of $SiO_2$ and it shows up for all three samples indicate that the vibration mode of the substrates keeps the same with different annealing temperature. The broad peak (B) mainly comes from the $A_{1g}$ mode of $Al_2O_3$ but with large broaden and distortions. This mainly due to the nano-scale of the clusters and the different orientations of nano-crystals. With increasing annealed temperature, the interface of $Al_2O_3$ clusters moves and the samples became crystalized, the number of vibration active mode decrease, which lead to the increase in the peak intensity and decrease in peak width.

The annealing temperature has an important influence on the photoluminescence(PL) performance. Fig.4 shows the PL intensity measurement of the $Er^{3+}$-$Yb^{3+}$ co-doped $Al_2O_3$ films annealed at various temperatures under 980nm laser excitation. Under the excitation at 980nm, both $Er^{3+}$ and $Yb^{3+}$ were excited. Energy transfer process between $Yb^{3+}$ to $Er^{3+}$ occurred due to the $^2F_{5/2} \rightarrow {}^2F_{7/2}$ transition of $Yb^{3+}$ and transfer its energy to $Er^{3+}$ , increase the population on $^4I_{11/2}$. The electrons on the$^4I_{11/2}$ level relax non-radiatively to the $^4I_{13/2}$ level and the $^4I_{13/2} \rightarrow {}^4I_{15/2}$ transition occurs, resulting in the emission at 1530nm[1][6]. The PL intensity peak of all the samples were observed around 1530nm observed can be assigned to the $^4I_{13/2} \rightarrow {}^4I_{15/2}$ transition of $Er^{3+}$ ions.

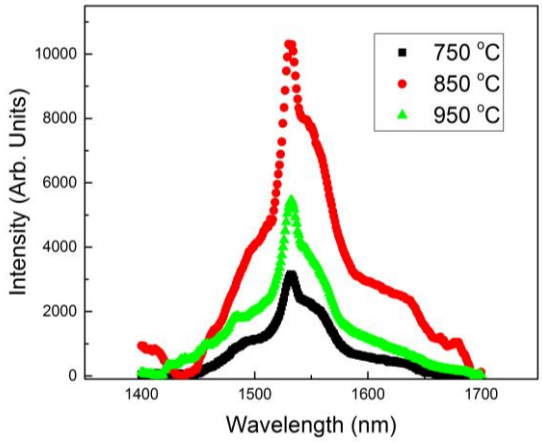


Fig.4 Photoluminescence spectra of Er-Yb co-doped $Al_2O_3$ films annealed at various temperature with the excitation wavelength of 980nm.

The PL intensity increased quickly and reached a maximum value at the annealing temperature 850℃, and then decreased under higher annealing temperatures. One possible reason is when the samples were annealed at 850℃, the strains introduce local distortion of the crystal structure around $Er^{3+}$ or $Yb^{3+}$ ions, which lead to different Er-O or Yb-O bond lengths and angles. Thus, some of the non-radiatively decay channels may be blocked and the lifetime of the PL increase. With further increasing annealing temperature, the strain relaxed, and local distortions disappeared, lead to the decrease of PL intensity.

## IV. Conclusions

We have fabricated $Er^{3+}$-$Yb^{3+}$ co-doped $Al_2O_3$ thin films on $SiO_2$ substrate by magnetron sputtering method. The photoluminescence of the samples annealed at different temperature were studied. The results show that the formation of strained Er-O or Yb-O clusters will enhance the photoluminescence intensity. With proper control of micro-structure of Er-Yb co-doped $Al_2O_3$ thin films, high intensity

and stable PL can be achieved for optical telecommunication system.

## REFERENCES


[1] M.Mahnke; S. Wiechmann, H.J. Heider, "Aluminum Oxide Doped with Erbium, Titanium and Chromium for Active Integrated Optical Applications*" AEU International Journal of Electronics and Communications* No.5,342-348, June 2001

[2] A. Polman;" Erbium implanted thin film photonic materials". *Journal of Applied Physics* 82, 1 July 1997

[3] Pinghua Tang;" Jun Liu," Stable and wavelength-locked Q-switched narrow-linewidth Er: YAG laser at 1645nm", *Optics Express* Vol.23, Issue9, 11037-11042, May 2015

[4] Saurabh Jain; Naresh Kumar;" Cladding-Pumped Er/Yb-coped Multi-Element Fiber Amplifier for Wideband Applications"; *IEEE Photonics Technology Letters*, Volume:27, Issue:4, Feb.15,15, Feb 2015

[5] J. Toudert; S. Nunez-Sanchez; M. Jimenez de Castro; R. Serna; J. Cortes, C.N. Afonso;" Efficient luminescence response from nanoscale controlled Er-Yb distribution in $Al_2O_3$ waveguides" *European Conference on Laser& Electro-optics*, June 2007

[6] Yan Wang, Xingyuan Guo, Shusen Liu, "controllable synthesis of β-NaLuF4:$Yb^{3+}$, $Er^{3+}$ nanocrystals and their application in polymer-based optical waveguide amplifiers", *Journal of Fluorine Chemistry* 175, 125-128 Jul. 2015

[7] Luis.a. Gomez; Leonardo de S. Menezes; Cid B.de Araujo; "Upconversion luminescence in Er3+ doped and Er3+/Yb3+ co-doped zirconia and hafnia nanocrystals excited at 980nm" *Journal of Applied Physics* 107, 113508, Jun. 2010

[8] D.Solis; T. Lopez-Luke; E. De la Rosa;" Surfactant effect on the up-conversion emission and decay time of ZrO2: Yb-Er nanocrystals" *Journal of Luminescence*, Volume 129, Issue 5 449-455, May 2009

[9] G.a. Kumar; M. Pokherl;" Intense visible and near infrared up-conversion in M2O2S: Er (M=Y, Gd, La) phosphor under 1550nm excitation" *Materials Letters*, Volume 68, pages 395-398, Feb 2012

[10] G.N.van den Hoven; R.J.I.M. Koper; A. Polman; "Net optical gain at 1.53um in Er-doped Al2O3 waveguides on silicon" *Applied Physics Letters*68, 1886, Feb. 1996

# Improving Efficiency of Thin Film CdS/CdTe Solar Cells with Layered BSF

Urmi Debnath[1] and Shaikh Asif Mahmood[1,*]

[1]Department of Electrical and Electronics Engineering
Bangladesh University of Engineering and Technology
Dhaka, Bangladesh
[*]asifmahmood@eee.buet.ac.bd

*Abstract*—**Cadmium Telluride (CdTe) thin film solar cells have tremendous potential in renewable energy research for their reduced cost and high efficiency. In this work, a high efficiency CdTe solar cell structure using Zinc Telluride (ZnTe) and Tin Telluride (SnTe) heterojunction as the back surface field (BSF) is investigated. The proposed structure is analysed using AMPS by considering Shockley-Reed-Hall recombination in the defect states. It has been observed that the inserting ZnTe between the SnTe BSF layer and the absorber layer reduces back surface recombination and increases the efficiency of the cell. The highest efficiency is achieved by optimizing the ZnTe thickness. The proposed ultra-thin solar cell also shows better temperature stability under global AM 1.5 condition.**

***Index Terms***—**Thin-film solar cell; Cadmium Telluride; BSF; numerical analysis; AMPS.**

## I. Introduction

Polycrystalline Cadmium Telluride (CdTe) is mainly used as the semiconducting material in photovoltaic technology [1]. It is the second most utilized solar cell material in the world and provides a most promising field of research [2]. CdTe solar cells have low manufacturing cost and high-quality thin films. It has high optical absorbance and its bandgap is near perfect match to the photon distribution in the solar spectrum [3].The Shockley-Queissar limit for CdTe solar cell is about 29%, which is the limiting theoretical efficiency [4]. Recently, First Solar, a leading organization of solar cell manufacturer, has reported record 22.1% efficiency achieved by CdTe solar cell [5].

Conventionally, a CdTe thin film solar cells is generally composed of four layers. The top layer comprises of a transparent conducting oxide (TCO) that acts as a front contact, the window layer is of n-doped Cadmium Sulphide (CdS), a p-CdTe functions as absorber layer below the window layer, and a back contact is at the bottom. Polycrystalline n-CdS with p-CdTe heterojunction gives higher efficiency, as higher bandgap CdS is used as window layer and lower bandgap CdTe is used as absorber layer. The most common back contact material used is Copper (Cu), but the efficiency reduces with time due to Cu diffusion to the front contact.

Performance of ultra-thin CdS/CdTe solar cells can be improved by introducing a back surface field (BSF) layer after absorber layer. Research work has been done using several materials as BSF, such as, Antimony Telluride ($Sb_2Te_3$), Arsenic Telluride ($As_2Te_3$), Copper Telluride ($Cu_2Te$), Zinc Telluride (ZnTe), Lead Telluride (PbTe) and Germanium Telluride (GeTe) [6] - [10]. Among these, ZnTe is the most common BSF material, since CdTe is easily grown over ZnTe by forming superlattice structure [11]. The scope and challenge of CdTe thin film solar cells lies in maximizing the efficiency by reducing the loss mechanisms.

The low open circuit voltage ($V_{oc}$) of CdS/CdTe cells can be improved by increasing carrier density and absorber lifetime of CdTe, and reducing the back-contact barrier height. The carrier recombination loss at the back contact, which is a major impairment in solar cell, degrades the short circuit current density ($J_{sc}$). Adding a stable back surface reflector improves the stability of the solar cell. The BSF may be of low bandgap material, such as, Tin Telluride (SnTe) or of higher bandgap material of low dielectric constant e.g. ZnTe [12]. Thus, the prospect of using both ZnTe and SnTe in BSF must be studied to make the CdTe solar cells more efficient.

A CdS/CdTe solar cell with SnTe BSF hast been taken as reference for this work. The front contact is considered to be Indium Tin Oxide (ITO) and the back contact is Indium (In). The reference cell is modified with a layer of ZnTe above the SnTe layer. The simulation results of the proposed structures is compared with that of the reference cell and analyzed to optimize the thickness of the ZnTe and CdTe layer.

## II. Modeling and Simulation

AMPS (Analysis of Microelectronic and Photonic Structures) software is used for numerical analysis of solar cells in this paper [13]-[14]. The basic equations of semiconductors are solved numerically to get the characteristic graphs of CdS/CdTe solar cells. The Shockley-Reed-Hall recombination has also been considered here.

The reference structure of CdTe solar cell is shown in Fig. 1(a). The analysis considers deep trap to be in the mid-gap energy level. About $10^{14} \sim 10^{16}$ $cm^{-3}$ defect density is used in the calculation [15]. The surface velocity of the carriers is considered as $10^8$ cm/s. The top contact reflectivity of 0.1 and the bottom contact reflectivity of 0.9 are used in the calculation. The capture cross section ($\sigma_e$) for electrons is taken as $10^{-12}$ $cm^2$. In the window layer, $\sigma_e$ is taken as $10^{-15}$ $cm^2$.

The modified structure is shown in Fig. 1(b). Depending on the fabrication and deposition methods, the solar cell paremeters vary even for the same batch in same technology. Table I lists the solar cell parameters used in the numerical

978-1-5386-3374-8/17/$31.00 ©2017 IEEE

simulation, which are selected based on experimental data and literature values [15]-[18].

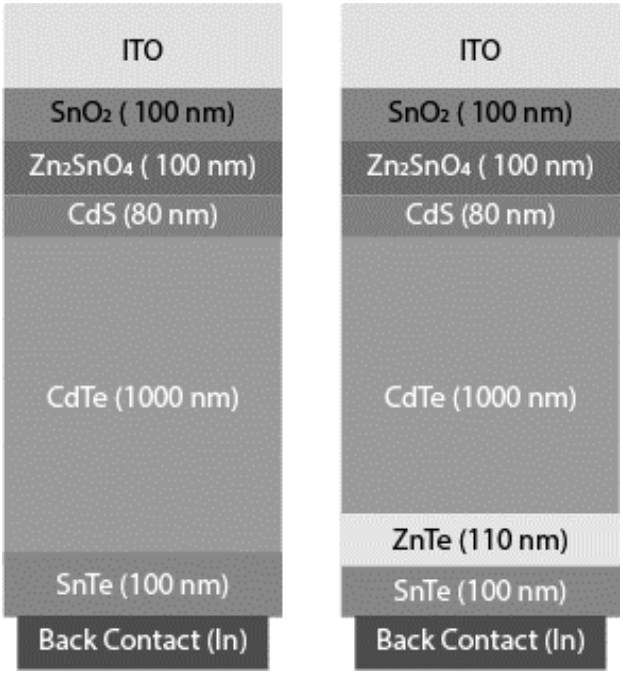


(a) (b)

Fig. 1: Schematic of CdS/CdTe solar cell; (a) Reference structure, (b) Modified structure

TABLE I
THE CELL PARAMETERS USED FOR THE NUMERICAL ANALYSIS

| Parameters | n-CdS | p-CdTe | p-ZnTe | p-SnTe |
|---|---|---|---|---|
| Dielectric constant, $\epsilon/\epsilon_o$ | 9 | 9.4 | 9.67 | 100 |
| Bandgap Energy, $E_g$ (eV) | 2.42 | 1.45 | 2.26 | 0.18 |
| Electron Affinity, $\chi$ (eV) | 4.5 | 4.28 | 3.5 | 5.1 |
| Conduction band effective density of states, $N_c$ ($cm^{-3}$) | $1.8\times10^{19}$ | $7.5\times10^{17}$ | $7\times10^{16}$ | $10^{16}$ |
| Valance band effective density of states, $N_v$ ($cm^{-3}$) | $2.4\times10^{18}$ | $1.8\times10^{18}$ | $2\times10^{19}$ | $10^{17}$ |
| Electron mobility, $\mu_n$($cm^2V^{-1}s^{-1}$) | 350 | 100 | 330 | 500 |
| Hole mobility, $\mu_p$($cm^2V^{-1}s^{-1}$) | 50 | 60 | 80 | 2720 |
| Doping Density, $N_D/N_A$ ($cm^{-3}$) | $1.1\times10^{17}$ | $10^{17}$ | $6\times10^{19}$ | $7.5\times10^{19}$ |

## III. RESULTS AND DISCUSSION

With the purpose of reducing the barrier height at the back contact and possible recombination loss of ultra-thin CdTe solar cell, a high band gap material with low dielectric constant (ZnTe) is placed between the SnTe BSF layer and absorber layer that causes reduction of back surface recombination rate at the CdTe/SnTe interface. This heterojunction bounces back the carriers from the CdTe/SnTe junction and hence increases the carrier flow. Different layers (CdTe, SnTe and ZnTe) have significant lattice mismatch, but they can be grown on top of each other as superlattice [11].

The ZnTe layer thickness is optimized to maximize the efficiency of the proposed structure. The variation of the solar cell efficiency with ZnTe thickness is shown in Fig. 2(a). From the analysis, the optimized thickness of ZnTe is found to be 110 nm.

The effect of inserting ZnTe layer on the thickness of the CdTe (absorber layer) is studied by optimizing the thickness of CdTe layer. The performance of the cell depends on the thickness of the absorber layer. By thinning the CdTe absorber layer, the structure becomes cost effective. But on the other hand, if the CdTe layer is too thin, the cell performance will decrease due to deep level absorption, and back contact recombination [19]. The effect of CdTe thickness on the solar cell efficiency is shown in Fig. 2(b). The optimum thickness of CdTe layer is found to be 1000 nm.

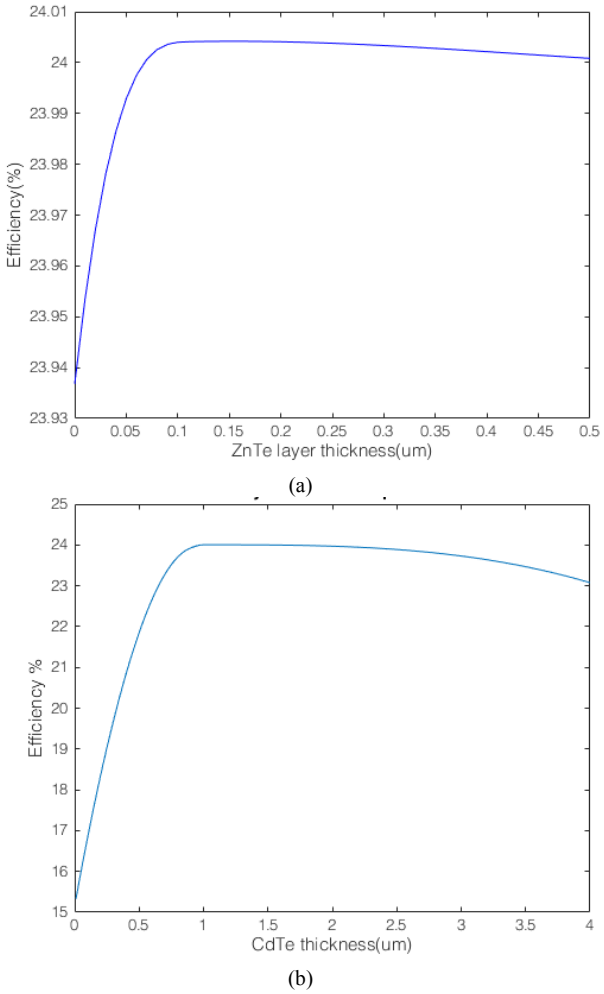


(a)

(b)

Fig. 2: Cell efficiency vs thickness of (a) ZnTe layer; (b) CdTe layer

The J-V and P-V characteristics of the reference cell and the modified cell is shown in Fig. 3. The characteristics of the reference cell closely matches with another work [17]. The reference structure has an efficiency of 18.9%. The modified structure with ZnTe over the SnTe BSF layer shows a

conversion efficiency of 24.03%. Parameters of these two structures are listed in Table II for comparison.

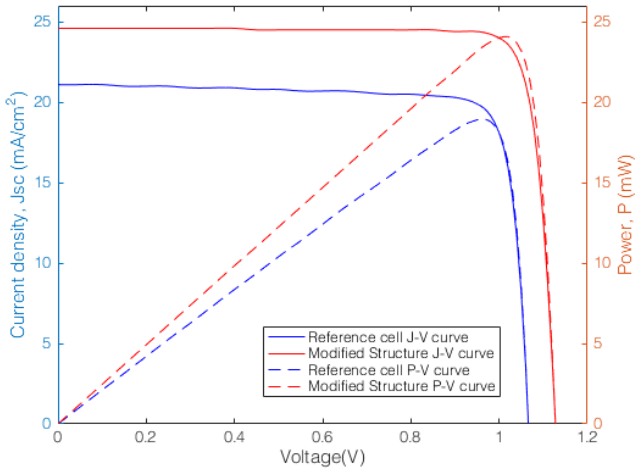


Fig. 3: J-V and P-V curve of the reference and the modified structures

TABLE III
THE OUTPUT PARAMETERS OF REFERENCE STRUCTURE AND MODIFIED STRUCTURE

| | **Reference Structure** | **Modified Structure** |
|---|---|---|
| $J_{SC}$ (mA/cm$^2$) | 21.10 | 24.60 |
| $V_{OC}$ (V) | 1.06 | 1.13 |
| Fill Factor (%) | 84.45 | 86.83 |
| Efficiency (%) | 18.90 | 24.03 |
| Temperature Coefficient (%/$^o$C) | -0.16% | -0.14% |

Figure 4 shows the external quantum efficiency of the modified structure plotted against wavelength. The quantum efficiency is current per unit flux for each band width.The Fig. shows that the spectral response of the modified structure is greater than the reference cell, i.e., it utilizes more of the solar spectrum and converts it into electrical power.

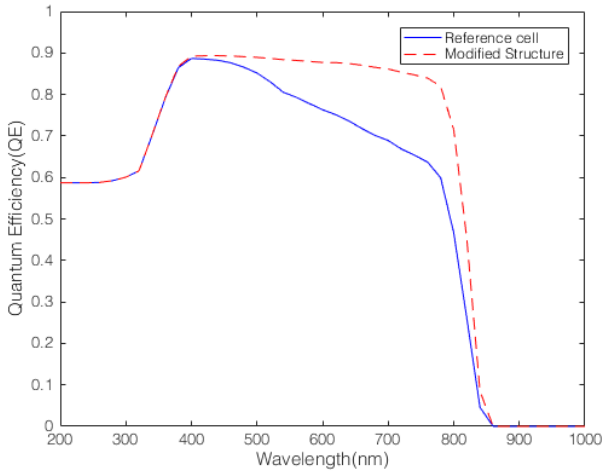


Fig. 4: Quantum efficiency (QE) vs wavelength curve

The normalized efficiency versus temperature curve of the modified structure is shown in Fig. 5. The Fig. compares the temperature stability of the reference and modified cell. The slope of this curve represents the percentage change in the efficiency of cell with temperature. Steeper curve represents less temperature stability. From the Fig., it is evident that inserting ZnTe layer in the reference cell increases the temperature stability.

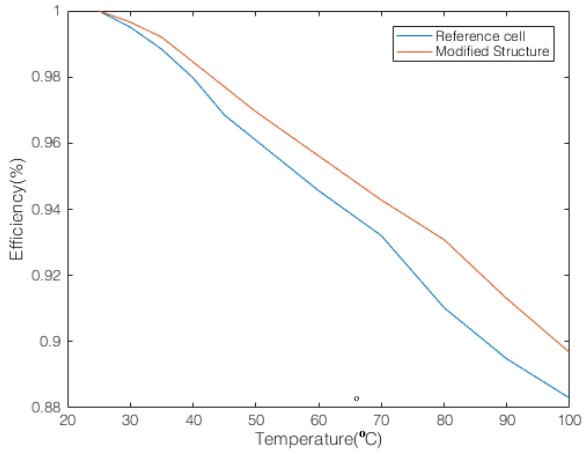


Fig. 5: Normalized Efficiency vs temperature curve

Fig. 6 shows the energy band diagrams of the reference and modified cells. The band diagram indicates that inserting ZnTe between the SnTe BSF layer and absorber layer creates a higher barrier before reaching the back contact. Hence, minority carriers get reflected, which reduces back surface recombination and increases the efficiency of the cell.

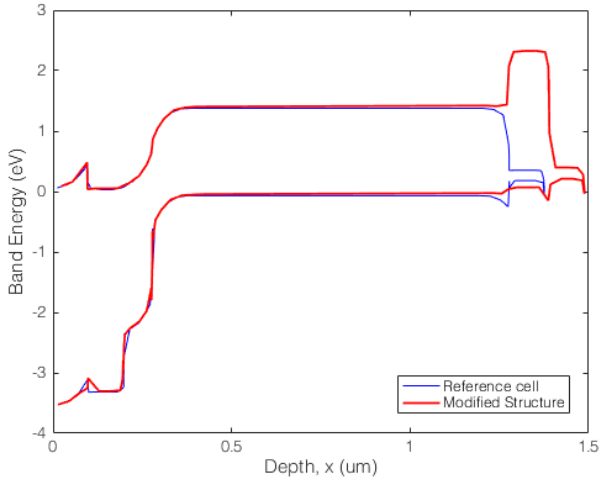


Fig. 6: The band diagram of the reference cell and modified cell.

## IV. CONCLUSIONS

A CdS/CdTe solar cell is modified by adding ZnTe over SnTe as BSF. Comparing with 18.90% efficiency of the reference cell, the proposed structure shows the efficiency of 24.03%. The highest efficiency is achieved with $J_{sc}$ = 24.60 mA/cm$^2$, $V_{oc}$ = 1.13V and fill factor = 86.83%. A lower temperature coefficient of -0.14%/C shows improved temperature stability. Optimization of these solar cell structures open up the possibility of further research to use thinner CdTe absorption layer and ZnTe/SnTe BSF layer for efficiency enhancement.

## ACKNOWLEDGMENT

This work has been supported by the Department of Electrical and Electronic Engineering (EEE), Bangladesh University of Engineering and Technology (BUET), Bangladesh.

## REFERENCES


[1] D.A.Cusano, “CdTe solar cells and photovoltaic heterojunctions in II–VI compounds”, Solid-State Electronics, Volume 6, Issue 3, Pages 217-232, May–June 1963.

[2] Fraunhofer Institute for Solar Energy Systems, "Photovoltaics Report", Freiburg, 2017.

[3] Saha, S., Pal, U., Chaudhuri, A. K., Rao, V. V. & Banerjee, H. D.,“Optical Properties of CdTe Thin Films”, Physica Status Solidi (a), 114, 721-729, 1989.

[4] William Shockley & Hans J. Queisser,“Detailed Balance Limit of efficiency of p‐n Junction Solar Cells”, Journal of Applied Physics, 32, 510-519, 1961.

[5] C. Roselund, "First Solar sets new cadmium telluride thin-film cell efficiency record at 22.1%", pv magazine International, 2017. [Online]. Available: https://www.pv-magazine.com/2016/02/23/first-solar-sets-new-cadmium-telluride-thin-film-cell-efficiency-record-at-22-1_100023341/. [Accessed: 19- Sep- 2017].

[6] D. L. Bätzner, A. Romeo, H. Zogg, A. N. Tiwari and R. Wendt, “Development of efficient and stable back contacts on CdTe/CdS solar cells,” Thin Solid Films, vol. 387, no. 1-2, pp. 151-154, May 2001.

[7] N. Romeo, A. Bosio, S. Mazzamuto, A. Romeo, and L. Vaillant-Roca, “High efficiency CdTe/CdS thin film solar cells with a novel back contact,” in Proceedings of the 22nd European Photovoltaic Solar Energy Conference, pp. 1919–1927, Milan, Italy, 2007.

[8] M. D. S. Hossain, N. Amin, M. A. Matin, M. M. MannirAliyu, T. Razykov, and K. Sopian, “A numerical study on the prospects of high efficiency ultra-thin ZnxCd1-xS/CdTe solar cell,” Chalcogenide Letters, vol. 8, no. 4, pp. 263–272, 2011.

[9] M. A. Matin and Mrinmoy Dey, “High Performance Ultra-Thin CdTe Solar Cell with Lead Telluride BSF,” in Proceedings of the 3rd International Conference on Informatics, Electronics & Vision, pp. 1-5, Dhaka, Bangladesh, May 2014.

[10] Mrinmoy Dey, M. A. Matin, Nipu Kumar Das and MaitryDey, “Germanium Telluride as a BSF material for high efficiency ultra-thin CdTe solar cell,” in Proceedings of the 9th International Forum on Strategic Technology, pp. 334-338, October 2014.

[11] R. H. Miles, T. C. McGillS. Sivananthan, X. Chu, and J. P. Faurie, "Structure of CdTe/ZnTeSuperlattices", Journal of Vacuum Science & Technology B, Nanotechnology and Microelectronics: Materials, Processing, Measurement, and Phenomena 5, 1263, April 1987.

[12] G. Fossum, “Physical operation of back-surface-field silicon solar cells”, ,IEEE Transactions on Electron Devices ,Volume: 24, Issue: 4, 322 – 325,Apr 1977

[13] Liu, Yiming, et al. “A New Simulation Software of Solar Cells -- wxAMPS.” Solar Energy Materials and Solar Cells, vol. 98, 2012, pp. 124–128., doi:10.1016/j.solmat.2011.10.010

[14] S. J. Fonash, “A Manual for AMPS-ID,” The Centre for Nanotechnology Education and Utilization, Pennsylvania State University, PA 16802, 2008.

[15] M. Gloeckler, A. L. Fahrenbruch, and J. R. Sites, “Numerical modeling of CIGS and CdTe solar cells: setting the baseline,” in Proceedings of the 3rd World Conference on Photovoltaic Energy Conversion, vol. 1, pp. 491–494, May 2003.

[16] Khosroabadi, S.; Keshmiri, S. H.; Marjani, S., “Design of a high efficiency CdS/CdTe solar cell with optimized step doping, film thickness, and carrier lifetime of the absorption layer”, Journal of the European Optical Society - Rapid publications, Europe, v. 9, dec. 2014. ISSN 1990-2573..

[17] Dey, M., Dey, M., Matin, M. A., & Amin, N. (2015), “Design of high performance and ultra-thin CdTe solar cells with SnTe BSF from numerical analysis”, 18th International Conference on Computer and Information Technology (ICCIT), 2015.

[18] M. A. Matin, M. M. Aliyu, A. H. Quadery, and N. Amin, “Prospects of novel front and back contacts for high efficiency cadmium telluride thin film solar cells from numerical analysis,” Solar Energy Materials and Solar Cells, vol. 94, no. 9, pp. 1496–1500, 2010

[19] Rucksana Safa Sultana, Ali Newaz Bahar, Md. Asaduzzaman & Kawsar Ahmed,“Numerical modeling of a CdS/CdTe photovoltaic cell based on ZnTe BSF layer with optimum thickness of absorber layer”, Cogent Engineering, 4, 0, 2017.

# Plasmonic Solar Cell with Annular Apertures and Ag Grating Supporting Fabry-Perot Modes

Zubayer Islam, and Md Zahurul Islam*
Department of Electrical and Electronic Engineering
Bangladesh University of Engineering and Technology, Dhaka-1205, Bangladesh
* mdzahurulislam@eee.buet.ac.bd

*Abstract*— **In this paper, we propound a solar cell structure that can enhance the absorption in the active layer as compared to the contemporary nano-structured solar cells reported in the literature. We propose a novel multi-layered structure in which a thin film Si semiconductor is sandwiched in between a top layer of annular apertures which support Fabry-Perot Modes and a bottom layer of Ag gratings that increase the active path length. Finite-Difference-Time-Domain simulation method has been performed for the proposed structure to evaluate the generation rate, short-circuit current and open-circuit voltage. The performance parameter values show significant improvement over those of the the conventional thin film solar cells.**

***Index Terms***— **Plasmonic solar cell, Ag grating, annular apertures, Frequency Selective Surfaces.**

## I. Introduction

In today's world the shift to renewable sources of energy is an utter necessity and in this regard photovoltaics or the conversion of light to electricity is a major achievement. The commercially available solar cells trap light within their structures and increase the optical path length through reflection in order that maximum light can be absorbed [1-3]. This requires large scale geomotries. The main drawback of these geometries are that the greater surface area results in recombination of the minority carriers. Moreover, intuitively, there is larger production cost.

Plasmonics or the interaction of light with metal nanoparticles is the way out in this regard. These offer us with a viable solution to reduce the physical thickness without compromising with the optical thickness. These structures [4] with a much thinner absorber layer will exactly absorb the same amount of light compared to a typical thicker solar cell. Over a past years different types of structures have been proposed. First of all, metal nanoparticles have been placed on top of conventional solar cells to increase light absorption. Silver gratings have been placed below the structure to couple more light through reflection. Furthermore, tandem geometries have be made by placing semiconductors with different bandgaps over one another [5]. Each layer couples light waves of different frequency bands. Also notable is quantum-dot solar cells [6] in which light is confined in the plane of silver and ultrathin dot layers. Quantum dots can also be electrically excited to generate plasmons [7]. Also available are examples of nanoscale antennas of coaxial holes drilled in a metal film, which show localized plasmonic modes due to Fabry-Perot resonances [8-10]. A surprising field enhancement of about 50 are reported in structures where semiconductors are poured inside the plasmonic cavity.

In general, light confinement, and hence enhancement of electric field due to the use of plasmonic nanostructures in the active layer of any type of solar cell is beneficial [11]. In this paper, we have simulated the performances of a solar cell structure that can support Fabry-Perot resonances.

## II. Proposed Cell Structure

Fig. 1 shows the proposed solar cell structure as simulated in Lumerical. The annular apertures are important in the sense that they help in active light trapping. At some particular frequencies the annular rings absorbs all of the incident light and for other frequencies, the absorption rate is still very high. Only at a particular narrow-band range, the annular rings are transparent [8]. To add to this exciting effect, we incorporated Ag grating underneath so that if light escaping at any particular frequency can be further reflected back to the active layer.

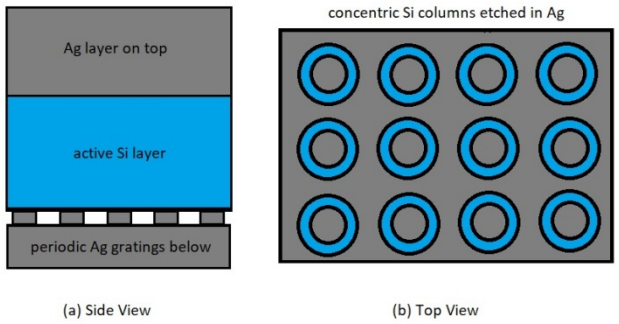


Fig. 1 Schematic representation of the proposed solar cell structure as simulated in Lumerical.

The front view of Fig. 1 shows that the active layer is sandwiched between a top Ag layer and a bottom Ag grating. The top view shows the annular grids that is present in the top Ag layer. The regions marked with blue indicate Si and those with ash indicate Ag. Any structure that can transmit or reflect electromagnetic radiation are called FSS. Generally these are metallic grids on a metal plate which can selectively transmit frequencies. The special feature is that frequencies near visible and infrared domain are transmitted or reflected independent of the incidence angle of light and independent of polarization. The grids or apertures are sub-wavelength in dimension. According to Ref [11], the high transmission and the general shape of the spectra do not rely on surface modes. These are angle independent because the cavity modes it depends on is angle-independent. Often a coupling between surface modes and cavity modes occur. In these cases, the Fabry-Perot spectrum is disturbed. For a particular metal thickness, angleindependent transmission bands are obtained. The absolute transmission in any FSS is more than 0.8. The tolerance on polarization is also excellent. A cavity resonance is the prime cause of these interesting properties. Popov et al.

978-1-5386-3374-8/17/$31.00 ©2017 IEEE

[12] presented the results in the far-infrared or microwave domains. The high transmission is due to nonplasmon resonances for one and two-dimensional gratings (Fabry-Perot, waveguide or cavity resonances). The thoeretical description of the bandpass property in the microwave regoin can be found in the study of A. Roberts et al. [13]. T.K. Wu [14] has shown the filtering properties of thin FSS grids that are designed for applications in the infrared, with circular or square loops patterns. All of these showed stable performances inspite of variations in the illumination angle and polarization. These properties remain secured in the visible region as well, as shown by D. V. Labeke et al. [8].

## III. Numerical Modelling

We simulated the solar cell structure, as shown schematically in Fig. 1, employing FDTD algorithm using the commercially available software Lumerical. For the source we have used AM 1.5G spectrum. We first found out the genration profile in FDTD and then using this result we resimulated the design in DEVICE to obtain other specifications of the proposed cell. In the latter case, we doped the structure as well to obtain a *p-i-n* structure. The *p-i-n* device structure is supposed to be superior to a *p-n* structure in the sense that the middle layer (the intrinsic layer *i*) has high resistivity due to low doping. So only a small reverse bias voltage value is necessary to extend the depletion layer in the *p* region all the way through to the *n* region and thus this structure provides a large sensitive volume or active area. In addition, due to the symmetry of this structure it is possible to reduce the computational domain in the simulation software and we take the full advantage of this opportunity. This leads to lesser computational resource requirement in terms of both computation time and memory volume.

## IV. Result and Discussion

We show different absorption enhancements for different combinations. Fig. 2 shows absorption enhancement, *g*, of a Si solar cell with Ag grating compared to another Si solar cell with no grating. Fig. 3 then displays absorption enhancement of a solar cell with only FP modes on top as compared to a bare Si solar cell. The absorption enhancement of a cell with FP modes as compared to a Si cell with Ag grating below is shown in Fig. 4.

Enhancement of about a factor of a maximum of 44 and an average of 15 is obtained, as can be seen from Fig. 3. Thus we can easily conclude that there has been immense light absorption if we compare with a bare Si cell. Even if we compare our current model to that of a cell with Ag grating below, we still notice from Fig. 4 an enhancement of a maximum of 33 with an average of about 12. These are encouraging results even as compared to plasmonic solar cells with nanoparticles embedded on it.

It can be inferred from the device structure that there are two different types of electromagnetic modes are induced in the cell: propagating surface plasmon modes that are propating along the horizontal metal-dielectric interface and vertical cavity or resonator modes circulating within the annular apertures. The high absorption and the resulting enhancement factor can be assumed to be the result of strong coupling between these two types of electromagnetic modes. Due to the role of the vertical modes, the transmission remains pretty small. For the case of the Ag layer placed on the top of the solar cell structure, we would expect the surface plasmons or Raleigh anomalies to be the cause of the enhanced transmission, which is actually not the case. It is the excitation of the cavity modes inside the apertures in a resonant manner that causes this increased transmission. It is more like a $TE_{11}$ mode with a small attenuation.

The results also confirms that although the width of the air-gap is small, all the cavities are acting like Fabry-Perot resonators. Moreover, the spectral response of the excited modes are independent of their periodicity. However the periodicity has an valuable role of converting the guided modes to the plane waves at the output of the device.

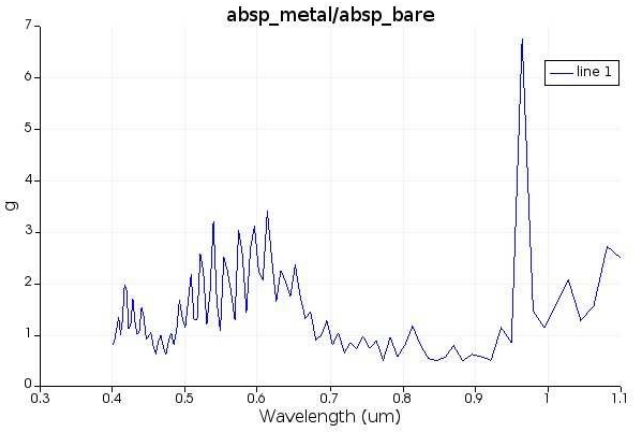


Fig. 2 Absorption enhancement of a Si solar cell with Ag grating compared to a Si solar cell with no grating.

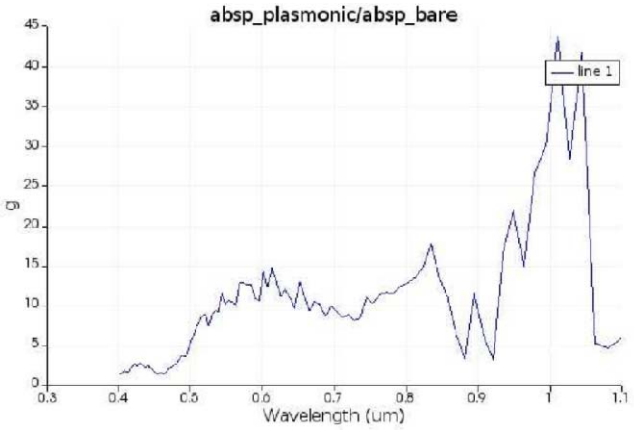


Fig. 3 Absorption enhancement of a solar cell with only FP modes on top as compared to a bare Si solar cell.

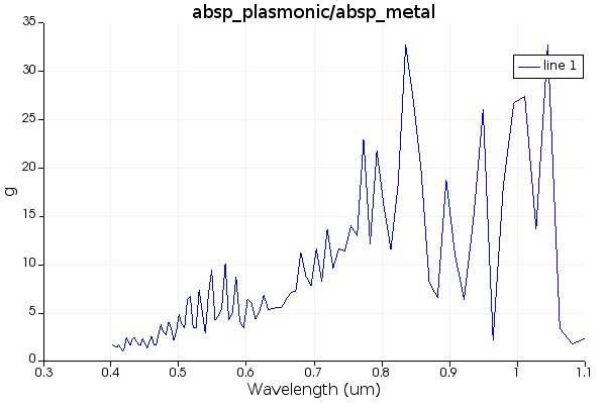


Fig. 4 Absorption enhancement of a cell with FP modes as compared to a Si cell with Ag grating below.

The transmission coefficient can be expressed by a simple analytical model which corresponds to the excitation of a mode in the cavity by the equation [16],

$$t = \frac{t_1 t_2 e^{ikh}}{1 + r_1 r_2 e^{2ikh}} \quad (1)$$

Here, $t$ is the transmission coefficient through the device. This equation is similar to those expressing the transmission through a dielectric slab or a Fabry-Perot resonator. Here, $t_1$ and $t_2$ the transmission coefficients of the two interfaces. Similarly, $r_1$ and $r_2$ are the reflection coefficients of the two interfaces.

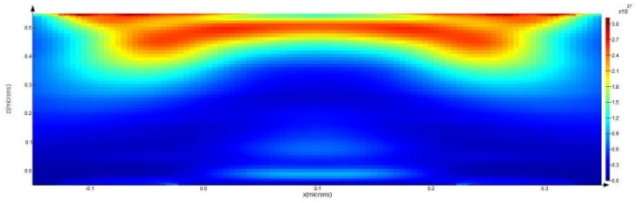

Fig. 5 Generation profile on the surface. Large amount of EHP generations on the upper portion is due to the FP resonance modes in the apertures.

Now we have a look at the generation profile of such a cell. Fig. 5 shows the electron-hole pairs (EHP) generated within the Si solar cell. $x$ and $z$ axes have been shown while $y$ axis is perpendicular to the paper. As can be seen, there are large amount of electron hole pairs generated owing to FP resonance.

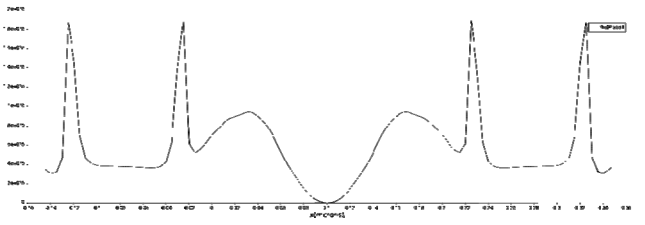

Fig. 6 Generation profile along a horizontal line on the surface. Very high EHP at some points is due to the coupling of cavity modes and surface plasmonic modes.

Fig. 6 shows the generation profile along a single line. We note two places where we have enormous electron-hole pair generation due to coupling between cavity modes and surface plasmons.

TABLE 1

Common solar cell parameters for the proposed design

| Parameters | Values |
|---|---|
| $V_{sc}$ | 0.48 V |
| Isc | 8.07 mA/cm$^2$ |
| FF | 0.80 |
| Pmax | 3.11 mW/cm$^2$ |
| eta | 3.12% |

Finally we doped the Si to collect the generated electron-hole pairs. A small photocurrent may result if the doping profile is not optimum for collecting the photo-generated electrons and holes. In a solar cell we need to have a built-in electric field to drive the electrons and holes to opposite contacts. This field is usually created using a *pn* junction. In our structure we have a *pn* junction, however it only covers the silicon substrate and not the silicon ring above. Also, we need to have some back surface doping to prevent minority carriers from getting collected at the contacts.

The common solar cell parameters extracted from the model are shown in Table 1.

## V. CONCLUSIONS

A plasmonic solar cell can be very thin structurally but very thick optically. This types of solar cell is attractive because of its low fabrication and manufacturing cost. It can made optically thick by increasing the path lengths of the traversing light waves through the cell or by keeping them inside the cell for longer time, which can be implemented, respectively, by using nanostrucures as the resonant scatterers and by using arrays of metal nanoparticles to trap or confine light in between them. Path length can also be increased by coupling the light energy to the surface plasmonic and photonic modes where the direction of the energy flow changes from the vertical to the horizontal direction, along the surface of the active semiconductor layer, thereby increasing the path length. In our design, we propose a novel solar cell structure containing metal resonant cavities. In the current design we did not add any nanoparticles. In the future we would add nanoparticles in the top layer to form even effective coupling of light in the Si ring.

## REFERENCES


[1] E. Yablonovitch and G. D. Cody, "Intensity enhancement in textured optical sheets for solar cells," *IEEE Transactions on Electron Devices*, vol. 29, no. 2, pp. 300–305, 1982.

[2] M. A. Green, "Solar cells: operating principles, technology, and system applications," 1982.

[3] H. Deckman, C. Roxlo, and E. Yablonovitch, "Maximum statistical increase of optical absorption in textured semiconductor films," *Optics letters*, vol. 8, no. 9, pp. 491–493, 1983.

[4] H. A. Atwater and A. Polman, "Plasmonics for improved photovoltaic devices," *Nature materials*, vol. 9, no. 3, p. 205, 2010.

[5] S. Fahr, C. Rockstuhl, and F. Lederer, "Metallic nanoparticles as intermediate reflectors in tandem solar cells," *Applied Physics Letters*, vol. 95, no. 12, p. 121105, 2009.

[6] D. Pacifici, H. J. Lezec, and H. A. Atwater, "All-optical modulation by plasmonic excitation of cdse quantum dots," *Nature photonics*, vol. 1, no. 7, pp. 402–406, 2007.

[7] P. Neutens, L. Lagae, G. Borghs, and P. Van Dorpe, "Electrical excitation of confined surface plasmon polaritons in metallic slot waveguides," *Nano letters*, vol. 10, no. 4, pp. 1429–1432, 2010.

[8] D. Van Labeke, D. Gerard,´ B. Guizal, F. I. Baida, and L. Li, "An angleindependent frequency selective surface in the optical range," *Optics express*, vol. 14, no. 25, pp. 11945–11951, 2006.

[9] R. De Waele, S. P. Burgos, A. Polman, and H. A. Atwater, "Plasmon dispersion in coaxial waveguides from single-cavity optical transmission measurements," *Nano letters*, vol. 9, no. 8, pp. 2832–2837, 2009.

[10] E. Kroekenstoel, E. Verhagen, R. Walters, L. Kuipers, and A. Polman, "Enhanced spontaneous emission rate in annular plasmonic nanocavities," *Applied Physics Letters*, vol. 95, no. 26, p. 263106, 2009.

[11] T. Peshek, Z. Tang, L. Zhang, R. Singh, B. To, T. Gessert, T. Coutts, N. Newman, and M. Van Schilfgaarde, "Zngeas 2 thin films properties: A potentially useful semiconductor for photovoltaic applications," in *Photovoltaic Specialists Conference (PVSC), 2009 34th IEEE*. IEEE, 2009, pp. 001367–001369.

[12] D. Van Labeke, D. Gerard,´ B. Guizal, F. I. Baida, and L. Li, "An angleindependent frequency selective surface in the optical range," *Optics express*, vol. 14, no. 25, pp. 11945–11951, 2006.

[13] E. Popov, S. Enoch, G. Tayeb, M. Neviere, B. Gralak, and N. Bonod, "Enhanced transmission due to nonplasmon resonances in one-and twodimensional gratings," *Applied optics*, vol. 43, no. 5, pp. 999–1008, 2004.

[14] A. Roberts and R. C. McPhedran, “Bandpass grids with annular apertures,” *IEEE transactions on antennas and propagation*, vol. 36, no. 5, pp. 607–611, 1988.

[15] T.-K. Wu, “Infrared filters for high-efficiency thermovoltaic devices,” *Microwave and optical technology letters*, vol. 15, no. 1, pp. 9–12, 1997.

[16] P. Lalanne, J. Rodier, and J. Hugonin, “Surface plasmons of metallic surfaces perforated by nanohole arrays,” *Journal of Optics A: Pure and Applied Optics*, vol. 7, no. 8, p. 422, 2005.

# A Non-Invasive Electrical Measurement Method for Junction Temperature Measurement of Highpower PC LEDs under Tropical Condition

A. Chakraborty[1,*], R. Ganguly[2] and M. Mitra[3,**]
[1]Institute of Engineering & Management, Department of ECE, West Bengal, India
[2]University of Engineering & Management, West Bengal, India
[3]IIEST, Shibpur, Department of ETCE, West Bengal, India
[*]arindam.chakraborty@iemcal.com
[**]rajivganguly72@gmail.com

*Abstract*— **With the current technological expansion in the world's economic market, it is essential for any proposed method to give maximum efficiency with minimum loss. LEDs are basically PN junction diodes developed with compound semiconductor materials. Now like other diodes in LEDs also some of the input power will be dissipated as a heat and which result a very high junction temperature. This high junction temperature may not only degrade the material property but at the same time reduces the life of the diode. Here we will discuss, not only how the junction temperature will be determined efficiently, but also the advantage of this non-invasive technique will have on an industrial scale. In this experiment we had devised a way to find out the junction temperature in a non-invasive method, which is simple, accurate and precise. We utilise the forward voltage drop across the p-n junction as a temperature sensor to conclude our results in a uncomplicated method. This is the new way of estimating the junction temperature for any semiconductor p-n junction, with minimum effort to get maximum output. This also gives a rough estimate of the useful life of the LED, as junction temperature is one of the major factors in determining lifetime of an LED.**

***Index Terms***— **Junction temperature, forward voltage, non-invasive method, ambient temperature.**

## I. INTRODUCTION

From 1960 onwards Red, Green and Yellow LEDs have been used mainly as indicator til the year 1993[1] when scientists Isamu Akasaki, Hiroshi Amano, and Shuji Nakamura made their pioneering research and created the world's first blue light emitting diodes—LEDs which actually showed the world the extent to which LEDs can be utilised as an economical and efficient source for fiber optic communication. LEDs are generally categorized based on their applications and compositions. The most basic kind of LEDs were the traditional inorganic LEDs. These LEDs were used primarily as indicator lamps on circuit boards, are typically small and have been used just for indication.

The next advancement came in the world of LEDs with the introduction of High Brightness LEDs also known as HBLEDs [2] which are capable of actual illuminating and are used for lighting purposes. It is quite similar to ILEDs [3] but having much greater light output, thus being able to handle far greater current and power dissipation making it useful for commercial purposes. Because of its high efficiency, it is replacing incandescent bulbs with CFLs (Compact Fluorescent Light bulbs) in worldwide market. LEDs have a long lifespan and can withstand constant switching ON/OFF and random power cuts. Due to high power consumption they did not appear to be very efficient and were soon replaced by OLEDs[4] (Organic LEDs). They have taken over the economic market of the world primarily because of some factors[4] like high brightness, low power consumption as compared to LCDs, lesser future cost as they are economic to manufacture, and can generate all colors and are thin to be used in LED TV-sets and cell phones.

These OLEDs use half as much power [2,3] as the CFLs, giving the same brightness, efficiency and is expandable to be used in any technological application. Due to high power consumptions CFLs have been rapidly replaced by OLEDs, specifically SSLs) as evident from the survey in Fig 1[5].

The main factors on which the life span and performance of LED depends are [6]:

- Ambient temperature.
- Current through the LED.
- The material of heat sinking on the LED.
- Bulb Casing Temperatures.
- LED Power supply.
- Capacitors and LED drivers.
- Thermal Pad (T-PAD) present in the newer versions of the LEDs reduces thermal dissipation thus reducing junction temperature and extending lifespan.

We have already seen that determination of junction temperature is a very complicated method, as well as long and tedious. Also with the size of the LED generally being quite small, it is extremely difficult to measure it from the solder points of the LEDs.

978-1-5386-3374-8/17/$31.00 ©2017 IEEE

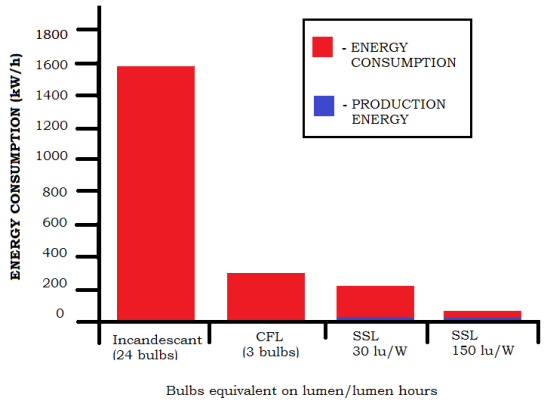


Fig. 1 Comparison of Light Technologies[5].

Therefore, in our research, we have developed a non-invasive method to measure the junction temperature of an LED at a constant current by utilising the "forward voltage" of the circuit.

## II. COMPARISON OF CONVENTIONAL AND PROPOSED METHODS

The temperature that develops across the junction of the semiconductor device is called the junction temperature ($T_j$) [7]. This temperature is generally higher than the ambient temperature and the difference between the two indicate the amount of heat transferred from the junction to the ambience during the operation of the device. Generally, with the rise in junction temperature the performance and ultimately the life span of the device fades away.

Generally the ideal measurement of junction temperature is to monitor the device temperature as close as it could get to the heat source[1]. One of the conventional methods for measuring junction temperature is to place a temperature sensor near the PN junction of the LED and measure the sensor output signal. Heat will be dissipated from the junction as current is applied and flow to the environment, thus raising the temperature of the ambient and tripping the sensor.

This conventional method does seem very simple and acute but there are certain limitations and constrains when performing it physically in a laboratory. One such constrain is the size of the sensor, sometimes it is too big compared to the junction that is to be measured. This large size of the sensor adds a large amount of additional thermal mass to the system, thus reducing the accuracy of the measurements. Hence this method is avoided in most experiments for the amount of error.

To overcome this problem and to gain much accuracy as needed a new and better technique is proposed to measure the Junction Temperature, not just for an LED but for any semiconductor device having a PN Junction. A process via which we could measure the junction temperature with accuracy without tampering with the circuit physically, a non-invasive method is proposed for this reason. A non-invasive method which is simple and efficient in both determining the $T_j$ with ease and accuracy, using the most basic instruments thus making the method cost-effective.

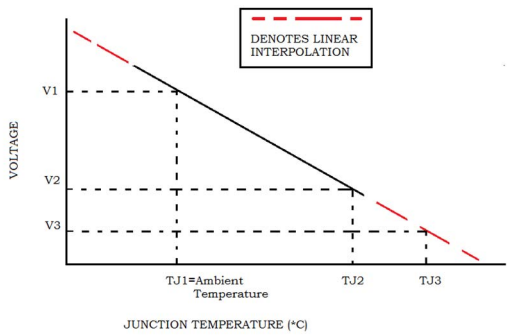


Fig. 2 This graph depicts the linearity of junction temperature versus forward voltage drop [8].

There is a strong correlation between the junction temperature and the forward voltage drop across the LED. The relationship of forward voltage and junction temperature is ideally linear as it is visible from the graph in Fig 2.

## II. PROPOSED METHODOLOGY

Here, we use the junction as a temperature sensor indicated by their forward voltage to measure the junction temperature of a LED with absolute accuracy and precision. The relationship between forward voltage and current is utilized to obtain the junction temperature such that, minor changes in the voltage can bring huge changes in the current as shown in the Fig. 3.

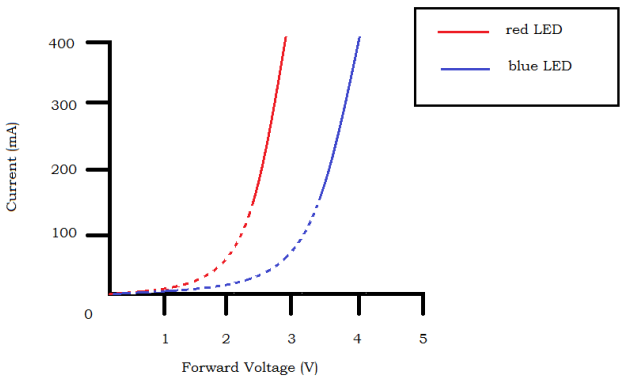


Fig. 3. Relationship between Voltage and Current [9].

The relationship between LED output and current is linear. Therefore, if the current that is supplied is not checked over a long period of time it will result in abridged useful life.

Fig 4, represents the proposed circuit diagram for this study.

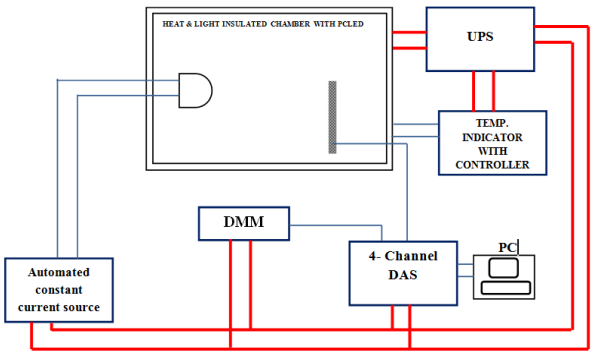


Fig. 4. Proposed Circuit Diagram

The above block diagram is the current varying circuit, to conduct the experiment. Here, at first the necessary connections to the LED are made and it is tested for minimum current just to check if the circuit's operation ability (As shown in Figure 5).

Now for a fixed current $I_1$ (say 25mA), the circuit is calibrated for that corresponding current at different temperatures which is created artificially by placing the circuit inside a heat chamber and then recording the voltage drop across the LED for each of the temperatures in the range considered here 30°C to 65°C according to the wattage of the LED. Then the results are plotted in a voltage versus time graph for the readings acquired as shown in Fig 4.

Once all the voltage drops have been recorded for the respective temperatures, and then the circuit brought out of the heat chamber and allow it to cool down to the ambient temperature.

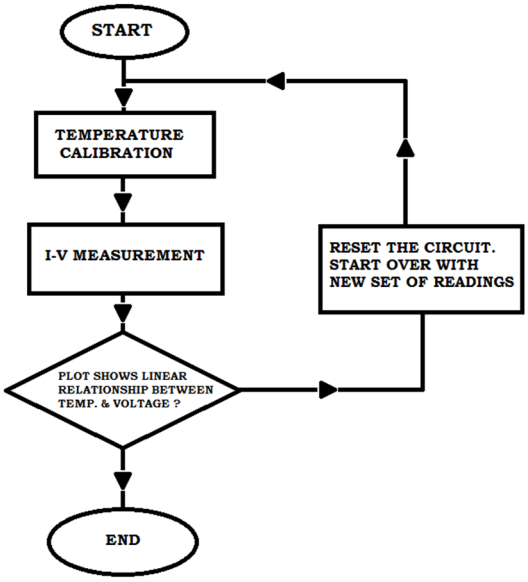


Fig. 5. The Flow Chart of the Process.

Then the current $I_1$ is applied in a constant supply and wait till the circuit stabilizes and we get a constant voltage drop across it. Let us say the fixed voltage drop is $V_1$, for the corresponding current $I_1$. Now for the current $I_1$, a graph of voltage verse time is drawn as per the figure the calibrations and then plot the voltage $V_1$ in the already established graph. From here we finally arrive at the junction temperature via a non-invasive method only with utilisation of the forward voltage drop across an LED which is much more precise and accurate. Now as it is done for the current $I_1$, the experiment is repeated for different currents, $I_2$, $I_3$, $I_4$, etc., for each deriving their respective voltage drops and ultimately their junction temperatures. Thus, by plotting all the graphs, we can predict a trend for the LED being considered.

Using the methodology explained above experiment was conducted for three different cases:

### A. *Case A. 0.25 watt LED for initial testing purpose*

As the wattage of this LED is quite low, it was evident that it is not meant for commercial purposes, yet I conducted the first experiment on this particular LED on purpose to get a proper idea of how to determine the junction temperature by implementing this method in real life. Thus, the initial approach met the expected results and now it was time to raise the stakes and move on to commercially available LEDs of 1 watt.

### B. *Case B. 1 WATT HIGH POWER LED WITHOUT HEAT SINK*

After the initial success we now move on to commercially useful 1 watt white PC LED. Since a 1 watt LED can support a greater amount of current than the previous recipient I purposely divided the experiment in two parts. The first part would be to test it with a range of currents we used previously 10 mA to 30 mA which is very comfortable for this DUT and requires no heat sink.

### C. *Case C. 1 WATT HIGH POWER LED WITH HEAT SINK*

This is the final part of the experiment were used heat sink, as this time the range of the currents taken into consideration varies from 55 mA to 115mA. Thus, to avoid any harm to the DUT the heat sink has been used.

## III. RESULTS OBTAINED

Here, we have conducted the experiment with a 0.25 watt LED and a 1 watt LED, with heat-sink and without heat-sink. Based on the plots depicted below we can determine the nature and behaviour of the LEDs with respect to each of the three cases considered here. From the plots given below we can clearly see the variations in the junction temperature for each case under a fixed current supply for different voltage drops.

### *A. Case A. 0.25 watt LED for initial testing purpose*

TABLE I
READINGS OF 0.25 WATT

| I(mA) | V(v) | T(°C) |
|---|---|---|
| 10.5 | 2.74 | 32 |
| 16.9 | 2.78 | 30 |
| 22.5 | 2.83 | 30 |
| 28.7 | 2.88 | 32 |
| 36.9 | 2.90 | 30 |

*A = ampere, V = volt, m = mili, T = temp, °C = celsius*

Ambient Temperature: 22°C.

Temperature Range: 30°C to 60°C

At the end of the experiment we see that for a range of currents from 10.5 mA to 36.9 mA, the junction temperature varies from 5°C to 7°C above the ambient temperature of 25°C.

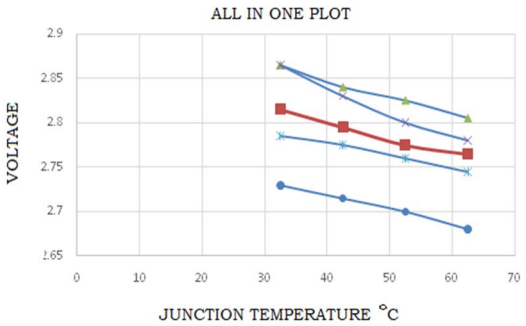


Fig. 6. All the five plots for their respective plots of initial testing

### *B. Case B. 1 watt high power LED without heat sink*

TABLE III

READINGS OF 1 WATT LED WITHOUT HEAT SINK

| I (mA) | V (v) | T (°C) |
|---|---|---|
| 10.9 | 2.72 | 40 |
| 15.6 | 2.77 | 45 |
| 20.1 | 2.80 | 40 |
| 25.7 | 2.84 | 42 |
| 30.0 | 2.85 | 40 |

*A = ampere, V = volt, m = mili, T = temp, °C = celsius*

Ambient temperature: 22°C.
Temperature range: 30°C to 60°C

From the plots we can see that the graphs are nearly stable and support the ideal Voltage vs Temperatures plot as seen previously in Figure 2. Here, the junction temperature is around 20°C to 23°C above the ambient temperature.

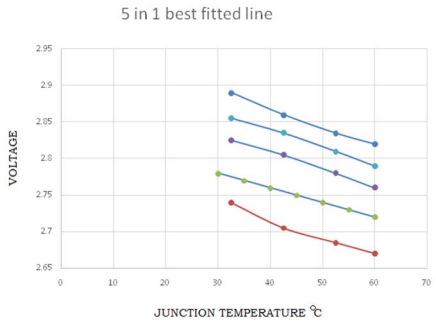


Fig. 7. All the five plots for their respective plots of without heat sink

### C. *Case C. 1 watt high power LED with heat sink*

TABLE III

READINGS OF 1 WATT LED (WITH HEAT SINK)

| I (mA) | V (v) | T (°C) |
|---|---|---|
| 55 | 2.99 | 45 |
| 65 | 3.03 | 42 |
| 75 | 3.06 | 45 |
| 85 | 3.10 | 41 |
| 95 | 3.14 | 45 |

A = ampere, V = volt, m = mili, T = temp, °C = celsius

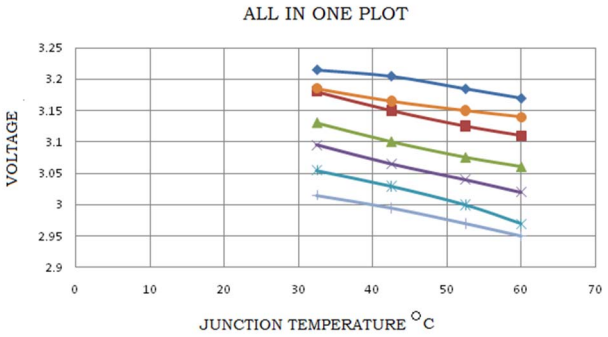


Fig. 8. All the five plots for their respective plots of with heat sink

Ambient temperature: 20°C.
Temperature range: 55°C to 115°C.
Here the junction temperature varies from 20°C to 25°C above ambient temperature and as seen from the plot, the graphs show linearity.

## IV. CONCLUSIONS

After conducting the experiment for two LEDs in three portions we can conclude that this is by far the most efficient way of determining the junction temperature by using the forward voltage drop across the LED. Here all we need to do is make sure the readings are accurate and then mapped them. Hence, it is known as a non-invasive method. From the plots displayed above, we can say that the logic of the experiment is sound as the graphs nearly coincide with the ideal Voltage verse Temperature plot.

Now, the old conventional methods were not just tedious and complicated in terms of calculations, but there was a problem that was even more accurate. LEDs are extremely small in size so, to physically measure their junction temperature from the solder points is not just inefficient sometimes it is physically not possible to touch the exact point from where the temperature should be noted and thus generates faulty readings. Thus, invasive methods such as this one mentioned here is a thing of the past now.

## ACKNOWLEDGMENT

We take this opportunity to express our profound gratitude and deep regards to our professor, Dr. M. K. Mukherjee, Emeritus Professor of Jadavpur University, for providing us with valuable guidance throughout the project. Also our thanks goes to authority of IEM for providing us some infrastructural facility.

## REFERENCES

[1] http://www.radio-electronics.com/info/data/semicond/leds-light-emitting-diodes/technology-tutorial.php
[2] http://www.radio-electronics.com/info/data/semicond/leds-light-emitting-diodes/high-brightness-hbled-basics-tutorial.php
[3] http://www.radio-electronics.com/info/data/semicond/leds-light-emitting-diodes/led-types.php
[4] http://www.radio-electronics.com/info/data/semicond/leds-light-emitting-diodes/organic-oled-basics-tutorial.php
[5] http://www.led-professional.com/resources-1/white-papers/cree-study-shows-led-lighting-is-best-bet-for-energy-efficiency
[6] http://www.radio-electronics.com/info/data/semicond/leds-light-emitting-diodes/lifespan-lifetime-expectancy-mtbf.php
[7] http://www.cypress.com/file/38656/download
[8] http://electronicdesign.com/lighting/use-forward-voltage-drop-measure-junction-temperature

[9] http://www.lrc.rpi.edu/programs/nlpip/lightinganswers/led/controlCurreco.asp
[10] http://www.lrc.rpi.edu/programs/nlpip/lightinganswers/led/heat.asp
[11] http://furniture.about.com/od/accessoriesguide/a/cfladvant.htm
[12] A.Chakraborty, R.Ganguly,''Study &Implementation of White Power-LED Based Indoor Lighting Application for the Healthcare Sector'', Advances in Optical Science and Engineering, 521-531, Advances in Optical Science and Engineering, 2015.
[13] S. Bhattacharya, A. Chakraborty& R. Ganguly, "A Novel Technique for Fast Determination of 'Useful Life' of White Phosphor-converted LED by Measuring Lumen Depreciation Characteristics for Different Forward Currents for Solid State Lighting Applications", 18th International Photovoltaic Science & Engineering Conference & Exhibition, 19-23 January,2009, Kolkata, India.
[14] http://www.sunrom.com/p/analog-data-logger-to-usb-pen-drive
[15] S. Bhattacharya, A. Chakraborty & R. Ganguly,"Role of forward current of white pcLED on its 'useful life' for solar PV based solid state lighting applications: An experimental study"